

FEASIBILITY STUDY AND PRELIMINARY DESIGN OF GRAVITY-GRADIENT-STABILIZED LENTICULAR TEST SATELLITE

GPO PRICE \$
CFSTI PRICE(S) \$
Hard copy (HC) \$ 10.49
Microfiche (MF) 3.50

853 July 65

N66-22379
(ACCESSION NUMBER)
750
(PAGES)
CR-66053
(NASA CR OR TMX OR AD NUMBER)

FACILITY FORM 602

Interim Technical Report, Contract NAS-1-3114

National Aeronautics and Space Administration
Langley Research Center
Langley Station, Hampton, Virginia

Distribution of this report is provided in the interest of
information exchange. Responsibility for the contents
resides in the author or organization that prepared it.

GER-11502

1 June 1964

Copy No. 17

GOODYEAR AEROSPACE CORPORATION

AKRON, OHIO

ABSTRACT

GER 11502

The feasibility of a gravity-gradient stabilized, lenticular satellite for passive communications was established. Studies were based upon a lenticular reflector, having a 200 foot radius of curvature, which would provide horizon to horizon communications coverage at an orbital altitude of 2000 nautical miles. Key elements of the study, conducted in four phases, consisted of satellite stabilization, damping systems, orientation, microwave reflectivity, structural analyses, and the development of materials, packaging, and deployment concepts. Component and model tests were conducted to verify deployment concepts, microwave reflectivity theories, material photolyzation rates, and material and structural tests which did not require a zero gravity environment. Phase I consisted of analytical studies of the satellite and a scaled model suitable for flight evaluation using a Scout launch vehicle. Phase II, conducted concurrently with Phase I, consisted of ground tests. In Phase III, preliminary designs of the flight-test model were evolved, and in Phase IV, a ground and flight test program was prepared.

GOODYEAR AEROSPACE CORPORATION

AKRON 15, OHIO

Copy No. 17

FEASIBILITY STUDY AND
PRELIMINARY DESIGN OF
GRAVITY-GRADIENT-STABILIZED
LENTICULAR TEST SATELLITE

GER-11502

1 June 1964

FOREWORD

This report covers the feasibility study and preliminary design of a gravity-gradient-stabilized lenticular test satellite performed by Goodyear Aerospace Corporation (GAC) from July 1963 through March 1964. The technical objectives and contract requirements were based on NASA, Langley Research Center (LRC) Statement of Work L-3308 dated 10 June 1963 which comprised the original scope of Contract NAS 1-3114.

The work was administered by the Applied Materials and Physics Division of LRC under the direction of W. E. Bressette, Program Manager, and D. C. Grana, Project Engineer, from the Spacecraft Applications Section.

F. J. Stimler of the Space Systems Division was the GAC Project Engineer with H. E. Henjum as Associate Project Engineer. The work was conducted as a cooperative effort by personnel from several divisions within GAC for the various specialties listed below:

Design	R. R. Carman H. W. Barrett
Material Development	R. W. Nordlie W. B. Cross P. F. Myers
Stabilization Orientation	A. C. Buxton D. E. Campbell K. Losch
Structural Analysis	E. Rottmayer J. D. Marketos
Fabrication	D. R. Thompson
Microwave Analysis	L. D. Barnett F. Fischer
Testing	R. I. Scoville, Jr.
Instrumentation	J. C. Kryah

Reliability	H. E. Whisler
Ground Test Plan	J. B. Wright
Flight Test Plan	D. T. Wight
Planning	J. B. Boughton
Contract Administration	A. F. Tinker

Philco Western Development Laboratories of Palo Alto, California, were sub-contracted for digital computer support in analyzing the satellite transient and steady-state libration characteristics.

TABLE OF CONTENTS

	<u>Page</u>
FOREWORD	iii
LIST OF ILLUSTRATIONS	xiii
LIST OF TABLES	xxv

<u>Section</u>	<u>Title</u>	
I	INTRODUCTION	1
II	SUMMARY	5
	1. General	5
	2. Design Analyses	5
	3. Model Scaling Considerations	10
	4. R-F Review	14
III	TECHNICAL DISCUSSION - PHASES I AND II . . .	17
One	Design Considerations	17
	1. General	17
	2. Full-Scale Satellite	18
	a. Conceptual Design Study	18
	b. Inflation and Deployment System	27
	3. Flight-Test Model	30
	a. Conceptual Design Study	30
	b. Inflation System	36
	4. Deployment Models and Tests	38
	a. General	38
	b. Six-Foot-Diameter Deployment Model . . .	39
	c. Five-Foot-Diameter Deployment Models . .	39
	d. Analysis of Model Test Results	52
	e. Twenty-Foot-Diameter Deployment Model 20-1	52
	f. Twenty-Foot-Diameter Deployment Model 20-2	86

<u>Section</u>	<u>Title</u>	<u>Page</u>
	g. Fabrication Forecast	89
	h. Deployment Tests in LRC Vacuum Chamber	93
Two	Systems Analysis	101
	1. General	101
	2. Full-Scale Satellite	101
	a. Lens	101
	b. Torus	104
	c. Rim	108
	d. Tripod	112
	e. Deployment	117
	f. Launch	122
	g. Pressurization Study	122
	h. Temperature Distribution Studies	130
	i. Error Analysis	143
	j. Weights and Inertias	147
	3. Fifty-Foot-Diameter Flight Test Model	148
	a. Lens	148
	b. Torus	150
	c. Rim	151
	d. Tripod	155
	e. Deployment	158
	f. Launch	160
	g. Pressurization Studies	160
	h. Temperature Distribution Study	168
	i. Error Analysis	168
	j. Weights and Inertias	171
	4. Comparative Studies	171
	a. General	171
	b. Sphere	172
	c. Lenticular Satellite with Echo A-12 Lens Material	174
	d. Parametric Study of Tripod-Boom Structure	177
	e. Summary	197
	5. Conclusions and Recommendations	199
	6. List of Symbols	200
Three	Stabilization and Orientation Systems	203
	1. General	203
	2. Stabilization System	205
	a. General	205
	b. Equations of Motion for Lenticular Satellite with Rice-Wilberforce Damper	206

<u>Section</u>	<u>Title</u>	<u>Page</u>
	c. Rice-Wilberforce Spring Equations	214
	d. Optimum Tuning and Energy Dissipation of Rice-Wilberforce Damper	233
	e. Transient Response Studies	251
	f. Steady-State Response Studies	272
	3. Orientation System	294
	a. General	294
	b. Spin-Up and Coning Angle	300
	c. Despin of the Canister	300
	d. Initial Orientation	302
	4. Conclusions and Recommendations	302
Four	Microwave Analysis and Tests	305
	1. General	305
	2. Edge Diffraction Analysis	306
	a. Theoretical Approach	306
	b. Reflectivity Tests	307
	c. Test Data Analysis	321
	3. Lens Surface Tolerance Effects	327
	4. Boom and Canister Effects on R-F Return	328
	5. Lens Surface Reflectivity Study	332
	6. Electrical Continuity of Lens Surface	334
	7. Predicted R-F Return of Full-Scale and Flight- Test Satellites	335
	8. Conclusions and Recommendations	344
	a. General	344
	b. Conclusions	344
	c. Recommendations	346
Five	Material Development	349
	1. General	349
	2. Wire and Wire Cloth	350
	3. Photolyzable Film	351
	4. Film-Cloth Composite	352
	5. Seams	352
	6. Conclusions and Recommendations	354
	a. General	354
	b. Wire and Wire Cloth	354
	c. Film	354

<u>Section</u>	<u>Title</u>	<u>Page</u>
	d. Film Cloth Composite	355
	e. Seams	355
	f. Model Fabrication	355
Six	Material and Component Tests	357
	1. Material Tests	357
	a. Wire and Wire Cloth	357
	b. Photolyzable Film	357
	c. Film-Cloth Composite	366
	d. Seams	366
	2. Component Tests	369
	a. Torus	369
	b. Rim Section	392
	c. Lens - 12-In. Diameter Diaphragm	413
	3. Lens Sphericity	434
	a. Purpose	434
	b. Test Specimen	434
	c. Test Setup and Procedure	436
	d. Test Results	436
Seven	Instrumentation and Control Parameters	443
	1. General	443
	2. Sequence Control System	443
	a. Canister Pressure Equalization	443
	b. Canister Separation from Launch Vehicle	444
	c. Canister Despin	444
	d. Canister Separation	444
	3. Inflation System	450
	a. Torus and Boom Inflation	450
	b. Lens Inflation	454
	4. Orbital Orientation Data Acquisition	455
	a. General	455
	b. Temperature Profile	455
	c. Pressure Sensors	455
	d. Attitude Sensing	456
	e. Attitude Rate Sensors	457
	5. Data Link	458
	a. General	458
	b. Command Control System	458
	c. Beacon System	459
	d. Commutation and Signal Conditioning	459
	e. Recording and Reproducing	460
	f. Telemetry	460

<u>Section</u>	<u>Title</u>	<u>Page</u>
	g. Antenna System	462
	6. Power Supply	463
	7. Ground Environment and Processing	464
	8. Hardware Summary	466
Eight	Reliability Considerations	467
	1. General	467
	2. Over-All Program Plan	467
	3. Program Definition Phase	469
	a. Reliability Block Diagram	469
	b. Reliability Goals	475
	c. Structural Reliability	476
	4. Conceptual Design Phase	476
	a. General	476
	b. Failure Mode Studies	476
	c. Material Review	477
	5. Ground Tests: Materials and Models	479
	6. Conclusions	479
	7. Recommendations	479
IV	TECHNICAL DISCUSSION - PHASES III AND IV	481
	1. Preliminary Spacecraft Design	481
	a. General	481
	b. Interface and Separation	481
	c. Despin System	481
	d. Canister Separation	482
	2. Program Planning	482
	a. General	482
	b. Master Plan	482
	3. Ground Test Development Plan	494
	a. Introduction	494
	b. Development Tests	498
	c. Functional Testing	524
	d. Checkout of Flight Payloads	525
	e. Reliability Tests	525
	4. Flight Test Development	530
	a. General	530
	b. Prelaunch Activities	530
	c. Orbital Test and Support	547

<u>Section</u>	<u>Title</u>	<u>Page</u>
V	LENTICULAR SATELLITE TRADE-OFF STUDIES .	559
	1. General	559
	2. Review of Lenticular Concept and Geometry . .	559
	3. Lenticular Physical Characteristics and Weight Scaling	561
	4. Microwave Communication Parameters	562
	5. Lenticular Comsat Communication System Capability	564
	6. Lenticular Angle Criteria and Coverage Con- siderations	567
	7. Advanced Lenticular Concept for Synchronous Orbit	574
	8. Conclusions and Recommendations	576
VI	CONCLUSIONS AND RECOMMENDATIONS	581
	1. Conclusions	581
	2. Recommendations	582
	LIST OF REFERENCES	585
<u>Appendix</u>		
A	ORBITAL DESIGN CONDITIONS FOR COMPONENTS OF GRAVITY-GRADIENT-STABILIZED LENTICU- LAR SATELLITE	589
B	LENTICULAR SATELLITE PRESSURIZATION STUDY REPORT	597
C	TORUS PRESSURIZATION STUDY	609
D	ERROR ANALYSIS FOR LENS OF LENTICULAR SATELLITE	621
E	PROPERTIES OF SATELLITE COMPONENTS . . .	629
F	LENTICULAR RETURN VERSUS $2\pi R/\lambda$ AND FRE- QUENCY	631
G	CALCULATION OF BOOM RETURN	639

<u>Appendix</u>	<u>Title</u>	<u>Page</u>
H	MICROWAVE REFLECTIVITY DATA	641
I	SELECTION OF LARGE DIAMETER DIAPHRAGM TEST SPECIMEN	645
J	RELIABILITY PREDICTION	651
K	SEQUENCE OF OPERATIONS AND FAILURE MODES DURING DEPLOYMENT	659
L	FAILURE MODES DURING OPERATION	663
M	EXAMINATION OF DISTURBING TORQUE ON FULL- SCALE SATELLITE CAUSED BY NONUNIFORM GAS LEAKAGE	665
N	ESTIMATED FLIGHT ENVIRONMENT OF THE SCOUT LAUNCH VEHICLE	671
O	POTENTIAL PASSIVE SATELLITE COMMUNICATION SYSTEM FOR ALL NATIONS	677

LIST OF ILLUSTRATIONS

		<u>Page</u>
FRONTISPIECE		xxx
<u>Figure</u>	<u>Title</u>	
1	Program Schedule	2
2	Schematic of Full-Scale and Flight Units of Gravity-Gradient-Stabilized Lenticular Satellite	3
3	Design Summary of Full-Scale Lenticular Satellite	6
4	Design Summary of Flight-Test Model of Lenticular Satellite	7
5	Flight-Test Satellite Booster Performance Data	11
6	Five- and Twenty-Foot-Diameter Mylar Deployment Models	13
7	General Area of Satellite R-F Operational Characteristics	15
8	Summary of Model Configurations	19
9	General Arrangement, Full-Scale Lenticular Satellite	21
10	Collapsible Rim Functional Schematic	24
11	Full-Scale Satellite Deployment Sequence	26
12	Inflation System Schematic	28
13	Lenticular Satellite, 50-Ft Diameter, General Arrangement	31
14	Test Satellite Detailed Deployment Sequence	35
15	Flight Test Inflation System Schematic	37

<u>Figure</u>	<u>Title</u>	<u>Page</u>
16	Packaging Sequence, Six-Foot Model	40
17	Five-Foot Deployment Model Final Configuration . .	41
18	Five-Foot Deployment Model	43
19	Packaging Sequence for Five-Foot-Diameter Model Torus	44
20	Deployment of Five-Foot-Diameter Torus	45
21	Deployment Test, Five-Foot-Diameter Model, Final Configuration	46
22	Tool and Part Forming Method for Torus of Five- Foot-Diameter Deployment Model.	47
23	Bulkhead Forming Tool	49
24	Bulkhead Installation	49
25	Rim-to-Torus Assembly Sequence	50
26	Lens-to-Torus Attachment	52
27	Twenty-Foot Deployment Model, Lenticular Satellite	55
28	Torus Male Mold Pattern	57
29	Torus Mold	58
30	Torus Female Forming Mold and Part Fabrication .	59
31	Torus Assembly Tool	61
32	Torus Assembly	62
33	Form for 20-Ft Deployment Model	63
34	Lens Tooling, Fabrication, and Assembly	65
35	Support Frame Assembly, Collapsible 20-Ft Torus and Lens Fabrication	67
36	Model Satellite Assembly	69

<u>Figure</u>	<u>Title</u>	<u>Page</u>
37	Schematic of Rim-Tape Arrangement	72
38	Model Fabrication, Turn-Over Operation	73
39	Boom and Air-Feed Line Attachment	75
40	Putting Deflation Holes in Lens and Torus of Model .	77
41	Packaging Sequence, 20-Ft Model	78
42	Canister, 20-Ft Deployment Model, Lenticular Satellite	81
43	Deployment Test Setup, 20-Ft Model	83
44	Deployment Sequence, 20-Ft Model	84
45	Breadboard of 20-Ft Model Inflation System, Lenticu- lar Satellite	87
46	Fabrication and Contour Check, 10-Ft-Diameter Solar Concentrator	90
47	Fabrication Technique, 44.5-Ft-Diameter Solar Con- centrator	91
48	Fabrication and Contour Checkout Fixture, 44.5-Ft- Diameter Solar Concentrator	92
49	Procedures and Facilities for Fabricating Wire-Grid Sphere	94
50	Grid-Sphere Models	95
51	Vacuum Deployment Test Schematic	97
52	Deployment Sequence for Model 20-1 Vacuum Sphere Tests	98
53	Full-Scale Satellite Principal Features	102
54	Torus-Lens Axial Section	106
55	Rim Plan View with Loads Causing Critical In-Plane Deflection	110

<u>Figure</u>	<u>Title</u>	<u>Page</u>
56	Rim Plan View with Loads Causing Critical Out-of-Plane Deflection	111
57	Tripod Boom Critically Loaded as a Beam-Column .	114
58	Torus Pressures versus Time (Full-Scale Model). .	126
59	Satellite Inflation Pressures versus Time (Full-Scale Model)	127
60	Satellite Deflation Pressures versus Time (Full-Scale Model)	129
61	Thermal Schematic of Lenticular Satellite	133
62	Principal Elements of Full-Scale Satellite	148
63	Tripod-Boom as a Beam-Column	158
64	Torus Pressures versus Time (Flight-Test Model) .	164
65	Satellite Inflation Pressures versus Time (Flight-Test Model)	165
66	Satellite Deflation Pressures versus Time (Flight-Test Model)	167
67	Principal Elements of Flight-Test-Model Satellite .	172
68	Exact Solution	179
69	Approximate Solution	180
70	Tripod Construction	182
71	Weight, Torque, and Drag versus Tripod Radius . .	188
72	Inflation Pressure versus Tripod Radius.	189
73	Torque and Drag Comparison.	196
74	Rice-Wilberforce Damper Applied to Lenticular Satellite	204
75	System Configuration and Attitude Parameters . . .	207

Figure	Title	Page
76	Comparison of Spring Parameters	217.
77	Geometric Parameters of Helical Spring.	218
78	Elastic Characteristics of Helical Spring	222
79	Helical-Spring Stiffness Coefficients.	229
80	Helical-Spring Parameters for Unstressed Helical Angle $\theta_o = 0$ Deg	231
81	Schematic Diagram and Definition of Symbols for Damper Analysis	234
82	Mechanical Impedance Diagram of Rice-Wilberforce Damper	236
83	Alternate Mechanical Impedance Diagram	237
84	Final Equivalent Mechanical Impedance Diagram for Torsional Mode	239
85	Determination of Rice-Wilberforce Damper Para- meters - Helix Angle = 30 Deg	243
86	Determination of Rice-Wilberforce Damper Para- meters - Helix Angle = 17.5 Deg	245
87	Relative Steady-State Dissipation versus Excitation Frequency	250
88	Analog-Computer Run - Case I	256
89	Analog-Computer Run - Case II.	257
90	Analog-Computer Run - Case III-A	258
91	Analog-Computer Run - Case III-B	259
92	Analog-Computer Run - Case IV-A	260
93	Analog-Computer Run - Case IV-B	261
94	Analog-Computer Run - Case V-A	262
95	Analog-Computer Run - Case V-B	263

Figure	Title	Page
96	Analog-Computer Run - Case VI-A	264
97	Analog-Computer Run - Case VI-B	265
98	Analog-Computer Run - Case VII-A	267
99	Analog-Computer Run - Case VII-B	269
100	Relative Power Dissipation for Case IV	271
101	Lens Subconfiguration	277
102	Torus Subconfiguration	278
103	Booms Subconfiguration	279
104	Canister Subconfiguration	281
105	Eclipse Diagram	286
106	Solar Torques on Full-Scale Satellite - Positive α 's .	288
107	Solar Torques on Full-Scale Satellite - Negative α 's	289
108	Solar Torques on Test Satellite - Positive α 's . . .	290
109	Solar Torques on Test Satellite - Negative α 's . . .	291
110	Pitch Axis Response - Rice-Wilberforce	295
111	Pitch-Axis Response - Rice-Wilberforce Alternate .	296
112	Pitch-Axis Response - Dual Mode, Lossy Spring . .	297
113	Pitch-Axis Response - Single Mode, Lossy Spring .	298
114	Launch and Deployment Sequence	299
115	Reflectivity Test Model (Front View)	309
116	Reflectivity Test Model (Side View)	310
117	Reflectivity Test Model Dimensions	311
118	Reflectivity Range (Side View)	312

Figure	Title	Page
119	Reflectivity Range (Side View)	312
120	Monostatic Reflectivity Measurements	316
121	Reflectivity Pattern - 9830 Mc	317
122	Reflectivity Pattern - 9030 Mc	318
123	Reflectivity Pattern - 9370 Mc	319
124	Average Lenticular Return with Respect to Reference Sphere versus Frequency	322
125	Nose-On Return with Respect to Reference Sphere versus Frequency	323
126	Nose-On Return with Respect to Average Lenticular Return versus Frequency	324
127	Maximum Lenticular Variation of Lenticular Return versus Frequency	325
128	Vectors A and B	326
129	Boom Radar Return versus Angle of Incidence to Boom	329
130	Magnitude and Phase Angle of Backscattered Radiation from Lenticular Satellite	331
131	Transmission Line	332
132	Grid Material Configuration	334
133	Worst Case Reflectivity of Area around Cap as Function of Cap Radius	336
134	Lenticular Configuration	337
135	Monostatic Region of Large Variations	337
136	Bistatic Region of Large Variations	338
137	Satellite Attitude and Position - Case 1	339
138	Satellite Attitude and Position - Case 2	340

Figure	Title	Page
139	Satellite Attitude and Position - Case 3	341
140	Satellite Attitude and Position - Case 4	342
141	The Goodyear Tire and Rubber Company Research Casting Belt	353
142	Stress-Strain Curves of Various Wires	359
143	Apparatus for Controlled Environment Weight-Loss Measurements by Sample Removal Method	361
144	Effect of Nigrosine Dye E-8037 on Weight-Loss Be- havior of Photolyzable Film - Long Time Exposure .	362
145	Carbon-Arc Solar Radiation Simulator Test Ap- paratus	364
146	Effect of Nigrosine E-8037 Dye on Ultraviolet and Visible Transmittance of 0.7-Mil Photolyzable Film	365
147	Stress versus Strain, 1.6-Mil Phosphor-Bronze Wire, 24 Wires per Inch - 0.7-Mil Spreadcoat Photolyzable Film at 72 F	368
148	Effective Modulus of Elasticity of Splices in 1.6-Mil Phosphor Bronze Cloth, 24 Wires per Inch at 72 F .	370
149	Effective Modulus of Elasticity of Splices in 1.6-Mil Phosphor Bronze Cloth, 24 Wires per Inch at 200 F.	371
150	Torus Model No. 1	372
151	Torus Model No. 2	372
152	Torus Model No. 1 - Schematic of Test Setup . . .	373
153	Torus Model No. 1 - Test Setup	374
154	Diagram of Torus Model No. 1 - Test Setup	375
155	Torus Model No. 2 - Test Setup on Flat Table . . .	376
156	Torus Model No. 2 - Test Setup Hanging Vertically .	377
157	Location of Deflection Points	378

<u>Figure</u>	<u>Title</u>	<u>Page</u>
158	Pressure versus Diameter Change, Torus Model No. 1	381
159	Lens Pressure versus Torus Diameter, Model No. 2, Specimen on Flat Table	384
160	Lens Pressure versus Torus Diameter, Model No. 2, Specimen Hanging Vertically	385
161	Lens Pressure versus Torus Diameter, Model No. 2	386
162	Torus-Lens Axial Section	387
163	Critical Pressure in the Lens versus Pressure in the Torus for Various Lens Angles α	390
164	Rim Cross Section	393
165	Rim Section Bending Test Setup.	394
166	Rim Section Torsion Test Setup and Failure	396
167	Load versus Deflection, Rim Section Bending Test	399
168	Rim Section Bending Test, Specimen No. 1 Failure	400
169	Torque versus Twist Angle, Rim Section Torsion Test	402
170	One-Quarter Rim Cross Section for Bending Analysis	403
171	Geometric Construction of One-Quarter Rim Cross-Section from Measured Dimensions	405
172	One-Quarter Rim Cross Section for Moment of Inertia Analysis	406
173	Diaphragm Test Specimen	413
174	Twelve-Inch Diaphragm Test Apparatus	414
175	Twelve-Inch Diaphragm in Fixture	415
176	Diaphragm Collapse Pressure versus Radius of Curvature of Diaphragm	429

Figure	Title	Page
177	Load versus Strain, 12-In. Diaphragm Test	430
178	Twelve-Inch Diaphragm Attached at End of Rigid Cylinder	433
179	Lens Sphericity Test Setup	435
180	Large Diaphragm, 0.36-In. H ₂ O Pressure	437
181	Large Diaphragm, Zero Return after 0.36-In. H ₂ O Pressure	439
182	Large Diaphragm, 0.40-In. H ₂ O Pressure	440
183	Large Diaphragm, Zero Return After 0.40-In. H ₂ O Pressure	441
184	Telemetry and Programming Systems Block Diagram for 50-Ft Flight-Test Satellite	445
185	Sequence and Control System Block Diagram for Full-Scale Satellite	447
186	Spin-Rate Sensor Housing	458
187	Antenna Tipped 90 Deg (Worst Case) to Determine Coverage Requirements	462
188	Antenna Pattern	463
189	Telemetry Data Acquisition and Reduction	465
190	Over-all Plan for Reliability Program	468
191	Reliability Block Diagram for Gravity-Gradient- Stabilized Lenticular Satellite System and Monitoring System	470
192	Reliability Block Diagram of Deployment Subsystem	471
193	Reliability Block Diagram for Deployment Monitor- ing Subsystem	473
194	Reliability Block Diagram for Operation Monitoring Subsystem	474

<u>Figure</u>	<u>Title</u>	<u>Page</u>
195	Payload Separation and Despin System	483
196	Master Program Plan	485
197	Product Design Plan.	489
198	Manufacturing Plan	490
199	Program Management Plan.	492
200	Documentation Plan	495
201	Ground Test Schedule	497
202	Setup for Satellite Model Contour Measurement. . .	503
203	Radio Frequency Ground-Test Schedule	514
204	Edge Diffraction Returns.	516
205	Diagram of Monostatic and Distatic Reflectivity Tests	517
206	Edge Modifications	518
207	Effect of Increased h Dimension.	520
208	Flight Test Plan and Schedule - Months Before and After Launch	531
209	Flight Test Plan and Schedule - Days Before Launch	532
210	Flight Test Plan and Schedule - Launch Day	533
211	Flight Test Orbits and Operational Sequences for 800-Mile Orbit	555
212	Ground Station Acquisition Times	557
213	Lenticular Geometry	560
214	Lenticular Angle and Lenticular Advantage.	560
215	Satellite Weight versus Lenticular Angle and Diameter	562
216	Equivalent Reflected Power versus Slant Range. . .	565

<u>Figure</u>	<u>Title</u>	<u>Page</u>
217	Band Width versus Receiving Antenna Diameter for 2000-Naut-Mi Orbit	566
218	Band Width versus Satellite Diameter for Synchro- nous Orbit	568
219	Lenticular Angle versus Orbital Altitude.	570
220	Mutual Coverage, Example A.	572
221	Mutual Coverage, Example B.	573
222	Number of Satellites for Worldwide Random System.	575
223	Advanced Lenticular Concept Communication Capa- bility: Band Width versus Receiving Antenna Diame- ter	577

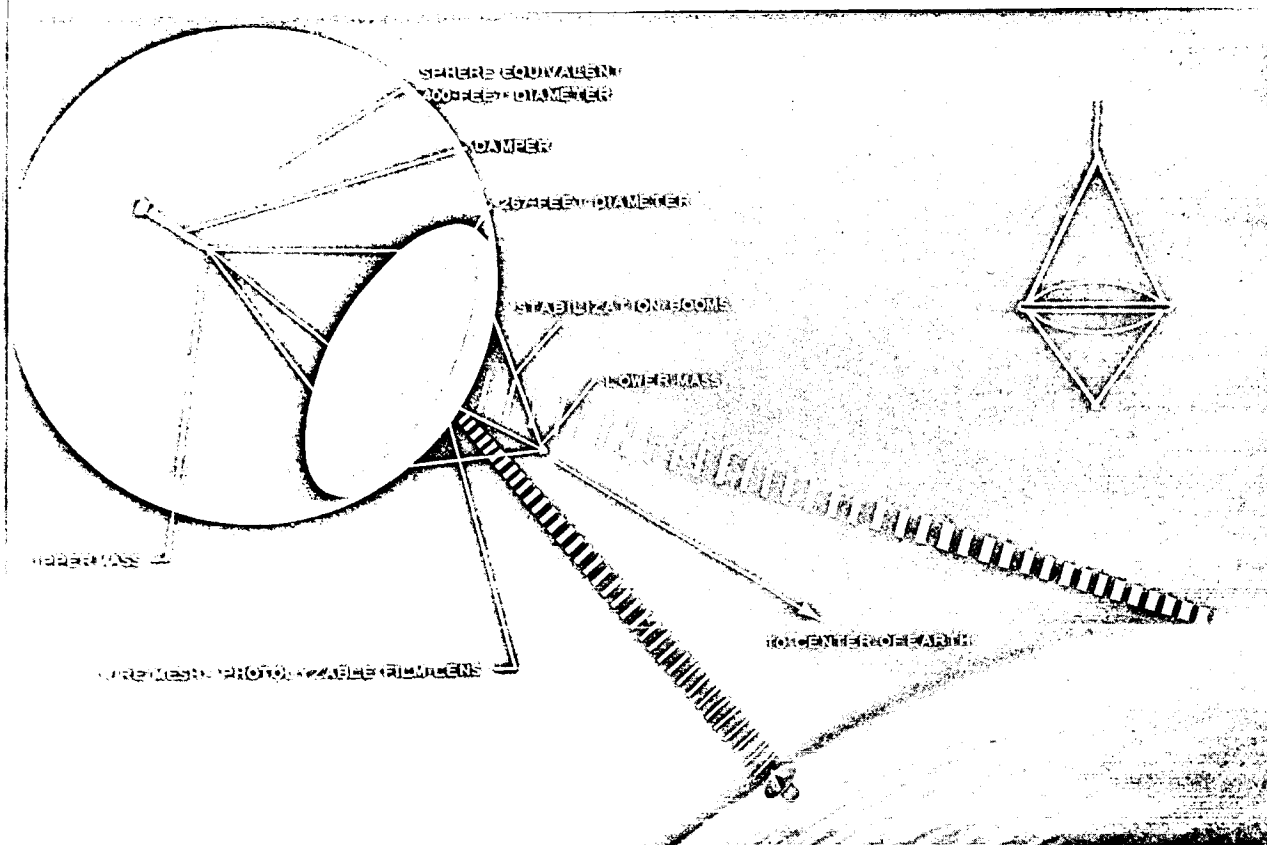
LIST OF TABLES

<u>Table</u>	<u>Title</u>	<u>Page</u>
I	Weight and Inertia Summary of Full-Scale and Flight-Test Satellite	9
II	Full-Scale Satellite System Weight and Volume . .	23
III	Flight-Test Satellite System Weight and Volume .	33
IV	Critical Gravity-Gradient and Inertia Net Loads for In-Plane and Out-of-Plane Rim Deflection . .	109
V	Transverse Deflections of Tripod Booms Subjected to Critical Load Condition	118
VI	Thermal Properties of Film	132
VII	Satellite Temperatures.	138
VIII	Partially Photolyzed Lens Temperatures	139
IX	Effect of Torus Pressure Variation on Lens Radius of Curvature for Full-Scale Satellite	146
X	Lens Radius of Curvature Errors for Full-Scale Satellite	157
XI	Weights and Inertias of Full-Scale Satellite . . .	149
XII	Effect of Torus Pressure Variation on Lens Radius of Curvature for Flight-Test Model	170
XIII	Lens Radius of Curvature Errors for Flight-Test Model	171
XIV	Weights and Inertias.	173
XV	Weight Comparison of Various Satellite Configurations.	178
XVI	Calculations for Alternate I	186

Table	Title	Page
XVII	Weight, Torque, and Drag Values versus Tripod Radius	187
XVIII	Calculations for S/S_s	195
XIX	Transient Response Study - Analog Simulation . . .	255
XX	Digital Simulation of Lens at Transient Response - Eight Degrees of Freedom	273
XXI	Solar Torque and Gravity Equilibrium Angle for Various Photolyzed Versions of the Lenticular Satellite	292
XXII	Test Equipment for 20-In. Model Reflectivity Tests .	313
XXIII	Data Obtained from Reflectivity Patterns	320
XXIV	Summary of Wire Physical Property Tests	358
XXV	Summary of Tensile Tests on Film Cloth Material .	367
XXVI	Torus Diameter Change - Model No. 1	380
XXVII	Recorded Deflections of Model No. 2 on Flat Plate .	382
XXVIII	Recorded Deflections of Model No. 2 Hanging Vertically	383
XXIX	Critical Pressure in Lens versus Pressure in Torus for Various Lens Angles	389
XXX	Rim Section Bending Test Specimen No. 1	397
XXXI	Rim Section Bending Test Specimen No. 2	398
XXXII	Rim Section Torsion Test	401
XXXIII	Twelve-Inch Diaphragm, Specimen No. 1, Belt Side In	417
XXXIV	Twelve-Inch Diaphragm, Specimen No. 2, Belt Side In	418
XXXV	Twelve-Inch Diaphragm, Specimen No. 3, Belt Side In	419

<u>Table</u>	<u>Title</u>	<u>Page</u>
XXXVI	Twelve-Inch Diaphragm, Specimen No. 4, Belt Side In	420
XXXVII	Twelve-Inch Diaphragm, Specimen No. 5, Belt Side Out	421
XXXVIII	Twelve-Inch Diaphragm, Specimen No. 6, Belt Side Out	422
XXXIX	Twelve-Inch Diaphragm, Specimen No. 7, Belt Side In	423
XL	Twelve-Inch Diaphragm, Specimen No. 8 at 200 F, Belt Side Out	424
XLI	Twelve-Inch Diaphragm, Specimen No. 9 at 200 F, Belt Side In	425
XLII	Twelve-Inch Diaphragm, Specimen No. 10 at 200 F, Belt Side In	426
XLIII	Twelve-Inch Diaphragm, Specimen No. 11 at 200 F, Belt Side In	427
XLIV	Twelve-Inch Diaphragm, Specimen No. 12 at 200 F, Belt Side Out	428
XLV	Lens Material Data, 1.6-Mil Phosphor Bronze Wire	432
XLVI	Recorded Deflections, Six-Foot Diaphragm	438
XLVII	Instrumentation Details for 50-Ft Flight-Test Satellite	448
XLVIII	Instrumentation Details for Full-Scale Satellite	449
XLIX	Functional Sequence for 50-Ft Test Vehicle	451
L	Functional Sequence for Full-Scale Vehicle	452
LI	Summary of Ground Test Requirements	496
LII	Tracking Station and Equipment Requirements During Ascent and Orbit Injection	550

<u>Table</u>	<u>Title</u>	<u>Page</u>
LIII	Geodetic Location of Minitrack Stations	552
LIV	Minitrack Facilities Required for Tracking and Data Acquisition	553
LV	Lenticular Angle and Lenticular Advantage for Various Orbital Altitudes.	561
LVI	Lenticular Angle as Function of Communication Links	569



SECTION I - INTRODUCTION

Goodyear Aerospace Corporation conducted a feasibility study and preliminary design of a gravity-gradient-stabilized lenticular test satellite for the NASA, Langley Research Center (LRC), in accordance with Contract NAS 1-3114.

This interim report covers the work of the original contract. Several contract amendments have been made for additional work in related areas; however, these efforts will be documented separately. A short document will be prepared at the end of the complete contract to summarize the total effort. It will be suitable for wide distribution of the technical information.

The original contract effort was basically of nine-month duration as shown in Figure 1. The four-phase program was oriented so that LRC approval could be obtained at the end of six months, prior to initiation of Phases III and IV. Program documentation requirements are shown in Figure 1. Additional technical and background information can be obtained from the Goodyear Aerospace proposal ^{1,a} submitted for this program and the NASA contract. ²

The program philosophy in Phases I and II was first to consider the conceptual design of a full-scale satellite (Figure 2) to establish design factors and second to design a test satellite system for the Scout launch vehicle. Ground tests of materials and models were conducted to validate design decisions. Several small models were designed, fabricated, and tested during the first two phases of the program. A major milestone of these phases was the delivery of two 20-ft-diameter inflation models to LRC for general deployment and inflation tests by NASA in the LRC 60-ft-diameter vacuum sphere.

Key elements considered in establishing a meaningful small-scale model test

^aSuperior numbers in the text refer to items in the List of References.

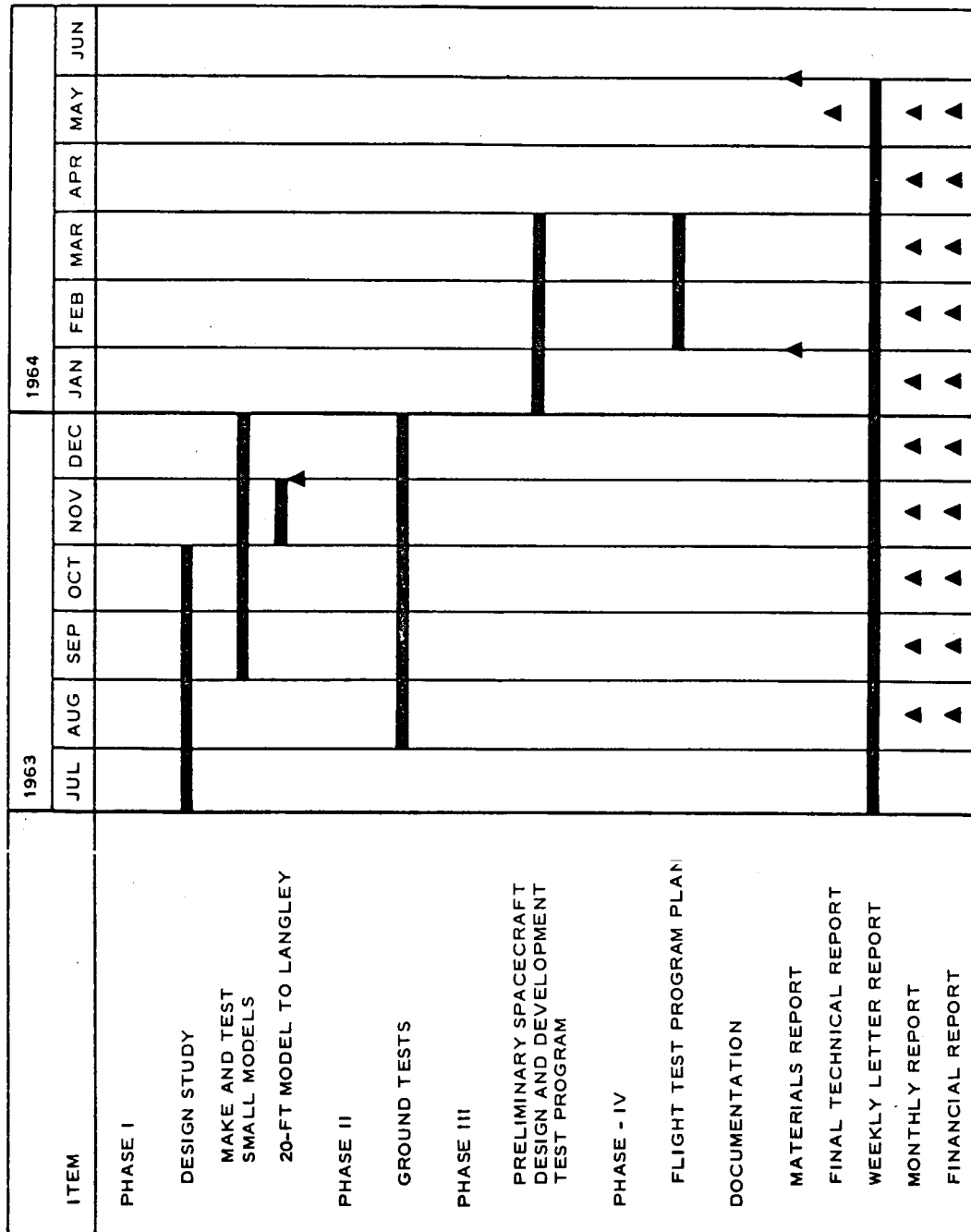


Figure 1 - Program Schedule

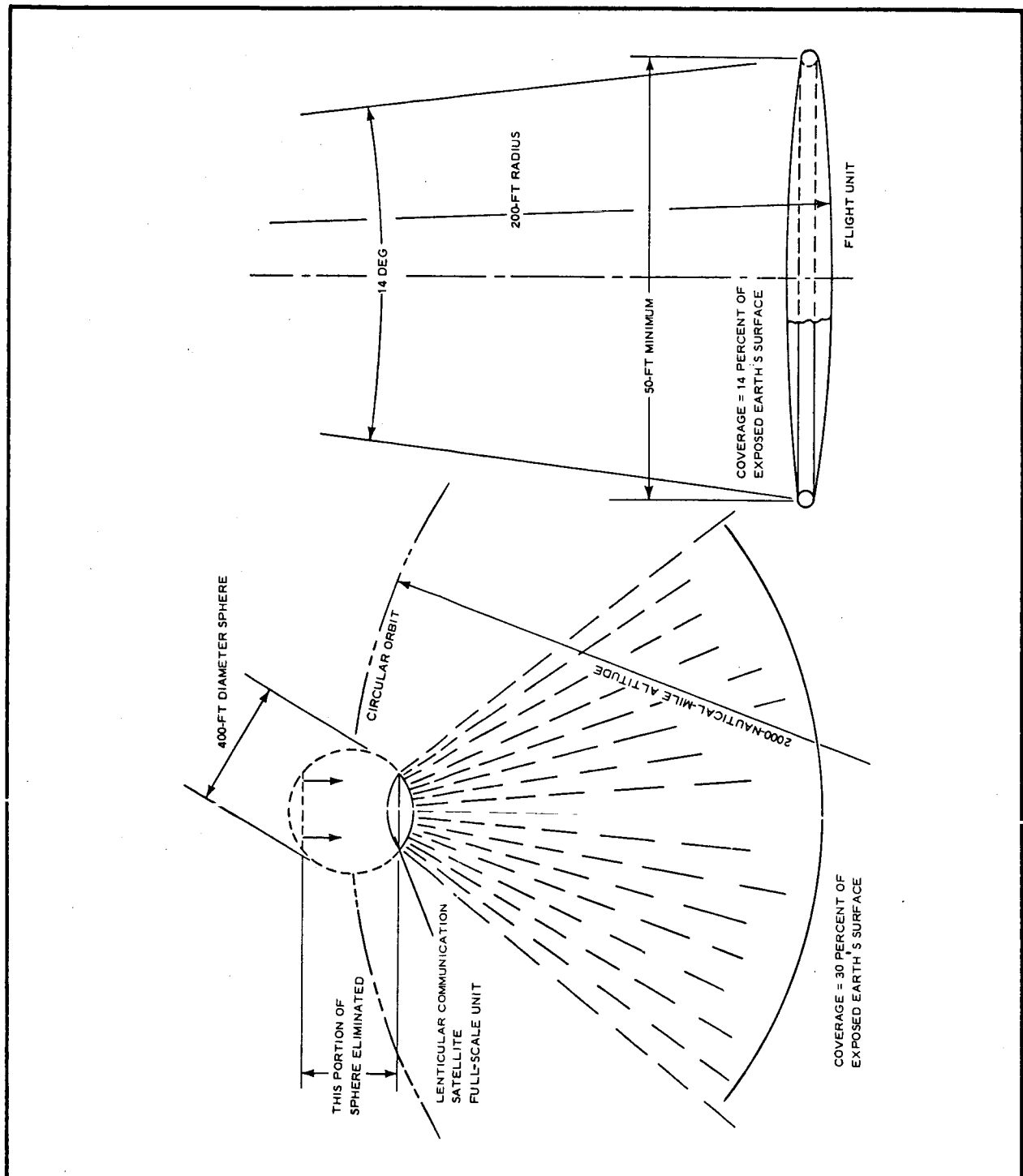


Figure 2 - Schematic of Full Scale and Flight Units of Gravity-Gradient-Stabilized Lenticular Satellite

were stabilization and orientation systems, including damping methods; satellite deployment; satellite r-f reflectivity characteristics; packaging methods; design tolerances; fabrication techniques; and the effects of perturbing forces on satellite performance. In general, emphasis was placed on analysis of the Rice-Wilberforce damping system and the use of the wire mesh, photolyzable film materials in the construction of the satellite lens and related components because they showed many advantages over other available methods and materials. Program results have substantiated this choice of damper and lens material as being very suitable for the satellite design under consideration.

Phase III consisted of the preliminary design of the spacecraft and formulation of ground tests that would qualify the components, the subsystems, and the instrumentation. Phase IV was for preparation of the flight test program plan for establishing the performance characteristics of the flight test satellite. This included such items as launch requirements, launch support, and flight and ground instrumentation that would be needed to acquire the performance and stabilization data.

SECTION II - SUMMARY

1. GENERAL

A review is presented of some of the items of major interest to consolidate the fundamental information that was generated during the program and to emphasize the achievements in the critical technical areas. In some cases complete solutions of the technical problems were available while in others new problem areas were pinpointed. In all cases however, solution of the technical problems is considered to be within the grasp of the next development phase, the flight test program.

Phases I and II of the program consisted of concurrent six-month design studies and detailed ground tests of lenticular satellite materials, components, and numerous models. Structural analyses and corroboratory tests were made to substantiate design decisions. Studies were also made in related areas of stabilization, orientation, reliability, instrumentation, materials development, and radio reflectivity to supply further technical design information. Successful deployment of a 20-ft-diameter model in the NASA-LRC vacuum chamber substantiated the design concept.

Phases III and IV were concurrent three-month studies of preliminary spacecraft design and ground and flight test planning for a satellite system development program. A master program plan was prepared to correlate model and test requirements. Deliveries were based on realistic lead times established for material procurement, tooling, fabrication, and model checkout, based on past experience.

2. DESIGN ANALYSES

Theoretical and experimental investigations of Phases I and II resulted in similar lenticular satellite designs for the 267-ft-diameter full-scale unit (see Figure 3). and the 50-ft-diameter flight-test unit (see Figure 4). These figures include definition of the materials involved and miscellaneous key design information. Further information can be obtained from

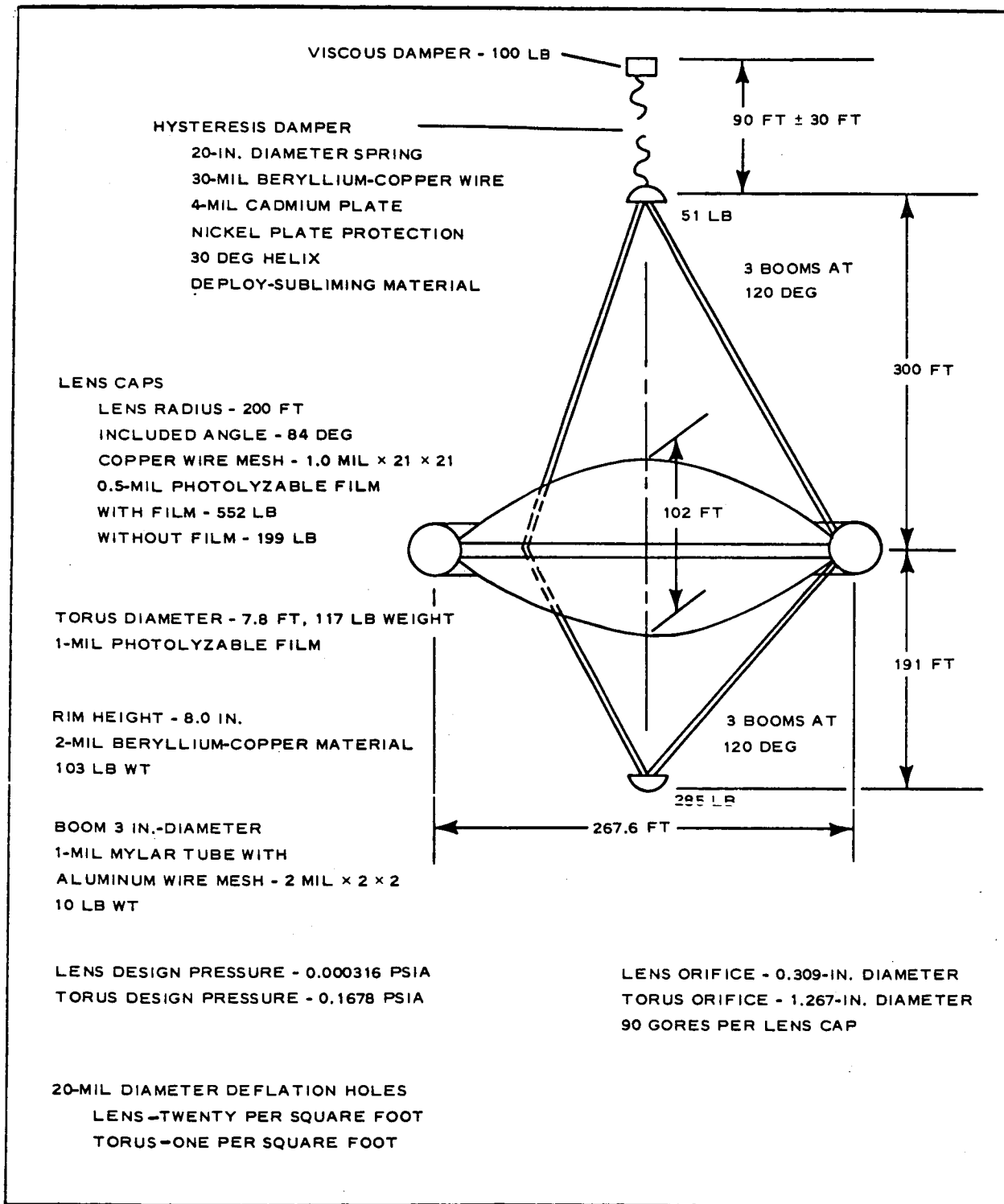


Figure 3 - Design Summary of Full-Scale Lenticular Satellite

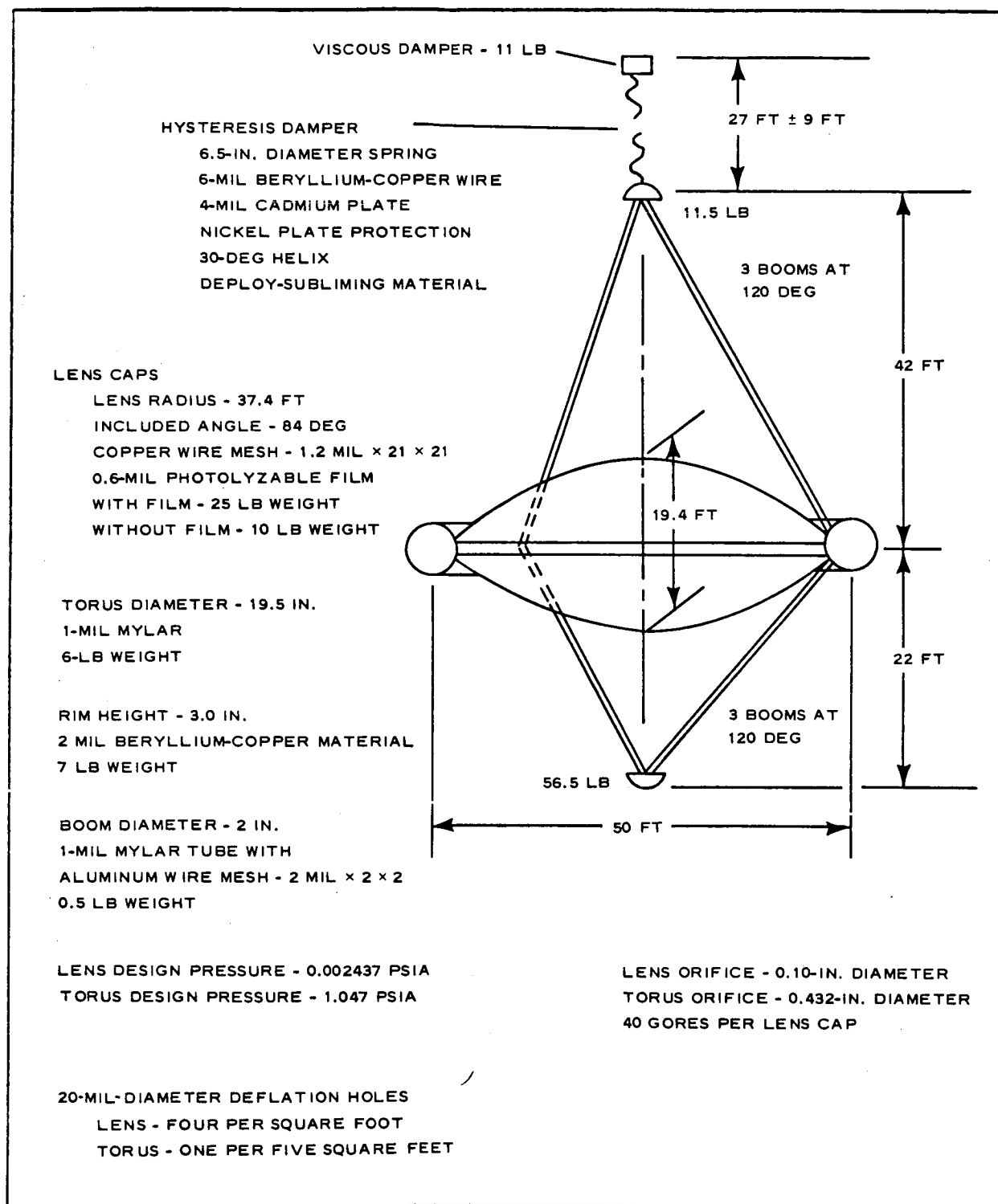


Figure 4 - Design Summary of Flight-Test Model of Lenticular Satellite

the appropriate sections of the report. The weights and inertias of the satellite designs are summarized in Table I.

The metal rim located on the inner diameter of the torus maintains lens accuracy during the rigidization process wherein the lens is pressurized to yield the metal wire of the mesh-photolyzable-film lens material. The metal rim makes it necessary to roll up the collapsed lens and torus surfaces during the initial phase of packaging rather than to use a conventional accordion fold. Model deployment tests under ambient and vacuum chamber conditions have shown that this packaging method is acceptable.

For the full-scale satellite, torus inflation to design pressures is completed in five minutes followed by lens inflation in another five-minute period. The lens is maintained at design pressure for two minutes and the torus for four minutes during the rigidization process, which is started ten minutes after the beginning of torus inflation. Automatic pressure relief is accomplished through evenly distributed holes that are made in the torus and lens surfaces to minimize destabilizing moments that might result from uneven gas discharge. Sufficient helium gas is provided to allow for leakage through the depressurization holes during the inflation period and through punctures that might occur from micrometeoroids. A similar inflation system is provided for the 50-ft-diameter flight-test unit. Initiation of satellite deployment is controlled to ensure proper attitude orientation within the gravity-gradient constraints of the design. A two-step yo-yo despin method is utilized to minimize residual spin of the payload prior to deployment.

Structural analyses of the static and dynamic conditions indicate that no major problem areas should be encountered utilizing available materials and proven fabrication techniques. Analysis indicates that the lens radius of curvature can be held to within ± 1 percent for both the full-scale and flight-test units, particularly if manufacturing tolerances and lens pressures are given careful attention. More model construction and test data

**TABLE I - WEIGHT AND INERTIA SUMMARY OF
FULL-SCALE AND FLIGHT-TEST SATELLITE**

Item	Weight (lb)		Volume (cu in.)	Moments of inertia (lb ft ²) *			Inertia ratio	Spacecraft envelope (in.)	
	Launch	Orbit		Roll	Pitch	Yaw		Diameter	Height
Flight-test model	136.7	106.3	4,700 (2.7 cu ft)	56,800 ⁺ 53,900	56,800 ⁺ 53,900	16,500 ⁺ 11,700	3.4 4.6	25	26
Control and instrumentation	23.0	23.0	800
Damping system	14.2	13.0
Structure and hardware	28.0	28.0
Satellite	38.5	23.5	3,500
Inflation system	17.0	16.0	400
Despin system	3.5	2.8
Separation system	12.5
Full-scale model	1250.0	758.0	68,572 (40 cu ft)	20 X 10 ⁶ 17 X 10 ⁶ †	20 X 10 ⁶ 17 X 10 ⁶ †	9.2 X 10 ⁶ 3.7 X 10 ⁶ †	2.2 4.6	50	68
Control system	18.0	18.0	372
Damping system	115.0	115.0
Structure and hardware	92.0	92.0
Satellite	782.0	312.0	65,200
Inflation system	233.0	216.0	3,000
Separation system	10.0	5.0

* Neglecting damper

† With film

‡ Without film

are needed to verify whether local radius of curvature variations of less than ± 30 percent of design spherical radius and maximum surface discontinuities of less than 0.10 in., peak to valley, for any square foot of inflated lens surface are realistic. Programs are under way at the present time toward further definition of surface tolerances of representative satellites.

Preliminary theoretical investigations show that the Rice-Wilberforce damper will be satisfactory for the lenticular satellite under consideration. The proposed design utilizes hysteresis damping in a coil spring during the elongation process and viscous damping in an end weight during the rotational motion imparted by the spring elongation. Proper tuning of the damper components is being studied to optimize the design.

The compatibility of the flight test satellite with the Scout vehicle is based on Figure 5. Additional detailed design analysis of the satellite might indicate the need for a larger booster, possibly in the Thor-Delta category.

GAC performed preliminary reliability studies and statistical analyses to establish reliability requirements and goals for the satellite system. During this limited effort emphasis was placed on minimizing system complexity, maximizing the use of design state-of-the-art, and incorporation of redundancy where needed. Techniques were discussed with cognizant NASA-LRC personnel to improve the effectiveness of data presentation and to fulfill NASA over-all reliability requirements for a space vehicle system.

3. MODEL SCALING CONSIDERATIONS

The major goal of the program was to show the feasibility of simulating technically the full-scale gravity-gradient-stabilized lenticular satellite by a flight-test model experiment.

Many scaling parameters must be considered when designing a relatively small flight-test unit so that the results of the experiment will give good

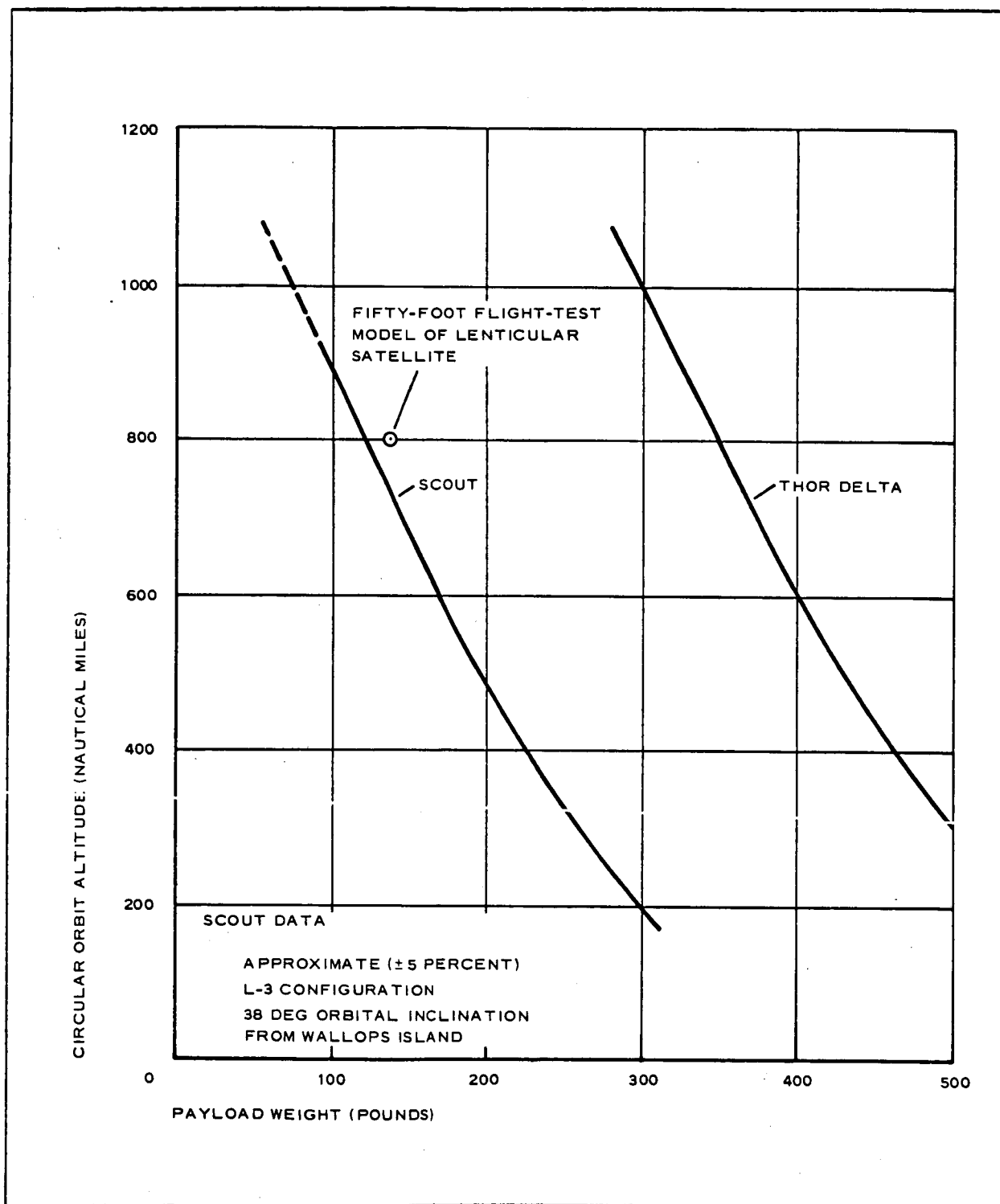


Figure 5 - Flight-Test Satellite Booster Performance Data

correlation to the dynamic and operational characteristics of a large full-scale passive communication satellite.

A fairly complete analysis indicated that it will be advisable to maintain the lens included angle of 84 deg between models rather than the 200-ft radius of curvature of the radio-reflecting lens surfaces. Geometric similarity was maintained for the 5-ft-diameter test models and the 20-ft-diameter deployment models (see Figure 6) to correlate correctly fabrication, packaging, and deployment characteristics between models.

By maintaining satellite geometric similarity the fabrication techniques, gore patterns, component tolerances, packaging methods and volumes, deployment methods and forces, and r-f reflectivity are representative.

The flight experiment goals are to investigate the major problems anticipated with the full-scale satellite, to verify theory with experimental data, to check the suitability of the gravity-gradient stabilization system, and to corroborate r-f theoretical predictions. By maintaining geometric similarity between model and full scale, the forces and component loadings are predictable because the structural theory and test methods correspond. In the stabilization and orientation area theoretical predictions of the flight-test model dynamics can be verified experimentally and, once modified wherever necessary, can be applied readily to the full-scale satellite if the proper inertia ratios are maintained. Geometric similarity is necessary in the r-f area to keep the r-f returns representative and predictable, based on simplified model tests.

The differences in r-f return for the flight-test model and the full-scale satellite can be determined readily by correcting for the lens radii of curvature and the flight altitudes because the r-f return, σ , varies as the square of the lens radius of curvature, ρ , and inversely as the fourth power of the altitude.

Maintaining model similarity should enhance reliability predictions for the full-scale satellite and show logically when controlling instrumentation will be advisable on the basis of flight-test model results. Ground

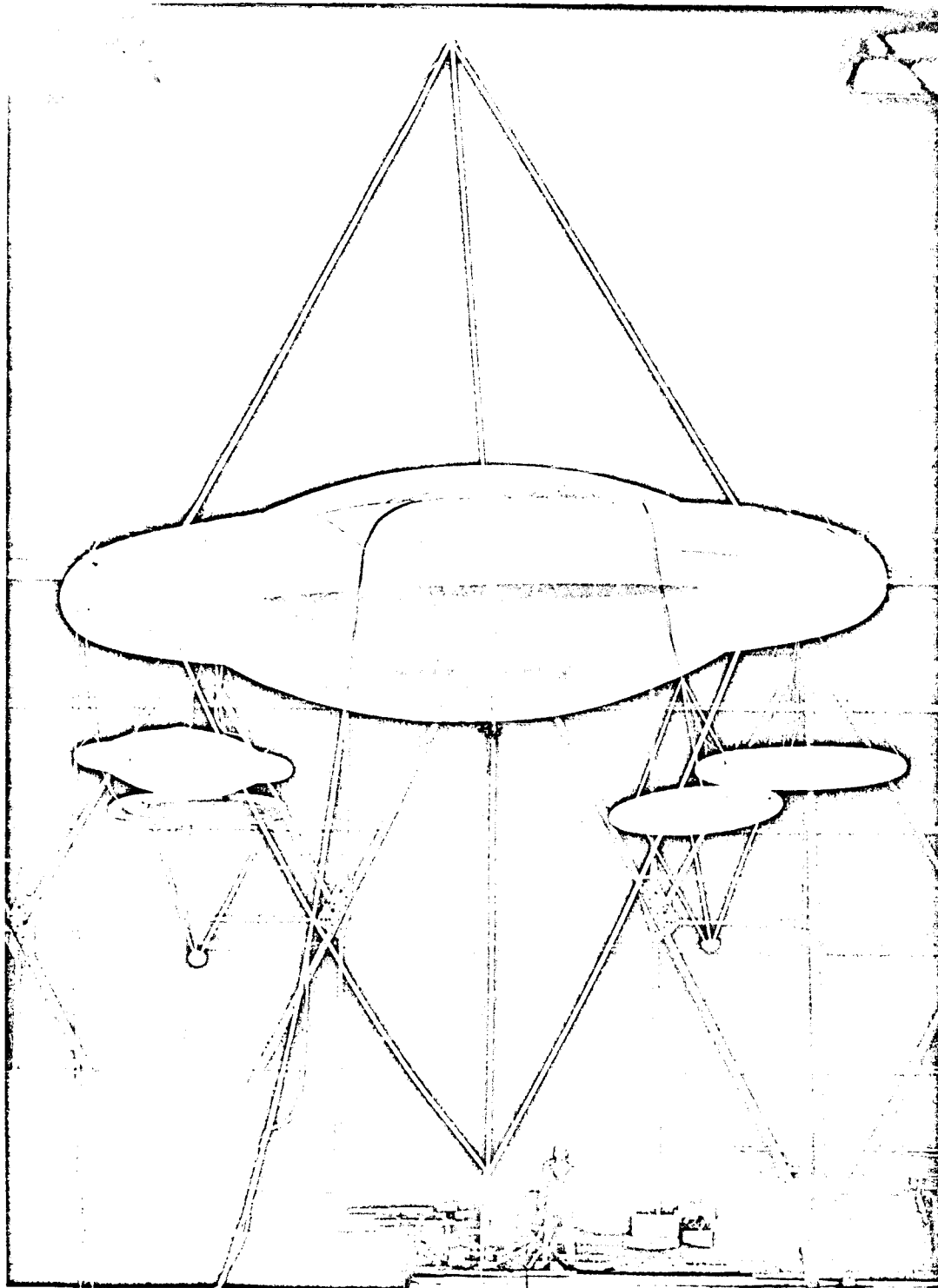


Figure 6 - Five- and Twenty-Foot-Diameter Mylar Deployment Models

test procedures for these units will be representative. Flight-test procedures will, however, be booster and launch area dependent.

4. R-F REVIEW

Theoretical predictions of nose-on monostatic r-f returns indicate that 21.5-db variations can be expected within the ± 1.5 -deg region from the satellite centerline. This variation is due to edge diffraction phenomena resulting from the lens edge radius being considerably smaller than the wave length of interest: (Frequency range is 2,000 to 10,000 mc.) The general operational picture is shown in Figure 7. The troublesome areas of Cases 1 and 2 are of no particular interest operationally. Cases 3, 4, and 5 are considered representative for both in-plane and out-of-plane equipment locations. For this reason, until some bistatic tests are conducted, indications are that the present satellite design concept has satisfactory r-f characteristics for the general operational areas to be considered.

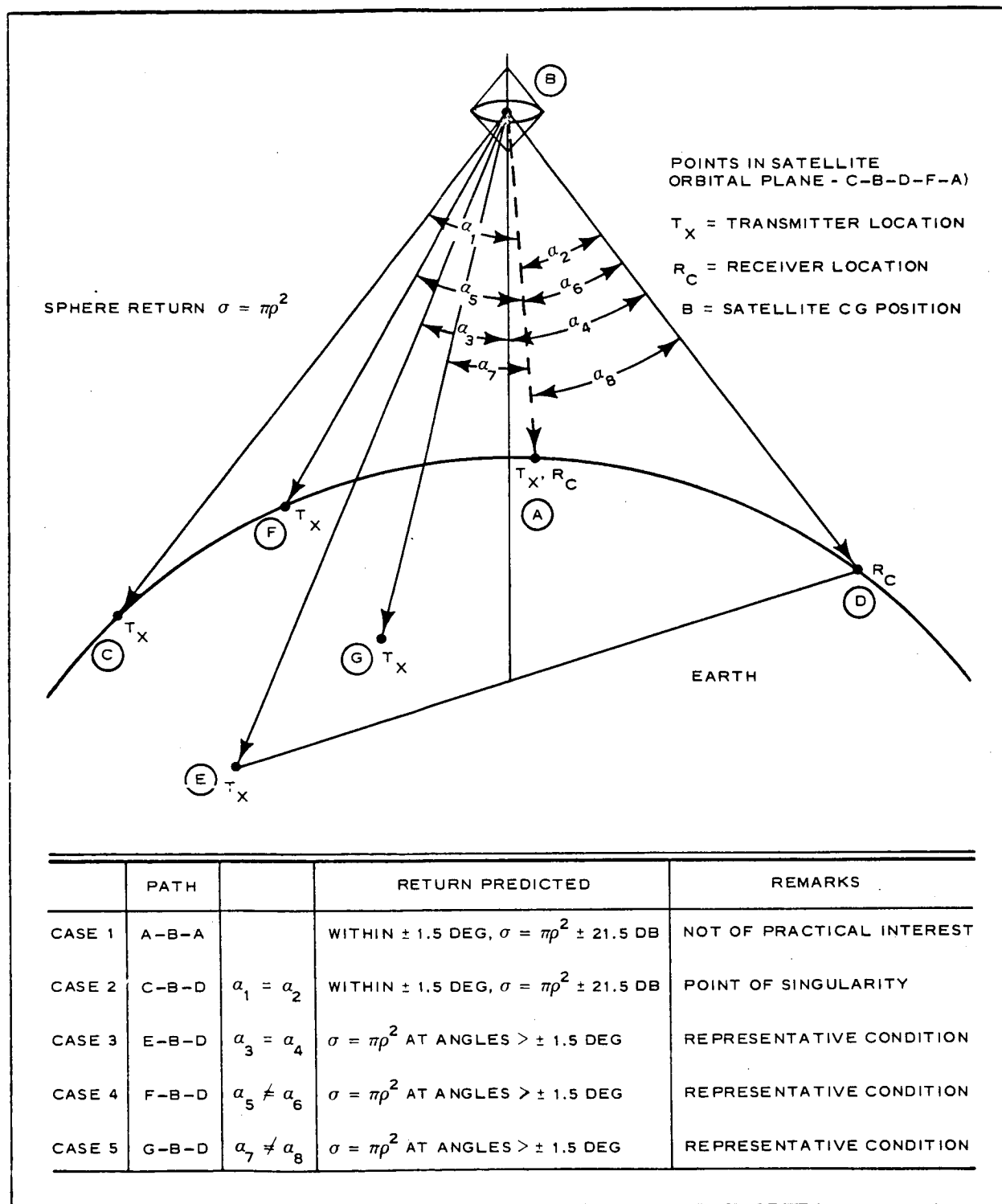


Figure 7 - General Area of Satellite R-F Operational Characteristics

SECTION III - TECHNICAL DISCUSSION - PHASES I AND II

Subsection One - Design Considerations

1. GENERAL

The design objectives of Phases I and II were to:

1. Establish the configuration design of a full-scale satellite including such factors as weight and inertia, packaging arrangement, packaging volume, deployment, configuration geometry, r-f characteristics, and structural integrity.
2. Establish the configuration design of a flight-test satellite, approximately 50-ft-diameter and capable of launch on a Scout vehicle, that will prove functional feasibility and produce meaningful test results in support of the full-scale satellite.
3. Design, fabricate, and deliver a 20 ft diameter deployment model, to be deployable in a vacuum chamber in support of the full-scale and flight-test configuration designs.
4. Design, fabricate, and deliver a breadboard inflation system to be used for the vacuum deployment of the 20-ft-diameter model.
5. Design and fabricate small-scale models as required in support of packaging and deployment studies.

A summation of the work done in support of the above objectives follows. Supporting analyses, trade offs, and material development accomplishments are covered in subsequent subsections and sections of this report.

Figure 8 summarizes the various model configurations that were pertinent to the design effort under Phases I and II.

2. FULL-SCALE SATELLITE

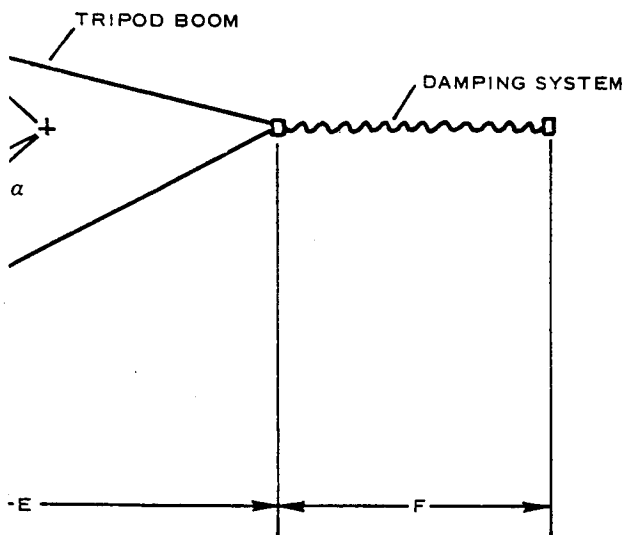
a. Conceptual Design Study

The general arrangement of the full-scale satellite is shown in Figure 9. Table II lists the weight and volume requirements of the system by components. The satellite consists of a lenticular lens bounded by a peripheral rim-torus and two displaced masses, each supported from the rim by a tripod structure.

The lenticular lens is comprised of two spherical segments with surfaces of 200-ft radius. The lens diameter is 267.6 ft.

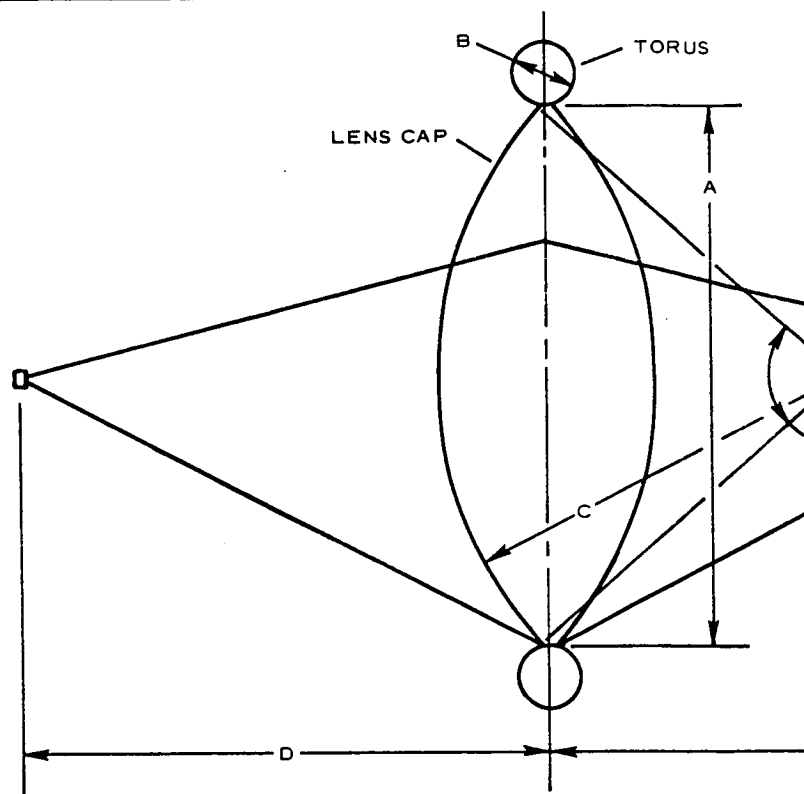
The lenticular lens surface is fabricated of 0.5-mil photolyzable film cast on a 1-mil copper wire plain-weave mesh (21 wires per inch). The film surface is perforated to allow bleed-off of residual gases prior to deployment, with approximately twenty 0.020-in. -diameter holes per square foot. These holes also provide automatic pressure relief of the system. The inflation of the entire system elongates the mesh beyond its yield point to rigidize the lenticular surfaces. After sublimation of the photolyzable gas barrier this screen, brazed to the lens rim, forms the reflective surface of the satellite.

The two spherical segments are interconnected through a metal rim of collapsible cross section (see Section E-E of Figure 9 and Figure 10). The rim is made of 2-mil beryllium copper with two hinged joints, 180 deg apart, to permit proper packaging of the system. To package the system, the rim cross section is flattened and then coiled on a storage drum. The important consideration is not to exceed the proportional limit of the material, with the stresses imposed by flattening and coiling and through deployment of the system, so that the structural section will be re-established after deployment.



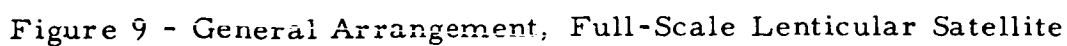
COMMENTS	STATUS
FLAR LENS	FINAL CONFIGURATION, FIGURE 9
PHOTOLYZABLE FILM-WIRE MESH LENS	FINAL CONFIGURATION, FIGURE 13
DRUS ONLY	DELIVERED TO NASA
DR GAC DEPLOYMENT TESTS	DELIVERED TO NASA
DR NASA EVALUATION	TESTED TO DESTRUCTION
DR GAC DEPLOYMENT TESTS	TESTED TO DESTRUCTION
DR STRUCTURAL EVALUATION	DELIVERED TO NASA
DR FOLDING AND PACKAGING TECHNIQUES EVALUATION	TESTED TO DESTRUCTION
	STILL AVAILABLE
	STILL AVAILABLE

Figure 8 - Summary of Model Configurations



MODEL	DIMENSION						ANGLE α (DEG)	
	A (FT)	B (IN.)	C (FT)	D (FT)	E (FT)	F (FT)		
FULL-SCALE	267.6	92.00	200.00	190.53	300.0	90.00	84	
FLIGHT-TEST	50.0	19.54	37.36	22.02	42.03	27.11	84	
TWENTY-FOOT NO. 20-1	20.0	26.00	14.94	*	17.32	*	84	M
TWENTY-FOOT NO. 20-2	20.0	26.00	14.94	*	17.32	*	84	PH
SIX-FOOT	6.0	2.38	*	*	*	*	*	TC
FIVE-FOOT NO. 1	5.0	3.75	3.5	*	*	*	91	FC
FIVE-FOOT NO. 2	5.0	3.75	3.5	*	*	*	91	FC
FIVE-FOOT NO. 3	5.0	3.75	3.5	*	4.00	*	91	FC
FIVE-FOOT NO. 4	5.0	3.75	3.9	*	*	*	100	FC
FIVE-FOOT NO. 5	5.0	3.75	3.5	*	4.32	7	91	FC

* NOT APPLICABLE



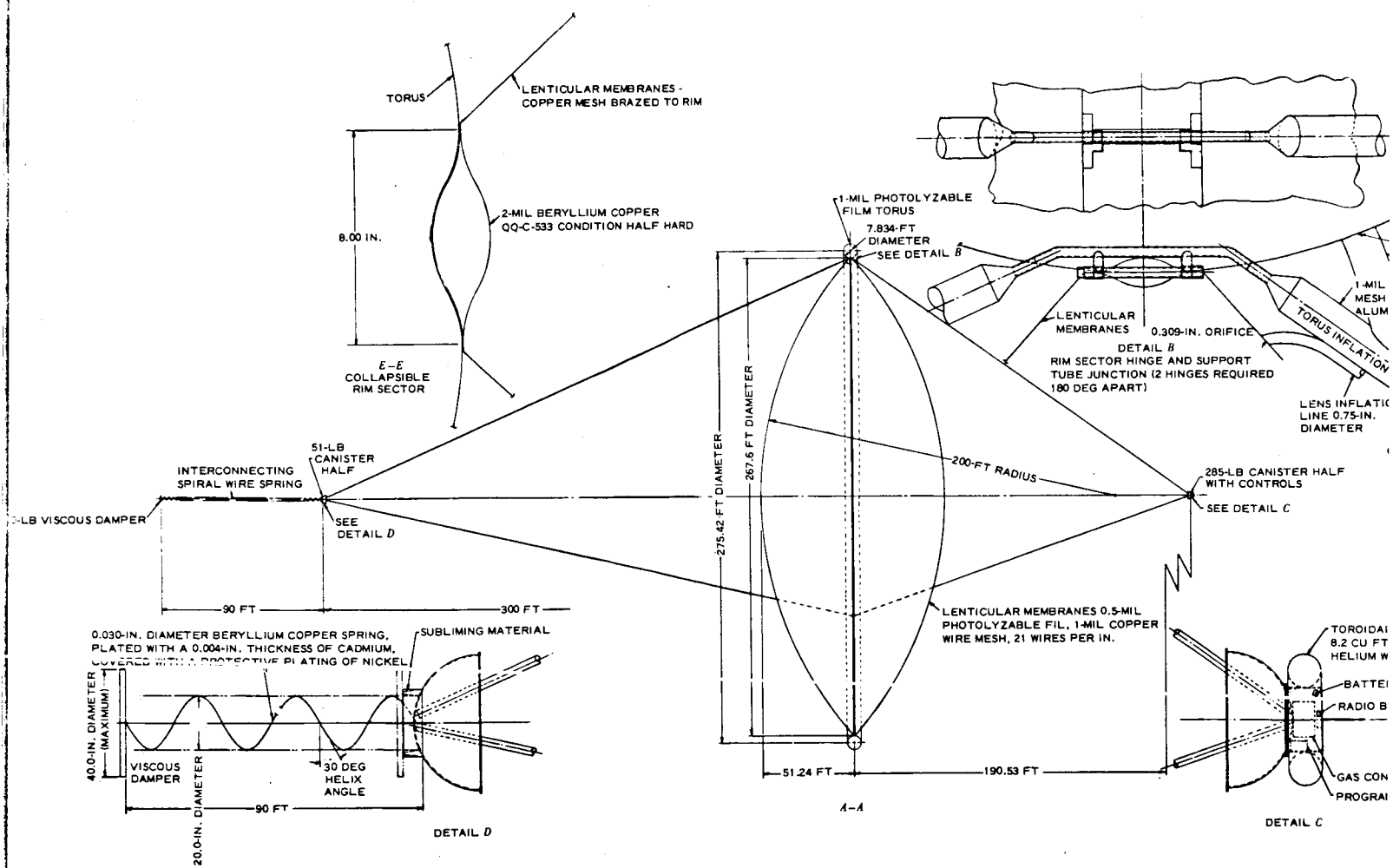


TABLE II - FULL-SCALE SATELLITE SYSTEM
WEIGHT AND VOLUME

Component	Weight (lb)			Volume (cu in.)
	Unit	Launch	Orbit	
Control electronic system		18	18	372
Radio beacon	1			
Sequence control	2			
Power control and regulation	15			
Damping system		115	115	. . .
Viscous damper	100			
Spring	5			
Damper cover and support	10			
Structure and hardware		92	92	. . .
Canister shell	80			
Mounting brackets	12			
Satellite		782	312	65,200
Lens with film	552			
Lens without film	199			
Photolyzable torus	117			
Rim	103			
Booms	10			
Inflation system		233	216	3,000
Gas bottle	191			
Gas (helium)	17			
Gas valves and hardware	25			
Separation system		10	5	. . .
Total		1250	758	68,572

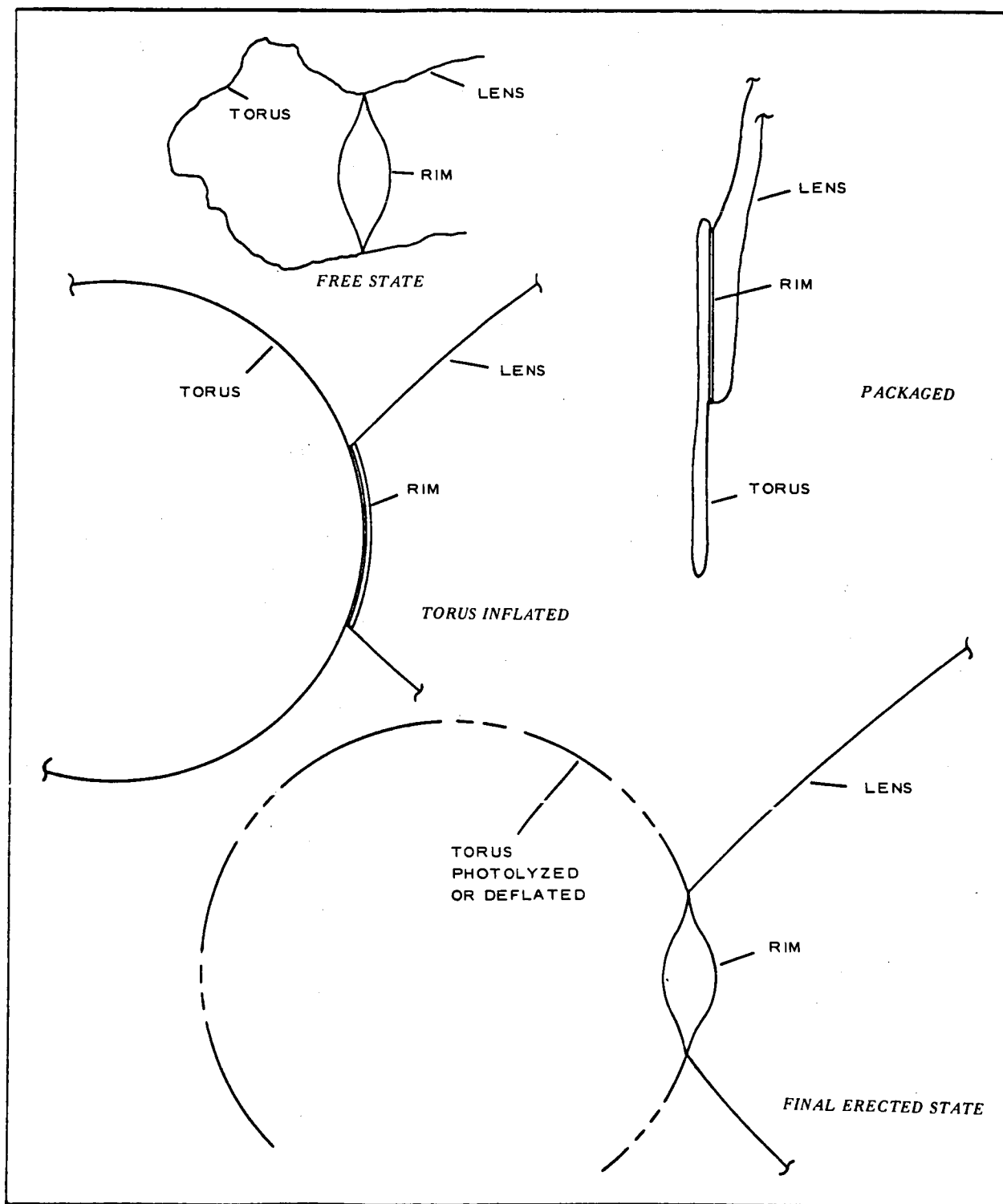


Figure 10 - Collapsible Rim Functional Schematic

The rim also provides the three structural attachments for the tripod booms that support the gravity-gradient masses.

The effective lenticular lens and metal rim are encircled by a torus of 7.83-ft-diameter cross section and 275.43-ft pitch diameter. The torus is inflated first, to unfurl the packaged lens surfaces, and is maintained under a relatively high pressure to support the erection loads that are imposed during pressure yielding of the lens surfaces. The torus is made of 1-mil photolyzable film material and has a series of compartments interconnected by sized orifices so that its cells will inflate in sequence to control the deployment of the overall system (see Figure 11) and to prevent buckling of the metal rim. The torus surface is perforated with approximately one 0.020-in.-diameter hole per square feet to allow bleed-off of residual gases prior to deployment. After deployment of the entire satellite the photolyzable torus material will sublime, leaving the metal rim as the structural interface for the lens caps and tripod booms.

Two masses, one on each side of the lenticular shape, are supported at the apexes of tripod booms. These masses are used as gravity-gradient weights and consist of the packaging canister halves and fixed equipment such as inflation system, damping system, and control and electronics elements.

The individual elements of the tripod booms are 3-in.-diameter tubes of 1-mil Mylar laminated to 0.5-in. square mesh aluminum wire 2-mil diameter.

The inflatable elements of the satellite are packaged in a 50-in.-diameter spherical canister which, at deployment, separates at its equator. A screen-type liner is spaced off the inner surface of the canister to permit passage of entrapped air to an evacuation valve. This valve is used for initial pump-down of the canister and is solenoid controlled to be opened at orbital altitude to stabilize pressures prior to deployment.

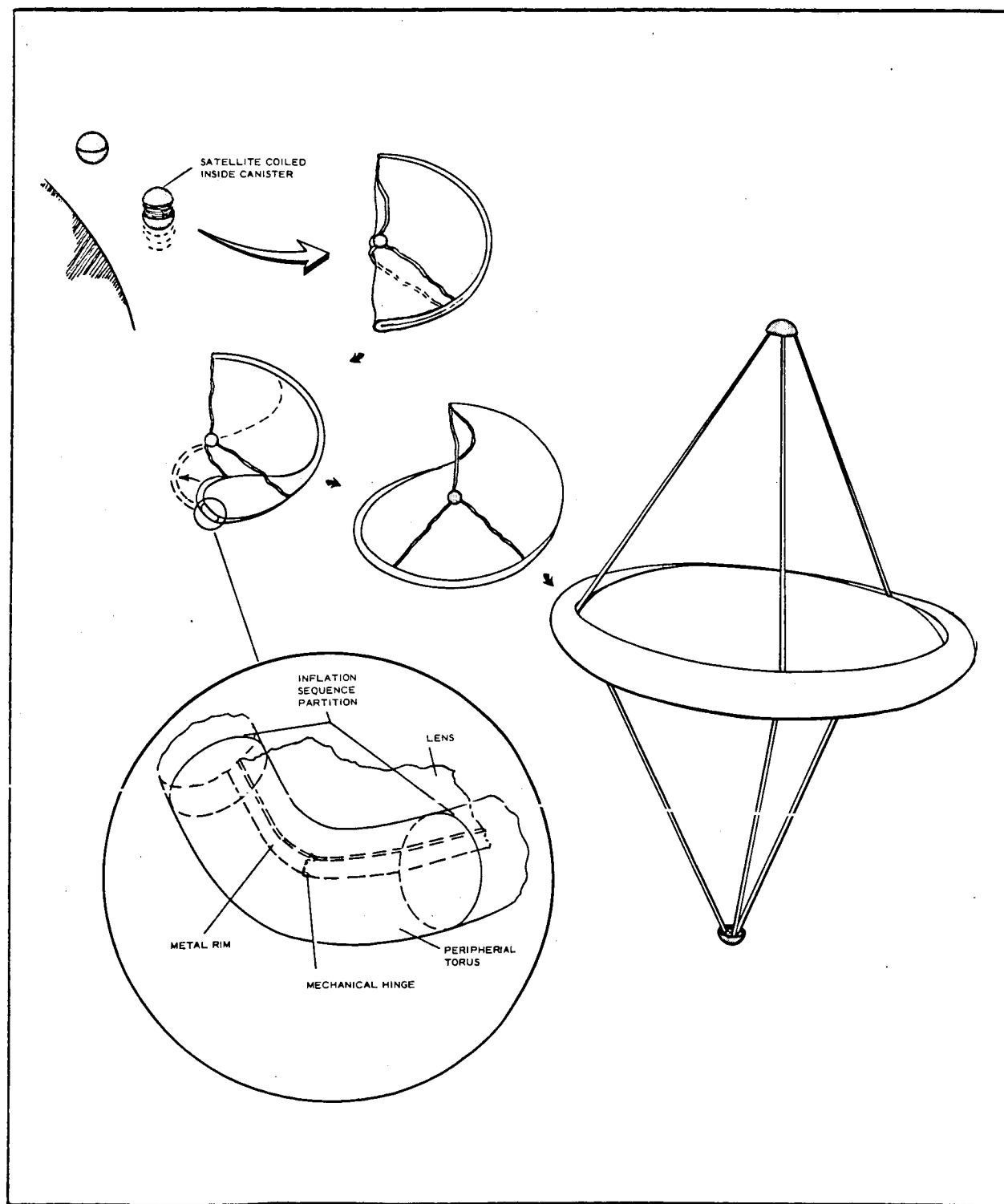


Figure 11 - Full-Scale Satellite Deployment Sequence

The earth-side canister half, when considering satellite-stabilized attitude, provides the mounting interface of the inflation system components, the communication system components, and the electrical system components. The opposite canister half provides the mounting interface for the damping system.

b. Inflation and Deployment System

Prior to initiation of the deployment sequence it is mandatory that entrapped air be evacuated from the satellite envelope and also from the canister. A two-step process will be used to accomplish the evacuation. First, partial evacuation will be effected on the ground by pumping down the canister and sealing it. Second, the canister will be vented in the orbital atmosphere for further evacuation. A solenoid-actuated valve will be mounted in the canister shell and fixed to initiate the second step at the proper time. The satellite skin will be perforated to allow entrapped air to escape during this period. The time required to carry out the above process successfully will be determined.

To effect successful satellite deployment, a sequential order of element inflation will be required, first the booms and torus and then the lens, with the torus remaining pressurized during lens inflation.

Likewise an orderly pressure relief sequence will be required to preclude the possibility of uncontrolled exhaust gas upsetting the system dynamics. After the deployment has been completed, the gas in the lens and torus will exhaust through the perforated surfaces, thus effecting uniform depressurization.

Deployment will be effected by helium gas inflation. The gas system and its controls are shown schematically in Figure 12. At the predetermined gas pressure, the grid-wire element of the lens skin will exceed its yield strength and rigidize. The system is based on the following data:

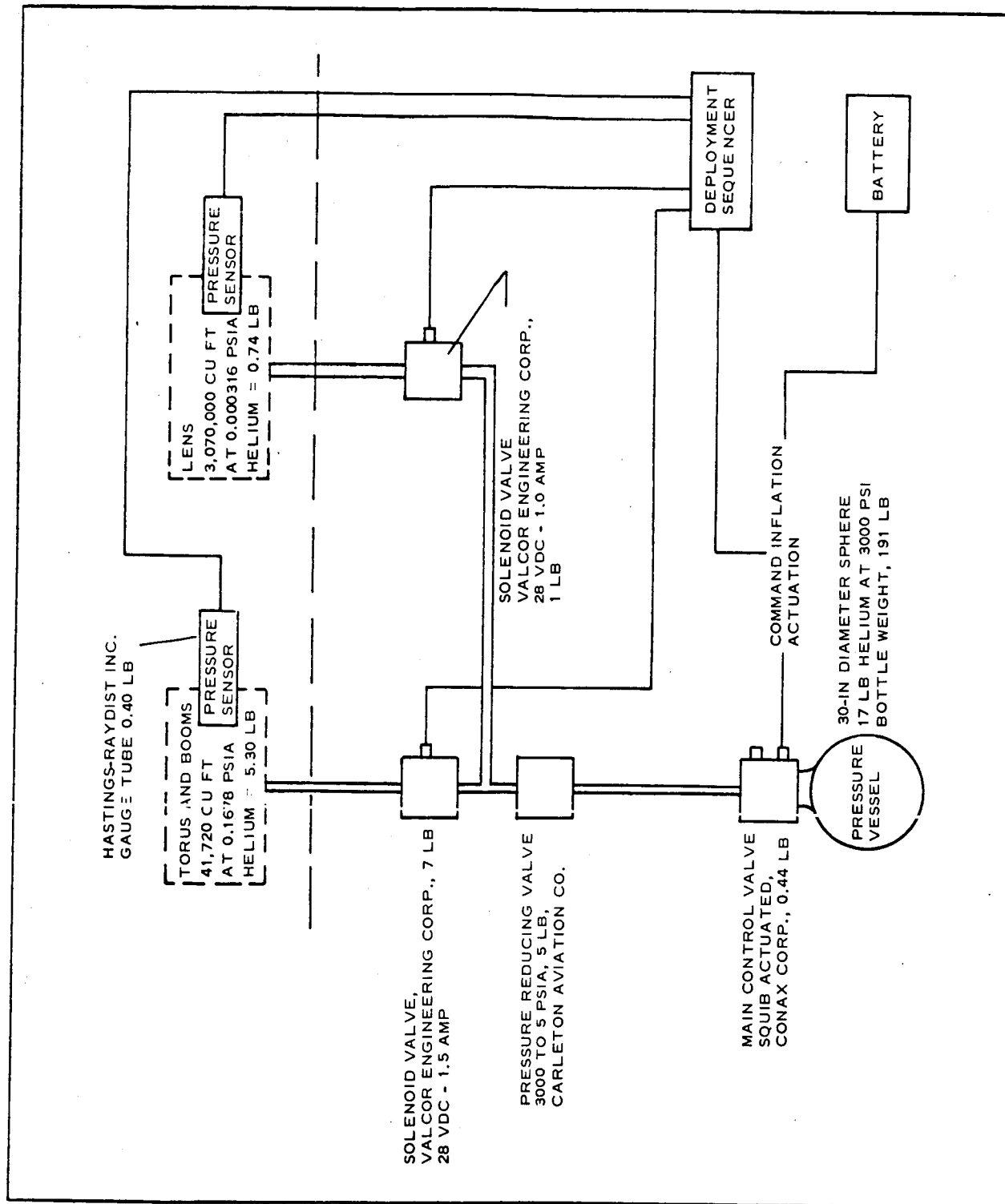


Figure 12 - Inflation System Schematic

1. Torus
 - a. Volume - 41,700 cu ft
 - b. Surface area - 21,300 sq ft
 - c. Surface perforation - One hole, 0.020-in-diameter per sq ft
 - d. Pressure required - 0.168 psia
 - e. Inflation time to pressure - 5 min
 - f. Inflation hold time - 9 min
2. Lens
 - a. Volume - 3,070,000 cu ft
 - b. Surface area - 129,000 sq ft
 - c. Surface perforation - 20 holes, 0.020 diameter per sq ft
 - d. Pressure required - 0.000316 psia
 - e. Inflation time to pressure - 5 min
 - f. Inflation hold time - 2 min

Based on above data the helium provided will weigh 17 lb, which is 133 percent of the calculated requirement. The pressure vessel will be a toroid and will weigh approximately 191 lb.

A complete analysis of the system as summarized herein is included in Subsection Two.

A test program will be developed to evaluate and verify the proposed deployment system capability. This program will include:

1. Air evacuation on a test envelope to demonstrate effectiveness of both skin perforation and soaking time versus entrapped air remaining
2. Individual component testing to demonstrate ability to carry out assigned functions in a simulated low-pressure and low-temperature environment.
3. Simulated system tests in a low-pressure chamber.

Special tests to demonstrate sensing capability and also the deployment concept will be developed.

3. FLIGHT-TEST MODEL

a. Conceptual Design Study

The test satellite is designed to be launched with the Scout vehicle and will be packaged within the envelope of an Echo I canister. The general arrangement of the flight-test satellite is shown in Figure 13. Table III lists the weight and volume requirements of the system by components. The satellite design consists of a lenticular lens bounded by a peripheral rim-torus and two displaced masses, each supported from the rim by a tripod structure.

The lenticular lens will be comprised of two spherical segments with surfaces of 37.36-ft radius and a lens diameter of 50 ft.

The lenticular lens surface will be made of 0.6-mil photolyzable film, cast on a 1.2-mil copper wire plain-weave mesh (21 wires per inch). The film surface will be perforated, to allow bleed-off of residual gases prior to deployment, with approximately four 0.020-in. diameter holes per sq ft. The inflation of the entire system will elongate this mesh beyond the yield point of the screen to rigidize the lenticular surfaces. After sublimation of the photolyzable gas barrier, this screen, brazed to the lens rim, will form the reflective surface of the satellite.

The two spherical segments will be interconnected by a metal rim of collapsible cross section. (See Section B-B of Figure 13.) The rim will be made of 2-mil beryllium copper and will include two hinged joints, 180 deg apart, to permit proper packaging of the system. The rim also will provide the three structural attachments for the tripod booms to support the gravity-gradient masses.

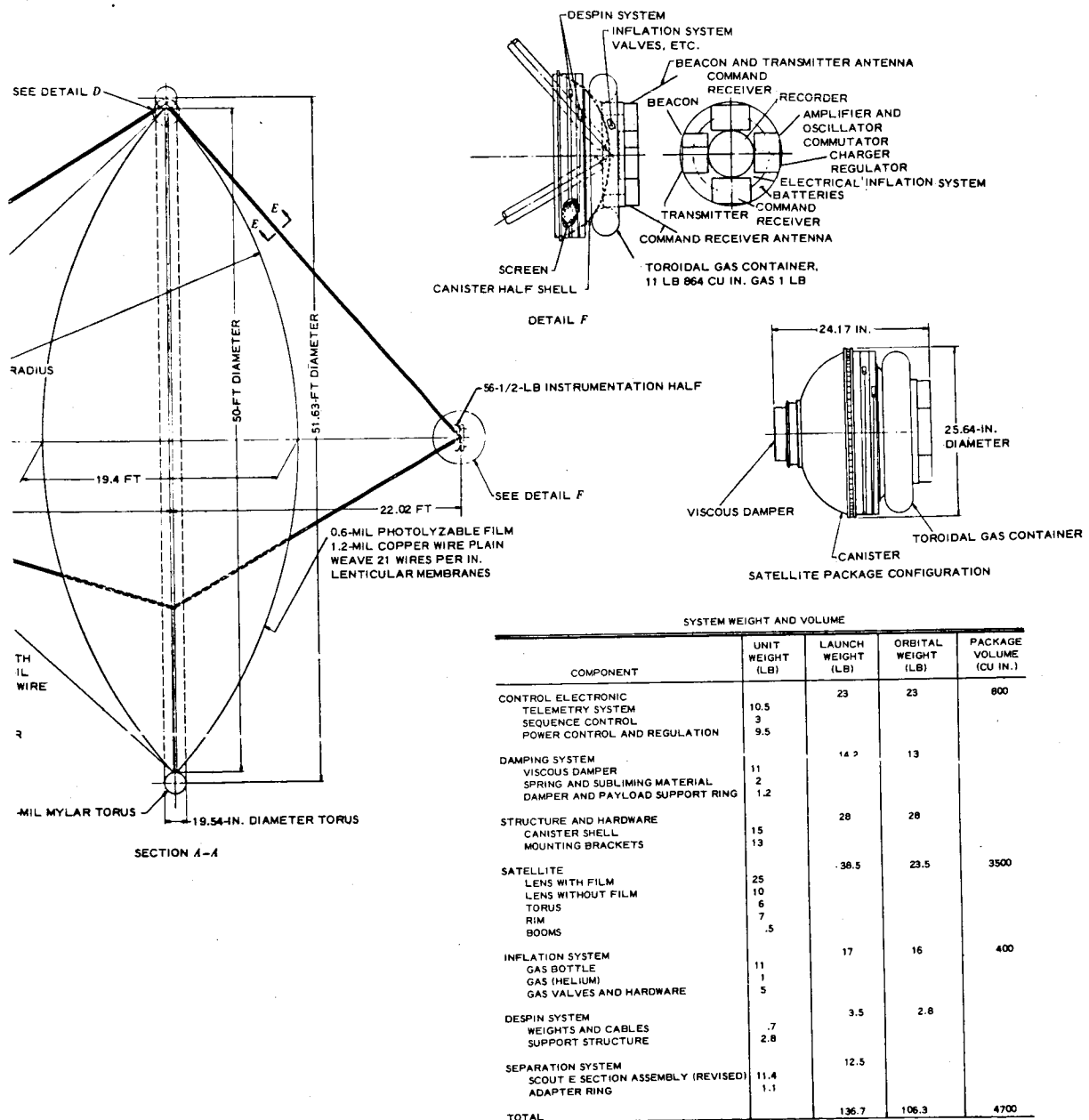


Figure 13 - Lenticular Satellite, 50-Ft Diameter, General Arrangement

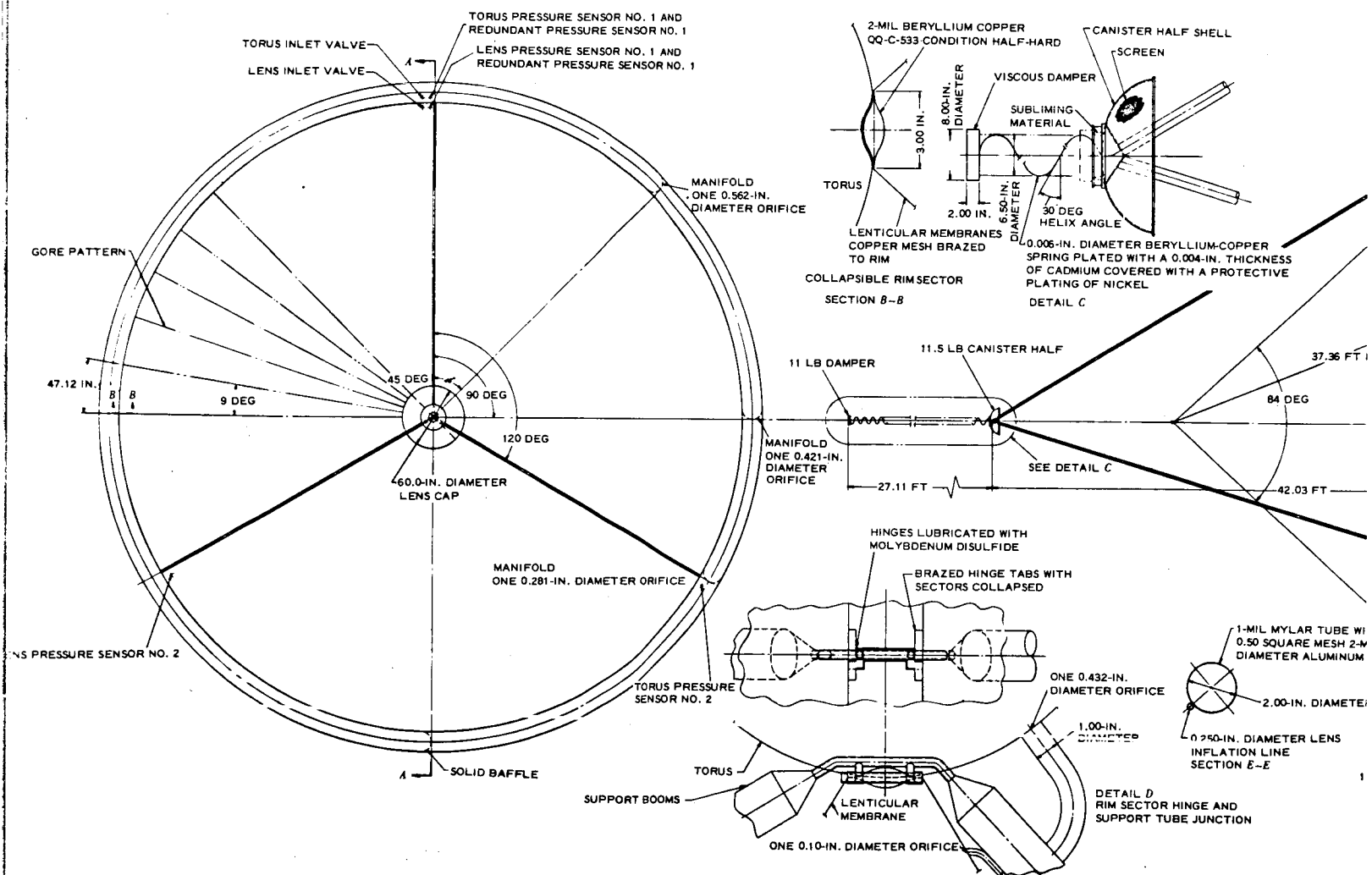


TABLE III - FLIGHT-TEST SATELLITE SYSTEM
WEIGHT AND VOLUME

Component	Weight (lb)			Package Volume (cu in.)
	Unit	Launch	Orbit	
Control electronic		23.0	23.0	800
Telemetry system	10.5			
Sequence control	3.0			
Power control and regu- later	9.5			
Damping system		14.2	13.0	
Viscous damper	11.0			
Spring and subliming material	2.0			
Damper and payload sup- port ring	1.2			
Structure and hardware		28.0	28.0	
Canister shell	15.0			
Mounting brackets	13.0			
Satellite		38.5	23.5	3,500
Lens with film	25.0			
Lens without film	10.0			
Torus	6.0			
Rim	7.0			
Booms	0.5			
Inflation system		17.0	16.0	400
Gas bottle	11.0			
Gas (helium)	1.0			
Gas valves and hardware	5.0			
Despin system		3.5	2.8	
Weights and cables	0.7			
Support structure	2.8			

TABLE III - FLIGHT-TEST SATELLITE SYSTEM
WEIGHT AND VOLUME (Continued)

Component	Weight (lb)			Package Volume (cu in.)
	Unit	Launch	Orbit	
Separation system		12.5		
Scout "E" section assembly (revised)	11.4			
Adapter ring	1.1			
Total		136.7	106.3	4,700

The effective lenticular lens and metal rim are encircled by a torus section with a 19.54-in. -diameter cross section and a pitch diameter of 51.63 ft. The torus will be inflated first, thereby unfurling the packaged lens surfaces, and will be maintained under a relatively high pressure to support the erection loads imposed by pressure yielding the lens surfaces. The torus is fabricated from 1-mil Mylar and has a series of compartments interconnected by sized orifices so that the cells inflate in sequence to control the deployment of the over-all system (see Figure 14) and to prevent buckling of the metal rim. The torus surface is perforated with one 0.020-in. -diameter hole per 5 sq ft to allow bleed-off of residual gases prior to deployment.

Two masses, one on each side of the lenticular shape, are supported at the apexes of tripod booms. These masses are used as gravity-gradient weights and consist of the packaging canister halves and fixed equipment such as inflation system, damping system, and control and electronic elements. The individual elements of the tripod booms are 2-in. -diameter tubes of 1-mil Mylar laminated to 0.5-in. square mesh aluminum wire, 2-mil diameter. The inflatable elements of the satellite are packaged within the volume of a 24-in.

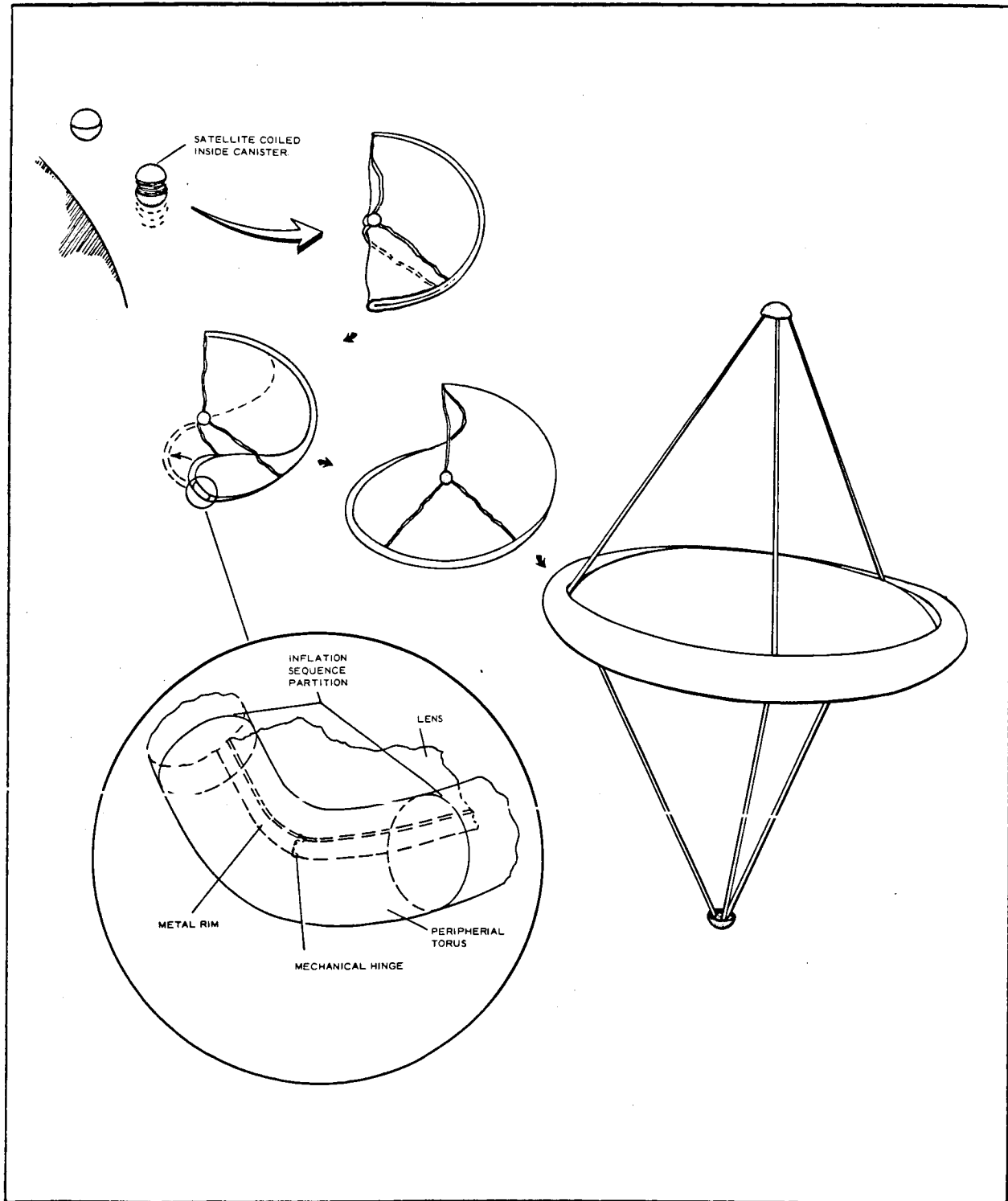


Figure 14 - Test Satellite Detailed Deployment Sequence

major diameter spheroid canister which, at deployment, separates at the equator. A screen-type liner is spaced off of the inner surface of the canister to permit passage of entrapped air to an evacuation valve. This valve is used for initial pump-down of the canister and is solenoid controlled to be opened at orbital altitude to stabilize pressures prior to deployment.

The earth-side canister half, when considering satellite stabilized attitude, provides the mounting interface of the inflation system components, the communication system components, test equipments, and the electrical system components. The opposite canister half provides the mounting interface for the damping system.

b. Inflation System

The flight-test satellite inflation system is functionally the same as the full-scale model, except as shown in Figure 15 and noted in the data listed below:

1. Torus

- | | |
|-------------------------------|--|
| a. Volume | - 337.6 cu ft |
| b. Surface area | - 830 sq ft |
| c. Surface perforation | - One hole, 0.020-in. - diameter per 5 sq ft |
| d. Pressure required | - 1.047 psia |
| e. Inflation time to pressure | - 2 min. |
| f. Inflation hold time | - 6 min. |

2. Lens

- | | |
|-------------------------------|--|
| a. Volume | - 20,257 cu ft |
| b. Surface area | - 4,510 sq ft |
| c. Surface perforation | - Four holes, 0.020-in. - diameter per sq ft |
| d. Pressure required | - 0.002437 psia |
| e. Inflation time to pressure | - 2 min. |
| f. Inflation hold time | - 2 min. |

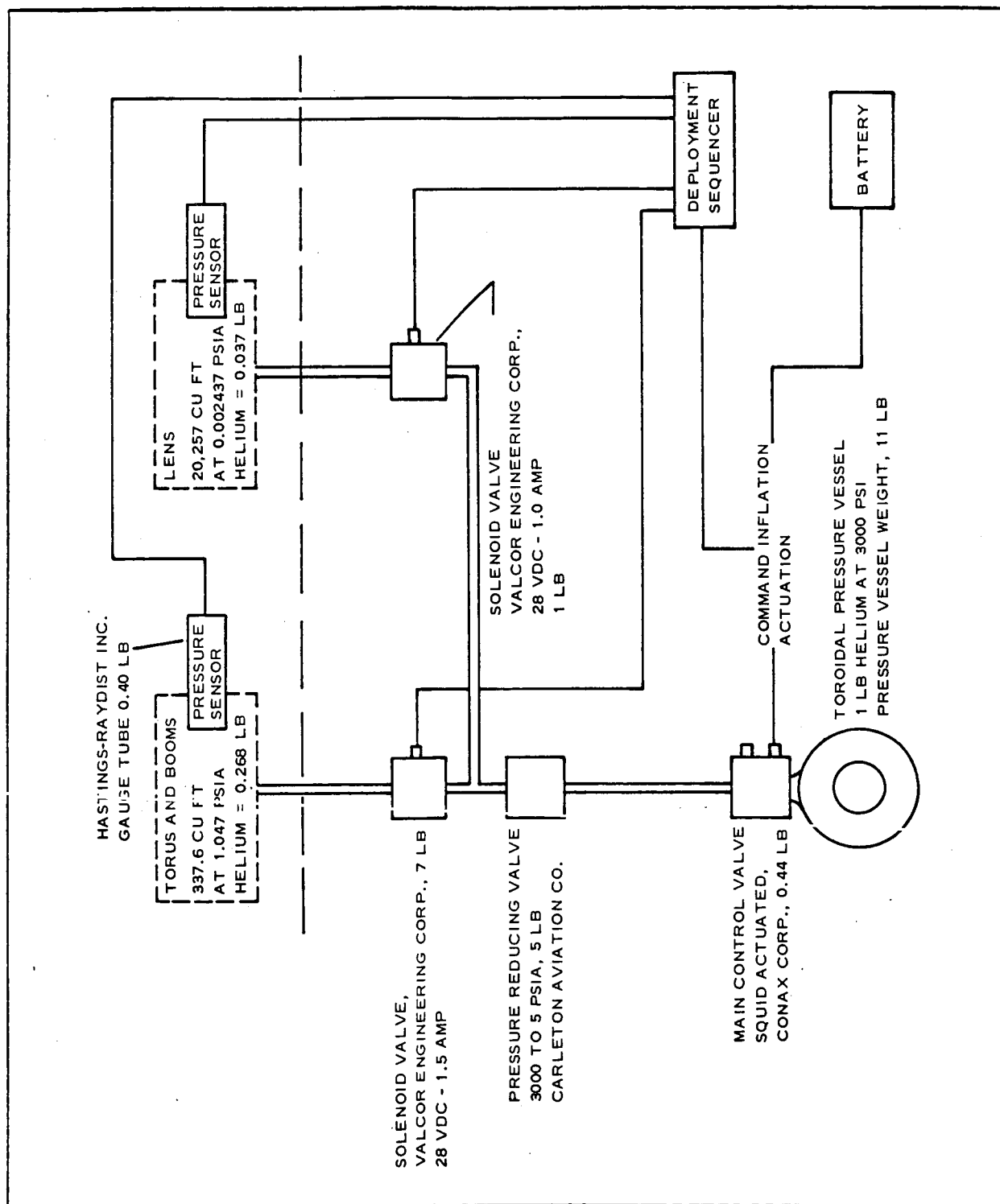


Figure 15 - Flight Test Inflation System Schematic

Based on above data 1 lb of helium is provided which is 150 percent of the calculated requirement. The pressure vessel will be a toroid and will weigh approximately 11 lb. A complete analysis of the system, as summarized herein, is included as part of Subsection Two.

4. DEPLOYMENT MODELS AND TESTS

a. General

A requirement of the contract was to deliver a 20-ft-diameter deployment model for vacuum deployment and an inflation system breadboard to be used with the model. The contract also provided for small-scale models to be built as required in support of the deliverable item. To this end one 6- and three 5-ft-diameter models were fabricated. The 5-ft-diameter models (torus) were dimensionally scaled to the design of the full-scale torus (which has subsequently been changed as part of the final design studies). The 6-ft model was not dimensionally scaled and was built from existing tooling to get an early evaluation of the deployment concept.

As previously noted, it is of primary importance to have an organized deployment of the torus to prevent local failures (buckling) of the metal rim cross section. This consideration and the assurance that there will not be any locking and subsequent tearing of the films due to packaging forms have been the dominant factors in the deployment work performed to date. Although packaging and deployment have not been optimized, reasonable and satisfactory solutions have been adequately demonstrated. A brief history and results of this work are given below.

Early testing proved that, with the relatively low pressure differentials involved, successful deployment of the torus element could not be effected on a table surface (including one coated with soapstone) because of friction due to gravity. All subsequent testing,

and results reported herein, was performed on a water surface, which effectively reduces friction due to gravity, and is therefore more representative of a gravity-free condition.

b. Six-Foot-Diameter Deployment Model

The 6-ft-diameter torus (2.375-in. cross-sectional diameter) was fabricated from 1-mil Mylar and included a 5-mil stainless steel rim with two mechanical hinges approximately 180 deg opposed. Figure 16 shows the approximate manifolded bulkhead arrangement and the folding technique that was used.

Test data were not recorded but the model was deployed successfully and served as a basis for the work that followed.

c. Five-Foot-Diameter Deployment Models

(1) General

Several five-foot-diameter deployment models, itemized in Figure 8, were fabricated and tested. Such parameters as number and location of bulkheads, bulkhead hole size, method of packaging, and deployment time were varied to determine design characteristics. Figures 17 and 18 show the final configuration used. Figures 19, 20, and 21 are photographic records of the testing. Also 16-mm film strips of some of the deployment tests are available.

(2) Fabrication and Tooling

(a) Torus

The tool used for the five-foot model was a solid-steel form representing half the torus cross section and slightly more than one-fourth of the torus circumference. A hollow form might have been better but time and cost favored a solid section. The tool shown in Figure 22 was used for both forming and assembly of the model torus. Each piece formed on the tool comprised one-eighth of the complete torus.

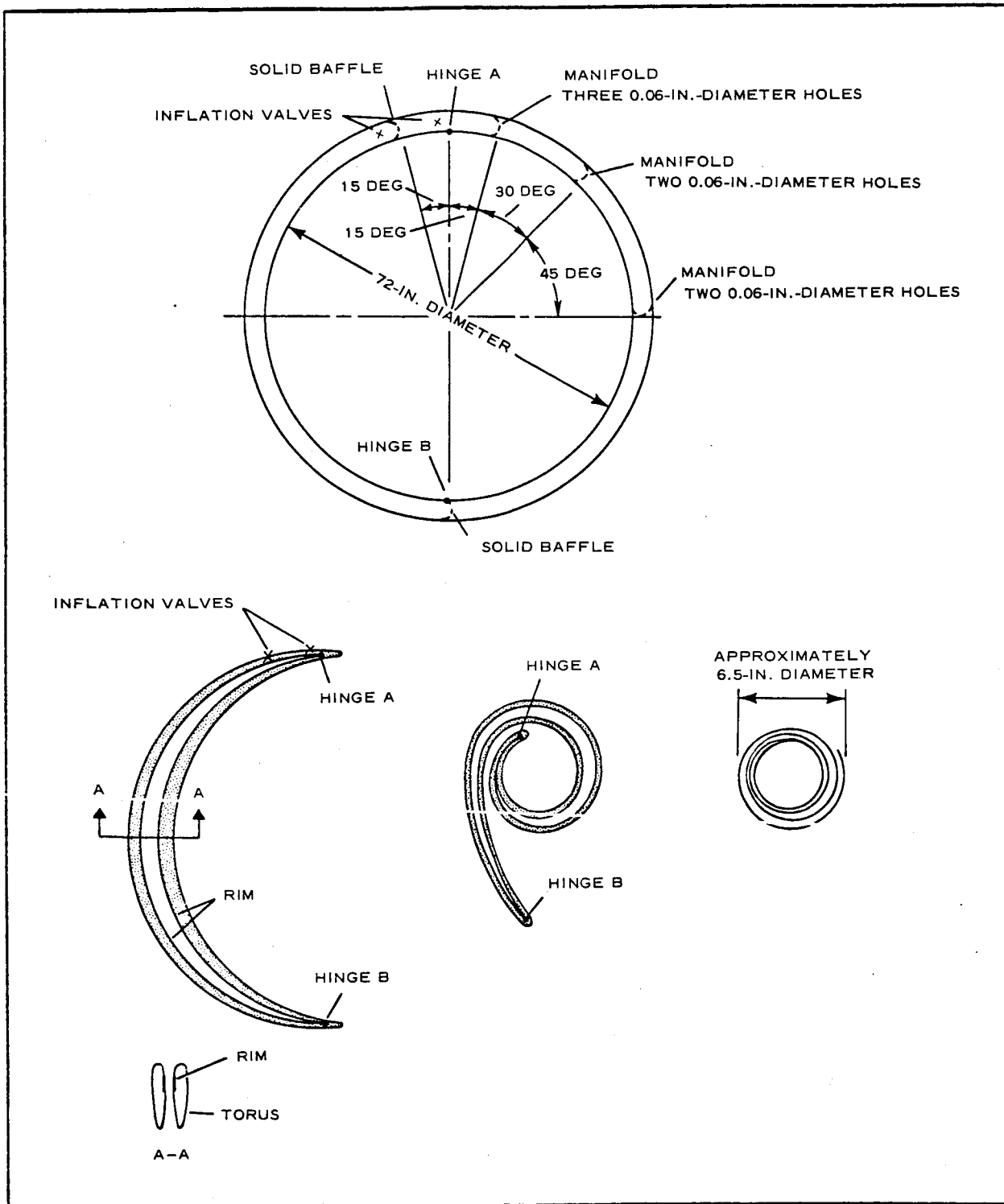
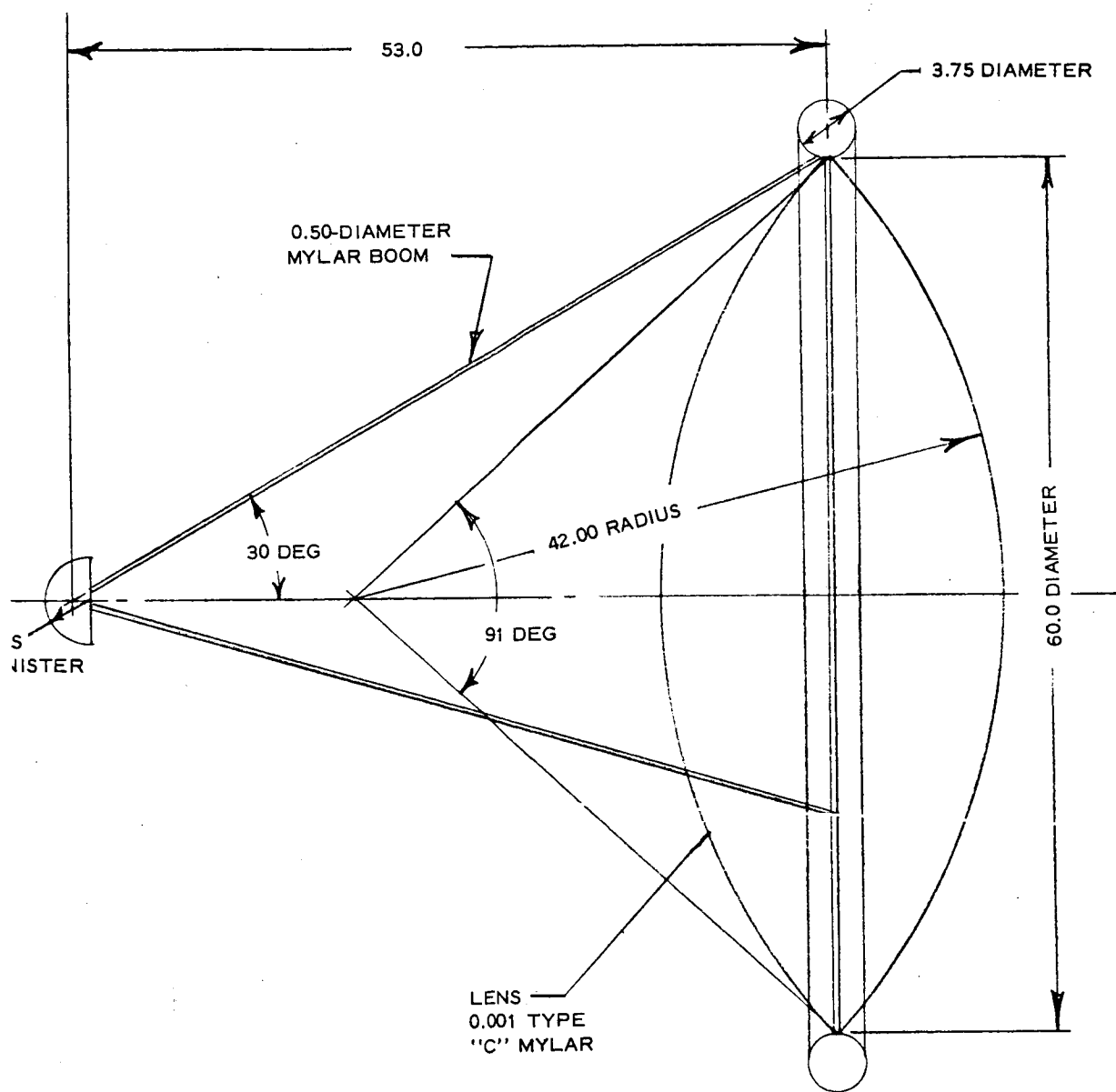
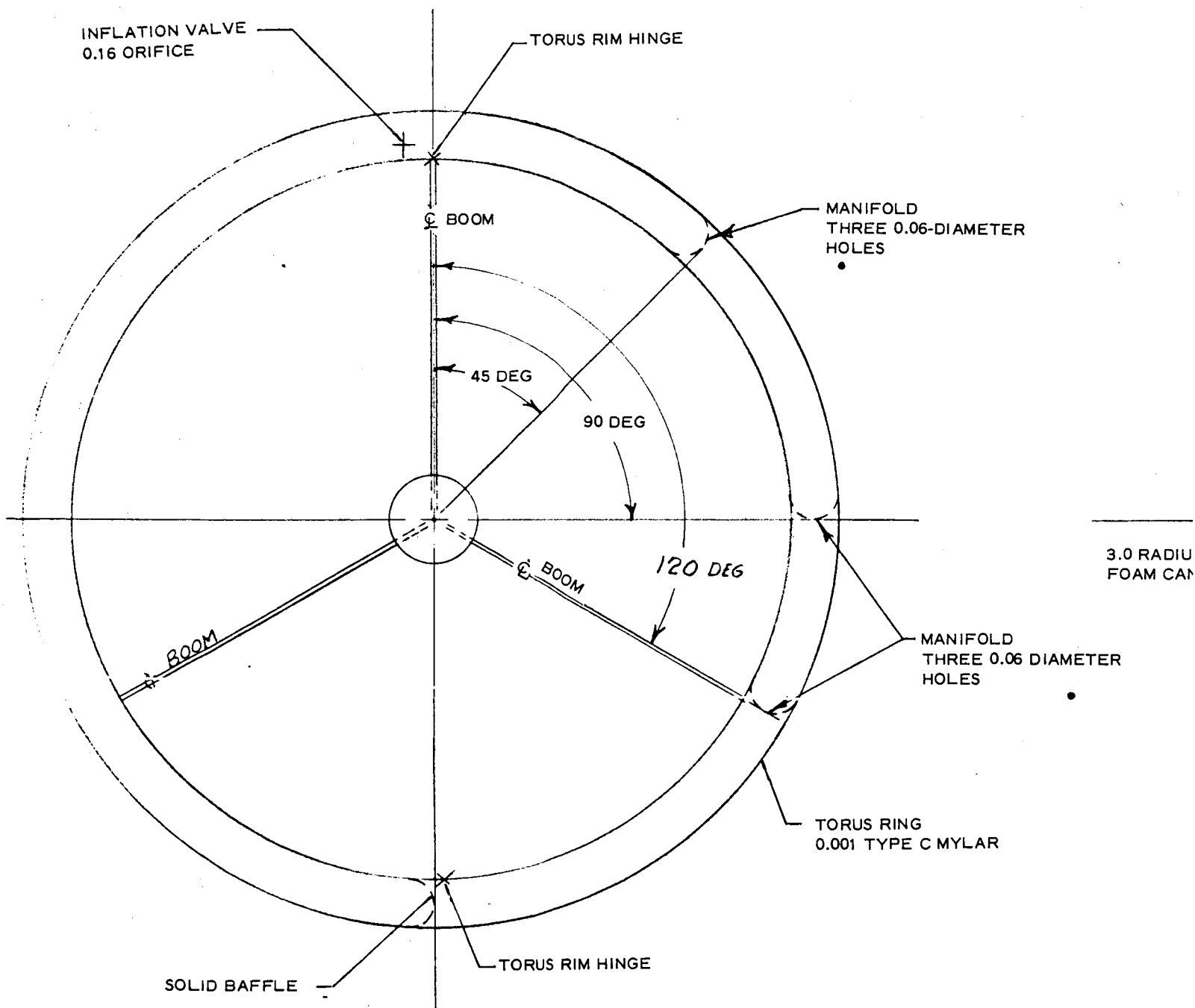


Figure 16 - Packaging Sequence, Six-Foot Model



NOTE: DIMENSIONS ARE IN INCHES

Figure 17 - Five-Foot Deployment Model Final Configuration



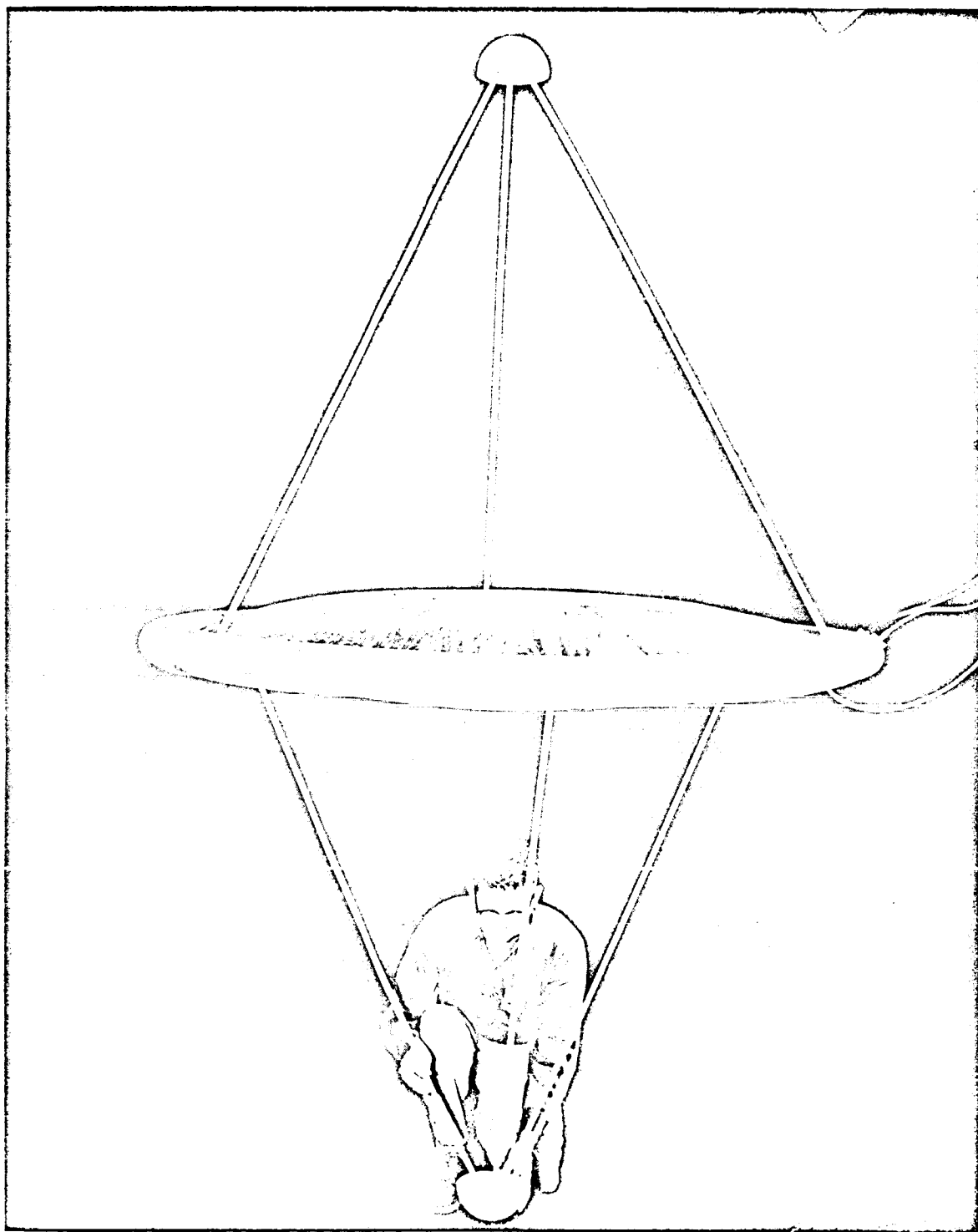
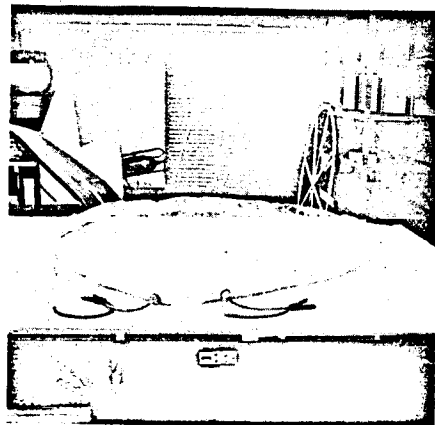


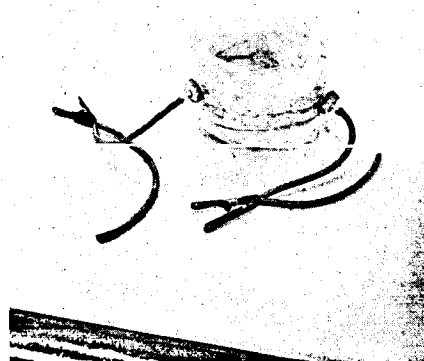
Figure 18 - Five-Foot Deployment Model



EVACUATED

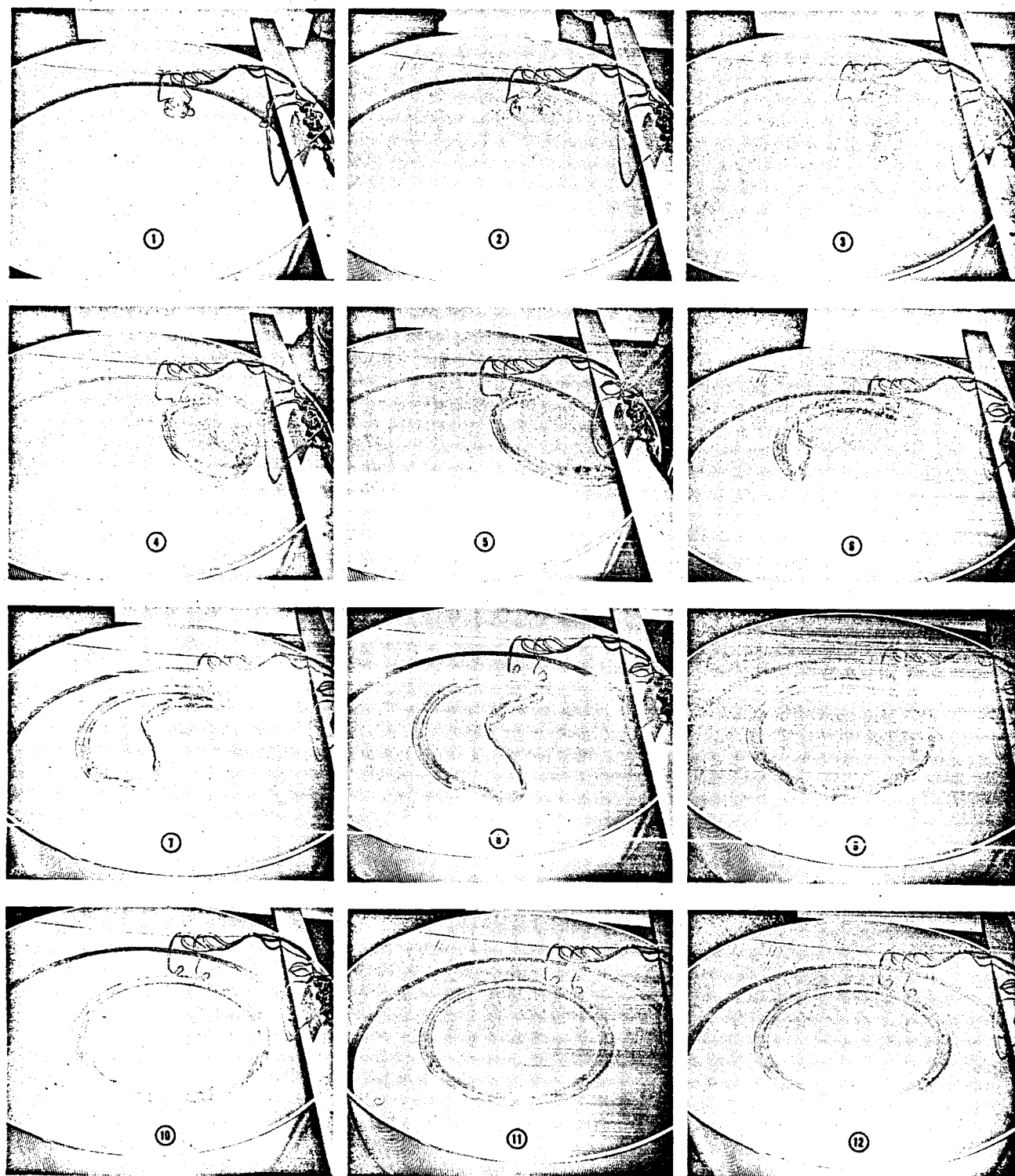


FOLDED



FINAL PACKAGE

Figure 19 - Packaging Sequence for Five-Foot-Diameter Model Torus



ELAPSED TIME 30 SECONDS

INFLATION PRESSURE 30-IN. WATER (1.1 PSI)

Figure 20 - Deployment of Five-Foot-Diameter Torus

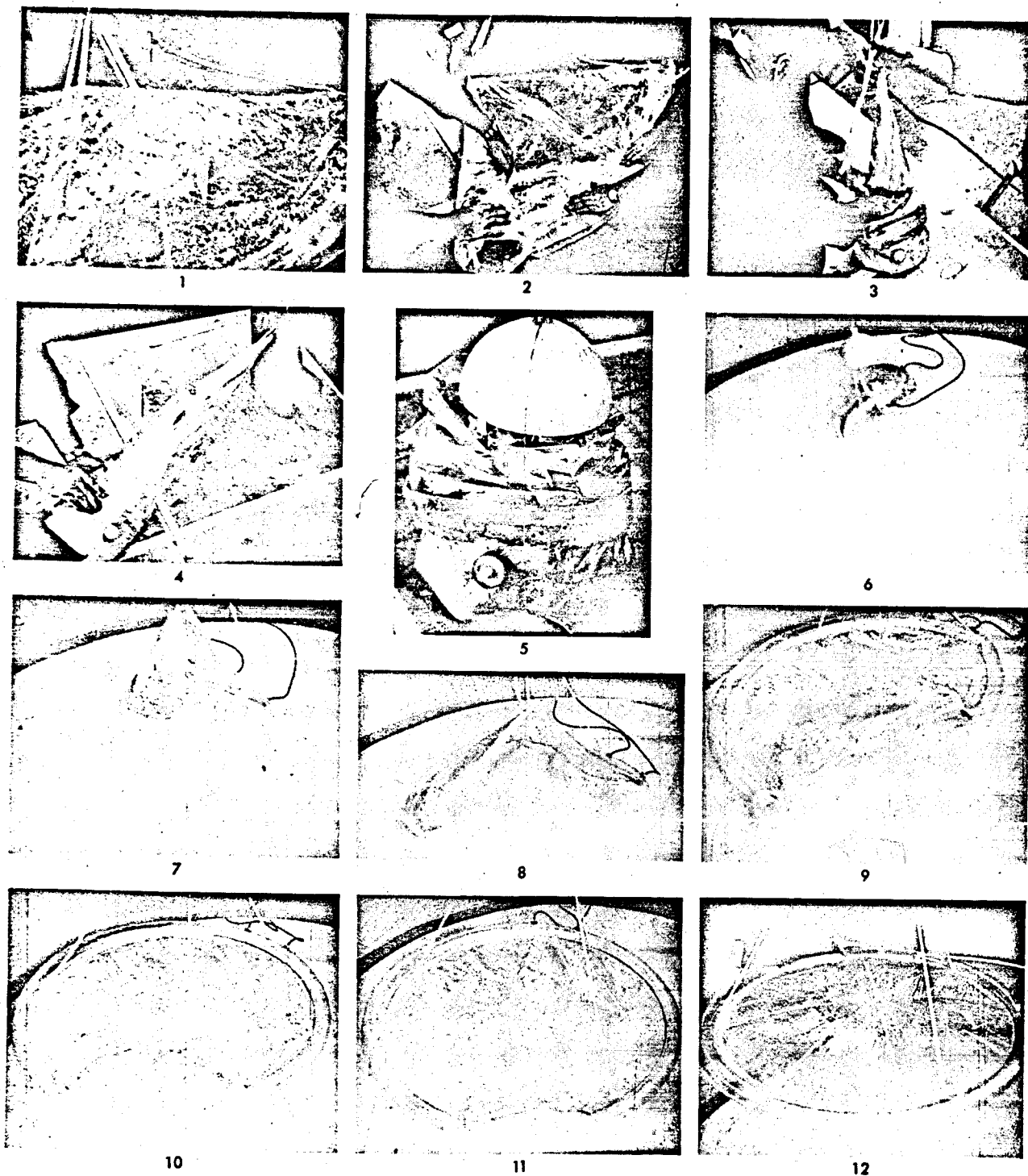
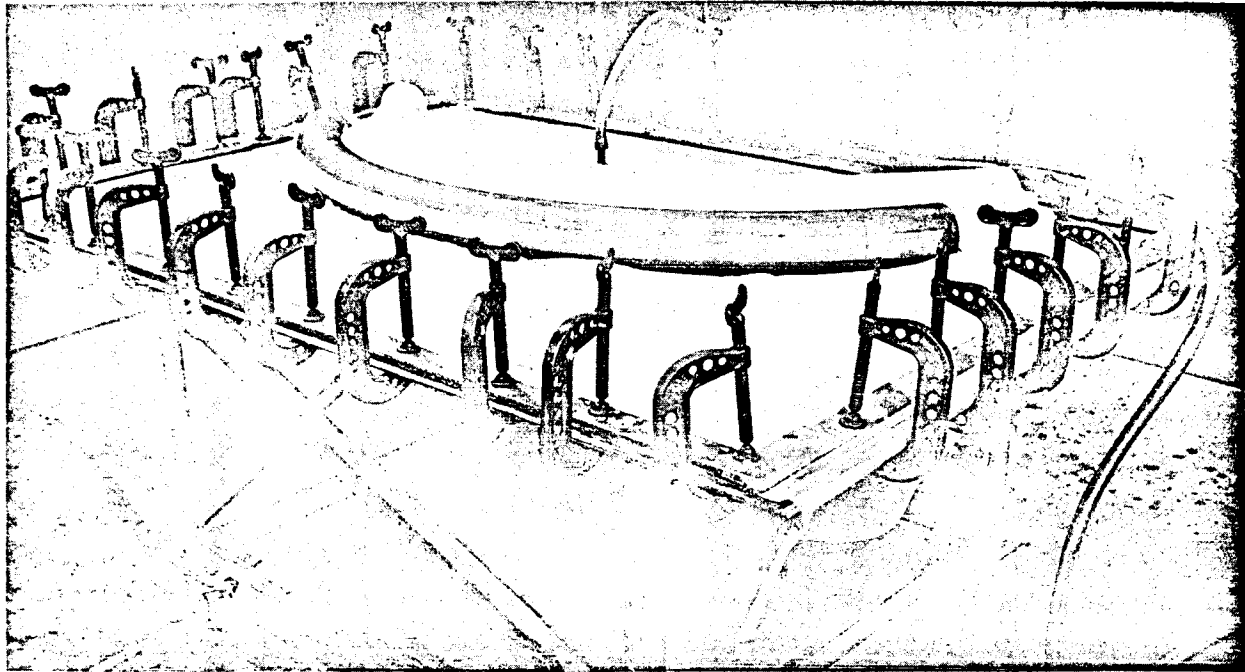
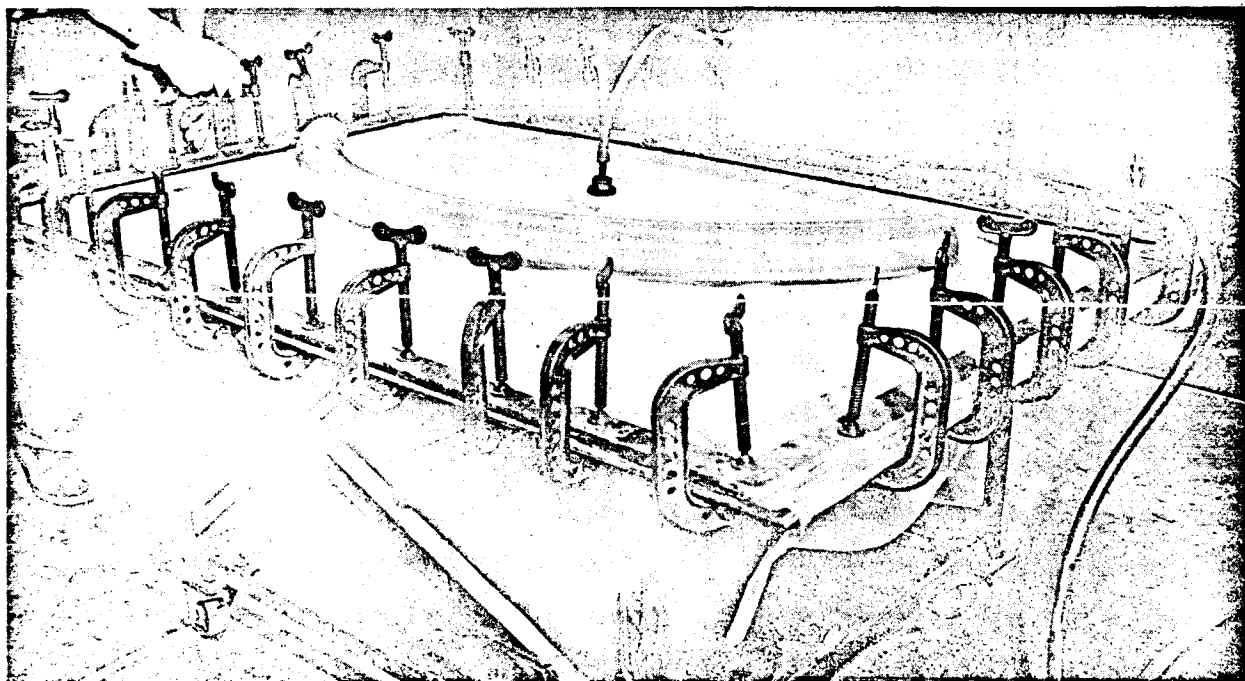


Figure 21 - Deployment Test, Five-Foot-Diameter Model,
Final Configuration



TOOL AND FORMED PART



PART FORMING METHOD

Figure 22 - Tool and Part Forming Method for Torus of Five-Foot-Diameter Deployment Model

One-mil Mylar was laid over the form and sealed to a flat metal plate on which the form was mounted. The Mylar was then slowly vacuum-formed to the tool contour in a 320 F oven for about 15 min after which it was cooled and removed to make the tool available for subsequent pieces.

To assemble the torus, two rough trimmed sections were placed on the form and held in place with magnets and rubber bands. Trim lines were matched to form and both halves butt-trimmed simultaneously on the torus inner and outer peripheral center lines. One-mil Schjeldbond GT300 tape was used to heat-seal the splice. Four 90-deg segments and three end-to-end splices were made on the form. The closing splice was made in the flat. Flow control bulkheads were located in the torus as it was assembled.

(b) Bulkheads

The tool used to make the bulkheads is shown in Figure 23.

A 10-in. square of 0.5-mil Mylar was centered on the form at point A and draped along the sides. The film was then pulled tight in eight places at 45-deg spacing and the excess material trimmed off to make butt splices. The splices were seamed with 0.5-mil GT300 tape and trimmed to line B after which the trimmed-off material was removed. A 0.75-in. -wide GT300 tape was then centered on trim line B and heat sealed to the bulkhead. This made the bulkhead ready for installation in the torus.

The bulkhead was turned inside out to place the tape adhesive outward and replaced on the wood forming tool as shown in Figure 24. The tool with the bulkhead was then inserted and positioned to a predetermined location in the torus. The bulkhead was then heat-sealed to the torus and the wood form removed for the next bulkhead installation.

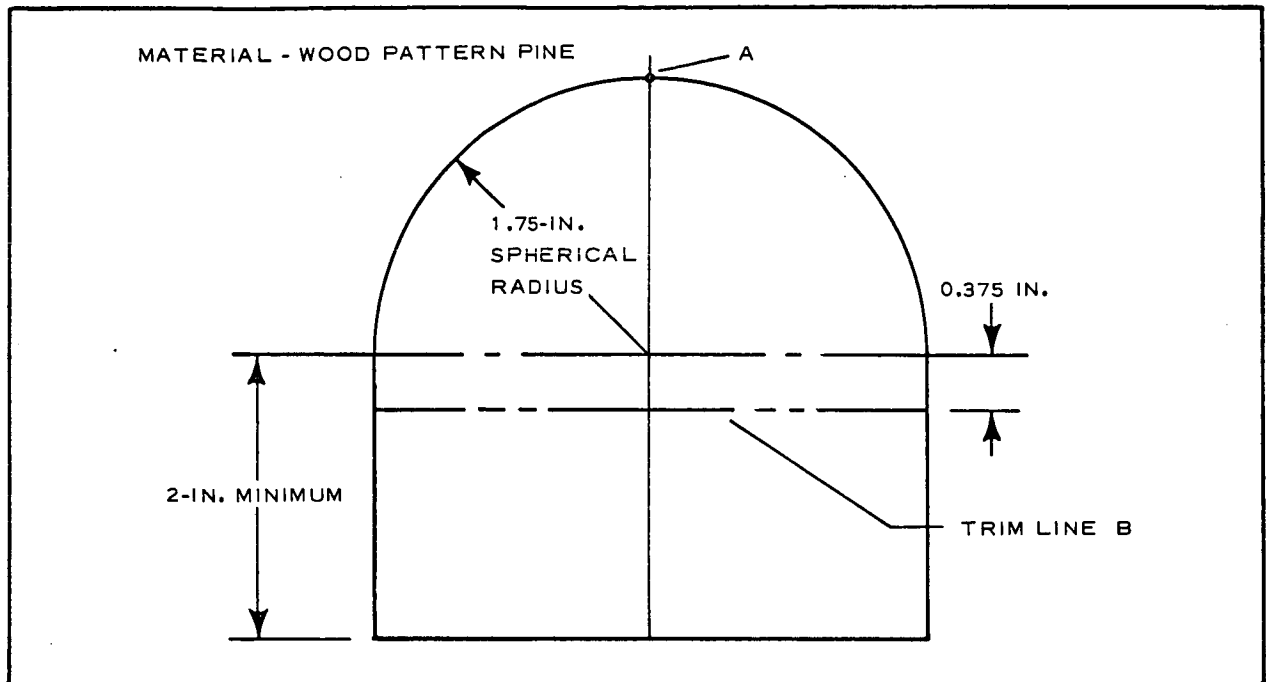


Figure 23 - Bulkhead Forming Tool

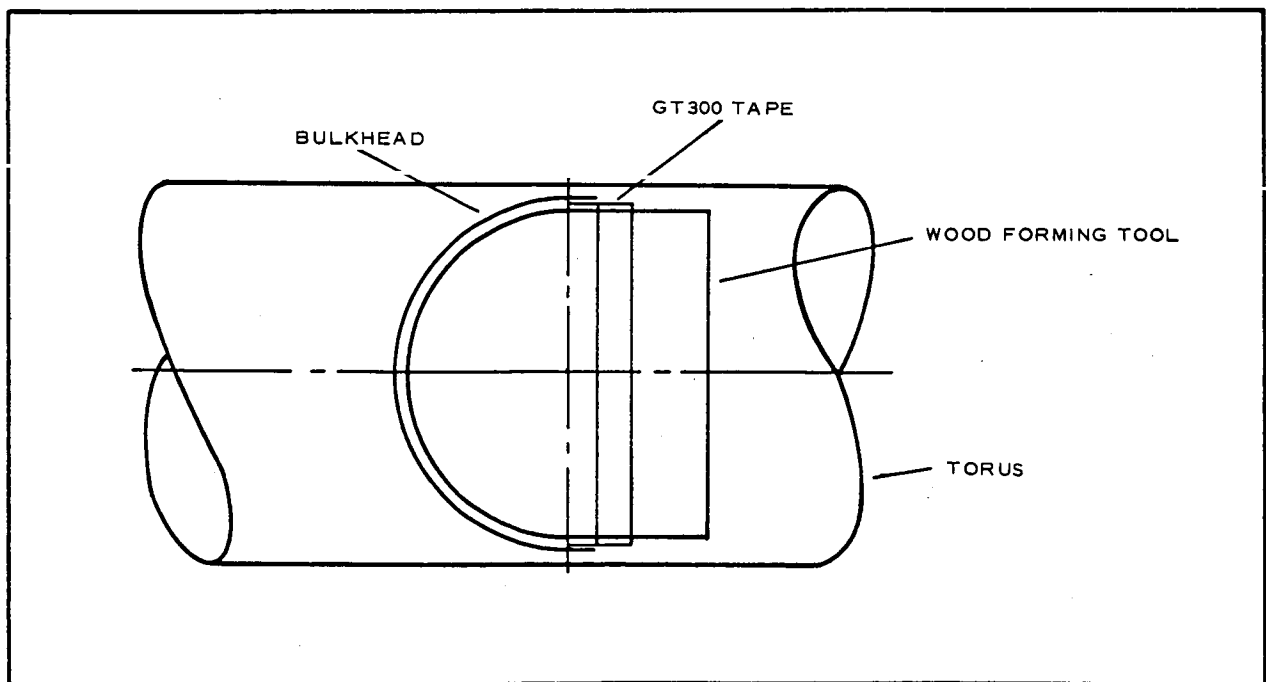


Figure 24 - Bulkhead Installation

(c) Rim-to-Torus Attachment

An assembly fixture was built comprised of a wood wheel with eight sections in the rim, eight spokes, and a hub designed so that all sections could be removed through a 4-in. -diameter hole. This tool also was used to assemble the lens to the torus through the rim. Figure 25 is an exploded diagram of the assembly sequence.

The rim with one hinge in place was wrapped around the wheel. The second hinge was located 0.5 in. from diametrically opposite the first hinge. The location of the second hinge was scribed on the rim, the rim removed, and the second hinge brazed in place. The rim was then replaced on the assembly fixture and GT100 tape tacked to the rim with a heat-sealing iron. The first Mylar tab was positioned and heat-sealed in place. The second GT100 tape was then

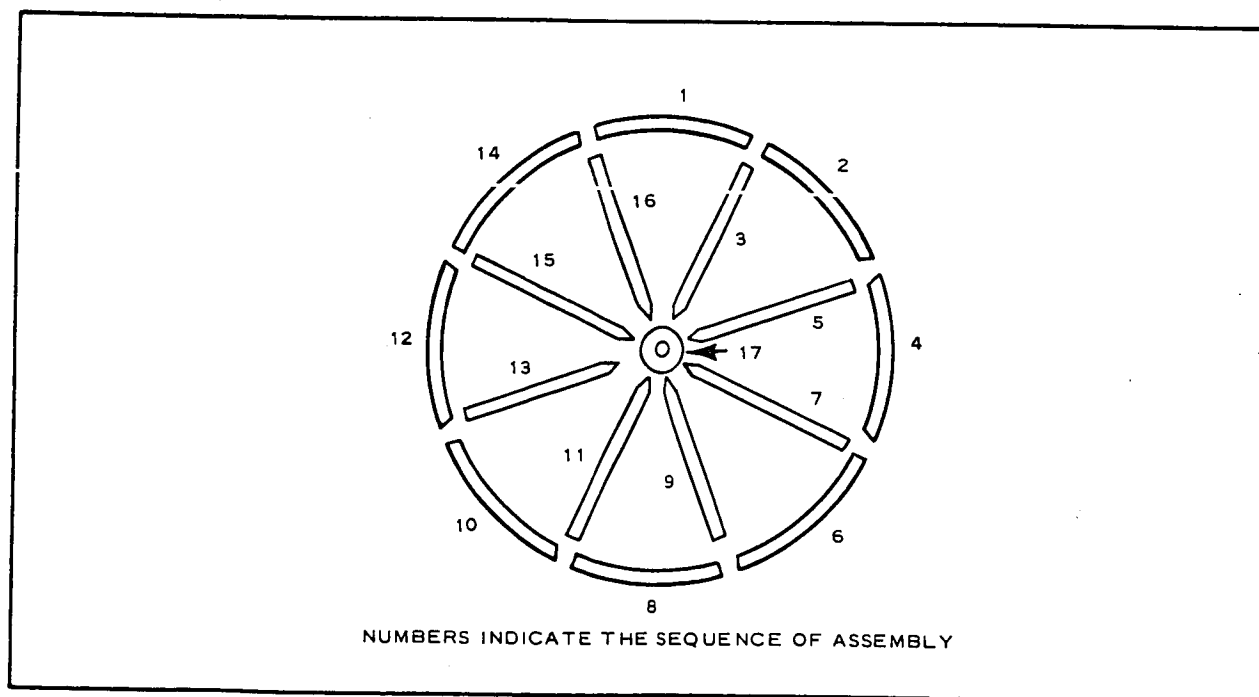


Figure 25 - Rim-to-Torus Assembly Sequence

tacked in place and the second tab positioned and heat sealed. The third GT100 tape was then tacked in place, the GT300 tape placed over it with its adhesive side facing toward the torus, and then heat-sealed in place. The inflated torus then was slipped over the above assembly so that the center of the inside diameter torus seam centered on the assembly. The GT300 tab on one side was heat-sealed to the torus, the unit turned over and the GT300 tab on the opposite side heat-sealed to the torus.

The orientation of hinges with the torus bulkheads is established when the torus is placed over the fixture.

(d) Lens Fabrication and Attachment

The lens was not built to scaled radius for the models used for deployment evaluation. Eight gores comprised each lens, cut and seamed in the flat. The diameter in the flat was 60 in. When assembled to the torus the lens was set for a 59-in. diameter to provide enough fullness to simulate a scaled lens. GT100 tape was used between the torus tab and the lens with 0.5-in. -wide GT300 tape for final tie in. (See Figure 26.)

One model was made for structural evaluation of the torus. In this instance the lens was scaled for an 80-deg angle, using 20 gores for a 46.6-in. lens radius. No bulkheads were used in the torus, and assembly to the torus was the same as in the other models.

The lens for all models was made of 0.5-mil Mylar, seamed with 1-mil GT300 tape.

(e) Inflation Hardware

Special inflation ports were machined from 1.5-in. diameter nylon rod because no commercial lightweight hardware was available.

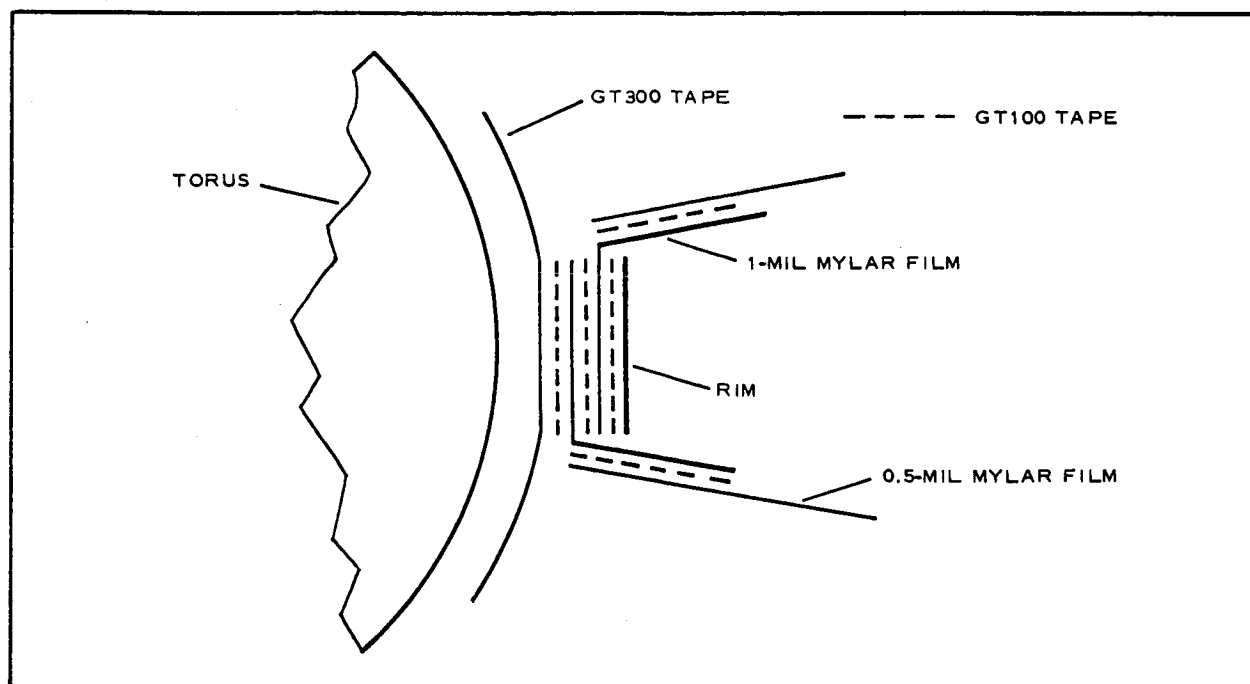


Figure 26 - Lens-to-Torus Attachment

d. Analysis of Model Test Results

The five-foot model testing served as a basis for the configuration design and testing of the 20-ft model. The test program did not optimize packaging and deployment but it did verify that an organized and controlled deployment, which satisfied the critical conditions of the lenticular system, was feasible. As a result of testing the five-foot models several simplifying changes to the manifolding arrangement of the torus were incorporated. These tests showed that further simplification, and hence greater reliability, could be effected by a comprehensive test program.

e. Twenty-Foot-Diameter Deployment Model 20-1

(1) Design

The 20-ft model configuration design was based on dimensional scaling of the design of the full-scale satellite (which subsequently

was changed as part of the final design studies), the model testing work on the 6- and 5-ft models, and the contract requirement for vacuum deployment.

Model 20-1 was made with Mylar lens surfaces. Model 20-2, described later, used wire mesh-photolyzable film for the lens surfaces.

Vacuum deployment dictated torus manifold design and inflation orifice sizes. The model was made initially with manifolding and orifice sizes suitable for the atmospheric deployment that was performed at GAC.

A modified Echo I canister was used as the packaging container.

Figure 27 defines the configuration and materials used for the 20-ft model. The main views of the figure define the configuration for vacuum deployment with an auxiliary view provided to show the configuration for atmospheric deployment. To facilitate ground deployment the tripod boom was provided on one side only.

The importance of controlling the effects of residual air for vacuum deployment has been discussed elsewhere in this report. To obtain a minimum pressure differential between the interior of the canister and the exterior environment the lens and torus were perforated and the interior of the canister arranged to permit the flow of gas to a solenoid-operated valve. The canister was initially pumped down as low as practical and then placed in the vacuum chamber. After vacuum was reached, the solenoid-operated valve was opened and soak time allowed for pressure stabilization.

(2) Fabrication and Tooling

(a) Torus

The torus was made by vacuum-forming 1.5-mil Mylar in

a female mold using techniques that resulted in stretching all areas in the forming process and minimizing the wrinkles and seaming operations.

Figure 28 shows two views of the master model from which the forming mold was made. The trim line for the part is one inch above the mounting plate. The form was made as shown in Figure 29.

Figure 30A shows the mold with necessary glass-cloth bleeder strips in place to assure complete air evacuation between the mold and film. Figure 30B shows the first operation for placing the film on the form. Figure 30C shows the film draped in the form prior to placement of the sealing clamp ring. The film, as draped, is clear of the bottom of the mold by approximately 1.25 in. Figure 30D shows the formed part being cooled prior to removal. The hemispherical ends are used later to make the air flow control bulkheads.

A 320 F oven was used to apply heat. A thermocouple attached to the film in the bottom area, between the mold surface and film, was used to record film temperature. The average film temperature when the vacuum was applied was 220 to 240 F. The vacuum was applied over a three-minute interval, after the film was up to temperature, in an attempt to equalize the amount of stretch throughout the part. When the film came in contact with the mold its temperature fell immediately to the mold temperature, which never exceeded 140 F. The thermocouple on the film confirmed this. The oven cycle for forming took 10 to 12 min.

Figure 30E shows one segment of 1-mil formed Mylar with ends closed and pressurized to 4-in. of water. This was

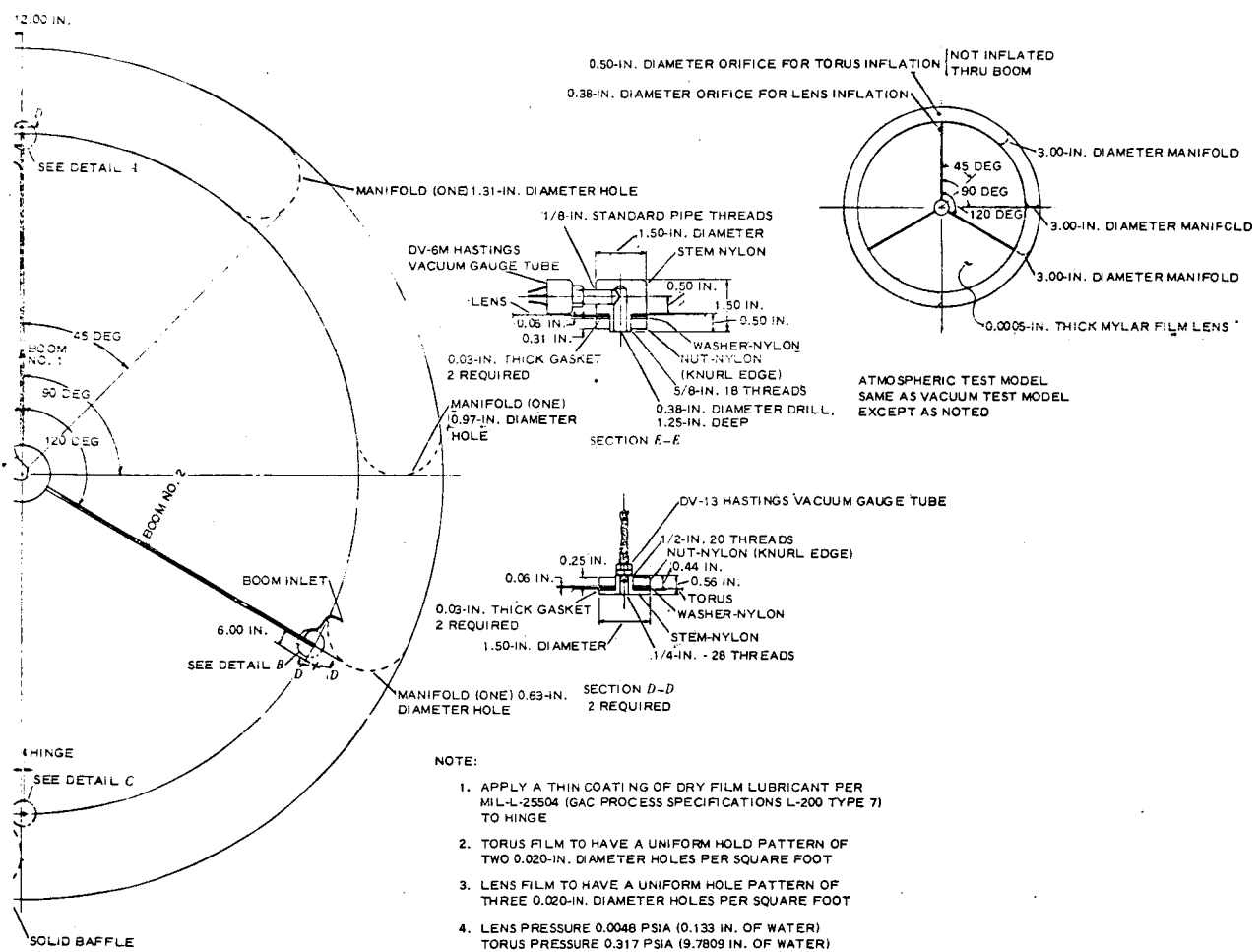
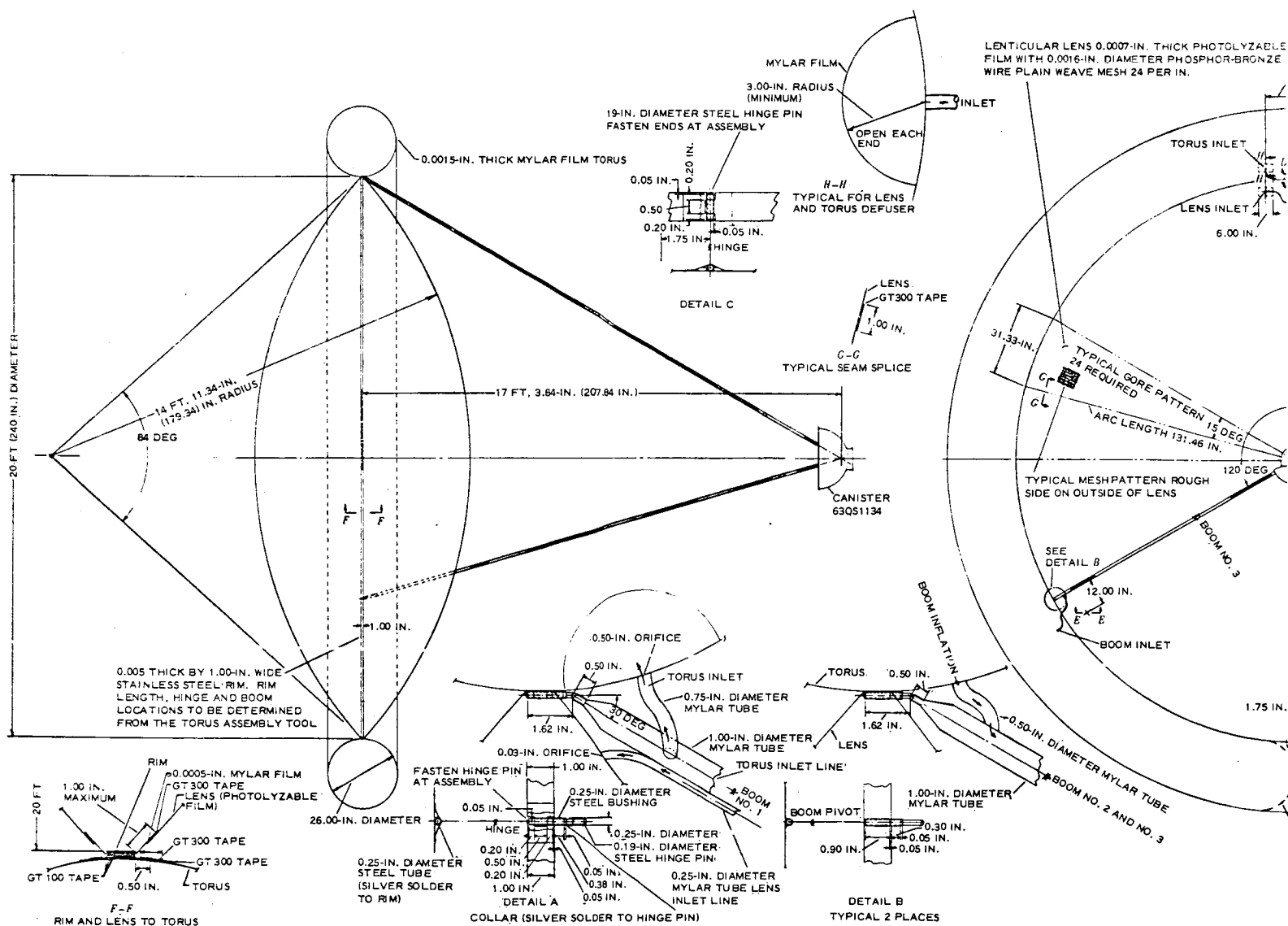
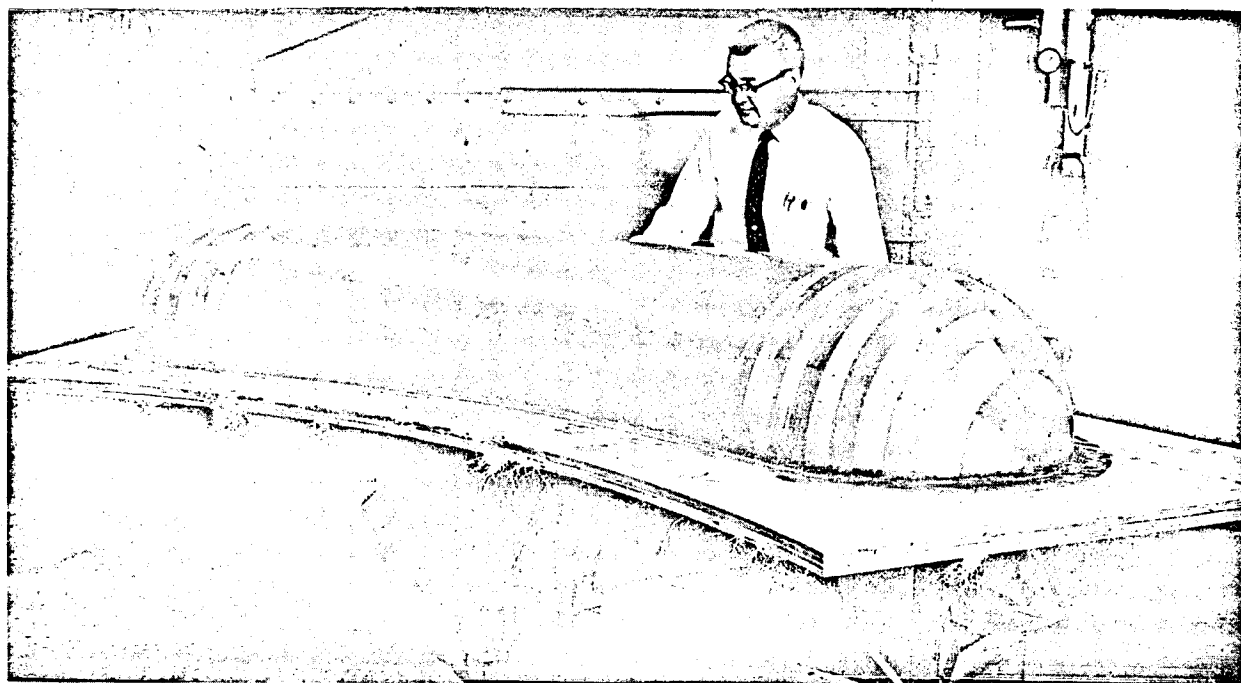
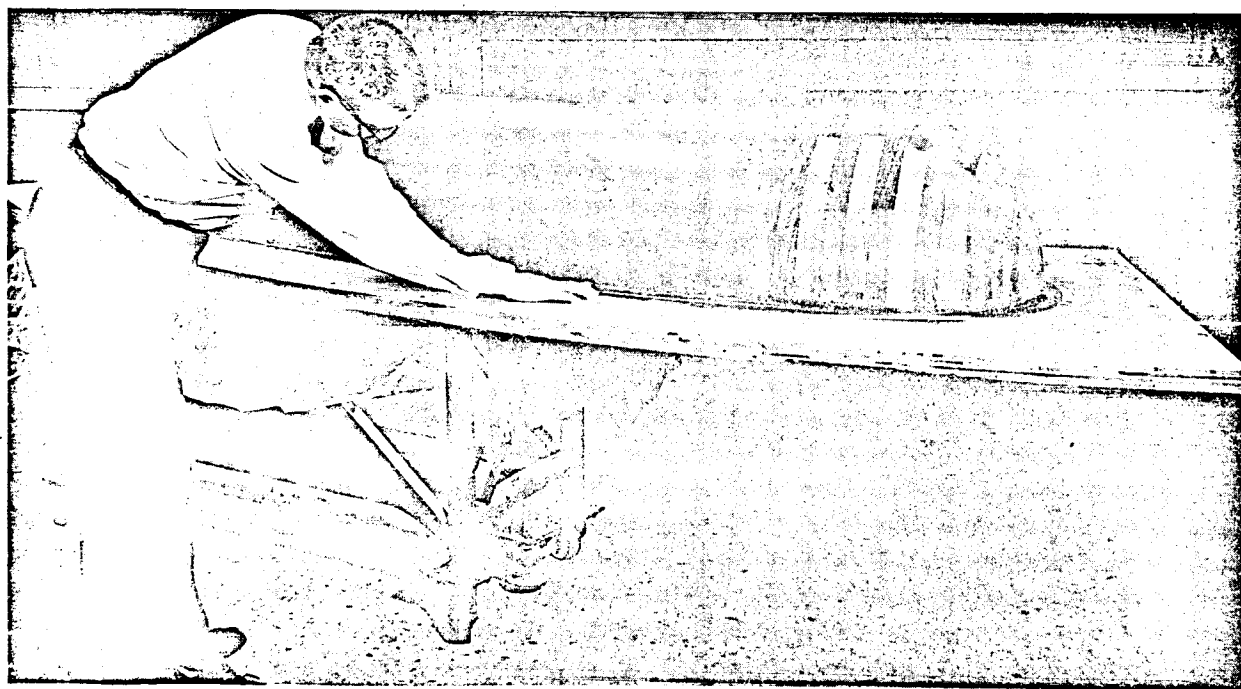


Figure 27 - Twenty-Foot Deployment Model, Lenticular Satellite



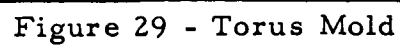


INSIDE



OUTSIDE

Figure 28 - Torus Male Mold Pattern





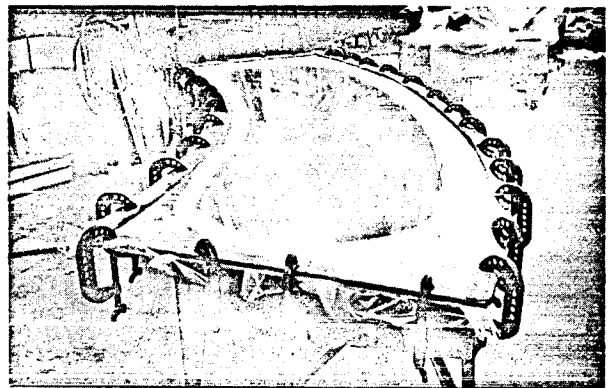
BLEEDER STRIPS IN PLACE



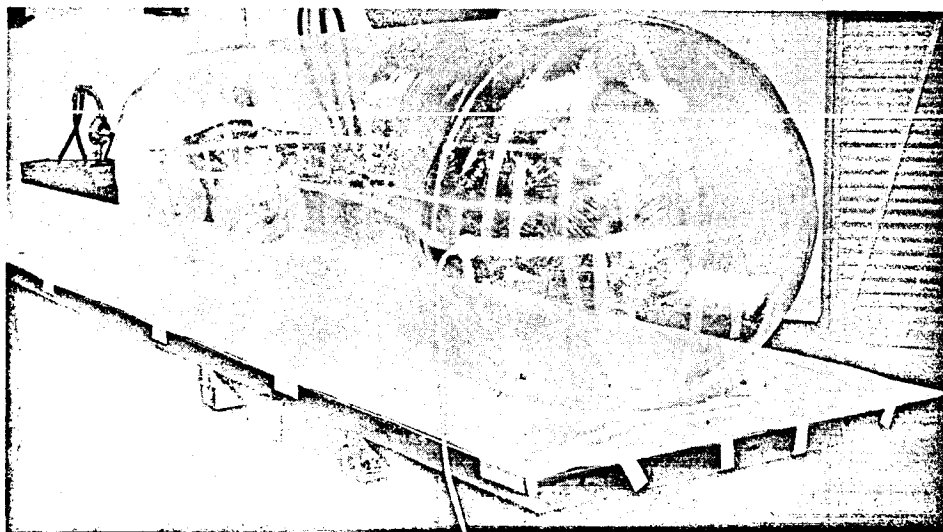
PLACING MYLAR SHEET ON FORM



MYLAR SHEET DRAPED IN FORM



FINAL FORMED SHEET



30-DEG TORUS SEGMENT

Figure 30 - Torus Female Forming Mold and Part Fabrication

done to check the ability of formed sections to retain shape under pressure with the ends free. No problems in this respect were evident with visual inspection.

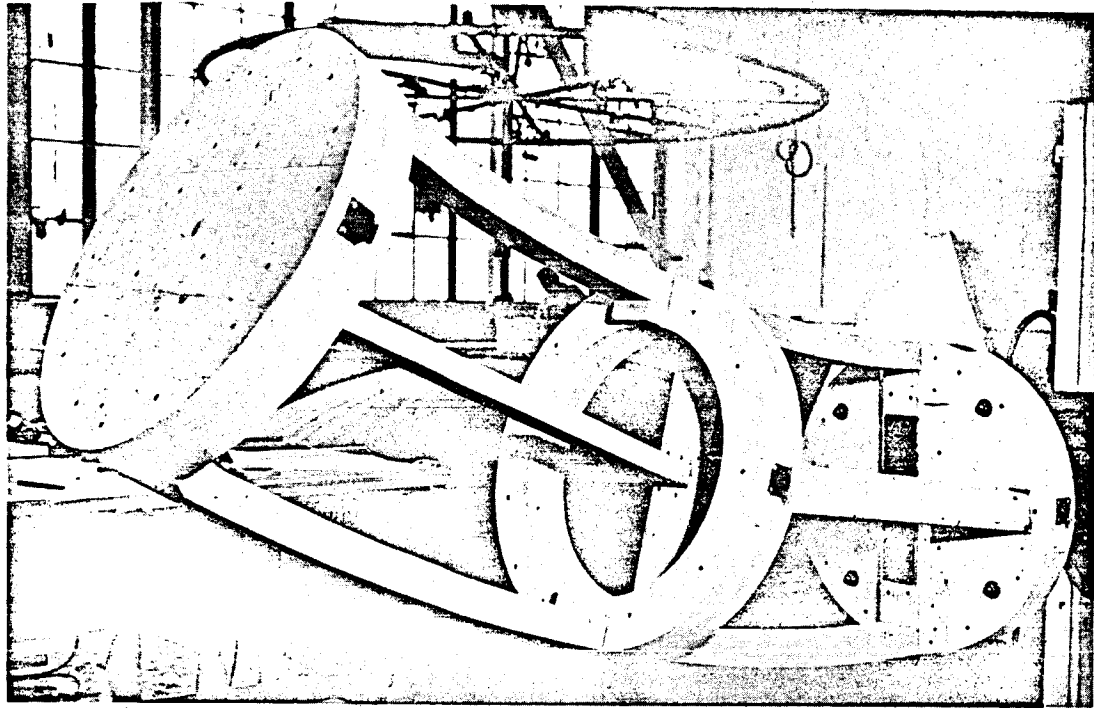
Figure 31 shows the torus assembly tool in two positions. The tool can be turned a full 360 deg and locked in four positions. Figure 32A shows the assembled bulkhead having the GT300 tape applied for bonding to the torus. After this operation the bulkhead was turned inside-out to put the adhesive side of the tape against the torus wall. Figure 32B shows the bulkhead mounted and being heat-sealed in place.

The formed torus sections were mounted on this tool, trimmed to 30-deg segments to lines on the tool, butt-trimmed along the inside and outside diameters, and seamed with heat-sealing tape. When all 30-deg segments had been pre-assembled and numbered the bulkheads were installed in designated places and the segments joined as shown in Figure 32C and D. The last seam was joined on this tool except that only one-half the circumference could be set up at one time. All seam material other than bulkheads was one-in. - wide GT301 tape of 1-mil Mylar.

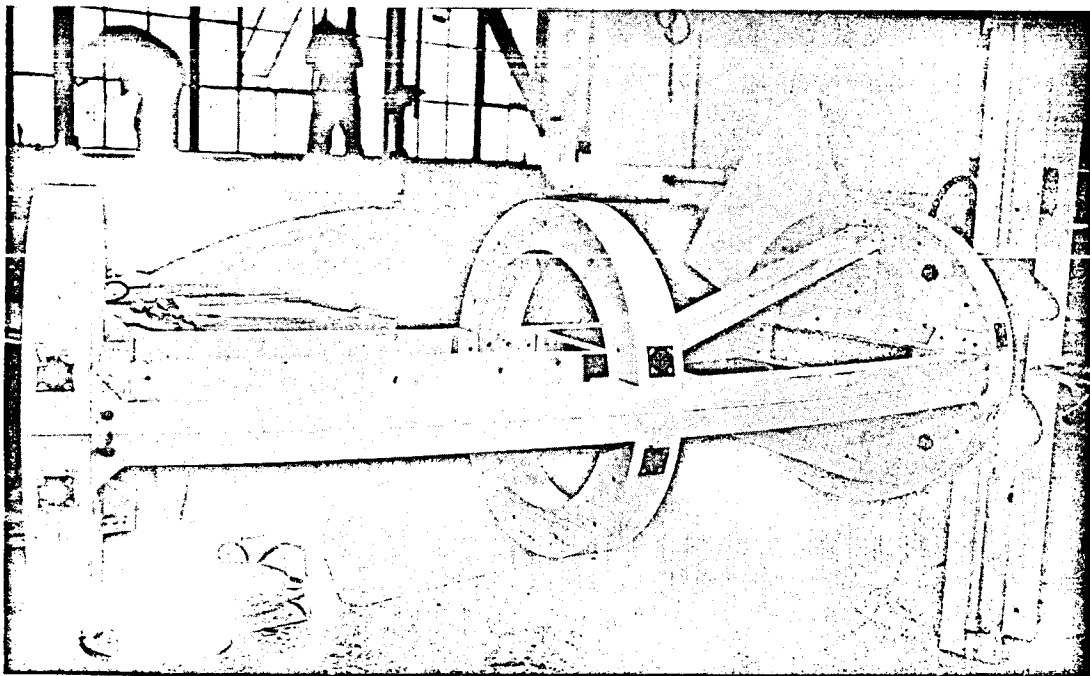
Figure 32E shows the completed torus pressurized for visual inspection of all seams and for any tendency to go out of plane. The assembly passed a visual inspection by responsible personnel.

(b) Lens

To fabricate the lens a form (Figure 33) for a four-gore section was made with a number of metal plates imbedded on both sides of the gore trim line. After placement of the lens material, magnets were placed over these plates to clamp the film to the form, as shown in Figure 34.

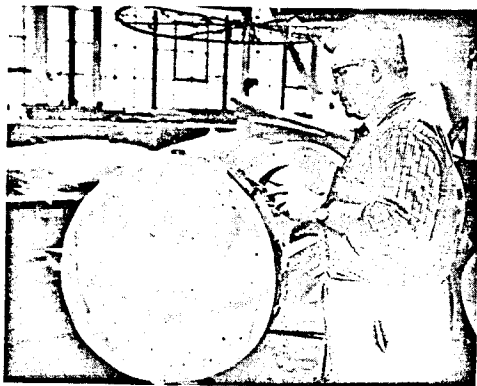


TOP VIEW



SIDE VIEW

Figure 31 - Torus Assembly Tool



ASSEMBLED BULKHEAD



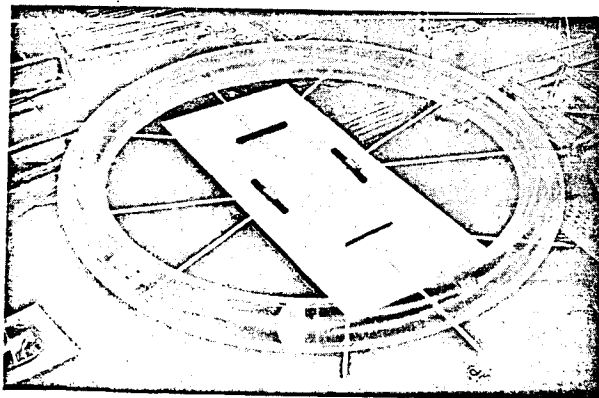
BULKHEAD TORUS ATTACHMENT



SEGMENT ALIGNMENT



SEGMENT SEAMING



COMPLETED TORUS

Figure 32 - Torus Assembly

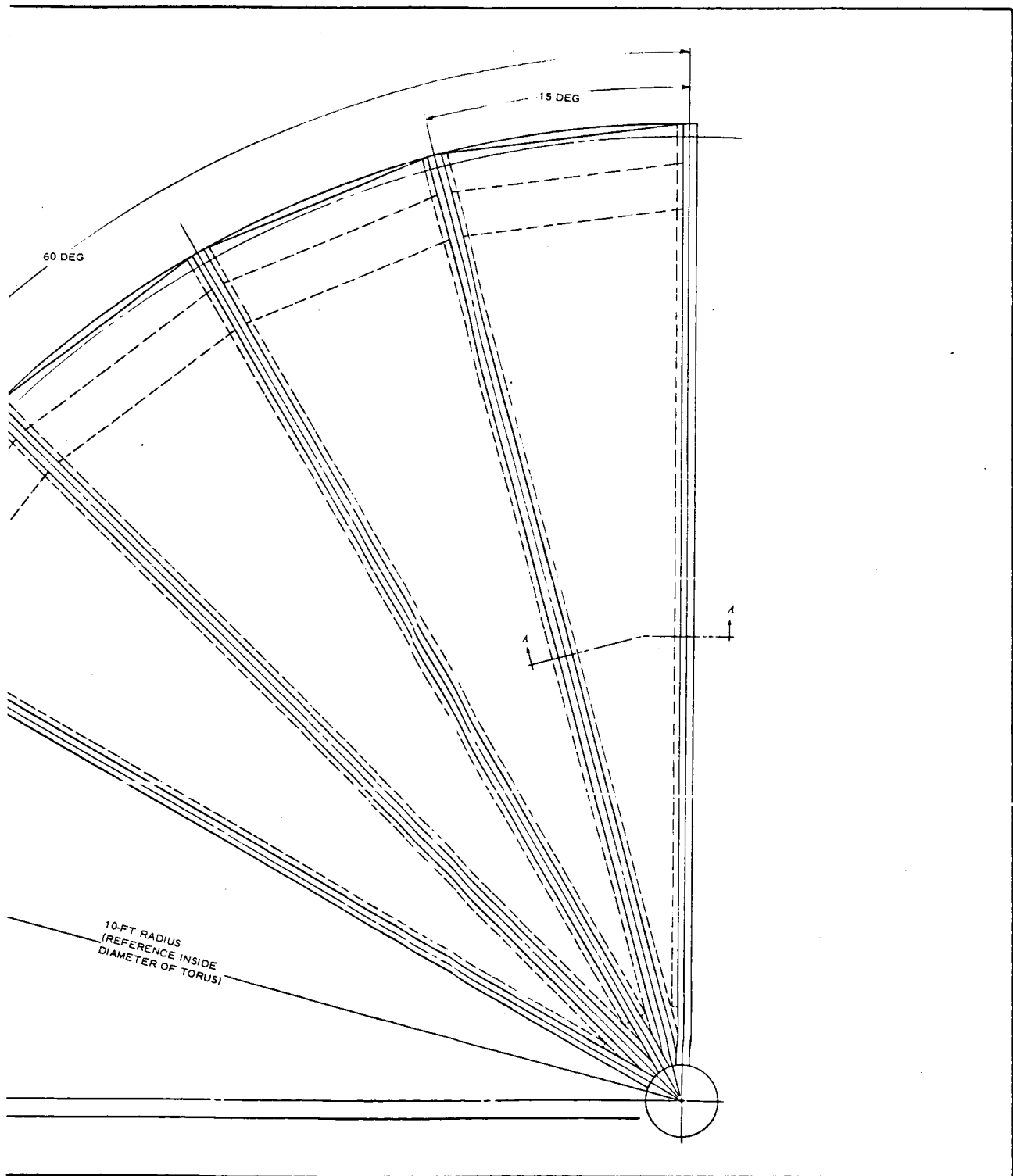


Figure 33 - Form for 20-Ft Deployment Model

FLOOR LINE
2 IN. (APPROXIMATE)
INSIDE DIAMETER OF
TORUS

2-BY 6-IN. FLOOR
TIE, FOUR REQUIRED

14.94-IN.
(179.34-IN.) RADIUS
6 IN. MINIMUM

INSIDE SHAPE OPTIONAL MUST
CLEAR EXISTING MOLD

40.5 IN. (APPROXIMATE) — TOP OF EXISTING
MOLD
0.5 IN. MINIMUM

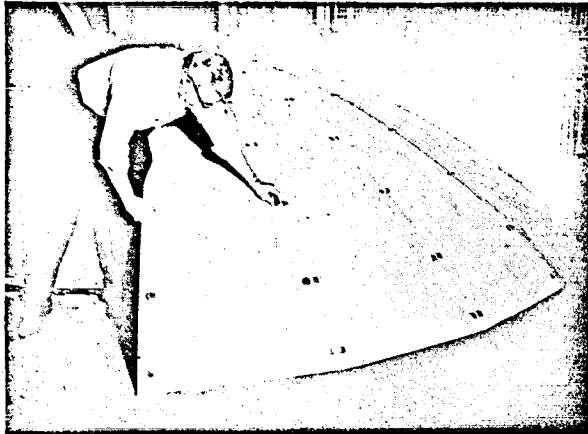
2-BY 8-IN. PATTERN PINE
RIB - FIVE REQUIRED

1/4-IN. PLYWOOD GORES

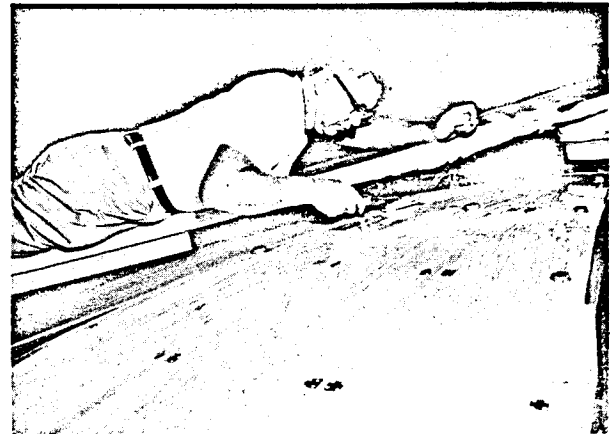
1-BY 2-IN. CLEAT
EIGHT REQUIRED

A-A

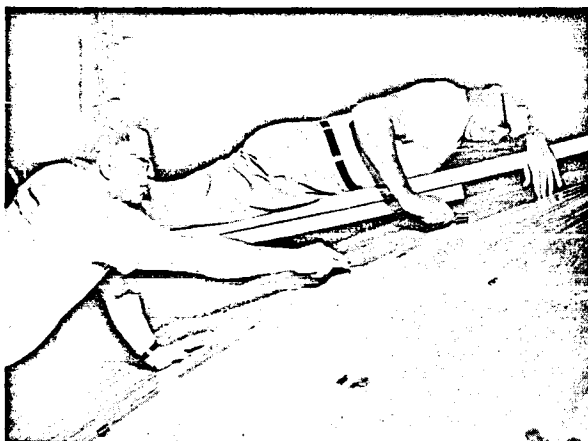
9-IN. DIAMETER
HUB (SOLID)



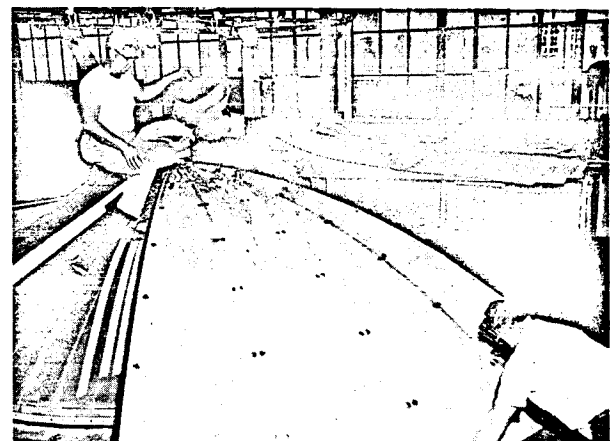
LENS TOOL



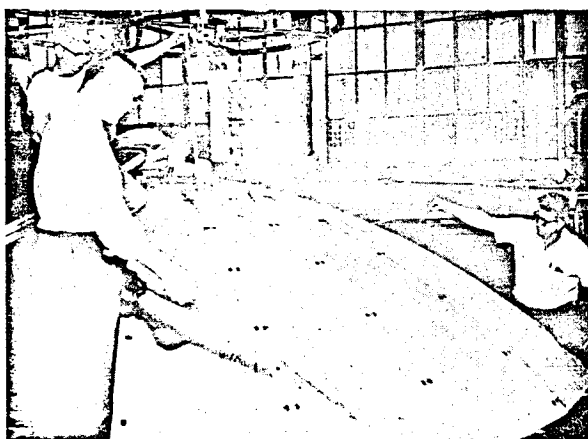
GORE PLACEMENT



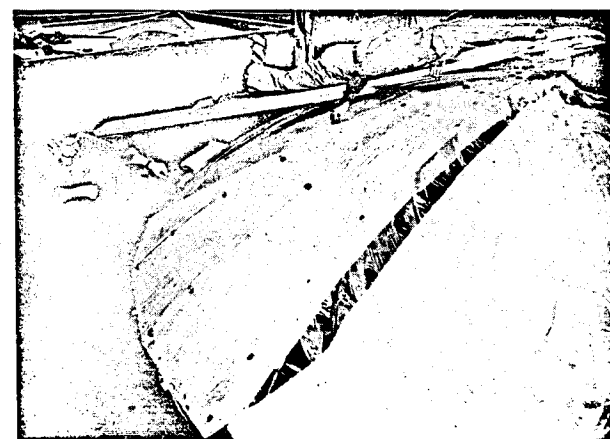
GORE MATCH TRIMMING



LENS SEAMING



FOUR-GORE PANEL



LENS PANEL ASSEMBLY

Figure 34 - Lens Tooling, Fabrication, and Assembly

The gores were precut oversize 0.75 in. on each side and four gores placed on the form at one time. Figure 34C shows the butt trimming of adjacent gores. The trimmed-off material was removed and the seam made by first tacking the tape in place followed by a finish seaming operation. The seam material was 0.75-in. wide GT300 tape of 1-mil Mylar.

When a four-gore segment was completed, the assembly was removed from the form and carefully folded and stored. For a complete model, 12 such assemblies were made. Figure 34E shows a four-gore assembly being removed. When the four-gore assemblies were complete, two were replaced on the form, with two gores of each adjacent to the mating line supported and realigned to orientation marks on the form and on the segments. The attachment seam was then trimmed and heat-sealed, as previously described.

This was continued until six segments of four gores each had been joined into one side of the lens. Figure 34F shows the tape application on the closing seam of one lens. This assembly was again carefully folded and stored, ready for use.

(3) Assembly and Checkout

A tool (Figure 35) was built to perform the assembly of the metal rim to the torus and of the lens to the torus. The design was based primarily on the anticipated need for removal through a lens cap opening 9 in. in diameter. This tool was used to establish the rim diameter, the location of the hinges, and the boom pins. It also served as a measuring device for checking the torus inside diameter. Figure 36A shows the placement of the last peripheral segment in the tool. Figure 36B shows the installation of the fish cords for removal of parts after the model assembly was complete.

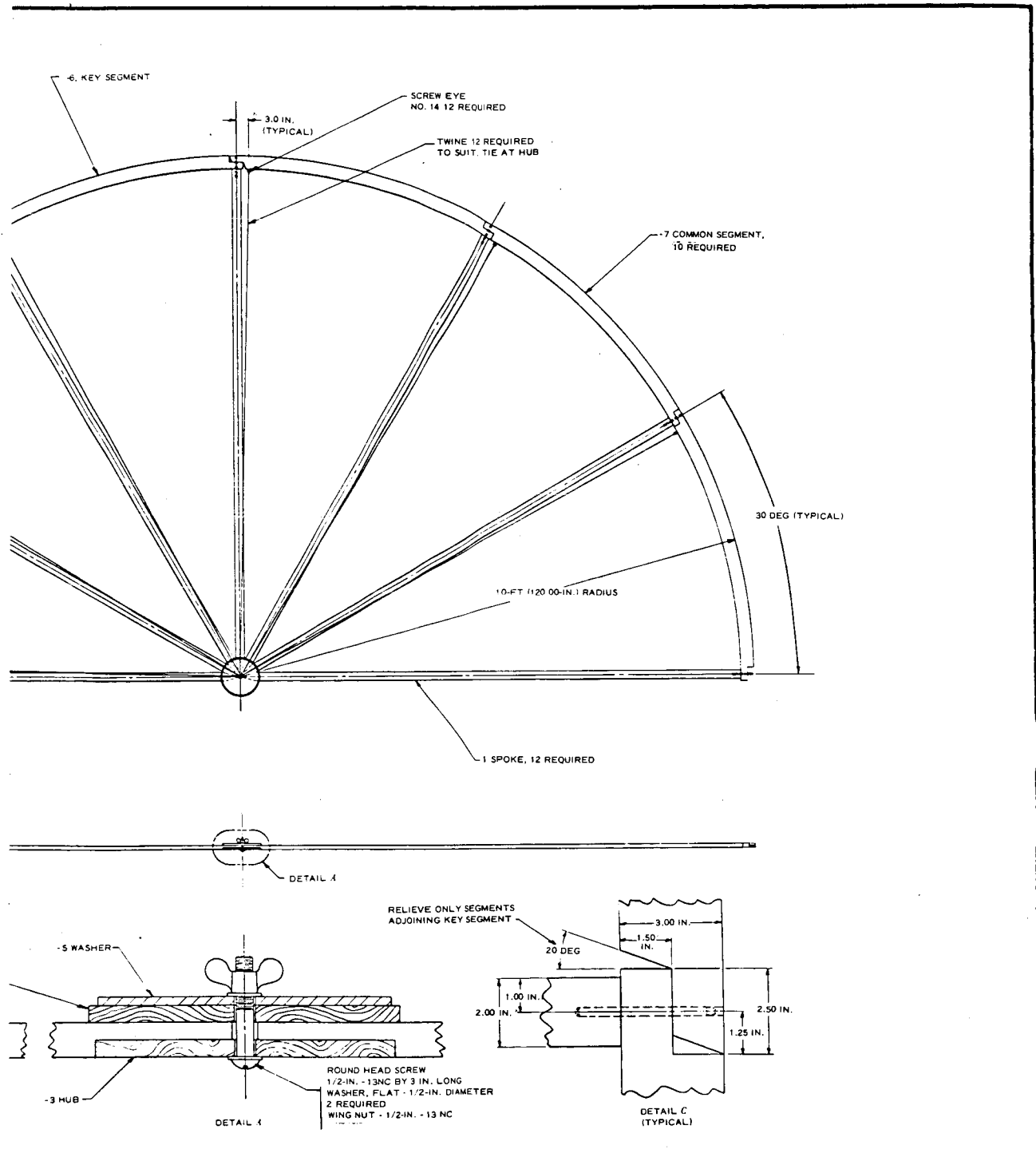
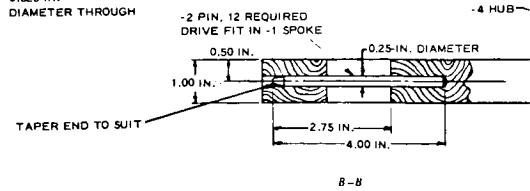
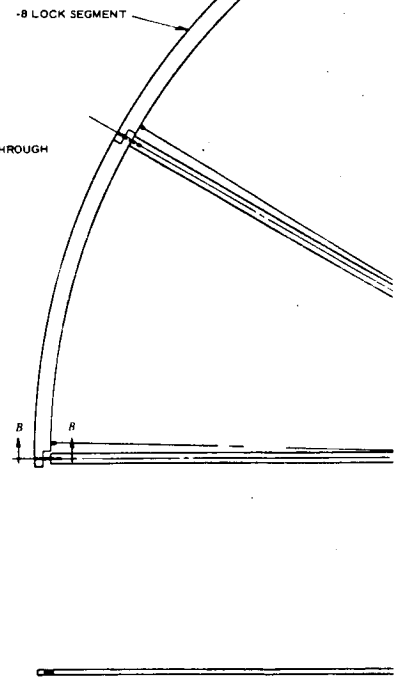
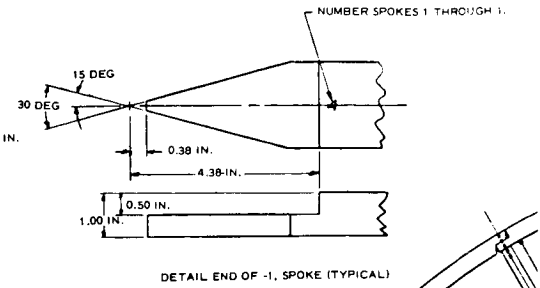
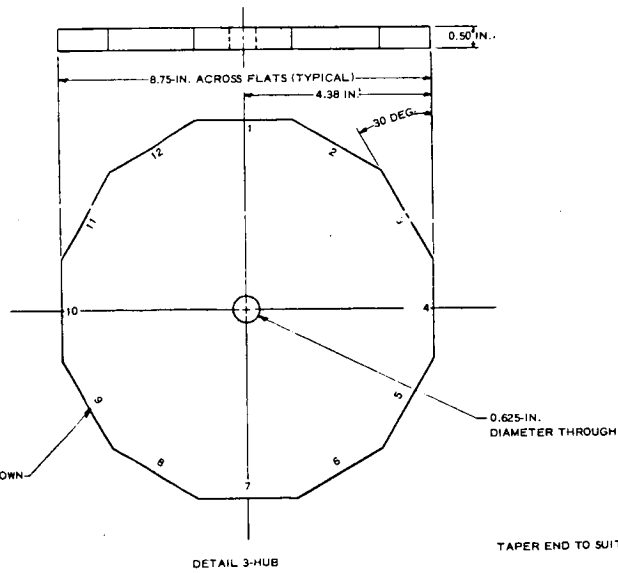
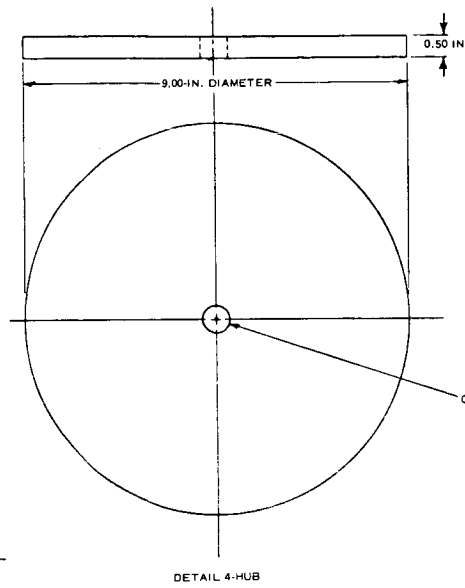
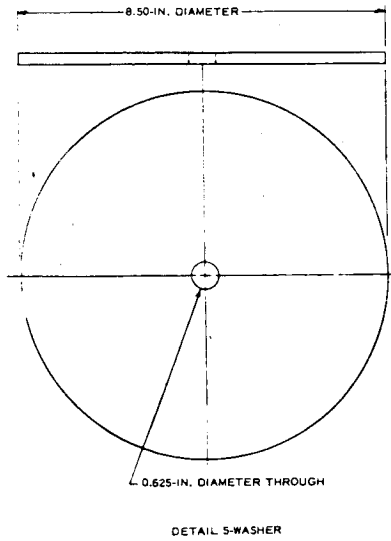
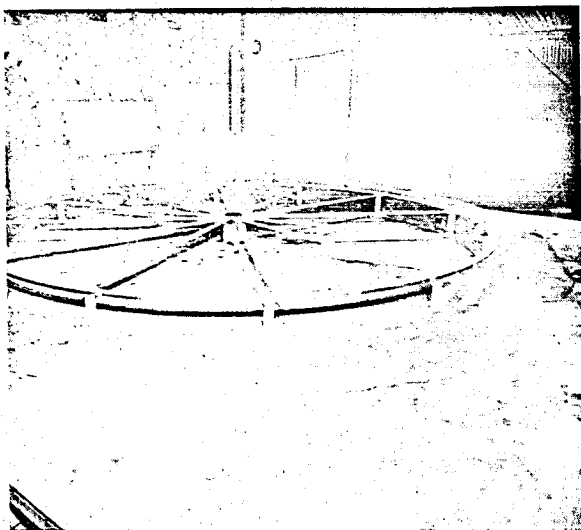
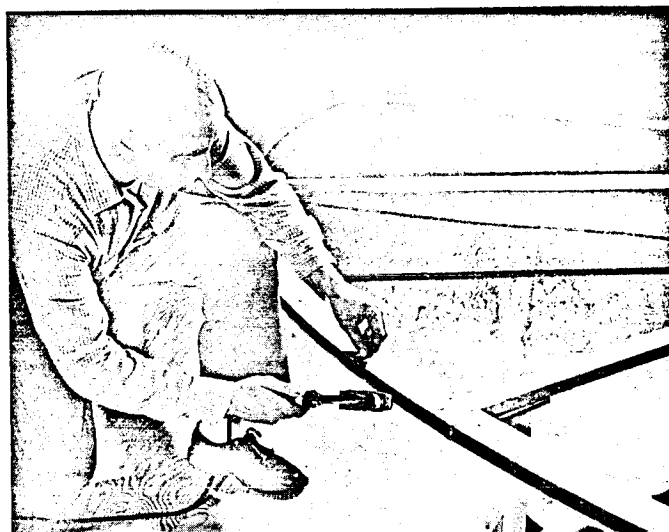


Figure 35 - Support Frame Assembly, Collapsible
20-Ft Torus and Lens Fabrication





METAL RIM ON TOOL



MYLAR TABS ON METAL RIM

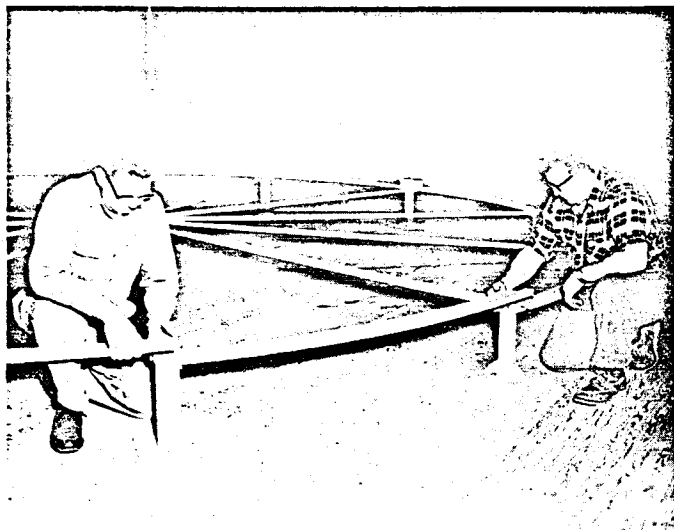


TORUS ATTACHMENT TO RIM

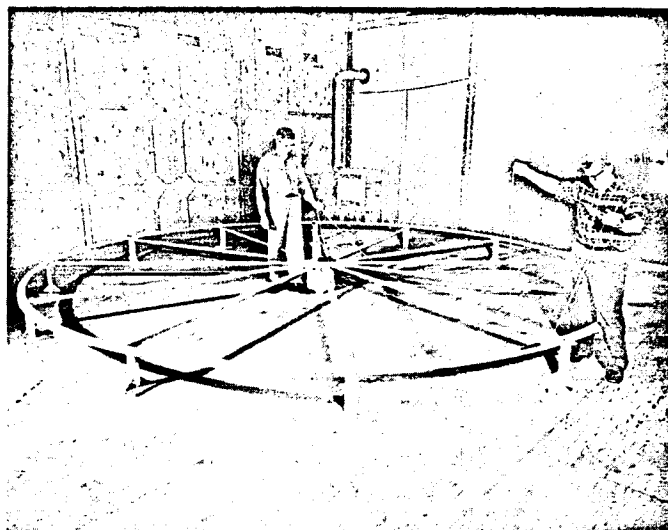


INSTALLING REINFORCING TAPE

Figure 36 - Model Satellite Assembly



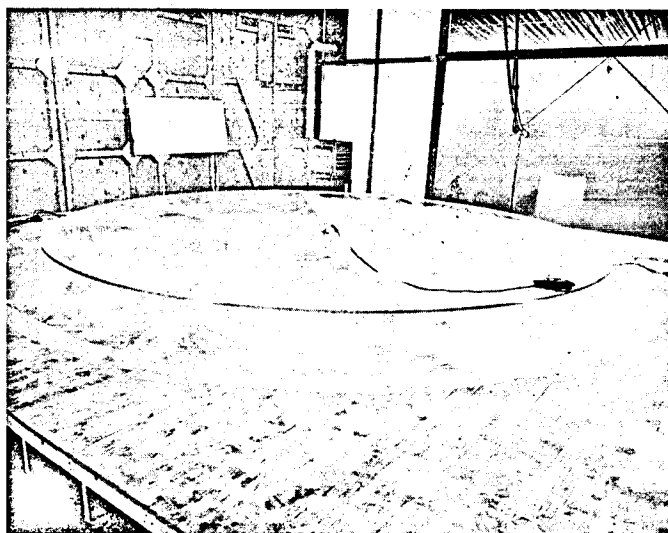
ASSEMBLY TOOL



ASSEMBLY TOOL REMOVAL SYSTEM



LENS CAP TO RIM



LENS ATTACHED TO RIM, TORUS IN POSITION

The first step in the assembly was to mount the rim section with only one hinge installed on the rim tool. The location of the second hinge and of the boom pins was marked on the rim, the rim removed and finishing operations completed. The rim was then replaced on the tool and the torus positioned and inflated to check its fit. Figure 36C shows the metal rim in place on the tool and the torus in position, ready for fit checkout. A section of torus can be added or removed, as required, to make a satisfactory fit. On the first torus (Model 20-1), it was necessary to remove one inch of torus circumference to accomplish what was judged to be a good match.

The next step was to apply the tie-in tabs of 1-mil Mylar to the rim. Figure 37 is a schematic diagram of the arrangement used.

One-inch wide GT100 tape (2.5-mil of resin without a backing material) was tacked to the metal rim. A 2.5-in. -wide strip of 1-mil Mylar film was then heat-sealed to the rim. The tabs were formed by heat-setting a crease at the edge of the rim over the entire rim periphery.

A second GT100 tape was tacked to the assembly and a 2-in. -wide GT300 tape heat-sealed in place. The GT300 tape was 1-mil Mylar with a 0.5-mil of resin on one side. In this case the resin side was placed as shown in Figure 37. To provide a wider seam area for attachment to the torus 7-in. -wide GT300 tape was applied as shown. This tape attachment was made using 3-in. -wide GT300 to avoid the extra operation. This entire operation was performed with the torus deflated and out of the way as shown in Figure 36C. Figure 36D shows the heat-sealing operation during the application of the 2.5-in. -wide tab element.

The next step was to attach the first lens to the tab. GT100 tape, 0.75-in. -wide, was tacked to the tab, one edge being aligned with the rim edge. The lens was positioned and tacked in place,

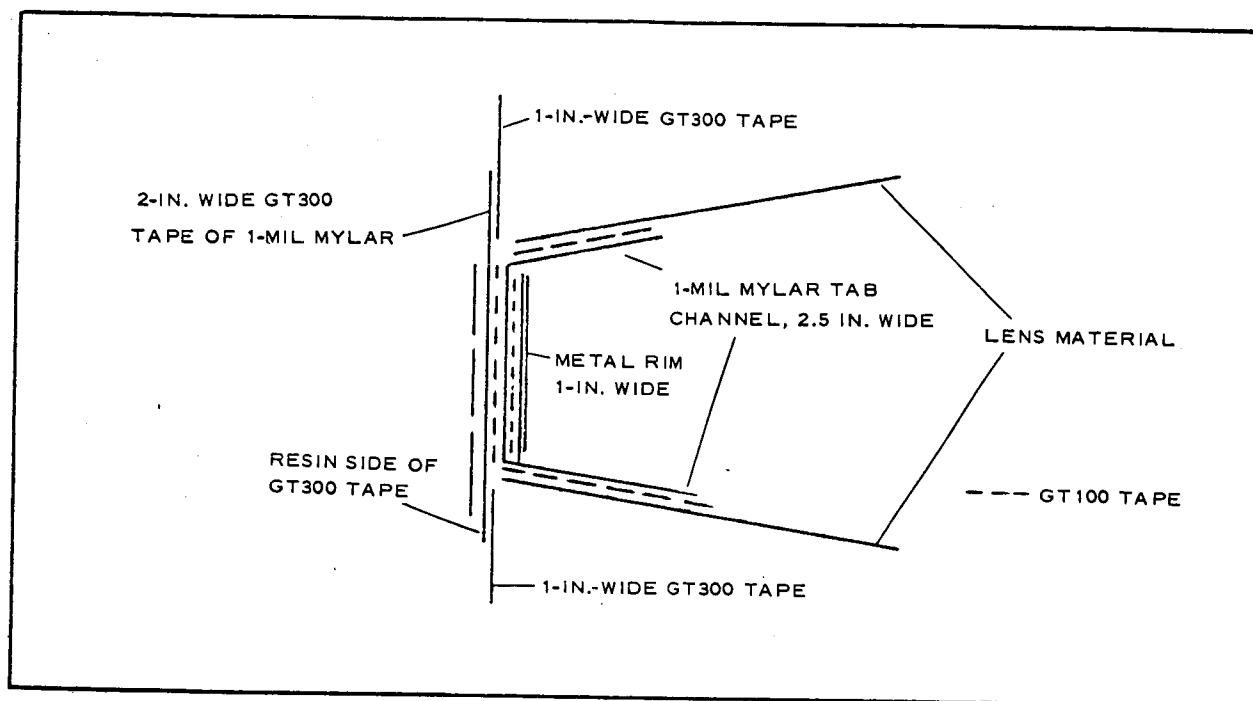
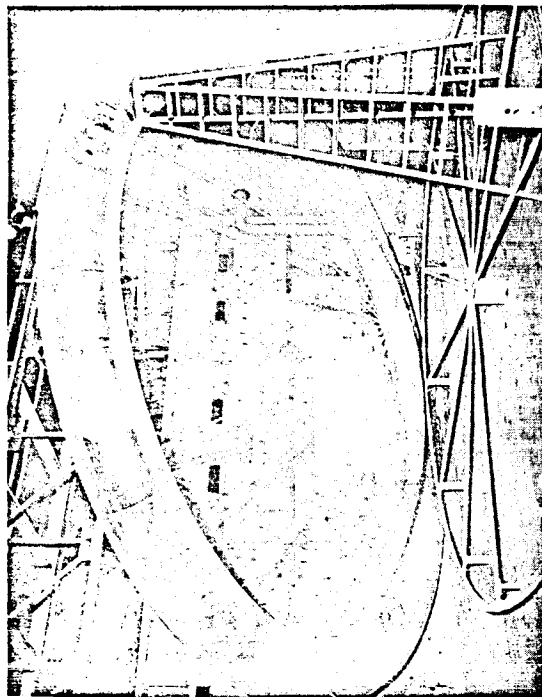


Figure 37 - Schematic of Rim-Tape Arrangement

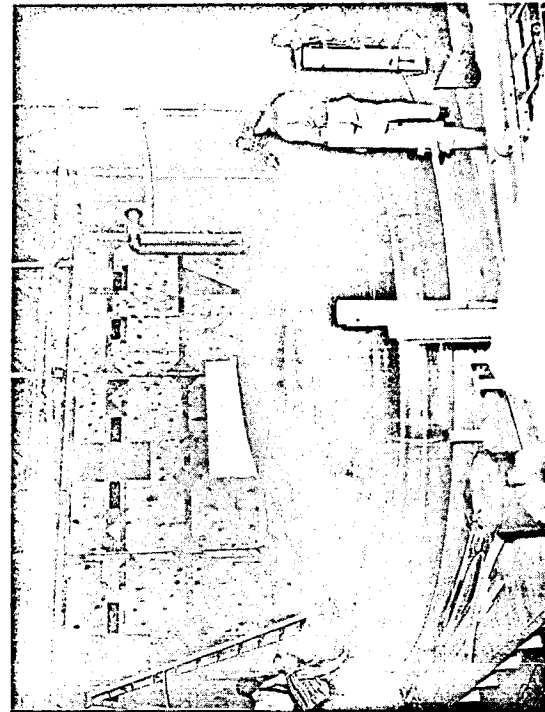
followed by the heat-sealing operation. Figure 36E shows the heat-sealing operation being performed. There are 12 segments in the torus and 24 gores in the lens. Orientation of the lens to the torus was set up on the basis of every other gore seam being lined up with a torus seam.

When the first lens attachment operation was complete the torus was attached on one side. This operation was introduced at this point so that the inflated torus could be used as a rigid structure for the turn-over operation. Figure 36F shows the placement of the torus prior to inflation; Figure 36G shows the heat-sealing operation of attachment to the torus, and Figure 36H shows the heat-sealing of the 1-in. -wide reinforcing GT300 tape shown in Figure 37. The reinforcing tape was applied at this stage because the operation was easier to perform under these conditions.

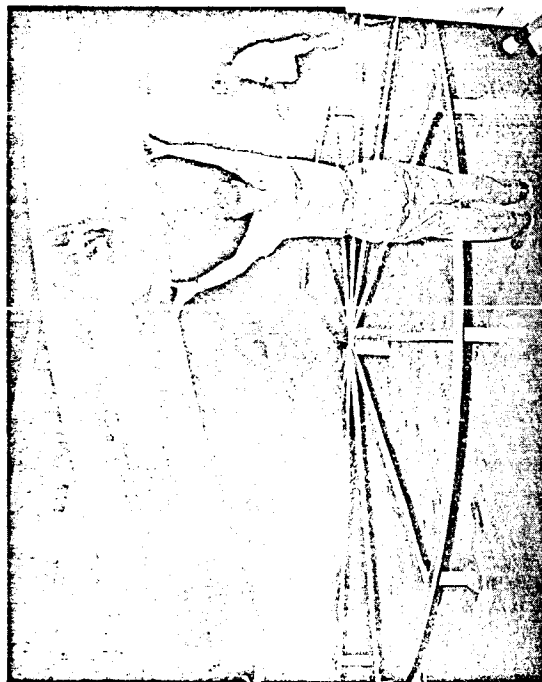
The assembly was now ready for turn over to install the second lens (See Figure 38). Figure 38A shows the first stage of this



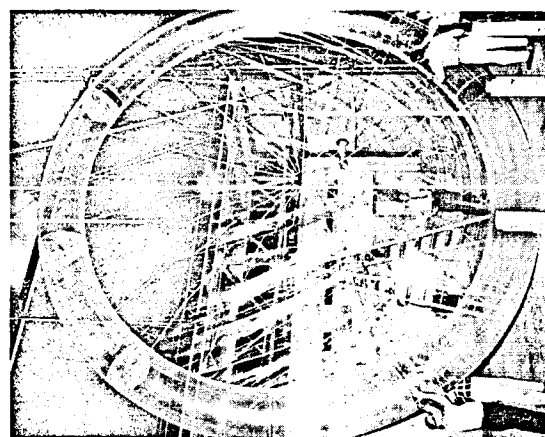
STAGE 2



STAGE 4 (COMPLETE)



STAGE 1



STAGE 3

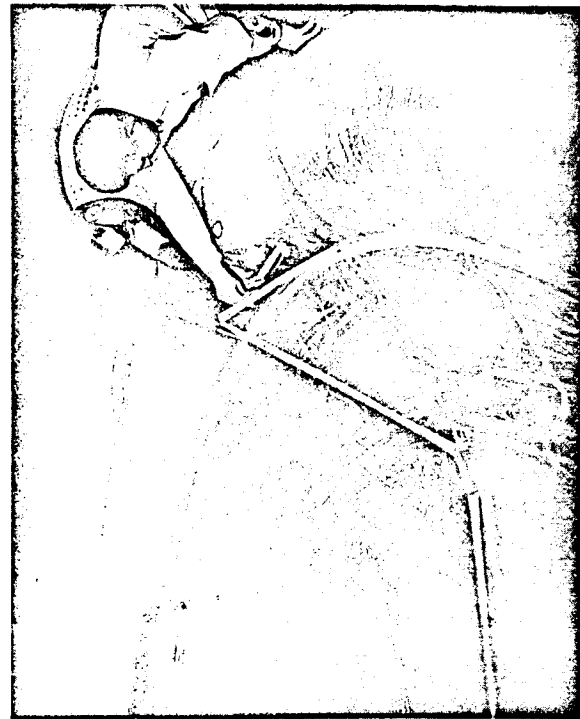
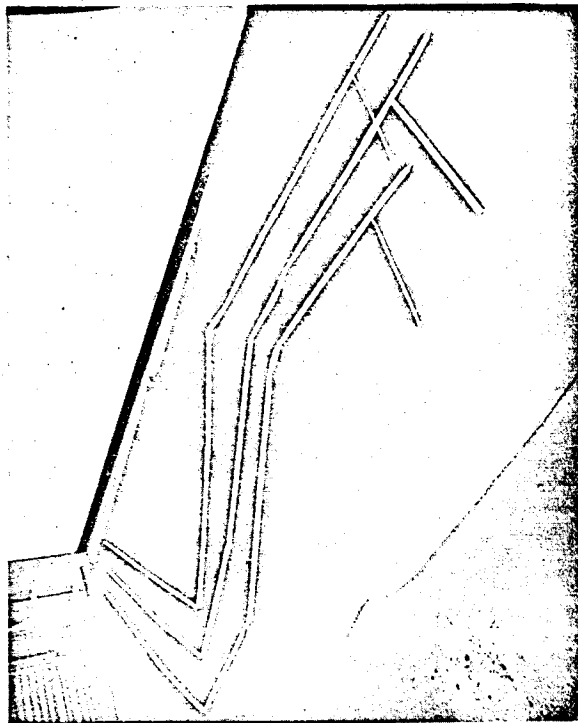
Figure 38 - Model Fabrication, Turn-Over Operation

operation. It was anticipated that the assembly tool would be locked in place firmly enough to stay with the part. However, the weight of the tool was too great and there was separation as shown in Figure 38. Figure 38B shows the second stage of the turnover.

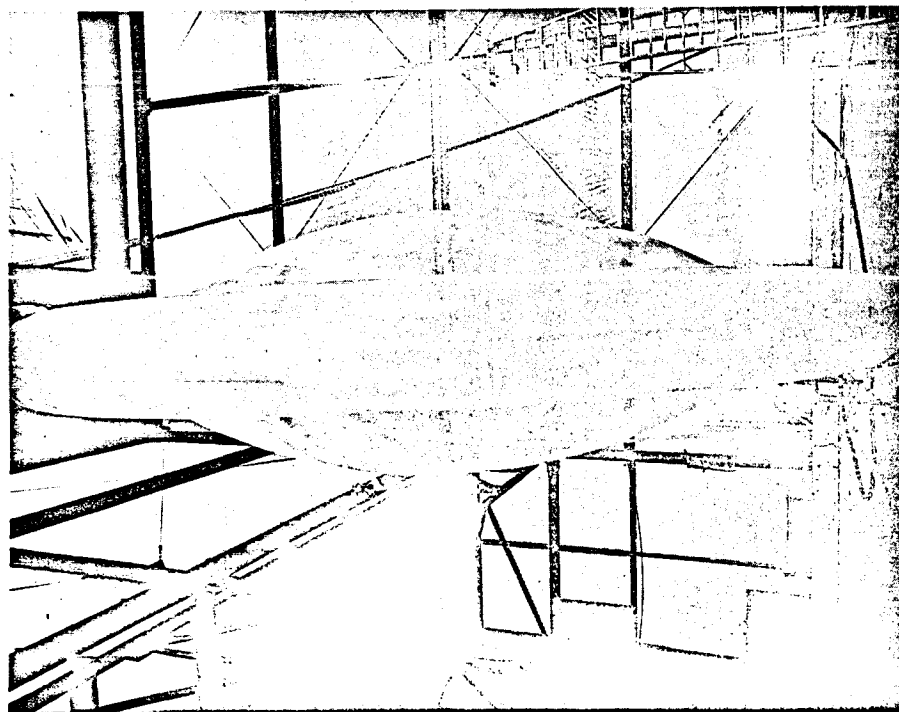
At this point the assembly tool was removed and set aside in the disassembled state. Figure 38C shows the third stage of the turn-over operation, and Figure 38D shows the last stage. The high billowing of the lens was due to air trapped between the floor and the lens.

Figure 39A is a view of the model inflated, with both lenses and the booms in place. Figure 39B shows the 1-in. -diameter booms fabricated from 1.5-mil Mylar film with air feed umbilicals that attach to the torus and lens. Burst of three 36-in. -long boom test specimens at 45-psi test pressure was equivalent to a factor greater than 100. Rupture did not always occur at the seam. Figure 39C shows the attachment of the booms to the boom pins on the rim. A polyurethane resin, GTR D1569-F838, was used. The resin, which is a two-part system, was catalyzed and painted on the pins and allowed to dry tack-free. The Mylar tube was slid into place and heat-sealed at 250 F. To attach the umbilicals to the torus, flanged Mylar fittings were formed and attached by heat-sealing methods, using a combination of GT100 and GT300 tapes. The booms were bonded to the canister by the same procedures that were used for bonding to the boom pins. Figure 39D shows the attachment of the umbilicals to the torus.

The Model 20-1 lens and the torus were perforated with 0.020-in. -diameter holes; three per square foot for the lens and two per square foot for the torus. The perforation was accomplished using a soldering iron modified by brazing a needle to the tip and insulating the assembly to guide the heat to the needle tip.



AIR-FEED LINE ATTACHMENT



COMPLETED MODEL (20-1)



BOOM ATTACHMENT TO RIM

Figure 39 - Boom and Air-Feed Line Attachment

Approximately 3/8 in. of the needle tip was left bare. Figure 40 shows the perforating operation in process. A paper pattern was used, as shown, to permit a fair degree of control of hole pattern. The assembly was in the inflated condition while the perforating operation was being performed. As more and more holes were completed the air feed had to be increased to keep the model inflated. This fact attested to successful perforation. This operation was performed after the atmospheric deployment tests on Model 20-1.

The model was deflated completely, using a vacuum cleaner for air removal, and then inflated to check out inflation sequence. Before the model was shipped the bulkheads were modified by reducing the hole sizes. To make this modification a cut through the torus was made and later repaired.

(4) Packaging

As previously noted, optimum packaging was not attempted. The objective was to package the satellite so that organized deployment of the torus, to prevent local failures (buckling) of the metal rim cross section, would be effected, free from any locking and subsequent tearing of the films.

The packaging arrangement developed through the five-foot model testing and successfully used for the GAC tests on the 20-ft model is shown in Figure 41. A 16-mm film strip is available that shows actual packaging.

To start the packaging operation, both the torus and lens were evacuated and laid flat on the floor. The torus was made into a C configuration with the two hinges in the metal rim and the metal rims lined up. A 10-in. -diameter aluminum drum 48-in. long was positioned at the end of the C opposite the inflation ports. The assembly then was rolled so that the half section of the torus containing the bulkheads was on the inside of the pack.

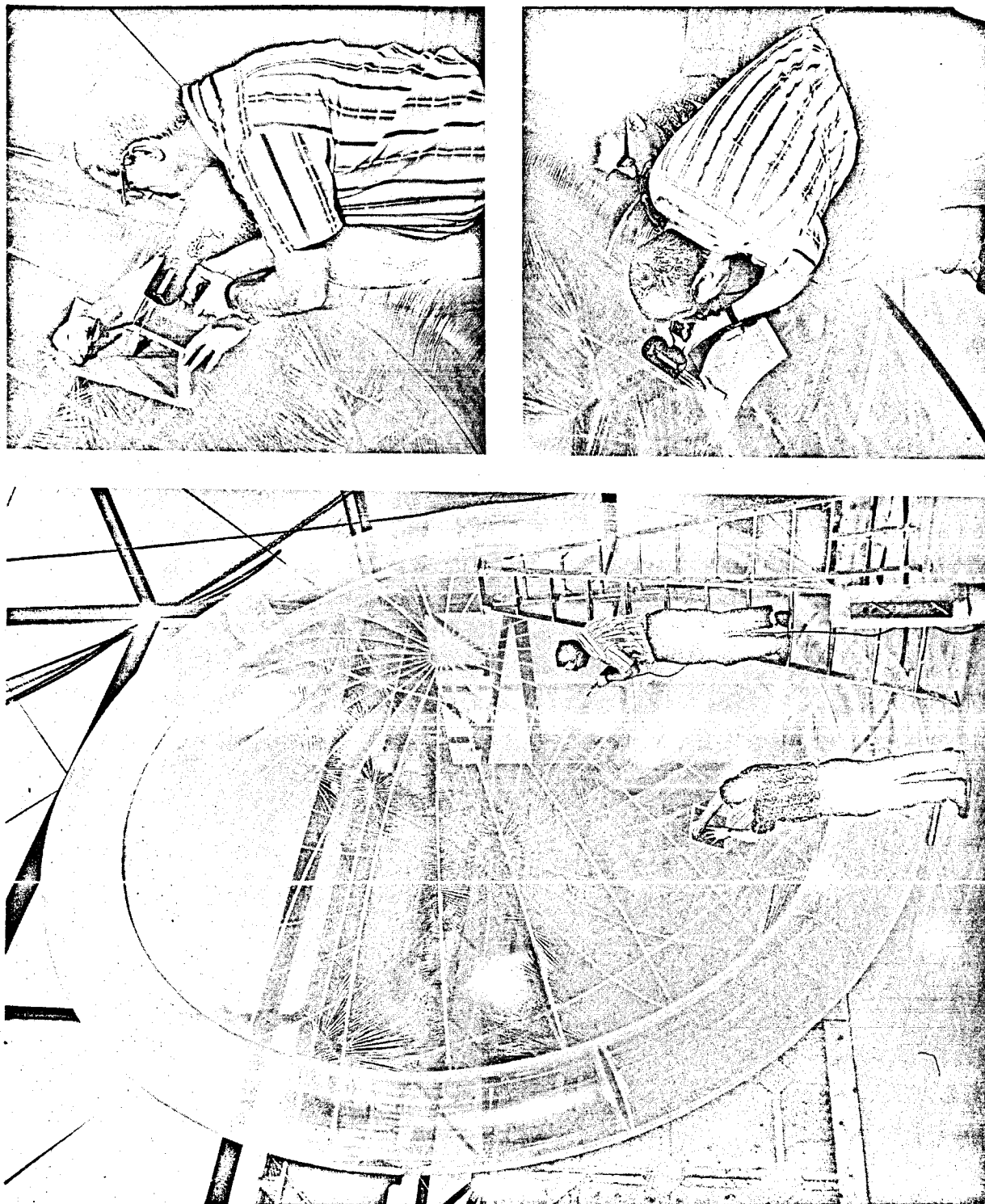


Figure 40 - Putting Deflation Holes in Lens and Torus of Model

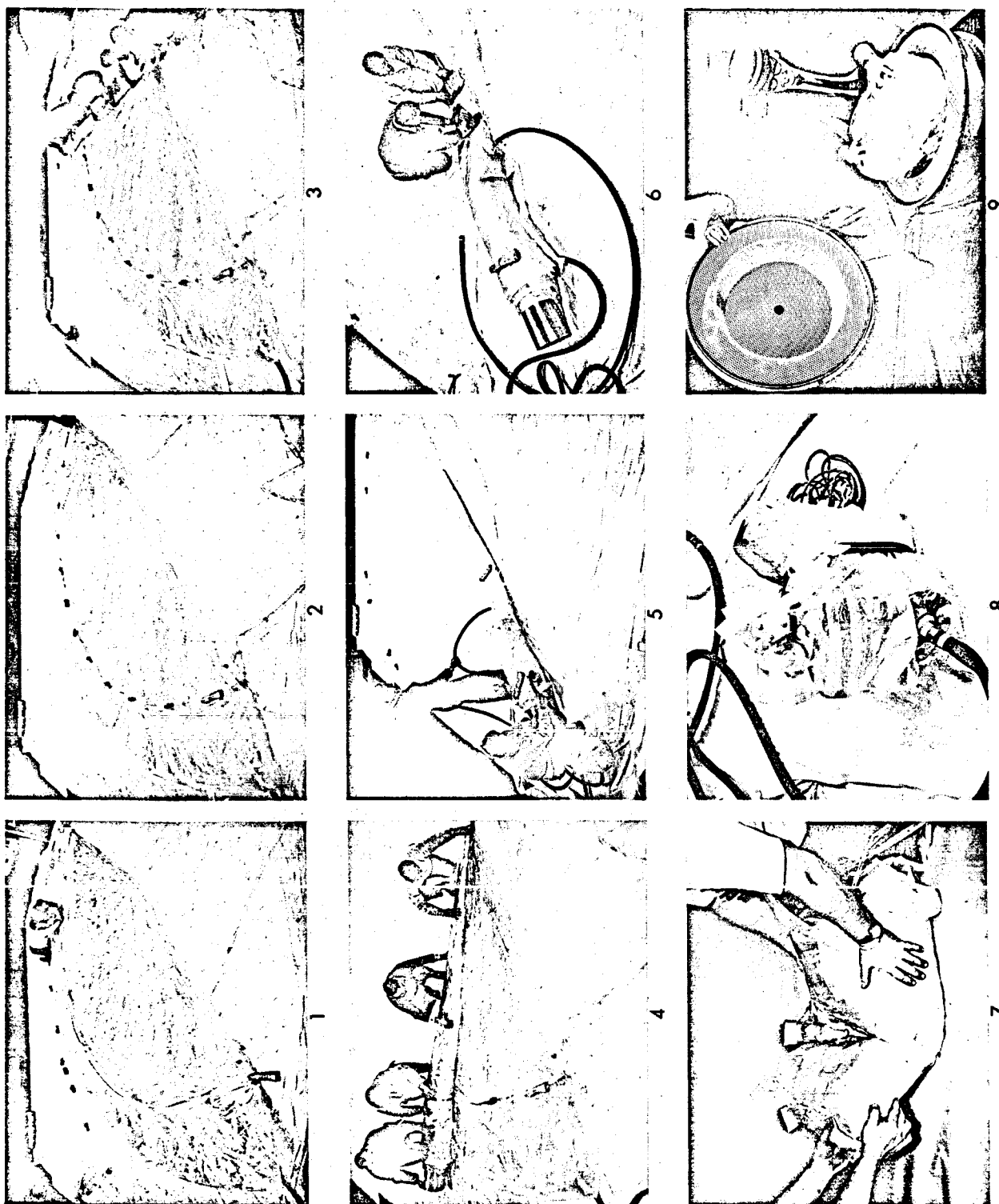


Figure 41 - Packaging Sequence, 20-Ft Model

The lens and torus were rolled together, keeping the inflation boom out of the pack. The lens was then folded in an accordion pleat, starting at the cone apex formed by the rolling operation. The torus was then folded to compact the package further. The roll was creased inward along two sides and then an accordion fold made. During this study no attempt was made to minimize the package volume of the models.

(5) Canister Details

An Echo I canister was modified as shown in Figure 42. Basically the modification consisted of (1) adding a perforated inner liner to reduce the effective volume and (2) adding an adapter fitting that serves as a termination of the tripod boom, provides inflation lines and electrical lines interface, and provides the canister evacuation value.

(6) Deployment

A deployment test under atmospheric conditions was run at GAC on Model 20-1 before installation of the deflation holes. The modifications to the model (torus manifold and inflation orifices) are as noted in Figure 27, and the inflation system analysis is as shown in Appendix C. Certain times, (1) to reach torus pressure, then hold and (2) to reach lens pressure, were assumed in the inflation system analysis and served as a basis for the inflation system design details such as torus manifold, inlet orifice sizes, supply pressure, and supply line sizes. Because the assumed times were believed to be conservative (minimum) and as such dictated the supply pressure required (which in turn relates directly to the energy to be absorbed by the system) it was determined to run the actual test at reduced supply pressure. The selected supply pressure, 35 psig, resulted in a satisfactory deployment. Because inflation time is related directly to supply pressure (for fixed manifold, inlet orifices, and line sizes) a study of the test results shows a close correlation to the inflation analysis.

A schematic of the setup is shown in Figure 43 and a photo sequence of the test in Figure 44. A 16-mm film of the actual packaging and deployment also is available.

The deployment was run on a water surface and was completely unattended except for a line attached to the booms to balance manually the effect of gravity.

The deployment was successful and demonstrated the feasibility of the system as designed. The effects of residual air on deployment were investigated at LRC during deployment tests in the 60-ft-diameter vacuum chamber.

(7) Repair Techniques

(a) Torus

Wherever a tear occurs or an entrance must be made into the torus, the opening can be repaired as follows.

1. Deflate the torus sufficiently to allow it to lay flat.
2. Line up the edges of the opening so they fit together properly.
3. Tack GT301 tape in place, centered over the opening.
4. Heat-seal the tape in place with a 340F iron. Be careful to minimize contact of the iron beyond the edge of the tape.
5. If the edge to be repaired is jagged it might be necessary to apply more than one strip of tape, with tape ends overlapping. Such a condition will destroy the continuity of the radius of curvature, but will not affect the operational function of the torus.

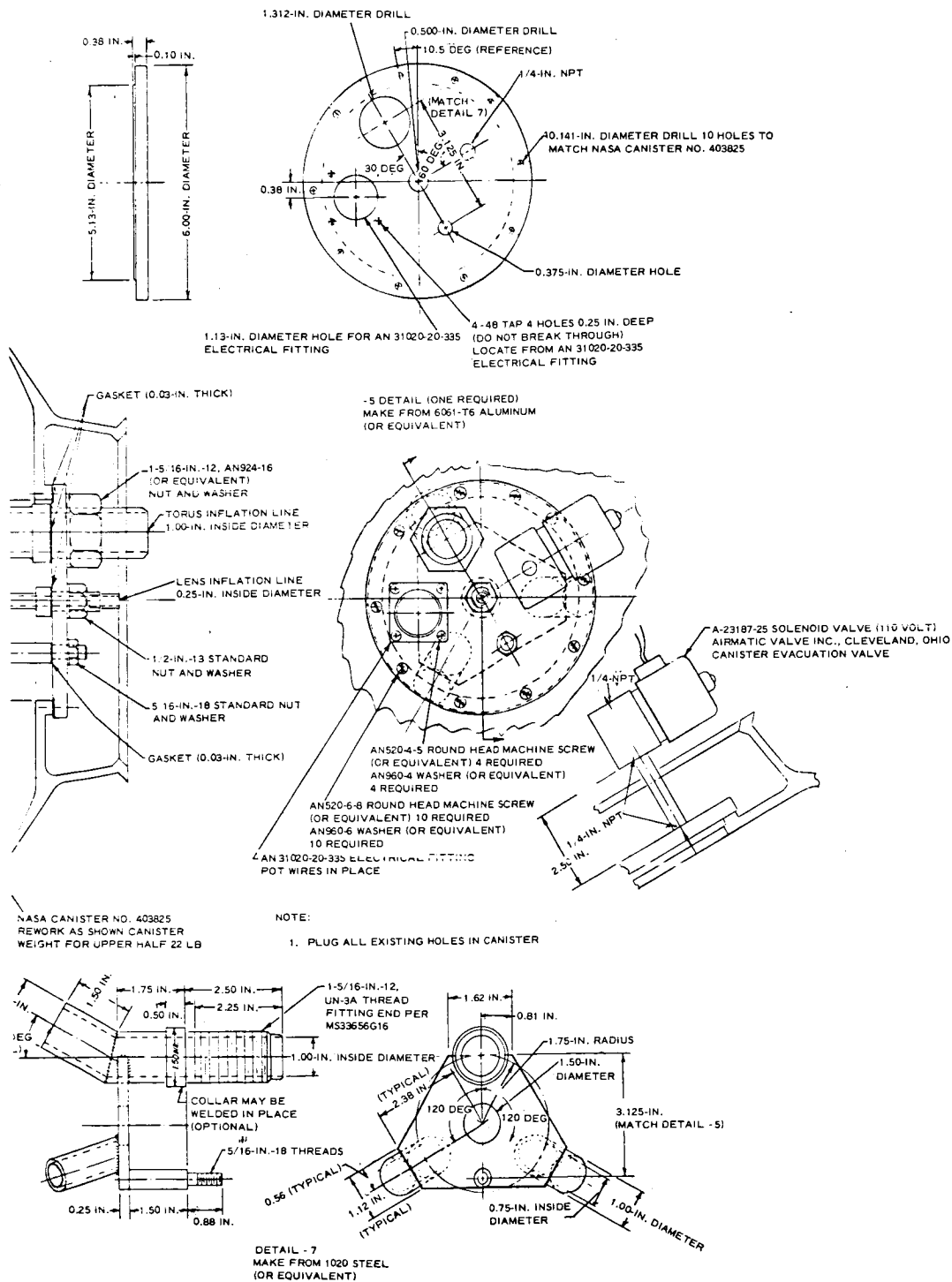
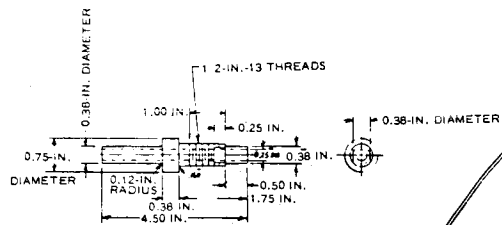
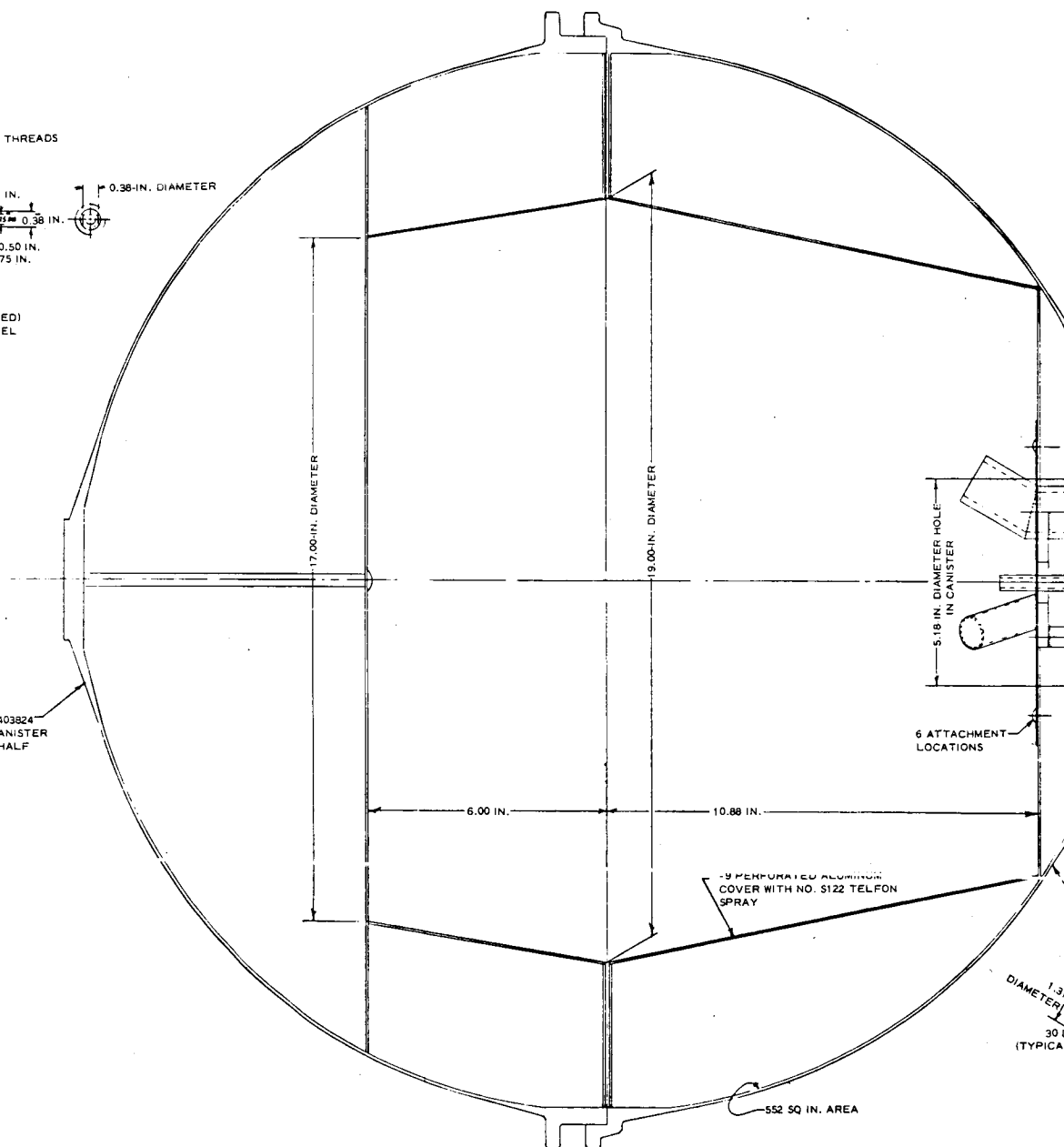


Figure 42 - Canister, 20-Ft Deployment Model, Lenticular Satellite



3 DETAIL (1 REQUIRED)
MAKE FROM 1020 STEEL
OR EQUIVALENT

NASA CANISTER NO. 403824
REWORK AS SHOWN CANISTER
WEIGHT FOR LOWER HALF
16.25 LB



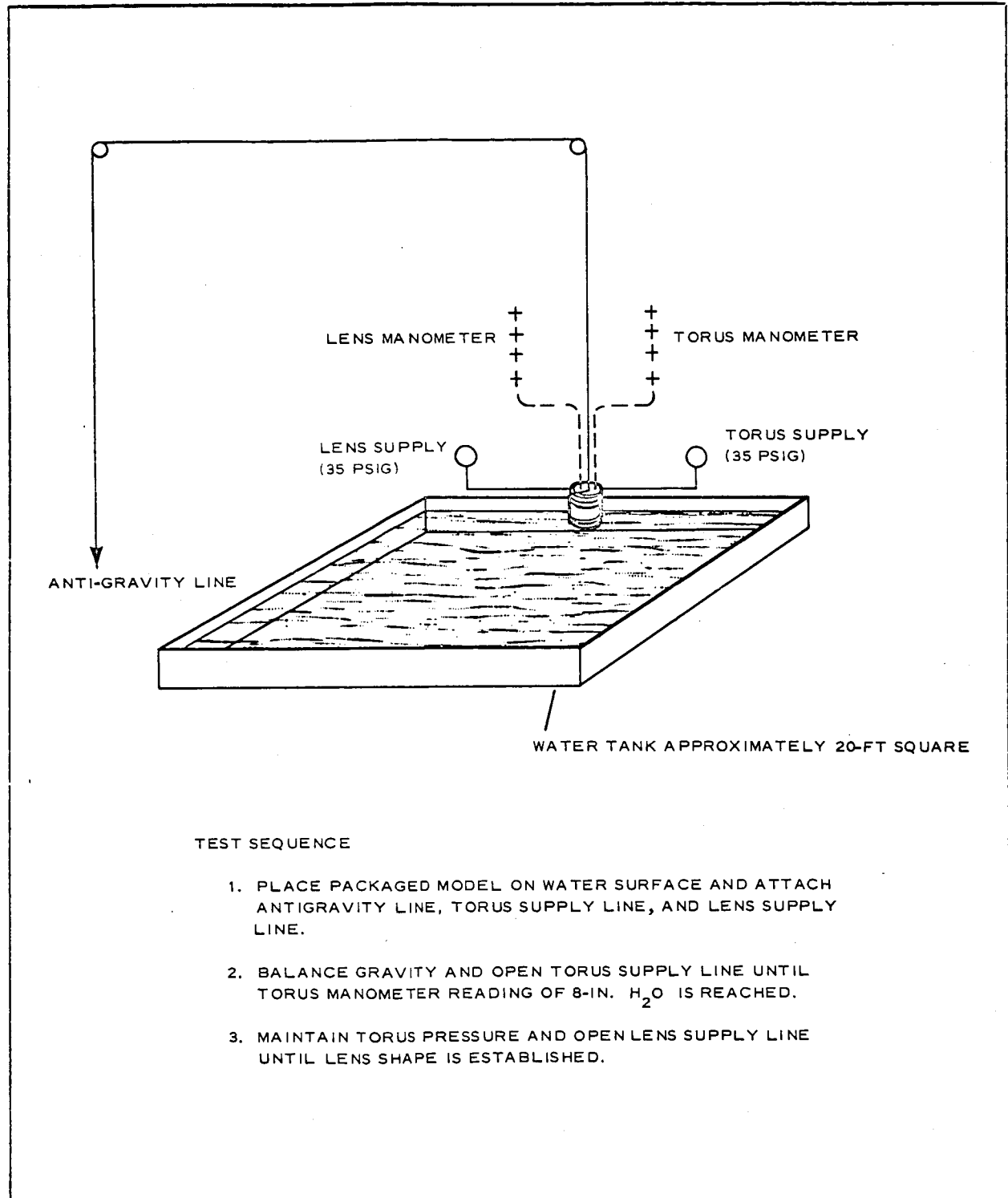


Figure 43 - Deployment Test Setup, 20-Ft Model

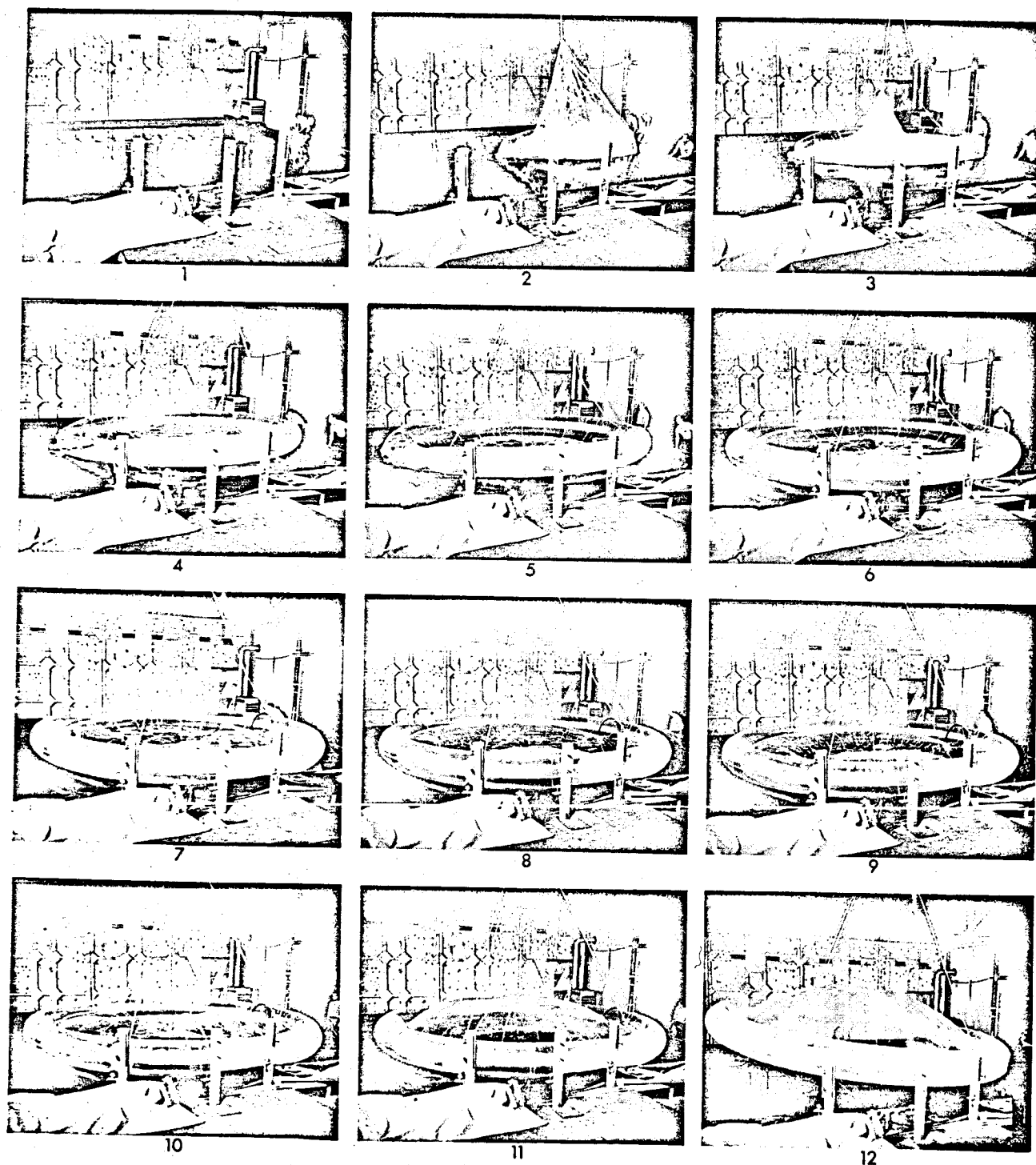


Figure 44 - Deployment Sequence, 20-Ft Model

(b) Mylar Lens

The Mylar lens can be repaired in the same manner as the torus except that GT300 tape should be used instead of GT301. It is also possible to remove seaming tape on the lens by heating and peeling it back. The used tape can be replaced although it is preferable to use fresh stock.

(c) Photolyzable Lens

Presently the best method of repairing tears and cuts is to use a Mylar pressure-sensitive tape. It is also possible to use other pressure-sensitive film-backed tapes for repairs, but Mylar is preferred.

(d) Boom Attachment

The booms were originally attached to the metal rim at both ends, using a two-part polyurethane resin. An epoxy system can also be used for field repairs. However, the bonding surfaces must be cleaned thoroughly with acetone before rebonding.

(e) Ring Separation

Unless the degree of ring separation from the torus is extensive, no repair attempt should be made. If repair should be necessary, the assembly should be returned to the manufacturer.

(8) Breadboard Inflation System

The breadboard inflation system was designed and fabricated to control and monitor the inflation of the 20-ft model under vacuum conditions. (See Figure 45.)

The breadboard consists of two pressure regulators to control inflation pressures. Hand-operated valves are provided to control inflation of the lens and torus. Two Hastings vacuum gages

are mounted on the panel for visual monitoring to prevent over-pressurization.

For satisfactory deployment in a vacuum chamber, the 20-ft model was designed to deploy under the following conditions:

1. Eliminate as much friction as possible on the deployment surface by mechanically raising the booms to overcome gravity and friction.
2. Set breadboard pressure regulator to 5 psia
3. Open canister (after residual air has been evacuated) and let model free fall
4. Open torus valve and inflate torus to 0.317 psia (16.4 mm Hg) and maintain this pressure while lens is inflating
5. Open lens valve and inflate lens to 0.0048 psia (248 micron Hg)

f. Twenty-Foot-Diameter Deployment Model 20-2

To fabricate Model 20-2 using a photolyzable film-wire lens, the same tools and procedures were used as for Model 20-1. The lens gores were put together with GT300 tape 0.75-in. wide. The four gore assemblies had been made approximately one month before final assembly into the lens. In the making of the torus, the hole sizes in the bulkheads were originally made for vacuum chamber deployment, so that changes that had to be made on Model 20-1 after atmospheric deployment were not required on Model 20-2.

The porosity of the lens material was high enough to eliminate the need for perforating the photolyzable lens, as was done on the Model 20-1 Mylar lens. Under ambient conditions it was necessary to put one of the large nylon fittings in the lens to achieve inflation to just slightly more than zero pressure.

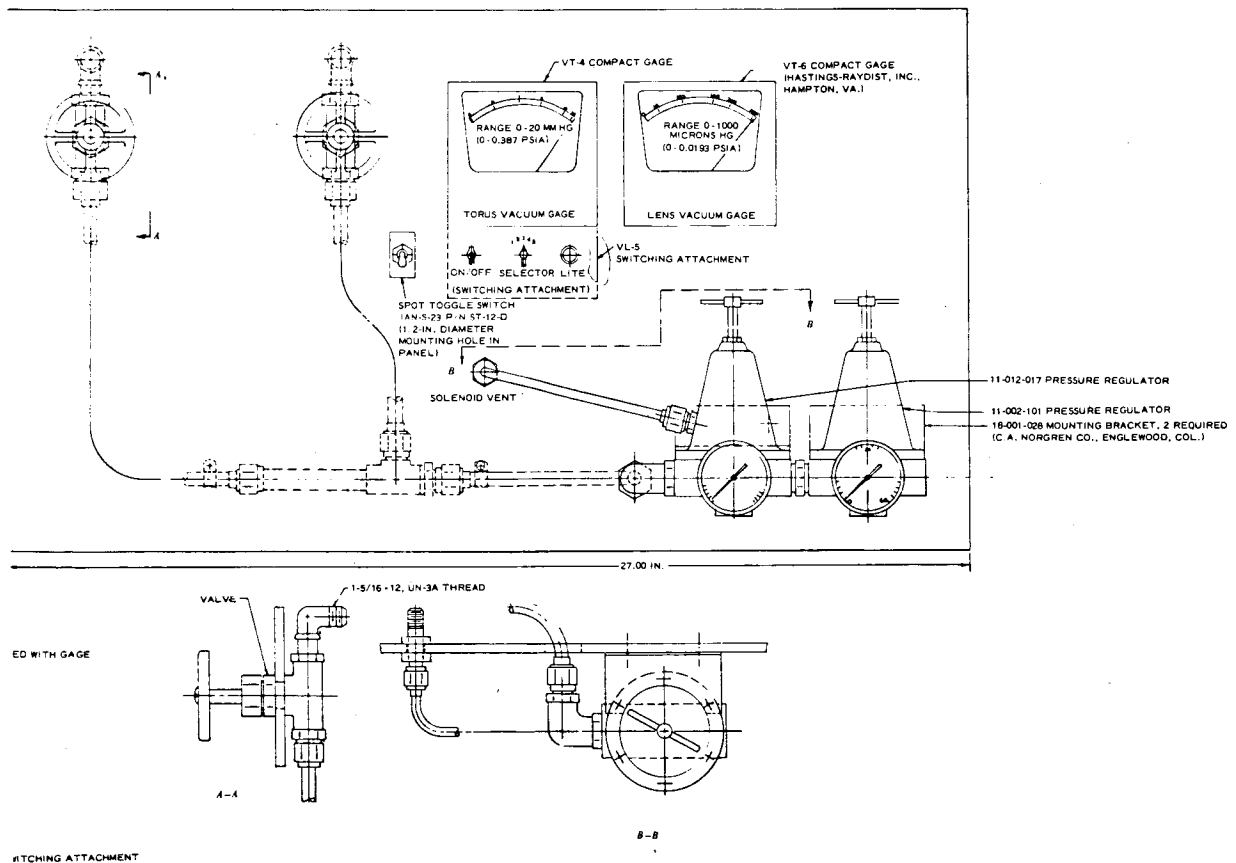
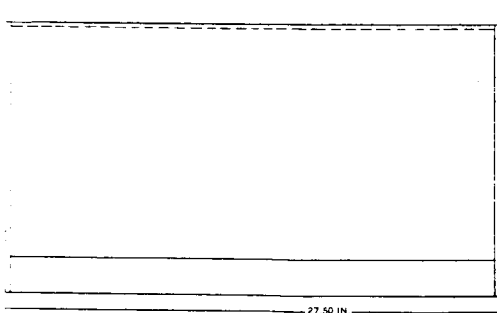
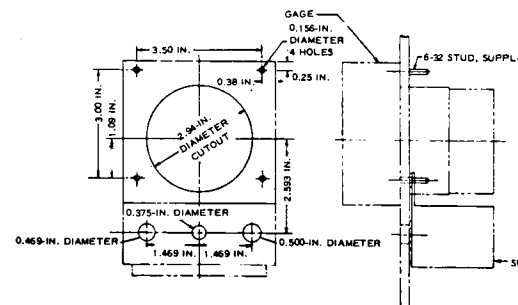
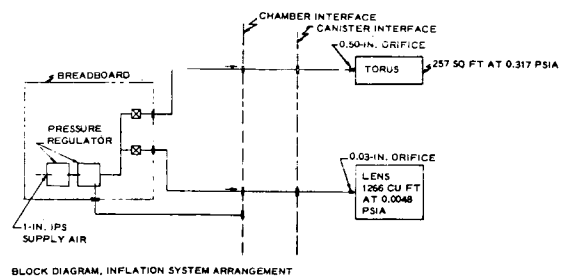
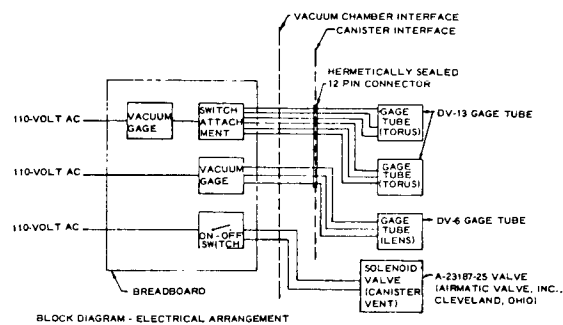
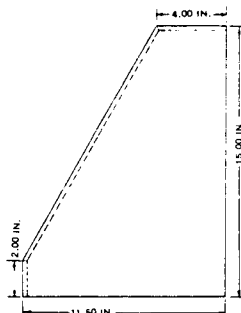


Figure 45 - Breadboard of 20-Ft Model Inflation System, Lenticular Satellite



OUTLINE - BREADBOARD ENVELOPE

FABRICATE FROM 1/4-IN. ALUMINUM



Packaging and deployment experience indicates that for any future models using photolyzable film-wire mesh, the center cap must be made of a stronger material to withstand the rigors of packaging.

g. Fabrication Forecast

(1) Flight Test Model

The fabrication procedures for the 50-ft model will be the same as for the 20-ft model. Because the torus cross section has been reduced to 19 in. the torus can be made from approximately 15 segments, only two more than for the 20-ft model. The number and width of the gores will depend on the width of material available at the time. There will be some handling problems to be solved for the lens gores. The only other major problems of fabrication will be the manufacture of the metal rim and an improvement of the method of attaching the rim to the torus. In this instance the problem will be to make the rim and the wire grid of the lens have a more intimate common bond than now exists.

Handling problems might occur when the packaging of the assembly takes place. These will involve floor space, head room, and the use of lightweight overhead block and tackle units.

Figure 46 shows the tooling and fabrication techniques that were used at GAC to construct a 10-ft-diameter solar concentrator, which are representative of lenticular satellite requirements. Methods of checking contour accuracy at ambient and vacuum conditions are also shown.

Figure 47 shows tooling and fabrication techniques that will be quite similar to the requirements of the 50-ft satellite flight-test model. Figure 48 shows the contour measuring system that could be used while the lens surface is pressurized on the

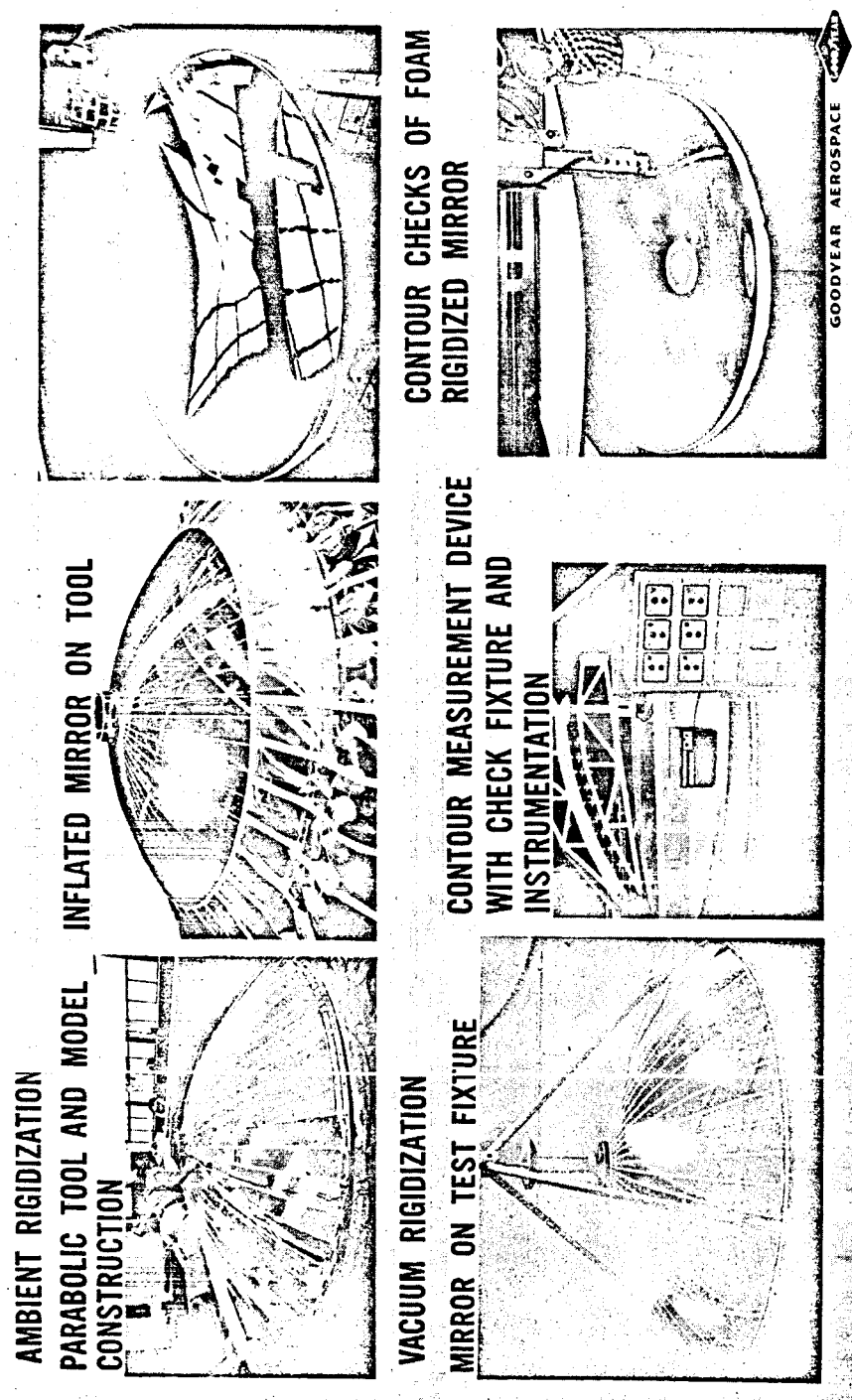


Figure 46 - Fabrication and Contour Check, 10-Ft-Diameter
Solar Concentrator

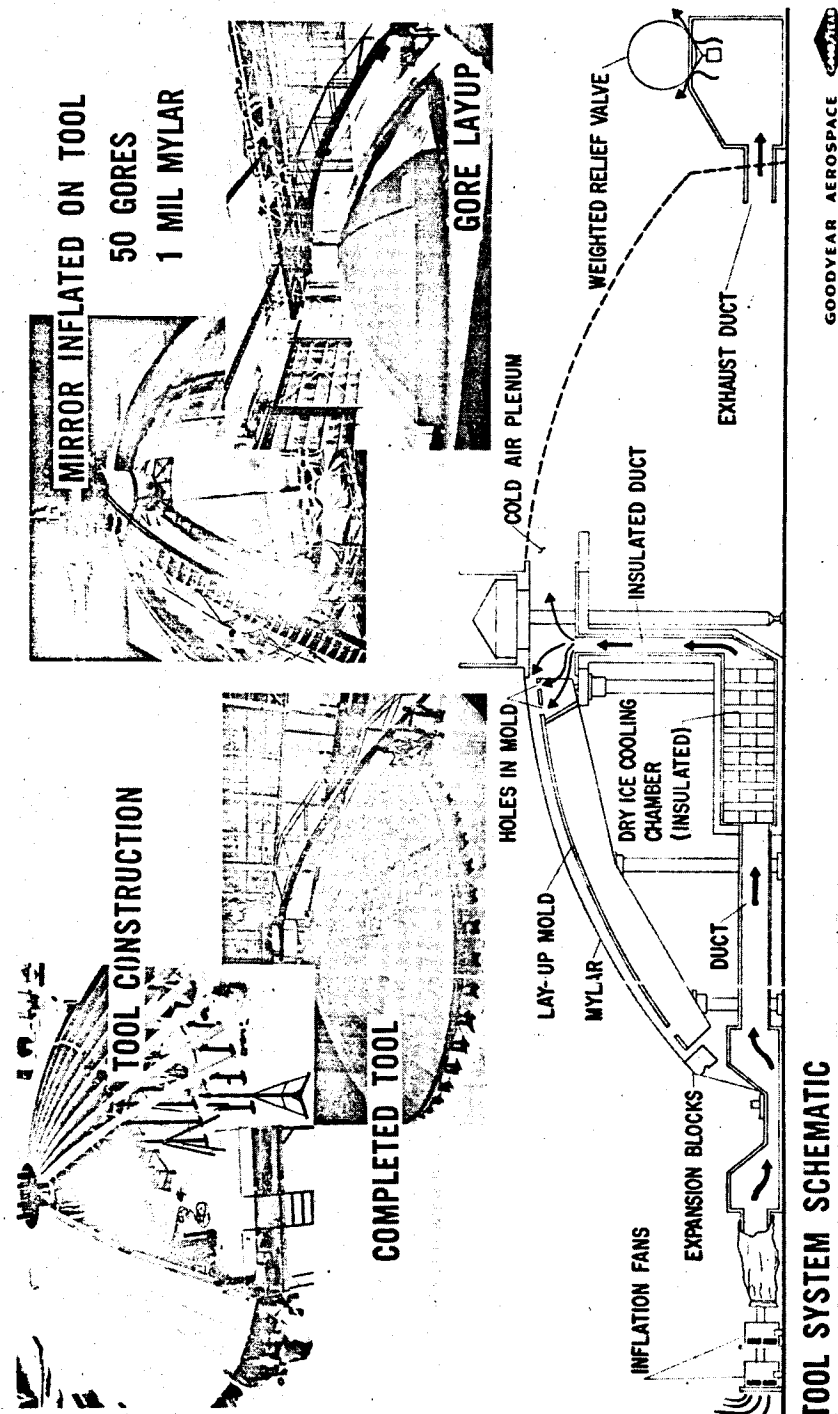


Figure 47 - Fabrication Technique, 44.5-Ft-Diameter Solar Concentrator

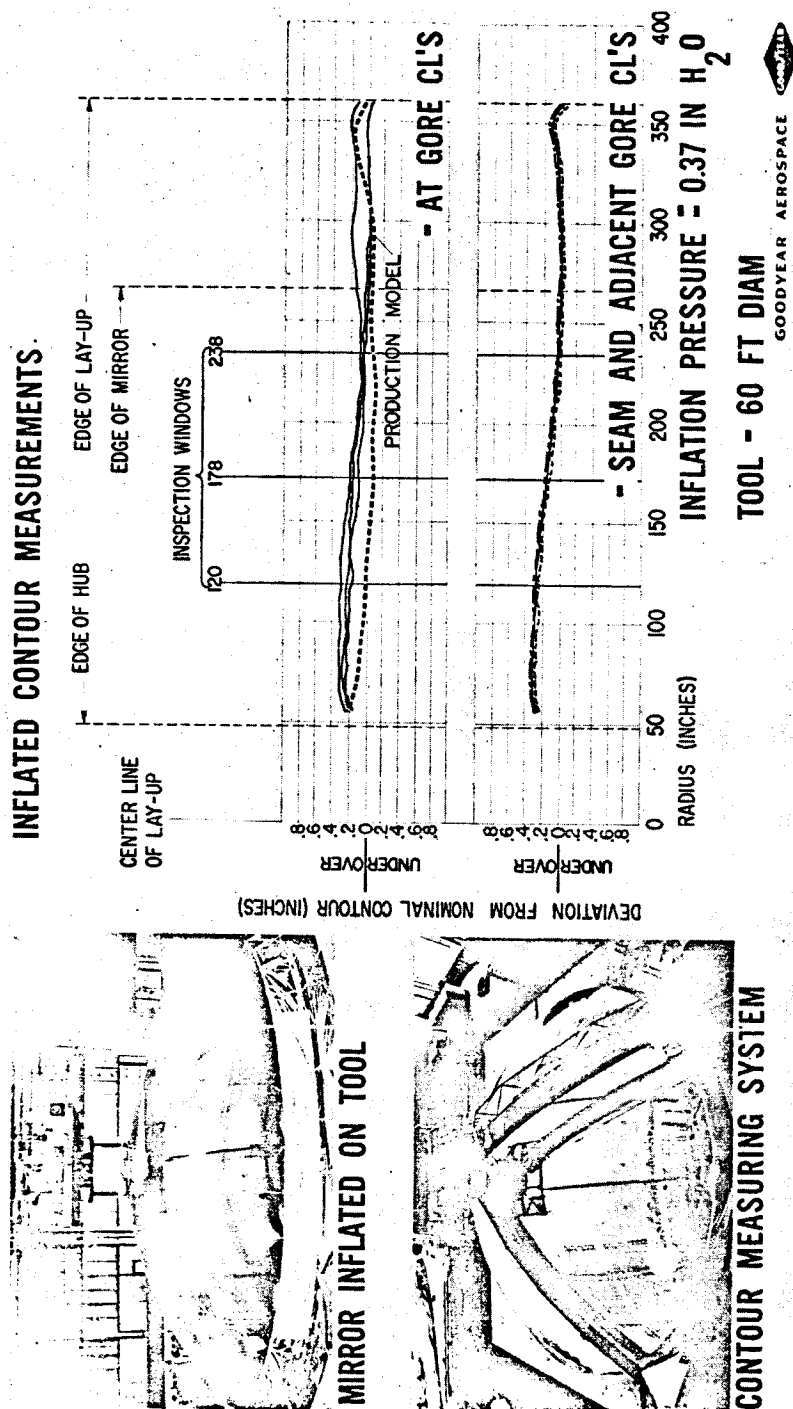


Figure 48 - Fabrication and Contour Checkout Fixture,
44.5-Ft-Diameter Solar Concentrator

tool. Contour accuracy data for several representative gores of the 44.5-ft-diameter solar concentrator indicate good overall construction characteristics.

Figures 49 and 50 show another method of fabricating wire-grid satellites used on grid-sphere models. Hexagonal and pentagonal preformed panels were assembled into a 14-ft-diameter sphere that had good r-f and dimensional characteristics.

(2) Full-Scale Satellite

The basic design of the full-scale unit has been established. However, an analysis of the design in terms of fabrication procedures has not been made. Essentially the same procedures that were used on the previous models will be used. The geometry of the subassemblies will probably vary considerably. The major causes of the variations will probably be controlled by material stock sizes that are available, and the desire to keep tooling within reasonable bounds. It is also possible that changes in the basic materials might cause changes in the fabrication approach.

The experience gained by LRC on Echo I and Echo II is directly related to fabrication and handling problems expected with the full-scale lenticular satellite.

h. Deployment Tests in LRC Vacuum Chamber

(1) General

Preliminary deployment tests were conducted on two 20-ft-diameter models of the proposed gravity-gradient-stabilized lenticular test satellite in the 60-ft vacuum chamber at LRC. Two tests were conducted on Model 20-1, which was the all-Mylar model. One deployment test was conducted on Model 20-2, which had a photolyzable film-wire mesh lens and a Mylar torus. The models were geometrically similar to the proposed full-scale lenticular satellite.

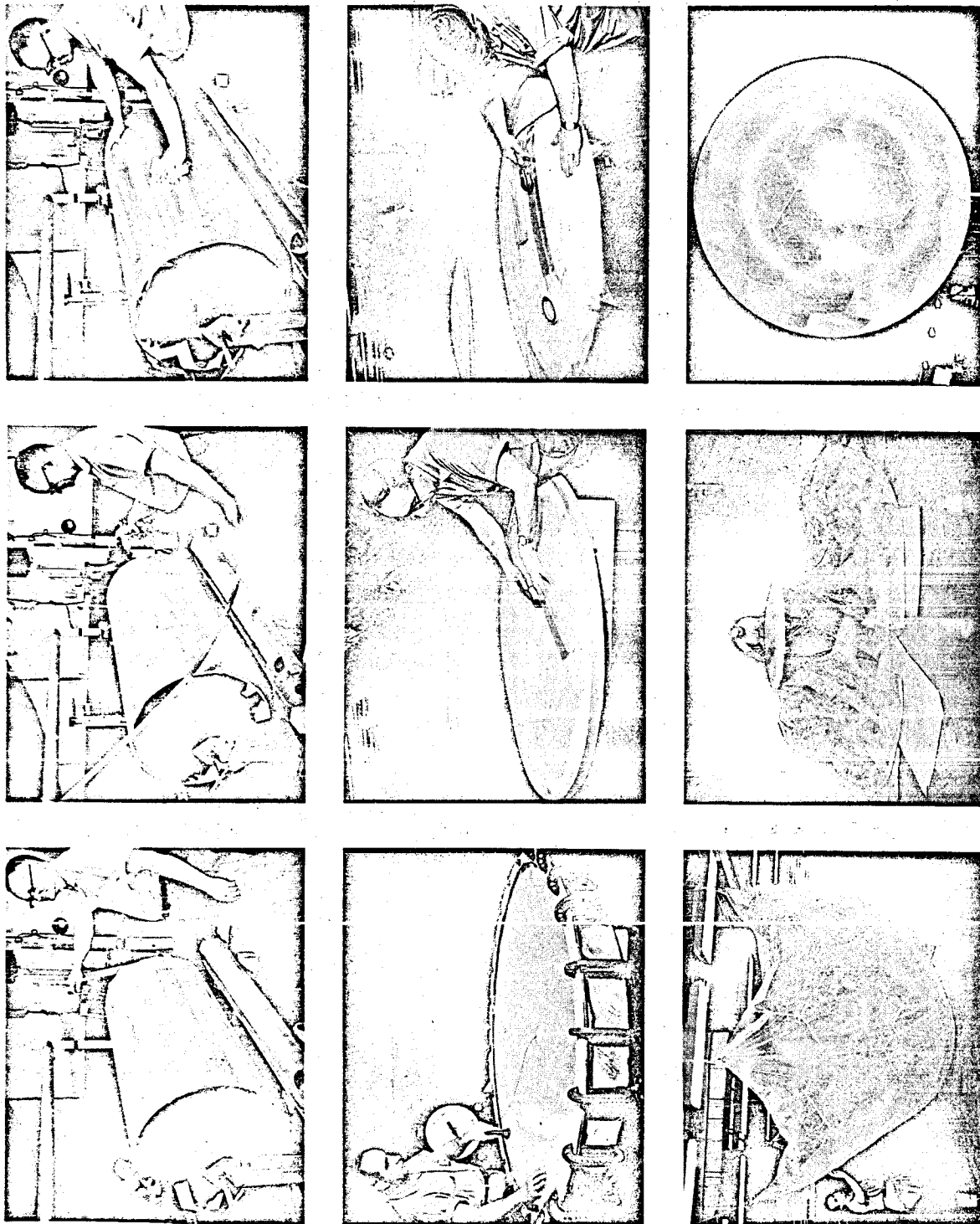


Figure 49 - Procedures and Facilities for Fabricating Wire-Grid Sphere



Figure 50 - Grid-Sphere Models

Instrumentation was provided to obtain pressure data on the various satellite components to control and analyze deployment. Suitable stop-action, high-speed, and real-time cameras were provided to document the deployment.

(2) Deployment Tests of Model 20-1

The test objectives of Model 20-1 were (1) to establish a reasonable canister pump-down procedure, (2) to evaluate the vacuum-sphere test arrangement and procedure, (3) to evaluate residual air effects on the satellite configuration, and (4) to evaluate the test under satellite configuration deployment and inflation sequence.

Figure 51 shows schematically the test setup used in the 60-ft sphere. Model and canister pressures were monitored through transducers at strategic locations within the model and the canister. Following canister separation the upper half was lifted to provide room for boom and lens deployment, and to help relieve friction forces between the model and the deployment surface. Figure 52 shows the deployment sequence along with characteristic pressures involved. Both the roll-accordion fold proposed by GAC and a pure-accordion fold method were tested to determine the effect on canister pump-down and model deployment. Each packaging method seemed satisfactory for the satellite design under consideration.

(3) Deployment Test of Model 20-2

The test objectives of Model 20-2 were to determine the characteristics of the wire-mesh lens after it had been packaged in the evacuated canister for a short time and to determine the effects of the lens material's inherent roughness and low strength on model deployment.

The only apparent effect of packaging the model, evacuating the canister, and shipping was that some of the lens wires worked

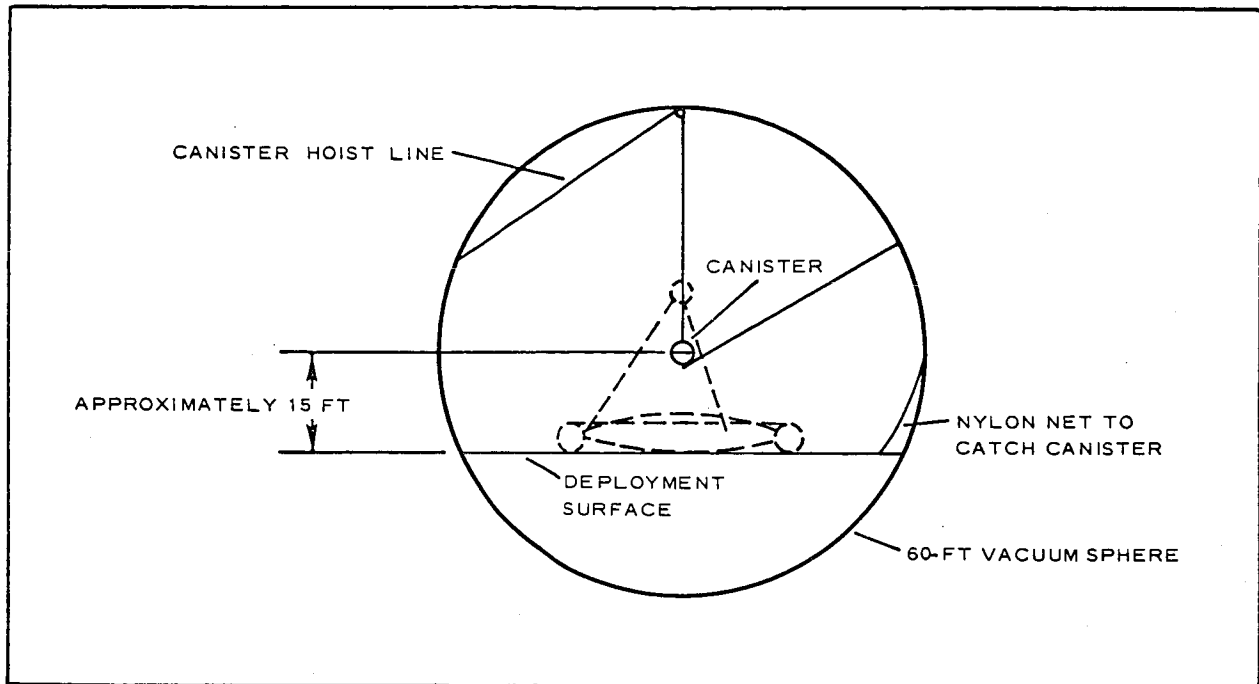


Figure 51 - Vacuum Deployment Test Schematic

loose of the photolyzable film in a small area close to the metal rim. This was the largest model fabricated of photolyzable-film, wire-mesh material up to that time. The model fabrication and tooling and handling techniques were very successful when it is considered that this first attempt primarily was to pinpoint the major problem areas.

Deployment of Model 20-2 in the vacuum chamber was unsuccessful when an adhesive failure separated a boom from the torus, thus making it impossible to complete the inflation process. It was found that the seam tape separated from the lens material in several areas. Subsequent testing has shown that the tapes that were used in the model construction are not compatible with the photolyzable film and that peel strength was lost after a short time. Several other tapes that are now readily available have been tested and found suitable for model construction of photolyzable film, based on preliminary test information. Construction

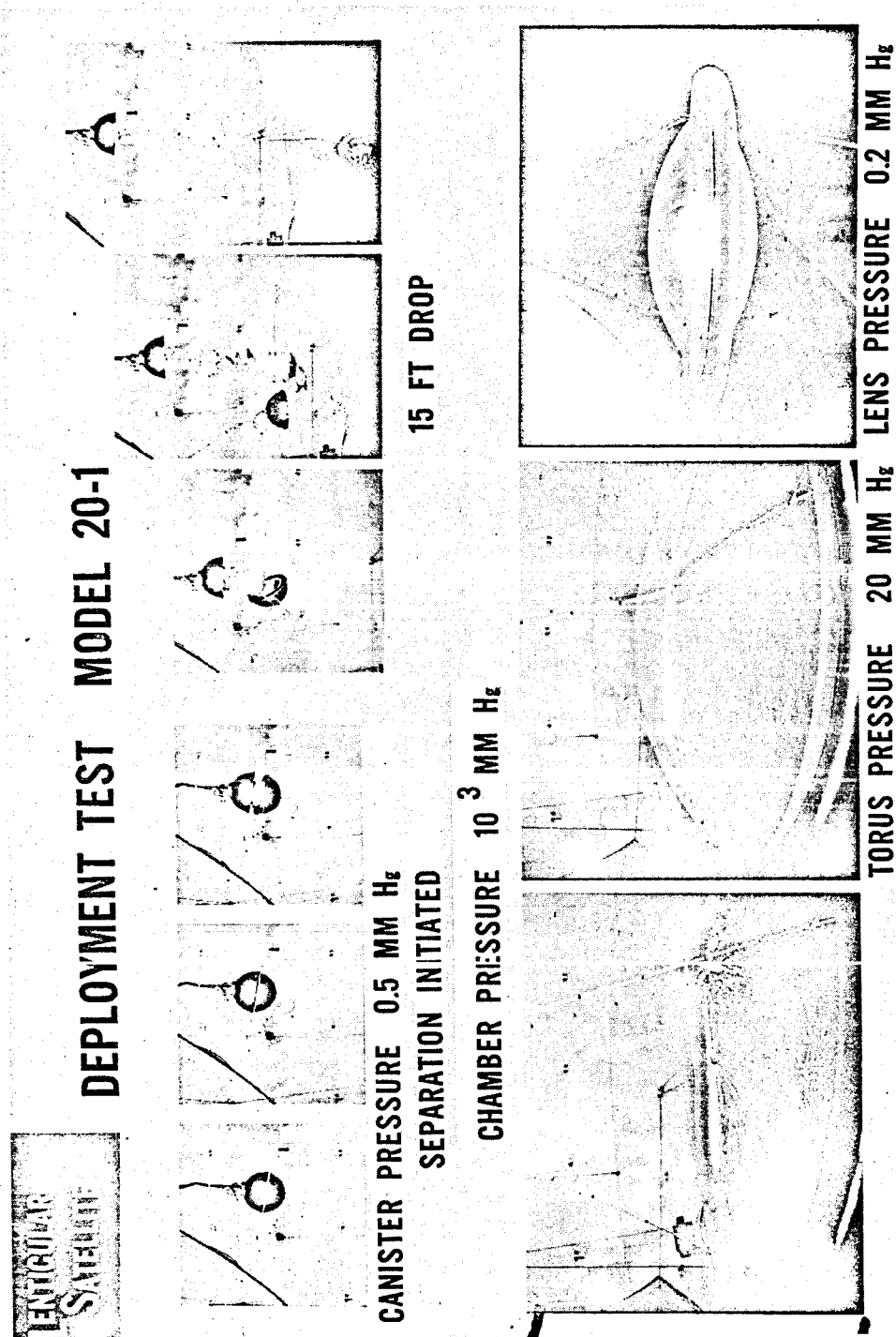


Figure 52 - Deployment Sequence for Model 20-1
Vacuum Sphere Tests

and testing of Model 20-2 provided information valuable for development of both larger and smaller models of prototype materials of the immediate future.

SECTION III - TECHNICAL DISCUSSION - PHASES I AND II

Subsection Two - Systems Analysis

1. GENERAL

Various studies, analyses, and tests have been made in support of the lenticular satellite program. These efforts were directed toward improving the configuration and raising the confidence level.

This subsection presents the structural and thermal analyses for the current designs for the full-scale and the flight-test models. A comparative study of alternate designs is also included as well as conclusions and recommendations. The design of the 20-ft deployment models was supported as needed³ but is not reported herein.

The full-scale and the flight-test designs are shown in Figures 9 and 13, respectively. For convenience in reading this section the principal features are shown in Figure 53.

Item 6 is a list of symbols that are applicable to all items of Subsection Two except 2g, 2h, and 3g - which include their own lists of symbols, and except for such other instances where symbols are defined in the immediate text.

2. FULL-SCALE SATELLITE

a. Lens

(1) Inflation Pressure

The lens material of the full-scale satellite consists of 1.0-mil copper wires woven in a plain weave pattern, 21 wires per inch in both directions, and bonded on a 0.5-mil photolyzable film.

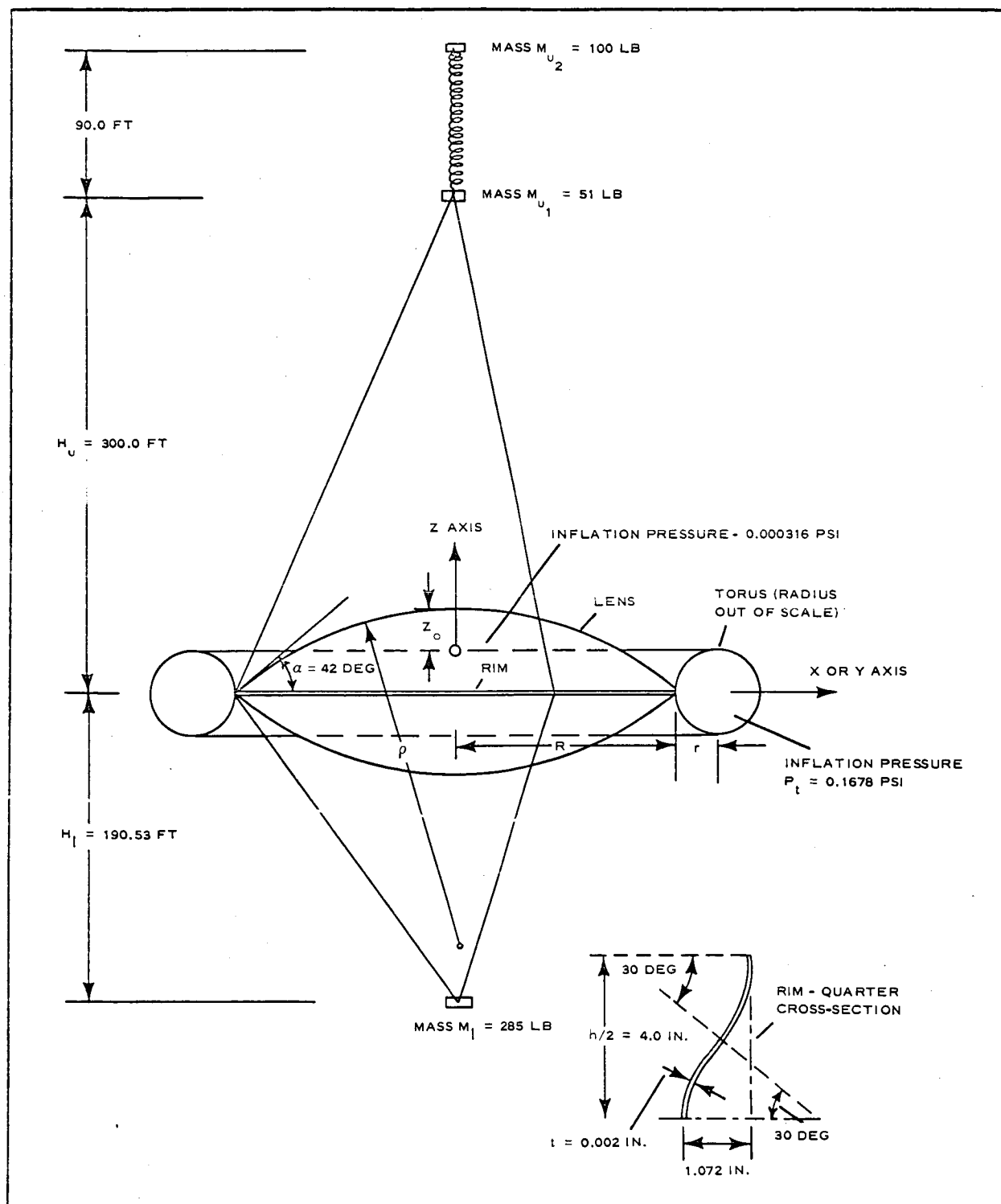


Figure 53 - Full-Scale Satellite Principal Features

For the determination of the lens rigidization pressure at the anticipated temperature of 200 F, the yield strength of the copper was taken as 23,000 psi while the photolyzable film was neglected. Hence, the required stress on the surface of the lens is,

$$\begin{aligned} f_{\rho y} &= 21 \left(\frac{\pi}{4} \right) (0.001)^2 (23,000) \\ &= 0.3793 \text{ lb/in.} \end{aligned}$$

Although the photolyzable film strength (about 1200 psi ultimate) was neglected in the determination of the yield strength of the lens material, it is, nevertheless, sufficient to seal the inflation gas in the lens. Diaphragm tests conducted at 200 F proved that the film held very satisfactorily much higher pressures than would be required to yield the lens material in the actual satellite lens. From five 12-in. diaphragms tested at 200 F (designated as specimens 8, 9, 10, 11, and 12), specimen 9 failed at 8.0 in. H₂O, (0.29 psi) which is about 1000 times as high as the pressure p_{ρ} that yields the lens material. All other specimens failed at pressures higher than 8.0-in. H₂O. (See Subsection Six, Tables XXXIII through XLIV.)

On the supposition that the lens surface consists of two identical spherical domes of 84-deg central angle, the uniform stress in the lens can be found⁴ from the equation

$$f_{\rho y} = \frac{p}{2} \quad (1)$$

Equation 1 can be solved for the lens rigidization pressure;

$$\begin{aligned} p_{\rho} &= \frac{2f_{\rho y}}{\rho} \\ &= \frac{2 \times 0.3793}{200 \times 12} \\ &= 0.316 \times 10^{-3} \text{ psi.} \end{aligned}$$

(2) Buckling Pressure

The critical buckling pressure of a spherical dome is given by the equation⁵

$$p_{cr} = 0.191 E_c \frac{d^3}{s \rho^2} \quad (2)$$

where

E_c = modulus of elasticity of copper wires =
 $10 - 16 \times 10^6$ psi,

d = wire diameter = 0.001 in.,

s = wire spacing = $\frac{1}{21}$ in. = 0.04762 in.,

ρ = radius of dome = $200 \times 12 = 2400$ in.

Substituting numerical values in Equation 2 results in

$$\begin{aligned} p_{cr} &= 0.191(10)10^6 \frac{(0.001)^3}{0.04762 \times (2400)^2} \\ &= 69.6 \times 10^{-10} \text{ psi.} \end{aligned}$$

Assuming specular reflection, the solar radiation pressure that hits the dome is $2 \times (6.8 \times 10^{-10}) = 13.6 \times 10^{-10}$ psi, which is about one-fifth the critical pressure.

As shown in Figure 176 the test points from four specimens on diaphragm tests are in good agreement with the collapse pressure curves. With a safety factor of five on the design pressure it is clear that even under the least favorable conditions the lens rigidization can be considered safe (all test points in the graph being above the theoretical curve).

b. Torus

The torus is a structural component that is fastened along its inner

equator to the edge (rim) of the lens. The torus serves two purposes:

1. By its gradual inflation, which is started at a point and proceeds in one direction around the circle the torus offers the first and most important step in the deployment of the satellite.
2. With its capability of carrying uniformly distributed radial compressive loads, the torus constitutes a supporting structure for the lens to assume its final shape upon inflation.

After the rigidization of the lens, the torus serves no purpose and therefore it should be photolyzed. The photolyzable film (Type II) for the construction of the torus, which is mentioned in References 1 and 3 is presently still in an experimental stage. Although modulus of elasticity and ultimate strength values (0.444×10^6 and 10,000 psi, respectively) are realistic values, the material is presently too brittle for packaging. Work is continuing on the development of high strength photolyzable film with good packaging characteristics.

The torus design criteria are three:

1. Buckling - the torus must have enough bending and torsional stiffness so that it will not collapse under the uniform radial pull from the lens.
2. Wrinkling - the torus must be pressurized high enough so that the circumferential inflation stresses will be greater than the compressive circumferential stresses caused by the radial pull of the lens (hoop compression).
3. Strength - the torus material (film) must be strong enough so that the maximum meridional

stress at the inner equator will be lower or equal to the strength of the film divided by the desired safety factor.

Extensive experimentation with a five-foot diameter (inner-equator diameter) torus indicated that the first of the above three design criteria can be neglected. In all tests, under various torus and lens pressures, the torus showed no signs of in-plane or out-of-plane collapse, even at lens pressures almost twice that theoretically required to collapse the torus. (See Subsection Six, Item 3, a.) The design criteria are established as follows (see Figure 54):

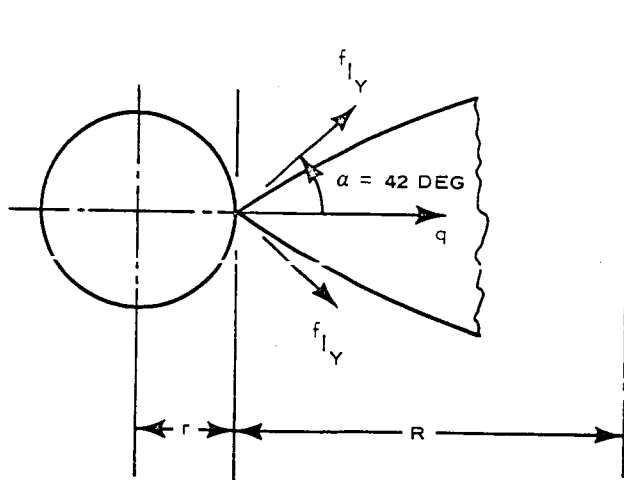


Figure 54 - Torus-Lens Axial Section

1. Buckling criterion:⁶

$$q \leq \frac{1}{(R + r)^3} \frac{12}{\frac{4}{EI} + \frac{1}{GJ}} \quad (3)$$

2. Wrinkling criterion

$$q(R + r) \leq p_t \pi r^2 \quad (4)$$

3. Strength criterion⁴

$$\frac{p_t r}{2t_t} \left(2 + \frac{r}{R} \right) \leq \frac{10,000}{F.S.} \quad (5)$$

Using a factor of 1.25 on the pressure in Equation 4, and the same value in the denominator of the right-hand side of Equation 5, these equations give respectively

$$p_t \pi r^2 \geq 1.25(2)(0.3793)(0.74314)(R + r)$$

or

$$p_t r^2 \geq 0.2243(R + r) \quad (6)$$

and

$$p_t r \leq \frac{16,000t_t}{2 + \frac{r}{R}} \quad (7)$$

Eliminating p_t between Equations 6 and 7 and solving the resulting equation for r/R and neglecting small quantities of higher order yields,

$$\frac{r}{R} = \frac{2}{71,333t_t - 3} \quad (8)$$

Let $t_t = 1$ mil.

Then Equation 8 gives

$$\frac{r}{R} = \frac{2}{68.333}$$

$$= 0.02927$$

$$r = 133.83 \times 0.02927$$

$$= 3.917 \text{ ft}$$

$$= 47 \text{ in.}$$

The inflation pressure can be found from Equation 7;

$$P_t = \left(\frac{1}{47} \right) \frac{16.0}{2.02927}$$

$$= 0.1678 \text{ psi}$$

c. Rim

(1) General

The stress analyses of the satellite configurations considered in Reference 3 have shown that insofar as the rim is concerned the stresses are negligibly small. Therefore, deflection calculations are presented for the final configuration. Preliminary investigation indicated that for in-plane deflection the condition IV-AM-OFF is critical, while for out-of-plane deflection the condition III-AM-ON is critical (see Appendix A, Tables A-III and A-V, and Reference 3, pages 338 through 340). Concentrated loads at the ends of the tripods and distributed loads around the rim are given in general terms in Table IV for these critical conditions.

(2) Maximum In-Plane Deflection

The maximum in-plane deflection is derived as follows (see Figure 55).

TABLE IV - CRITICAL GRAVITY-GRADIENT AND INERTIA NET LOADS FOR
IN-PLANE AND OUT-OF-PLANE RIM DEFLECTION

Load	Condition III		Condition IV	
	General values	Numerical values*	General values	Numerical values†
P_x	$+2M_q H_q \omega^2 (1 - \lambda) \sin^2 \beta$	$0.6034 \times 10^{-3} \text{ lb}$		
P_z	$+M_q H_q \omega^2 (1 - 4 \cos^2 \beta)$	$-0.5573 \times 10^{-3} \text{ lb}$	$-M_q H_q \omega^2 (3 + 4\lambda \sin^2 \beta_o)$	$-3.0019 \times 10^{-3} \text{ lb}$
q_{rx}	$Rm_r' \omega^2 (1 - 4 \sin^2 \beta) \sin \phi$	$-123.46 \times 10^{-9} \sin \phi \text{ lb/in.}$	$Rm_r' \omega^2 (1 - 4\lambda \sin^2 \beta_o) \sin \phi$	$-27.248 \times 10^{-9} \sin \phi \text{ lb/in.}$
q_{rz}	$2Rm_r' \omega^2 (1 + \lambda) \sin^2 \beta \sin$	$+380.50 \times 10^{-9} \sin \phi \text{ lb/in.}$		

* $\beta = 45 \text{ deg;}$

$\omega = 0.6243 \times 10^{-3} \text{ sec}^{-1}$ (altitude 2000 mi);

$\lambda = (I_x - x - I_z - z) \div I_x - x = 1 - \frac{1}{2177} = 1 - 0.459 = 0.541$ (photolizable film on);

$M_q = \frac{285}{32.2} = 8.851 \text{ slugs;}$

$m_r' =$ rim load per unit length, assuming that rim, torus, and lens weights are uniformly distributed around the rim, $m_r' =$

$$\frac{1}{g} (552.2 + 100.4 + 116.6) \div [2\pi(133.83 \times 12)] = 0.002367 \text{ slugs/in.}$$

+ $\beta_o = 45 \text{ deg;}$

$\lambda = 1 - 1 \div 4.621 = 0.7836;$

$$m_r' = \frac{1}{g} (199 + 100.4) \div [2\pi(133.83 \times 12)] = 0.000921 \frac{\text{slugs}}{\text{in.}}$$

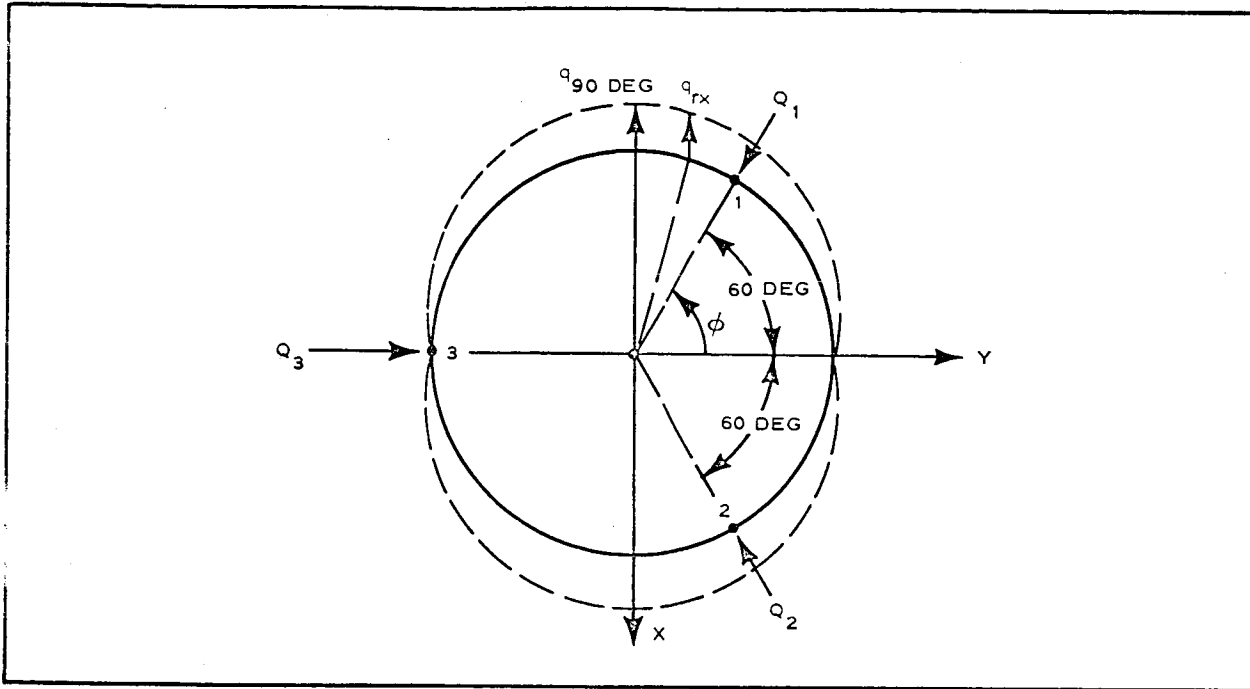


Figure 55 - Rim Plan View with Loads Causing Critical In-Plane Deflection

$$\begin{aligned}
 Q_1 &= Q_2 \\
 &= Q_3 \\
 &= -\frac{1}{3}(3.0019) \times 10^{-3} \left(\frac{133.83}{190.53} + \frac{133.83}{300.00} \right) \\
 &= -1.1492 \times 10^{-3} \text{ lb} \\
 q_{rx} &= -27.248 \times 10^{-9} \sin \phi \text{ lb/in.}
 \end{aligned}$$

Maximum deflection at point 1 ($\phi = 60 \text{ deg}$) due to the concentrated loads Q (Reference 3, page 128).

$$\begin{aligned}
 w_Q &= 0.0079 \frac{2P_Z R^4}{3EI_Z} \left(\frac{1}{H_\ell} + \frac{1}{H_u} \right) \\
 &= 0.0079 \left(\frac{2}{3} \right) \frac{3.0019 \times 10^{-3} \times 1606^4}{3 \times 18 \times 10^6 \times 0.01488} \left(\frac{1}{12} \right) \left(\frac{1}{190.53} + \frac{1}{300} \right) \\
 &= 0.094 \text{ in. (very small)}
 \end{aligned}$$

Maximum deflection at point $\phi = 90$ deg due to distributed load q_{rx} (Reference 3, pages 206-208).

$$w_q = \frac{q_{90} R^4}{6EI_Z} = \frac{27.248 \times 10^{-9} \times 1606^4}{6 \times 18 \times 10^{-6} \times 0.01488}$$

$$= 0.226 \text{ in. (very small) .}$$

Because both maximum deflection due to Q and q are very small, (these deflections occur at different places) the maximum deflection, w , due to the combined effect of the forces Q and q need not be determined.

(3) Maximum Out-of-Plane Deflection

The maximum out-of-plane deflection is derived as follows (see Figure 56). From Reference 7, page 28 the loads F are

$$F_1 = -F_2 = \frac{P}{\sqrt{3}} (\cot \alpha_u + \cot \alpha_\phi)$$

$$= \frac{0.6034 \times 10^{-3}}{\sqrt{3}} \frac{190.53 + 300.00}{133.83} = 1.2769 \times 10^{-3} \text{ lb.}$$

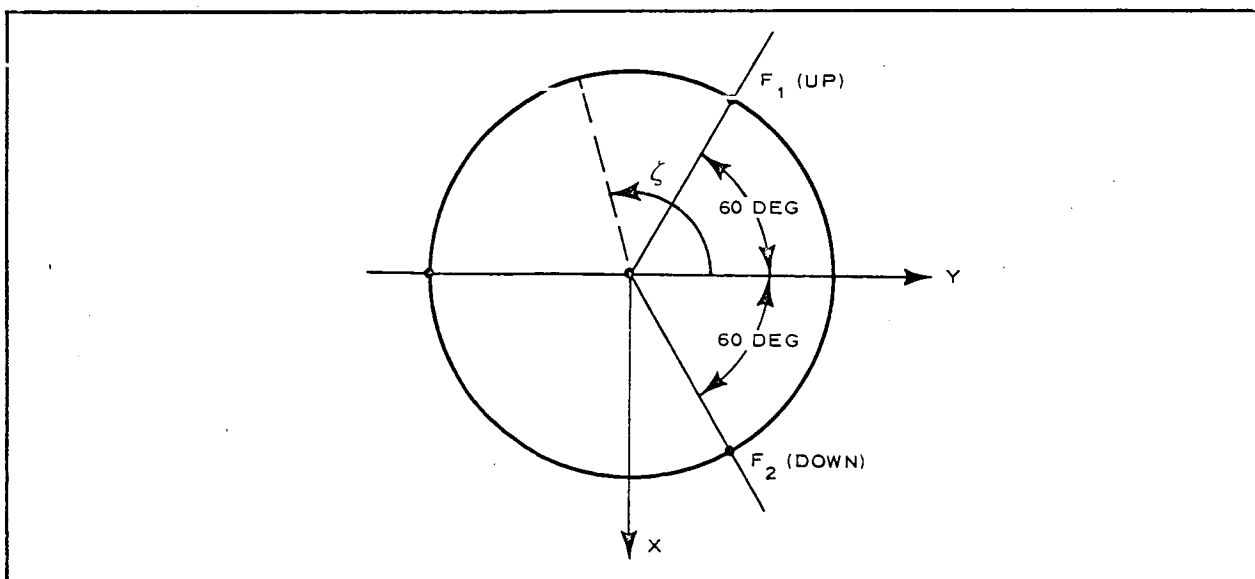


Figure 56 - Rim Plan View with Loads Causing Critical Out-of-Plane Deflection

The deflection (Reference 3, page 542) at five places ($\zeta = 60, 90, 120, 150, \text{ and } 180 \text{ deg}$) is given by equation

$$\delta_{\zeta} = \frac{F_1 R^3}{EI_x} \begin{bmatrix} 0 \\ 0.5823 \\ 0.9872 \\ 0.6396 \\ 0 \end{bmatrix} + \frac{F_1 R^3}{GJ} \begin{bmatrix} 0 \\ 0.7891 \\ 1.0061 \\ 0.6859 \\ 0 \end{bmatrix}$$

Substituting numerical values in the above equation yields $F_1 R^3 / EI_x = 1.648$, $F_1 R^3 / GJ = 22.325$, and

$$\delta = \begin{bmatrix} 0.0 \\ 18.6 \\ 24.1 \\ 16.4 \\ 0.0 \end{bmatrix} \text{ inches at } \zeta = \begin{bmatrix} 60 \\ 90 \\ 120 \\ 150 \\ 180 \end{bmatrix}, \text{ respectively,}$$

from which it is concluded that the maximum out-of-plane deflection, at about $\zeta = 115 \text{ deg}$, is 24.5 in.

d. Tripod

The tripod booms are analyzed for the maximum anticipated axial compression in combination with distributed loads, that come from gravity-gradient, inertia, and solar radiation in the most critical condition, which is specular reflection with the solar rays normal to the axis of the boom. Table A-I of Appendix A shows that the critical condition for the booms is either I-B or III-B (in both cases Boom No. 1 is critically loaded). Of these two conditions, the first is the most critical when $\alpha = 90 \text{ deg}$ and with the photolyzable film on.

The maximum compressive load, L , in the boom is

$$\begin{aligned} L &= M_u H_u \omega^2 \left[\frac{\cos \alpha}{\cos \alpha_u} - 2\sqrt{3}(1 - \lambda) \frac{\sin \alpha}{\sin \alpha_u} \right] \\ &= M_u H_u \omega^2 \left[0 - 2\sqrt{3}(1 - 0.541) \frac{1.0}{0.4074} \right] \\ &= -3.903 M_u H_u \omega^2 . \end{aligned}$$

$$\begin{aligned} (\alpha_u &= \tan^{-1} \frac{133.83}{300.00} \\ &= 24 \text{ deg } 2.5 \text{ min}) \end{aligned}$$

But

$$\begin{aligned} M_u H_u &= M_l H_l \\ &= \frac{285 \times 190.53}{32.2} \\ &= 1686.4 \text{ slug-ft.} \end{aligned}$$

Therefore,

$$\begin{aligned} L &= -3.903 \times 1686.4 (0.6243)^2 \times 10^{-6} \\ &= -2.565 \times 10^{-3} \text{ lb.} \end{aligned} \quad (9)$$

Gravity-gradient and inertia distributed load for $\alpha = 90$ deg can be found from the first of Equations 25 of Reference 7, page 20; then

$$\begin{aligned} \frac{dF_n}{d\ell} &= q_n \\ &= -3m_b \omega^2 \cos \alpha_u \{-y\} \\ &= 3m_b y \omega^2 \cos \alpha_u . \end{aligned}$$

The solar radiation pressure for specular reflection per unit length of boom is given by equation

$$q_S = \frac{8}{3} r_o \left(\frac{p_i}{c} \right)$$

$$= 1815 \times 10^{-12} r_o \text{ lb/in. (Reference 3, page 212) .}$$

Then the total distributed load, q , is

$$q = 3m_b y \omega^2 \cos \alpha_u + 1815(10^{-12}) r_o , \quad (10)$$

where y is measured in feet along the radius of the rim ($0 \leq y \leq R$), m_b the mass per unit length (inch) of boom, and r_o the boom radius in inches; the units of q are lb per inch.

Assuming that the booms are made of 2-mil aluminum wires^a forming a 0.5-square in. grid, bonded on 1-mil Mylar film and that the boom radius is $r_o = 1.5$ in., the trapezoidal load on the boom can be determined from Equation 10, as shown in Figure 57.

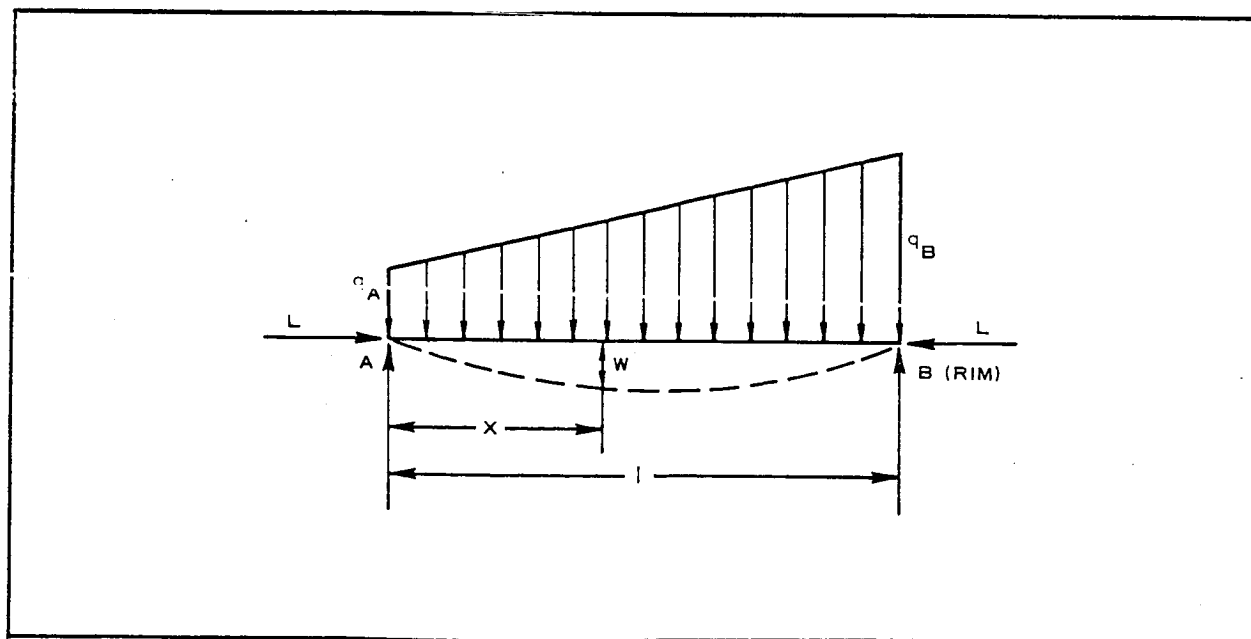


Figure 57 - Tripod Boom Critically Loaded as a Beam-Column

^a Purpose of the wires is to provide some local stiffness so that, when the pressure in the booms is lost, the skin is prevented from wrinkling back to the folds that form during packaging.

Axial compression $L = 2.565 \times 10^{-3}$ lb (Equation 9)

$$m_b = 2\pi(1.5) \left[(0.05)(0.001) + 2 \times 2 \times \frac{\pi}{4} (0.002)^2 (0.1) \right] \div 32.2$$

$$= 15.025 \times 10^{-6} \text{ slugs/in.}$$

Beam length $l = (300^2 + 133.83^2)^{1/2} = 328.5 \text{ ft} = 3942 \text{ in.}$

$$q_A = 3 \times 15.025 \times 10^{-6} (0)(0.38975) 10^{-6} (0.91325) + 1815 \times 10^{-12} (1.5)$$

$$= 2.7225 \times 10^{-9}$$

$$q_B = 3 \times 15.025 \times 10^{-6} \times 133.83 \times 0.38975 \times 10^{-6} (0.91325) +$$

$$2.7225 \times 10^{-9}$$

$$= (2.1470 + 2.7225) \times 10^{-9}$$

$$= 4.8695 \times 10^{-9}$$

(10)

If a factor 1.5 is used to convert limit to ultimate loads, then

$$L = 3.848 \times 10^{-3} \text{ lb}$$

$$q_A = 4.084 \times 10^{-9} \text{ lb/in.}$$

$$q_B = 7.304 \times 10^{-9} \text{ lb/in.}$$

Because stresses are of no particular interest (Reference 3, pages 214, 215) only derivation of deflections is given below.

Reactions A and B:

$$\left. \begin{aligned} A &= \frac{q_A \ell}{2} + \frac{1}{3} \frac{1}{2} (q_B - q_A) \ell = \frac{1}{6} \ell (2q_A + q_B) \\ B &= \frac{q_A \ell}{2} + \frac{2}{3} \frac{1}{2} (q_B - q_A) \ell = \frac{1}{6} \ell (q_A + 2q_B) \end{aligned} \right\} \quad (11)$$

Bending moment at x:

$$M_x = Ax + Lw - \frac{1}{2} q_A x^2 - \frac{1}{6} (q_B - q_A) \frac{x^3}{\ell} \quad (12)$$

Differentiating this equation twice with respect to x, and noting that $d^2 w/dx^2 = -M_x/EI$ results in

$$\frac{d^2 M_x}{dx^2} + \frac{L}{EI} M_x = -q_A - \frac{x}{\ell} (q_B - q_A) \quad (13)$$

The general solution of Equation 13 is

$$M_x = C_1 \sin\left(\frac{x}{j}\right) + C_2 \cos\left(\frac{x}{j}\right) - j^2 \left[q_A + \frac{x}{\ell} (q_B - q_A) \right] \quad (14)$$

where

$$j^2 = \frac{EI}{L} \quad (15)$$

With the boundary conditions $M_{x=0} = M_{x=\ell} = 0$, the constants of integration C_1 and C_2 are determined:

$$C_1 = j^2 \frac{q_B - q_A \cos A\left(\frac{\ell}{j}\right)}{\sin\left(\frac{\ell}{j}\right)} ; \quad C_2 = j^2 q_A$$

Hence, Equation 14 becomes

$$M_x = j^2 \frac{q_B - q_A \cos\left(\frac{\ell}{j}\right)}{\sin\left(\frac{\ell}{j}\right)} \sin\left(\frac{x}{j}\right) + j^2 q_A \cos\left(\frac{x}{j}\right) - j^2 \left[q_A + \frac{x}{\ell} (q_B - q_A) \right] \quad (16)$$

Substituting Equations 11 and 16 into Equation 12 and solving the resulting equation for the deflection w yields,

$$w = \frac{j^2}{L} \frac{q_B - q_A \cos\left(\frac{\ell}{j}\right)}{\sin\left(\frac{\ell}{j}\right)} \sin\left(\frac{\ell}{j} \frac{x}{\ell}\right) + \frac{j^2}{L} q_A \cos\left(\frac{\ell}{j} \frac{x}{\ell}\right) -$$

$$\left[\frac{j^2}{L} (q_B - q_A) + \frac{\ell^2}{6L} (2q_A - q_B) \right] \left(\frac{x}{\ell}\right) + \frac{q_A \ell^2}{2L} \left(\frac{x}{\ell}\right)^2 + \frac{(q_B - q_A) \ell^2}{6L} \left(\frac{x}{\ell}\right)^3 - \frac{j^2}{L} q_A$$

(17)

Substituting numerical values into Equation 17 and simplifying results in

$$w = 14.726 \sin\left(2.7205 \frac{x}{\ell}\right) + 2.2286 \cos\left(2.7205 \frac{x}{\ell}\right) - 12.170 \left(\frac{x}{\ell}\right) +$$

$$8.2462 \left(\frac{x}{\ell}\right)^2 + 2.1672 \left(\frac{x}{\ell}\right)^3 - 2.2286$$

(18)

Values of w (inches) are given in Table V for several values of the ratio x/ℓ . The maximum transverse deflection of the boom is about 9.0 in. (small).

e. Deployment

Deployment in this item is limited to the transient phase from separation of the canister until inflation of the satellite is started. The inflation phase has been demonstrated by deployment on a water surface and in a vacuum chamber. These tests show that this phase of the deployment proceeds in an orderly fashion and that no structural damage to the satellite is to be anticipated.

The effect of trapped air on the structure merits some attention. The trapped air will expand when the satellite is deployed and consequently will do work on the surrounding structure. The amount of work done

TABLE V - TRANSVERSE DEFLECTIONS OF TRIPOD BOOMS
SUBJECTED TO CRITICAL LOAD CONDITION

(1) $\frac{x}{l}$	(2) $\left(\frac{x}{l}\right)^2$	(3) $\left(\frac{x}{l}\right)^3$	(4) $2.7205 \frac{x}{l}$	(5) $\sin 2.7205 \frac{x}{l}$	(6) $\cos 2.7205 \frac{x}{l}$	(7) $14.726 \times \sin \frac{x}{l}$ $2.7205 \frac{x}{l}$	(8) $2.2286 \times \cos \frac{x}{l}$ $2.7205 \frac{x}{l}$	(9) $12.170 \frac{x}{l}$	(10) $8.2462 \left(\frac{x}{l}\right)^2$	(11) $2.1672 \left(\frac{x}{l}\right)^3$	(12) w^*
0.0	0.0	0.0	0.0	0.0	1.000	0.0	2.2286	0.0	0.0	0.0	0.0
0.1	0.01	0.001	0.2721	0.26874	0.96320	3.9575	2.1466	1.2170	0.0825	0.0022	2.7432
0.2	0.04	0.008	0.5441	0.51764	0.85558	7.6228	1.9067	2.4340	0.3298	0.0173	5.2110
0.3	0.09	0.027	0.8162	0.72854	0.68499	10.7285	1.5266	3.6510	0.7422	0.0585	7.1762
0.4	0.16	0.064	1.0882	0.88579	0.46408	13.0441	1.0342	4.8680	1.3194	0.1387	8.4398
0.5	0.25	0.125	1.3603	0.97791	0.20905	14.4007	0.4659	6.0850	2.0616	0.2709	8.8855
0.6	0.36	0.216	1.6323	0.99812	-0.06134	14.6983	-0.1367	7.3020	2.9686	0.4681	8.4677
0.7	0.49	0.343	1.9044	0.93485	-0.32749	13.7666	-0.7298	8.5190	4.0406	0.7433	7.0731
0.8	0.64	0.512	2.1764	0.82214	-0.56928	12.1068	-1.2687	9.7360	5.2776	1.1096	5.2607
0.9	0.81	0.729	2.4485	0.63899	-0.76921	9.4098	-1.7143	10.9530	6.6794	1.5799	2.7732
1.0	1.0	1.0	2.7205	0.40875	-0.91264	6.0193	-2.0339	12.170	8.2462	2.1672	0.0

* $w = 14.726 \sin 2.2286 \frac{x}{l} + 2.2286 \cos 2.7205 \frac{x}{l} - 12.170 \frac{x}{l} + 8.2462 \left(\frac{x}{l}\right)^2 + 2.1672 \left(\frac{x}{l}\right)^3 - 2.2286$.

is given by the following equation, which conservatively assumes that the pressure-volume product of the trapped air remains constant

$$W = p_o V_f \left(\frac{V_o}{V_f} \right) \log_e \frac{V_f}{V_o} , \quad (19)$$

where

W = work done,

p_o = initial pressure,

V_o = initial volume of trapped air,

V_f = final volume.

If p_o and V_o/V_f are constant then the effect of size is that the work that will be done is proportional to the final volume.

This work must be absorbed by work required to unfold the packaged material and by strain energy in the material after it unfolds. If the material of satellites or components compared is the same, then the effect of the size is that the energy absorption capacity is proportional to the surface area.

Since the energy absorbed by the satellite shell must be equal to the work done on it, the important size parameter is the ratio of volume to area.

Designating the size parameter as \bar{h} , then

$$\bar{h} = \frac{\text{final volume}}{\text{surface area}} .$$

For comparison it is interesting to note that for a sphere

$$\bar{h} = \frac{\frac{4}{3}\pi R^3}{4\pi R^2} = \frac{R}{3} = \frac{D}{6} \text{ ft} ,$$

for Echo I

$$\begin{aligned}\bar{h} &= \frac{100}{6} \\ &= 16.7 \text{ ft ,}\end{aligned}$$

and for Echo II

$$\begin{aligned}\bar{h} &= \frac{135}{6} \\ &= 22.5 \text{ ft .}\end{aligned}$$

The lenticular satellite consists of three inflatable portions, torus, lens, and tripod. These are interconnected by small passageways and consequently the three portions can be considered independent of one another for the short times involved during deployment.

For the torus.

$$\begin{aligned}\bar{h} &= \frac{41,720}{21,302} \\ &= 1.96 \text{ ft .}\end{aligned}$$

This value is very small compared to that of Echo I and it can be concluded that trapped air will not be a problem.

For the lens.

$$\begin{aligned}\bar{h} &= \frac{3,070,000}{129,112} \\ &= 23.7 \text{ ft .}\end{aligned}$$

This is slightly greater than the value for Echo II and indicates that the lens might present a problem. However, the packaging arrangement is such that the lens cannot develop directly into its final shape and the effective \bar{h} therefore is probably much less than the above value. This is to some extent borne out by the deployment of the 20-ft model in a vacuum chamber.

The tripods are simply cylinders and

$$\begin{aligned}\bar{h} &= \frac{D}{4} \\ &= \frac{1}{4 \times 4} \\ &= \frac{1}{16} \text{ ft.}\end{aligned}$$

Hence, the effect of the trapped air on the tripod itself is negligible. Another problem, however, is the outward velocity that might be imparted to the canister halves and other masses attached to the tripods by the elements expanding between them. For the upper part of the satellite the pertinent parameters are:

$$\begin{aligned}m &= \frac{151}{32.2} \\ &= 4.69 \text{ slugs}\end{aligned}$$

Length of tripod = 328.5 ft

Diameter of tripod = 0.25 ft

The final volume V_f of the three legs of the tripod

$$\begin{aligned}V_f &= \frac{3 \times \pi(0.25)^2 \times 328.5}{4} \\ &= 48.3 \text{ cu ft.}\end{aligned}$$

If it is assumed that the initial pressure

$$\begin{aligned}p_o &= 1 \text{ mm Hg} \\ &= 2.8 \text{ psf}\end{aligned}$$

and that the final-to-initial volume ratio is

$$\frac{V_f}{V_o} = 1000,$$

then the total work done could be

$$W = \frac{2.8 \times 48.3 \times 6.908}{1000}$$
$$= 0.92 \text{ ft lb .}$$

Assuming all of this work is converted into kinetic energy of the attached mass, the velocity is given by

$$v = \left(\frac{2W}{m} \right)^{1/2}$$
$$= \left(\frac{2 \times 0.92}{4.69} \right)^{1/2}$$
$$= 0.626 \text{ fps .} \quad (20)$$

The total time for the mass to reach its full travel (fully extended booms) would be

$$\text{Time} = \frac{300}{0.626}$$
$$= 480 \text{ sec .}$$

Inflation of the system will be initiated shortly after separation (15 sec) and the tripod booms will be at least partially inflated as columns before their elasticity can start the mass on its return trip toward the center of the satellite. Even partially inflated tripods should be capable of arresting the return velocity of the mass.

f. Launch

No analysis is shown for the launch conditions. This phase of the operation cannot be treated until the detail design stage of the program. Past experience indicates that proper support can be provided for critical elements to meet the accelerations, vibration, and shock loads that will be encountered during boost.

g. Pressurization Study

(1) Introduction

The objective of the pressurization study was to size tentatively

the flow control orifices and to predict the pressure-time relationships for the full-scale lenticular satellite. The concepts and methods of analysis described in Appendixes B and C were used in this analysis.

(2) Assumed System Parameters

The full-scale satellite is shown in Figure 9. The lens has a volume of approximately 3,100,000 cu ft and a surface area of 129,000 sq ft, while the torus has a total volume of 41,700 cu ft and a surface area of 21,300 sq ft. Torus bulkheads are located at 45, 90, 120, and 180 deg from the gas inlet port, clockwise around the torus.

The pressurizing or inflating gas was assumed to be helium stored at 3000 psi. This gas will pass through a pressure regulator set for 5 psia and then through individual flow-limiting orifices before entering the lens and torus. On-off valves and pressure sensors will prevent the pressures from exceeding design values, or will maintain these pressures as required.

The first chamber of the torus will be pressurized to the design value of 0.1678 psia in approximately 80 sec and maintained at this pressure. A total of five minutes has been allotted for pressurization of the torus chambers, followed by five minutes for pressurization of the lens to the design pressure of 0.000316 psia. After lens inflation the design pressures will then be maintained for an additional period of two and four minutes for the lens and torus, respectively, followed by shut-off of the pressurization system with pressure decay resulting.

(3) Analysis

The lens and torus must be perforated with exhaust holes to permit depressurization. These holes are presumed to be 0.020-in. diameter, and the torus is assumed to have one hole in each

square foot of surface area. Rigidity considerations indicate that the lens should depressurize at least as rapidly as the torus, and on this basis the number of exhaust holes per unit area can be computed for the lens.

Appendix B presents the flow equations for the exhaust holes. For free molecular flow in terms of upstream pressure:

$$\frac{W\sqrt{T}}{PA} = \frac{135.7}{\sqrt{R}} \quad (21)$$

or, for helium:

$$\frac{W\sqrt{T}}{PA} = 6.905. \quad (22)$$

For choked continuum flow in terms of upstream pressure:

$$\frac{W\sqrt{T}}{PA} = 340.3 C_D \sqrt{\frac{K}{R} \left(\frac{2}{K+1} \right) \frac{K+1}{K-1}} \quad (23)$$

or, for helium with a coefficient of discharge of 0.9:

$$\frac{W\sqrt{T}}{PA} = 11.302. \quad (24)$$

Appendix B also indicates the transitional pressure as being in the order of 0.0063 psia. For pressures near design values, the flow from the torus will primarily be continuum and from the lens free molecular.

The depressurization equation was also derived in Appendix B and can be expressed:

$$\frac{P}{P_o} = e^{-\frac{R\sqrt{T}}{144 \times 60} \frac{A}{V} \left(\frac{W\sqrt{T}}{PA} \right) (\theta - \theta_o)}. \quad (25)$$

The depressurization rate is therefore a function of $(A/V) \times (W\sqrt{T}/PA)$. For the lens to have the same depressurization rate as the torus:

$$\left[\frac{A}{V} \left(\frac{W\sqrt{T}}{PA} \right) \right]_{\text{lens}} = \left[\frac{A}{V} \left(\frac{W\sqrt{T}}{PA} \right) \right]_{\text{torus}} \quad (26)$$

Utilizing Equations 22, 24, and 26, it was computed that the lens should have 20.1 exhaust holes per square foot of surface area. The lens was presumed to have 22 exhaust holes per square foot.

Appendix C presents the method for sizing torus bulkhead orifices. Several constants in the analysis were changed because the gas is helium rather than air; the helium values are 11.302 in Equation C-7, 14.69 in Equation C-8, 0.4083 for the pressure ratio determining applicability of Equations C-7 and C-8, and 0.04470 for Equations C-9 and C-12. Only the analysis in the vacuum condition was used. A supply flow rate of 3.1 lb/min and bulkhead flow control orifice sizes of 4.5-, 3.375-, and 2.25-in. diameters respectively, seemed to meet the specified conditions. The resultant pressure-time curves are given in Figure 58. The quantity of helium required for the 14 min of torus pressurization is 11.92 lb. The stabilized pressure values, $dP/d\theta = 0$, are 0.1678, 0.1655, 0.1624, and 0.1555 psia, respectively, which is a variation of 7.4 percent.

Appendix B presents the method for determining the lens flow rates and pressure-time curves. The pressurization equation can be expressed as:

$$P = 0.007369 \frac{\sqrt{RT}}{A} W_o \left(1 - e^{-0.015707 \sqrt{RT} \frac{A}{V} \theta} \right), \quad (27)$$

which reduces to

$$P = 0.003736 W_o (1 - e^{-0.002042\theta}) \quad (28)$$

For the specified time of five minutes and design pressure of 0.000316 psia, Equation 28 yields a mass flow rate (W_o) of 0.1846 lb/min. Figure 59 presents a plot of Equation 28.

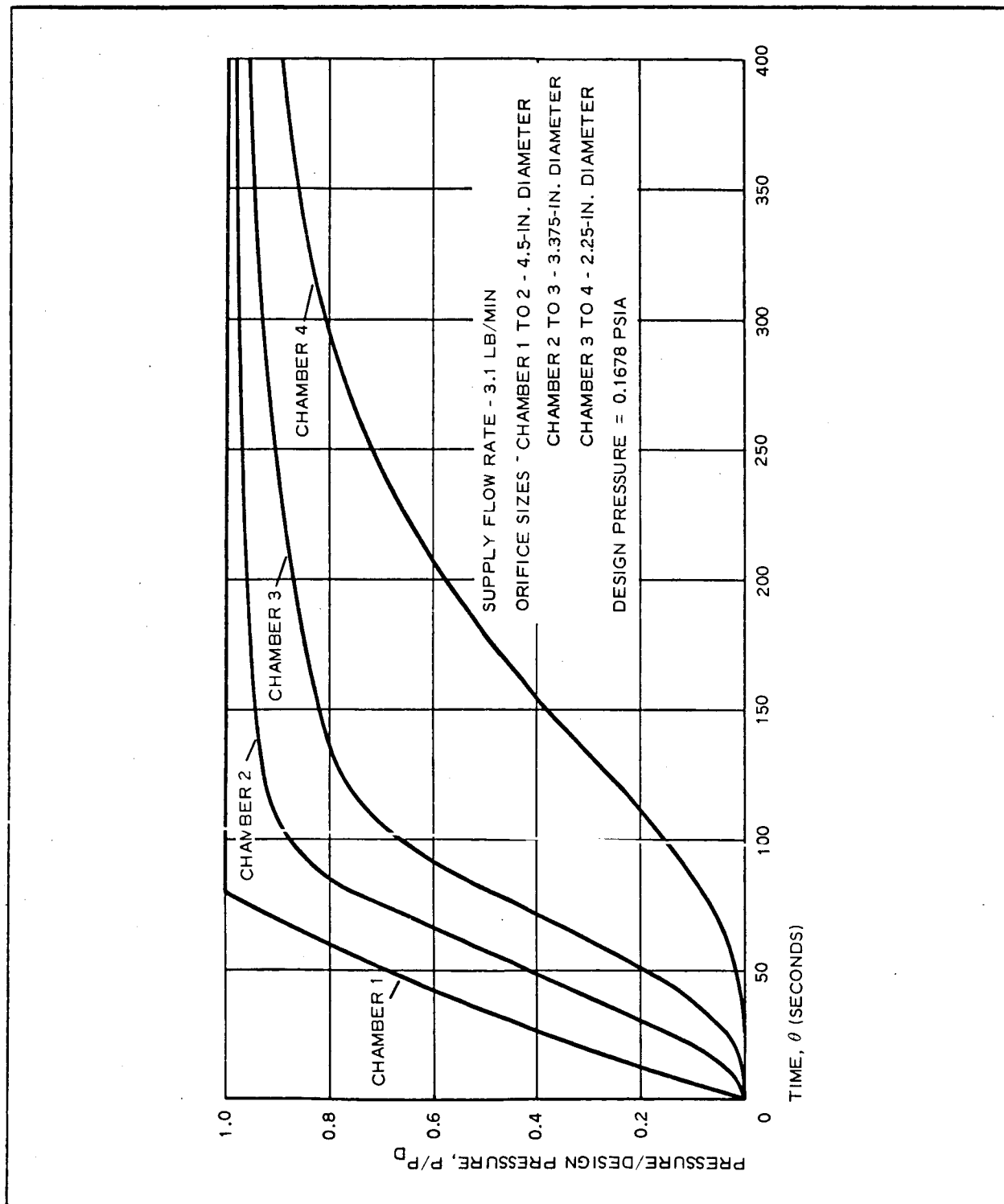


Figure 58 - Torus Pressures versus Time (Full-Scale Model)

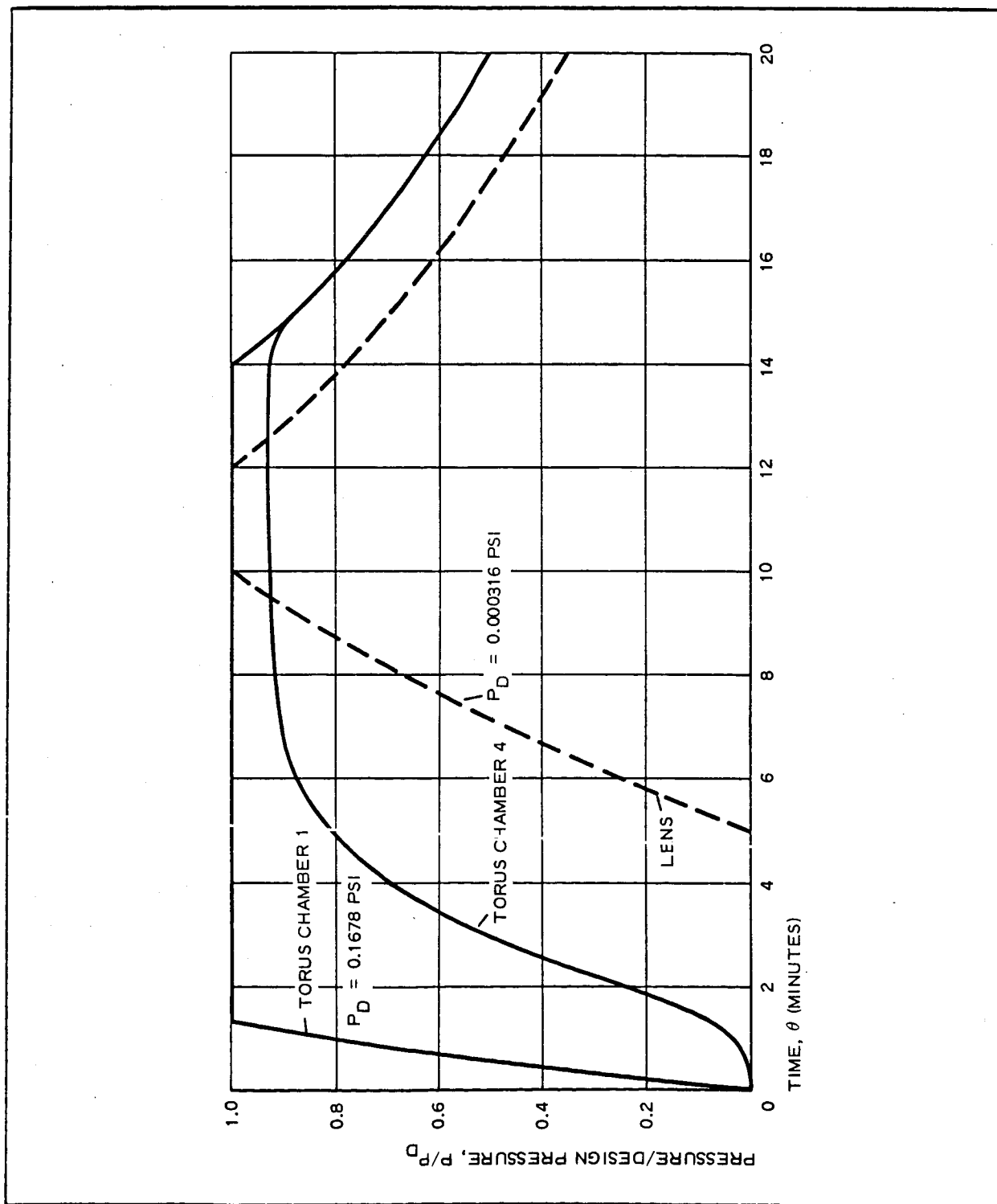


Figure 59 - Satellite Inflation Pressures versus Time (Full-Scale Model)

To maintain the design pressure, the supplied mass flow rate must equal the mass flow rate through the exhaust holes. Equation 22 yields this mass flow rate as 0.08458 lb/min. The quantity of helium required for the seven minutes of lens pressurization is 1.09 lb.

The depressurization equation has previously been expressed as Equation 25, and is applicable for the lens and torus. Figure 60 presents Equation 25 in graphical form for the lens and torus.

The total quantity of helium required is the sum of the 11.92 lb for the torus and 1.09 lb for the lens, or 13.01 lb. When stored at 3000 psi the required volume is 6.16 cu ft.

The supply orifice sizes can be computed from Equation 24, using the upstream pressure of 5 psia and the computed supply flow rates. The computed orifice sizes are 1.267- and 0.309-in. diameters for the torus and lens, respectively. The supply lines upstream of the orifices should be at least twice the orifice diameters or 2.75- and 0.75-in. diameters for the torus and lens, respectively.

(4) Summary

For the full-scale satellite the helium storage volume should exceed 6.16 cu ft at 3000 psia. The supply orifices should be 1.267- and 0.309-in. diameters for the torus and lens, respectively. Bulkhead orifices for the torus should be 4.5-, 3.375-, and 2.25-in. diameters in order from the inlet port. If 0.020-in. diameter exhaust holes are used, the torus should have one and the lens 22 holes per square foot of surface area.

The predicted pressure-time curves are given in Figures 58, 59, and 60.

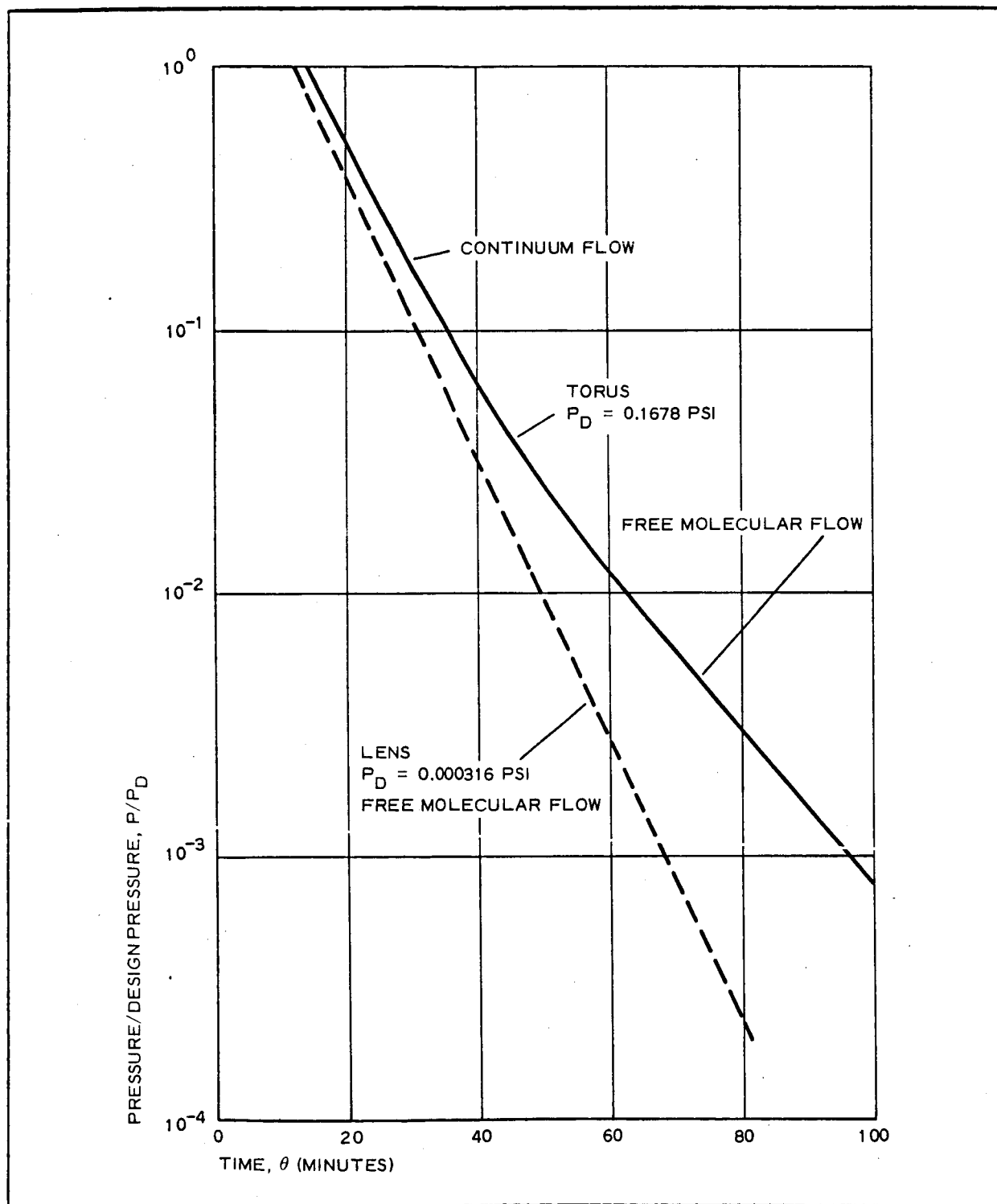


Figure 60 - Satellite Deflation Pressures versus Time (Full-Scale Model)

(5) List of Symbols

- A = orifice area
- C_D = coefficient of discharge
- K = ratio of specific heats
- P = total pressure in torus chamber, lens,
or ducts
- P_D = design pressure in torus or lens
- P_o = initial total pressure
- R = gas constant
- T = total temperature
- V = volume of gas in torus chambers or lens
- W = mass flow rate
- W_o = initial mass flow rate
- θ = time
- θ_o = initial time

h. Temperature Distribution Studies

(1) Introduction

The objective of the temperature distribution study was to predict lenticular satellite temperatures. These temperatures were used in material evaluations and confirm that orbital temperatures are adequate to cause photolysis of the lens and possibly of the torus. Measured values of the photolysis film thermal properties were used in this analysis.

After this study was completed the radius of the torus was decreased. This will reduce the radiation view factor from the lens to the torus and slightly increase the view factor from the

torus to the lens. The predicted temperatures for the new geometry would be slightly lower for the lens and slightly higher for the torus. These temperature changes are of negligible magnitude and the temperature distribution shown herein for the large torus radius can be considered applicable to the final configuration with the small torus radius.

(2) Assumed System Parameters

The satellite analyzed was the full-scale model shown in Figure 9, and was presumed to be in a low earth orbit (altitude approximately 250 mi) that passes through or near the earth-sun line. The lens and torus were assumed to be constructed of 0.7-mil (nominal) thick gridded film which is photolyzable on the lens and might be photolyzable on the torus. The apparent thermal properties of the film are given in Table VI for various dye concentrations. These properties are presumed independent of incidence angle. The satellite also was presumed to be gravity stabilized with respect to the earth.

The analysis considered the effects of film thickness, orbital altitude, and orbital position on the temperatures.

(3) Analysis

Thermal radiation is the only significant means of heat transfer within and to the satellite. External radiation inputs are direct solar radiation, albedo (earth-reflected solar radiation), and earth radiation.

The satellite was divided into 18 nodes as shown in Figure 61. The 10 lens nodes are circular strips of equal area. Since each half of the lens has a spherical radius of 42 deg, the node boundaries are 0 deg, 18 deg 27 min, 26 deg 12 min, 32 deg 14 min, 37 deg 23 min, and 42 deg. The eight torus nodes are also circular strips of equal area. Since each half of the torus has a

TABLE VI - THERMAL PROPERTIES OF FILM*

Property	Temperature of emitting body (F)	Dye concentration (parts dye per 100 parts resin by weight)	Value
Solar transmittance	~ 10, 000	0	0. 78
		2	0. 26
		3	0. 22
		5	0. 18
Solar absorptance	~ 10, 000	0	0. 19
		2	0. 72
		3	0. 76
		5	0. 80
Solar reflectance	~ 10, 000	0	0. 03
		2	0. 02
		3	0. 02
		5	0. 02
Infrared transmittance	-64	Any	0. 64
	8	Any	0. 61
	80	Any	0. 57
	152	Any	0. 55
	224	Any	0. 53
	296	Any	0. 53
Infrared absorptance (emittance)	-64	Any	0. 34
	8	Any	0. 37
	80	Any	0. 41
	152	Any	0. 43
	224	Any	0. 45
	296	Any	0. 45
Infrared reflectance	-64	Any	0. 02
	8	Any	0. 02
	80	Any	0. 02
	152	Any	0. 02
	224	Any	0. 02
	296	Any	0. 02

* 0. 7-mil film on 1. 6-mil phosphor bronze, 24 by 24 mesh grid.

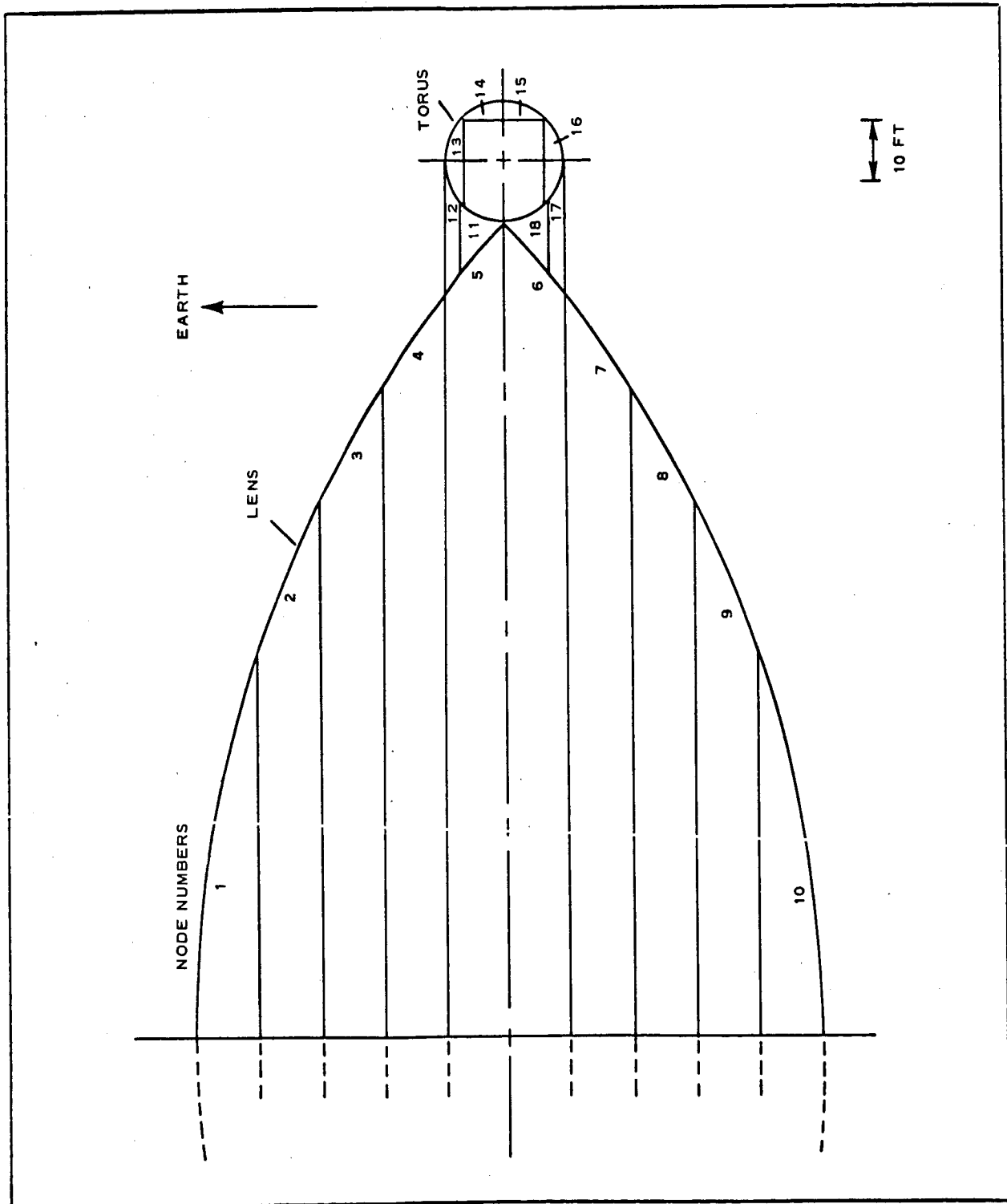


Figure 61 - Thermal Schematic of Lenticular Satellite

circular radius of 180 deg, the node boundaries are 0 deg, 48 deg 6 min, 94 deg 9 min, 137 deg 48 min, and 180 deg. This system of nodes presumes no temperature variation around the nodes, as is the case when the satellite is on the earth-sun line or in the earth's umbra. The above two orbital positions yield the highest and lowest satellite temperatures. To evaluate temperature distributions radially around the nodes, each of the 18 nodes would have to be divided into several nodes, thereby increasing the complexity of the analysis.

Thermal radiation heat or energy balances on each node are complicated by the transparency of the lens and torus. Each node views its surroundings (sun, earth, other nodes, and itself) through a series of overlays of transparent material. For example, the external surface of node 15 views the earth directly, while the internal surface views the earth through the torus film only and also through the torus film and two lens films. The most extreme case of overlays is four, with the internal surface of node 15 viewing itself through two lens films and two torus films.

Radiation view factors from the external and internal surfaces of each node to all 18 nodes, the earth, and the sun for each film overlay condition are fixed by the specified satellite geometry and orbital position. These view factors were computed by using standard equations and a unit hemisphere as described in pages 395 through 402 of Reference 8.

Incident radiation on each node consists of emitted radiation from all 18 nodes as well as solar, albedo, and earth radiation that might pass through intermediate layers of film. These radiation terms might come directly from the source to the receiving node, or might be reflected from one or more intermediate nodes. Because the reflectances are in the order of 0.02,

reflections are relatively unimportant. To simplify the analysis by eliminating reflections, effective film transmittances and absorptances were used, and are defined as follows. For spectral properties of a transparent film:

$$\tau_{\lambda}^A + \alpha_{\lambda}^A + r_{\lambda}^A = 1 \quad (29)$$

The effective transmittance is:

$$\tau_{\lambda} = \frac{\tau_{\lambda}^A}{1 - r_{\lambda}^A} \quad (30)$$

The effective absorptance is:

$$\alpha_{\lambda} = \frac{\alpha_{\lambda}^A}{1 - r_{\lambda}^A} \quad (31)$$

Then:

$$\tau_{\lambda} + \alpha_{\lambda} = 1 \quad (32)$$

An energy balance on each node (n) is then:

$$\begin{aligned} 2 \epsilon_n^A \sigma T_n^4 = & \sum_{m=1}^{m=18} \alpha_{n,m} \epsilon_m^A \sigma T_m^4 \sum_{J=0}^{J=4} \left[F_{J(n,m)}^E \tau_{o-J}^m + \right. \\ & \left. F_{J(n,m)}^I \tau_{o-J}^m \right] + \alpha_{n,B} \sum_{J=0}^{J=3} \left[F_{J(n,B)}^E \tau_{o-J}^B + F_{J(n,B)}^I \tau_{o-J}^B \right] + \\ & \alpha_{n,S^Q} \sum_{J=0}^{J=3} F_{J(n,B)}^E \tau_{o-J}^S + F_{J(n,B)}^I \tau_{o-J}^S + \\ & \alpha_{n,S^C} \sum_{J=0}^{J=1} \left[F_{J(n,S)}^E \tau_{o-J}^S + F_{J(n,S)}^I \tau_{o-J}^S \right] \end{aligned} \quad (33)$$

where

$$\tau_{o-J}^m = \tau_o^m \times \tau_1^m \times \tau_2^m \dots \tau_J^m \quad (34)$$

$$\tau_{o-J}^B = \tau_o^B \times \tau_1^B \dots \tau_J^B \quad (35)$$

$$\tau_{o-J}^S = \tau_o^S \times \tau_1^S \dots \tau_J^S \quad (36)$$

The subscripts 1, 2, . . . J in the above equations are defined as the respective film layers through which the radiation passes. The subscript o refers to zero layers, so that:

$$\begin{aligned} \tau_o^m &= \tau_o^B \\ &= \tau_o^S \\ &= 1. \end{aligned} \quad (37)$$

It is noted that the spectral properties of thermal radiation are altered somewhat when passing through one or more transparent films, due to the variation of spectral transmittance with wavelength. This effect is neglected in this analysis for simplicity. The radiation constants (B and Q) in Equation 33 are the values at the apparent surface of the earth, while the solar constant (C) is the value at one astronomical unit from the sun. Because the solar constant is defined in this manner, the radiation view factor to the sun must be defined as:

$$\begin{aligned} F_{J(n, S)}^E &= F_{J(n, S)}^I \\ &= \frac{A_{np}}{A_n}. \end{aligned} \quad (38)$$

By specifying the film properties and orbital position, Equation 33 yields a set of 18 linear equations involving the 18 values of

T_n^4 as the 18 unknown parameters. Simultaneous solution of these equations will produce the node temperatures.

Table VII presents 8 solutions of Equation 33. These solutions are for the lens film containing zero, 2, 3, and 5 parts dye per 100 parts resin by weight with the torus film being either clear (0 parts dye) or the same as the lens film. Two orbital positions were considered, the earth-sun line, and the earth's umbra with an altitude of approximately 250 mi. Dye concentrations of 2, 3, or 5 parts are sufficient to raise the temperatures of lens nodes 6 to 10 above the approximately 225 F required for photolysis, while the clear film (zero parts dye) is obviously inadequate. The torus is noted to be cooler than the lens, with only one or two nodes exceeding 225 F with dye concentrations of 2, 3, or 5 parts.

Although Table VII indicates that lens nodes 6 to 10 will photolyze with dye concentrations of 2, 3, or 5 parts, it must still be established that lens nodes 1 to 5 will also photolyze. This is accomplished by taking the case wherein the lens dye concentration is 2 parts with a clear torus, and presuming that certain nodes have been photolyzed, i. e., their transmittances approach unity. Equation 33 is again valid, and Table VIII presents the results of this investigation.

As a first step the two hottest nodes, 9 and 10, are presumed photolyzed. As shown, the effect on nodes 6, 7, and 8 is negligible; nodes 3, 4, and 5 are cooler; while nodes 1 and 2 receive direct solar heating and attain high temperatures. The order of photolysis might conceivably be one of two orders, depending upon photolysis rate with temperature. The first possibility is, in order, nodes 10, 9, 8, 7, 6, 1, 2, 3, 4, and 5; while the second possibility is nodes 10, 1, 9, 2, 8, 3, 7, 4, 6, and 5. If nodes 1 and 10 are photolyzed, the effect on nodes 6 to 9 is

TABLE VII - SATELLITE TEMPERATURES

Dye concentration (parts dye per 100 parts resin by weight)		Orbital,* position	Temperature at node number (F)																	
Lens	Torus		1	2	3	4	5	6	7	9	10	11	12	13	14	15	16	17	18	
0	0	1	104	98	91	88	92	95	90	94	100	106	37	71	63	6	61	68	29	
2	2	1	213	207	199	195	198	247	244	251	259	267	126	160	152	89	219	227	151	
2	0	1	212	206	198	192	191	241	243	250	258	266	76	81	72	22	68	77	66	
3	3	1	213	207	199	195	198	252	249	256	265	273	126	159	151	89	225	233	155	
3	0	1	212	206	198	192	192	246	248	255	264	272	77	82	72	23	68	77	67	
5	5	1	213	207	200	195	198	258	256	263	271	283	125	157	149	89	232	240	159	
5	0	1	212	206	198	193	192	252	255	262	271	279	79	82	72	23	69	78	68	
any	any	2	-72	-76	-82	-84	-86	-112	-116	-114	-111	-108	-106	-87	-91	-113	-139	-135	-138	

* Orbital positions

1 = earth-sun line, 250-mi altitude

2 = umbra, 250-mi altitude

TABLE VIII - PARTIALLY PHOTOLYZED LENS TEMPERATURES*

Nodes photolyzed	Temperature of node number (F)									
	1	2	3	4	5	6	7	8	9	10
None	212	206	198	192	191	241	243	250	258	266
9, 10	294	287	178	179	183	241	245	254
1, 10	...	192	187	184	186	239	242	250	259	...
6, 7, 8, 9, 10	282	273	262	254	247

* Orbital position = earth-sun line, 250-mi altitude.

Dye concentration of lens = 2 parts dye per 100 parts resin by weight.

Dye concentration of torus = 0 parts dye per 100 parts resin by weight.

Thickness of films = 0.7 mils (nominal).

again negligible, while nodes 2 to 5 are cooler. It is therefore obvious that nodes 6 to 10 will photolyze no matter what order of photolyzation occurs. With nodes 6 to 10 photolyzed, nodes 1 to 5 all exceed 225 F, and will also photolyze. Higher dye concentrations will, of course, accelerate the process.

Another question of interest is the effect of film thickness on temperature. In order to evaluate this effect the properties of the 2 parts dye film will be estimated for a thickness of 0.5 mils (nominal) and compared to the values for a thickness of 0.7 mils (nominal). With an 0.7-mil thickness the values of emittance and solar absorptance are 0.45 and 0.72 respectively, with apparent reflectances of 0.02. The values of emittance and solar absorptance probably vary exponentially with thickness, so that:

$$\frac{\epsilon^A}{1 - r^A} \approx 1 - e^{-D_1 t} \quad (39)$$

and

$$\frac{\alpha_S^A}{1 - r^A} \approx 1 - e^{-D_2 t} \quad (40)$$

where D_1 and D_2 are constants. Using the 0.7-mil values, D_1 and D_2 are found to be 0.877 and 1.894 respectively. Neglecting any variation of reflectance with thickness, the emittance and solar absorptance with an 0.5-mil thickness are 0.35 and 0.61 respectively. The ratio of solar absorptance to emittance for the 0.7- and 0.5-mil films is 1.60 and 1.74, respectively, which indicates that the thinner film will have a higher temperature. For a double-wall transparent object the following ratio $\alpha_S^A(2 - \alpha_S^A)/\epsilon^A(2 - \epsilon^A)$ is probably more indicative of temperatures than the α_S^A/ϵ^A ratio; the same conclusion is attained by use of this ratio.

The above discussion on film thickness is also applicable during the photolyzation process. The film being photolyzed is expected to decrease in thickness until it disappears completely because the resin will photolyze more rapidly than the dye and the dye concentration increase during photolyzation. Both of these effects tend to increase film temperatures.

Orbital altitudes greater than 250 mi and positions other than on the earth-sun line will decrease temperatures from the listed values. Although no formal computations have been made on these variations, it is estimated that increasing the altitude to 2000 mi will decrease temperatures by approximately 40 F, and moving 30 deg from the earth-sun line will decrease temperatures by approximately 15 F.

Another computation of interest is the thermal response time of the film. For thermal radiation the thermal response time is a variable dependent upon initial and final temperatures. As an estimate consider a single sheet of 0.7-mil (nominal) film of

unit area initially at -100 F (360 R) seeking an equilibrium temperature of 225 F (685 R). The energy balance equation can be written:

$$2\epsilon^A \sigma (685^4 - T^4) = WC_p \frac{dT}{d\theta} \quad (41)$$

Integrating:

$$2 \tan^{-1} \frac{T}{685} - \ln \left[\frac{1 - \frac{T}{685}}{1 + \frac{T}{685}} \right] = 2 \tan^{-1} \frac{360}{685} - \ln \left[\frac{1 - \frac{360}{685}}{1 + \frac{360}{685}} \right] + \frac{8\epsilon^A \sigma (685)^3 \theta}{WC_p} \quad (42)$$

The emittance (ϵ^A) is 0.41 and WC_p is estimated as 0.0031 Btu/sq ft/R. Taking the temperature as 105 F (565 R), which means the temperature has risen $(1 - 1/\epsilon)$ of the maximum, the time is found to be approximately 9 sec.

(4) Conclusions

By the addition of small amounts of dye to the photolyzable film the lens and torus temperatures can be raised to the levels required for photolyzation. The precise amount of dye required cannot be established at this time. Additional data regarding thermal properties and photolyzation rates together with system requirements such as orbital altitude and inclination and time required for the inflation-deflation sequence must be defined in order to do this.

(5) List of Symbols

A_n = area of node n (one side)

A_{np} = projected area of node n with respect to sun

B = earth radiation constant (66.36)

C = solar constant (442.4)

C_p = specific heat of gridded film

D = constant

F^E = radiation view factor from external surface

F^I = radiation view factor from internal surface

J = number of intermediate films

n = node number

Q = albedo constant (176.96 on earth-sun line)

r^A = apparent reflectance

T = temperature

W = mass of gridded film

α = effective absorptance

α^A = apparent absorptance

ϵ^A = apparent emittance

θ = time

σ = Stefan-Boltzmann constant (0.1714×10^{-8})

τ = effective transmittance

τ^A = apparent transmittance

τ^B = effective transmittance to radiation from earth

τ^m = effective transmittance to radiation from node m

τ^S = effective transmittance to radiation
from sun

Subscripts

J = number of intermediate films

m = node number

n = node number

n, B = node n to earth

n, m = node n to node m

n, S = node n to sun

S = solar

λ = spectral

i. Error Analysis

(1) General

The equations required for the error analyses were developed in Reference 3, and are included herein in Appendix D. The basic equation is:

$$\rho = \rho_0 + \left. \frac{\partial \rho}{\partial S} \right|_0 (\Delta S) + \left. \frac{\partial \rho}{\partial D} \right|_0 (\Delta D) \quad (43)$$

For this case the included half angle is 42 deg and from Figure D-3 of Appendix D the values of the coefficient are:

$$\left. \frac{\partial \rho}{\partial S} \right|_0 = -3$$

$$\left. \frac{\partial \rho}{\partial D} \right|_0 = 4$$

The basic equation for the full-scale satellite becomes:

$$\rho = \rho_0 - 3(\Delta S) + 4(\Delta D) \quad (44)$$

Under ideal conditions the radius of curvature of the lens would be ρ_0 . Variations in arc length, ΔS , and chord, ΔD , from the ideal values S_0 and D_0 will arise from several sources. These will be discussed below.

(2) Manufacturing Tolerances

It is planned to determine the diameter of the torus by measurement before the lens is assembled to it. This will make ΔD essentially zero. A tolerance of two inches is estimated to be reasonable for the arc length.

Therefore:

$$\begin{aligned} \Delta S &= \frac{2}{12} \\ &= 0.167 \text{ ft} \end{aligned}$$

and the error in radius of curvature

$$\begin{aligned} \Delta \rho &= \rho - \rho_0 \\ &= -3(0.167) \\ &= \pm 0.50 \text{ ft} . \end{aligned}$$

(3) In-plane Rim Deflection

The maximum rim in-plane deflections were obtained in Item c. Combining the two cases gives:

$$\begin{aligned} \Delta D &= \frac{2(0.226 + 0.094)}{12} \\ &= 0.057 \text{ ft} \end{aligned}$$

$$\begin{aligned}\Delta\rho &= 4 \times 0.057 \\ &= 0.228 \text{ ft.}\end{aligned}$$

(4) Torus Pressure

The nominal design pressure of the torus is 0.1678 psi (Item b) and the cross-sectional area is 6940 sq in. The total torus load is $6940 \times 0.1678 = 1165$ lb. Assuming that the pressure can be controlled to ± 10 percent the variation in load would be ± 116.5 lb.

It was conservatively assumed that the load variation is carried entirely by the rim which has a cross-sectional area of 0.03351 sq in. The change in diameter is:

$$\begin{aligned}\Delta D &= \frac{116.5 \times 267}{0.03351 \times 18 \times 10^6} \\ &= 0.051 \text{ ft} \\ \Delta\rho &= \pm 0.204 \text{ ft.}\end{aligned}$$

(5) Lens Pressure

The nominal lens pressure is 0.000316 psi, based on a wire stress of 23,000 psi (Item a). The load-strain curve for the lens material is not known but should be similar in form to the stress-strain curve shown on page 29 of Reference 10. Based on this assumption, the effect of a ± 10 -percent pressure variation on the lens radius of curvature will be as listed in Table IX.

(6) Temperature

The lens material is a composite with load-strain characteristics that are affected by temperature. The stress-strain curve of the copper wire is little affected in the temperature range of interest, but the photolyzable film is very sensitive. This is apparent from the stress-strain curves for photolyzable film at 74, 85

TABLE IX - EFFECT OF TORUS PRESSURE VARIATION ON LENS
RADIUS OF CURVATURE FOR FULL-SCALE SATELLITE

Pressure		Wire stress (psi)	Elongation, ϵ (in./in.)	$\Delta\epsilon$ (in./in.)	ΔS (ft)	$\Delta\rho$ (ft)
Torus	Lens (psi $\times 10^{-3}$)					
-10 percent	0.284	20,700	0.0018	-0.0005	-0.147	+0.44
Nominal	0.316	23,000	0.0023			
+10 percent	0.348	25,300	0.0035	0.0012	0.352	-1.06

and 100 F shown on page 72 of Reference 9. At 100 F the stress is less than 10 psi for strains less than 0.01 and the effect of the film on the characteristics of the composite material can be neglected for all temperatures above 100 F. No data are available on the cold temperature characteristic of photolyzable film but it is evident that it will significantly affect the load strain characteristics of the composite material.

From the above considerations plus the temperature distribution study given in Item h it can be concluded that:

1. In the sun, both sides of the lens will behave the same and depend only on the wire properties. Therefore, the error computed above due to lens pressure is directly applicable.
2. If the inflation is done in the dark the temperature will be about -100 F and the film properties must be taken into account.

(7) Summary

The computed errors are listed in Table X.

TABLE X - LENS RADIUS OF CURVATURE
ERRORS FOR FULL-SCALE SATELLITE

Source of error	Δp (ft)	
	Positive	Negative
Manufacturing tolerances	0.50	0.50
Rim deflections	0.23	0.23
Torus pressure	0.20	0.20
Lens pressure	0.44	1.06

Rim deflection and torus pressure contribute only small variations in the radius of curvature. Manufacturing tolerances and lens pressure will cause the larger sources of error and should be given careful attention in the future. The total errors, assuming that all signs are the same, are +1.37 ft and -1.99 ft. This indicates that it is feasible to obtain the tolerance of ± 2 ft specified for the over-all radius of curvature of the lens.

The above calculations assume that the seams have the same load-strain characteristics as the basic material. If this is not so, then the problem is primarily one of meeting the local radius of curvature requirements. Attempts to match the seams and the basic material appear promising (Reference 9, Figure 39). From this figure it is evident that the 1.5-mil videne and the 1.0-mil slotted Mylar show the most promise.

j. Weights and Inertias

The weights and inertias of the principal elements of the full-scale satellite (see Figure 62), computed in accordance with the formulas shown in Appendix E, are listed in Table XI.

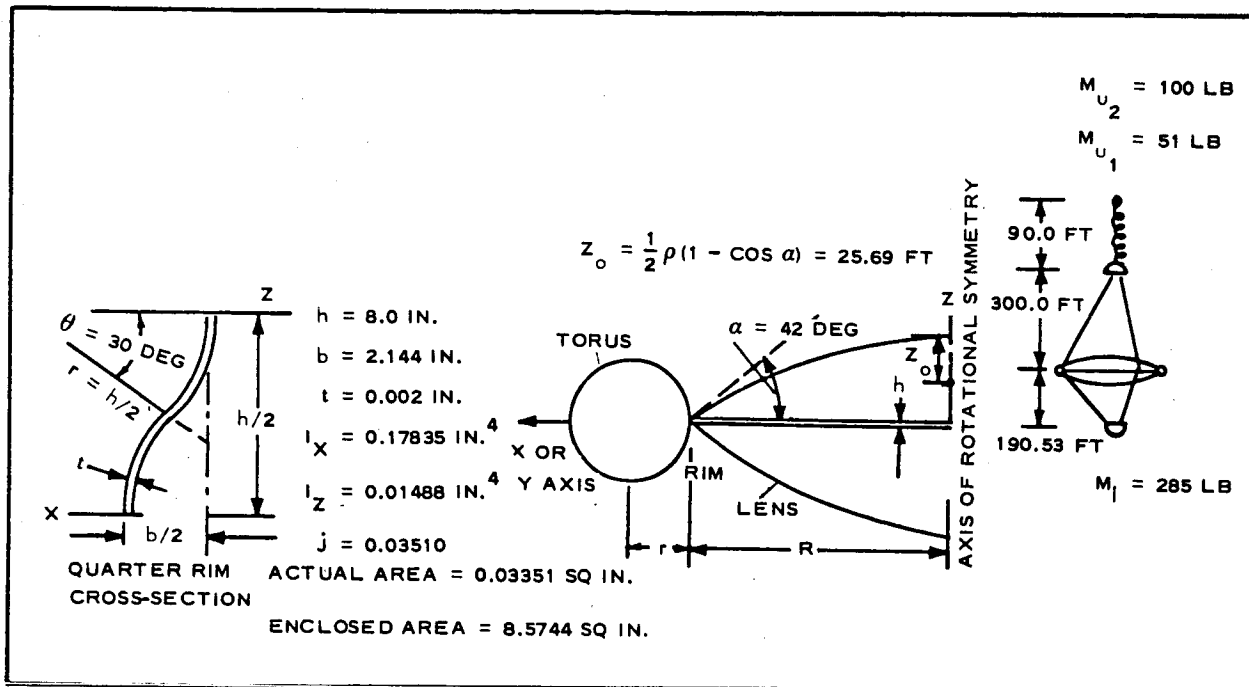


Figure 62 - Principal Elements of Full-Scale Satellite

3. FIFTY-FOOT-DIAMETER FLIGHT TEST MODEL

a. Lens

(1) Inflation Pressure

The lens material of the 50-ft flight test model will be 1.2-mil copper wires spaced 21 per inch bonded on 0.6-mil photoiyzable film.

$$\begin{aligned}
 \text{Yield stress} &= f_{ly} \\
 &= 21 \frac{\pi}{4} (0.0012)^2 (23,000) \\
 &= 0.5463 \text{ lb/in.} \quad (45)
 \end{aligned}$$

TABLE XI - WEIGHTS AND INERTIAS OF FULL-SCALE SATELLITE

Materials and properties	Satellite component					
	Lens (spherical zone)	Torus	Rim	Mass		
				M_l	M_{u_1}	M_{u_2}
Material	1-mil copper wire at 21 per inch. 0.5-mil photolyzable film	1-mil photolyzable film	0.002-in. beryllium-copper alloy			
Young's modulus, E.	Only copper $10 - 16 \times 10^6$ psi	0.444×10^6 psi	18×10^6 psi			
Poisson's ratio, μ		0.4	1/3			
Surface area (sq ft)	One cap 64,556	21,302	Actual foil area - 1174.1			
Enclosed volume (cu ft)	Between two spherical zones and rim 3,070,000	41,720				
Weight per sq in. of surface when photolyzable film is ON (lb)	0.0000297	0.0000380	0.000594			
Weight per sq in. of surface when photolyzable film is OFF (lb)	0.0000107	0	0.000594			
Total weight (lb) *	Two caps ON - 552.2 OFF - 199.0	ON - 116.6 OFF - 0	100.4	285	51	100
Weight of helium (lb)	0.74	5.30				
Polar moment of inertia I_{z-z} (lb ft sq)	ON* - 5,187,496 OFF - 1,868,896	ON - 2,214,352 OFF - 0	1,798,696	0	0	0
Moment of inertia† I_{x-x} or I_{y-y} (lb ft sq)	ON - 3,089,019 OFF - 1,112,879	ON - 1,108,070 OFF - 0	899,348	10,345,979	4,590,000	

* The designations ON or OFF in the table refer to the lens and torus photolyzable film before and after its disappearance, respectively.

† Principal Moments of Inertia of Satellite

- Without photolyzable film

$$I_{x-x} = I_{y-y} = 16,948,206 \text{ lb ft sq}, I_{z-z} = 3,667,592 \text{ lb ft sq}; \frac{I_{x-x}}{I_{z-z}} = 4.621$$

- With photolyzable film ON

$$I_{x-x} = I_{y-y} = 20,032,416 \text{ lb ft sq}, I_{z-z} = 9,200,544 \text{ lb ft sq}; \frac{I_{x-x}}{I_{z-z}} = 2.177$$

$$\begin{aligned}\rho &= 200 \times \frac{25}{133.83} \\ &= 37.36 \text{ ft} \\ &= 448.32 \text{ in.}\end{aligned}\tag{46}$$

$$\begin{aligned}p_l &= \frac{2f_l y}{\rho} \\ &= \frac{2 \times 0.5463}{448.32} \\ &= 0.002437 \text{ psi.}\end{aligned}\tag{47}$$

(2) Buckling Pressure.

$$\begin{aligned}p_{cr} &= 0.191 E_c \frac{d^3}{s \rho^2} \\ &= 0.191 \times 10 \times 10^6 \frac{(0.0012)^3}{\left(\frac{1}{21}\right) (448.32)^2} \\ &= 34.48 \times 10^{-8} \text{ psi}\end{aligned}\tag{48}$$

This pressure is much higher than the solar radiation pressure of 13.6×10^{-10} psi (two orders of magnitude).

b. Torus

The torus material of the flight test model will be Mylar film. From equations similar to 4 and 5 of the full-scale model, the ratio r/R can be found,

$$\frac{r}{R} = \frac{2}{64,400 t_t - 3}\tag{49}$$

For $t_t = 1$ mil,

$$\begin{aligned}\frac{r}{R} &= \frac{2}{61.4} \\ &= 0.03257\end{aligned}$$

Then

$$\begin{aligned} r &= 25 \times 0.03257 \\ &= 0.814 \text{ ft} \\ &= 9.77 \text{ in.} \end{aligned}$$

The inflation pressure can be found from Equation 5, in which F.S = 1.25 and the number 10,000 should be replaced by 13,000; hence

$$\begin{aligned} P &= \frac{\left[\frac{13,000}{1.25} (2 \times 0.001) \right]}{9.77 \times 2.03257} \\ &= 1.047 \text{ psi.} \end{aligned}$$

c. Rim

(1) General

For material, cross sections, dimensions, and other properties see Item j.

As in the full-scale model critical conditions are (1) IV-AM-OFF for in-plane deflection and (2) III-AM-ON for out-of-plane deflection.

Concentrated loads at the ends of the tripods and distributed loads around the rim can, in general terms, be taken from Table IV.

In the present configuration

$$\omega = \frac{R_E}{\rho_o} \sqrt{\frac{g}{\rho_o}}$$

where R_E = earth radius = 3437.7 naut mi, and $\rho_o = R_E + 700 = 4137.7$ naut mi. Then

$$\begin{aligned} \omega &= \frac{3437.7}{4137.7} \sqrt{\frac{32.2}{4137.7 \times 1.15 \times 5280}} \\ &= 0.9404 \times 10^{-3} \text{ sec}^{-1}, \end{aligned}$$

$$\omega^2 = 0.88435 \times 10^{-6} \text{ sec}^{-2},$$

$$M_\rho = \frac{56.5}{32.2}$$

$$= 1.7547 \text{ slugs, and}$$

$$H_\rho = 22.02 \text{ ft.}$$

The above values are common for conditions III and IV.

For condition III (photolyzable film on)

$$\begin{aligned}\lambda &= (I_{x-x} - I_{z-z}) \div I_{x-x} \\ &= 1 - \frac{1}{3.438} \\ &= 0.7091\end{aligned}\tag{51}$$

$$\begin{aligned}m_r' &= \frac{1}{g}(24.8 + 6.0 + 7.0) \div 2\pi(25 \times 12) \\ &= 0.000623 \text{ slugs/in.}\end{aligned}\tag{52}$$

For condition IV (photolyzable film off)

$$\begin{aligned}\lambda &= (I_{x-x} - I_{z-z}) \div I_{x-x} \\ &= 1 - \frac{1}{4.620} \\ &= 0.7835\end{aligned}\tag{53}$$

$$\begin{aligned}m_r' &= \frac{1}{g}(10.0 + 6.0 + 7.0) \div 2\pi(25 \times 12) \\ &= 0.000379 \text{ slugs/in.}\end{aligned}\tag{54}$$

(2) Maximum In-Plane Deflection

The maximum in-plane deflection is derived in the same manner as for the full-scale satellite [see Item 2, c, (2)].

$$\begin{aligned}
 P_z &= -M_\lambda H_\lambda \omega^2 (3 + 4\lambda \sin^2 \beta_o) \\
 &= -1.7547 \times 22.02 \times 0.88435 \times 10^{-6} \left(3 + 4 \times 0.7835 \times \frac{1}{2}\right) \\
 &= -0.156 \times 10^{-3} \text{ lb.}
 \end{aligned} \tag{55}$$

$$\begin{aligned}
 q_{rx} &= R m_r' \omega^2 \left(1 - 4\lambda \sin^2 \beta_o\right) \sin \phi \\
 &= 25 \times 0.000379(0.88435)10^{-6} \left(1 - 4 \times 0.7835 \times \frac{1}{2}\right) \sin \phi \\
 &= -4.75 \times 10^{-9} \sin \phi \text{ lb/in.}
 \end{aligned} \tag{56}$$

$$\begin{aligned}
 Q_1 &= Q_2 \\
 &= Q_3 \\
 &= -\frac{1}{3}(0.156)10^{-3} \left(\frac{25}{22.02} + \frac{25}{42.03}\right) \\
 &= -0.0900 \times 10^{-3} \text{ lb.}
 \end{aligned}$$

Maximum deflection at point 1 (see Figure 55) due to the concentrated loads Q:

$$\begin{aligned}
 W_Q &= 0.0079 \frac{2P_z R^4}{3EI_z} \left(\frac{1}{H_\ell} + \frac{1}{H_u}\right) \\
 &= 0.0079 \times \left(\frac{2}{3}\right) \frac{2(0.156)10^{-3}(25 \times 12)^4}{3 \times 18 \times 10^6 \times 0.0007776} \left(\frac{1}{12}\right) \left(\frac{1}{22.02} + \frac{1}{42.03}\right) \\
 &= 0.00183 \text{ in. (very small),}
 \end{aligned} \tag{57}$$

Maximum deflection at point $\phi = 90$ deg due to distributed load

q_{rx}

$$\begin{aligned}
 w_q &= \frac{q_{90 \text{ deg}} R^4}{6EI_z} \\
 &= \frac{4.75 \times (25 \times 12)^4 \times 10^{-9}}{6 \times 18 \times 10^6 \times 0.0007776} \\
 &= 0.00046 \text{ in. (very small)}
 \end{aligned} \tag{58}$$

(3) Maximum Out-of-Plane Deflection [See Item 2 c (3)]

$$\begin{aligned}
 P_x &= 2M_\lambda H_\lambda \omega^2 (1 - \lambda) \sin 2\beta \\
 &= 2 \times 1.7547 \times 22.02 \times 0.88450 \times 10^{-6} (0.2909) \\
 &= 0.0199 \times 10^{-3} \text{ lb.}
 \end{aligned} \tag{59}$$

$$\begin{aligned}
 q_{rz} &= 2Rm_r' \omega^2 (1 + \lambda) \sin 2\beta \sin \phi \\
 &= 2(25)(0.000379)(0.88435)10^{-6}(1.7091) \sin \phi \\
 &= 28.64 \times 10^{-9} \sin \phi
 \end{aligned} \tag{60}$$

$$\begin{aligned}
 F_1 &= -F_2 \\
 &= \frac{P_x}{\sqrt{3}} (\cot \alpha_u + \cot \alpha_\lambda) \\
 &= \frac{0.0199}{\sqrt{3}} \left(\frac{22.02 + 42.03}{25.0} \right) \times 10^{-3} \\
 &= 0.02944 \times 10^{-3} \text{ lb.}
 \end{aligned} \tag{61}$$

The deflection at five places is given by equation

$$\delta_{\zeta} = \frac{F_1 R^3}{EI_x} \begin{bmatrix} 0 \\ 0.5823 \\ 0.9872 \\ 0.6396 \\ 0 \end{bmatrix} + \frac{F_1 R^3}{GJ} \begin{bmatrix} 0 \\ 0.7891 \\ 1.0061 \\ 0.6859 \\ 0 \end{bmatrix} \text{ at } \zeta = \begin{bmatrix} 60 \text{ deg} \\ 90 \text{ deg} \\ 120 \text{ deg} \\ 150 \text{ deg} \\ 180 \text{ deg} \end{bmatrix}$$

Substituting numerical values in the above equation ($F_1 R^3/EI_x = 0.0047$ and $F_1 R^3/GJ = 0.0636$) yields

$$\delta_{\zeta} = \begin{bmatrix} 0 \\ 0.0529 \\ 0.0686 \\ 0.0466 \\ 0 \end{bmatrix} \text{ inches at } \zeta = \begin{bmatrix} 60 \text{ deg} \\ 90 \text{ deg} \\ 120 \text{ deg} \\ 150 \text{ deg} \\ 180 \text{ deg} \end{bmatrix}, \text{ respectively,}$$

from which the maximum out-of-plane deflection is about $\delta_{\zeta=120} = 0.070$ inches (very small).

d. Tripod

As in the full-scale model analysis (Item 2, d) the maximum compressive load is given by equation

$$L = M_u H_u \omega^2 \left[\frac{\cos \alpha}{\cos \alpha_u} - 2\sqrt{3}(1 - \lambda) \frac{\sin \alpha}{\sin \alpha_u} \right],$$

for $\alpha = 90$ deg and with the photolyzable film on.

$$\alpha_u = \tan^{-1} \frac{25.0}{42.03} = 30 \text{ deg } 45 \text{ min};$$

$$\sin \alpha_u = 0.51120;$$

$$\cos \alpha_u = 0.85946;$$

$$\lambda = 0.7091$$

Hence,

$$\begin{aligned}
 L &= -1.7547(22.02)(0.88435)10^{-6}2\sqrt{3}(0.2909)\frac{1}{0.51120} \\
 &= -0.0674 \times 10^{-3} \text{ lb.}
 \end{aligned}
 \tag{62}$$

Gravity-gradient and inertia distributed load for $\alpha = 90$ deg,

$$q_n = 3m_b \omega^2 y \cos \alpha_u \tag{63}$$

Solar radiation pressure for specular reflection per unit length of boom

$$q_s = 1815 \times 10^{-12} r_o \text{ lb/in.} \tag{64}$$

Total distributed load

$$q = 3m_b \omega^2 y \cos \alpha_u + 1815(10^{-12})r_o \text{ lb/in.} , \tag{65}$$

where y is measured in feet along the radius of the rim ($0 \leq y \leq R$), m_b the mass per unit length (inch) of boom, and r_o the boom radius in inches.

Assuming that the material for the booms is the same as that of the full-scale satellite (see Item 2, d), and that $r_o = 1.0$ in. the mass, m_b , per unit length of boom can be found from the corresponding value for the full-scale model by proportioning; thus

$$\begin{aligned}
 m_b &= 15.025 \times \frac{1.0}{1.5} \times 10^{-6} \\
 &\cong 10 \times 10^{-6} \text{ slugs/in.}
 \end{aligned}$$

Then,

$$\begin{aligned}
 q &= 3(10)(10^{-6})(0.88435)(10^{-6})(0.85946)y + 1815(10^{-12})(1.0) \\
 &= 22.802y(10^{-12}) + 1815(10^{-12}) .
 \end{aligned}$$

For $y = 0$

$$q_A = 1815 \times 10^{-12} \text{ lb/in.}$$

For $y = 25 \text{ ft}$

$$\begin{aligned} q_B &\approx 570 \times 10^{-12} + 1815 \times 10^{-12} \\ &= 2385 \times 10^{-12} \text{ lb/in.} \end{aligned}$$

If a factor 1.5 is used to convert limit to ultimate loads (see Figure 63), then

$$\begin{aligned} L &= 0.0674 \times 10^{-3} \times 1.5 \\ &= 0.1011 \times 10^{-3} \text{ lb} \end{aligned}$$

$$\begin{aligned} q_A &= 1815 \times 10^{-12} \times 1.5 \\ &= 2.723 \times 10^{-9} \text{ lb/in.} \end{aligned}$$

$$\begin{aligned} q_B &= 2385 \times 10^{-12} \times 1.5 \\ &= 3.578 \times 10^{-9} \text{ lb/in.} \end{aligned}$$

$$\begin{aligned} \text{Beam length } l &= (25.0^2 + 42.03^2)^{1/2} \\ &= 48.9 \text{ ft} \\ &= 586.8 \text{ in.} \end{aligned}$$

For the determination of the maximum deflection in the beam (stresses are of no particular interest because they are negligibly small), the same procedure - Equations 11 through 17 - applies here as in the full-scale satellite.

The constant quantity j in this configuration is equal to

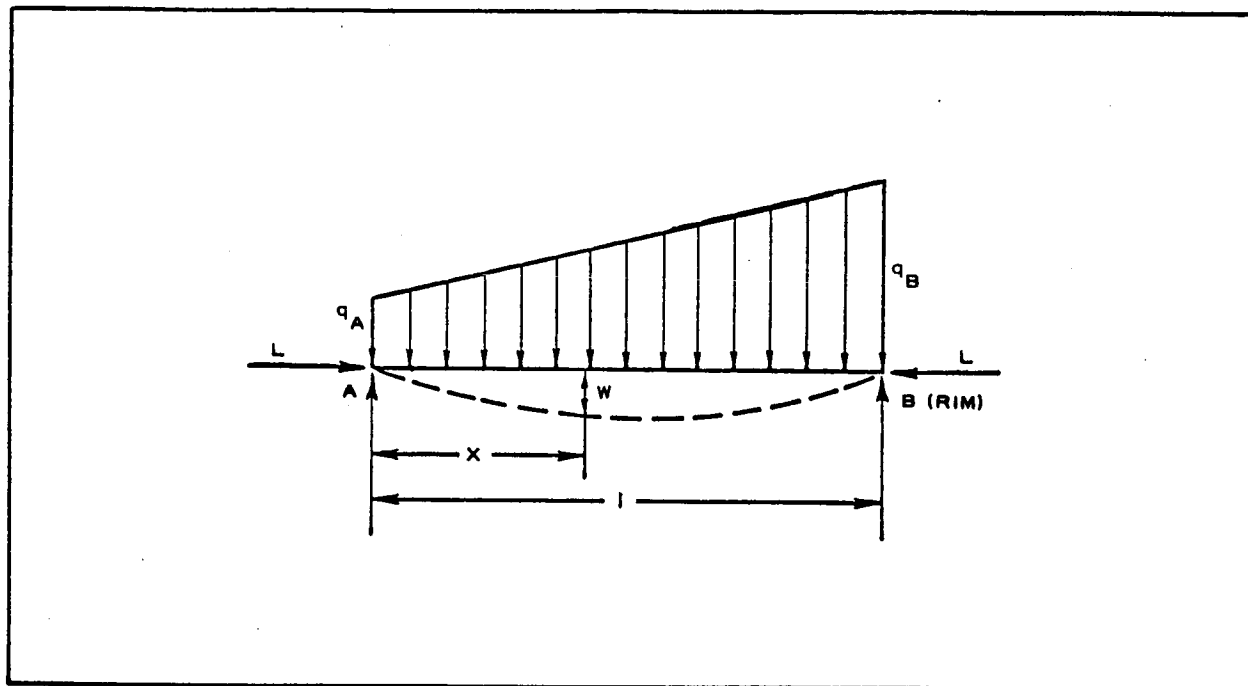


Figure 63 - Tripod-Boom as a Beam-Column

$$\sqrt{\frac{EI}{L}} = \left[\frac{0.762 \times 10^6 \times \pi(1.0)^3(0.001)}{0.1011 \times 10^{-3}} \right]^{1/2}$$

$$= 4866 .$$

Because the ratio l/j equals $586.8/4866 = 0.1206$, which is a number much less than π , the axial compression, L , of the boom contributes very little to the transverse deflection; hence, the maximum transverse deflection can be approximately found from equation

$$w = \frac{5}{384} \cdot \frac{ql^4}{EI} , \quad (66)$$

where q is taken equal to the average between q_A and q_B . Substituting numerical values in the above equation yields $w = 0.002$ in., which is negligibly small.

e. Deployment

The effects of trapped air on the flight-test model can be evaluated

by examining the volume-to-area ratios as was done for the full-scale satellite in Item 2, e. The resulting values are

1. Torus - $\bar{h} = 338/830 = 0.41 \text{ ft}$
2. Lens - $\bar{h} = 20,256/4,505 = 4.5 \text{ ft}$
3. Tripod - $\bar{h} = 1/(6 \times 4) = 0.0416 \text{ ft}$

In each case the value of h for the flight-test model is less than the corresponding value for the full-scale satellite. From this it is concluded that the effects of trapped air will be less critical for the flight-test model.

The effects of the masses attached to the tripods were examined in the same manner as for the full-scale satellite, using the following parameters:

$$m = \frac{22.5}{32.2}$$
$$= 0.698 \text{ slugs}$$

$$\text{Length of tripod} = 48.8 \text{ ft}$$

$$\text{Diameter of tripod} = 1/6 \text{ ft}$$

$$V_f = \frac{3 \times \pi \left(\frac{1}{6}\right)^2 \times 48.8}{4}$$
$$= 3.19 \text{ cu ft .}$$

With the same assumption in regard to initial pressure and the ratio of final-to-initial volume the total work done is

$$W = \frac{2.8 \times 3.19 \times 6.908}{1000}$$
$$= 0.0617 \text{ ft lb}$$

The velocity becomes

$$v = \left(\frac{2 \times 0.0617}{0.698} \right)^{1/2}$$
$$= 0.42 \text{ fps}$$

and the time to reach its full travel is

$$\text{time} = \frac{42}{0.42}$$
$$= 100 \text{ sec.}$$

This is approximately 1/5 the time required for the full-scale satellite and is therefore more critical. However, this is still plenty of time for the tripods to be at least partially inflated and to be capable of arresting the return velocity of the attached mass.

f. Launch

No analysis is shown for the launch conditions. This phase of the operation cannot be treated until the detail design stage of the program. Past experience indicates that proper support can be provided for critical elements to meet the accelerations, vibration, and shock loads that will be encountered during boost.

g. Pressurization Studies

(1) Introduction

The objective of the pressurization study was to size tentatively the flow control orifices and to predict the pressure-time relationships for the flight-test model lenticular satellite. The concepts and methods of analysis described in Appendixes B and C were used in this analysis.

(2) Assumed System Parameters

The flight-test satellite is shown in Figure 13. The lens has a volume of 20,300 cu ft and a surface area of 4,510 sq ft, while the torus has a total volume of 338 cu ft and a surface area of

830 sq ft. Torus bulkheads are located at 45, 90, 120, and 180 deg from the gas inlet port, clockwise around the torus.

The pressurizing or inflating gas was assumed to be helium stored at 3000 psi. This gas will pass through a pressure regulator set for 5 psia and then through individual flow-limiting orifices before entering the lens and torus. On-off valves and pressure sensors will prevent pressures from exceeding design values, or will maintain these pressures as required.

The first chamber of the torus will be pressurized to the design value of 1.047 psia in approximately 32 sec, and maintained at this pressure. A total of two minutes has been allotted for pressurization of the torus chambers, followed by two minutes for pressurization of the lens to the design pressure of 0.002437 psia. After lens inflation the design pressures will then be maintained for an additional period of two and four minutes for the lens and torus respectively, followed by shut-off of the pressurization system with pressure decay resulting.

(3) Analysis

The lens and torus must be perforated with exhaust holes to permit depressurization. These holes are presumed to be 0.020 in. in diameter, and the torus is assumed to have one hole in each five square feet of surface area. Rigidity considerations indicate that the lens should depressurize at least as rapidly as the torus, and on this basis the number of exhaust holes per unit area can be computed for the lens.

Appendix B presents the flow equations for the exhaust holes. For free molecular flow in terms of upstream pressure:

$$\frac{W\sqrt{T}}{PA} = \frac{135.7}{\sqrt{R}} \quad (67)$$

or, for helium:

$$\frac{W\sqrt{T}}{PA} = 6.905 . \quad (68)$$

For choked continuum flow in terms of upstream pressure:

$$\frac{W\sqrt{T}}{PA} = 340.3 C_D \sqrt{\frac{K}{R} \left(\frac{2}{K+1} \right) \frac{K+1}{K-1}} \quad (69)$$

or, for helium with a coefficient of discharge of 0.9:

$$\frac{W\sqrt{T}}{PA} = 11.302 \quad (70)$$

Appendix B also indicates the transitional pressure as being in the order of 0.0063 psia. For pressures near design values, the flow from the torus will be continuum and from the lens free molecular.

The depressurization equation was also derived in Appendix B, and can be expressed:

$$\frac{P}{P_o} = e^{-\frac{R\sqrt{T}}{144 \times 60 V} \frac{A}{\left(\frac{W\sqrt{T}}{PA} \right)} (\theta - \theta_o)} \quad (71)$$

The depressurization rate is therefore a function of (A/V) $(W\sqrt{T}/PA)$. For the lens to have the same depressurization rate as the torus:

$$\left[\frac{A}{V} \left(\frac{W\sqrt{T}}{PA} \right) \right]_{\text{lens}} = \left[\frac{A}{V} \left(\frac{W\sqrt{T}}{PA} \right) \right]_{\text{torus}} \quad (72)$$

Utilizing Equations 68, 70, and 72, it was computed that the lens should have 3.62 exhaust holes per square foot of surface area. The lens was presumed to have 4 exhaust holes per square foot.

Appendix C presents the method for sizing torus bulkhead

orifices. Several constants were changed because the gas is helium rather than air; the helium values are 11.302 in Equation C-7, 14.69 in Equation C-8, 0.4083 for the pressure ratio determining applicability of Equations C-7 and C-8, and 0.04470 for Equations C-9 and C-12. Only the analysis in the vacuum condition was used.

A supply flow rate of 0.36 lb/min and bulkhead flow control orifice sizes of 9/16-, 27/64-, and 9/32-in. diameters, respectively, seem to meet the specified conditions. The resultant pressure-time curves are presented in Figure 64. The quantity of helium required for the eight minutes of torus pressurization is 0.449 lb. The stabilized pressure values (i. e., $dP/d\theta = 0$) are 1.047, 1.043, 1.038, and 1.026 psia, respectively, which is a variation of 2.0 percent.

Appendix B presents the method for determining the lens flow rates and pressure-time curves. The pressurization equation can be expressed:

$$P = 0.007369 \frac{\sqrt{RT}}{A} W_o \left(1 - e^{-0.015707 \sqrt{RT} \frac{A}{V} \theta} \right), \quad (73)$$

which reduces to:

$$P = 0.5877 W_o (1 - e^{-0.001982 \theta}) \quad (74)$$

For the specified time of two minutes and design pressure of 0.002437 psia, Equation 74 yields a mass flow rate (W_o) of 0.01959 lb/min. Figure 65 presents a plot of Equation 74.

To maintain design pressure, the supplied mass flow rate must equal the mass flow rate exhausting through the exhaust holes. Equation 68 yields this mass flow rate as 0.004146 lb/min. The quantity of helium required for the four minutes of lens pressurization is 0.0475 lb.

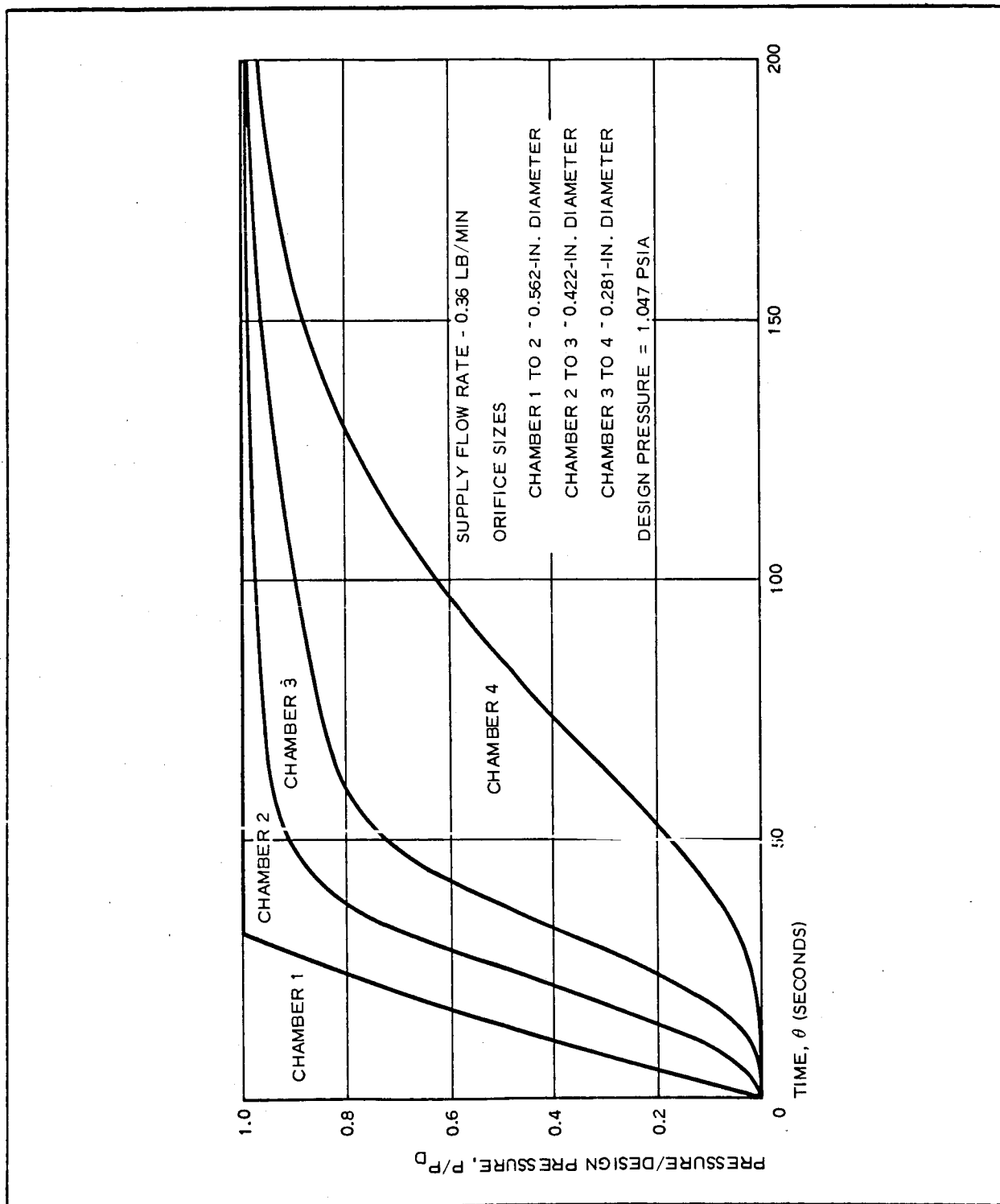


Figure 64 - Torus Pressures versus Time (Flight-Test Model)

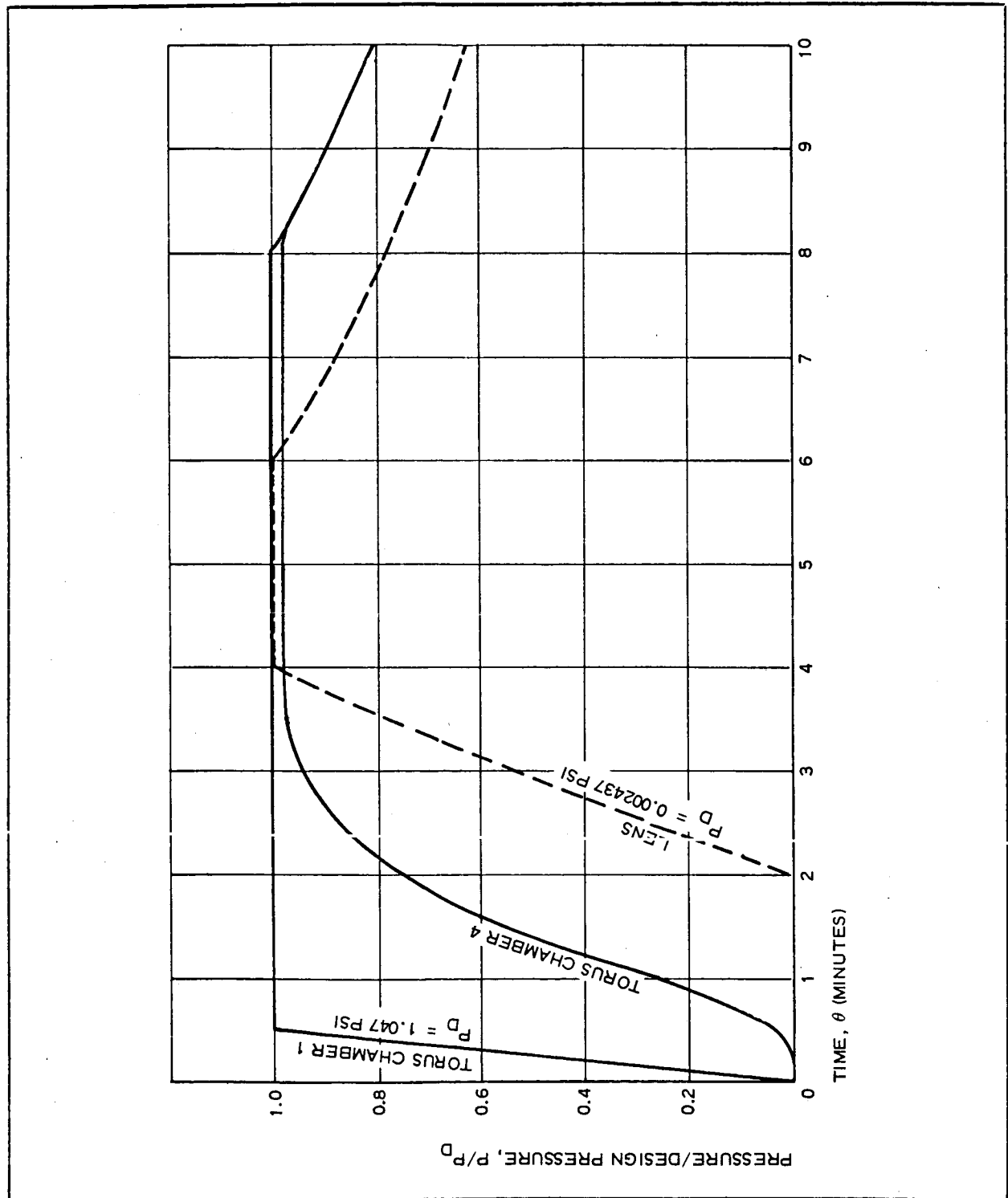


Figure 65 - Satellite Inflation Pressures versus Time (Flight-Test Model)

The depressurization equation has previously been expressed as Equation 71, and is applicable for the lens and torus. Figure 66 presents Equation 71 in graphical form for the lens and torus.

The total quantity of helium required will be the sum of the 0.449 lb for the torus and 0.0475 lb for the lens, or 0.497 lb. When stored at 3000 psi the required volume will be 0.236 cu ft.

The supply orifice sizes can be computed from Equation 70, utilizing the upstream pressure of 5 psia and the computed supply flow rates. The computed orifice sizes are 0.432- and 0.1008-in. diameters for the torus and lens, respectively. The supply lines upstream of the orifices should be at least twice the orifice diameters of 1.0- and 0.25-in. diameters for the torus and lens, respectively.

(4) Summary

For the flight-test satellite the helium storage volume should be in excess of 0.236 cu ft at 3000 psia. The supply orifices should be 0.432- and 0.1008-in. diameters for the torus and lens, respectively. Bulkhead orifices for the torus should be 9.16-, 27/64-, and 9/32-in. diameters in order from the inlet port. If 0.020-in. diameter exhaust holes are used, the torus should have 0.2 and the lens 4 holes per square foot of surface area.

The predicted pressure-time curves are presented in Figures 64, 65, and 66.

(5) List of Symbols

A = orifice area

C_D = coefficient of discharge

K = ratio of specific heats

P = total pressure in torus chamber, lens,
or ducts

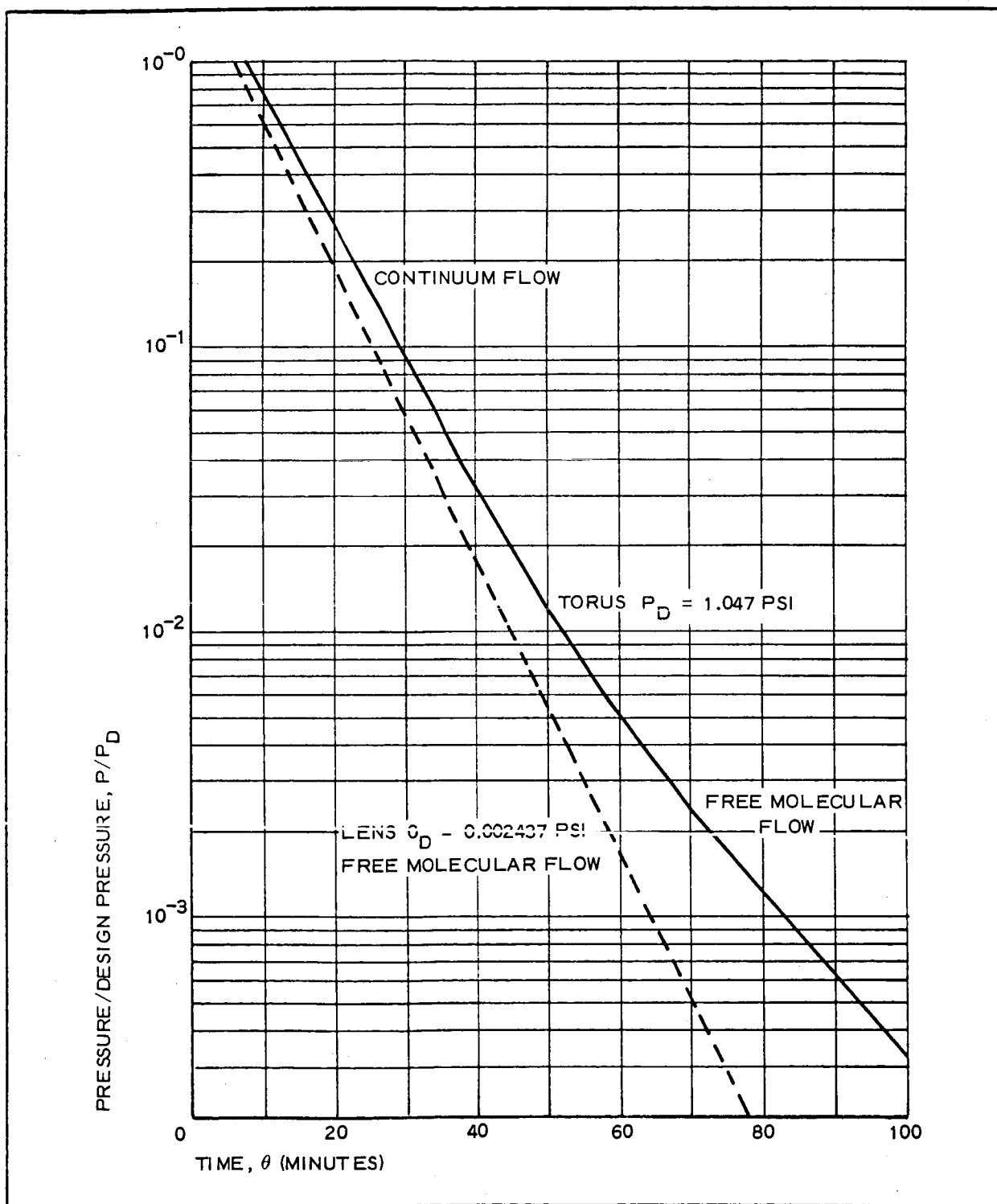


Figure 66 - Satellite Deflation Pressures versus Time (Flight-Test Model)

P_D = design pressure in torus or lens

P_o = initial total pressure

R = gas constant

T = total temperature

V = volume of gas in torus chambers or lens

W = mass flow rate

W_o = initial mass flow rate

θ = time

θ_o = initial time

h. Temperature Distribution Study

The flight-test lenticular satellite is, from a temperature viewpoint, a nearly perfectly scaled version of the full-scale satellite.

The temperature distribution study for the full-scale satellite given in Item 2, h, is therefore applicable to the flight-test model.

i. Error Analysis

(1) General

As in the case of the full-scale satellite the coefficients $\partial\rho/\partial S$ and $\partial\rho/\partial D$ for $\alpha = 42$ deg are -3 and 4 respectively. The basic equation then becomes,

$$\rho = \rho_o - 3\Delta S + 4\Delta D .$$

$$\rho_o = 37.36 \text{ ft};$$

$$D_o = 50 \text{ ft};$$

$$S_o = 2\alpha\rho_o = 54.77 \text{ ft} .$$

Under ideal conditions the radius of curvature of the lens would be $\rho_o = 37.36$ ft. Variations ΔS and ΔD in arc length and lens

diameter respectively from the ideal values S_o and D_o arise from the sources described below.

(2) Manufacturing Tolerances

It is planned to determine the diameter of the torus by measurement before the lens is assembled to it. This will make ΔD essentially zero. A tolerance of 0.5 in. is estimated to be reasonable for the arc length. Therefore,

$$\Delta S = \frac{1}{24} \text{ ft} ,$$

and

$$\begin{aligned} \Delta \rho &= \rho - \rho_o \\ &= -3 \left(\frac{1}{24} \right) \\ &= -0.125 \text{ ft} . \end{aligned}$$

(3) In-Plane Rim Deflection

The maximum in-plane rim deflections, from Item c, is less than $0.00183 + 0.00046 = 0.00229$ inches; then

$$\begin{aligned} \Delta D &\leq \frac{2 \times 0.00229}{12} \\ &= 0.00038 \text{ ft} \end{aligned}$$

and

$$\begin{aligned} \Delta \rho &= \rho - \rho_o \\ &\leq 4 \times 0.00038 \\ &= 0.00152 \text{ ft} . \end{aligned}$$

(4) Torus Pressure

The nominal design pressure for the torus is 1.047 psi (see Item 3, b), and the cross-sectional area is $\pi(9.77)^2 = 300$ sq in. The

total torus load is $300 \times 1.047 = 314$ lb. Assuming that the pressure can be controlled to ± 10 percent the variation in load will be ± 31.4 lb. To be conservative it is assumed that the load variation is carried entirely by the rim, which has a cross-sectional area of 0.01257 sq in. The change in diameter is

$$\Delta D = \frac{31.4 \times 50}{0.01257 \times 18 \times 10^6}$$

$$= 0.007 \text{ ft}$$

$$\Delta \rho = \pm 4(0.007)$$

$$= \pm 0.028 \text{ ft.}$$

(5) Lens Pressure

The nominal lens pressure is 0.002437 psi, based on a wire stress 23,000 psi (see Item 3, a). Using the stress-strain curve of Reference 10 as in Item 2, i, and for the expected pressure tolerance of ± 10 percent the effect on the radius of curvature can be determined as shown in Table XII.

(6) Temperature

For the temperature effect, see Item 2, i, (6).

TABLE XII - EFFECT OF TORUS PRESSURE VARIATION ON LENS
RADIUS OF CURVATURE FOR FLIGHT-TEST MODEL

Pressure		Wire stress (psi)	Elongation, (in./in.)	$\Delta \epsilon$ (in./in.)	ΔS (ft)	$\Delta \rho$ (ft)
Torus	Lens (psi $\times 10^{-3}$)					
-10 percent	2.112	20,700	0.0010	-0.0005	-0.0274	+0.082
Nominal	2.347	23,000	0.0023
+10 percent	2.582	25,300	0.0035	+0.0012	+0.0657	-0.197

(7) Summary

The computed errors are summarized in Table XIII.

TABLE XIII - LENS RADIUS OF CURVATURE
ERRORS FOR FLIGHT-TEST MODEL

Source of error	$\Delta\rho$ (ft)	
	Positive	Negative
Manufacturing tolerances	0.125	0.125
Rim deflections	0.0015	0.0015
Torus pressure	0.028	0.028
Lens pressure	0.082	0.197
Total	0.2365	0.3515

As in the full-scale model, the sources of large error are the manufacturing tolerances and the lens pressure tolerance ± 10 percent; hence, these sources should be given careful attention in the future. The maximum error in the radius is 0.3515 ft from all sources. This is about 1 percent of the radius of the lens, which compares with the 1.99-ft error in the full-scale model.

j. Weights and Inertias

The weights and inertias of the principal elements of the flight-test model satellite (see Figure 67), computed in accordance with the formulas shown in Appendix E are listed in Table XIV.

4. COMPARATIVE STUDIES

a. General

In this item a weight comparison is made of the full-scale lenticular satellite as analyzed in Item 2 of this Subsection with (1) a spherical

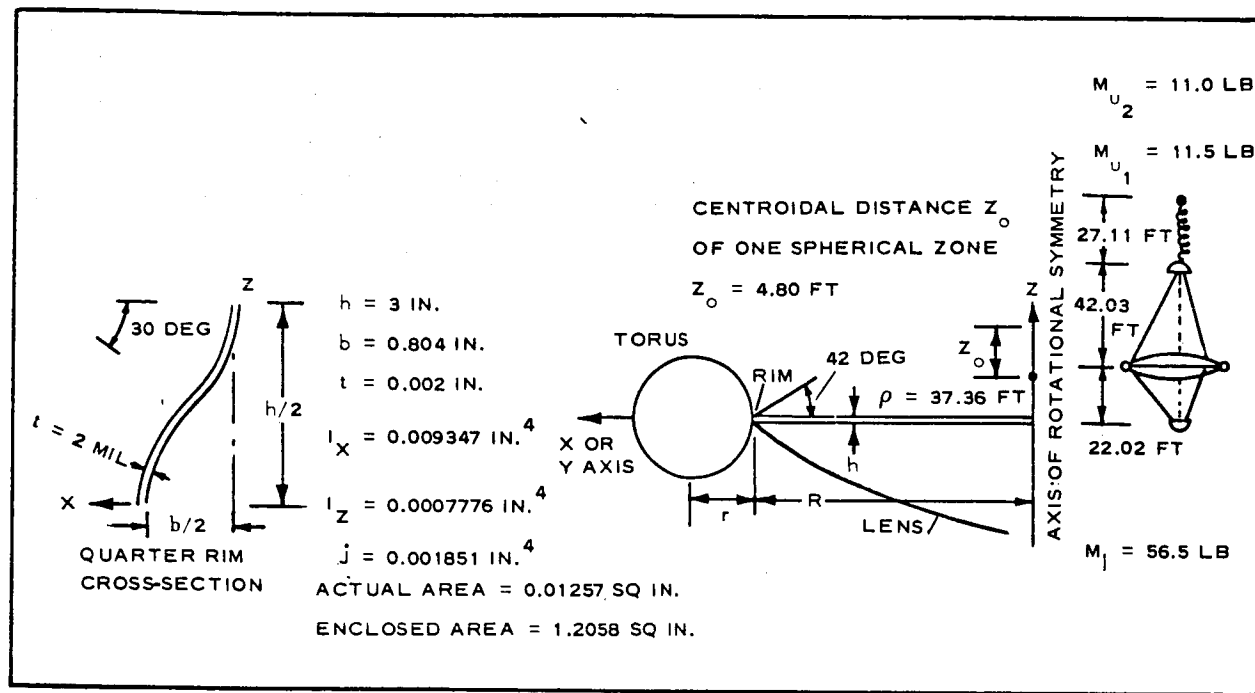


Figure 67 - Principal Elements of Flight-Test-Model Satellite

satellite made of the same material as the lens of the lenticular satellite, and (2) a lenticular satellite in which the lens material is that of Echo A-12. In the latter case the comparison assumes equal length booms for both configurations or equal concentrated masses. Finally, in all cases the radius of curvature of the reflecting surface was taken as 200 ft, and in the cases of the lenticular shapes the mass moment of inertia ratios I_{X-X}/I_{Z-Z} were taken equal.

Also included in this item is a parametric study of tripod boom structure. The effect on weight, perturbing torque due to solar pressure, and aerodynamic drag for two alternate methods of boom construction are compared with the proposed full-scale satellite design.

b. Sphere

The sphere used in this comparison has the following characteristics:

$$\text{Total area, } A = 4\pi\rho^2 = 4\pi(200 \times 12)^2 = 72.35 \times 10^6 \text{ sq in.}$$

TABLE XIV - WEIGHTS AND INERTIAS

Materials and properties	Satellite component					
	Lens (spherical zone)	Torus	Rim	Mass		
				M_l	M_{u_1}	M_{u_2}
Material	1.2-mil copper wire at 21 per inch. 0.6-mil photolyzable film	1-mil Mylar $\sigma_Y = 13,000$ psi $\sigma_{TU} = 20,500$ psi	0.002-in. beryllium-copper			
Young's modulus, E	Only copper $10 - 16 \times 10^6$ psi	0.762×10^6 psi	18×10^6 psi			
Poisson's ratio, μ		0.4	1/3			
Surface area (sq ft)	One cap 2252.6	829.6	Actual foil area - 82.25			
Enclosed volume (cu ft)	Between two spherical zones and rim 20,256.5	337.6				
Weight in lb sq in. of surface when the photolyzable film is						
ON	0.0000382	0.000050	0.000594			
OFF	0.0000154	0.000050	0.000594			
Total weight (lb)*	Two caps ON - 24.80 OFF - 10.00	6.00	7.00	56.5	11.5	11.0
Weight of helium (lb)	0.037	0.268				
Polar moment of inertia I_{z-z} (lb ft sq)*	ON - 8124.0 OFF - 3275.1	3986	4396.92			
Moment of inertia*† I_{x-x} or I_{y-y} (lb ft sq)	ON - 4853.4 OFF - 1956.2	1995	2198.46	27,395.7	20,315.0	

*The designations ON and OFF in the table refer to the lens photolyzable film before and after its disappearance, respectively.

†Principal Moments of Inertia of Satellite

- Without photolyzable film

$$I_{x-x} = I_{y-y} = 53,860.4 \text{ lb ft sq}; I_{z-z} = 11,658 \text{ lb ft sq}; \frac{I_{x-x}}{I_{z-z}} = 4.620$$

- With photolyzable film ON

$$I_{x-x} = I_{y-y} = 56,757.6 \text{ lb ft sq}; I_{z-z} = 16,506.9 \text{ lb ft sq}; \frac{I_{x-x}}{I_{z-z}} = 3.438$$

$$\text{Volume, } V = \frac{4}{3}\pi\rho^3 = 33.5 \times 10^6 \text{ cu ft} = 57.89 \times 10^9 \text{ cu in.}$$

$$\text{Inflation pressure, } p = 0.316 \times 10^{-3} \text{ psi [see Item 2, a, (1)]}$$

$$\text{Sphere skin weight} = 72.35 \times 10^6 \times 29.7 \times 10^{-6} = 2150 \text{ lb}$$

$$\begin{aligned} \text{Weight of inflation gas (helium)} &= 33.5 \times 10^6 \\ &\times \frac{0.316 \times 10^{-3}}{14.7} \times 0.01115 = 8.0 \text{ lb (weight of} \\ &\text{helium under normal pressure and temperature} \\ &\text{is 0.01115 pcf).} \end{aligned}$$

$$\begin{aligned} \text{Weight of helium bottle} &= w_b = \frac{3}{2} 57.89 \times 10^9 \times \\ &0.316 \times 10^{-3} \times 1.5 \times \frac{0.16}{160,000} \approx 50 \text{ lb (titanium,} \\ &F_{tu} = 160,000 \text{ psi, density} = 0.16 \text{ pci, safety} \\ &\text{factor, 1.5)} \end{aligned}$$

c. Lenticular Satellite with Echo A-12 Lens Material

(1) General

The Echo A-12 material is a sandwich consisting of

Aluminum foil	0.00018 in. thick
Mylar film	0.00035 in. thick
Aluminum foil	<u>0.00018 in. thick</u>
Total thickness	0.00071 in.

The lens rigidization pressure must stress the aluminum foil at 5000 psi. Considering the moduli of elasticity of aluminum and Mylar ($E_A = 10 \times 10^6$ psi and $E_M \approx 0.5 \times 10^6$ psi) and

noting that strains in the Mylar and in the aluminum must be equal the lens inflation pressure can be derived from the following simple calculations

$$F_M = \sigma_M(0.00035)$$

$$F_A = \sigma_A(0.00018)$$

$$= 5000 \times 0.00018$$

$$= 0.9 \text{ lb}$$

$$\frac{\sigma_M}{E_M} = \frac{\sigma_A}{E_A}$$

$$= \frac{F_M}{0.00035E_M}$$

$$= \frac{0.9}{0.00018E_A}$$

$$= \frac{0.9}{1800}$$

$$= 5 \times 10^{-4} \quad (75)$$

Then,

$$F_M = 0.0875 \text{ lb,}$$

$$f_s = F_M + 2F_A$$

$$= 0.0875 + 2 \times 0.9$$

$$= 1.8875 \text{ lb/in,}$$

$$\frac{P_L \rho}{2} = 1.8875, \text{ and}$$

$$p = 0.001576 \text{ psi.}$$

Because the torus buckling criterion was decided to be neglected [see Item 2, a, (2)] the torus radius and inflation pressure will be found from Equations 4 and 5. Selecting a torus radius $r = 47$ in., the film thickness and inflation pressure can be found to be about five times as high as the respective quantities of a lenticular satellite with copper wire-photolyzable film lens (pressure $p = 0.839$ psi, film thickness $t_t = 5$ mil, torus radius $r = 47$ in.).

(2) Equal Length Booms (without photolyzable film torus)

$$I_{z-z(\text{lens})} = 1,868,896 \times \frac{0.000054}{0.0000107}$$

$$\approx 9,344,500 \text{ lb ft sq}$$

$$I_{z-z(\text{rim})} = 1,798,696 \text{ lb ft sq}$$

$$I_{(z-z)(\text{torus})} = 0$$

$$I_{z-z(\text{total})} = 11,143,200 \text{ lb ft sq}$$

$$I_{x-x(\text{lens})} = 1,112,879 \times \frac{0.000054}{0.0000107}$$

$$\approx 5,564,400$$

$$I_{x-x(\text{rim})} = 899,350$$

$$I_{x-x(\text{torus})} = 0$$

$$I_{x-x(\text{masses})} = 300^2(M_{u_1}) + 190.53^2(M_l)$$

$$\frac{I_{x-x}}{I_{z-z}} = 4.621 = \frac{6,463,750 + 90,000M_{u_1} + 36,302M_l}{11,143,200}$$

(76)

From statics (satellite centroid),

$$300M_{u_1} + 390\left(\frac{100}{51}M_{u_1}\right) = 285M_\lambda \quad (77)$$

Solving these two equations for M_λ and M_u yields $M_{u_1} = 200$ lb, $M_\lambda = 748$ lb. Then

$$\begin{aligned} M_{u_2} &= M_{u_1} \frac{100}{51} \\ &= 393 \text{ lb.} \end{aligned}$$

Table XV compares the results of the preceding investigation to the full-scale lenticular satellite.

d. Parametric Study of Tripod-Boom Structure

(1) Introduction

The tripod analysis for the full-scale satellite is given in Item 2, d. In this design it is assumed that only the Mylar is effective structurally and the contribution of the wires is neglected. The wires are used to provide local stiffness to the Mylar which, due to its memory, might have a tendency to wrinkle along the fold lines that are introduced during packaging.

There are other tripod designs that might be advantageous from a system standpoint. It is the purpose of this study to examine these other possibilities and to discuss their relative merits.

(2) Equivalent Structural Problem

The proposed tripod was analyzed as a beam-column with a trapezoidally distributed load. This is a lengthy calculation that can be replaced by a much simpler problem to facilitate the study with very little sacrifice in accuracy. This is demonstrated below.

TABLE XV - WEIGHT COMPARISON OF VARIOUS SATELLITE
CONFIGURATIONS

Component	Satellite configuration			
	1-mil copper wire at 21 per inch, 0.5-mil photolyzable film		Echo A-12 material	
	Lenticular satellite (lb)	Sphere (lb)	Boom lengths equal (lb)	Concentrated masses equal (lb)
Lens	552.2	2150.0	1000.0	1000.0
Torus	116.6	. . .	583.0	583.0
Rim	100.4	. . .	100.4	100.4
Mass M_{u_1}	51.0	. . .	200.0	51.0
Mass M_{u_2}	100.0	. . .	393.0	100.0
Mass M_{λ}	285.0	. . .	748.0	285.0
Inflation gas	6.0	8.0	30.0	30.0
Gas bottle	38.0	50.0	190.0	190.0
Canister	. . .	120.0
Miscellaneous (tripods, etc.)	200.0	200.0	200.0	200.0
Total weight	1413.8	2528.0	3444.4	2539.4

Pertinent data from the exact solution (Figure 68) are given below.

$$P = 3.848 \times 10^{-3} \text{ lb}$$

$$q_A = 4.084 \times 10^{-9} \text{ lb/in.}$$

$$q_B = 7.304 \times 10^{-9} \text{ lb/in.}$$

$$\lambda = 3942 \text{ in.}$$

$$\delta = 8.8855 \text{ in. about mid-span}$$

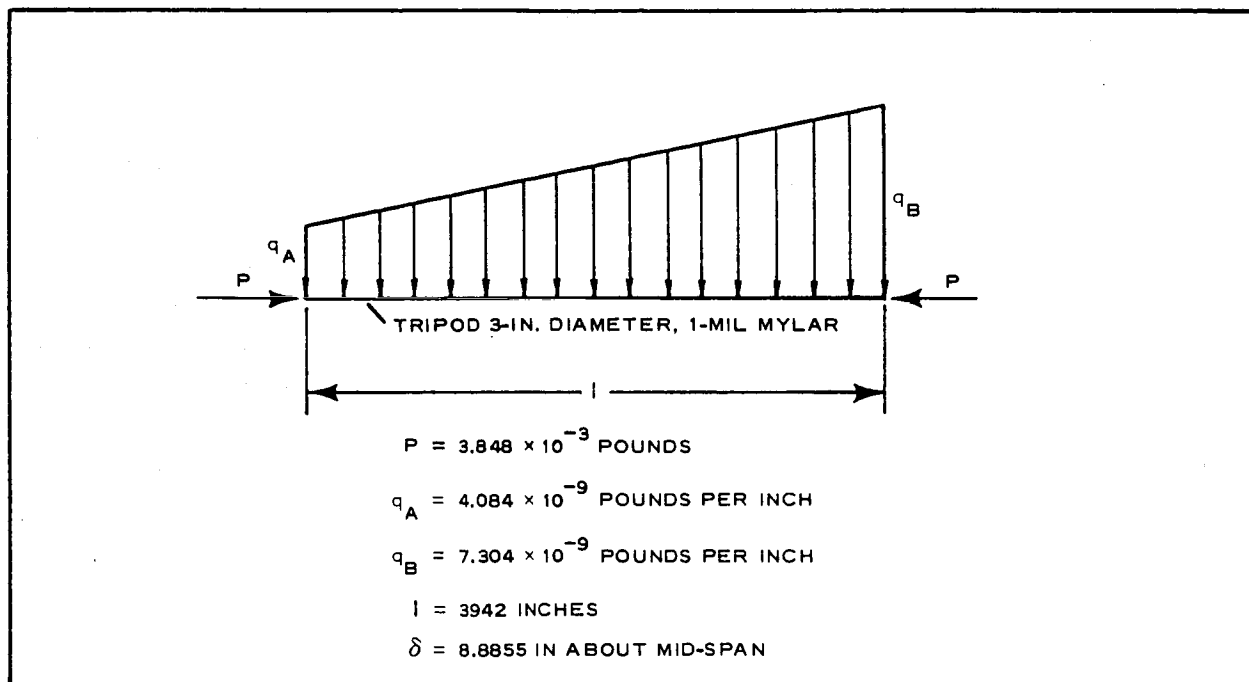


Figure 68 - Exact Solution

The equivalent problem uses the same axial load with a uniformly distributed load equal to the average load of the exact problem (see Figure 69). A very good approximation to the deflection at the center of the span is given by

$$\delta = \frac{\delta_o}{1 - \frac{P}{P_{cr}}} \quad (78)$$

where

$$\delta_o = \frac{5ql^4}{384EI} \quad (79)$$

$$P_{cr} = \frac{\pi^2 EI}{l^2} \quad (80)$$

Substituting the same values used in the exact solution

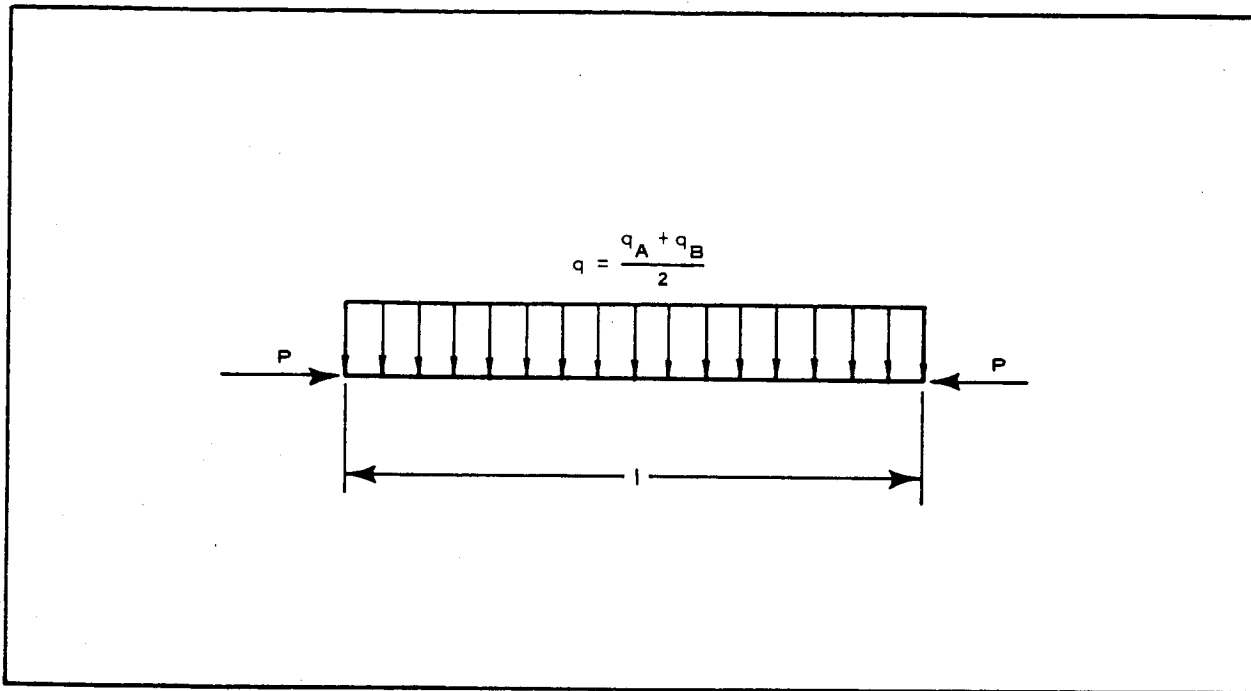


Figure 69 - Approximate Solution

$$I = \pi R^3 t = \pi (1.5)^3 \times 10^{-3} = 10.6 \times 10^{-3} \text{ in.}^4$$

$$P_{cr} = \frac{\pi^2 \times 760,000 \times 10.6 \times 10^{-3}}{(3942)^2} = 5.13 \times 10^{-3} \text{ lb}$$

$$q = \frac{(4.084 + 7.304)}{2} \times 10^{-9} = 5.694 \times 10^{-9} \text{ lb/in.}$$

$$\delta_o = \frac{5 \times 5.694 \times 10^{-9} \times (3942)^4}{384 \times 760,000 \times 10.6 \times 10^{-3}} = 2.21 \text{ in.}$$

$$\delta = \frac{2.21}{1 - \frac{3.848}{5.13}} = \frac{2.21}{0.25} = 8.84 \text{ in.}$$

The approximate and exact deflections are then 8.84 and 8.885 in., respectively, or an error of about 1/2 percent. This is sufficiently accurate for the intended study.

(3) Design Alternate I

Alternate I is a wire-film material of aluminum wire and 0.25-mil Mylar. The difference between the full-scale design and Alternate I is that in the full scale only the Mylar is considered structurally effective whereas in Alternate I the wire only is considered effective and the Mylar serves primarily to contain the inflation pressure required for rigidization.

Alternate I material has been under investigation at GAC for some time and analytical methods and test data pertinent to such a design have been developed.^{1, 3, 9} These data are sufficient to estimate the weight of the tripod as a function of the radius.

The comparison is made on the basis that the axial load and length of the tripod are the same and that the wires are selected to give the same deflection at the midpoint. That is:

$$P = 3.848 \times 10^{-3} \text{ lb}$$

$$l = 3942 \text{ in.}$$

$$\delta = 8.84 \text{ in.}$$

The distributed load will be a function of tripod radius and weight. From Item 2, d, the distributed loads, including a factor of safety of 1.5, are:

From solar pressure

$$\begin{aligned} q_s &= 1.815 \times 10^{-9} \times 1.5 \times R \\ &= 2.7225 \times 10^{-9} R \text{ lb/in.} \end{aligned} \quad (81)$$

From gravity gradient the average load is

$$\begin{aligned} q_g &= \frac{3 \times 66.91 \times 0.38975 \times 10^{-6} \times 0.91325 \times 1.5W}{32.2} \\ &= 3.32 \times 10^{-6} W \text{ lb/in.} \end{aligned} \quad (82)$$

W is the weight per inch of tripod .

The tripod construction, as shown in Figure 70, consists of 0.25-mil Mylar with wires in the circumferential and hoop directions.

Let A_W be the total wire area at a cross-section

$$\begin{aligned} A_W &= 2\pi R \frac{\pi d^2}{4S} \\ &= \frac{\pi^2 R d^2}{2S} \end{aligned} \quad (83)$$

The spacing of the hoop wires must be one-half the spacing of the longitudinal wires to make the wire stresses the same in both directions due to inflation pressure required for rigidization. The tripod weight then becomes for 0.25-mil Mylar and aluminum wire

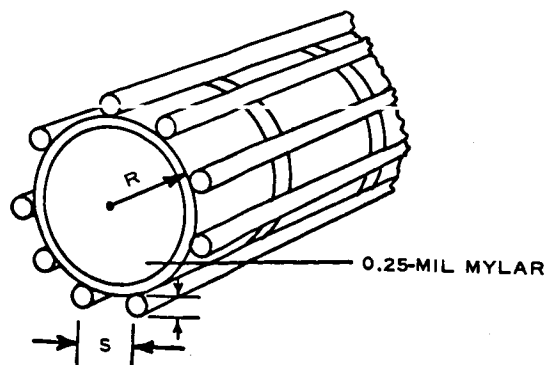


Figure 70 - Tripod Construction

$$\begin{aligned}
 W &= 2\pi R t \gamma_F + (A_W + 2A_W) \gamma_W \\
 &= 2\pi \times \frac{1}{4} \times 10^{-3} \times 0.05R + 3A_W(0.1) \\
 &= 0.0785 \times 10^{-3}R + 0.3A_W.
 \end{aligned} \tag{84}$$

The total loading is then obtained by combining Equations 81, 82, and 84.

$$\begin{aligned}
 q &= 2.7225R \times 10^{-9} + 3.32 \times 10^{-6}(0.0785 \times 10^{-3}R + 0.3A_W) \\
 &= 2.983 \times 10^{-9}R + 0.996 \times 10^{-6}A_W \\
 &= C_1R + C_2A_W
 \end{aligned} \tag{85}$$

Equation 78 can be rearranged into the following form

$$P_{cr} - \frac{\delta_o P_{cr}}{\delta} = P \tag{86}$$

Substituting Equations 79 and 80, Equation 86 becomes:

$$\frac{\pi^2 EI}{l^2} - \frac{\pi^2 EI}{l^2 \delta} \frac{5(C_1R + C_2A_W)^4}{384EI} = P \tag{87}$$

or

$$EI - \frac{5l^4(C_1R + C_2A_W)}{384\delta} = \frac{Pl^2}{\pi^2} \tag{88}$$

Noting that

$$I = \frac{A_W R^2}{2} \tag{89}$$

Equation 88 can be written

$$\frac{ER^2}{2}A_W - \frac{5\ell^4}{384\delta}C_2A_W = \frac{Pl^2}{\pi^2} + \frac{5\ell^4}{384\delta}C_1R \quad (90)$$

Solving for A_W gives

$$A_W = \frac{\frac{Pl^2}{\pi^2} + \frac{5\ell^4}{384\delta}C_1R}{\frac{ER^2}{2} - \frac{5\ell^4}{384\delta}C_2} \quad (91)$$

The above equations relate the wire area required to the radius of the tripod. For this particular case the magnitudes of the various quantities are:

$$\frac{Pl^2}{\pi^2} = \frac{3.848 \times (3942)^2 \times 10^{-3}}{\pi^2} = 6050$$

$$\frac{5\ell^4}{384\delta}C_1 = \frac{5(3942)^4 2.983 \times 10^{-9}}{384 \times 8.84} = 1055$$

$$\frac{5\ell^4}{384\delta}C_2 = \frac{1055C_2}{C_1} = \frac{1055 \times 0.996 \times 10^{-6}}{2.983 \times 10^{-9}} = 352,000$$

$$\frac{E}{2} = \frac{10^7}{2} = 5,000,000$$

Substituting the above values into Equation 91

$$A_W = \frac{6050 + 1055R}{(5kR^2 - 0.352)10^6} \quad (92)$$

In the above equation it should be noted that a new factor k has been added. This factor is less than one and amounts to a reduction in the modulus of elasticity. It has been found in preliminary tests conducted to date that the effective stiffness can be much less than that computed by conventional means.

The rigidization pressure, p , required is also of interest and is given by

$$\sigma_y A_W = \pi R^2 p$$

or

$$p = \frac{\sigma_y A_W}{\pi R^2}, \quad (93)$$

where σ_y is the yield stress of the wires.

The perturbing torque and aerodynamic drag is also of interest. This will not be determined directly but as a ratio, assuming that these forces are proportional to the projected area, S , of the members. Because the configurations are the same and only the diameter of the tripod is varied it follows that

$$\begin{aligned} \frac{T}{T_S} &= \frac{D}{D_S} \\ &= \frac{S}{S_S} \\ &= \frac{R}{R_S} \\ &= \frac{R}{1.5} \end{aligned} \quad (94)$$

where the subscript S refers to the proposed full-scale design.

The results of the following computations are given in Table XVI for several radii varying from 0.8 to 2.0 in.

$$A_W = \frac{6.050 + 1.055R}{5kR^2 - 0.352} \times 10^{-3} \text{ sq in.}$$

$$W = 0.0785R \times 10^{-3} + 0.3A_W \text{ lb/in.}$$

$$\begin{aligned}\frac{W}{W_S} &= \frac{W}{2\pi R t \gamma} \\ &= \frac{W}{3\pi \times 0.05 \times 10^{-3}} \\ &= \frac{W}{0.472 \times 10^{-3}} \\ \frac{T}{T_S} &= \frac{D}{D_S} \frac{R}{1.5} \\ p &= \frac{6,500 A_W}{\pi R^2} \\ &= 2065 \frac{A_W}{R^2}\end{aligned}$$

TABLE XVI - CALCULATIONS FOR ALTERNATE I

Item	Radius					
	0.80 in.	0.90 in.	1.0 in.	1.25 in.	1.50 in.	2.00 in.
For k = 1.0						
R^2 (sq in.)	0.640	0.81	1.00	1.5625	2.25	4.00
$1.055R$ (in.)	0.845	0.950	1.055	1.320	1.583	2.110
$5R^2$ (sq in.)	3.200	4.05	5.00	7.812	11.250	20.00
$6.050 + 1.055R$ (in.)	6.895	7.000	7.105	7.377	7.633	8.160
$5R^2 - 0.352$ (sq in.)	2.848	3.698	4.648	7.460	10.898	19.648
$A_W \times 10^3$ (sq in.)	2.420	1.89	1.53	0.987	0.701	0.415
$0.0785R \times 10^3$ (in.)	0.063	0.071	0.078	0.098	0.118	0.157
$0.3A_W \times 10^3$ (sq in.)	0.727	0.567	0.459	0.296	0.210	0.124
$W \times 10^3$ (lb/in.)	0.790	0.638	0.537	0.394	0.328	0.281
W/W_S	1.670	1.35	1.14	0.835	0.695	0.596
T/T_S or D/D_S	0.532	0.600	0.667	0.834	1.000	1.333
p (psi)	7.810	4.82	3.16	1.29	0.643	0.214
For k = 0.5						
$5kR^2$ (sq in.)	1.600	1.025	2.500	3.906	5.625	10.000
$5kR^2 - 0.352$ (sq in.)	1.248	1.673	2.148	3.554	5.273	9.648
$6.050 + 1.055R$ (in.)	6.895	7.000	7.105	7.377	7.633	8.160
$A_W \times 10^3$ (sq in.)	5.51	4.18	3.31	2.07	1.445	0.847
$0.3A_W \times 10^3$ (sq in.)	1.653	1.254	0.993	0.621	0.433	0.254
$0.0785R \times 10^3$ (in.)	0.063	0.071	0.078	0.098	0.118	0.157
$W \times 10^3$ (lb/in.)	1.716	1.325	1.071	0.719	0.551	0.411
W/W_S	3.63	2.81	2.27	1.52	1.17	0.870
p (psi)	17.8	10.6	6.85	2.74	1.33	0.44

Two values of k were used, 1.0 and 0.5. The results are plotted in Figures 71 and 72. Figure 71 shows the effect of radius on weight and perturbing torque. Figure 72 shows the effect of radius on the inflation pressure required for rigidization.

Figure 71 shows the trade-off between tripod weight and perturbing torque due to solar pressure or aerodynamic drag. It is evident that if k approaching unity can be realized, this method of construction is definitely superior, for it is possible to reduce both weight and torque. Several particular points of interest are given in Table XVII.

If k approaches 0.5 then the advantage is not clear cut. Weight can be reduced then only at the expense of increasing torque or torque can be reduced at the expense of increasing weight.

Regardless of the value of k it is apparent from Figure 72 that the inflation pressure required will be greater than that required for the torus or lens. Three pressures must be regulated if this method of construction is employed instead of two, as in the present design. This makes the Alternate I system more complicated and less reliable, which is a definite disadvantage.

TABLE XVII - WEIGHT, TORQUE,
AND DRAG VALUES VERSUS
TRIPOD RADIUS

Radius	$\frac{W}{W_S}$	$\frac{T}{T_S}$ and $\frac{D}{D_S}$
1.10	1.00	0.74
1.25	0.84	0.84
1.50	0.69	1.00
2.00	0.60	1.33

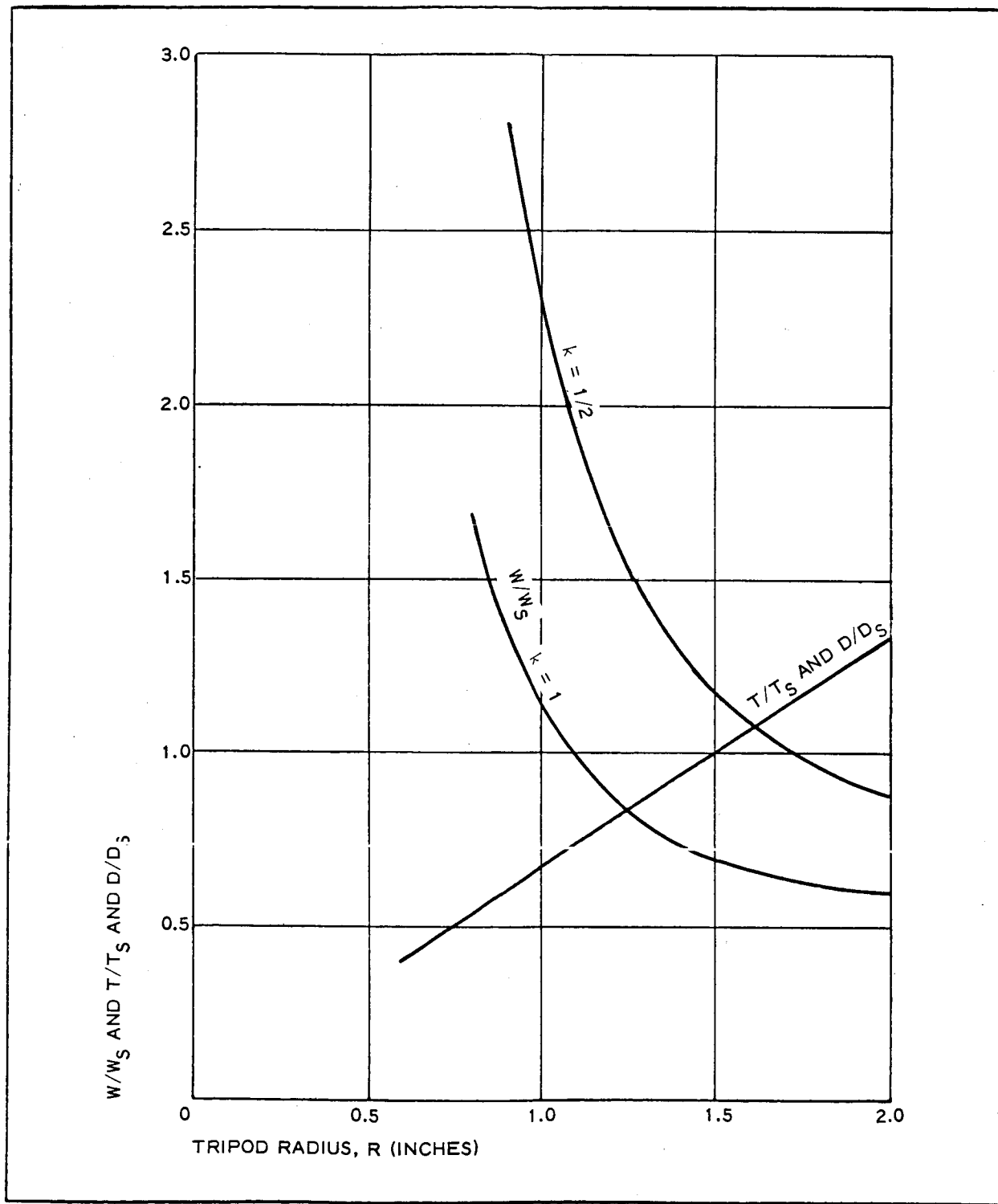


Figure 71 - Weight, Torque, and Drag versus Tripod Radius

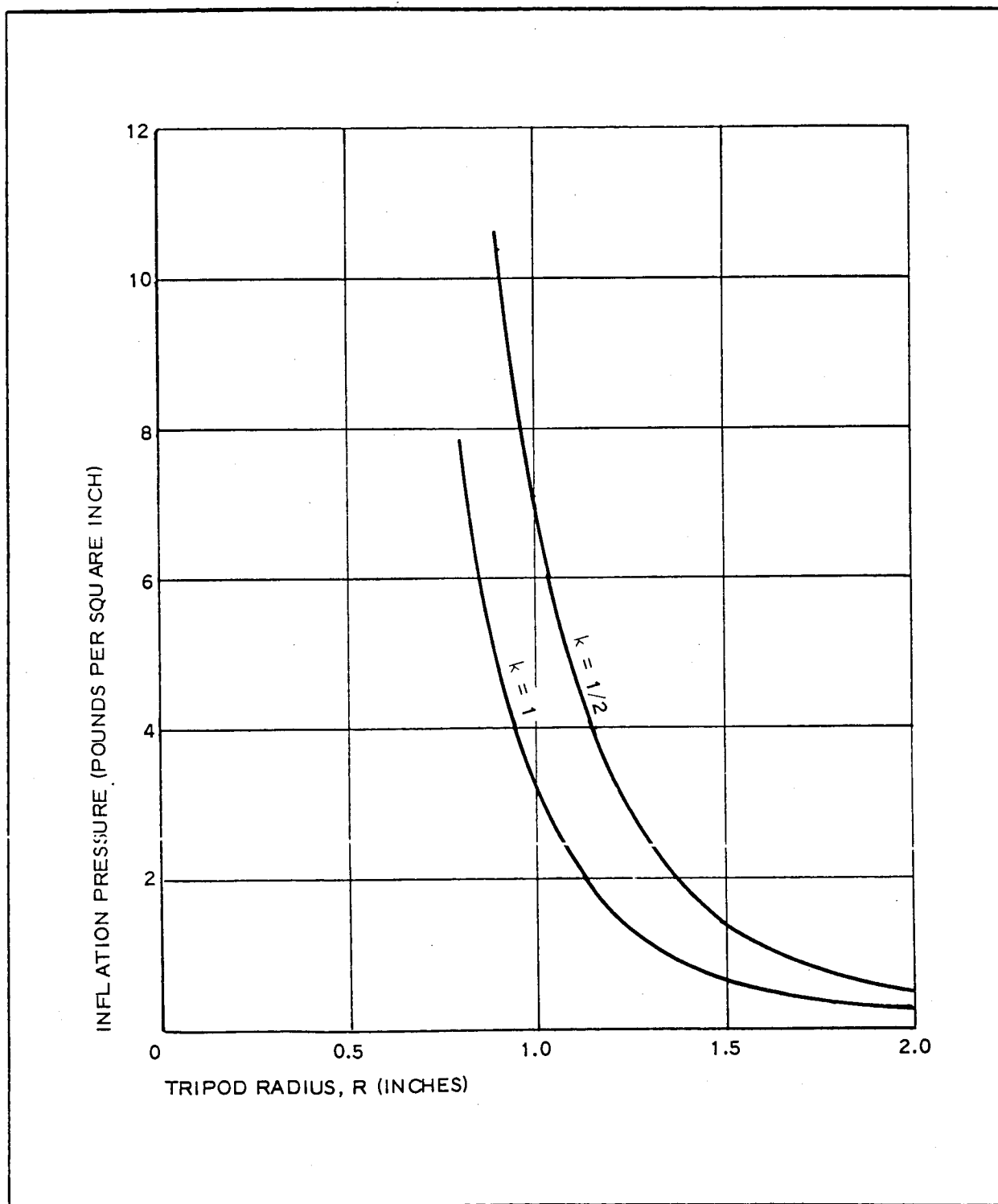


Figure 72 - Inflation Pressure versus Tripod Radius

(4) Design Alternate II

In this case it is proposed to use wire-film material as in Alternate I except that the film will be photolyzable film rather than Mylar. The advantage of photolyzable film would be a reduction in solar torque and aerodynamic drag after the film has disappeared.

Immediately after deployment, while the film is still present, the design condition will be the same as for Alternate I, assuming that the photolyzable film weight required is the same as the 0.25-mil Mylar used in Alternate I. If this is so, then the previous analysis applies and no saving in launch weight would be realized.

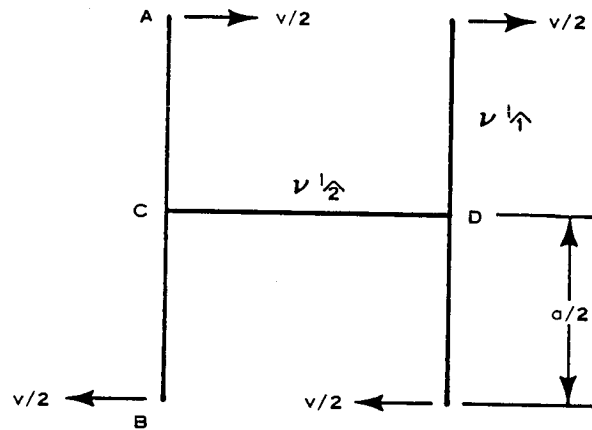
After the film disappears, the structure is altered in that the shear must be carried in the wires instead of in the film. It is therefore necessary to investigate the effect of shear deflections on the structural integrity of the tripods.

The approach used is that given for latticed columns in Reference 10. Using the nomenclature of Reference 10 a shear stiffness is defined as

$$\begin{aligned}\frac{1}{P_d} &= \frac{\alpha}{AG} \\ &= \frac{ab}{12EI_2} + \frac{a^2}{24EI_1}\end{aligned}\tag{95}$$

In the wire film application, member AB corresponds to the longitudinal wires, member CD corresponds to the hoop wires, and b, a are the wire spacing, respectively.

The quantities in Equation 95 are then for the wire film application:



$$I_1 = I_2$$

$$= \frac{\pi d^4}{64}$$

$$b = S$$

$$a = \frac{S}{2}$$

Substituting the above in Equation 95 gives

$$\frac{1}{P_d} = \frac{\alpha}{AG} = \alpha \left[\frac{\left(\frac{S}{2}\right)S}{\frac{12E\pi d^4}{64}} + \frac{\left(\frac{S}{2}\right)}{\frac{24E\pi d^4}{64}} \right]$$

$$= \frac{10}{3\pi} \frac{S^2 \alpha}{Ed^4} \quad (96)$$

The general expression for shear deflection is

$$\delta_S = \int_0^x \frac{\alpha V_n}{AG} dx , \quad (97)$$

where αV_n is interpreted here to be the load at the neutral axis, or the maximum shear flow times the wire spacing

$$\alpha V_n = \frac{VS}{\pi R} . \quad (98)$$

Substituting Equation 98 into Equation 97 gives

$$\delta_S = \int_0^x \left(\frac{10}{3\pi^2} \frac{S^3}{ERd^4} \right) V dx . \quad (99)$$

For a beam of length, ℓ , with a uniformly distributed load, q , the deflection due to shear at the mid-span is

$$\delta_S = \frac{10}{3\pi^2} \frac{S^3}{ERd^4} \left(\frac{q\ell^2}{8} \right) . \quad (100)$$

The bending deflection is obtained by combining Equations 79, 83, and 89, which gives

$$\begin{aligned} \delta_B &= \frac{5q\ell^4}{384E \left(\frac{R^2}{2} \right) \left(\frac{\pi^2 R d^2}{2S} \right)} \\ &= \frac{20q\ell^4 S}{384\pi^2 E R^3 d^2} \end{aligned} \quad (101)$$

The ratio of shear to bending deflection is then

$$\frac{\delta_S}{\delta_B} = \frac{8S^2 R^2}{d^2 \ell^2} \quad (102)$$

For this application the approximate values of the above quantities are

$$S \approx 0.25 \text{ in.}$$

$$R \approx 1.0 \text{ in.}$$

$$d \approx 0.01 \text{ in.}$$

$$l \approx 4000 \text{ in.}$$

Substituting these into Equation 102 yields

$$\frac{\delta_S}{\delta_B} \approx \frac{1}{3000} \quad (103)$$

From this it is apparent that the shear contribution to the deflection is small and can be neglected in this application. Therefore, after the film disappears, the strength and stiffness of the tripod is for all practical purposes unchanged, the loads are reduced, and it can be concluded that if the structure is satisfactory with film it will also be satisfactory without film. The weights obtained for Alternate I, therefore, are applicable to Alternate II.

The reduction in solar torque and aerodynamic drag can be estimated roughly by assuming that the torque and drag are proportional to the total projected area of the wires. This can be expressed conveniently as a ratio of projected area, S , to the standard area, S_s .

The projected area of the longitudinal wires per inch of tripod

$$\begin{aligned} S_L &= (d \times l) \frac{2\pi R}{S} \\ &= \frac{2\pi R d}{S} \end{aligned} \quad (104)$$

There is twice as much hoop wire as longitudinal wire so the total projected area of the wires is

$$\begin{aligned} S &= 3S_L \\ &= \frac{6\pi R d}{S} \end{aligned} \quad (105)$$

The standard area S_s is 3, since the proposed design has 3-in.-diameter tubes, so

$$\frac{S}{S_s} = \frac{2\pi R d}{S} \quad (106)$$

For Alternate I the wire area required was determined as a function of the radius R . These results are valid for this application and can be used to evaluate Equation 106. Equation 83 can be rewritten in the form

$$d^2 = \frac{2SA_W}{\pi^2 R} \quad (107)$$

or

$$d = \frac{1}{\pi} \sqrt{\frac{2SA_W}{R}} \quad (108)$$

Substituting into Equation 106 gives

$$\frac{S}{S_s} = 2\sqrt{2} \sqrt{\frac{RA_W}{S}} \quad (109)$$

Equation 109 is evaluated using the values of R and A_W from Table XVI and assuming S is 0.25 in. These calculations are shown in Table XVIII.

The values of S/S_s are plotted as a function of R in Figure 73. The most interesting feature is that the value of S/S_s decreases with increasing R for the cases without film. Since the weight decreases as R increases (note Figure 71), it must be concluded

TABLE XVIII - CALCULATIONS FOR S/S_s

R	k = 1.0				k = 0.5			
	$A_W \times 10^4$	$RA_W \times 10^4$	$\sqrt{RA_W}$	S/S_s^*	$A_W \times 10^4$	$RA_W \times 10^4$	$\sqrt{RA_W}$	S/S_s^*
0.80	24.2	19.3	0.0440	0.249	55.1	44.1	0.0664	0.375
0.90	18.9	17.0	0.0412	0.233	41.8	37.6	0.0614	0.346
1.00	15.3	15.3	0.0392	0.222	33.1	33.1	0.0576	0.326
1.25	9.87	12.3	0.0351	0.198	20.7	25.8	0.0508	0.287
1.50	7.01	10.5	0.0324	0.183	14.45	21.7	0.0466	0.264
2.00	4.15	8.3	0.0289	0.163	8.47	16.9	0.0411	0.232

$$* \frac{S}{S_s} = 5.656 \sqrt{RA_W}$$

where R and A_W are obtained from Table XVI.

that the wire-film tripod with photolyzable film (Alternate II) is the best design.

(5) Summary

Two alternate tripod designs have been investigated and the results are summarized below:

1. Proposed full-scale design - The proposed design, see Item 2, d, consists of three-inch-diameter tubes of one-mil Mylar. This design is light in weight and simple to fabricate. Structurally the memory of the Mylar might be a problem, but the addition of wire reinforcement as proposed to stabilize the section locally should resolve this problem.
2. Alternate I - A wire-film material in which

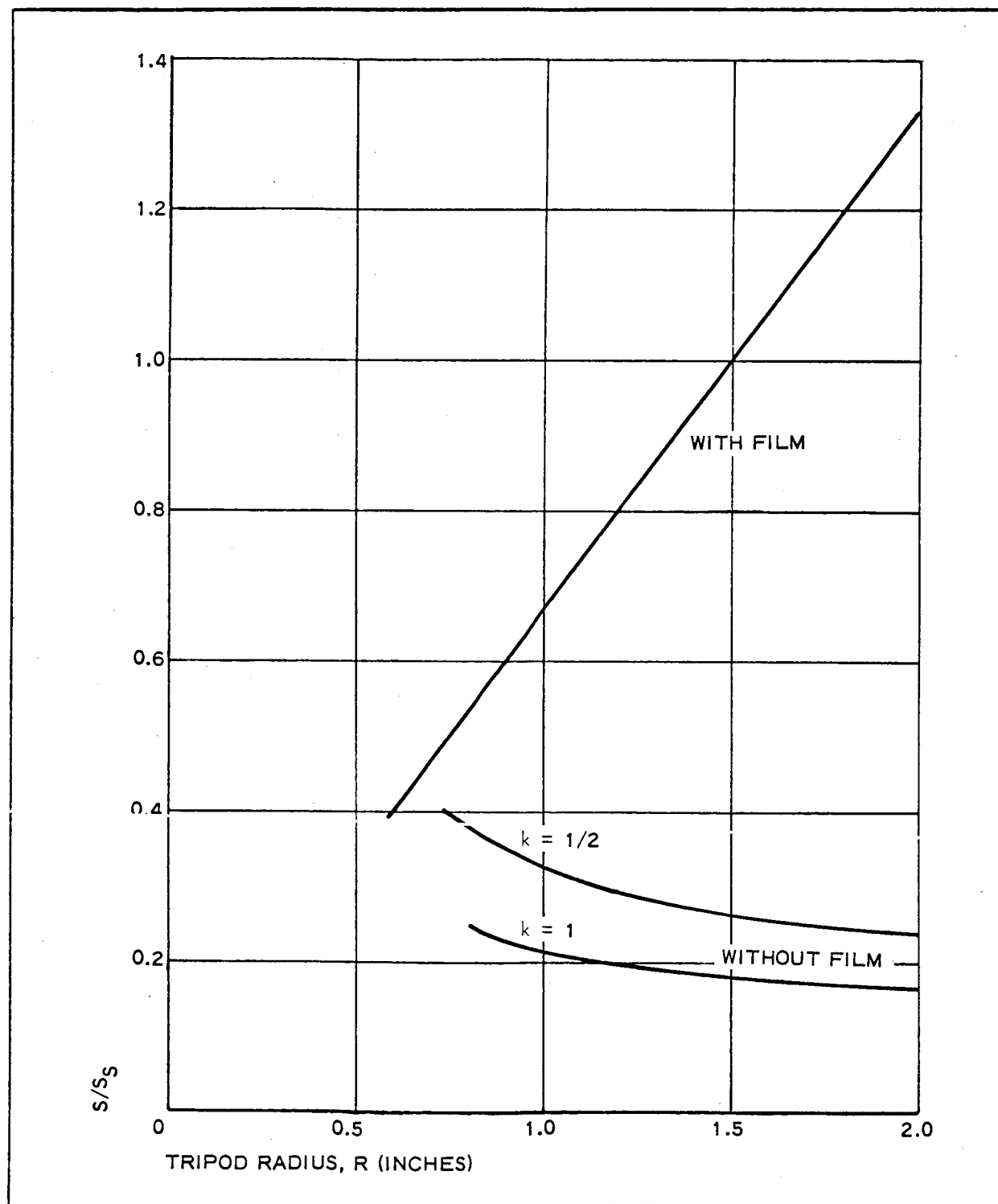


Figure 73 - Torque and Drag Comparison

a practical minimum weight film is used to contain the inflation pressure with the loads carried entirely by the wires. This approach is definitely advantageous (note Figure 71) if a value of k approaching unity can be realized. One disadvantage is that a separate pressure control will probably be required for the tripods (note Figure 72).

3. Alternate II - This is the same as Alternate I except that photolyzable film is used. The weight should be the same as for Alternate I but substantial reductions in solar torque and aerodynamic drag are possible (see Figure 73). On the other hand considerable development effort might be required to answer the following questions:

1. What k can be used?
2. Can the inflation pressure be contained with photolyzable film at the expected temperature?
3. Can the wire intersections be made such that no relative rotation occurs between the longitudinal and hoop wires?

e. Summary

This study shows that the full-scale lenticular satellite as proposed herein is substantially lighter in weight than either an equivalent sphere or a lenticular satellite with Echo A-12 material for the lens. Compared to the sphere the weight saving amounts to 1115 lb or 44

percent of the sphere weight. The comparison with the Echo A-12 material is approximately the same, the weight saving being 1126 lb when compared to the case where the concentrated masses are kept the same.

The weight breakdowns presented in Table XV provide information from which the following conclusions can be drawn.

1. The principal part of the sphere weight (2150 lb) is in the shell and can be reduced only by the use of lighter weight material.
2. The inflation system weight is relatively small (58 lb), but it should be pointed out that the relative properties are dependent on size and that the inflation system weight will increase more rapidly than the shell weight.
3. The weight increase with the Echo A-12 material can be attributed to two causes. The first is the unit weight of the lens material, which increases the lens weight 448 lb (from 552 to 1000 lb). The second is the increased strength of the A-12 material, which in turn requires a higher inflation pressure. This affects both the torus and the inflation system weights. The torus weight increases 446 lb (from 117 to 583 lb) and the inflation system 176 lb (from 44 to 220 lb). Therefore, the increased weight of the material accounts for 448 lb and the increased strength for 642 lb or a total of 1090 lb.

The study of alternate materials for the tripod booms show that Alternate II, aluminum wire with photolyzable film, is the best. The

weight, torque due to solar pressure, and aerodynamic drag can be reduced simultaneously from the corresponding values for the full-scale satellite. On the other hand considerable development work might be required to establish the desired level of confidence in this approach. Alternate I, aluminum wire plus 0.25-mil Mylar might have advantages over the present concept, but additional work on this approach is required to establish the value of the parameter, k , before specific conclusions can be made.

5. CONCLUSIONS AND RECOMMENDATIONS

As a result of the studies and analyses made during Phases I and II it is concluded that:

1. It is feasible to meet the system requirements with the full-scale satellite proposed herein.
2. The flight-test model will in general be structurally less critical than the full-scale satellite.
3. A flight-test model is desirable to demonstrate and to obtain information regarding packaging, deployment, rigidization, and orbital behavior to increase confidence in the basic concept and to improve the design of the full-scale satellite.
4. Alternate studies show that the proposed design is lighter than a similar lenticular using Echo A-12 material for the lens or for a 400-ft-diameter sphere.
5. A further reduction in weight is possible by refinement in design and development of improved materials.

It is recommended that:

1. Work to be continued on material and fabrication development, design studies, and component testing with the objective of decreasing launch weight and increasing the confidence level.
2. A detail design and test program for a flight-test model be initiated.

6. LIST OF SYMBOLS

A = area enclosed by the periphery
of the rim cross-section

D = lens chord

E = modulus of elasticity

F = concentrated load normal to the
rim plane

f = stress, in general

F.S = factor of safety

G = shear modulus

g = acceleration of gravity on the
surface of the earth

H = distance of rim center from
the tripod apex

$I_x - x', I_y - y', I_z - z$ = mass moments of inertia of
satellite about principal axes
x, y, and z

I_x, I_z = moments of inertia of rim cross
section about centroidal axes x
and z

$J = 4A^2 \int \frac{ds}{t}$ for the rim cross
section

$j = \sqrt{\frac{EI}{L}}$ in a beam-column

- L = boom axial load
- ℓ = boom length
- M = concentrated mass
- M_x = bending moment at station X
- m = mass per unit area
- m_r = mass per rim unit length, assuming that rim, torus, and lens masses are uniformly distributed around the rim
- P = load at the tripod apex
- p = inflation pressure
- Q = concentrated load in the plane of the rim
- q = uniform radial pull on the torus from the lens also (with subscripts) any distributed load
- R = rim radius
- r = radius of torus meridional section
- r_c = radius of tripod leg (boom) cross section
- S = lens arc length
- t = thickness in general
- w = in-plane rim deflection; also tripod boom transverse deflection
- x, y, z = Cartesian coordinates originating from the center of the rim (x and y in the plane of the rim, z along the polar axis of the satellite)

α, α_o = angular deviation in the orbital plane between the polar axis of the satellite and the radius of the earth

β, β_o = angle between the polar axis of the satellite and its orbital plane, degrees

δ = rim deflection normal to its plane

ϵ = elongation

ζ, ϕ = parameter angles

$\lambda = (I_x - x - I_z - z) \div I_x - x$

μ = Poisson's ratio

ρ = lens radius of curvature

ω = angular velocity of satellite in its rotation around the earth

Subscripts:

c = copper

cr = critical

ℓ = lower or lens

u = upper

t = torus

y = yield

b = boom

r = rim

1, 2, 3 = locations on the rim corresponding to the values $\phi = 60, 180, \text{ and } 300 \text{ deg, respectively}$

x, y, z = associated with respective axis

SECTION III - TECHNICAL DISCUSSION - PHASES I AND II

Subsection Three - Stabilization and Orientation Systems

1. GENERAL

The gravity-gradient stabilization system and the orientation system for the proposed passive lenticular satellite have been studied.

The purpose of the stabilization system is to maintain the attitude of the lenticular satellite in an upright position within a nominal accuracy of ± 3 deg. To accomplish this, the stabilization system must ensure that initial attitude errors are damped out within a reasonable time limit and must also ensure that steady-state perturbing torques on the satellite, such as those due to solar pressure and orbital eccentricity, are prevented from building up attitude errors in excess of the nominal accuracy. The gravity-gradient stabilization system consists of gravity-gradient booms with attached canister load and a libration damping device. Figure 74 presents a schematic of the system. For gravity stabilization purposes, the important considerations are the moments of inertia of the principal axes of the satellite, including the contribution of the gravity-gradient booms and their associated canister loads, as well as the energy dissipation capability of the damping device.

The purpose of the orientation system is to provide proper attitude of the spacecraft prior to the time when the gravity-gradient stabilization captures the attitude of the lenticular satellite in its fully deployed configuration. The orientation system thus functions from shortly after orbital injection until the gravity-gradient stabilization system is ready to capture the attitude of the fully deployed satellite. In this interval of time, the orbiting payload is going through a metamorphosis that changes its configuration from a pair of hemispherically sealed canisters to its final

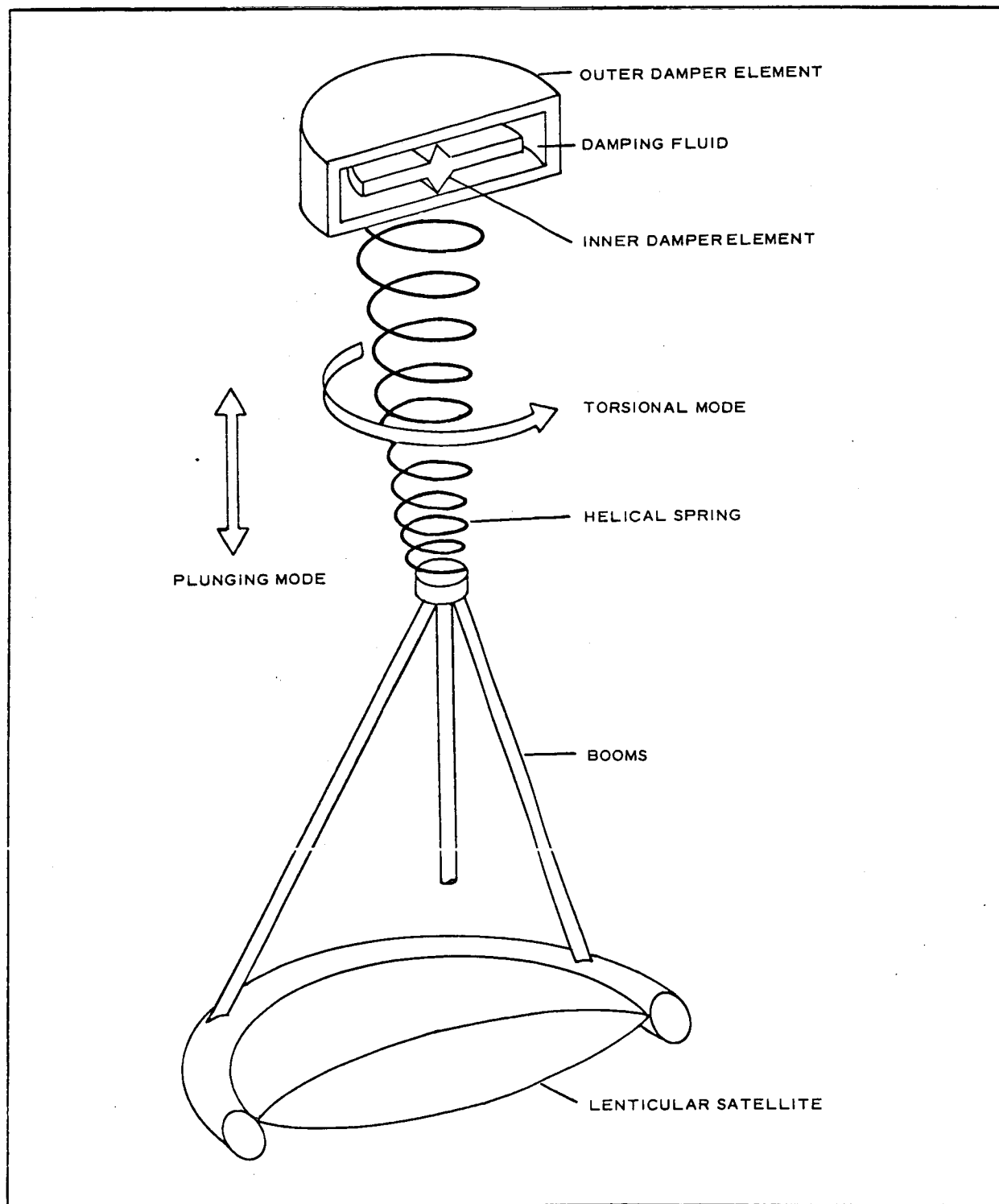


Figure 74 - Rice-Wilberforce Damper Applied to Lenticular Satellite

configuration. The orientation system consists of a timing device and a despin mechanism, which ensure that the angular momentum of the payload (as established by the orbital injection stage of the propulsion system) is reduced to a low value at that point in the orbit where the momentum vector originally due to spin is vertical. On the basis of studies made so far, it appears that the orientation system does not require any active attitude control jets or magnetic torquing coils. The tolerance on the accuracy with which the orientation system kills the momentum vector is relatively crude, but the gravity-gradient stabilization system is able to capture the attitude of the satellite with initial attitude errors on the order of 40 deg and attitude rate errors on the order of the orbital rate. (See Reference 1, Figure 7.)

2. STABILIZATION SYSTEM

a. General

The stabilization system for the passive lenticular communication satellite consists of the set of gravity-gradient booms with the attached canisters as inertia loads and a damping device. Performance requirements of the damping system are assumed to be a damping time constant of less than five orbits and the suppression of steady-state forced errors in pitch and roll to less than 3 deg. On the basis of studies made so far, it appears that these performance requirements can be met. Studies made to date have been primarily concerned with the stabilization performance achievable on the operational satellite configuration. There is no reason to expect that adequate performance cannot be achieved on a test satellite of much less weight and inertia.

Studies of the gravity-gradient stabilization system were made for both transient conditions as well as for steady-state disturbing conditions. The equations of motion applicable to the gravity-gradient stabilization problem were developed using the classical method of

Lagrange. These equations were simulated on both analog and digital computers. Various forms of the Rice-Wilberforce gravity-gradient damping device were investigated, including forms such as a simple single-mode lossy spring and tip mass, a dual-mode lossy spring with the tip mass, and a dual-mode lossy spring with tip mass and internal fluid damper within the tip mass. Figure 74 presents a sketch of the dual-mode lossy spring and fluid damper as applied to the lenticular satellite. This last mentioned form of the damper is an optimum one, being very efficient as a gravity-gradient device giving damping time constants in both pitch and roll axes of the order of $1\frac{1}{2}$ orbits and with no steady bias or hang-off errors. However, further studies must be done to assess the full effect of cross-coupling in the equations of motion. The results are therefore somewhat tentative.

b. Equations of Motion for Lenticular Satellite with Rice-Wilberforce Damper

(1) General

The equations of motion presented here are the basis for study of the stabilization and damping of the gravity-gradient-stabilized lenticular satellite. They have been used for both analog and digital computer studies. They are an adaptation and extension of the equations developed by Dr. J. L. Vanderslice at APL-JHU for studying the dynamics of the TRAAC satellite. The original equations are published in TG-502.¹¹

The coordinate systems, Euler angle set, and nomenclature are identical to those used in the reference, with the addition of terms necessary to describe the additional degree of freedom of the Rice-Wilberforce damper concept. The system configuration and the YXZ Euler angle orientation are depicted in Figure 75. The applicable simplifying assumptions from the reference with changes in wording as believed necessary along with two additional assumptions are presented below:

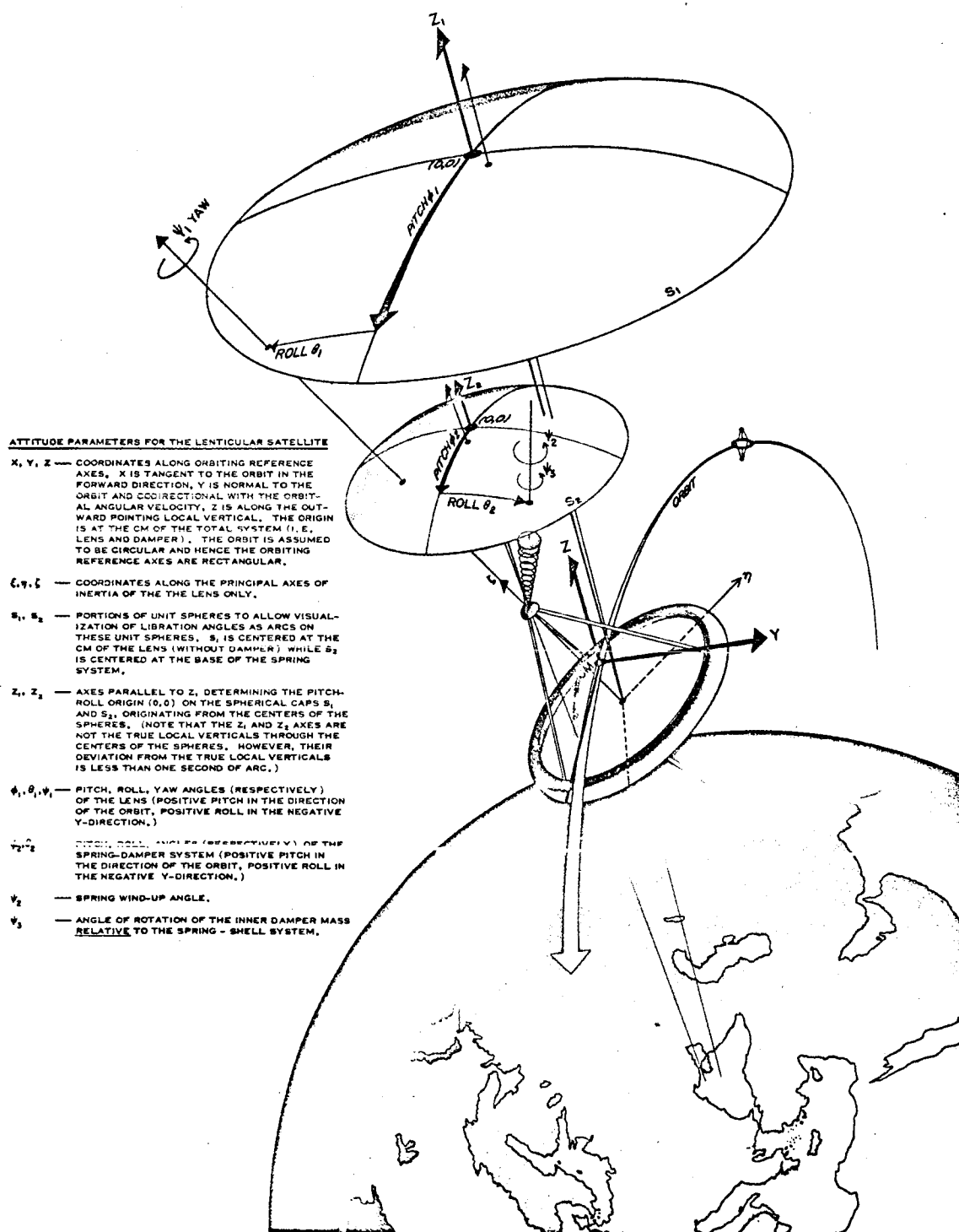


Figure 75 - System Configuration and Attitude Parameters

1. The orbit of the center of mass (C. M.) of the satellite-damper system is inexorably circular.
2. The inner and outer masses at the end of the spring are considered as point masses. The weight of the spring is neglected.
3. The axis of the helical spring remains rectilinear, and the spin axis of the end masses lies along the spring axis. There is no torsion in the spring connection to the canister.
4. Although the spring loss is expected to be principally hysteretic, it has been represented by an equivalent viscous damping.
5. In the collection of trigonometric terms in the final differential equations of motion, third-order terms are negligible except where ψ is concerned (see next assumption); that is, $\sin \theta = \theta$, $\sin^2 \theta = \theta^2$, $\cos \theta = 1 - (\theta^2/2)$, $\cos^2 \theta = 1 - \theta^2$, $\sin \theta \cos \theta = \theta$, and $\cos \theta \cos \phi = 1 - (\theta^2/2) - \phi^2/2$.
6. Third-order terms containing $\dot{\psi}_1$ when multiplied by I_s or I_m are negligible.
7. The nonlinear spring can be simulated by a "constant" spring constant, based on desired equilibrium length and helix angle, and a bias in the \ddot{r} equation, which results in static equilibrium about r_e .

The original equations in the reference contained seven degrees of freedom. The equations presented here have one more degree of freedom, resulting from inclusion in the dynamics of the Rice-Wilberforce damping concept. The term $M/(m + M)$

has been retained as a multiplying factor in the energy expressions, therefore resulting in differences from the reference equations. Depending on the damping and weight requirements, this term may or may not be approximated by unity.

The revised nomenclature and the energy and dissipation functions are presented first, followed by the revised equations of motion obtained by applying Lagrange's methods.

(2) Nomenclature

$$(\dot{}) = d()/dt$$

$$\omega = \text{constant orbital angular velocity, rad per second}$$

$$R = \text{distance from system C.M. to earth center, ft}$$

$$L = \text{distance from satellite c.g. to spring attachment, ft}$$

$$r, r_e = \text{instantaneous and equilibrium length of spring, ft}$$

$$M, m = \text{mass of satellite, combined weights on end of spring, slugs}$$

$$\bar{m} = \text{modified mass of spring weights, } \bar{m} = mM/M + m$$

$$X, Y, Z = \text{basic rectangular coordinate systems, rotating about Y at orbital speed}$$

$$X_M, X_m, \text{ etc.} = \text{rectangular coordinates of } M, m$$

$$\xi, \eta, \zeta = \text{principal body axes of satellite}$$

$$I_\xi, I_\eta, I_\zeta = \text{principal moments of inertia of satellite, slug-ft}^2$$

$$I_S, I_m = \text{spin moment of inertia of fixed mass at end of spring, inner mass, slug-ft}^2$$

$$\phi_1, \theta_1, \psi_1 = \text{Euler angles for satellite, rad}$$

SECTION III

Subsection Three - Stabilization and Orientation Systems

GER-11502

ϕ_1, θ_2 = first two Euler angles for fixed mass, rad

ψ_2 = spin angle of spring and outer mass relative to attachment, rad

ψ_3 = spin angle of inner mass relative to the fixed (container) mass, rad

$k_1 m \omega^2$ = Hooke's constant of spring, lb/ft

$k_2 m \omega$ = equivalent viscous damping constant of spring, lb-sec/ft

$k_3 I_S \omega^2$ = torsional spring constant, ft-lb/rad

$k_4 \sqrt{m I_S \omega^2}$ = spring cross-coupling extension and wind-up, ft-lb/ft or lb/rad

$k_5 I_S \omega$ = spring torsional damping, ft-lb sec/rad

$k_6 I_m \omega$ = torsional (viscous) damping constant acting on inner mass, ft-lb-sec/rad

$L_{\phi_1}, L_{\theta_1}, L_{\psi_1}$ = external torques acting on satellite about Euler axes 1, 2, 3, ft-lb

T, V, D = system kinetic, potential, and dissipation functions

N = ratio of masses (m + M)/M

Subscripts 0, 1, 2, 3 = orderly rotations in a 3-Euler angle rotation

(3) Equations

(a) Kinetic Energy

$$T = \frac{\bar{m}}{2} \left\{ L^2 (\dot{\theta}_1^2 + \dot{\phi}_1^2 c^2 \theta_1) + r^2 (\dot{\theta}_2^2 + \dot{\phi}_2^2 c^2 \theta_1) + \dot{r}^2 + 2Lr \left[\dot{\theta}_1 \dot{\theta}_2 (c\theta_1 c\theta_2 + s\theta_1 s\theta_2 c(\phi_2 - \phi_1) + \dot{\theta}_1 \dot{\phi}_2 s\theta_1 c\theta_2 s(\phi_2 - \phi_1) - \dot{\theta}_2 \dot{\phi}_1 c\theta_1 s\theta_2 s(\phi_2 - \phi_1) + \dot{\phi}_1 \dot{\phi}_2 c\theta_1 c\theta_2 c(\phi_2 - \phi_1) \right] + 2Lr \left[\dot{\theta}_1 (c\theta_1 s\theta_2 - s\theta_1 c\theta_2 c(\phi_2 - \phi_1) + \right. \right.$$

$$\begin{aligned}
& \dot{\phi}_1 c\theta_1 c\theta_2 s(\phi_2 - \phi_1) \Big] + 2\omega \Big[L^2 \dot{\phi}_1 c^2\theta_1 + Lr(\dot{\theta}_1 s\theta_1 c\theta_2 s(\phi_2 - \phi_1) - \\
& \dot{\theta}_2 c\theta_1 s\theta_2 s(\phi_2 - \phi_1) + \dot{\phi}_1 c\theta_1 c\theta_2 c(\phi_2 - \phi_1) + \dot{\phi}_2 c\theta_1 c\theta_2 c(\phi_2 - \phi_1) + \\
& r^2 \dot{\phi}_2 c^2\theta_2 + Lrc\theta_1 c\theta_2 s(\phi_2 - \phi_1) \Big] + \omega^2 \Big[L^2 c^2\theta_1 + 2Lrc\theta_2 c(\phi_2 - \phi_1) + \\
& r^2 c^2\theta_2 \Big] \Big\} + \omega^2 R \frac{(m+M)}{2} + \frac{1}{2} \Big\{ I_\xi \Big[\dot{\theta}_1^2 c^2\psi_1 + \dot{\theta}_1(\omega + \dot{\phi}_1) c\theta_1 s2\psi_1 + \\
& (\omega + \dot{\phi}_1)^2 c^2\theta_1 s^2\psi_1 \Big] + I_\eta \Big[\dot{\theta}_1^2 s^2\psi_1 - \dot{\theta}_1(\omega + \dot{\phi}_1) c\theta_1 s2\psi_1 + \\
& (\omega + \dot{\phi}_1)^2 c^2\theta_1 c^2\psi_1 \Big] + I_\zeta \Big[(\omega + \dot{\phi}_1)^2 s^2\theta_1 - 2\psi_1(\omega + \dot{\phi}_1) s\theta_1 + \dot{\psi}_1^2 \Big] + \\
& I_s(\dot{\psi}_1 c\phi_2 c\theta_2 + \dot{\psi}_2)^2 + I_m(\dot{\psi}_1 c\phi_2 c\theta_2 + \dot{\psi}_2 + \dot{\psi}_3)^2 \Big\} \quad (110)
\end{aligned}$$

(b) Potential Energy

$$\begin{aligned}
V = & \frac{\omega^2}{2} \Big[k_1 m r^2 + 2k_4 \sqrt{mI_s} (r - r_e) \psi_2 + k_3 I_s \psi_2^2 + \\
& \frac{\bar{m}\omega^2}{2} \Big[L^2(1 - 3c^2\phi_1 c^2\phi_1) + 2Lr(c\theta_1 c\theta_2 s\phi_1 s\phi_2 - 2c\theta_1 c\theta_2 c\phi_1 c\phi_2 + \\
& s\theta_1 s\theta_2) + r^2(1 - 3c^2\theta_2 c^2\phi_2) \Big] - \frac{3}{4} \omega^2 \Big\{ I_\xi \Big[(c^2\phi_1 s^2\theta_1 - s^2\phi_1) c2\psi_1 + \\
& s2\phi_1 s\theta_1 s2\psi_1 + c^2\phi_1 c^2\theta_1 \Big] + I_\eta \Big[-(c^2\phi_1 s^2\theta_1 - s^2\phi_1) c2\psi_1 - \\
& s2\phi_1 s\theta_1 s2\psi_1 + c^2\phi_1 c^2\theta_1 \Big] - I_\zeta \Big[2c^2\phi_1 c^2\theta_1 \Big] \Big\} \quad (111)
\end{aligned}$$

(c) Dissipation Function

$$D = \frac{\omega}{2} (mk_2 \dot{r}^2 + I_s k_5 \dot{\psi}_2^2 + I_m k_6 \dot{\psi}_3^2) \quad (112)$$

(d) System Differential Equations (8 Degrees of Freedom)

$$\begin{aligned} & (I_\xi - I_\eta) s \psi_1 c \psi_1 \ddot{\phi}_1 + (I_\xi c^2 \psi_1 + I_\eta s^2 \psi_1) \ddot{\theta}_1 + \bar{m} L (\theta_2 - \theta_1) \ddot{r} - \\ & 2(I_\xi - I_\eta) s \psi_1 c \psi_1 \dot{\theta}_1 \dot{\psi}_1 + \left[(I_\xi - I_\eta) c^2 \psi_1 + I_\zeta \right] \ddot{\phi}_1 \dot{\psi}_1 + 2\omega (I_\xi s^2 \psi_1 + \\ & I_\eta c^2 \psi_1 - I_\zeta) \theta_1 - \bar{m} L^2 (\theta_2 - \theta_1) \ddot{\phi}_1 - 2\omega \bar{m} L r (\theta_2 - \theta_1) \ddot{\phi}_2 + \\ & \left[(I_\xi - I_\eta) c^2 \psi_1 + I_\zeta \right] \left(1 - \frac{\theta_1^2}{2} \right) \omega \dot{\psi}_1 + \omega^2 \left[4(I_\xi s^2 \psi_1 + I_\eta c^2 \psi_1 - I_\zeta) \theta_1 - \right. \\ & \left. 3\bar{m} L (L + r) (\theta_2 - \theta_1) - 3s \psi_1 c \psi_1 (I_\xi - I_\eta) \phi_1 \right] = L \theta_1 \end{aligned} \quad (113)$$

$$\begin{aligned} & (I_\xi s^2 \psi_1 + I_\eta c^2 \psi_1) \ddot{\phi}_1 + (I_\xi - I_\eta) s \psi_1 c \psi_1 \ddot{\theta}_1 - I_\zeta \theta_1 \ddot{\psi}_1 + \bar{m} L (\phi_2 - \phi_1) \ddot{r} + \\ & 2(I_\xi - I_\eta) s \psi_1 c \psi_1 \dot{\theta}_1 \dot{\psi}_1 + \left[(I_\xi - I_\eta) c^2 \psi_1 - I_\zeta \right] \dot{\theta}_1 \dot{\psi}_1 + \end{aligned}$$

$$\begin{aligned} & \omega \left\{ -2\bar{m}L^2(\phi_2 - \phi_1)\ddot{\phi}_1 - 2(I_\xi s^2\psi_1 + I_\eta c^2\psi_1 - I_\zeta)\theta_1\dot{\theta}_1 - 2\bar{m}Lr(\phi_2 - \phi_1)\ddot{\phi}_2 + \right. \\ & \left. 2(I_\xi - I_\eta)s\psi_1 c\psi_1(1 - \theta_1^2)\psi_1 \right\} + \omega^2 \left\{ 3(I_\xi c^2\psi_1 + I_\eta s^2\psi_1 - I_\zeta)\phi_1 + \right. \\ & \left. 3\bar{m}L(L+r)(\phi_1 - \phi_2) - 3s\psi_1 c\psi_1(I_\xi - I_\eta)\theta_1 \right\} = L\phi_1 \end{aligned} \quad (114)$$

$$\begin{aligned} & (I_\zeta + I_s + I_m)\ddot{\psi}_1 + (I_s + I_m)\ddot{\psi}_2 + I_m\ddot{\psi}_3 - I_\zeta\theta_1\ddot{\phi}_1 - (I_\xi - I_\eta)s\psi_1 c\psi_1\ddot{\phi}_1^2 - \\ & \left[(I_\xi - I_\eta)c^2\psi_1 + I_\zeta \right] \phi_1\dot{\theta}_1 + (I_\xi - I_\eta)s\psi_1 c\psi_1\dot{\theta}_1^2 - \\ & \omega \left\{ 2(I_\xi - I_\eta)s\psi_1 c\psi_1\ddot{\phi}_1 + \left[(I_\xi - I_\eta)c^2\psi_1 + I_\zeta \right] \theta_1 \right\} - \\ & \omega^2 \left\{ (I_\xi - I_\eta)s\psi_1 c\psi_1 + (I_\xi - I_\eta)s\psi_1 c\psi_1(3\phi_1^2 - 4\theta_1^2) + \right. \\ & \left. 3\phi_1\theta_1 c^2\psi_1(I_\xi - I_\eta) \right\} = L\psi_1 \end{aligned} \quad (115)$$

$$L\ddot{\theta}_1 + r\ddot{\theta}_2 + 2\dot{r}\dot{\theta}_2 + 2\omega \left[L\theta_2\phi_1 + r\theta_2\phi_2 \right] + \omega^2 \left[L\theta_1 + (3L + 4r)\theta_2 \right] = 0 \quad (116)$$

$$L\ddot{\phi}_1 + r\ddot{\phi}_2 + 2\dot{r}\dot{\phi}_2 + 2\omega \left[L(\phi_2 - \phi_1)\ddot{\phi}_1 - L\theta_1\dot{\theta}_1 - r\theta_2\dot{\theta}_2 + \dot{r} \right] + 3\omega^2(L+r)\phi_2 = 0 \quad (117)$$

$$\begin{aligned}
& L(\phi_2 - \phi_1)\ddot{\phi}_1 + L(\theta_2 - \theta_1)\ddot{\theta}_1 + \ddot{r} - L\dot{\phi}_1^2 - L\dot{\theta}_1^2 - r\dot{\phi}_2^2 - r\dot{\theta}_2^2 - \\
& 2\omega \left[L\dot{\phi}_1 + r\dot{\phi}_2 - \frac{N}{2}k_2\dot{r} \right] + \omega^2 \left\{ \left[Nk_1 - 3 + 4\theta_2^2 + 3\phi_2^2 \right] r + \right. \\
& \left. \left[-3 + \frac{3}{2}(\theta_1^2 + \theta_2^2 + \phi_1^2 + \phi_2^2) + \theta_1\theta_2 \right] L + Nk_4\sqrt{I_s/m}\psi_2 + 3(r_e + L) - \right. \\
& \left. Nk_1r_e \right\} = 0
\end{aligned} \tag{118}$$

$$\begin{aligned}
& (I_s + I_m)\ddot{\psi}_1 + (I_s + I_m)\ddot{\psi}_2 + I_m\ddot{\psi}_3 + \omega k_5 I_s \dot{\psi}_2 + \\
& \omega^2 \left[k_3 I_s \psi_2 + k_4 \sqrt{I_s m} (r - r_e) \right] = 0
\end{aligned} \tag{119}$$

$$\ddot{\psi}_1 + \ddot{\psi}_2 + \ddot{\psi}_3 + \omega k_6 \dot{\psi}_3 = 0 \tag{120}$$

c. Rice-Wilberforce Spring Equations

(1) General

The basic concept of the Rice-Wilberforce damper involves use of the cross-coupling characteristics of the helical spring as a mechanism for converting plunging motion into rotary motion. At the beginning of this study it was found that the available literature and classic textbooks on spring characteristics did not provide an adequate coverage of properties of helical springs in the region of parameters needed in this application.

For this reason, the necessary equations were developed as a part of the study. Subsequently, a Russian paper¹² was found to be nearly identical to the work summarized here and served to corroborate the validity of the analysis.

The analysis which follows is not intended to be an all-encompassing treatise on the subject of helical springs but is reasonably broad within the following constraints:

1. It is assumed that the spring is made of wire of uniform-symmetrical cross section and that the helix angle and radius of the coil are uniform throughout the length of the spring
2. The wire diameter is small compared to the radius of the coil, so that curved beam effects on stress distribution and stiffness are negligible
3. It is assumed that all deflections of the spring result from bending and torsion of the wire; that is, that deflections due to direct stresses (axial and shear) are negligible
4. The wire behaves elastically

The general expressions for the axial load and rotational moment are developed as a function of the wire characteristics and geometry (including initial unloaded geometry).

The stiffness coefficients (spring constants) are evaluated by taking appropriate partial derivatives of the force equations. Note that the nomenclature used to denote these stiffness coefficients in this derivation differs from the nomenclature used in the equations of motion because of convenience.

Special cases of particular interest in this study are evaluated in more detail, and curves are plotted to facilitate the choice of parameters for the dynamic study. Figure 76 is included to show the result of linearization of the spring characteristics.

Further study of spring characteristics is desirable in the following areas:

1. The theoretical and practical implications of utilizing springs with various unloaded lengths.
2. The effects of using wire of noncircular cross sections, for example, flattened cross sections. The equations indicate that the cross-coupling can be enhanced by this means. Other characteristics associated with this need more study.
3. Practical design considerations of the geometry of the terminal of the coil.
4. The behavior of springs built from wire coated with inelastic materials.
5. Stability characteristics and associated vulnerability to entanglement.

(2) Helical Spring Geometry Relationships

A helical spring may be geometrically interpreted as the geometric figure that results from the bending and twisting of a straight uniform wire around a right circular cylinder at constant bending and twisting rates, so that the same longitudinal filament on the wire surface is always in contact with the surface of the right circular cylinder.

Figure 77 shows a helical spring with its various geometric parameters.

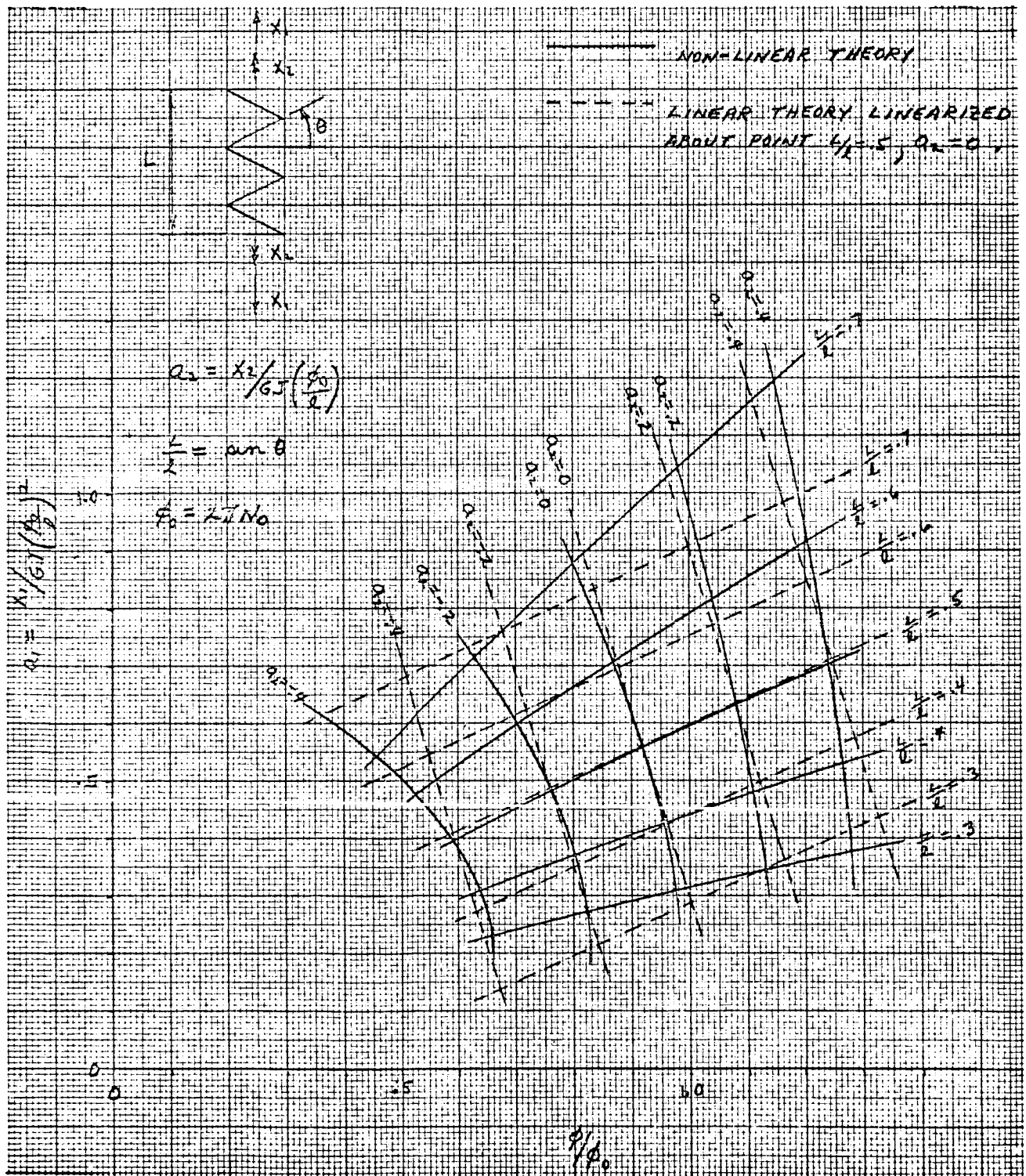


Figure 76 - Comparison of Spring Parameters

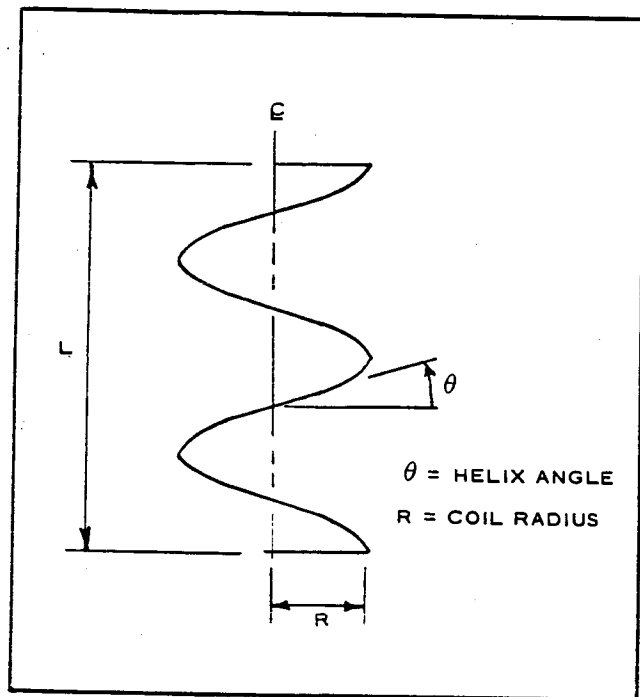


Figure 77 - Geometric Parameters of Helical Spring

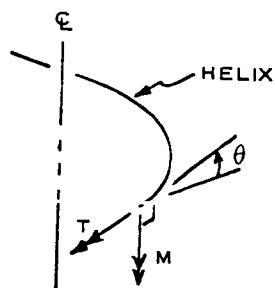
The bending and twisting of the wire around the right circular cylinder gives rise to the following relationships between:

1. The internal torque in the wire, T
2. The internal bending moment in the wire, M
3. The unit twist in the wire, α
4. The radius of curvature of the wire, ρ , associated with the moment, M (the subscript zero refers to initial unstressed conditions):

$$\frac{1}{\rho} = \frac{M}{EI} + \frac{1}{\rho_0}, \quad (121)$$

and

$$\alpha = \frac{T}{JG} + \alpha_0. \quad (122)$$

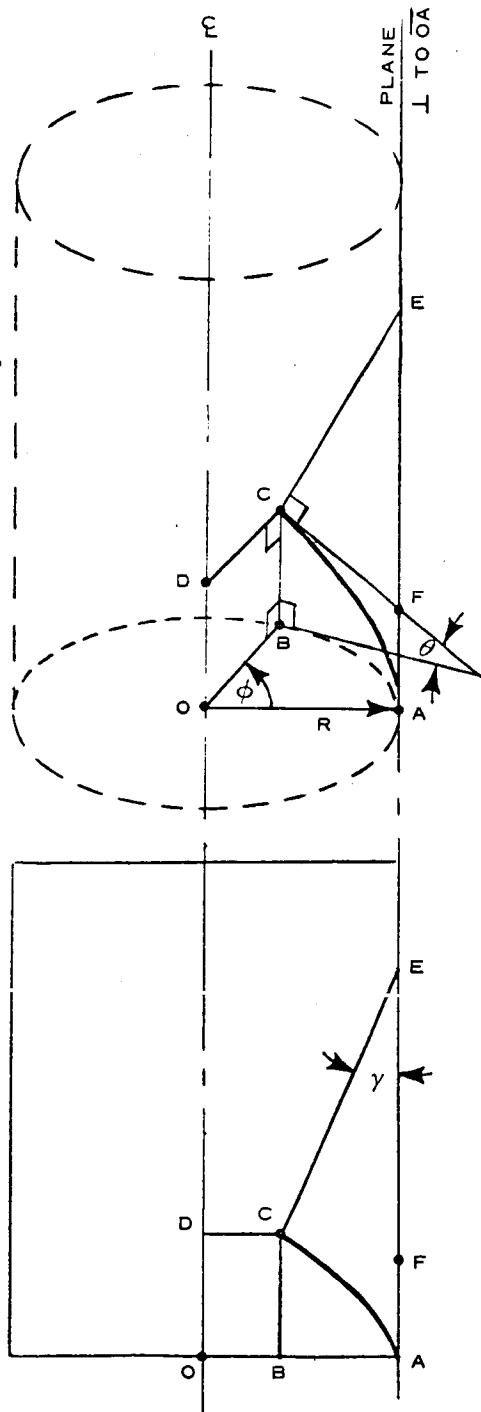


Note: Right-hand rule for moments

The following derivation gives the relationship of the helical-spring geometrical parameters R and θ to α .

Problem:

Determine the unit twist required to keep a longitudinal filament of the round wire of a helix spring in contact with the cylinder enclosed by the helix for any given helix angle and radius.

PROJECTION ON PLANE \overline{AOD} Definitions:

R = radius of helix

θ = helix angle

\overline{EC} is a line in a plane tangent to the helix cylinder and perpendicular to the helix.

A and C are two points on the helix.

Analysis:

The total twist of the helix between points A and C is the angle, $\overline{\alpha}$, defined by the angle \overline{EC} makes with the plane perpendicular to \overline{OA} as ϕ approaches zero.

The following relations are obtained from geometry:

$$\text{True angle } \angle CEF = \theta$$

$$\tan \gamma = \tan \theta \sin \phi$$

$$\text{as } \phi \rightarrow 0 \sin \phi \rightarrow \phi$$

Therefore,

$$\tan \gamma = \phi \tan \theta, \quad (123)$$

and

$$\text{arc } CA = \frac{R\phi}{\cos \theta}. \quad (124)$$

Since γ is the vector component of $\overline{\alpha}$ in the vertical direction, it follows that

$$\tan \overline{\alpha} = \tan \gamma \cos \theta. \quad (125)$$

Substituting Equation 112 into 114 gives

$$\tan \bar{\alpha} = \phi \tan \theta \cos \theta = \phi \sin \theta .$$

For small angles

$$\tan \bar{\alpha} \approx \bar{\alpha} ,$$

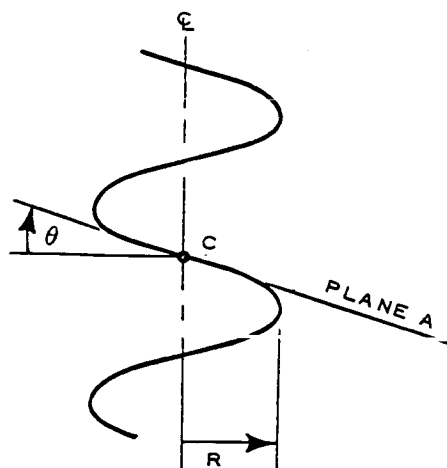
Therefore,

$$\bar{\alpha} = \phi \sin \theta .$$

Since the unit twist is defined as the total twist divided by the length, it follows that

$$\text{unit twist} = \alpha \text{ E } \frac{\bar{\alpha}}{CA} = \frac{\phi \sin \theta}{\frac{R\phi}{\cos \theta}} = \frac{\sin \theta \cos \theta}{R} .$$

The following derivation gives the relationship of R and θ to ρ .

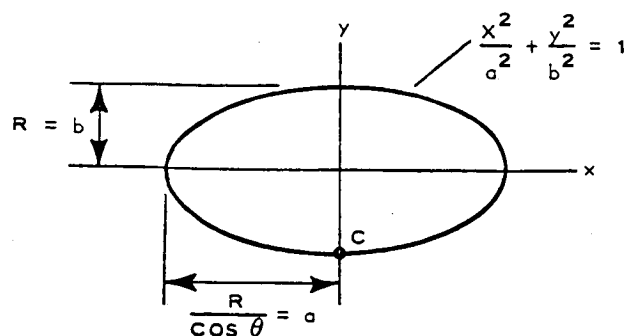


Problem:

Determine the radius of curvature, ρ , in the helix wire at point C on the helix. Point C is where plane A is tangent to the helix

Analysis:

The projection of the cylinder on plane A results in the ellipse shown here. The radius of curvature in general terms is given by



$$\rho = \frac{(1 + y'^2)^{3/2}}{y''} .$$

For the ellipse of the above sketch,

$$y' = -\left(\frac{b}{a}\right)\left(\frac{x}{\sqrt{a^2 - x^2}}\right),$$

and

$$y'' = -\left(\frac{b}{a}\right)\left[\frac{a^2}{(a^2 - x^2)^{3/2}}\right].$$

The radius of curvature is then equal to

$$\rho = \frac{1 + \left(\frac{b}{a}\right)^2 \left(\frac{x^2}{a^2 - x^2}\right)^{3/2}}{-\left(\frac{b}{a}\right) \left[\frac{a^2}{(a^2 - x^2)^{3/2}}\right]}. \quad (127)$$

Evaluating the radius of curvature at point C for $x = 0$ gives

$$\rho = -\frac{a^2}{b} = -\frac{R}{\cos^2 \theta}.$$

(3) Elastic Characteristics of a Helical Spring

Note: Right-hand rule for moments

R = radius of helix

R_0 = radius of helix for unstressed state

L = length of helix

L_0 = length of helix for unstressed state

l = total length of wire in helix

θ = helix angle

θ_0 = helix angle in unstressed state

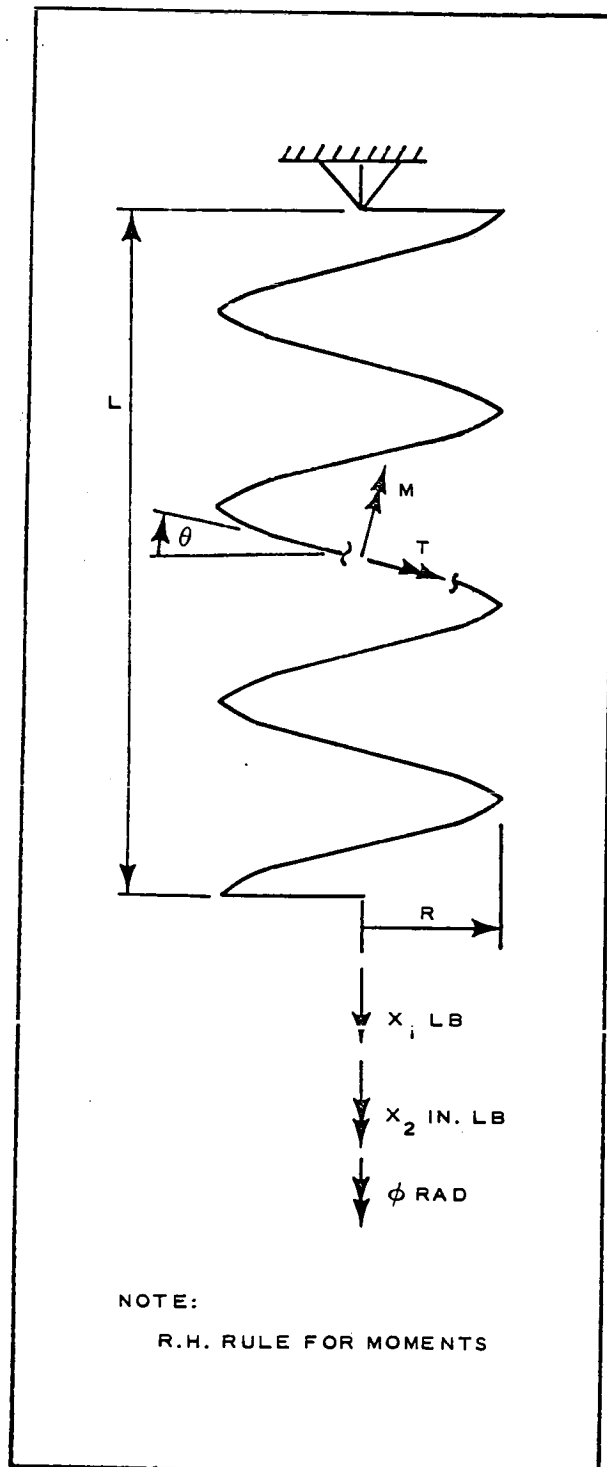


Figure 78 - Elastic Characteristics of Helical Spring

ϕ = helix rotation about of cylinder

ϕ_o = helix rotation, unstressed state

T = internal torque in helix wire

M = internal bending moment in helix wire

X_1 = external load applied along helix

X_2 = external torque applied along helix

I = moment of inertia of wire cross section

J = torsional stiffness factor

E = Young's modulus

G = shear modulus

In the following analysis of the elastic characteristics of helical springs (see Figure 78) the following assumptions are made:

1. The helix is constructed from a wire having a constant symmetrical cross section with a bending stiffness, EI , and a torsional stiffness, JG .
2. Deflections caused by axial and shear energies are negligible.
3. The external loads, X_1 and X_2 , are applied and reacted by infinitely rigid brackets.

From Equations 121, 122, 126, and 127, the relationships between the internal force system in the wire and the geometry of the helix spring can be found by substituting Equations 126 and 127 into Equations 121 and 122. The result is

$$M = EI \left(\frac{\cos^2 \theta}{R} \right) - \frac{1}{\rho_o} \quad (128)$$

and

$$T = JG \left(\frac{\sin \theta \cos \theta}{R} \right) - \alpha_o \quad (129)$$

Application of the external loads X_1 and X_2 will cause the stress state in the spring to go from its initial unstressed state to some other equilibrium stress state. Equations 128 and 129 can then be written

$$M = EI \left(\frac{\cos^2 \theta}{R} - \frac{\cos^2 \theta_o}{R_o} \right), \quad (130)$$

and

$$T = JG \left(\frac{\sin \theta \cos \theta}{R} - \frac{\sin \theta_o \cos \theta_o}{R_o} \right). \quad (131)$$

Statics give the following relationships:

$$X_1 = \frac{T \cos \theta}{R} - \frac{M \sin \theta}{R} \quad (132)$$

and

$$X_2 = T \sin \theta + M \cos \theta. \quad (133)$$

Solving Equations 132 and 133 for T and M gives

$$M = X_2 \cos \theta - X_1 R \sin \theta, \quad (134)$$

and

$$T = X_2 \cos \theta + X_1 R \cos \theta. \quad (135)$$

Substituting Equations 134 and 135 into Equations 130 and 131 and solving for X_1 and X_2 give the following equations:

$$X_1 = \frac{GJ \cos \theta}{R} \left(\frac{\sin \theta \cos \theta}{R} - \frac{\sin \theta_o \cos \theta_o}{R_o} \right) - \frac{EI \sin \theta}{R} \left(\frac{\cos^2 \theta}{R} - \frac{\cos^2 \theta_o}{R_o} \right), \quad (136)$$

and

$$X_2 = GJ \sin \theta \left(\frac{\sin \theta \cos \theta}{R} - \frac{\sin \theta_o \cos \theta_o}{R_o} \right) + EI \cos \theta \left(\frac{\cos^2 \theta}{R} - \frac{\cos^2 \theta_o}{R_o} \right). \quad (137)$$

X_1 and X_2 can also be written in terms of L and ϕ with the aid of the following geometric relationships:

$$\sin \theta = \frac{L}{\ell},$$

$$\cos^2 \theta = 1 - \frac{L^2}{\ell^2},$$

and

$$R = \frac{\ell \cos \theta}{\phi}.$$

Substituting the above relationships into Equations 135 and 136 gives

$$X_1 = \frac{GJ}{\ell^3} (\phi L - \phi_o L_o) \phi - \frac{EI}{\ell^3} \left(\phi L \left[1 - \left(\frac{L}{\ell} \right)^2 \right]^{\frac{1}{2}} \left\{ \phi \left[- \left(\frac{L}{\ell} \right)^2 \right]^{\frac{1}{2}} - \phi_o \left[1 - \left(\frac{L_o}{\ell} \right)^2 \right]^{\frac{1}{2}} \right\} \right) \quad (138)$$

and

$$X_2 = \frac{GJ}{\ell^3} (\phi L - \phi_o L_o) L + \frac{EI}{\ell} \left[1 - \left(\frac{L}{\ell} \right)^2 \right]^{\frac{1}{2}} \left\{ \phi \left[1 - \left(\frac{L}{\ell} \right)^2 \right]^{\frac{1}{2}} - \phi_o \left[1 - \left(\frac{L_o}{\ell} \right)^2 \right]^{\frac{1}{2}} \right\} .$$

(139)

Since both X_1 and X_2 are functions of the same two independent variables, L and ϕ , the total differentials of X_1 and X_2 are

$$dX_1 = \frac{\partial X_1}{\partial L} dL + \frac{\partial X_1}{\partial \phi} d\phi , \quad (140)$$

and

$$dX_2 = \frac{\partial X_2}{\partial L} dL + \frac{\partial X_2}{\partial \phi} d\phi . \quad (141)$$

The stiffness coefficients are defined as

$$K_{11} = \frac{\partial X_1}{\partial L} ,$$

$$K_{12} = \frac{\partial X_1}{\partial \phi} = K_{21} = \frac{\partial X_2}{\partial L} ,$$

and

$$K_{22} = \frac{\partial X_2}{\partial \phi} .$$

Performing the partial differentiation obtains the following equations for the stiffness coefficients:

$$K_{11} = \frac{GJ}{\ell^3} \phi^2 - \frac{EI}{\ell^3} \left(\phi^2 - \phi \phi_o \left[1 - \left(\frac{L_o}{\ell} \right)^2 \right] \left\{ \left[- \left(\frac{L}{\ell} \right)^2 \right]^{-\frac{1}{2}} + \left(\frac{L}{\ell} \right)^2 \left[1 - \left(\frac{L}{\ell} \right)^2 \right]^{-\frac{3}{2}} \right\} \right), \quad (142)$$

$$K_{12} = K_{21} = \frac{GJ}{\ell^3} (2L\phi - L_o\phi_o) - \frac{EI}{\ell^3} \left\{ 2L\phi - L_o\phi_o \left[1 - \left(\frac{L_o}{\ell} \right)^2 \right]^{\frac{1}{2}} \left[1 - \left(\frac{L}{\ell} \right)^2 \right]^{-\frac{1}{2}} \right\}, \quad (143)$$

and

$$K_{22} = \frac{GJ}{\ell} \left(\frac{L}{\ell} \right)^2 + \frac{EI}{\ell} \left[1 - \left(\frac{L}{\ell} \right)^2 \right]. \quad (144)$$

When converted to functions of R and θ , Equations 142, 143, and 144 are given by

$$K_{11} = \frac{GJ}{\ell R^2} \cos^2 \theta - \frac{EI}{\ell R^2} \left(\cos^2 \theta - \frac{R}{R_o} \frac{\cos^2 \theta_o}{\cos^2 \theta} \right), \quad (145)$$

$$K_{12} = K_{21} = \frac{GJ}{\ell} \left(\frac{2 \sin \theta \cos \theta}{R} - \frac{\sin \theta_o \cos \theta_o}{R_o} \right) - \frac{EI}{\ell} \left[\frac{2 \sin \theta \cos \theta}{R} - \frac{\sin \theta \cos \theta_o}{R_o} \left(\frac{\cos \theta_o}{\cos \theta} \right) \right], \quad (146)$$

and

$$K_{22} = \frac{GJ}{\ell} \sin^2 \theta + \frac{EI}{\ell} \cos^2 \theta. \quad (147)$$

- (4) Evaluation of Helical-Spring Stiffness Characteristics for the Unstressed Condition; $L_o = 0$, $\theta_o = 0$

The helical-spring characteristics of the most interest are those at an equilibrium length, L_e . This deflection of the spring results from the gravity-gradient attraction on the damper mass. Therefore, with $\theta_o = 0$, $\sin \theta_o = 0$, and $\cos \theta_o = 1$, Equations 146 and 147 reduce to the following equations, where the subscript "e" denotes the extended equilibrium position:

$$X_1 = GJ \frac{\cos \theta_e}{R_e^2} (\sin \theta_e \cos \theta_e) - EI \frac{\sin \theta_e}{R_e} \left(\frac{\cos^2 \theta_e}{R_e} - \frac{1}{R_o} \right) \quad (148)$$

and

$$X_2 = GJ \frac{\sin \theta_e}{R_e} (\sin \theta_e \cos \theta_e) + EI \cos \theta_e \left(\frac{\cos^2 \theta_e}{R_e} - \frac{1}{R_o} \right) \quad (149)$$

$X_2 = 0$ for the gravity-gradient equilibrium condition. Solving Equation 149 with $X_2 = 0$ gives

$$\frac{R_o}{R_e} = \frac{EI}{GJ \sin^2 \theta_e + EI \cos^2 \theta_e} \quad (150)$$

Substituting Equation 150 into Equations 145, 146, and 147 with $\sin \theta_o = 0$ and $\cos \theta_o = 1$ gives the following equations for the spring stiffness coefficients at the gravity-gradient equilibrium length:

$$\begin{aligned}
 K_{11} &= \left(\frac{\partial X_1}{\partial L} \right)_e \\
 &= \frac{GJ(\cos^2 \theta_e + \tan^2 \theta_e) + EI \sin^2 \theta_e}{\ell R_o^2 \left(\frac{GJ}{EI} \sin^2 \theta_e + \cos^2 \theta_e \right)^2} \\
 &= f_1 \frac{GJ}{\ell R_o^2} , \tag{151}
 \end{aligned}$$

$$\begin{aligned}
 K_{12} &= K_{21} = \left(\frac{\partial X_1}{\partial \phi} \right)_e = \left(\frac{\partial X_2}{\partial L} \right)_e \\
 &= \frac{GJ - EI}{R_o \ell} \left(\frac{2 \sin \theta_e \cos \theta_e}{\frac{GJ}{EI} \sin^2 \theta_e + \cos^2 \theta_e} \right) + \frac{EI}{R_o \ell} \tan \theta_e \\
 &= f_{12} \frac{GJ}{\ell R_o} , \tag{152}
 \end{aligned}$$

$$\begin{aligned}
 K_{22} &= \left(\frac{\partial X_2}{\partial \phi} \right)_e \\
 &= \frac{GJ}{\ell} \sin^2 \theta_e + \frac{EI}{\ell} \cos^2 \theta_e \\
 &= f_2 \frac{GJ}{\ell} . \tag{153}
 \end{aligned}$$

A plot of the spring stiffness coefficients is shown in Figure 79.

- (5) Helical-Spring Parameters for Unstressed Helix Angle $\theta_o = 0$ Deg

Equations 138 and 139 can be factored into the form shown below, if $\beta = GJ/EI = 0.77$ for round steel wire.

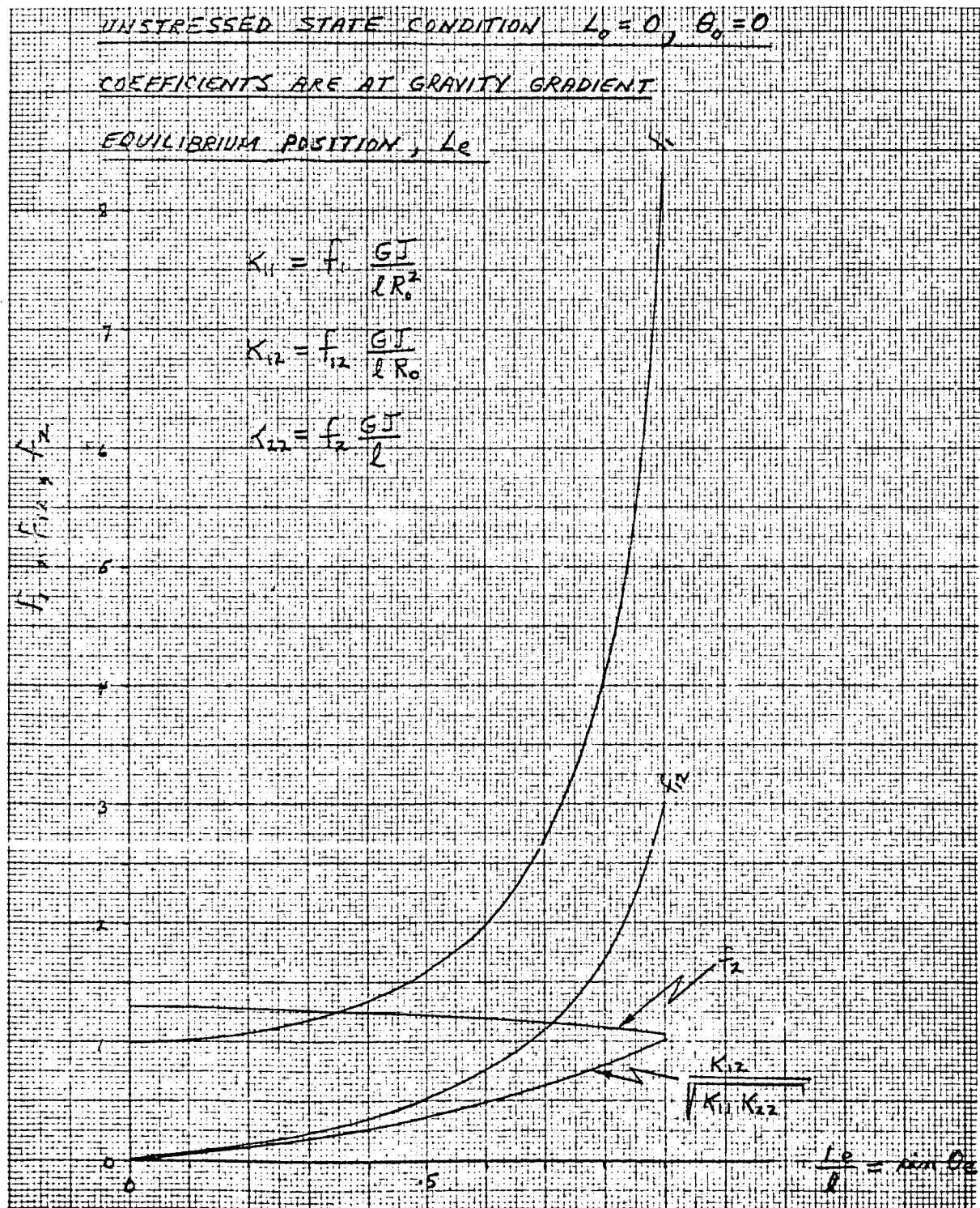


Figure 79 - Helical-Spring Stiffness Coefficients

$$X_1 = GJ \left(\frac{\phi_o}{\ell} \right)^2 \left(\frac{\phi}{\phi_o} \right)^2 \frac{L}{\ell} \left(1 - \frac{1}{\beta} \left\{ 1 - \frac{\phi_o}{\phi} \left[1 - \left(\frac{L}{\ell} \right)^2 \right]^{-\frac{1}{2}} \right\} \right) \quad (154)$$

and

$$X_2 = GJ \left(\frac{\phi_o}{\ell} \right)^2 \left[\frac{\phi}{\phi_o} \left(\frac{L}{\ell} \right)^2 \left(1 - \frac{1}{\beta} \left\{ 1 - \frac{\phi_o}{\phi} \left[1 - \left(\frac{L}{\ell} \right)^2 \right]^{-\frac{1}{2}} \right\} \right) + \frac{\phi}{\phi_o \beta} \left\{ 1 - \frac{\phi_o}{\phi} \left[1 - \left(\frac{L}{\ell} \right)^2 \right]^{-\frac{1}{2}} \right\} \right] \quad (155)$$

Equations 154 and 155 can also be written as

$$X_1 = GJ \left(\frac{\phi_o}{\ell} \right)^2 a_1 \quad (156)$$

and

$$X_2 = GJ \left(\frac{\phi_o}{\ell} \right)^2 a_2 \quad (157)$$

a_1 and a_2 are defined by Equations 154 and 155. The graphical presentation of X_1 , X_2 , a_1 , and a_2 is shown in Figure 80.

- (6) Stress Parameter Relationships for Helical Springs Made from Round Wire with Unstressed Helix Angle $\theta_o = 0$

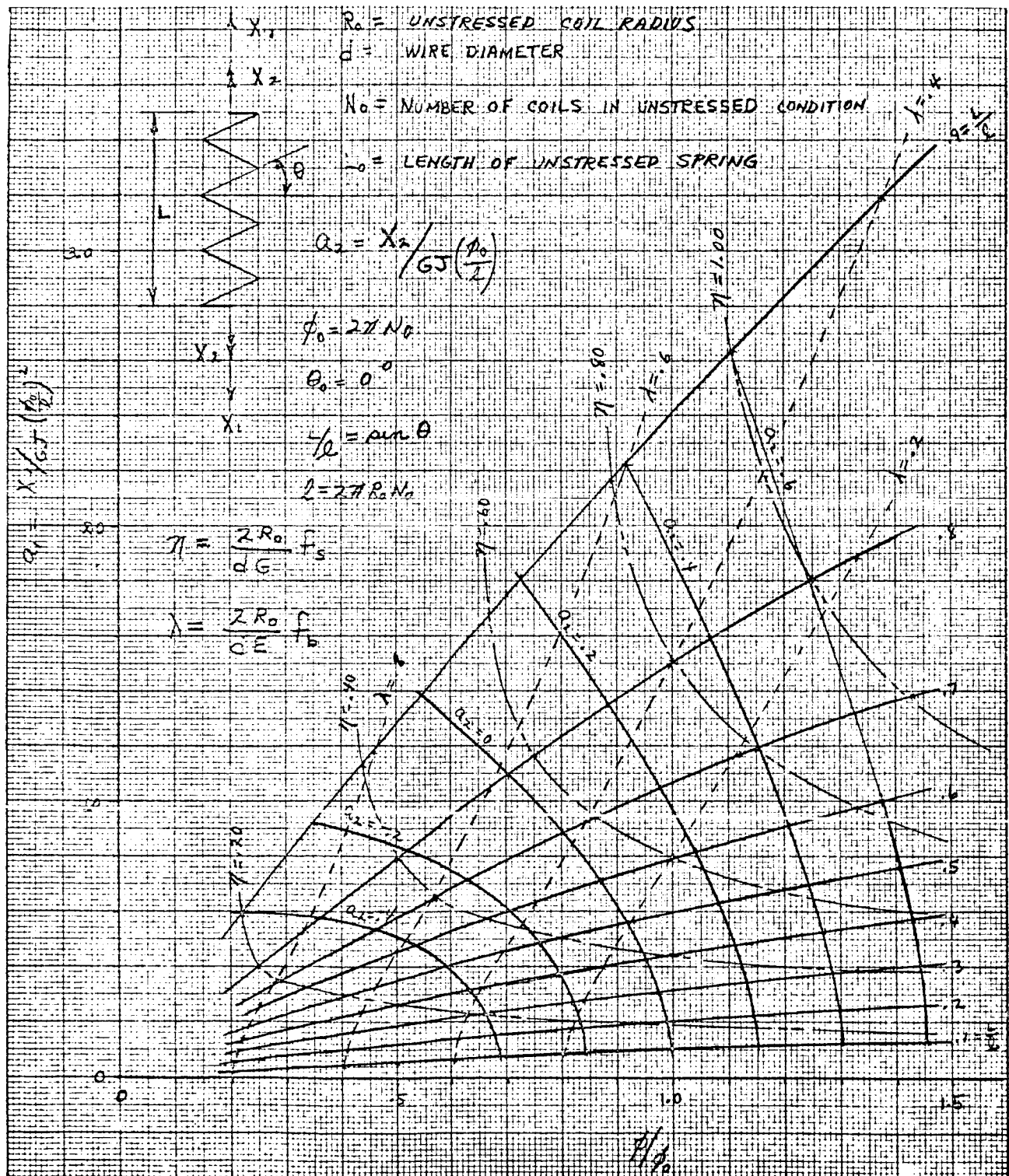
The torsional shear stress, f_s , in the wire is given as

$$f_s = \frac{Td}{4I} \quad (158)$$

The bending stress, f_b , in the wire is given as

$$f_b = \frac{Md}{2I} \quad (159)$$

Equations 130 and 131 yield equations for T and M as follows:

Figure 80 - Helical-Spring Parameters for Unstressed Helical Angle $\theta_0 = 0^\circ$

SECTION III

Subsection Three - Stabilization and Orientation Systems

GER-11502

$$M = EI \left(\frac{\cos^2 \theta}{R} - \frac{1}{R_o} \right), \quad (160)$$

and

$$T = 2IG \frac{\sin \theta \cos \theta}{R}. \quad (161)$$

Substituting Equations 160 and 161 into Equations 158 and 159 yields

$$f_s = \frac{dG}{2R} \sin \theta \cos \theta, \quad (162)$$

and

$$f_b = \frac{dE}{2} \left(\frac{\cos^2 \theta}{R} - \frac{1}{R_o} \right). \quad (163)$$

Equations 162 and 163 in terms of ϕ and L are as follows:

$$f_s = \frac{dGL\phi}{2\lambda^2} \quad (164)$$

and

$$f_b = -\frac{dE}{2\lambda} \left\{ \phi \left[1 - \left(\frac{L}{\lambda} \right)^2 \right]^{\frac{1}{2}} - \phi_o \right\}. \quad (165)$$

When written in nondimensional form, Equations 164 and 165 are

$$\frac{2R_o f_s}{dG} = \left(\frac{L}{\lambda} \right) \left(\frac{\phi}{\phi_o} \right) = \eta, \quad (166)$$

and

$$\frac{2R_o f_b}{dE} = 1 - \frac{\phi}{\phi_o} \left[1 - \left(\frac{L}{\lambda} \right)^2 \right]^{\frac{1}{2}} = \lambda. \quad (167)$$

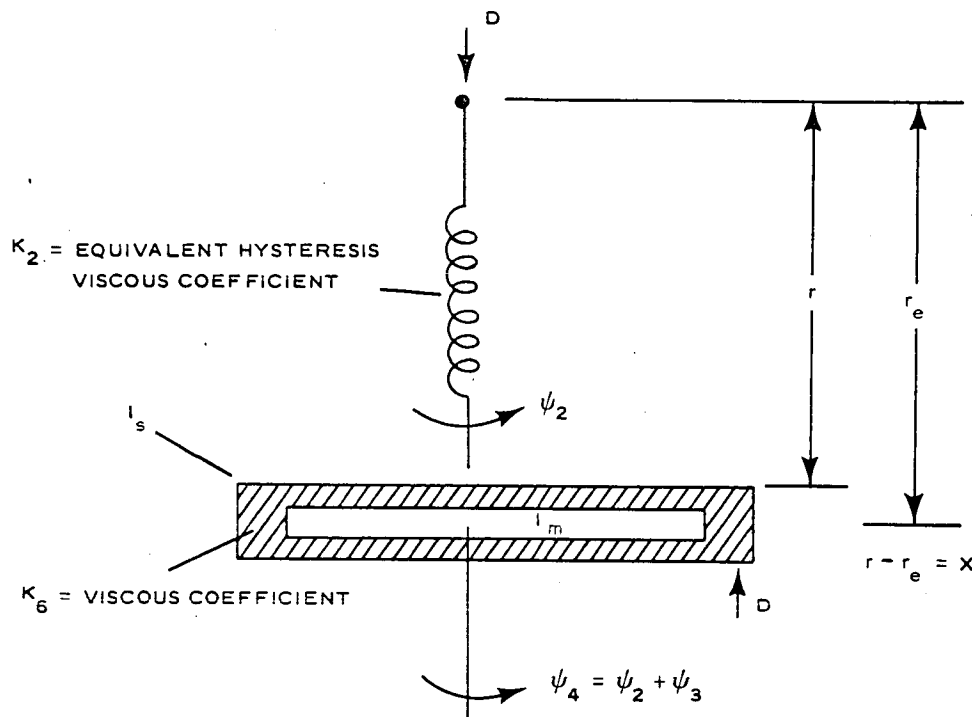
The stress parameters given in Equations 166 and 167 are shown graphically in Figure 80.

d. Optimum Tuning and Energy Dissipation of Rice-Wilberforce Damper

Optimization criteria that determine best values for the damper parameters were developed under assumed limits of total damper weight, maximum outside dimensions, and other constraints imposed by payload capability. Optimization is achieved by setting the natural frequencies of the two modes of damper articulation to lie at certain discrete frequencies that will be excited by satellite librations. The spring constants, masses, and inertias of the damper are selected to give the discrete frequencies at which maximum rates of energy dissipation will occur. The rate of energy dissipation in each of the two modes is adjusted for a compromise between high maximum rates of dissipation over a narrow band of frequencies and low maximum rates over a broad band of frequencies. The lossy elements of the damper, including the mechanical hysteresis of the plunging mode of the spring and the viscosity of the fluid in the torsional mode, are the parameters selected to give this compromise.

The analysis indicates how the usual low rate limitation of viscous dampers in gravity-gradient systems is overcome by the high articulation gain of the Rice Wilberforce damper, which transforms the low angular rates of satellite libration into relatively high rates of motion of the damping elements.

A schematic diagram and definition of symbols used for analysis of the Rice-Wilberforce damper are shown in Figure 81. For an analysis of optimum tuning and energy dissipation, it is convenient to work with rates of displacement as the basic variables, since the dissipative elements of the damper are treated as rate sensitive. The damper, when in orbital deployment (but neglecting spring libration angles), is described mathematically by the following differential equations of motion:



D = DRIVING FORCE APPLIED TO DAMPER BY SATELLITE

K_2 = EQUIVALENT HYSTERESIS VISCOUS COEFFICIENT IN PLUNGING

m = TOTAL MASS OF DAMPER

M = MASS OF SATELLITE TO WHICH DAMPER IS ATTACHED

I_m = INERTIA OF INNER MASS

I_s = INERTIA OF SHELL

K_1 = PLUNGING SPRING COEFFICIENT

K_3 = TORSIONAL SPRING COEFFICIENT

K_4 = CROSS COUPLING SPRING COEFFICIENT

K_6 = VISCOUS TORQUE COEFFICIENT

ψ_2 = ROTATION OF TIP MASS

ψ_3 = SLIPPAGE ANGLE IN VISCOUS DAMPER

ψ_4 = ROTATION OF INNER MASS = $\psi_2 + \psi_3$

$$\bar{m} = \frac{mM}{M+m}$$

Figure 81 - Schematic Diagram and Definition of Symbols for Damper Analysis

$$\left[\overline{m}p + K_2 + \frac{1}{p}(K_1 - 3\overline{m}\omega_o^2) \right] \dot{x} + \frac{K_4}{p} \dot{\psi}_2 + 0\dot{\psi}_4 = D, \quad (168)$$

$$\frac{K_4}{p} \dot{x} + \left(I_s p + K_6 + \frac{K_3}{p} \right) \dot{\psi}_2 - K_6 \dot{\psi}_4 = 0, \quad (169)$$

and

$$0\dot{x} - K_6 \dot{\psi}_2 + (I_m p + K_6) \dot{\psi}_4 = 0. \quad (170)$$

Note that the derivative of a variable is symbolized by either the Heaviside operator, p , preceding the variable or by a dot above the variable. In addition to other constraints, all which are developed later, spring parameters in the equations are constrained as follows:

$$K_1 > \frac{3Mm\omega_o^2}{M+m} = 3\overline{m}\omega_o^2; \quad (171)$$

that is, the negative spring constant contributed by gravity-gradient and centrifugal force must not be permitted to overpower the real positive spring constant, K_1 , of the plunging mode of the spring. Also,

$$K_4 \leq 0.34 \sqrt{K_1 K_3}; \quad (172)$$

that is, the physical characteristics of the spring such as modulus of elasticity, helix angle, and other factors, constrain the maximum cross-coupling that may be obtained. A mechanical impedance diagram for the equations of motion is shown in Figure 82. Figure 83 is an alternate representation that has been obtained by the application of Thevinin's network theorem to the mechanical impedance diagram of Figure 82 at points a and b. Thevinin's network theorem permits the replacement of any portion of a network, no matter how complicated that portion may be, by a single source of driving force

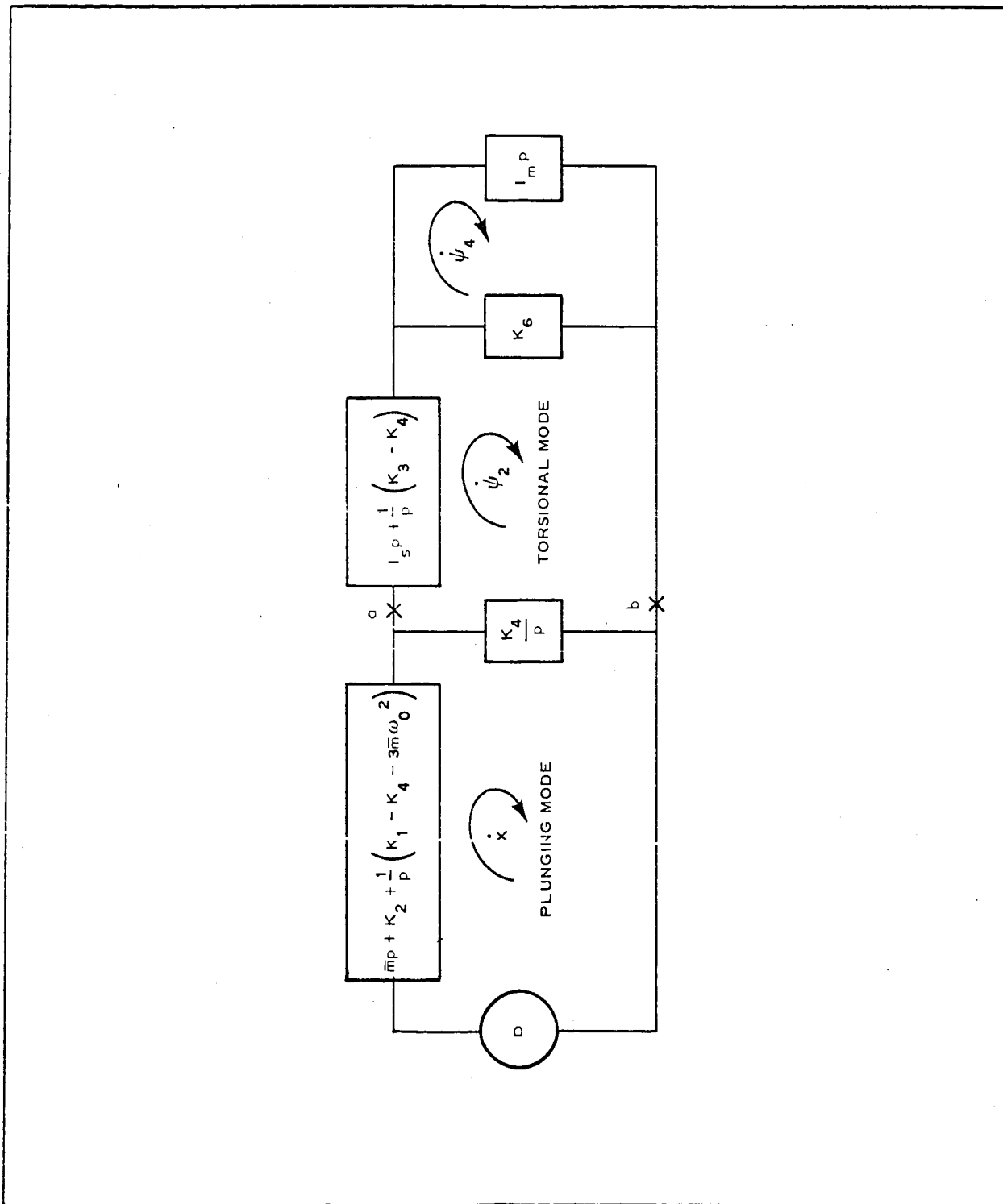


Figure 82 - Mechanical Impedance Diagram of Rice-Wilberforce Damper

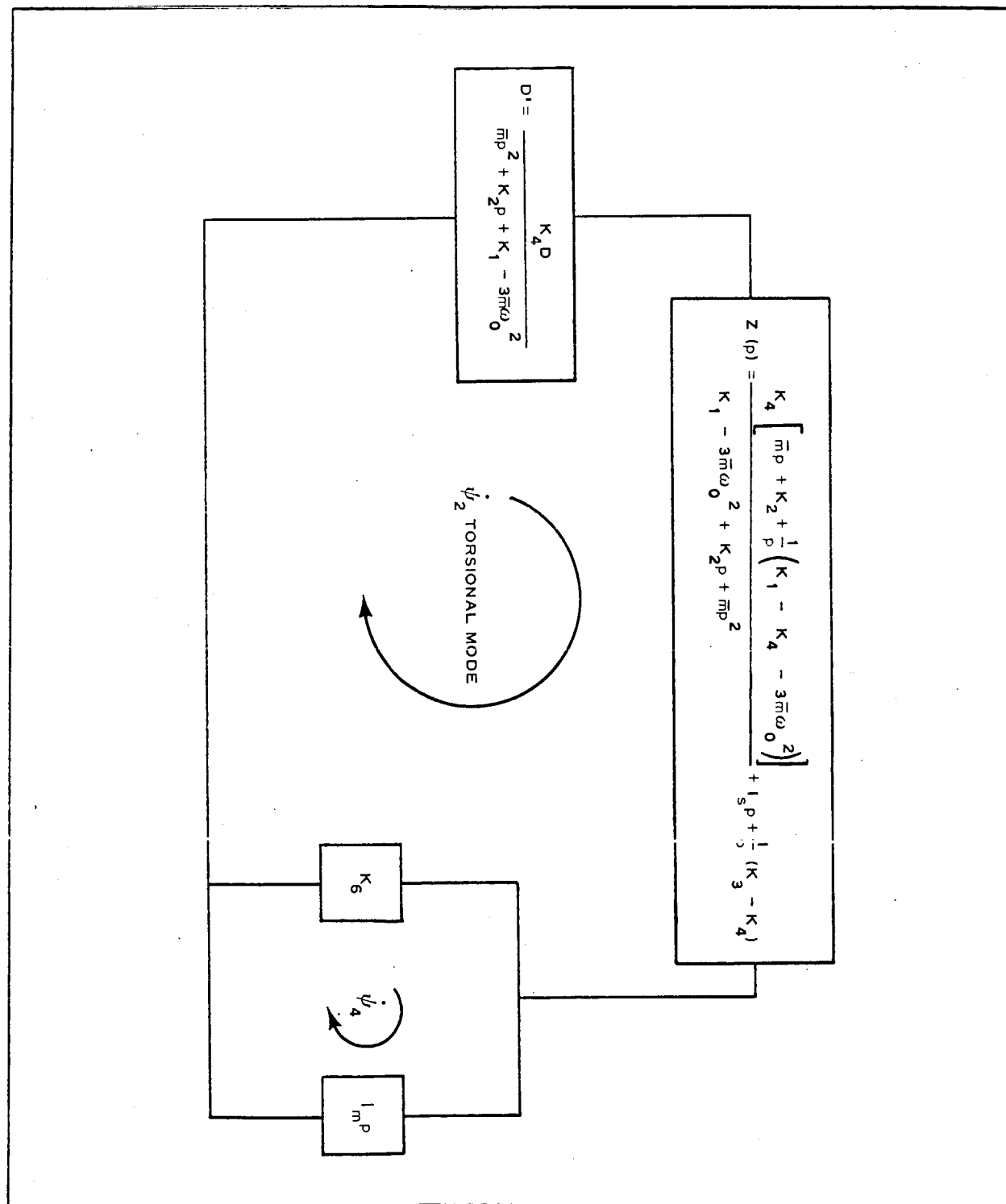


Figure 83 - Alternate Mechanical Impedance Diagram

and a series source impedance. The driving force is that seen when looking into the portion to be simplified, when it has been separated from the rest of the network. The source impedance is that seen when looking into the same portion when all the driving forces are replaced by short circuits.

Figure 84 is a final version of the mechanical impedance diagram obtained under the assumption

$$I_m \gg \frac{K_6}{p} . \quad (173)$$

Certain observations can be made by inspection of the various impedance diagrams. Figure 83 shows that the spring coupling coefficient, K_4 , between the plunging and torsional modes of the spring should be maximum if maximum excitation of the torsional mode is to be achieved. Remember that D represents the driving force or disturbing force applied to the damper by librations of the satellite. D' is the portion of the driving force that couples directly into ψ_2 . This coupled force is obviously maximum when K_4 is maximum, as shown by the expression for D' :

$$D' = \frac{K_4 D}{K_1 + \bar{m}p^2 - 3\bar{m}\omega_o^2 + K_2 p} . \quad (174)$$

The intuitive insight that K_4 should be as large as practical is thus confirmed analytically, giving

$$K_{4 \text{ opt}} = 0.34 \sqrt{K_1 K_3} . \quad (175)$$

The development of the optimum tuning requirement by application of impedance matching principles to the circuit of Figure 84 will now be continued. As previously stated, optimum tuning can be viewed as an impedance matching problem in which the source impedance is

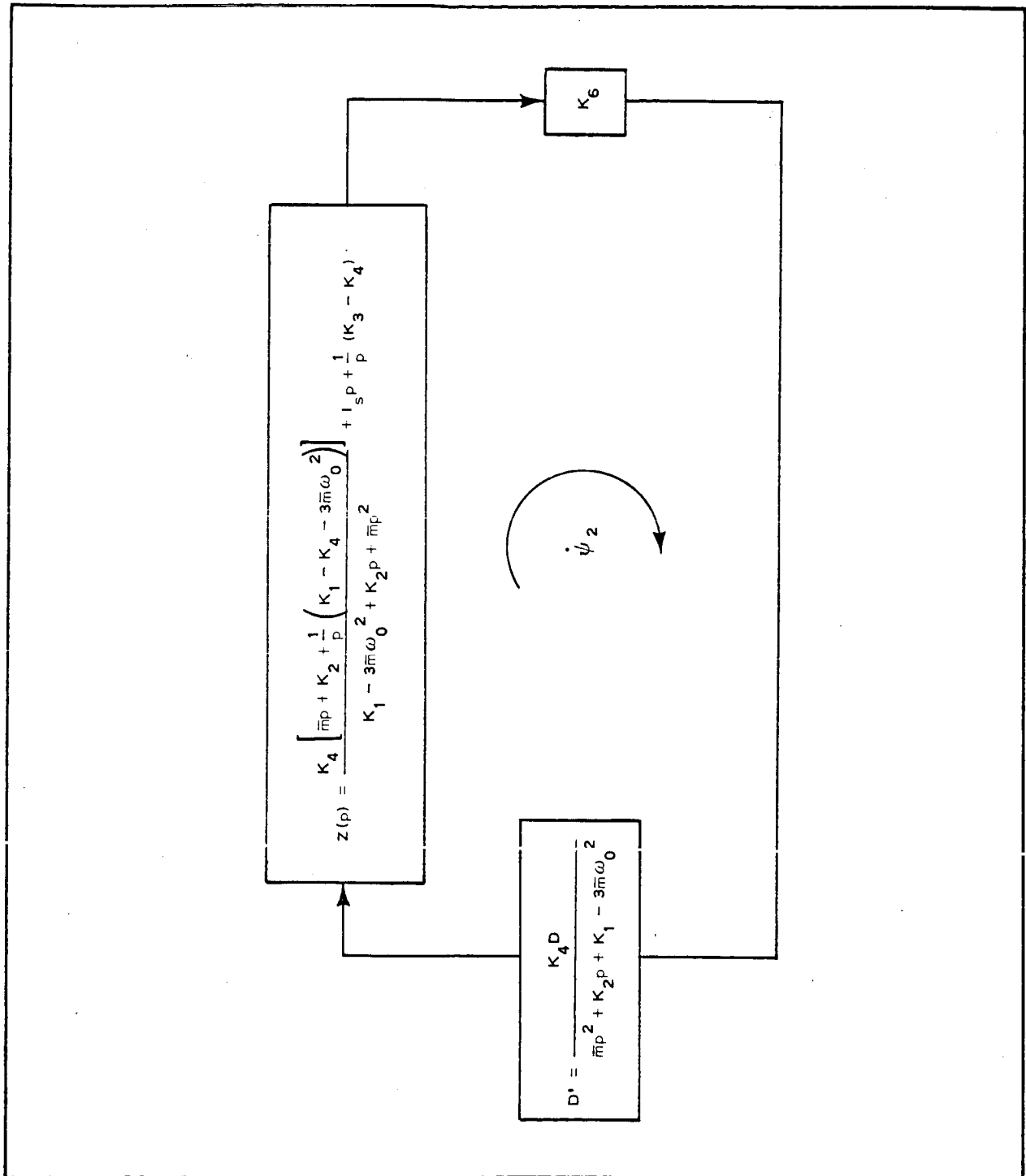


Figure 84 - Final Equivalent Mechanical Impedance Diagram for Torsional Mode

set equal to the conjugate at the load impedance. Note, however, that the load impedance K_6 is a pure real numeric and the source impedance is essentially a pure imaginary if the rather light dissipative term for the equivalent viscous effect of hysteresis is ignored. Therefore, the tuning criterion is obtained simply by equating the source impedance to zero and solving for the resulting values of spring constants and inertias. Thus, the tuning criterion is:

$$\frac{K_4 \left[\bar{m}p + K_2 + \frac{1}{p} (K_1 - K_4 - 3\bar{m}\omega_o^2) \right]}{mp^2 + K_2 + K_1 - 3m\omega_o^2} + I_s p + \frac{K_3 - K_4}{p} = 0. \quad (176)$$

After considerable manipulation, and neglecting K_2 , Equation 176 becomes

$$(K_3 + I_s p^2) (K_1 + \bar{m}p^2 - 3\bar{m}\omega_o^2) - K_4^2 = 0, \quad (177)$$

which is a somewhat more convenient statement of the optimum tuning equation of the damper.

Equation 177 is of fourth order in the variable p with odd-order powers of p missing. Thus there are two pairs of complex conjugate roots giving rise to two natural frequencies in the response of the damper. These natural frequencies are, of course, related to the isolated plunging and torsional modes of the damper, depending on the magnitude of the cross-coupling coefficient K_4 . If the cross-coupling term K_4 is set equal to zero, the two isolated or uncoupled natural frequencies of the damper can be seen:

$$\omega_{n_{\text{torsion}}} = \sqrt{\frac{K_3}{I_s}}, \quad (178)$$

and

$$\omega_{n_{\text{plunging}}} = \sqrt{\frac{K_1 - 3\bar{m}\omega_o^2}{\bar{m}}} \quad (179)$$

It is convenient to analyze the coupled natural frequencies that are the solution to Equation 177 in terms of the uncoupled natural frequencies. This has been done analytically, and the results are shown in Figures 85 and 86. Figure 85 is for the case of a spring helix angle of 30 deg, where the cross-coupling is given by

$$K_4 = 0.34 \sqrt{K_1 K_3} \quad ,$$

and Figure 86 is for the case of a helix angle of 17.5 deg, where the cross-coupling is given by

$$K_4 = 0.20 \sqrt{K_1 K_3} \quad .$$

It may be shown that when large values of fluid damping coefficient K_6 are employed, and for which the assumption of Equation 173 does not hold, the optimum tuning Equation 177 must be modified to include the reflected inertia of the inner member of the damper. The modification takes the form of substituting a new value, I_s' , for I_s into these equations. The new value is

$$I_s' = I_s + \frac{K_6^2 I_m}{K_6^2 - p_{I_m}^2} \quad (180)$$

Use of the optimum-tuning Equation 177 requires specifying the discrete frequencies at which the Rice-Wilberforce damper is to accept the librational energy of the satellite and dissipate that energy in the damping fluid and the hysteresis loss coating of the helical spring. Specifying the frequencies requires examination of the librational frequencies of the satellite and the manner in which the librational motion excites the Rice-Wilberforce spring. Basically, the spring is attached to the satellite by means of a long gravity

gradient boom, so there will be tension forces in the spring due to centrifugal and gravity-gradient forces that excite the plunging and torsional modes of the damper. First, consider the centrifugal forces in the spring due to the orbital-plane or pitch-axis motion of the satellite. In the presence of pitch-axis librations, the total angular rate of concern is orbital rate ω_o plus pitch libration rate $\dot{\phi}$. The resultant centrifugal force producing tension in the plunging mode of the spring is proportional to

$$(\omega_o + \dot{\phi})^2 = \omega_o^2 + 2\omega_o\dot{\phi} + \dot{\phi}^2. \quad (181)$$

Consideration of Equation 181 shows that tension forces in the spring due to centrifugal effects of pitch-axis motion are periodic at both the fundamental and second harmonic of the satellite natural frequency in pitch plus a zero frequency or steady component. Centrifugal forces due to roll-axis or traverse-plane librations can be shown to contain a zero-frequency term plus a second harmonic of the roll-axis natural frequency. However, there is no component of tension in the spring due to roll librations that are periodic at the satellite-roll natural frequency. Thus there is a significant difference in the frequency composition of tension forces in the spring between these due to centrifugal forces of pitch librations and those due to centrifugal forces of roll-axis librations; i. e., the pitch librations cause both fundamental and second harmonic terms that excite the spring, whereas the roll librations generate only second harmonic terms in the spring tension.

The discussion of the frequency composition of forces that excite the Rice-Wilberforce spring has emphasized so far those forces originating by centrifugal action. However, equally important are the forces in the spring which arise from differential gravity. It can be shown that the spring tension forces due to gravity gradient are periodic at twice the satellite natural libration frequencies. Recall that tension in a rod connecting the two masses of a dumbbell satellite is

SECTION III

Subsection Three - Stabilization and Orientation Systems

GER-11502

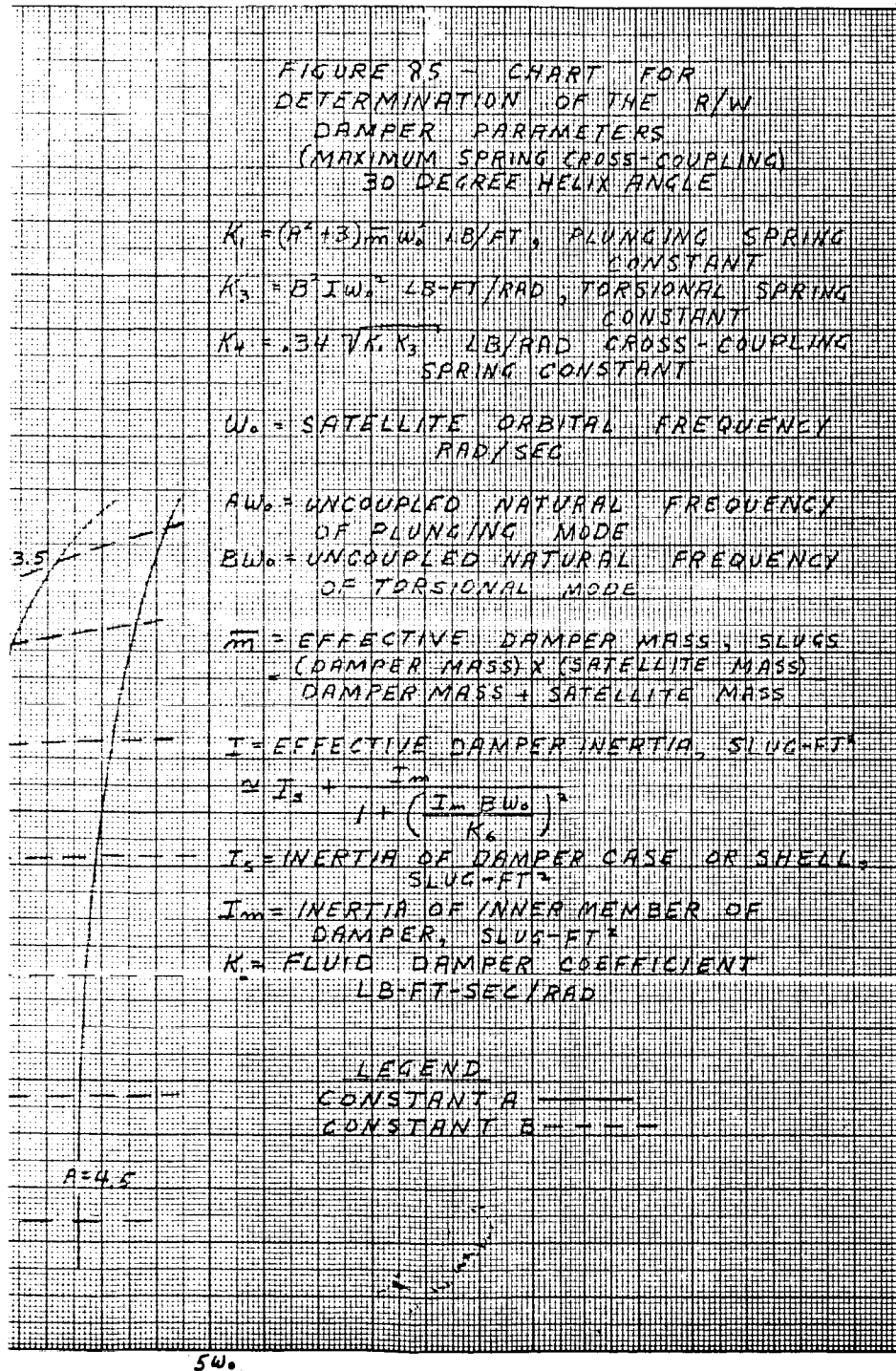
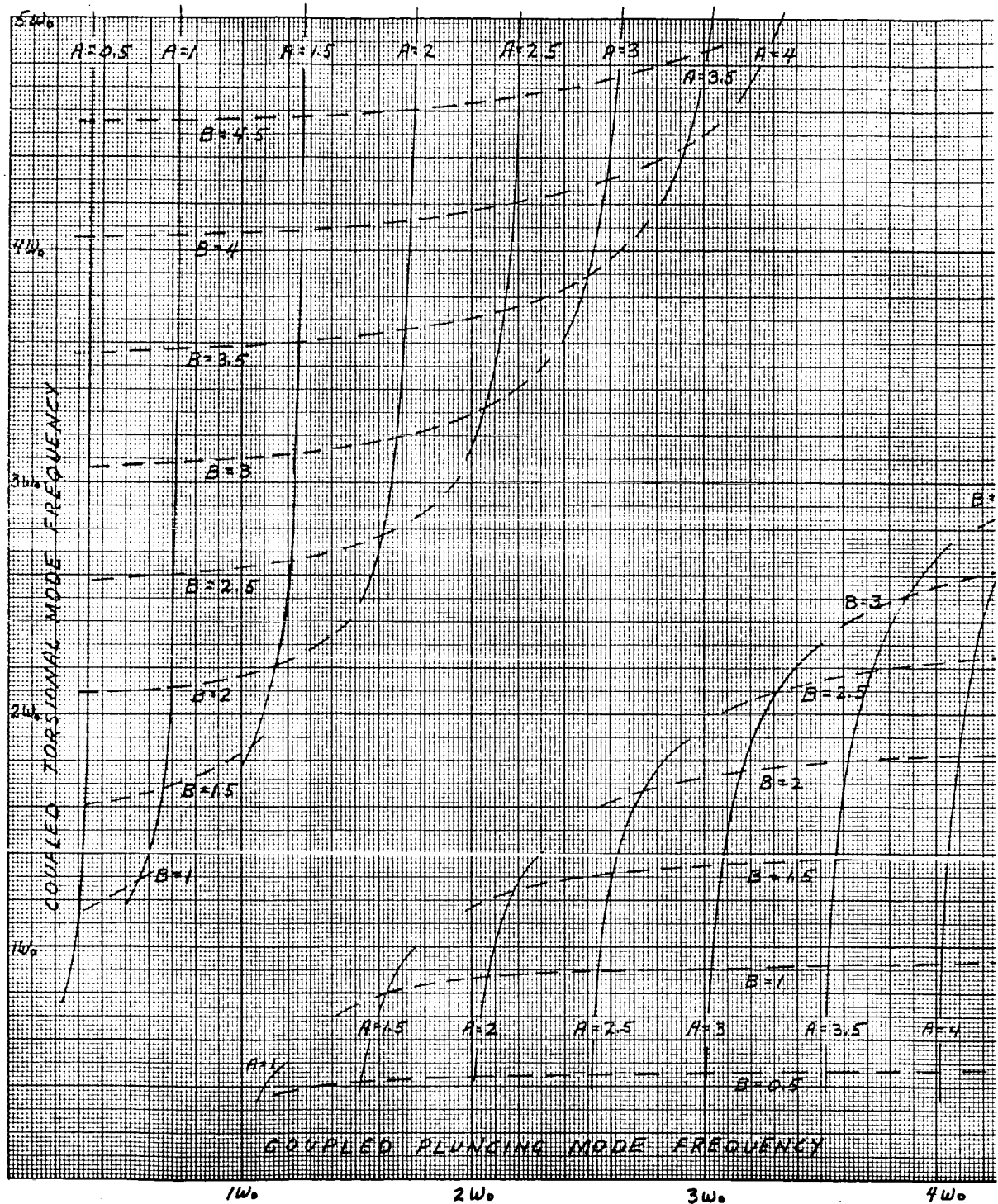


Figure 85 - Determination of Rice-Wilberforce Damper Parameters - Helix Angle = 30 Deg



SECTION III

Subsection Three - Stabilization and Orientation Systems

GER-11502

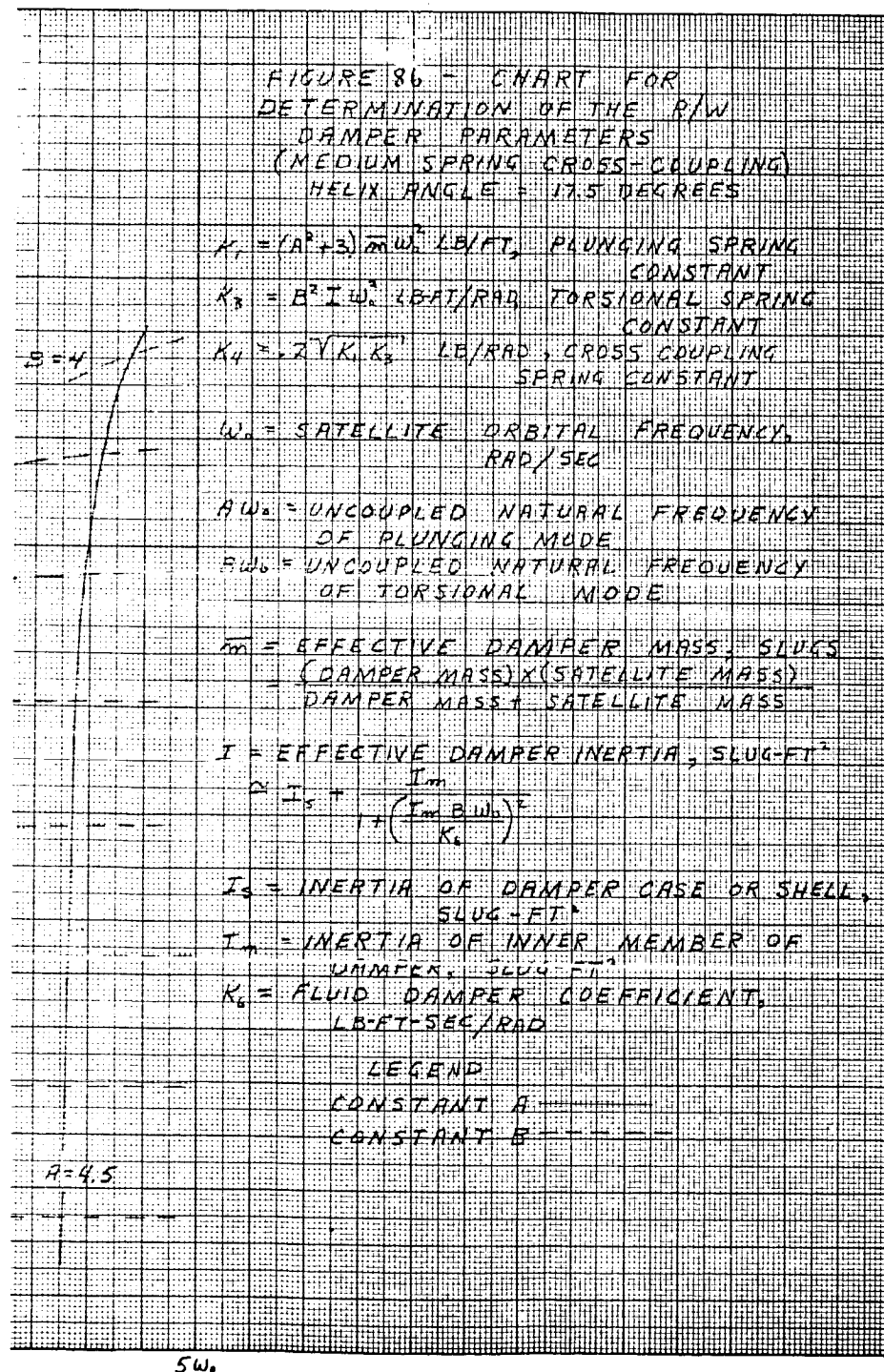
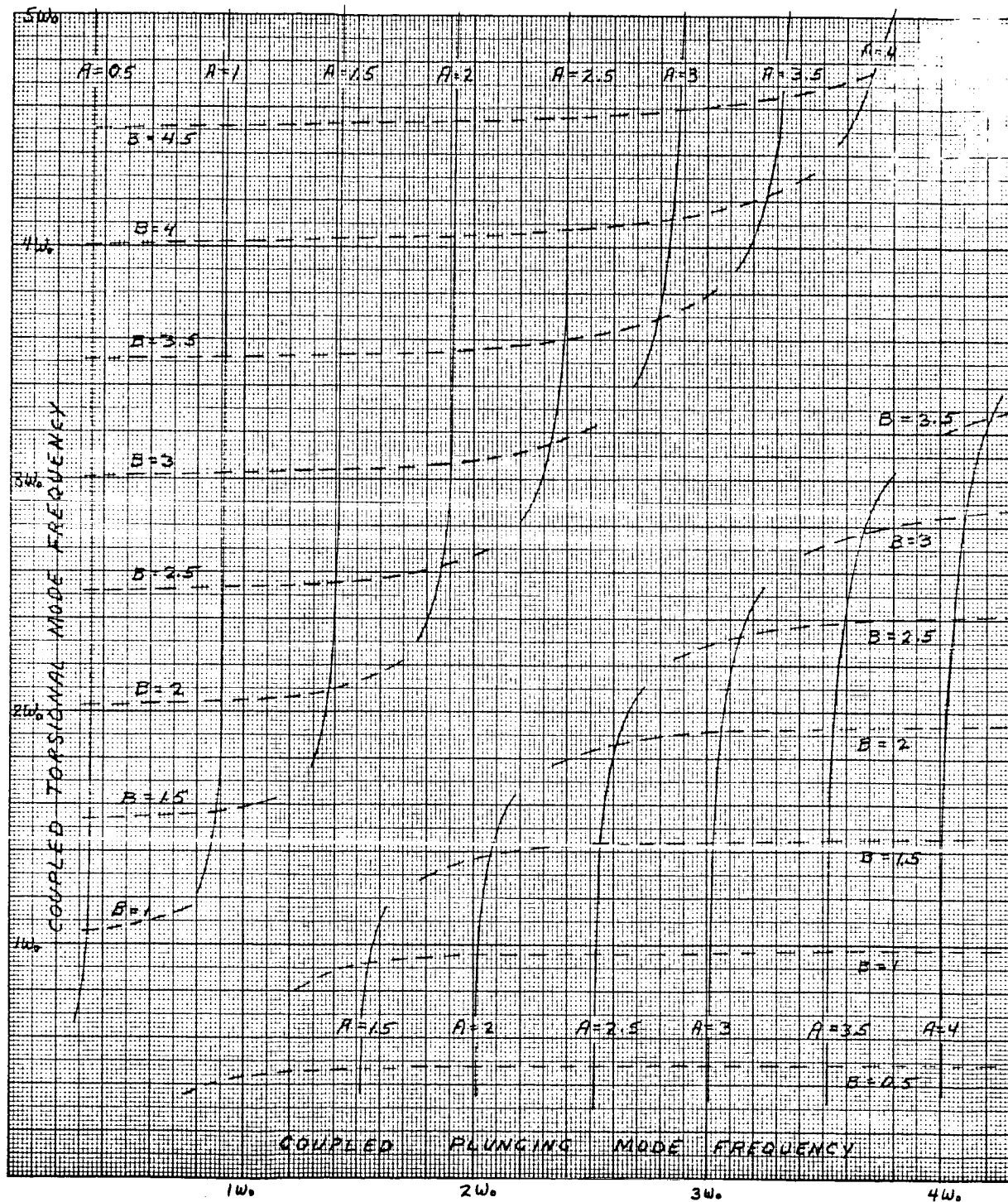


Figure 86 - Determination of Rice-Wilberforce Damper Parameters -
Helix Angle = 17.5 Deg



periodic at twice the libration frequency of the dumbbell. Thus there is excitation of the Rice-Wilberforce spring at the second harmonic of the satellite libration frequencies because of both centrifugal and differential gravity forces acting along the plunging axis of the spring.

In summary, pitch-axis librations excite the spring tension at both the fundamental and second harmonic of the pitch axis, whereas, in the case of roll, tension forces in the spring are periodic at only the second harmonic of the roll-libration natural frequency. The damper, of course, can dissipate no energy associated with any steady or zero-frequency forces.

Therefore, the damper tuning frequencies chosen must be constrained somewhat as follows. For damping of the roll-axis librations, either the plunging or torsional mode can be tuned to the second harmonic of the roll-axis natural frequency. There is somewhat more freedom in suppressing pitch-axis librations, with the choice of tuning either the plunging or torsion mode to either the fundamental or second harmonic of the pitch natural frequency. If certain practical aspects are considered, such a minimizing spring length and maximum spring stiffness, then the plunging mode should be tuned to the second harmonic of the satellite roll-axis frequency and the wind-up mode of the damper should be tuned to the pitch-axis natural frequency of satellite libration. Alternative choices can also be made.

Another practical consideration could be that of reversing the gyroscopic precession torques of the damper as frequently as possible. This consideration leads to tuning the plunging mode to the second harmonic of the pitch-axis librations and the torsional mode to the second harmonic of the roll-axis librations. The latter tuning is not possible for large cross-coupling coefficients of the Rice-Wilberforce spring, where the helix angle is in the region of 25 deg or more. However, if a low helix angle in the region of 15 to 20 deg is used in the spring, such tuning is possible. Figures 85 and 86 give insight

into this constraint on the physically realizable tuning frequencies. In general, if spring cross-coupling is increased by employment of a larger helix angle of the spring, then the two mode frequencies are constrained to be farther apart.

The influence of the fluid viscosity and the hysteresis loss of the cadmium-coated spring is as follows. It can be shown that the energy dissipation rate or power loss in the damper fluid is

$$W_F = K_6 (\dot{\psi}_2 - \dot{\psi}_4)^2, \quad (182)$$

where

K_6 = fluid drag torque coefficient, and

$(\dot{\psi}_2 - \dot{\psi}_4)$ = slip rate in the damper.

Similarly, the energy dissipation rate in the hysteresis of the cadmium coating of the spring is

$$W_H = K_2 \dot{X}^2, \quad (183)$$

where

K_2 = the equivalent viscous coefficient of the cadmium coating, and

\dot{X} = rate of spring deflection in plunging.

The expression for K_2 used for analysis is

$$K_2 = \frac{bK_1}{2\omega\pi}, \quad (184)$$

where

b = fractional energy loss per cycle of plunging of the spring,

K_1 = plunging spring constant, and

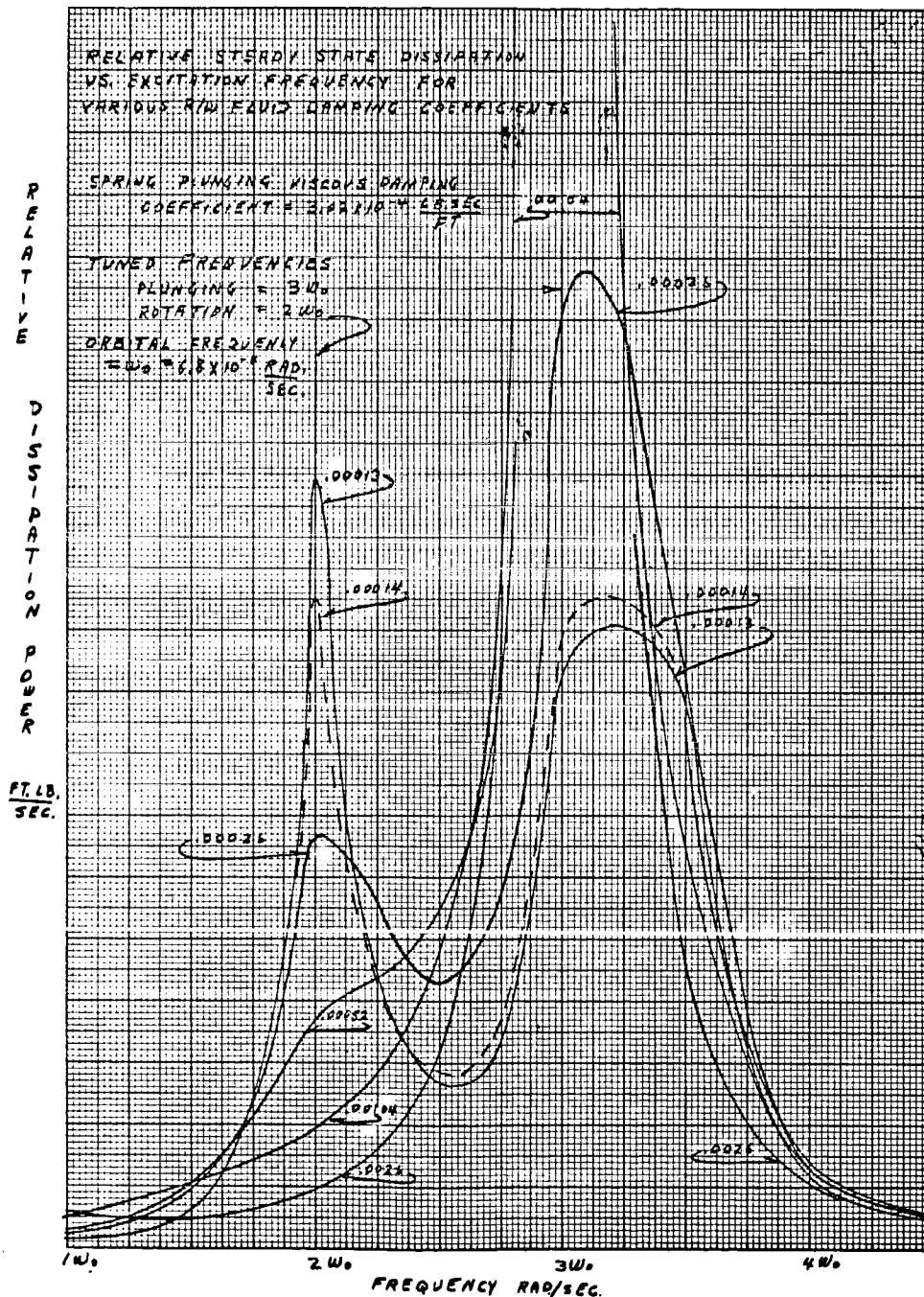
ω = plunging frequency.

Note that Equation 184 is valid at one frequency only, but, where the plunging mode is excited dominantly at a single discrete frequency, this expression holds relatively well.

Equations 182 and 183 are very complicated if the very complex expressions required to solve for $(\dot{\psi}_2 - \dot{\psi}_4)$ and \dot{X} are considered. No direct analytical calculation of power loss of the damper was therefore made. However, analog computer runs, including the damper dynamics for determining $(\dot{\psi}_2 - \dot{\psi}_4)$ and \dot{X} , were made, and power dissipation was studied as a function of frequency for a fixed value of K_2 and various values of K_6 . These curves are presented in Figure 87. Note that K_2 and K_6 determine the band width of dissipation capability but also higher maximum peak values of steady-state dissipation. Conversely, larger values of K_6 increase band width of dissipation capability at the expense of reducing the maximum rate of dissipation.

Thus the parameters K_2 and K_6 are very important and must be properly related to the tuning tolerances. Too low a band width makes the damper susceptible to failure due to a slight damper mistuning. Conversely, too broad a band width reduces the damping capability of the system. At the present time, the optimum trade-off of these two factors is believed to be in the region of values of K_6 and K_2 , giving approximately 0.1 of critical damping in their respective modes.

The influence of payload weight and space limitations on damper optimization is as follows. For an operational satellite with, for example, a 1000-lb payload limit, it is reasonable to allow 10 percent for gravity-gradient damping purposes, which gives a total mass of the damper of 100 lb. The parameter $M/(M + m)$ thus becomes 0.9. Assuming further that the maximum outside diameter of the payload container can accommodate a damper no larger than that of a disk with a radius of 18 in., for an orbital altitude of 2000 naut mi and



an orbital rate of $\omega_o = 6.2 \times 10^{-4}$ rad per second, the total tip mass inertia becomes 50 lb-in. -sec squared. Also, in attempting to make I_m as large as possible and yet holding the total tip mass inertia to no more than 50 lb-in. -sec squared, the best design could achieve a shell inertia of no less than 6.25-lb-in. -sec squared and an inner element inertia no greater than $I_m = 43.75$ lb-in. -sec squared.

e. Transient Response Studies

(1) General

Transient response studies were made to determine the damping capability of the Rice-Wilberforce damper in suppressing librations of the satellite due to initial condition errors at the time of satellite deployment. The dynamic equations employed were those presented in Item 2, b. Various satellite configurations and Rice-Wilberforce damper tuning conditions were investigated. The equations of motion were simulated at the GAC analog computer facility, Akron, Ohio, and digitally at Philco-WDL, Palo Alto, Calif. The equations used in both simulations were derived using LaGrange's method. However, two basic differences should be noted:

1. The digital simulation solved the complete set of equations consisting of eight degrees of freedom. Higher-order terms were neglected, and linearizing assumptions were made with respect to the trigonometric functions of some of the angular displacements to reduce the complexity of the simulation.
2. The analog simulation was simplified to five degrees of freedom in each case studied, namely, pitch and roll. This assumes each axis is decoupled from the others, which

appears quite satisfactory for pitch but is questionable for roll, particularly with respect to yaw coupling. The analog simulation maintained the trigonometric functions and the higher-order terms for the less-complex five-degree-of-freedom equations. Follow-on studies are planned to simulate all eight degrees of freedom on the analog computer.

In general, results of the two different simulations corroborated one another. The digital simulation made at Philco, however, was performed before the optimum tuning criteria of Item 2, c were developed and thus the digital simulation has no great significance so far as optimum tuning of the Rice-Wilberforce damper is concerned. Conversely, the analog simulation has investigated the transient performance under the conditions of optimum tuning of the damper; therefore, the analog simulation results are presented first.

(2) Analog-Computer Simulation of Transient Response

Analog computer runs were made of the settling out of various initial-condition errors of the lenticular satellite for different tuning conditions of the Rice-Wilberforce damper. The following equations for pitch, roll, and spring-mass-damper degrees of freedom were simulated on analog computers:

Spring-Mass-Damper

$$I_m \ddot{\psi}_3 + I_m \dot{\psi}_2 + K_6 \dot{\psi}_3 = 0, \quad (185)$$

$$I_s \ddot{\psi}_2 - K_6 \dot{\psi}_3 + K_5 \dot{\psi}_2 + K_3 \psi_2 + K_4(r - r_e) = 0, \quad (186)$$

$$\bar{m} \ddot{r} + K_2 \dot{r} + (K_1 - 3\bar{m}\omega_o^2)r + K_4 \psi_2 - 3\bar{m}\omega_o^2 L + C = 0. \quad (187)$$

where $C = 3\bar{m}\omega_o^2(L + r_e) - K_1 r_e$.

Pitch Plane

$$I_m \ddot{\psi}_3 + I_m \ddot{\psi}_2 + K_6 \dot{\psi}_3 = 0, \quad (188)$$

$$I_s \ddot{\psi}_2 - K_6 \dot{\psi}_3 + K_5 \dot{\psi}_2 + K_3 \psi_2 + K_4(r - r_e) = 0, \quad (189)$$

$$\begin{aligned} \bar{m}\ddot{r} + K_2 \dot{r} + (K_1 - 3\bar{m}\omega_o^2 C^2 \phi_2 - 2\bar{m}\omega_o \phi_2 - \bar{m}\dot{\phi}_2^2)r + \\ K_4 \psi_2 - \bar{m}L\dot{\phi}_1(2\omega_o + \dot{\phi}_1)C(\phi_2 - \phi_1) + \bar{m}L\ddot{\phi}_1 S(\phi_2 - \phi_1) - \\ 3\bar{m}\omega_o^2 LC\phi_1 C\phi_2 + C = 0, \end{aligned} \quad (190)$$

$$\begin{aligned} r\ddot{\phi}_2 + L\ddot{\phi}_1 C(\phi_2 - \phi_1) + 2\dot{r}(\omega_o + \dot{\phi}_2) + L\dot{\phi}_1(2\omega_o + \dot{\phi}_1)S(\phi_2 - \phi_1) + \\ 3\omega_o^2(LC\phi_1 + rC\phi_2)S\phi_2 = 0, \end{aligned} \quad (191)$$

$$\begin{aligned} (\bar{m}L^2 + I_n)\ddot{\phi}_1 + 3\omega_o^2(I_\xi - I_\zeta)C\phi_1 S\phi_1 + 3\bar{m}\omega_o^2 L(LC\phi_1 + rC\phi_2)S\phi_1 + \\ 2\bar{m}\omega_o L\dot{r}C(\phi_2 - \phi_1) + \bar{m}L(2\dot{r}\dot{\phi}_2 + r\ddot{\phi}_2)C(\phi_2 - \phi_1) + \\ \bar{m}L(\ddot{r} - 2\omega_o r\dot{\phi}_2 - r\dot{\phi}_2^2)S(\phi_2 - \phi_1) = L\phi_1. \end{aligned} \quad (192)$$

Roll Plane

$$I_m \ddot{\psi}_3 + I_m \ddot{\psi}_2 + K_6 \dot{\psi}_3 = 0, \quad (193)$$

$$I_s \ddot{\psi}_2 - K_6 \dot{\psi}_3 + K_5 \dot{\psi}_2 + K_3 \psi_2 + K_4(r - r_e) = 0, \quad (194)$$

$$\begin{aligned} \bar{m}\ddot{r} + K_2 \dot{r} + (K_1 - 4\bar{m}\omega_o^2 C^2 \theta_2 + \bar{m}\omega_o^2 - \bar{m}\dot{\theta}_2^2)r + K_4 \psi_2 - \\ \bar{m}L\dot{\theta}_1^2 C(\theta_2 - \theta_1) + \bar{m}L\ddot{\theta}_1 S(\theta_2 - \theta_1) + \\ \bar{m}\omega_o^2 L(-3C\theta_1 C\theta_2 + S\theta_1 S\theta_2) + C = 0, \end{aligned} \quad (195)$$

$$\begin{aligned}
& r\ddot{\theta}_2 + L\ddot{\theta}_1 C(\theta_2 - \theta_1) + 2\dot{r}\dot{\theta}_2 + L\dot{\theta}_1^2 S(\theta_2 - \theta_1) + \\
& \omega_o^2 (3LC\theta_1 + 4rC\theta_2)S\theta_2 + \omega_o^2 LC\theta_2 S\theta_1 = 0 \quad (196) \\
& (\bar{m}L^2 + I_\xi)\ddot{\theta}_1 + 4\omega_o^2 (I_\eta - I_\xi)C\theta_1 S\theta_1 + \bar{m}\omega_o^2 L \times \\
& (4LC\theta_1 + 3rC\theta_2)S\theta_1 + \bar{m}L(2\dot{r}\dot{\theta}_2 + r\ddot{\theta}_2)C(\theta_2 - \theta_1) + \\
& \bar{m}L(\ddot{r} - r\dot{\theta}_2^2)S(\theta_2 - \theta_1) + \bar{m}\omega_o^2 LrC\theta_1 S\theta_2 = L\theta_1 \quad (197)
\end{aligned}$$

Initially, servo resolvers were used to develop the desired trigonometric functions, but they caused the simulation to be unstable. This effect has been noted in other simulations of lightly damped systems. The functions were then developed using electronic multipliers and representing the sine and cosine by the first two terms in their respective series approximations. The resulting simulation was stable without noticeable loss in accuracy.

Table XIX shows the varying conditions used in studying the transient response for the analog-computer runs in Figures 88 through 99 for Cases I through VII-B. Figure 100 is the relative power dissipation curve for Case IV.

Cases I and II both confirm the damping capability of the damper in suppressing pitch librations when the spring plunging and torsion modes are near the fundamental pitch natural frequency. No roll damping, however, is provided for in this tuning condition. Case III is a somewhat more optimum tuning condition, where some use is made of the torsional mode but not maximum advantage of the tuning possibilities. Cases IV-A and IV-B show the damping capability of the Rice-Wilberforce damper when the plunging mode of the spring mass combination has been tuned to twice the fundamental natural response frequency of the satellite

TABLE XIX - TRANSIENT RESPONSE STUDY - ANALOG SIMULATION

Case	Initial attitude error (deg)	Damper tuning conditions						Transient settling time constant (orbits)	Remarks
		Plunging-mode frequency (ω_0)	Torsional-mode frequency (ω_0)	Spring length (ft)	Fluid coefficient (lb-ft-sec per rad)	Hysteresis viscous coefficient (lb-sec per ft)			
						Plunging	Torsion		
I	20 deg pitch	1.6	2.8	267	0.0005	0.00021	0	2-1/2 in pitch	Confirmed poor performance in roll axis when torsion mode is mistuned
II	20 deg pitch				0.001			No roll damping	
A	25 deg pitch	3.47	6.1	90	0.0035	0.00032	0	2-3/4 orbits in both pitch and roll	Confirmed acceptable performance of a somewhat near-optimum tuning condition
B	25 deg roll								
IV	20 deg pitch	3.9	1.55	94	0.02	0.00033	0	2 orbits in both pitch and roll	Confirmed Rice-Wilberforce damper optimum tuning theory
B	20 deg roll								
A	20 deg pitch	3.1	3.9	120	0.04	0.00027	0	2-1/2 orbits in both pitch and roll	Confirmed Rice-Wilberforce damper could operate very well when both modes tuned to second harmonics of satellite
B	20 deg roll								
VI	20 deg pitch	1.6	Unused mode	267	Fluid damper locked	0.0002	0.00025	2 orbits in pitch, 50 or more in roll	Confirmed APL damper as currently tuned did not give good damping in roll
B	20 deg roll								
A	20 deg pitch	3.9	1.55	94	Fluid damper locked	0.00031	0.00019	4 orbits in pitch, 6 in roll	Confirmed APL damper could be made to give good damping in both pitch and roll
VII	20 deg pitch								
B	20 deg roll								

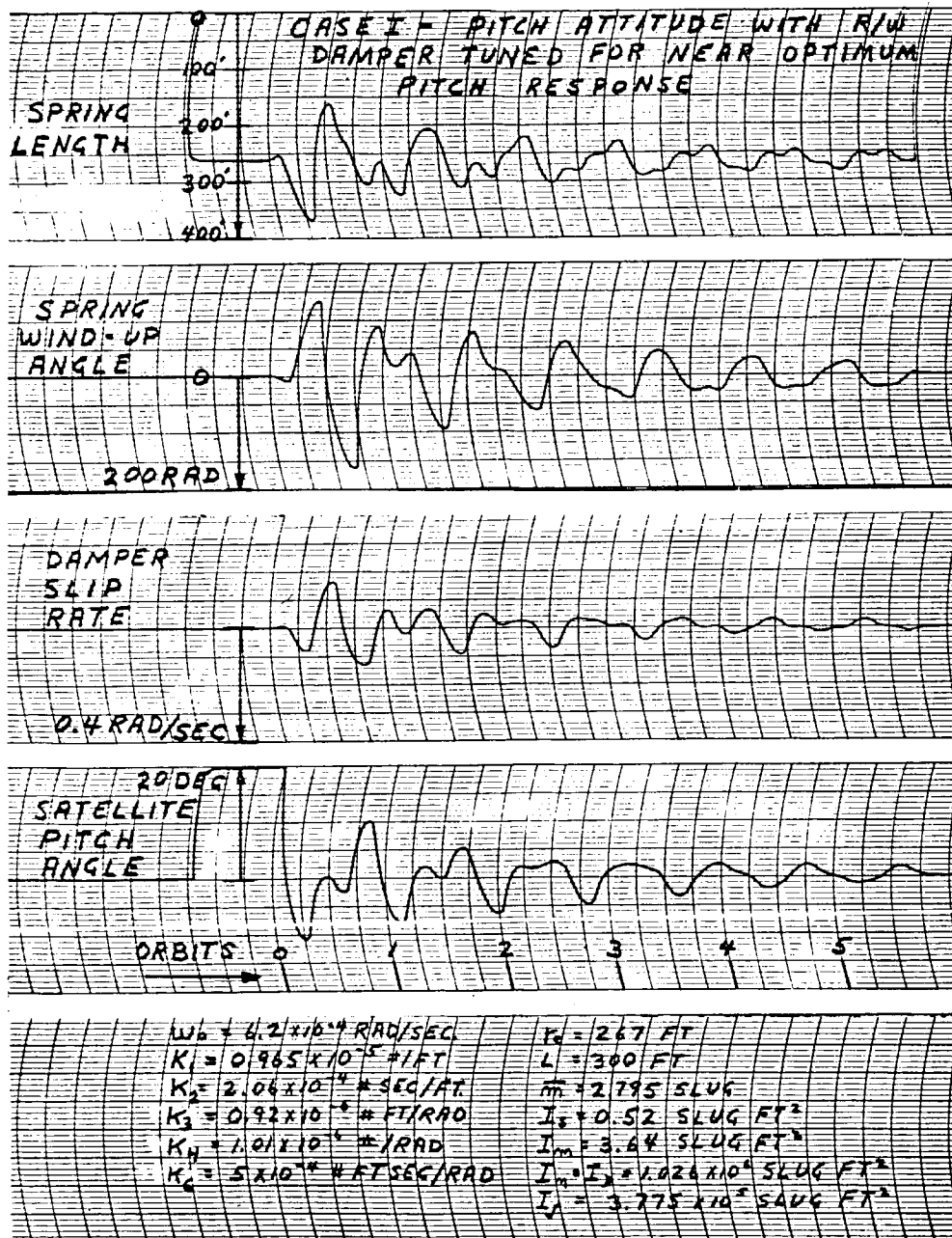


Figure 88 - Analog-Computer Run - Case I

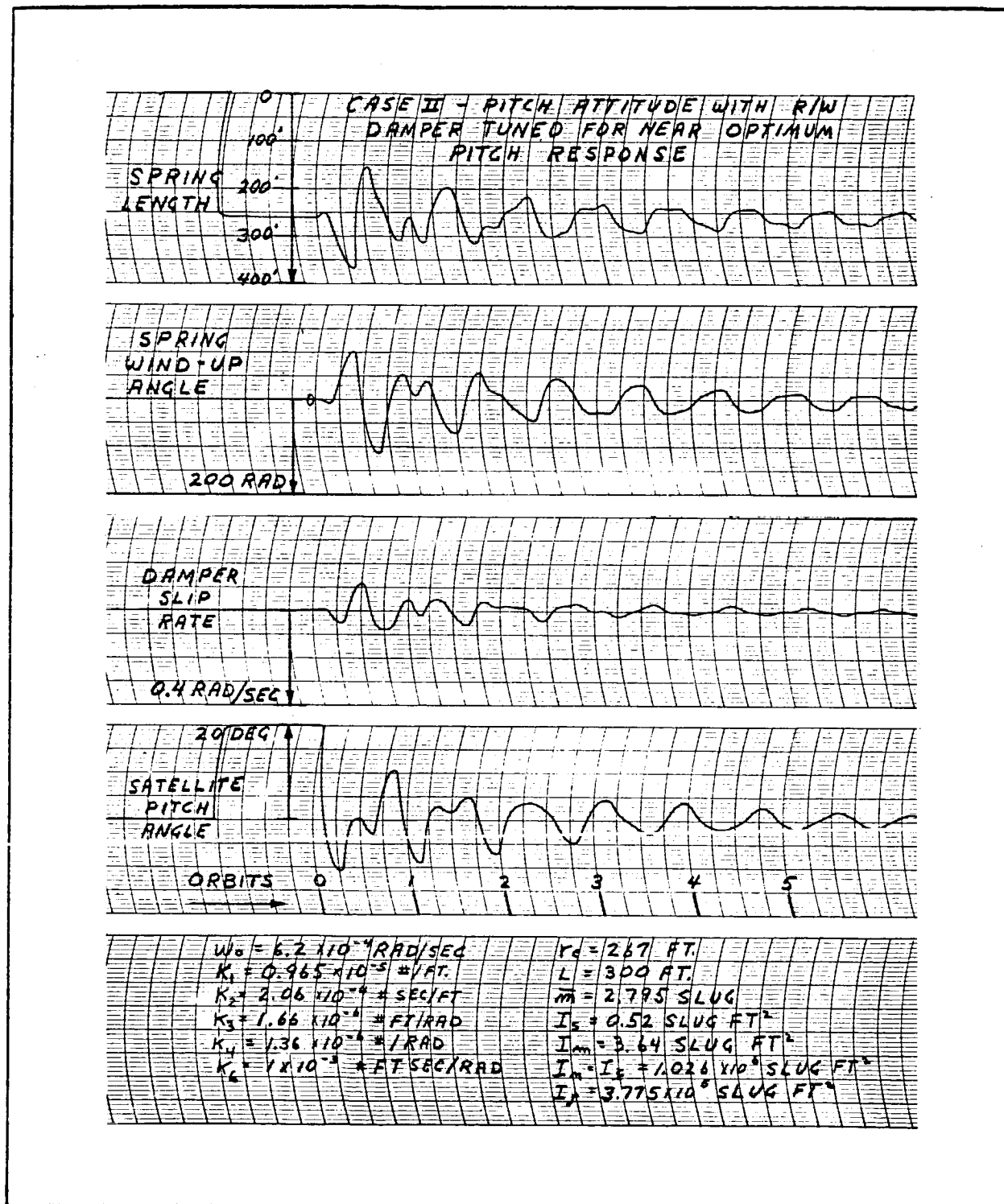


Figure 89 - Analog-Computer Run - Case II

SECTION III

Subsection Three - Stabilization and Orientation Systems

GER-11502

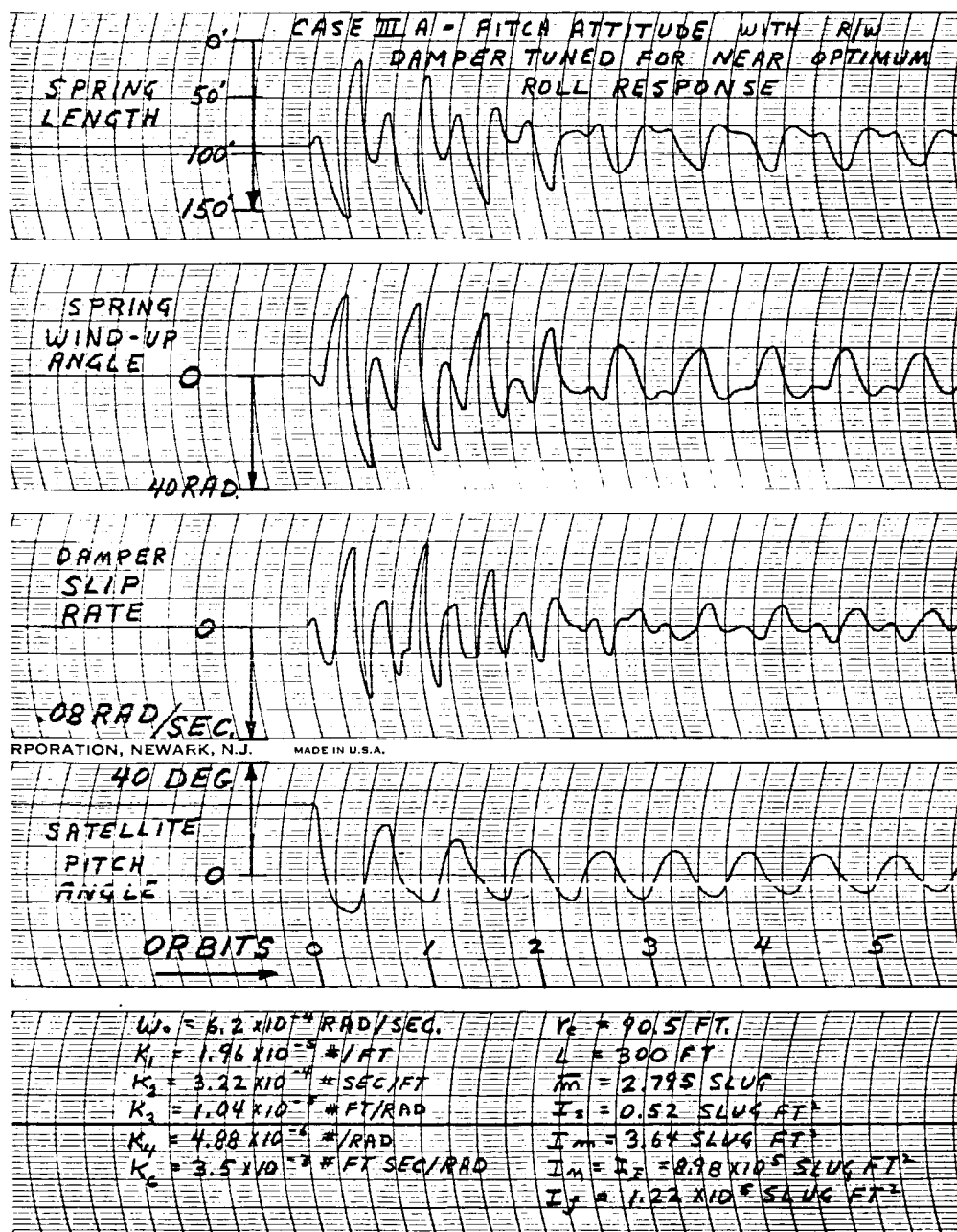


Figure 90 - Analog-Computer Run - Case III-A

SECTION III

Subsection Three - Stabilization and Orientation Systems

GER-11502

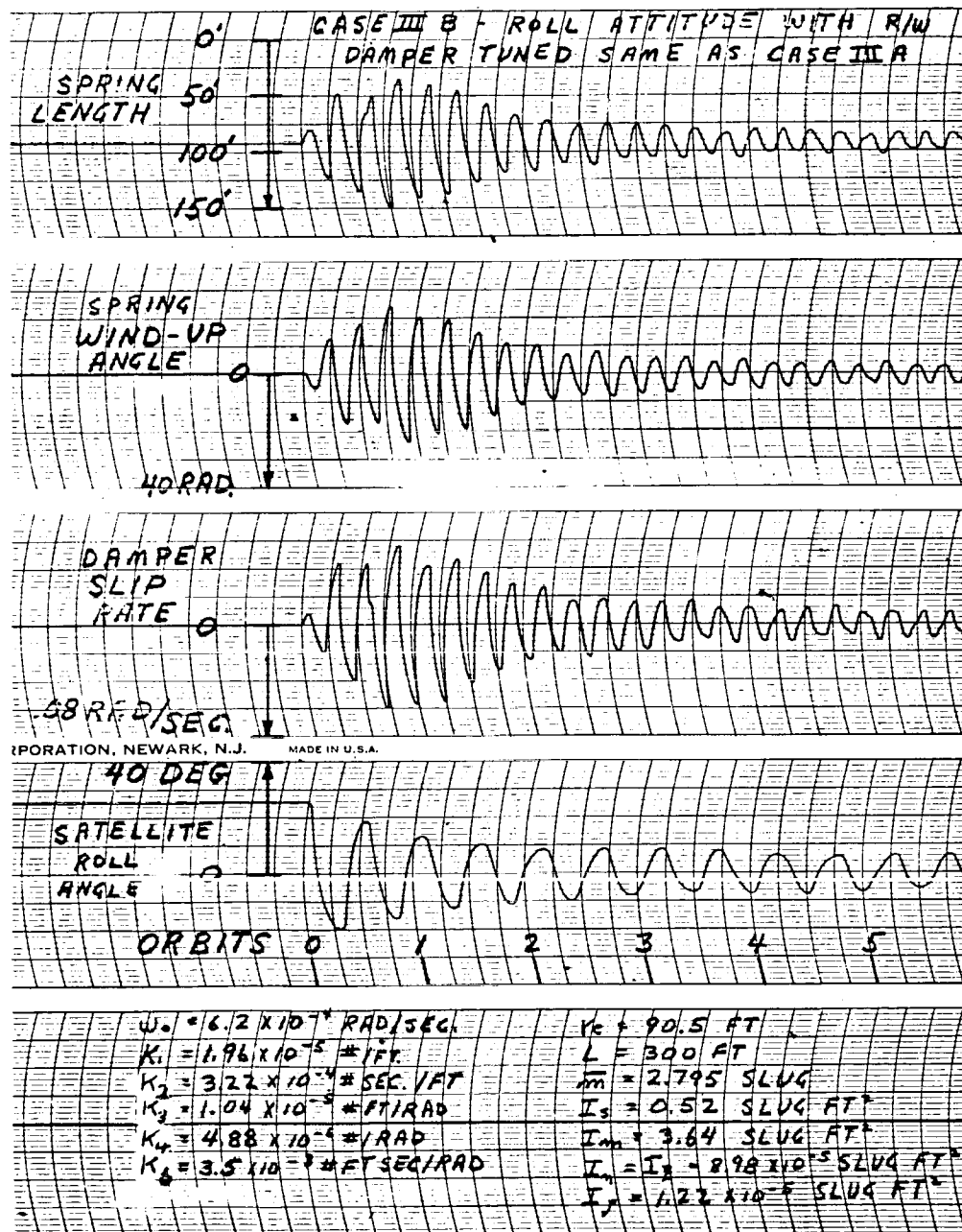


Figure 91 - Analog-Computer Run - Case III-B

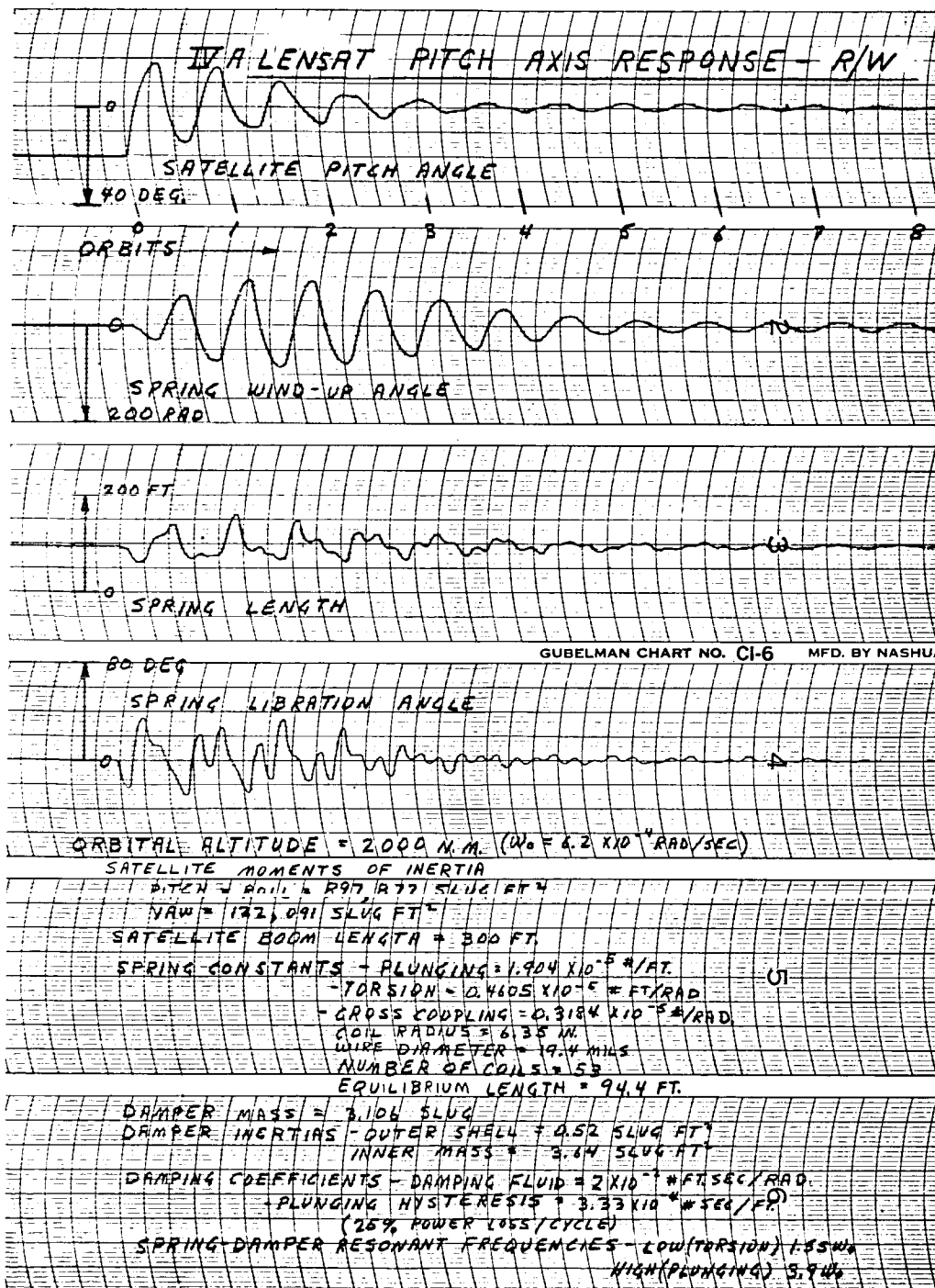


Figure 92 - Analog-Computer Run - Case IV-A

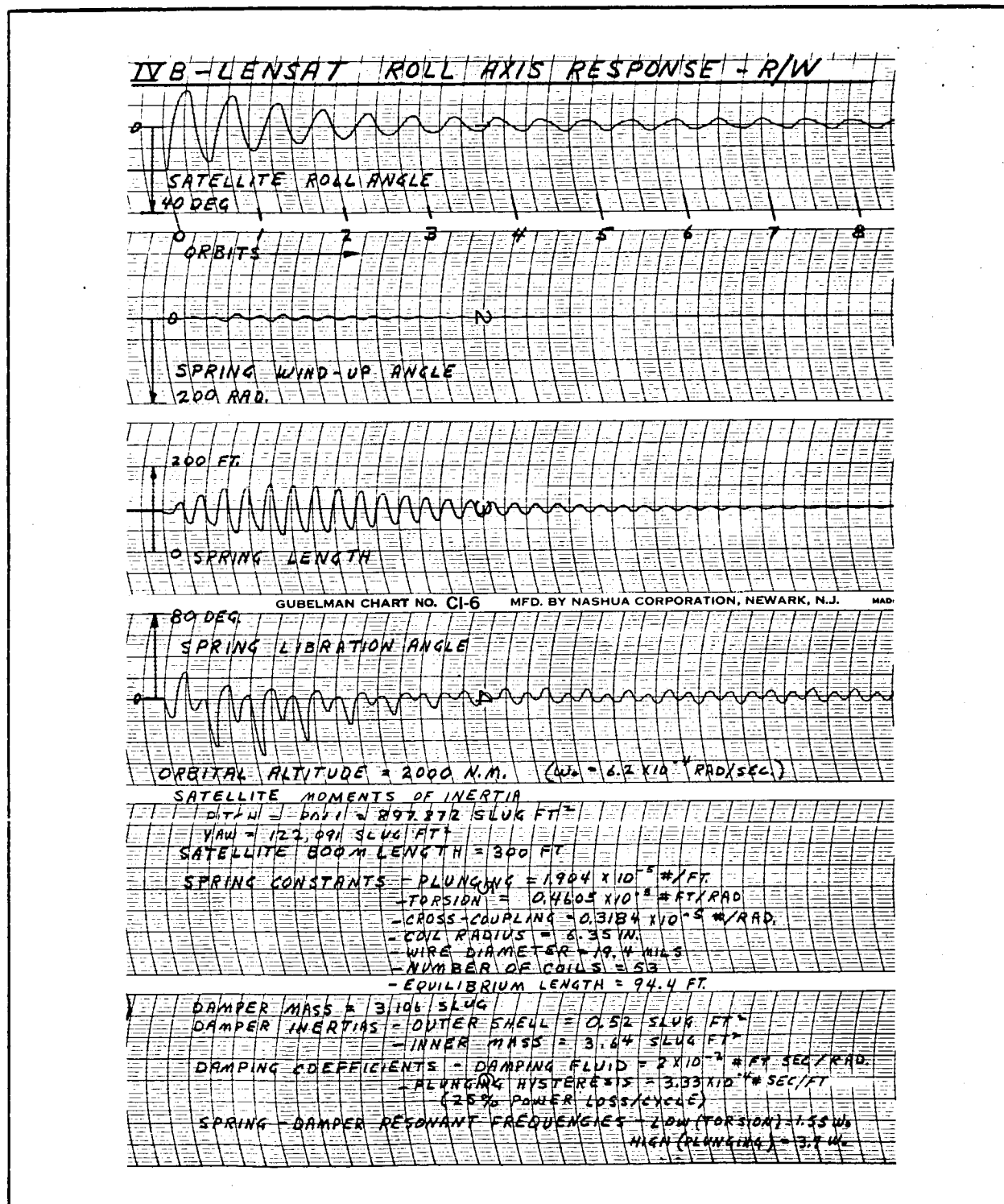


Figure 93 - Analog-Computer Run - Case IV-B

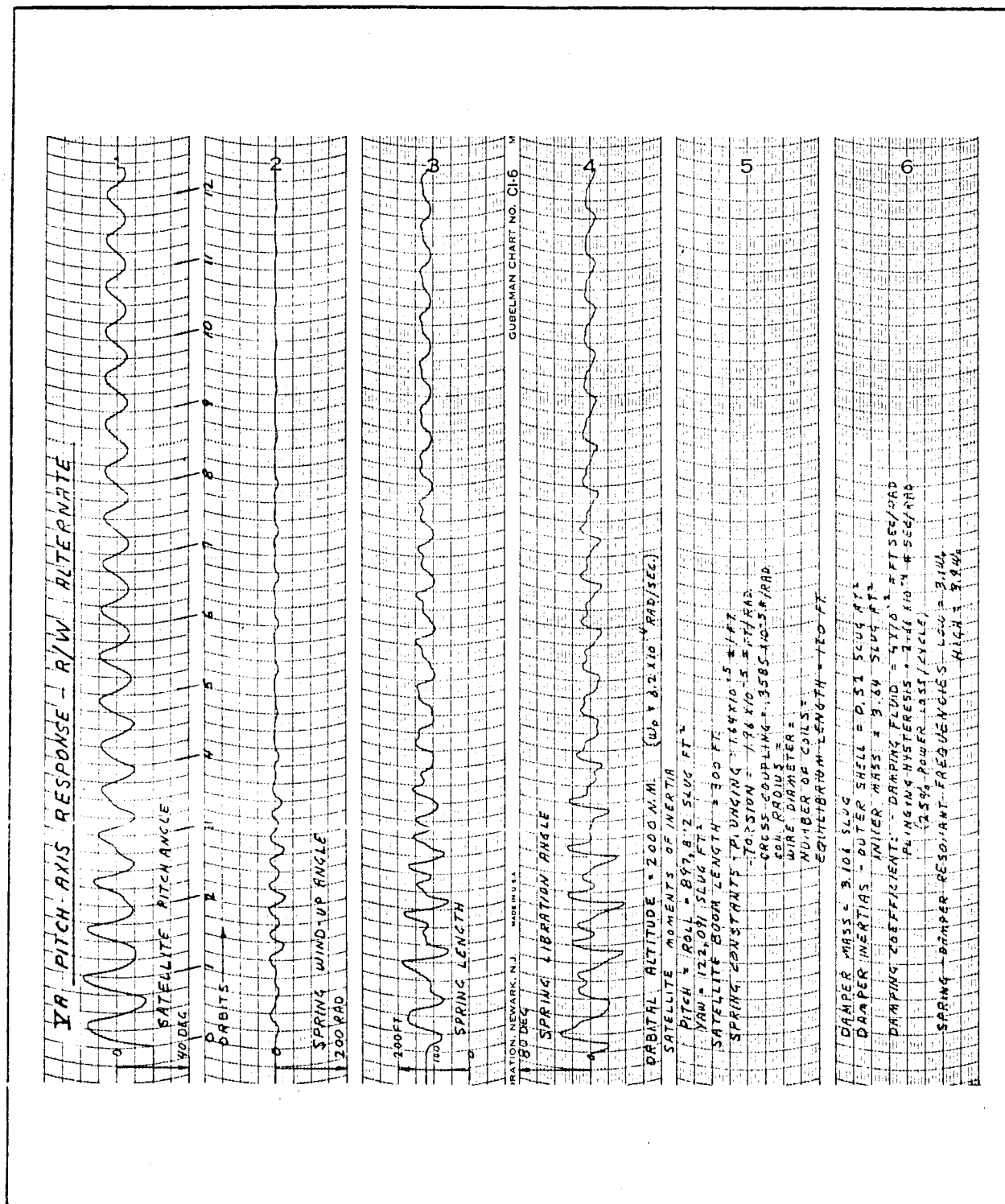


Figure 94 - Analog-Computer Run - Case V-A

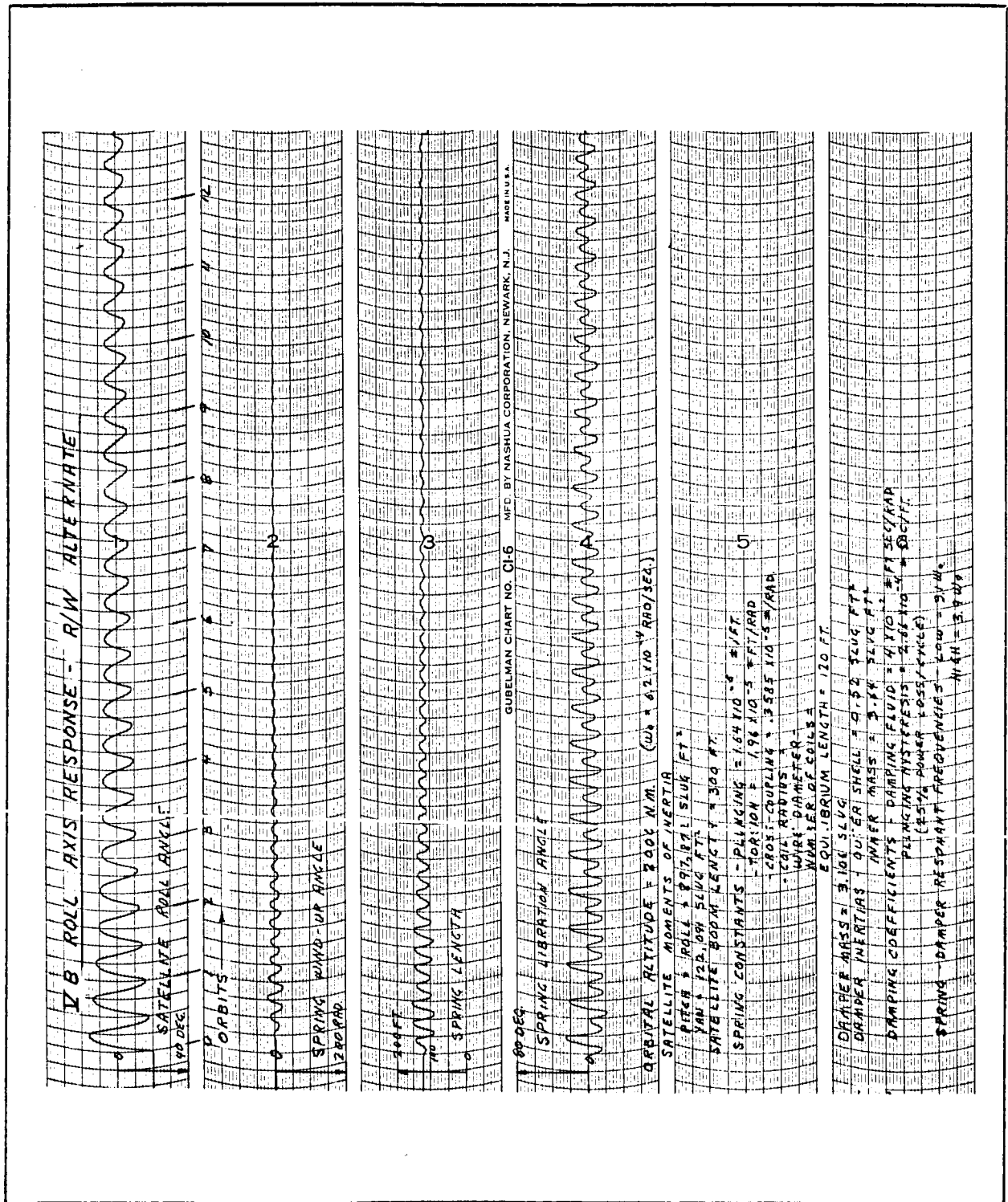


Figure 95 - Analog-Computer Run - Case V-B

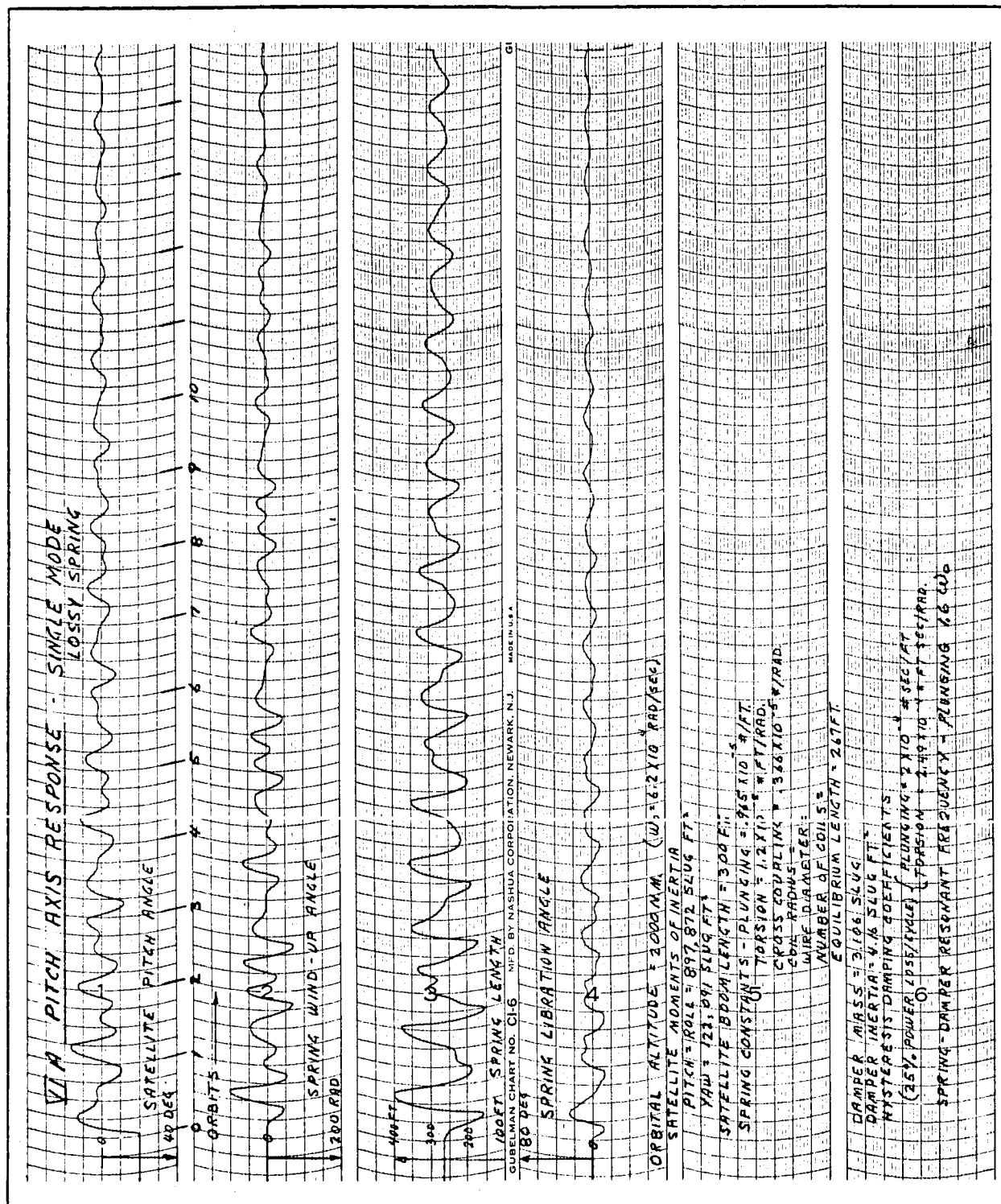


Figure 96 - Analog-Computer Run - Case VI-A

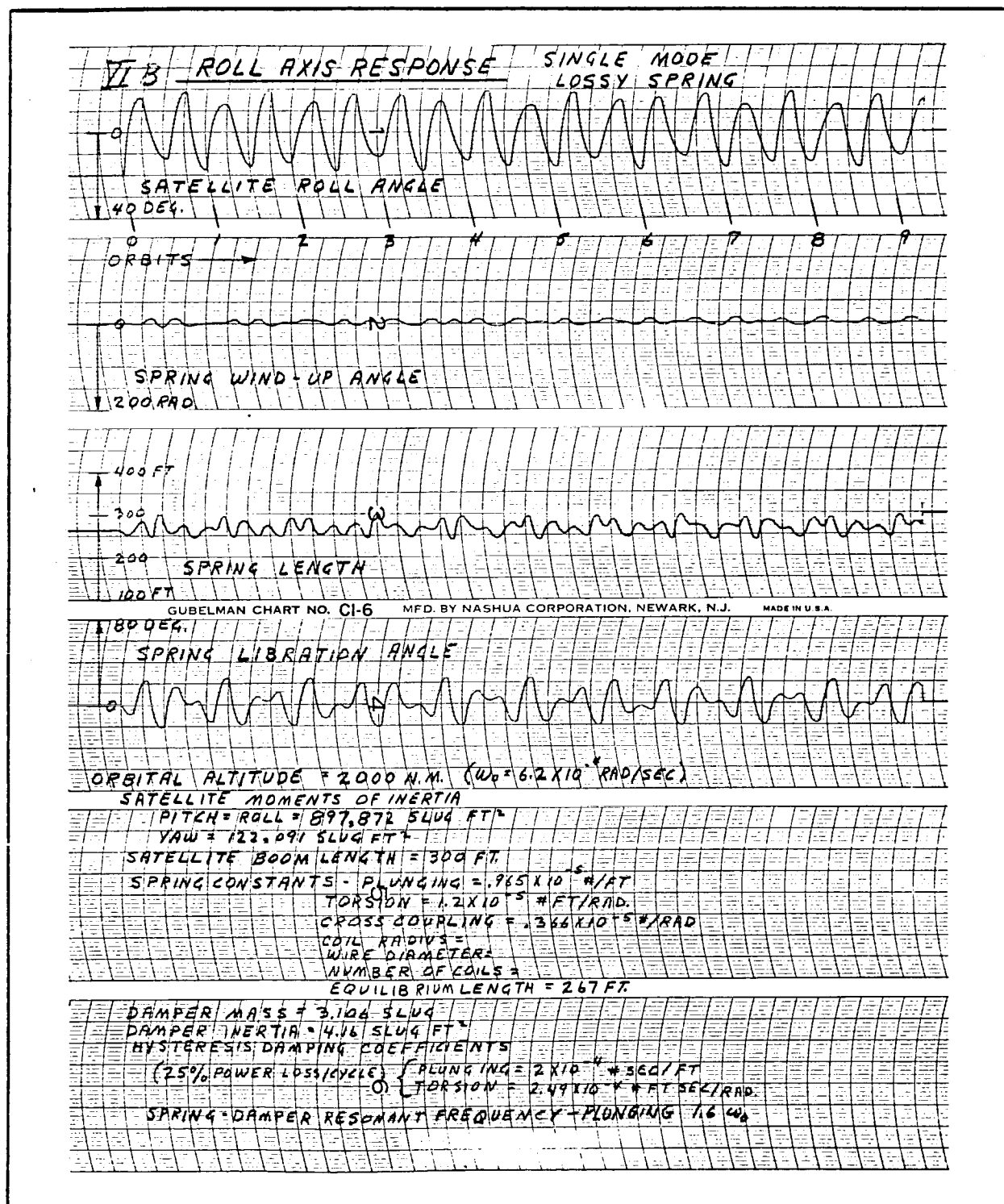


Figure 97 - Analog-Computer Run - Case VI-B

roll axis, and the torsional mode of the spring and rotational inertia of the damper have been tuned to the fundamental frequency of the satellite pitch axis. Cases V-A and V-B are for an alternate tuning condition in which the plunging and torsional modes are tuned to twice the natural frequency of the pitch and roll axes, respectively. These cases correspond to a relatively stiff short spring and have the advantage of having the gyroscopic precession of the damper disk go through approximately four full cycles per orbit, thereby reducing the tendency of the damper to precess out of the horizontal plane. Cases VI-A and VI-B show the capability of the purely lossy spring and tip mass damper when the plunging mode is essentially resonant to the pitch-libration frequency but with no use made of the torsional mode, thus not being able to achieve a damping capability in the roll axis. Cases VII-A and VII-B show the benefit made possible by utilizing the torsional mode of the lossy spring-tip mass damper as well as the plunging mode. The torsional mode has been tuned to the pitch frequency and the plunging mode has been tuned to twice the roll frequency of the satellite. Note that, in all the cases shown here, hysteresis loss in the spring was simulated in the plunging mode to complement the fluid damper in the torsional mode. If this hysteresis loss were not present, the satellite oscillation associated with the plunging-mode tuned frequency would exhibit poorer damping.

(3) Digital-Computer Simulation of Transient Response

The full eight-degree-of-freedom equations of Item 2, \underline{b} were simulated on the TRANSAC 2000 digital computer at Philco-WDL, Palo Alto, Calif. Twelve different cases were run with varying initial errors in pitch and roll attitudes, varying satellite moments of inertia corresponding to different types of satellite wire film material, and varying tuning arrangements of the Rice-Wilberforce gravity-gradient damper. These runs were made

SECTION III

Subsection Three - Stabilization and Orientation Systems

GER-11502

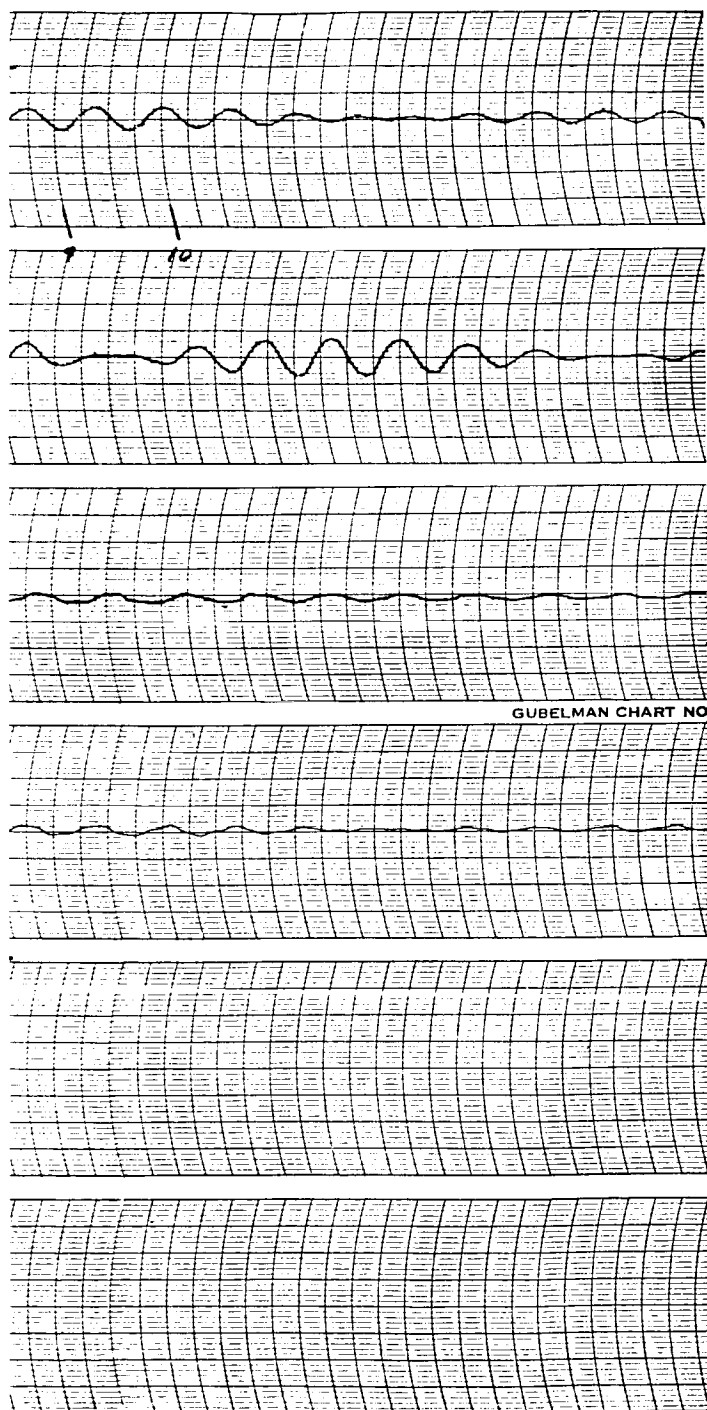
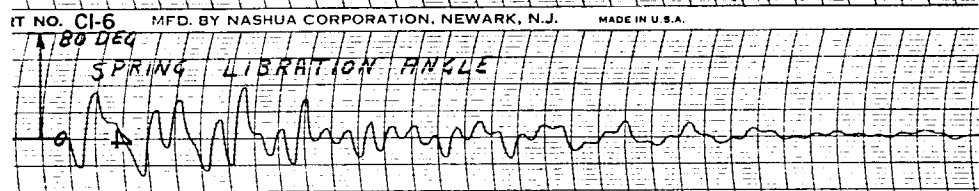
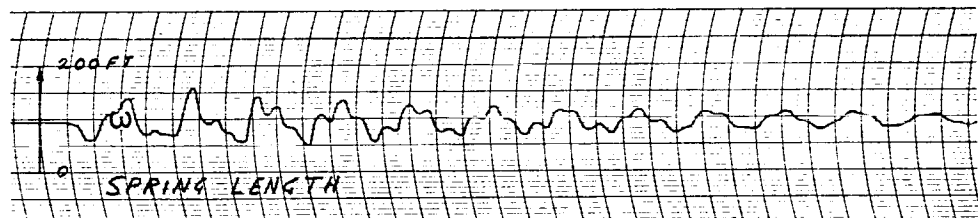
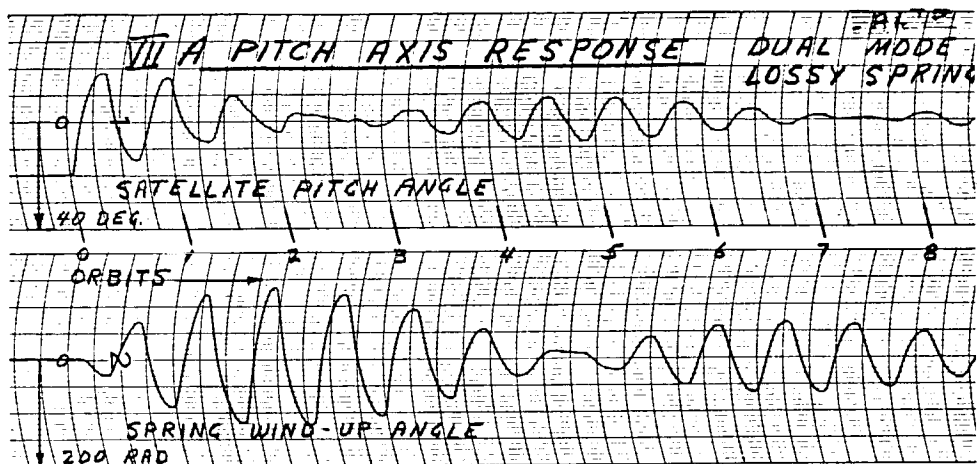


Figure 98 - Analog-Computer Run - Case VII-A



ORBITAL ALTITUDE = 2000 N.M. ($\omega_0 = 6.2 \times 10^{-4}$ RAD/SEC)

SATELLITE MOMENTS OF INERTIA

PITCH = ROLL = 897,872 SLUG FT²

YAW = 12,497 SLUG FT²

SATELLITE BOOM LENGTH = 300 FT.

SPRING CONSTANTS - PLUNGING = 1.904×10^{-5} #/FT.

- TORSION = 0.4605×10^{-5} # FT/RAD

- CROSS COUPLING = 0.3184×10^{-5} #/RAD.

COIL RADIUS = 6.35 IN.

WIRE DIAMETER = 19.4 MILS

NUMBER OF COILS = 53

EQUILIBRIUM LENGTH = 94.4 FT.

DAMPER MASS = 3.106 SLUG

DAMPER INERTIA = 4.16 SLUG FT²

HYSTERESIS DAMPING COEFFICIENTS

(25% POWER LOSS/CYCLE) { PLUNGING = 3.12×10^{-4} # SEC/FT
TORSION = 1.91×10^{-4} # FT SEC/RAD.

SPRING-DAMPER RESONANT FREQUENCIES

LOW (TORSION) = 1.55 ω_0

HIGH (PLUNGING) = 3.9 ω_0

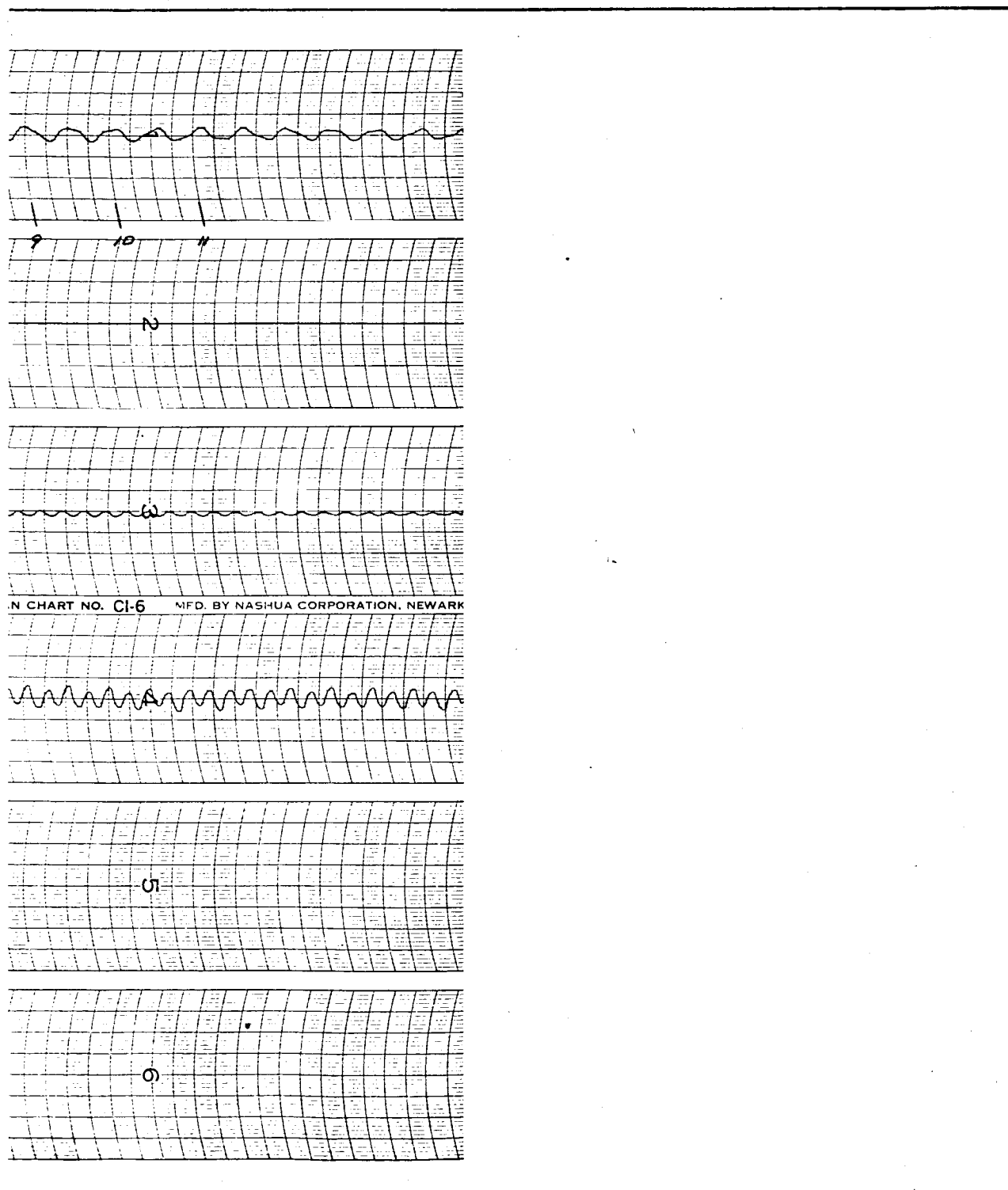
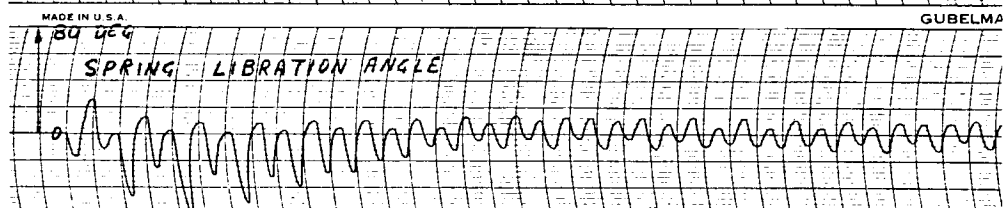
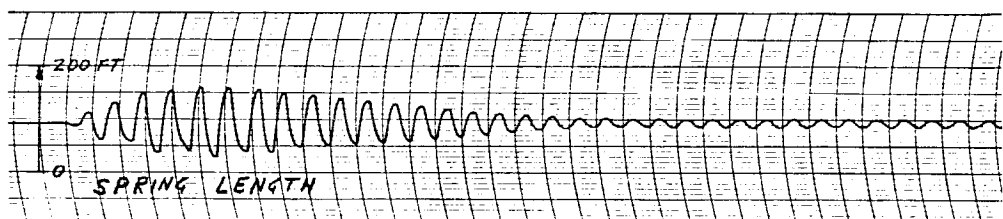
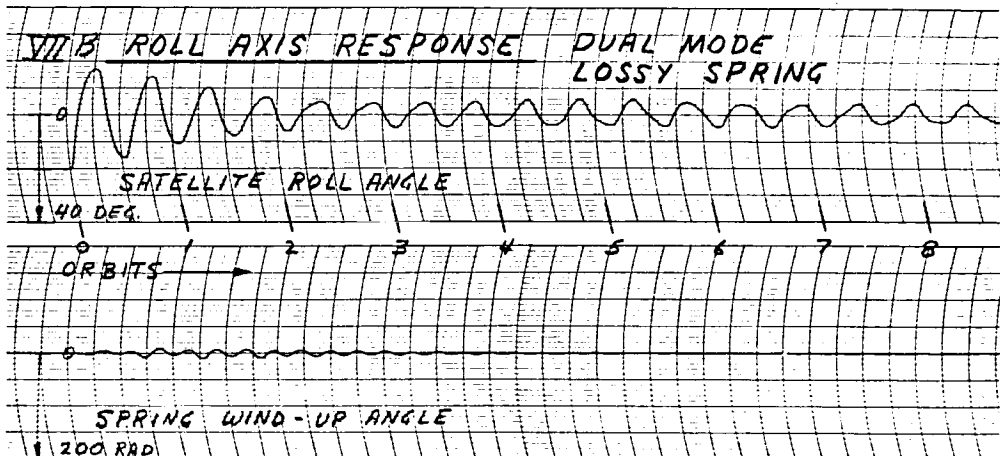


Figure 99 - Analog-Computer Run - Case VII-B



ORBITAL ALTITUDE = 2000 N.M. ($\omega_0 = 6.2 \times 10^{-4}$ RAD/SEC)

SATELLITE MOMENTS OF INERTIA

PITCH = ROLL = $871,814$ SLUG FT^2

YAW = $122,091$ SLUG FT^2

SATELLITE BOOM LENGTH = 300 FT.

SPRING CONSTANTS - PLUNGING = 1.904×10^{-5} #/FT.

- TORSION = 0.4605×10^{-5} # FT/RAD.

- CROSS COUPLING = 0.3184×10^{-5} #/RAD.

COIL RADIUS = 6.85 IN.

WIRE DIAMETER = 19.4 MILS

NUMBER OF COILS = 53

EQUILIBRIUM LENGTH = 94.4 FT.

DAMPER MASS = 3.106 SLUG

DAMPER INERTIA = 4.16 SLUG FT^2

HYSTERESIS DAMPING COEFFICIENTS

(25% POWER LOSS/CYCLE) (PLUNGING = 3.12×10^{-4} # SEC/FT.

TORSION = 1.91×10^{-4} # FT SEC/RAD.

SPRING-DAMPER RESONANT FREQUENCIES

LOW (TORSION) - 1.55 ω_0

HIGH (PLUNGING) - 3.9 ω_0

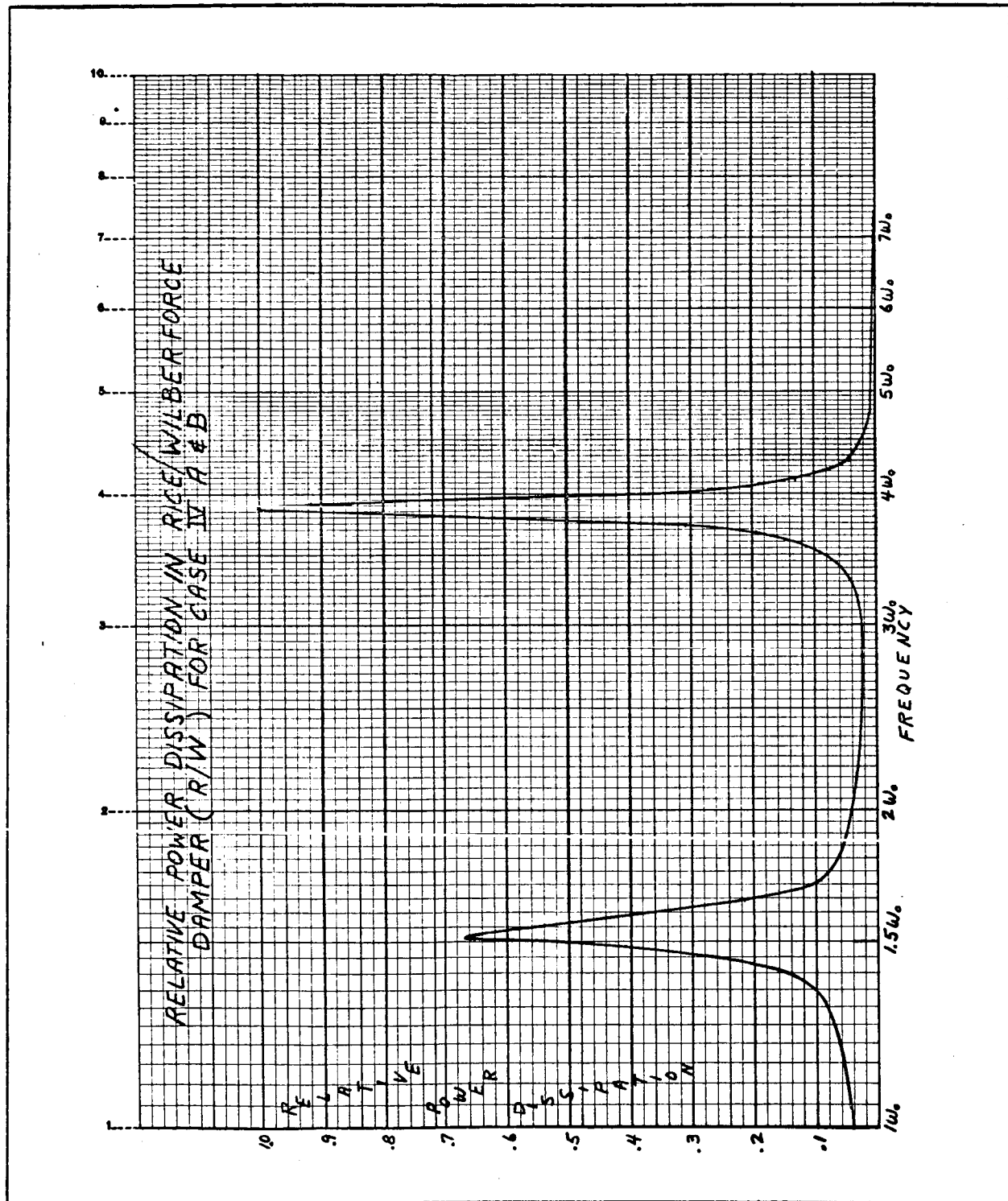


Figure 100 - Relative Power Dissipation for Case IV

before the optimum tuning theory of Item 2, d was available and hence do not show optimum performance. In fact, many of the runs are for cases where the Rice-Wilberforce damper is badly mistuned. Nevertheless, the runs do verify the feasibility of the damper with respect to damping pitch librations. They show that roll librations can also be damped by using hysteresis losses in the spring to dissipate energy rather than using body axis cross-coupling to direct energy into the pitch plane.

Additional runs will be made at Philco, using the optimum tuning theory of Item 2, e.

The data and curves generated at Philco are much too prolific to publish in this report, but are presented in a separate report, Reference 13. However, a summary of the most significant information obtained from the digital simulation is presented here in Table XX.

f. Steady-State Response Studies

(1) General

A knowledge of the steady-state response of the GAC lenticular satellite to solar pressure torque and orbital eccentricity is necessary to determine the magnitude of the libration angles from the vertical and also to determine whether there is some critical combination of initial conditions and steady-state disturbance torques. The derived solar torque equations show that the solar torque forcing frequencies are at one and two times orbital frequency, while the eccentricity effect appears at approximately orbital frequency. The critical nature of this problem is brought about because of the closeness of the satellite-libration natural frequencies to these forcing frequencies.

The effects of eccentricity on pitch attitude dynamics were studied with the GAC analog simulation referred to in Item 2, e, (2). The

SECTION III

Subsection Three - Stabilization and Orientation Systems

GER-11502

RESPONSE - EIGHT DEGREES OF FREEDOM

Super configuration			Initial attitude error (deg)		Settling time constant (orbits)		Notes/conclusions
ng sis. h)	Coupled mode frequency (multiple ω_o)						
	Plunging	Torsion	Pitch	Roll	Pitch	Roll	
sis	2.717	1.68	25	0	2.7	...	Confirmation of good pitch transient response for all types of damping. Fluid damping better than hysteresis. Best response obtained when both types of damping were used simultaneously
	2.76	1.735	25	0	4.0	...	
	2.717	1.68	25	0	2.3	...	
sis	2.717	1.68	0	25	...	~25	Roll response poor with fluid damping: effective only in torsional mode. Roll response much better with hysteresis damping used in both torsion and plunging modes of damper
	2.76	1.735	0	25	...	~4.0	
	2.717	1.68	0	25	...	~25	Response comparable to photolyzable response
	2.717	1.68	0	25	...	~25	Effects of increased asymmetry inconclusive
	2.717	1.68	0	25	...	~35	
	2.717	1.68	25	0	~2.7	...	Asymmetric satellite appears to have better damping in roll than symmetric satellite. Body-axis cross-coupling can enhance the roll damping
	2.717	1.68	0	25	...	~40	
	3.47	6.43	25	0	6.5	...	Roll response unacceptable. Pitch response poor. Torsional mode mistuned. Plunging mode tuned correctly, but no hysteresis damping used to remove energy
	3.47	6.43	0	25	...	75	

s simulated with 25-percent power loss per cycle effective at the coupled-mode

TABLE XX - DIGITAL SIMULATION OF LENS AT TRANSIENT RE

Run No		Purpose of run	Satellite configuration					Darr	
			Lens material	Satellite inertias (slug-ft ²)			Inertia ratios		Type dampi
				I _{pitch}	I _{roll}	I _{yaw}	$\frac{I_{pitch}}{I_{roll}}$	$\frac{I_{pitch}}{I_{yaw}}$	(Fluid hysteresis or bot
101	Comparison of pitch transient response for various damping configurations with 4-percent satellite asymmetry	Photolyzable	915, 739	879, 815	122, 091	1. 0408	7. 5005	Fluid	
102		Photolyzable	915, 739	879, 815	122, 091	1. 0408	7. 5005	Hystere	
103		Photolyzable	915, 739	879, 815	122, 091	1. 0408	7. 5005	Both	
104	Comparison of roll transient response for fluid and hysteresis damping with 4-percent asymmetry	Photolyzable	915, 739	879, 815	122, 091	1. 0408	7. 5005	Fluid	
105		Photolyzable	915, 739	879, 815	122, 091	1. 0408	7. 5005	Hystere	
106	Roll transient response for unphotolyzable satellite lens with 4-percent asymmetry	Unphotolyzable	1. 046, 696	1. 005, 650	377, 529	1. 0408	2. 7725	Fluid	
107	Compare roll transient response for photolyzable satellite lenses with increased asymmetry (~8 percent)	Photolyzable	943, 789	861, 959	122, 091	1. 0949	7. 730	Fluid	
108		Unphotolyzable	1, 067, 220	985, 126	377, 529	1. 083	2. 827	Fluid	
109	Pitch and roll transient response with fluid damping and symmetrical satellite	Photolyzable	897, 872	897, 872	122, 091	1. 00	7. 354	Fluid	
110		Photolyzable	897, 872	897, 872	122, 091	1. 00	7. 354	Fluid	
111	Compare pitch and roll response with one mode of damper tuned between second harmonics of pitch and roll	Photolyzable	879, 815	915, 739	122, 091	0. 9608	7. 206	Fluid	
112		Photolyzable	879, 815	915, 739	122, 091	0. 9608	7. 206	Fluid	

* Hysteresis damping was used for torsional and plunging spring motion. An equivalent viscous damping was frequency.

more complete equations-of-motion program at Philco [referred to in Item 2, e, (3)] is being modified to include solar pressure effects. However, as these torque equations have not been checked out in the Philco program at this time, steady-state response from eccentricity only are discussed in this report. The checkout of the Philco program, including solar torques, will be completed in the near future, and the response of the lenticular satellite and various Rice-Wilberforce damper configurations to solar torques will be obtained and published as a separate report. The solar torque equations relative to a satellite-fixed coordinate system, including an order-of-magnitude analysis of the solar torques, and the orbital eccentricity and its effects on the steady-state response are discussed in the following paragraphs.

(2) Moments Due to Solar Radiation Pressure

(a) General

The torque expressions presented here will be used in the digital computer study concerned with the steady-state response of the lenticular satellite. The method employed in deriving these expressions is similar to that employed in Reference 14.

The satellite configuration is subdivided into four subsystems: lens, torus (nonphotolyzed), booms, and canisters. The respective moments can be added to determine the composite moment. Because of the complexity of the exact derivations, simplifying assumptions are made. The order-of-magnitude analysis led to the conclusion that all subconfiguration moments are approximately the same order of magnitude and therefore must be included in the study.

The satellite subconfigurations and nomenclature and the derived subconfiguration moment expressions are presented in the following paragraphs. Also presented are the basic

solar-pressure force and moment equations necessary to obtain the final moment equations and the earth-satellite eclipsing logic. The general simplifying assumptions are as follows:

1. All material is partially transmissive or specular reflective to incident light or is a combination of both (for example, Mylar and wire screen). This property will be represented by the ratio of reflecting to total surface area, μ , as defined in Reference 14 and independent of angle of incidence.
2. Shadow effects of one subsystem on another are neglected.
3. Only direct radiation from the sun will be considered (i. e., no satellite or earth reflection is included).

(b) Satellite Subconfiguration Moment Expressions

The coordinate systems utilized in the analysis of each satellite subconfiguration along with nomenclature and solar torque expressions are presented in Figures 101 through 104.

(c) Basic Solar Radiation Force and Moment Equations

The basic equations utilized in obtaining the moment equations utilized in obtaining the moment equations for the satellite subconfigurations are presented here. These equations (from Reference 14), when integrated over a particular subconfiguration (lens, torus, etc.) surface area, result in the moment equations for each subconfiguration, which are presented in Figures 101 through 104.

The force on an element of area for a partially transmissive and partially specularly reflective surface is

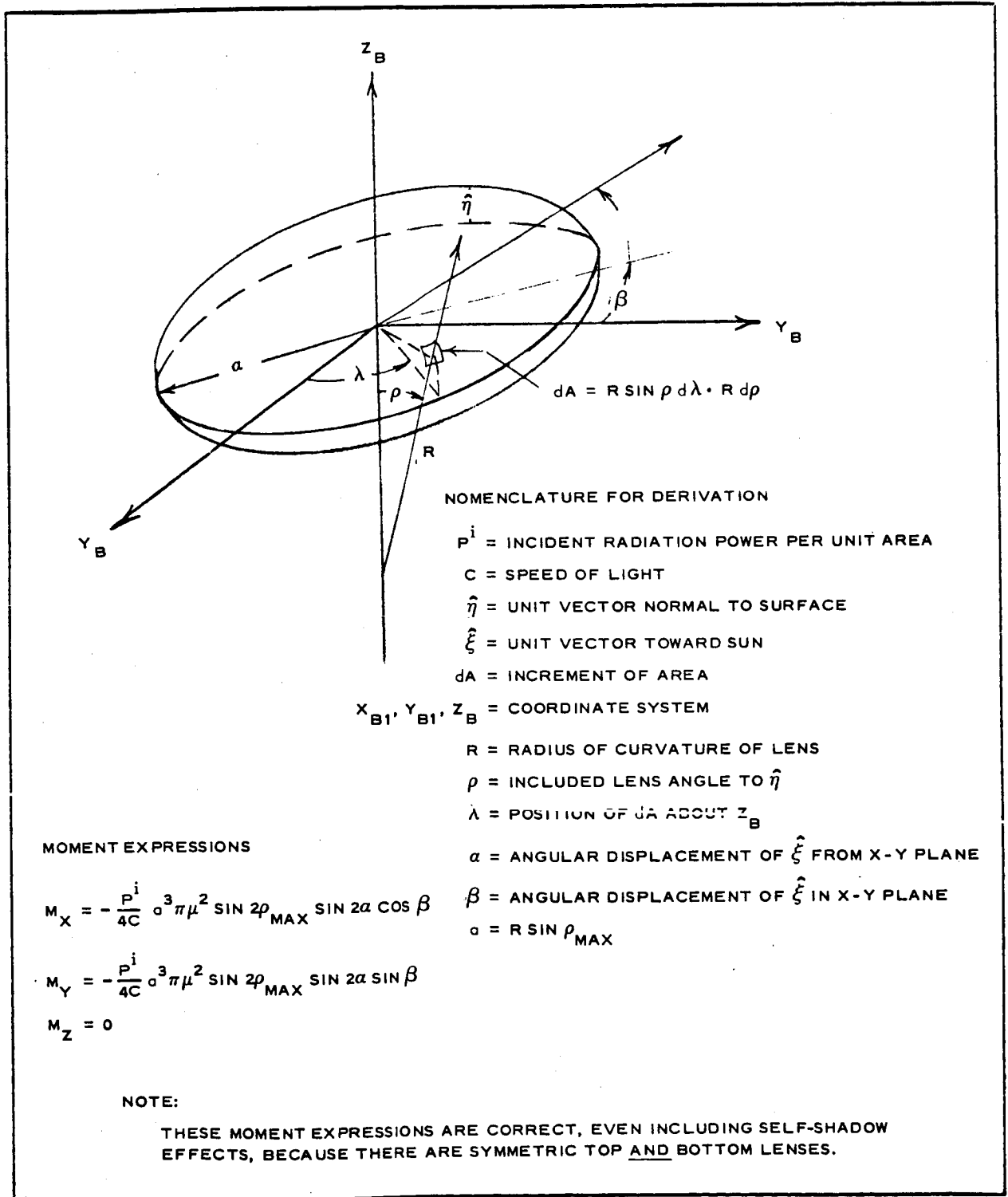
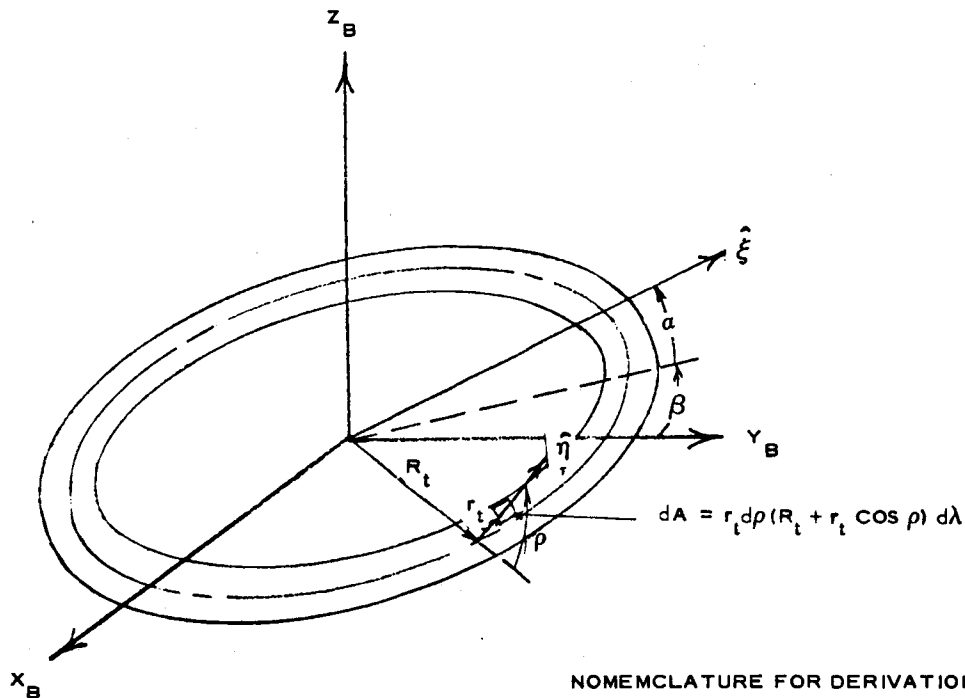


Figure 101 - Lens Subconfiguration



NOMENCLATURE FOR DERIVATION

R_t = RADIUS OF TORUS ABOUT z_B

r_t = RADIUS OF TORUS

ρ = ANGLE OF $\hat{\eta}$ ABOUT TORUS \hat{e}

MOMENT EXPRESSIONS

$$M_X = -\mu \frac{(2-\mu)P^i}{4C} r_t^2 R_t^2 \sin 2\alpha \cos \beta$$

$$M_Y = -\mu \frac{(2-\mu)P^i}{4C} r_t^2 R_t^2 \sin 2\alpha \sin \beta$$

$$M_Z = 0$$

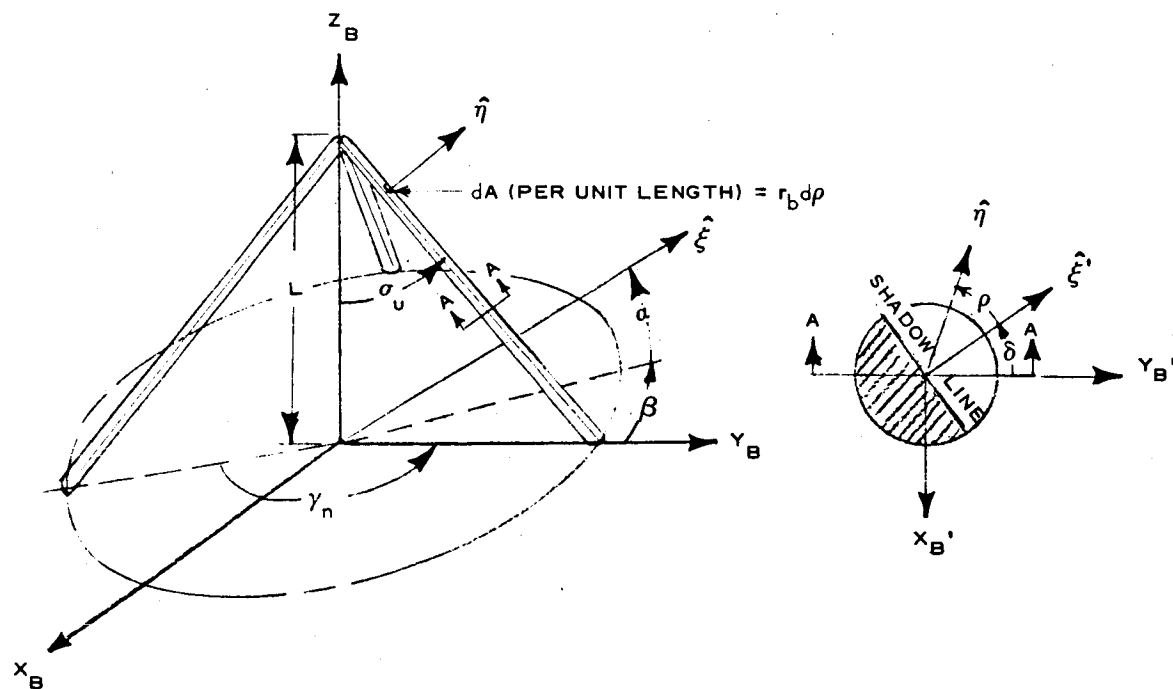
NOTE:

ALL OTHER NOMENCLATURE HAS BEEN PRESENTED.

NOTE:

TO OBTAIN A SIMPLER CLOSED-SOLUTION, AND BECAUSE IT IS CONSERVATIVE, THE LIMITS OF ρ FOR INTEGRATION PURPOSES ARE $0 \leq \rho \leq 180$ DEG.

Figure 102 - Torus Subconfiguration



$$\begin{aligned}
 &+ 2) + B \left[\cos \sigma_n \sin \gamma_n \cos \delta_n (\sin^2 \delta_n + 2) - \cos \gamma_n \sin^3 \delta_n \right] + C \left[\cos \sigma_n \sin \gamma_n \sin^3 \delta_n - \cos \gamma_n \cos^3 \delta_n \right] \Bigg\} \\
 &+ 2) + B \left[\cos \sigma_n \cos \gamma_n \cos \delta_n (\sin^2 \delta_n + 2) + \sin \gamma_n \sin^3 \delta_n \right] + C \left[\cos \sigma_n \cos \gamma_n \sin^3 \delta_n + \sin \gamma_n \cos^3 \delta_n \right] \Bigg\} \\
 &= \sin \sigma_n \sin^3 \delta_n \Bigg\} \\
 &(\beta + \gamma_n), B = \left[\cos \sigma_n \cos \alpha \cos (\beta + \gamma_n) + \sin \sigma_n \sin \alpha \right]^2,
 \end{aligned}$$

Figure 103 - Booms Subconfiguration

NOMENCLATURE FOR DERIVATION

r_b = RADIUS OF BOOMS

L = HEIGHT OF UPPER BOOMS

L_L = HEIGHT OF LOWER BOOMS

σ_u = ANGLE OF INCLINATION OF UPPER BOOMS

σ_L = ANGLE OF LOWER BOOMS (NEGATIVE)

γ_n = POSITION OF BOOM n TO Y_B

ρ = ANGLE TO $\hat{\eta}$ FROM $\hat{\xi}$

δ_n = ANGLE FROM Y_B TO $\hat{\xi}$ FOR BOOM n

$$M_X = \sum_{n=1}^3 M_{X_n}(\gamma_n, \sigma_n, L) + \sum_{n=4}^6 M_{X_n}(\gamma_n, \sigma_n, L_L)$$

$$M_Y = \sum_{n=1}^3 M_{Y_n}(\gamma_n, \sigma_n, L) + \sum_{n=4}^6 M_{Y_n}(\gamma_n, \sigma_n, L_L)$$

$$M_Z = \sum_{n=1}^3 M_{Z_n}(\gamma_n, \sigma_n, L) + \sum_{n=4}^6 M_{Z_n}(\gamma_n, \sigma_n, L_L)$$

WHERE

$$M_{X_n} = -\frac{F_{Y_n} L}{2} \Big|_{n=1,2,3} + \frac{F_{Y_n} L}{2} \Big|_{n=4,5,6} + F_{Z_n} \frac{\alpha \cos \gamma_n}{2}$$

$$M_{Y_n} = \frac{F_{X_n} L}{2} - \frac{F_{Z_n} \alpha \sin \gamma_n}{2}$$

$$M_{Z_n} = -\frac{F_{X_n} \alpha \cos \sigma_n}{2} + \frac{F_{Y_n} \alpha \sin \gamma_n}{2}$$

$$F_{X_n} = -\mu \frac{4(2-\mu)P^i L}{3C \cos \sigma_n} r_b \left\{ A \left[\cos \sigma_n \sin \gamma_n \cos^3 \delta_n - \cos \gamma_n \sin \delta_n (\cos^2 \delta_n \right.$$

$$F_{Y_n} = -\mu \frac{4(2-\mu)P^i L}{3C \cos \sigma_n} r_b \left\{ A \left[\cos \sigma_n \cos \gamma_n \cos^3 \delta_n + \sin \gamma_n \sin \delta_n (\cos^2 \delta_n \right.$$

$$F_{Z_n} = -\mu \frac{4(2-\mu)P^i L}{3C \cos \sigma_n} r_b \left\{ A \sin \sigma_n \cos^3 \delta_n + B \sin \sigma_n \cos \delta_n (\sin^2 \delta_n + 2) + \right.$$

$$\delta_n = \tan^{-1} \left[\frac{\cos \alpha \sin (\beta + \gamma_n)}{\cos \alpha \cos (\beta + \gamma_n) \cos \sigma_n + \sin \alpha \sin \sigma_n} \right], A = \cos^2 \alpha \sin^2$$

$$C = \cos \alpha \left[\cos \sigma_n \cos \alpha \sin 2(\gamma_n + \beta) + 2 \sin \alpha \sin \sigma_n \sin (\beta + \gamma_n) \right]$$

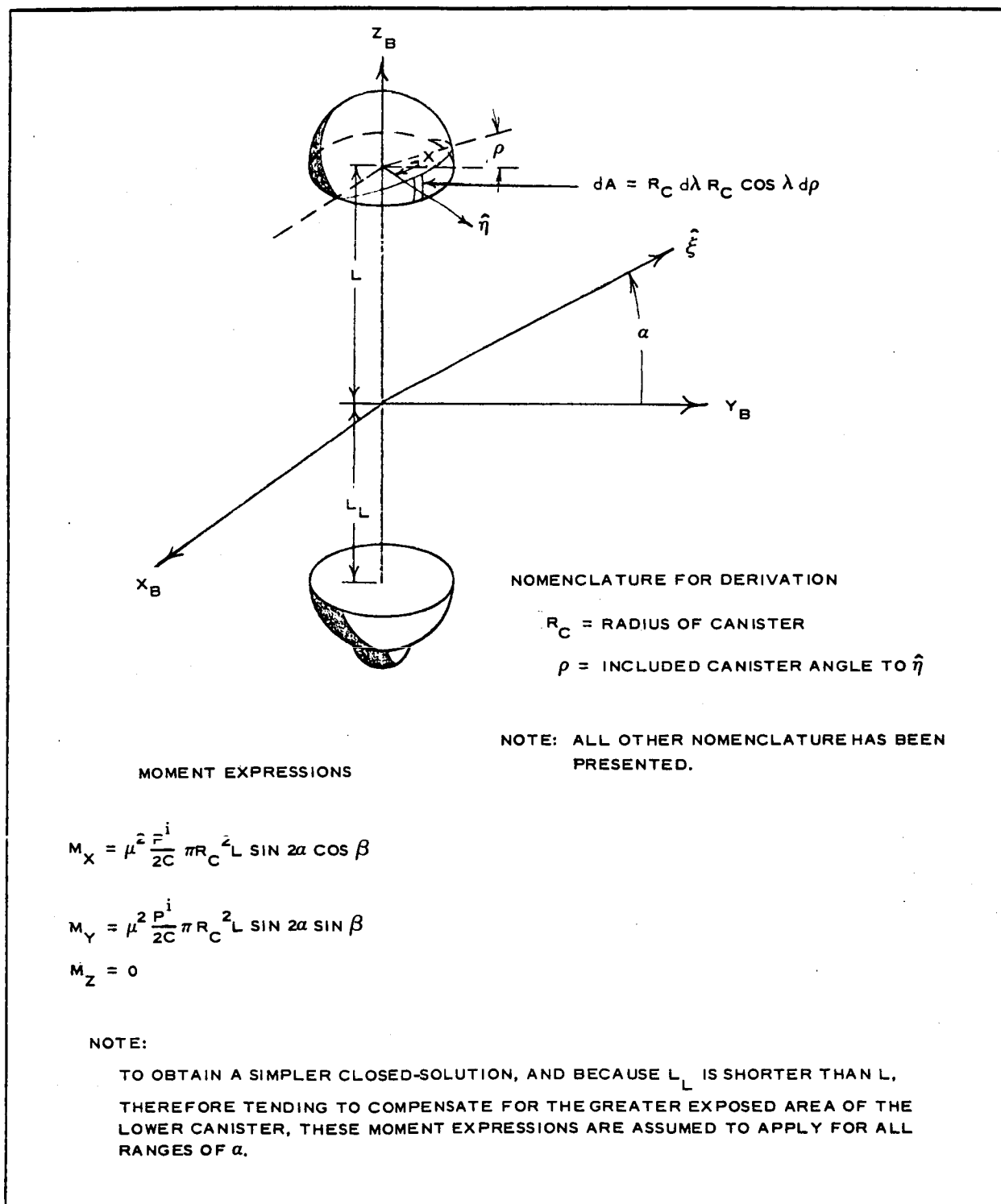


Figure 104 - Canister Subconfiguration

$$\begin{aligned}
 \overline{dF}_{\text{total}} &= \overline{dF}_{\text{outer surface}} + \overline{dF}_{\text{inner surface}} \\
 &= -\mu \frac{2P_d^L A}{C} (\hat{\xi} \cdot \hat{\eta})^2 \hat{\eta} - \mu \frac{2(1-\mu)P_d^L A}{C} (\hat{\xi} \cdot \hat{\eta})^2 \hat{\eta}
 \end{aligned}
 \tag{198}$$

Symbols used here and in subsequent equations are defined in Figures 101 through 104 or in the general simplifying assumptions.

The moments for various subconfigurations are

$$\begin{aligned}
 1. \quad \overline{dM}_{\text{lens}} &= \bar{r} \times \overline{dF}_{\text{lens}} = -\mu^2 \frac{2P_d^L A}{C} (\hat{\xi} \cdot \hat{\eta})^2 \times \\
 &\quad (\overline{-R \cos \rho_{\max}} \times \hat{\eta})
 \end{aligned}$$

or

$$\begin{aligned}
 \overline{M}_{\text{lens}} &= \int_0^{\rho_{\max}} \int_{-\pi}^{\pi} -\mu^2 \frac{2P_d^L A}{C} (\hat{\xi} \cdot \hat{\eta})^2 \times \\
 &\quad (\overline{-R \cos \rho_{\max}} \times \hat{\eta}) R^2 \sin \rho d\lambda d\rho
 \end{aligned}
 \tag{199}$$

where

$$\hat{\xi} = (-\cos \alpha \sin \beta_1 \cos d \cos \beta_1 \sin \alpha)$$

$$\hat{\eta} = (\sin \rho \cos \lambda_1 \sin \rho \sin \lambda_1 \cos \rho)$$

$$\begin{aligned}
 2. \quad \overline{dM}_{\text{canisters}} &= \sum_{n=1}^2 \left[-\mu^2 \frac{2P_d^L A_n}{C} \times \right. \\
 &\quad \left. (\hat{\xi}_n \cdot \hat{\eta}_n)^2 (\bar{L}_n \times \hat{\eta}_n) \right]
 \end{aligned}$$

or

$$\begin{aligned} \overline{M}_{\text{cans}} \quad (\beta = 0) = & \sum_{n=1}^2 \left[\int_{-\frac{\pi}{2}}^{\frac{\pi}{2}} \int_{\rho_{1n}}^{\rho_{2n}} -\mu^2 \times \right. \\ & \left. \frac{2P^L}{C} (\hat{\xi}_n \cdot \hat{\eta}_n)^2 (\overline{L}_n \times \hat{\eta}_n) \times \right. \\ & \left. R_L^2 \cos \lambda \, d\rho \, d\lambda \right] \quad (200) \end{aligned}$$

where

$$\hat{\xi} = (0, \cos \alpha, \sin \alpha)$$

$$\hat{\eta} = (-\sin \lambda_1 \cos \lambda \cos \rho_1 \cos \lambda \sin \rho)$$

For $\beta \neq 0$, the X_{B_2} and Y_B components of $\overline{M}_{\text{cans}}$ are easily obtained by rotation through β . The μ^2 factor in the case of the canisters is equivalent to a reflectance coefficient.

$$\begin{aligned} 3. \quad \overline{M}_{\text{booms}} = & \left[\sum_{n=1}^3 \left(-F_{Y_n} \frac{L_n}{2} + F_{Z_n} \frac{\alpha \cos \gamma_n}{2} \right) \text{ or} \right. \\ & \left. \sum_{n=4}^6 \left(F_{Y_n} \frac{L_n}{2} + F_{Z_n} \frac{\alpha \cos \gamma_n}{2} \right) \right] \hat{i} + \\ & \left[\sum_{n=1}^3 \left(F_{X_n} \frac{L_n}{2} - F_{Z_n} \frac{\alpha \sin \gamma_n}{2} \right) \text{ or} \right. \\ & \left. \sum_{n=4}^6 \left(F_{X_n} \frac{L_n}{2} - F_{Z_n} \frac{\alpha \sin \gamma_n}{2} \right) \right] \hat{j} + \end{aligned}$$

$$\bar{M}_{\text{booms}} = \left[\sum_{n=1}^6 \left(-F_{X_n} \frac{\alpha \cos \gamma_n}{2} + F_{Y_n} \frac{\alpha \sin \gamma_n}{2} \right) \right] \hat{k} \quad (201)$$

where

$$\bar{F}_{\text{booms}} = \frac{L_n}{\cos \sigma_n} \int_{-\frac{\pi}{2}}^{\frac{\pi}{2}} -\mu \frac{2(2-\mu)P^i}{C} r_b \times (\hat{\xi}_n \cdot \hat{\eta}_n)^2 \hat{\eta}_n d\rho$$

and

$$\hat{\xi}_n = (-\cos \alpha \sin \beta_1 \cos \alpha \cos \beta_1 \sin \alpha)$$

$$\hat{\eta} = \left[-\sin(\rho + \delta_n) \cos \gamma_n + \cos(\rho + \delta_n) \times \right. \\ \left. \cos \sigma \sin \gamma_n \cos(\rho + \delta_n) \cos \sigma_n \cos \gamma_n + \right. \\ \left. \sin(\rho + \delta_n) \sin \gamma_n \cos(\rho + \delta_n) \sin \sigma_n \right]$$

$$4. \quad d\bar{M}_{\text{torus}} = -\mu \frac{2(2-\mu)P^i dA}{C} (\hat{\xi} \cdot \hat{\eta})^2 (\bar{R}_t \times \hat{\eta})$$

or

$$\bar{M}_{\text{torus}} = \int_{+\pi}^{-\pi} \int_{\tan^{-1} \left[\frac{\sin \alpha}{\cos \alpha \cos (\lambda + \beta)} \right] - \frac{\pi}{2}}^{\tan^{-1} \left[\frac{\sin \alpha}{\cos \alpha \cos (\lambda + \beta)} \right] + \frac{\pi}{2}} \times$$

$$\begin{aligned} \bar{M}_{\text{torus}} = & -\mu \frac{2(2-\mu)P^i}{C} r_t (\hat{\xi} \cdot \hat{\eta})^2 (\bar{R}_t \times \hat{\eta}) \times \\ & (R_t + r_t \cos \rho) d\rho d\lambda \end{aligned} \quad (202)$$

where

$$\begin{aligned} \hat{\xi} &= (-\cos \alpha \sin \beta_1 \cos \alpha \cos \beta_1 \sin \alpha) \\ &= (\cos \rho \sin \lambda_1 \cos \rho \cos \lambda_1 \sin \rho) \end{aligned}$$

The total moment or body-axes components of the total moment can be obtained by adding these subconfiguration contributions. These contributions in terms of body-axes coordinates have been presented previously in Figures 101 through 104. Note that in the satellite equations of motion presented in Item 2, b, the input torques (L_{θ_1} , L_{ϕ_1} , L_{ψ_1}) are about rotational axes. Therefore, these body-axes solar-pressure moments must be rotated back through the angles ϕ_1 , and ϕ_1 and θ_1 , respectively, to obtain L_{ϕ_1} and L_{θ_1} .

(d) Earth Shadow Eclipsing

The satellite will be in the earth's shadow whenever the sun vector, $\hat{\xi}$, lies inside the cone whose vertex is at the satellite (considered as a point) and containing the earth tangentially (see Figure 105). Analytically, this condition can be embodied in an eclipsing function $\Delta (= 0 \text{ or } 1)$ defined by:

$$\Delta = \begin{cases} 0 & \text{if } \hat{\xi} \cdot \hat{Z} < -\sqrt{1 - \left(\frac{\text{earth radius}}{\text{orbit radius}}\right)^2} \\ 1 & \text{otherwise} \end{cases}$$

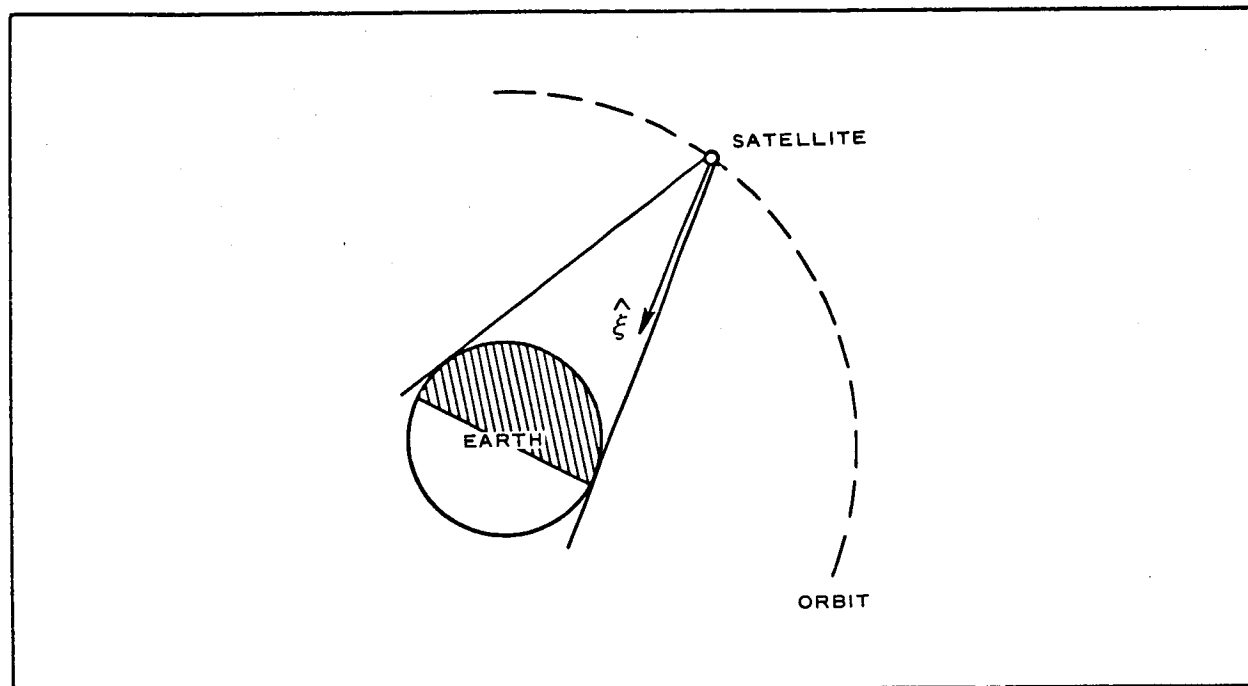


Figure 105 - Eclipse Diagram

NOTE: The sine of the cone half-angle is precisely earth radius/orbit radius. Also, since $\hat{\xi}$ is a unit vector and \hat{Z} the unit vector along the outward pointing local vertical, $-\hat{\xi} \cdot \hat{Z}$ is the cosine of the angle between $\hat{\xi}$ and the cone axis ($-\hat{Z}$). Hence (Δ) follows.

Thus, to include earth-shadowing effects, the total solar torque \bar{M} previously calculated must now be replaced by $\Delta \bar{M}$, with Δ given above.

(e) Order-of-Magnitude Analysis for Solar Pressure Moments

Order-of-magnitude analyses were conducted, which were concerned with the solar pressure moments for both the full-scale and test satellites. The contributions of the various subconfiguration surfaces over the complete sun-vector "angle-of-attack" range were compared. It was thought that some of these complex expressions could be neglected in the

steady-state response studies. However, as the data show, the subsystem moments are all of the same order of magnitude.

A breakdown of these subsystem moments about each of the ξ, η, ζ (denoted by X, Y, Z) body axes are presented in Figures 106 through 109 for a complete range of α 's at $\beta = 0$ deg. This particular β results in the largest solar moments encountered in this study, $\bar{M} = 0.0013$ ft-lb at $\alpha = -30$ deg and $\bar{M} = 0.0000079$ ft-lb at $\alpha = 0$ for the basic full-scale and test satellites, respectively. For $(I_x - I_z) = 78 \times 10^4$ slug-ft², in the full-scale-satellite case, the pitch angle for gravity-gradient equilibrium is 0.10 deg. For $(I_x - I_z) = 1310$ slug-ft² in the test-satellite case, the equilibrium pitch angle is 0.15 deg. Except for near-resonant conditions at low damping, these magnitudes of solar pressure torque should not be deleterious.

Table XXI presents a summary of the solar pressure moments and the gravity-equilibrium pitch for various photolyzed and nonphotolyzed versions of the full-scale satellite. The solar torque and equilibrium angle are also presented for the basic test satellite. These moments and the resulting angles are all for the maximum moment condition, $\beta = 0$ deg. Note that the maximum moment occurs at either $\alpha = -30$ or -45 deg in the full-scale case and $\alpha = 0$ in the test-satellite case. This occurs because the moment contribution of the booms is greatest at $\alpha = 0$, and all other subconfiguration moments are greatest at $\alpha = 45$ (or -45) deg.

As a matter of interest and comparison, an eccentricity of 0.02 (representative of Scout launch accuracy to 800-mi orbit) results in pitch oscillations of 0.9 deg for the full-scale satellite and 0.98 deg for the test satellite. The eccentricity

LENS		BOOMS		CANISTERS	
R = 200 FT		$r_b = 0.167$ FT		$R_C = 2.33$ FT	
$\rho_{MAX} = 42$ DEG		L = 300 FT		$\mu = \sqrt{0.8}$	
$\mu = 0.048$		$L_L = 188$ FT			
$P_i/C = 0.09 \times 10^{-6}$ PSF		$\sigma_U = \tan^{-1} 133.8/300$			
		$\sigma_L = -\tan^{-1} 133.8/188$			
TORUS		$\gamma_n = 0, -120$ DEG, -240 DEG			
$R_t = 143.52$ FT		$0, -120$ DEG, -240 DEG			
$r_t = 9.72$ FT		$\mu = 0.124$			
$\mu = 0.10$					
ALPHA	0. DEG	BETA	0. DEG	MOMENTS (FT-LB)	
		MX	MY	MZ	MTOT
LENS		0.00000000	0.00000000	0.00000000	0.00000000
TORUS		0.00000000	0.00000000	0.00000000	0.00000000
BOOMS		0.00072781	0.00000000	0.00000000	0.00072781
CANISTER		0.00000000	0.00000000	0.00000000	0.00000000
TOTALS		0.00072781	0.00000000	0.00000000	0.00072781
ALPHA	15.	BETA	0.		
		MX	MY	MZ	MTOT
LENS		-0.00019398	0.00000000	0.00000000	0.00019398
TORUS		-0.00028606	0.00000000	0.00000000	0.00028606
BOOMS		0.00065875	0.00000000	0.00000000	0.00065875
CANISTER		0.00009236	0.00000000	0.00000000	0.00009236
TOTALS		0.00027107	0.00000000	0.00000000	0.00027107
ALPHA	30.	BETA	0.		
		MX	MY	MZ	MTOT
LENS		-0.00033599	0.00000000	0.00000000	0.00033599
TORUS		-0.00049546	0.00000000	0.00000000	0.00049546
BOOMS		0.00051819	0.00000000	0.00000000	0.00051819
CANISTER		0.00015997	0.00000000	0.00000000	0.00015997
TOTALS		-0.00015330	0.00000000	0.00000000	0.00015330
ALPHA	45.	BETA	0.		
		MX	MY	MZ	MTOT
LENS		-0.00038797	0.00000000	0.00000000	0.00038797
TORUS		-0.00057211	0.00000000	0.00000000	0.00057211
BOOMS		0.00034432	0.00000000	0.00000000	0.00034432
CANISTER		0.00018472	0.00000000	0.00000000	0.00018472
TOTALS		-0.00043104	0.00000000	0.00000000	0.00043104
ALPHA	60.	BETA	0.		
		MX	MY	MZ	MTOT
LENS		-0.00033599	0.00000000	0.00000000	0.00033599
TORUS		-0.00049546	0.00000000	0.00000000	0.00049546
BOOMS		0.00018382	0.00000000	0.00000000	0.00018382
CANISTER		0.00015997	0.00000000	0.00000000	0.00015997
TOTALS		-0.00048767	0.00000000	0.00000000	0.00048767

Figure 106 - Solar Torques on Full-Scale Satellite - Positive α 's

SECTION III

Subsection Three - Stabilization and Orientation Systems

GER-11502

LENS		BOOMS		CANISTERS	
R = 200 FT		$r_b = 0.167$ FT		$R_C = 2.33$ FT	
$\rho_{MAX} = 42$ DEG		L = 300 FT		$\mu = \sqrt{0.8}$	
$\mu = 0.048$		$L_L = 188$ FT			
$P_i/C = 0.09 \times 10^{-6}$ PSF		$\sigma_U = \tan^{-1} 133.8/300$			
		$\sigma_L = -\tan^{-1} 133.8/188$			
TORUS					
$R_t = 143.52$ FT		$\gamma_n = 0, -120$ DEG, -240 DEG			
$r_t = 9.72$ FT		$0, -120$ DEG, -240 DEG			
$\mu = 0.10$		$\mu = 0.124$			

ALPHA -75. DEG	BETA 0. DEG	MOMENTS (FT-LB)		
		MX	MY	MTOT
LENS	0.00019399	0.00000000	0.00000000	0.00019399
TORUS	0.00028606	0.00000000	0.00000000	0.00028606
BOOMS	0.00011776	0.00000000	0.00000000	0.00011776
CANISTER	-0.00009236	0.00000000	0.00000000	0.00009236
TOTALS	0.00050544	0.00000000	0.00000000	0.00050544

ALPHA -60.	BETA 0.	MOMENTS (FT-LB)		
		MX	MY	MTOT
LENS	0.00033599	0.00000000	0.00000000	0.00033599
TORUS	0.00049546	0.00000000	0.00000000	0.00049546
BOOMS	0.00026005	0.00000000	0.00000000	0.00026005
CANISTER	-0.00015997	0.00000000	0.00000000	0.00015997
TOTALS	0.00093154	0.00000000	0.00000000	0.00093154

ALPHA -45.	BETA 0.	MOMENTS (FT-LB)		
		MX	MY	MTOT
LENS	0.00038797	0.00000000	0.00000000	0.00038797
TORUS	0.00057211	0.00000000	0.00000000	0.00057211
BOOMS	0.00043444	0.00000000	0.00000000	0.00043444
CANISTER	-0.00018472	0.00000000	0.00000000	0.00018472
TOTALS	0.00120980	0.00000000	0.00000000	0.00120980

ALPHA -30.	BETA 0.	MOMENTS (FT-LB)		
		MX	MY	MTOT
LENS	0.00033599	0.00000000	0.00000000	0.00033599
TORUS	0.00049546	0.00000000	0.00000000	0.00049546
BOOMS	0.00059873	0.00000000	0.00000000	0.00059873
CANISTER	-0.00015997	0.00000000	0.00000000	0.00015997
TOTALS	0.00127021	0.00000000	0.00000000	0.00127021

ALPHA -15.	BETA 0.	MOMENTS (FT-LB)		
		MX	MY	MTOT
LENS	0.00019398	0.00000000	0.00000000	0.00019398
TORUS	0.00028606	0.00000000	0.00000000	0.00028606
BOOMS	0.00070609	0.00000000	0.00000000	0.00070609
CANISTER	-0.00009236	0.00000000	0.00000000	0.00009236
TOTALS	0.00109377	0.00000000	0.00000000	0.00109377

Figure 107 - Solar Torques on Full-Scale Satellite - Negative α 's

SECTION III
Subsection Three - Stabilization and Orientation Systems

GER-11502

LENS		BOOMS		CANISTERS	
R = 37.4 FT		$r_b = 0.0833$ FT		$R_C = 0.833$ FT	
$\rho_{MAX} = 42$ DEG		L = 42.03 FT		$\mu = \sqrt{0.8}$	
$\mu = 0.048$		$L_L = 22.02$ FT			
$P_i/C = 0.09 \times 10^{-6}$ PSF		$\sigma_U = \tan^{-1} 25/42.03$			
		$\sigma_L = -\tan^{-1} 25/22.02$			
TORUS		$\gamma_n = 0, -120$ DEG, -240 DEG,			
$R_t = 25.81$ FT		0, -120 DEG, -240 DEG			
$r_t = 0.814$ FT		$\mu = 0.124$			
$\mu = 0.10$					

ALPHA	0. DEG	BETA	0. DEG	MOMENTS (FT-LB)	
		MX	MY	MZ	MTOT
LENS		0.00000000	0.00000000	0.00000000	0.00000000
TORUS		0.00000000	0.00000000	0.00000000	0.00000000
BOOMS		0.00000787	0.00000000	0.00000000	0.00000787
CANISTER		0.00000000	0.00000000	0.00000000	0.00000000
TOTALS		0.00000787	0.00000000	0.00000000	0.00000787

ALPHA	15.	BETA	0.	MOMENTS (FT-LB)	
		MX	MY	MZ	MTOT
LENS		-0.00000127	0.00000000	0.00000000	0.00000127
TORUS		-0.00000036	0.00000000	0.00000000	0.00000036
BOOMS		0.00000704	0.00000000	0.00000000	0.00000704
CANISTER		0.00000165	0.00000000	0.00000000	0.00000165
TOTALS		0.00000707	0.00000000	0.00000000	0.00000707

ALPHA	30.	BETA	0.	MOMENTS (FT-LB)	
		MX	MY	MZ	MTOT
LENS		-0.00000219	0.00000000	0.00000000	0.00000219
TORUS		-0.00000062	0.00000000	0.00000000	0.00000062
BOOMS		0.00000562	0.00000000	0.00000000	0.00000562
CANISTER		0.00000286	0.00000000	0.00000000	0.00000286
TOTALS		0.00000566	0.00000000	0.00000000	0.00000566

ALPHA	45.	BETA	0.	MOMENTS (FT-LB)	
		MX	MY	MZ	MTOT
LENS		-0.00000253	0.00000000	0.00000000	0.00000253
TORUS		-0.00000072	0.00000000	0.00000000	0.00000072
BOOMS		0.00000399	0.00000000	0.00000000	0.00000399
CANISTER		0.00000330	0.00000000	0.00000000	0.00000330
TOTALS		0.00000404	0.00000000	0.00000000	0.00000404

ALPHA	60.	BETA	0.	MOMENTS (FT-LB)	
		MX	MY	MZ	MTOT
LENS		-0.00000219	0.00000000	0.00000000	0.00000219
TORUS		-0.00000062	0.00000000	0.00000000	0.00000062
BOOMS		0.00000251	0.00000000	0.00000000	0.00000251
CANISTER		0.00000286	0.00000000	0.00000000	0.00000286
TOTALS		0.00000255	0.00000000	0.00000000	0.00000255

Figure 108 - Solar Torques on Test Satellite - Positive α 's

SECTION III

Subsection Three - Stabilization and Orientation Systems

GER-11502

LENS		BOOMS		CANISTERS	
R = 37.4 FT		$r_b = 0.0833$ FT		$R_c = 0.833$ FT	
$\rho_{MAX} = 42$ DEG		L = 42.03 FT		$\mu = \sqrt{0.8}$	
$\mu = 0.048$		$L_L = 22.02$ FT			
$P_i/C = 0.09 \times 10^{-6}$ PSF		$\sigma_u = \tan^{-1} 25/42.03$			
		$\sigma_L = -\tan^{-1} 25/22.02$			
		$\gamma_n = 0, -120$ DEG, -240 DEG,			
		0, -120 DEG, -240 DEG			
TORUS		$\mu = 0.124$			
$R_t = 25.81$ FT					
$r_t = 0.814$ FT					
$\mu = 0.10$					

ALPHA -75. DEG	BETA 0. DEG	MOMENTS (FT-LB)		
	MX	MY	MZ	MTOT
LENS	0.00000127	0.00000000	0.00000000	0.00000127
TORUS	0.00000036	0.00000000	0.00000000	0.00000036
BOOMS	0.00000171	0.00000000	0.00000000	0.00000171
CANISTER	-0.00000165	0.00000000	0.00000000	0.00000165
TOTALS	0.00000169	0.00000000	0.00000000	0.00000169

ALPHA -60.	BETA 0.	MOMENTS (FT-LB)		
	MX	MY	MZ	MTOT
LENS	0.00000219	0.00000000	0.00000000	0.00000219
TORUS	0.00000062	0.00000000	0.00000000	0.00000062
BOOMS	0.00000358	0.00000000	0.00000000	0.00000358
CANISTER	-0.00000286	0.00000000	0.00000000	0.00000286
TOTALS	0.00000353	0.00000000	0.00000000	0.00000353

ALPHA -45.	BETA 0.	MOMENTS (FT-LB)		
	MX	MY	MZ	MTOT
LENS	0.00000253	0.00000000	0.00000000	0.00000253
TORUS	0.00000072	0.00000000	0.00000000	0.00000072
BOOMS	0.00000537	0.00000000	0.00000000	0.00000537
CANISTER	-0.00000330	0.00000000	0.00000000	0.00000330
TOTALS	0.00000532	0.00000000	0.00000000	0.00000532

ALPHA -30.	BETA 0.	MOMENTS (FT-LB)		
	MX	MY	MZ	MTOT
LENS	0.00000219	0.00000000	0.00000000	0.00000219
TORUS	0.00000062	0.00000000	0.00000000	0.00000062
BOOMS	0.00000694	0.00000000	0.00000000	0.00000694
CANISTER	-0.00000286	0.00000000	0.00000000	0.00000286
TOTALS	0.00000689	0.00000000	0.00000000	0.00000689

ALPHA -15.	BETA 0.	MOMENTS (FT-LB)		
	MX	MY	MZ	MTOT
LENS	0.00000127	0.00000000	0.00000000	0.00000127
TORUS	0.00000036	0.00000000	0.00000000	0.00000036
BOOMS	0.00000784	0.00000000	0.00000000	0.00000784
CANISTER	-0.00000165	0.00000000	0.00000000	0.00000165
TOTALS	0.00000782	0.00000000	0.00000000	0.00000782

Figure 109 - Solar Torques on Test Satellite - Negative α 's

SECTION III

Subsection Three - Stabilization and Orientation Systems

GER-11502

TABLE XXI - SOLAR TORQUE AND GRAVITY EQUILIBRIUM ANGLE FOR
VARIOUS PHOTOLYZED VERSIONS OF THE LENTICULAR SATELLITE

No.	Satellite configuration	μ 's	β (deg)	α (deg)	M_{\max} (ft-lb)	ρ_e (deg)
1	Full-scale basic					
	Lens	0.048				
	Torus	0.100				
	Booms	0.124				
	Canisters	$\sqrt{0.8}$	0	-30	0.00127	0.097
2	Full-scale torus - photolyzed					
	Lens	0.048				
	Torus	0				
	Booms	0.124				
	Canisters	$\sqrt{0.8}$	0	-15	0.00081	0.052
3	Full-scale booms - photolyzed					
	Lens	0.048				
	Torus	0.100				
	Booms	0.024				
	Canisters	$\sqrt{0.8}$	0	-45	0.00086	0.065
4	Full-scale - all photolyzed					
	Lens	0.048				
	Torus	0				
	Booms	0.024				
	Canisters	$\sqrt{0.8}$	0	-30	0.00030	0.019
5	Full-scale - nonphotolyzed					
	Lens	0.148				
	Torus	0.100				
	Booms	0.124				
	Canisters	$\sqrt{0.8}$	0	-45	0.00451	0.363
6	Test-satellite basic					
	Lens	0.048				
	Torus	0.100				
	Booms	0.124				
	Canisters	$\sqrt{0.8}$	0	0	0.000008	0.152

effects are introduced at orbital frequency, while the solar torques enter at both one and two times orbital frequency.

(3) Orbital Eccentricity Effects

(a) General

A conservative philosophy of designing for the conditions attainable by the less sophisticated Scout-launched test satellite has been applied. From Reference 15, an altitude band encompassing a 95-percent probability for an 800-mi orbit and assuming a 2-deg tip-off error would be approximately 800 ± 115 mi. This results in an initial orbital eccentricity of 0.02, which for the test satellite results in a gravity-gradient equilibrium pitch angle of 0.98 deg; for this eccentricity, it is slightly less (0.9 deg) in the case of the full-scale satellite and mission.

Because of solar pressure effects upon the orbit, the perigee altitude of an eccentric orbit will oscillate, thus causing a variation in eccentricity after injection. Depending upon this eccentricity variation, which is a function of the time of day of launch and the initial orbital parameters, the lifetime of a satellite may vary by as much as a factor of 10.

The eccentricity appears at orbital frequency as a near-sinusoidal forcing function in pitch. For small eccentricities, this forcing function can be simulated by

$$L_y = 2eI_y \bar{\omega}^2 \sin \bar{\omega}t \text{ ft-lb}, \quad (203)$$

where

I_y = pitch moment of inertia, slug ft²;

e = eccentricity; and

$\bar{\omega}$ = average orbital frequency, rad per second.

The Rice-Wilberforce damping system has demonstrated that it will quite satisfactorily dissipate this energy input.

(b) Analog Computer Study

The effect of orbital eccentricity was introduced into the pitch-plane analog simulation as a sinusoidal torque acting about the pitch axis.

$$\begin{aligned} L_y(t) &= L_y \sin \omega_o t \\ &= 0.021 \text{ ft-lb} \end{aligned} \quad (204)$$

for $e = 0.03$.

The simulation was rescaled to improve accuracy of the small angular displacements resulting from this disturbance. Computer runs (Figures 110 through 113), show the combined effects of this disturbance and an initial-condition pitch error of 10 deg. The four damper configurations used for the transient response studies were used for these runs. The runs show that in all cases the final steady-state response for an eccentricity of 0.03 is approximately ± 1.5 deg. The Rice-Wilberforce/alternate-configuration run also shows that the damping of the fundamental pitch oscillation is poor at low amplitudes and results in a forced oscillation at ω_o from orbital eccentricity plus a very poorly damped pitch oscillation of comparable magnitude.

3. ORIENTATION SYSTEM

a. General

The orientation system will consist of a sequencer and two stages of yo-yo despin devices. Its task will be to minimize the angular displacement and rate relative to the moving local vertical at satellite deployment. The sequencer will be initiated by ground-radio command when the canister separates from the final boost stage,

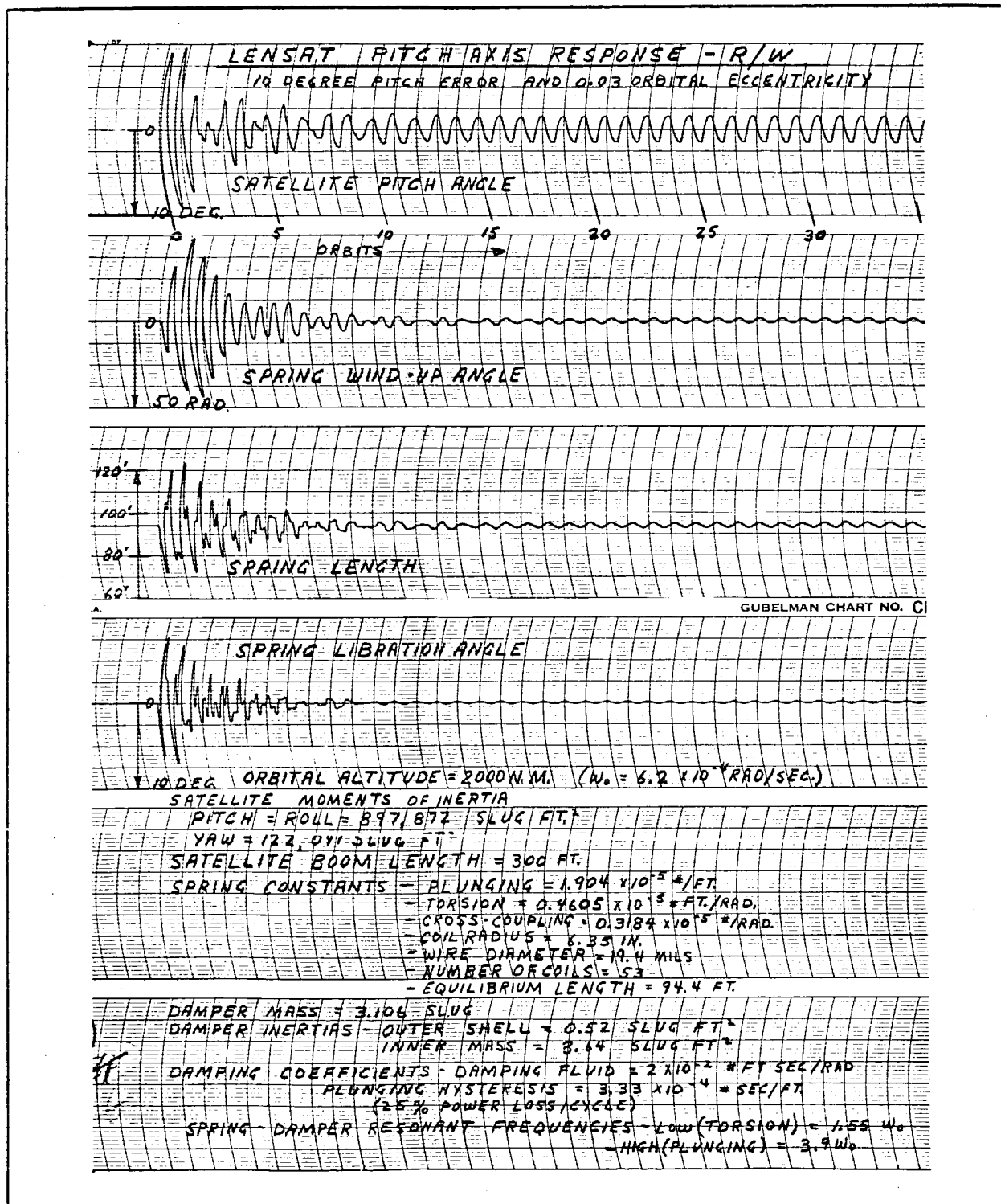


Figure 110 - Pitch-Axis Response - Rice-Wilberforce

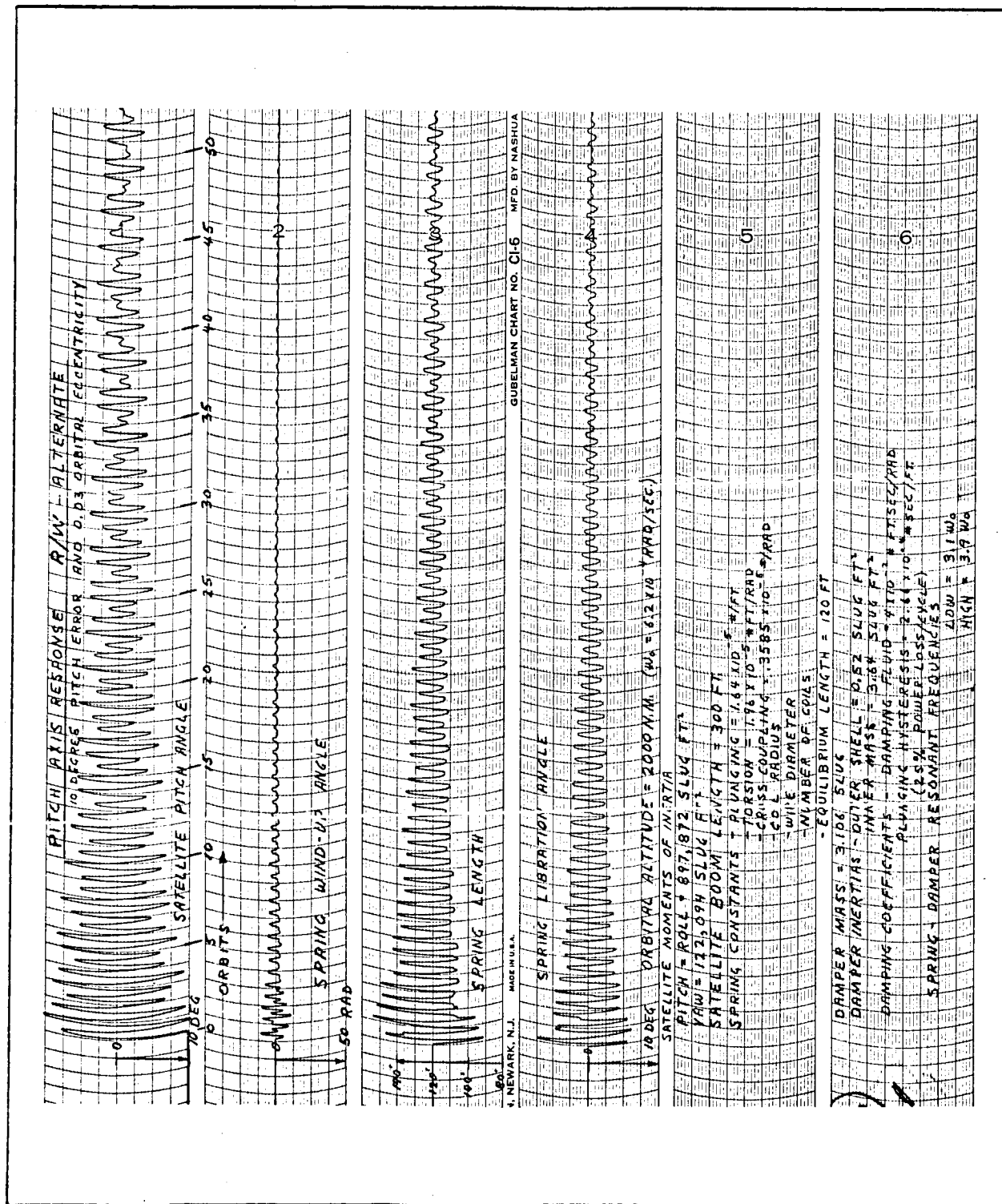


Figure 111 - Pitch-Axis Response - Rice-Wilberforce Alternate

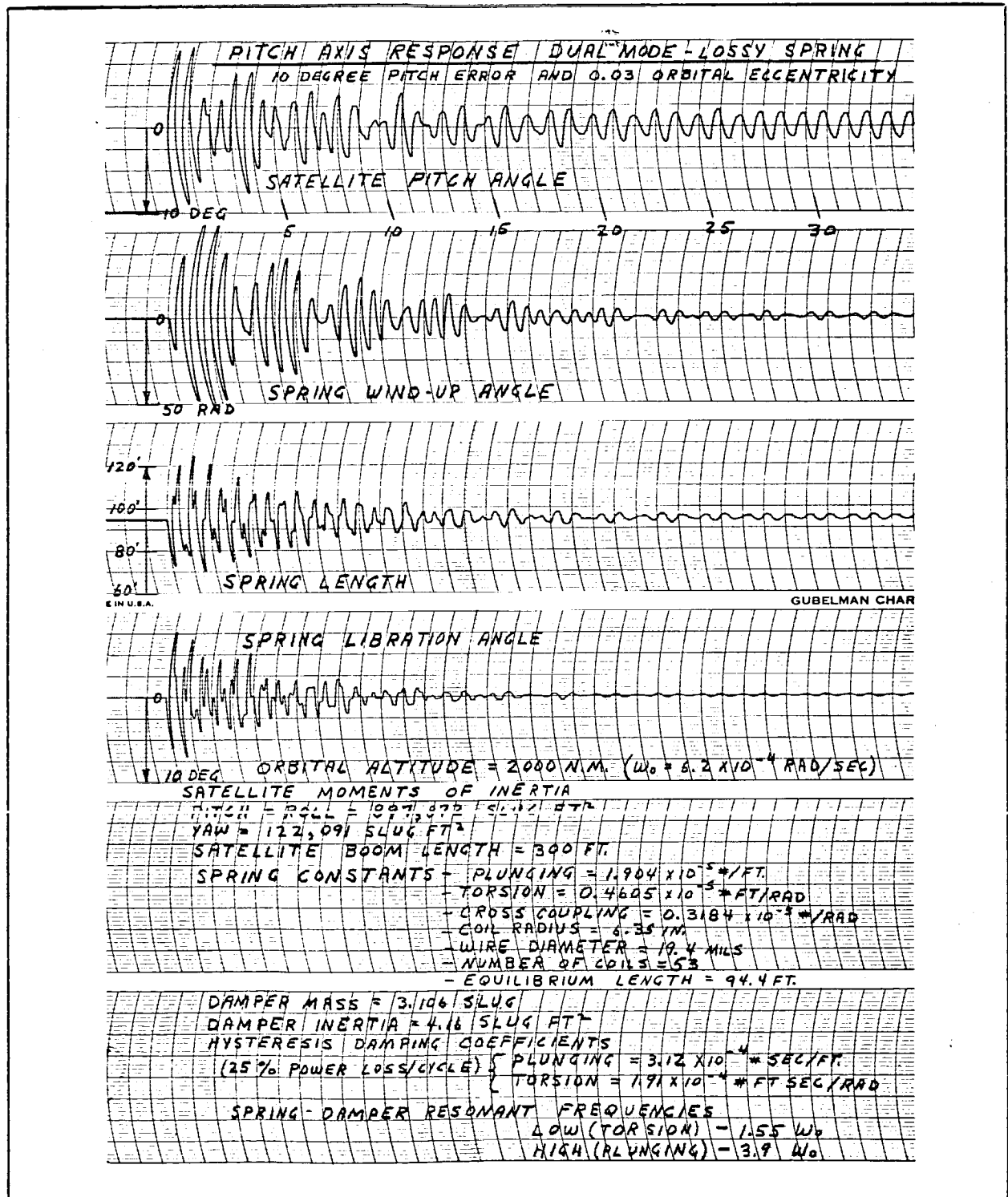


Figure 112 - Pitch-Axis Response - Dual Mode, Lossy Spring

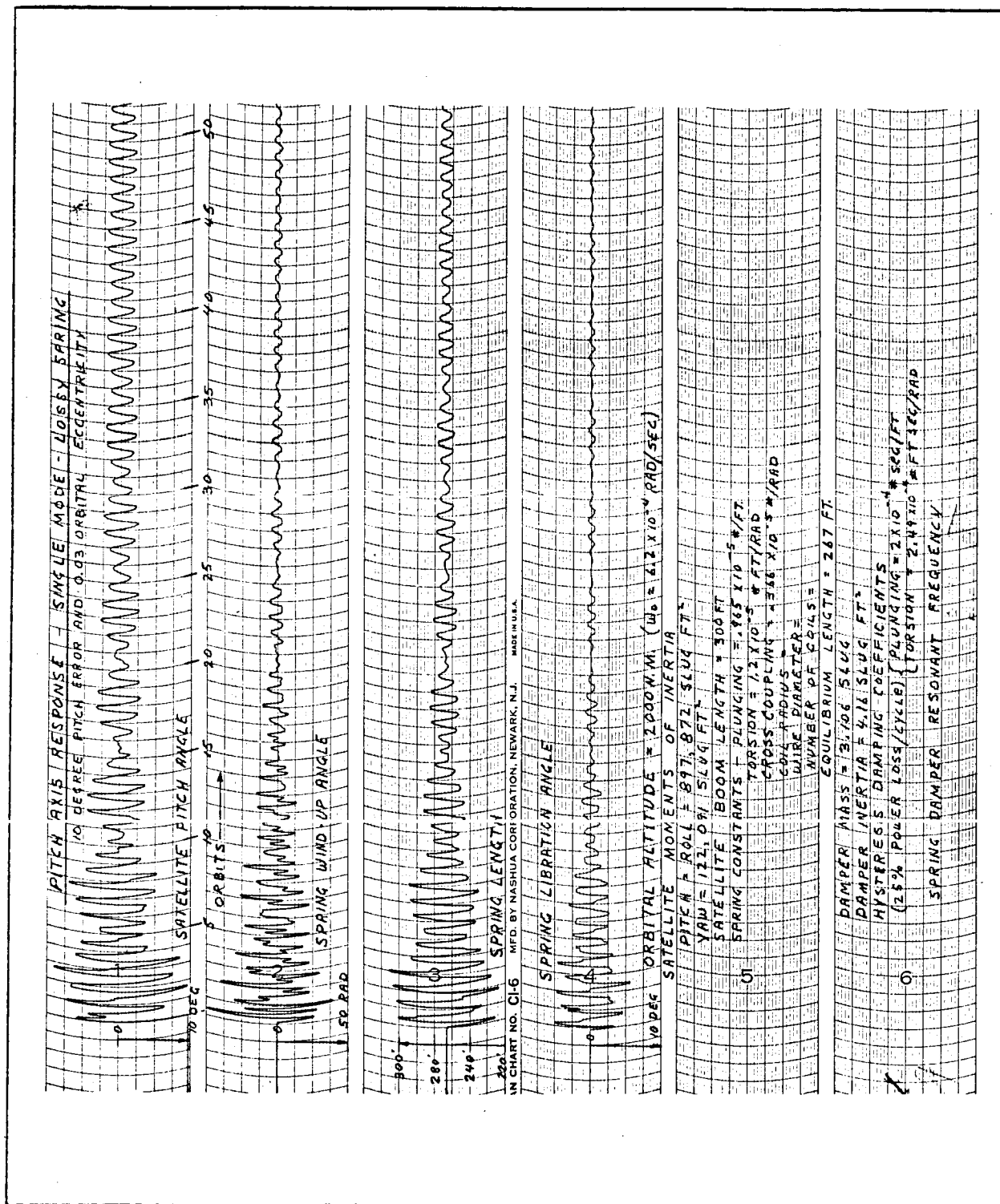


Figure 113 - Pitch-Axis Response - Single Mode, Lossy Spring

approximately three-fourths of the way around the earth from the launch site. The following sequence will then proceed automatically:

1. Despin canister
2. Separate canister halves
3. Deploy, inflate, and rigidize satellite
4. Exhaust inflation gas

The suggested sequence for placing the lenticular test satellite in orbit is shown in Figure 114.

A conservative philosophy has been applied in arriving at the initial orbital orientation for design purposes. The transient response study results show that the GAC stabilization and damping system will quite satisfactorily acquire the desired orbital dynamics for mission purposes from these conservative initial conditions. Because the guidance and control accuracy of boosters capable of placing the full-scale

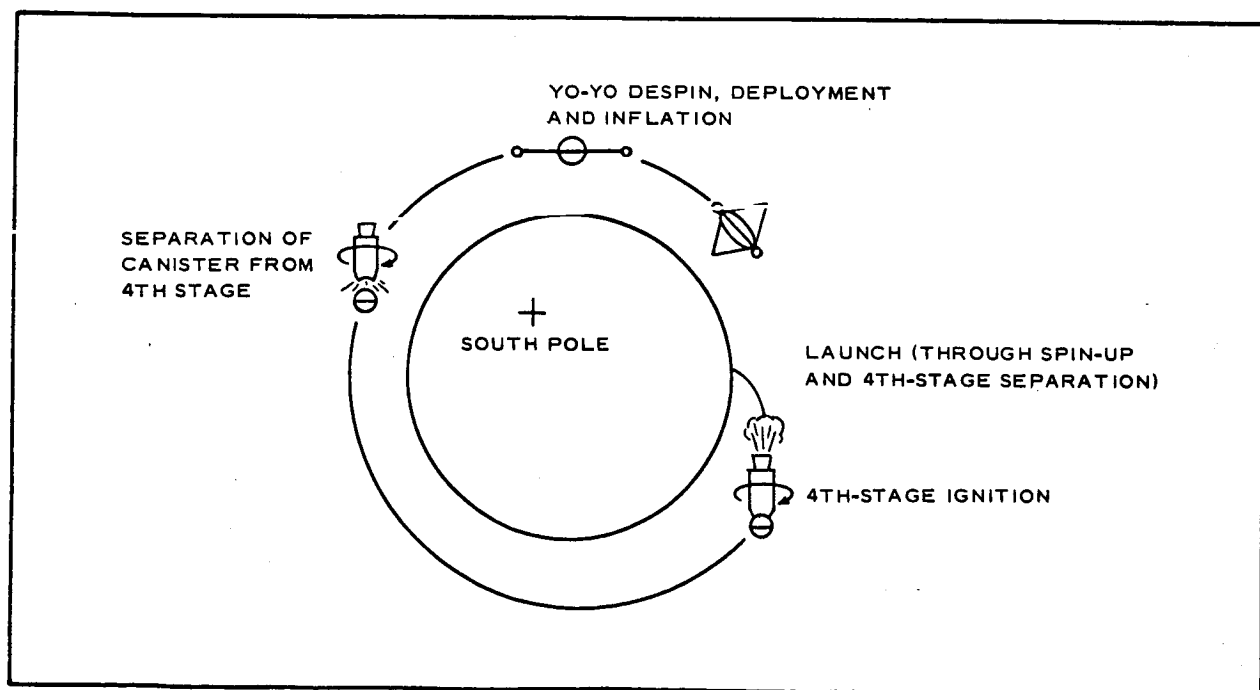


Figure 114 - Launch and Deployment Sequence

lenticular satellite in orbit is an order of magnitude better than the Scout launch vehicle, which is proposed for the test satellite, representative Scout injection errors have been used for design purposes. These injection errors will appear as initial orbit eccentricity and attitude angles and rates. Since the final stage of the Scout launch vehicle is spin stabilized, this will result in a residual yaw rate after despin in addition to other typical disturbances from sources such as thrust misalignment, mass unbalance, or tip-off error.

b. Spin-Up and Coning Angle

The Scout spin-up system (Reference 16) will, with a canister spin-axis moment of inertia of 1.50 slug-ft^2 , spin the fourth stage to approximately 146 rpm. Half cone angles from 2 to 3 deg are possible (Reference 17) from four disturbance sources: (1) dynamic unbalance of the fourth stage, (2) lateral impulse at fourth-stage ignition, (3) fourth-stage thrust misalignment, and (4) tip-off error at payload separation. The rms sum of these disturbances is 4.6 deg. Arithmetically, they add up to 10 deg. These half-cone angles would appear as pitch or roll angles after despin of the canister.

c. Despin of the Canister

The canister payload will be despun by a two-stage yo-yo despin system. The two-stage system is advantageous over a one-stage system because it results in greater despin accuracy. Another item to be considered in the actual design of a despin system is the internal stress caused by the rapid angular deceleration. The two-stage system does not alleviate the internal stress or packaging problem, but results in a less stringent release requirement at the end of the second stage. Utilizing smaller weights and unwinding the cables from a smaller diameter increases the time to despin and therefore tends to alleviate the internal stress problem.

In the lenticular satellite application, the objective is to despin to zero rpm. This is an advantage, since for a given spin moment of

inertia value, despin to zero is independent of the initial spin rate. The method of analysis employed in this study is presented in Reference 18. The data presented are based on unwinding two 2-oz and two 3-oz weights for the two stages, respectively, from the maximum 12-in. diameter about the spin axis and releasing them at a radial position. The following formula results in the necessary cord length to despin to any desired rpm:

$$\frac{I}{m(\ell + r)^2} = \frac{1 + \lambda}{1 - \lambda}, \quad (205)$$

where

I = canister spin moment of inertia, 1.50 slug-ft²;

m = mass of despin weights plus one-third mass of cords, 0.008 slugs;

ℓ = length of cords, feet;

r = radius of coiled cords, 1.0 ft; and

λ = ratio of desired final rpm to initial rpm.

Applying this formula, first-stage despin cord lengths of 12.2 ft will despin the canister from 146 rpm to 5.4 rpm in 0.94 sec, and second-stage cord lengths of 10.25 ft will despin the canister to 0 rpm in an additional 21.9 sec. Assuming a despin accuracy of ± 3 percent of initial-spin rpm for each stage results in an over-all despin accuracy of ± 0.11 percent, which for the initial 146 rpm leaves a residual spin of only 1 deg per second. This spin would appear as a yaw-angle rate and would be further attenuated by a factor of 240 as the satellite deploys to a yaw inertia of 360 slug-ft².

The maximum tension in any stage is encountered when the cords are unwinding but still tangent to the cylinder about which they are unwinding. The formula used to compute this tension is

$$T_{\max} = \frac{3\sqrt{3}}{4} \omega_o^2 \frac{I}{\sqrt{\frac{I}{m} + r^2}}, \quad (206)$$

where

T_{\max} = maximum tension in cords, lb; and

ω_o = initial spin rpm.

For the first stage, this results in a tension of 33.2 lb, and for the second stage a value of 0.055 lb. Piano wire of 0.015-in. diameter (tensile strength = 60 lb) will provide the necessary tensile strength.

d. Initial Orientation

For a fourth-stage tip-off error of 2 deg, a 95-percent probability encompasses an altitude variation of approximately 0 ± 115 mi for a desired circular orbital altitude of 800 mi (Reference 15). This results in an initial orbital eccentricity of 0.02. Half-cone angles as large as 10 deg are possible, which in combination with an initial rate error equivalent to the orbital rate of $8.7 \cdot 10^{-4}$ rad per second will result in initial oscillations in pitch or roll of approximately ± 40 deg for the test satellite. Initial oscillations of the full-scale satellite will be no greater than 40 deg because of the increased guidance and control accuracy anticipated for the full-scale satellite.

4. CONCLUSIONS AND RECOMMENDATIONS

On the basis of studies made so far, it has been shown that the application of gravity-gradient stabilization to a lenticular-shaped communication satellite is definitely feasible. It is therefore recommended that the study be continued. A very efficient gravity-gradient libration damper (the Rice-Wilberforce damper) has been discovered. Further study of the transient and steady-state stabilization accuracy needs to be done, however. The optimum-tuning theory for this damper, which has been

SECTION III

Subsection Three - Stabilization and Orientation Systems

GER-11502

developed during Phase I, needs to be verified with a complete eight-degree-of-freedom simulation of the equations of motion of the satellite. More studies need to be made of the effects of solar pressure and orbital eccentricity in generating steady-state attitude errors. Especially pertinent here is the influence of the various reflecting-to-total-surface-area ratios of the satellite subsystems as functions of the type of satellite structural material, wire mesh size, and degree of photolyzability of the film. Also, the effects of sun-line angle of attack on this reflecting-to-total-surface-area ratio and the effects of a non-lens-centered center of mass must be investigated.

Hardware studies of the Rice-Wilberforce damper should be made to examine the questions of physical realizability of the helical spring and required damping-fluid parameters, the pivot problem of the damper element, and the general questions of deployability of the damper. Also, the question of using an active orientation system to provide a relaxed gravity-gradient capture problem at the time of satellite deployment needs to be examined. Various approaches to the problems due to the rather indeterminate body-axis moments of inertia during inflation of the satellite also require further study.

SECTION III - TECHNICAL DISCUSSION - PHASES I AND II

Subsection Four - Microwave Analysis and Tests

1. GENERAL

A microwave analysis and test program was undertaken to prove the feasibility of the lenticular configuration as a passive relay satellite. A preliminary investigation of the lenticular shape indicated that a significant radar return was to be expected because of the edge diffraction phenomenon. This return combined with the return from the spherical portion of the lenticular shape would cause large amplitude variations with changes of frequency. Theoretical calculations of the edge diffraction were made, and a computer program was set up to calculate the expected radar returns as a function of frequency.

Reflectivity measurements were made on a scale model of the lenticular shape in an effort to accomplish the following:

1. Experimentally determine the magnitude of the edge diffraction return for correlation with the return predicted by theory.
2. Predict the over-all return that might be expected from the full-scale and flight-test satellites.

Technical literature was reviewed and consultants were used to determine the state-of-the-art of diffraction analysis, to direct further analysis, and to establish valid reflectivity measurement procedures. Theoretical consideration was given to the effect of the boom and canister on radar return, the reflectivity of the wire-grid material used for lens caps, and the effect of the lens surface tolerance.

2. EDGE DIFFRACTION ANALYSIS

a. Theoretical Approach

A theoretical analysis was undertaken to determine if the radar return due to the edge diffraction and the radar return from the front convex surface of the satellite are comparable in magnitude. The results of the analysis on the 267-ft-diameter, 200-ft-radius-of-curvature lenticular shape are as follows:

1. Radar cross section of convex surface (center spherical portion of the lenticular shape)¹⁹

$$\sigma_c = 1.2 \times 10^4 \text{ m}^2 \quad \leftarrow \text{Diagram of a lenticular shape with a single arrow pointing to its convex surface.} \quad (207)$$

2. Radar cross section of edge diffraction of 267-ft-diameter lenticular shape¹⁹

$$\sigma_e = 0.83 \times 10^4 \text{ m}^2 \quad \leftarrow \text{Diagram of a lenticular shape with two arrows pointing to its edges.} \quad (208)$$

Since the magnitude of the over-all lenticular return due to constructive and destructive interference between the two returns is given by

$$\sigma_T = (\sqrt{\sigma_c} \pm \sqrt{\sigma_e})^2, \quad (209)$$

it can be seen that the resultant return from the proposed configuration could suffer from large amplitude variations. The variation was

computed to be approximately 21.5 db for the nose-on monostatic conditions.

Equation 209 describes the magnitude of the variations but does not show the variations as a function of frequency. For this reason, the impulse scattering technique²⁰ was used to describe the radar cross section as a function of frequency for the cases where the low-frequency and high-frequency return and the shape of the scattering object are known.

After consultation with Dr. Kennough,^a the impulse scattering equations were simplified and the edge diffraction pulse was redefined from the work of Keller.²¹

A computer program was then set up to evaluate the equations and to obtain numerical results over a wide frequency band. The results of the computer analysis, an explanation of the graphs of return versus frequency, and the equations of the radar return are presented in Appendix F. In general, the results show that the nose-on monostatic return from the lenticular shape varies by 21.5 db and that a complete cycle of constructive and destructive interference occurs with a 10-mc frequency change for the 267-ft-diameter lenticular satellite.

b. Reflectivity Tests

(1) General

The purposes of the lenticular satellite reflectivity tests were:

1. To determine the peak magnitude of the edge scattering or diffraction return for correlation with the return predicted by theory.

^aOhio State University, Antenna Laboratory.

2. To determine the over-all return that might be obtained from the complete satellite.

A scale model of the lenticular satellite was fabricated, and reflectivity patterns were taken on a 150-ft test range. Although it would be desirable to determine the peak magnitude and distribution of the spectral return (the return from the center portion of the model, neglecting edge effects), it did not appear that this could be readily obtained from direct reflectivity measurements. However, the phase interference relationship between the edge effects and the center spectral return was apparent when patterns of the complete model were compared with the pattern of a reference sphere (essentially a constant return as the sphere is rotated). An approximation of the magnitude of the edge return could then be made, and the validity of the edge diffraction equations for the lenticular shape could be established by comparing the measured and theoretical edge return.

(2) Test Model

A scale model (Figures 115 and 116) of the lenticular satellite was constructed by gluing wooden strips together and forming them to the desired shape on a lathe. The model was then coated with conducting paint for the radar cross section measurements. A size was chosen that would enable valid reflectivity data to be obtained. Ease of model handling and the reception of a large signal for the far-field conditions were also considered. A 15-in.-radius-of-curvature model with an 84-deg included angle was chosen, thus providing a 20-in.-diameter model (Figure 117). The model width-to-wave-length ratio at X band is considerably out of the resonant region (the region where the radar cross section and the return from a spherical shape vary considerably with a change frequency). Also, the depth is 4 in. for one curved

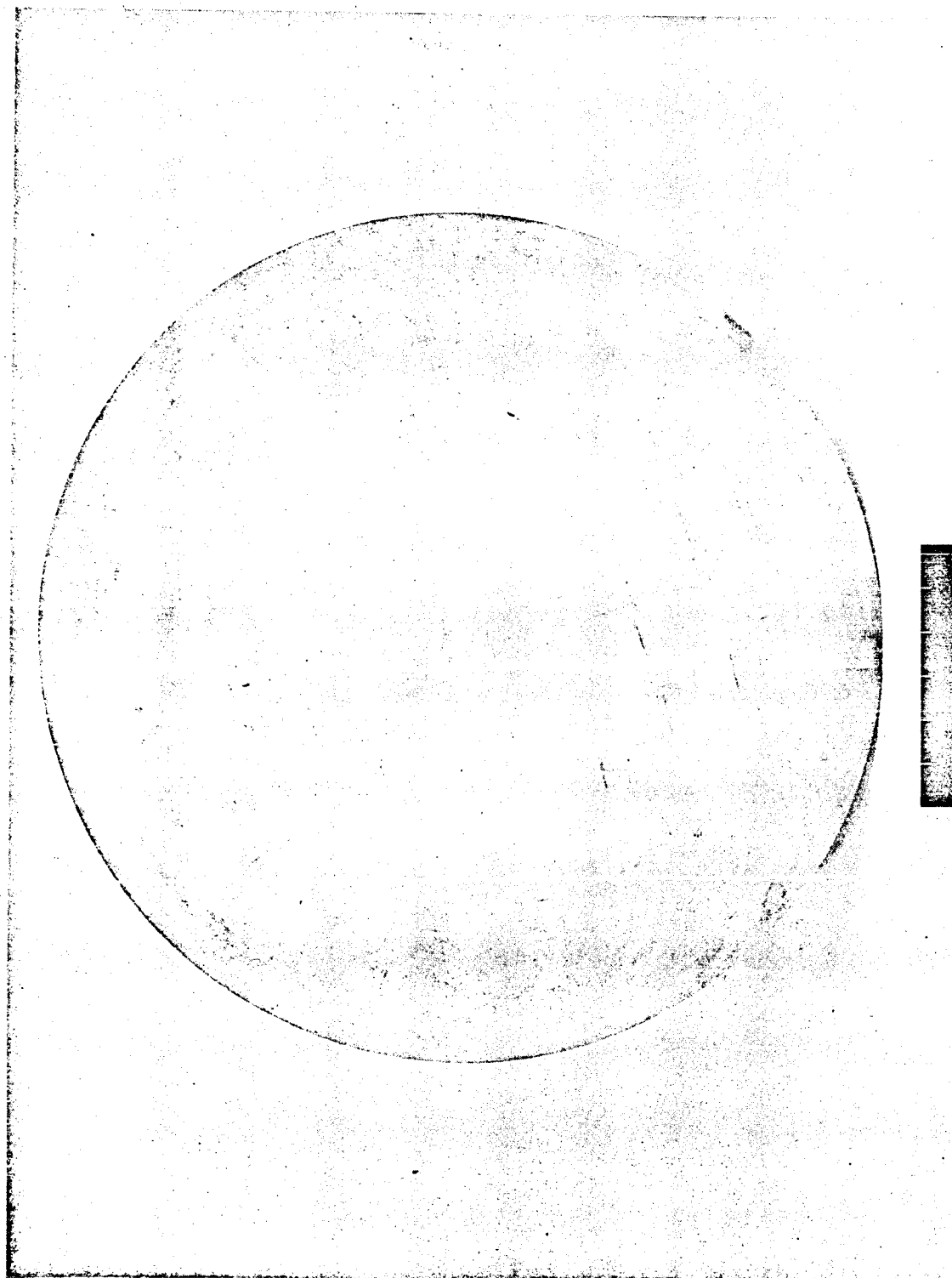


Figure 115 - Reflectivity Test Model (Front View)

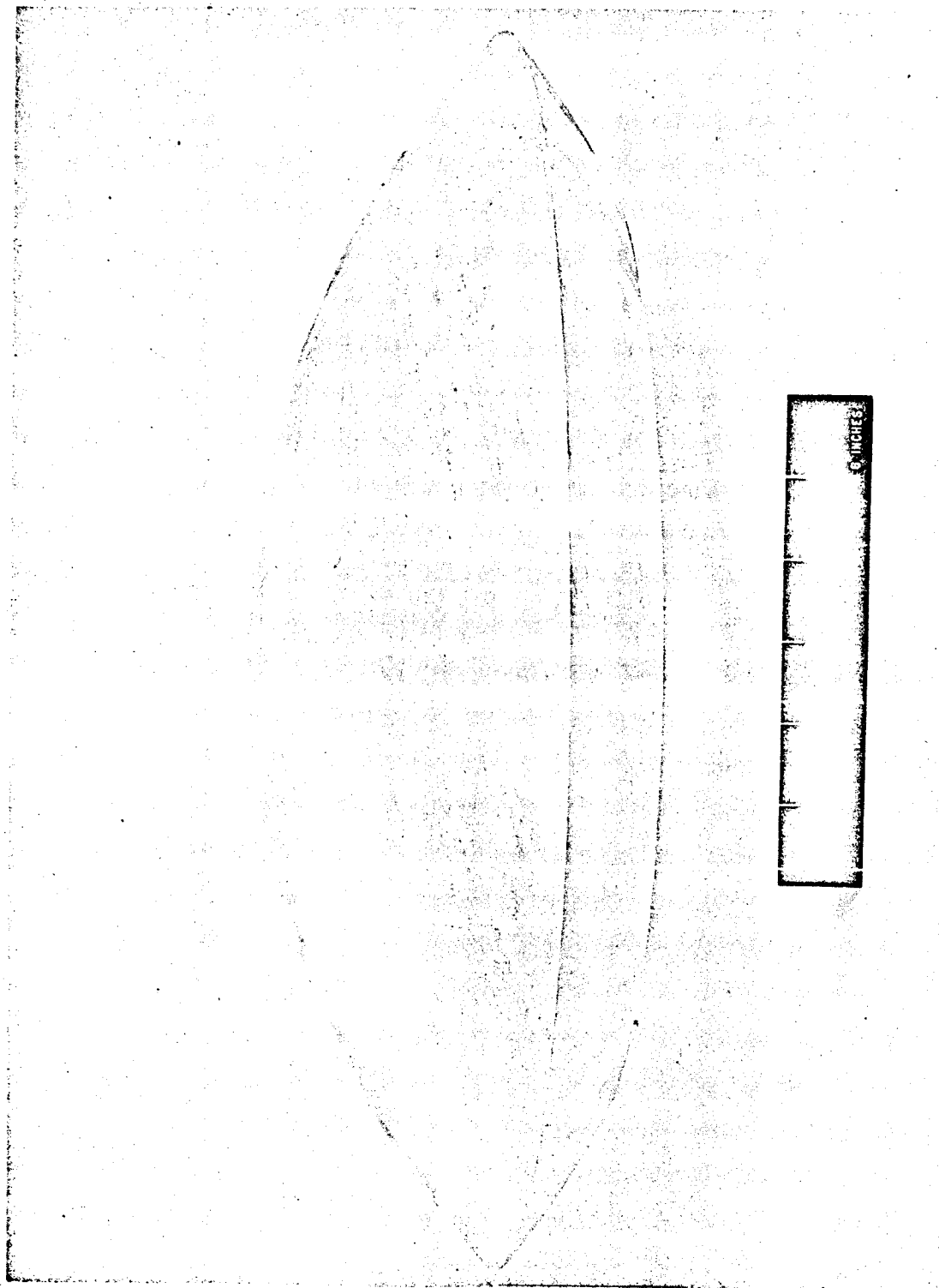


Figure 116 - Reflectivity Test Model (Side View)

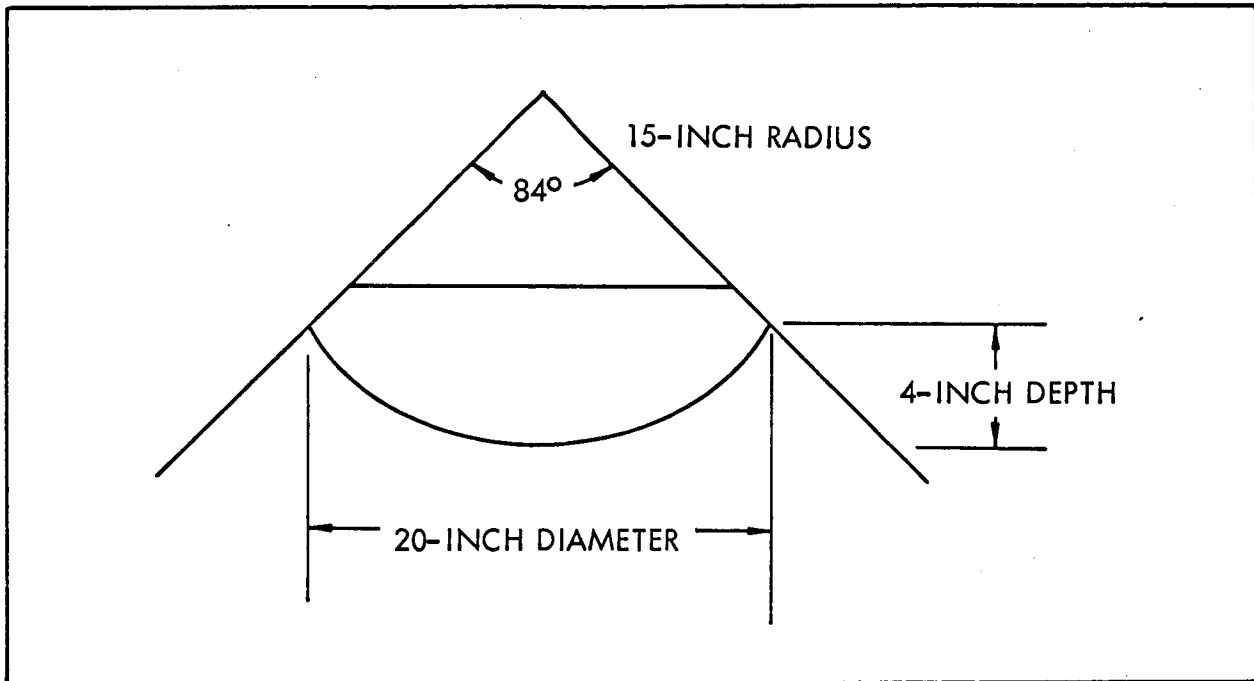


Figure 117 - Reflectivity Test Model Dimensions

portion of the model. Therefore, approximately 16 Fresnel zones illuminate the model in the nose-on direction, which is sufficient to obtain the spectral return of πR^2 (that of a sphere).²² It was not the intent of the reflectivity model tests to simulate the actual pattern of the full-scale model at its operating frequencies, but rather to determine the reflection characteristics that are independent of frequency. For example, while the actual interference pattern of the edge diffraction return and the center spectral return is dependent on frequency, the peak scattering and the envelope of the edge scattering are relatively independent of frequency.

(3) Test Range and Equipment

A 150-ft reflectivity range was set up to take reflectivity patterns of the 20-in. model at X band frequencies. A block diagram of the setup is shown in Figure 118 and a diagram of the range is shown in Figure 119. The range was of sufficient length to ensure

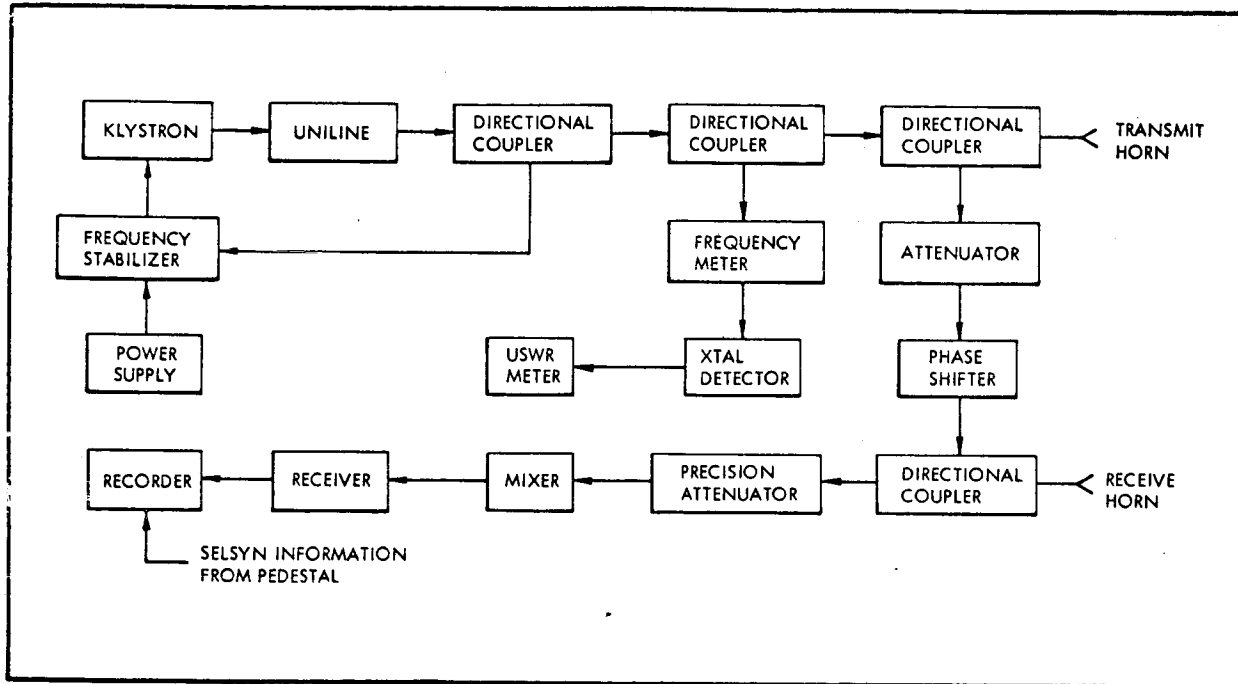


Figure 118 - Block Diagram of Reflectivity Range Equipments

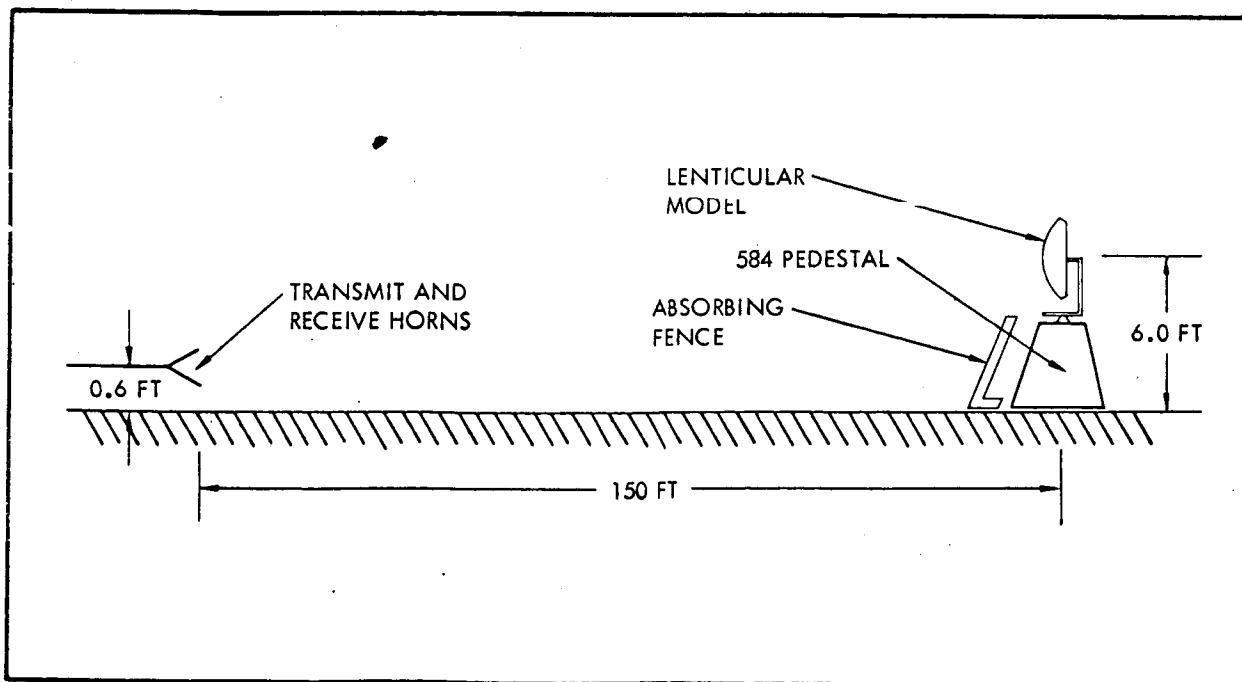


Figure 119 - Reflectivity Range (Side View)

far-field reflectivity characteristics and short enough to provide an adequate signal level to reduce errors caused by noise returns. The model was mounted 6-ft above the ground on a rotating pedestal and 150 ft from two standard-gain horns used as the transmitter and the receiver. These horns were mounted 0.6 ft above the ground. These conditions provide the following range parameters:

1. Phase variation over model - $< \lambda/16$
2. Amplitude variation over model
 - Width - < 0.25 db
 - Height - < 0.35 db

A noise cancelling network was used to decrease or null-out the background noise, and a fence of r-f absorbing material was placed in front of the pedestal to reduce the return signal from the pedestal and mount.

Table XXII lists the test equipment used for reflectivity measurements of the 20-in. lenticular model. All critical equipments were calibrated prior to reflectivity measurements.

TABLE XXII - TEST EQUIPMENT FOR 20-IN. MODEL
REFLECTIVITY TESTS

Item	Model number	Manufacturer
Directional couplers	402	PRD Electronics Inc.
Uniline	R-88.96	Cascade
Klystron	V-58	Variac Co.
Frequency stabilizer	2650A	Dymec Div. of Hewlett-Packard Co.
Power supply	801A	PRD Electronics Inc.
Attenuator	195B	PRD Electronics Inc.

TABLE XXII - TEST EQUIPMENT FOR 20-IN. MODEL
REFLECTIVITY TESTS (Continued)

Item	Model number	Manufacturer
Phase shifter	X-885A	Hewlett-Packard Co.
Frequency meter	585A	PRD Electronics Inc.
Detector
VSWR meter	415B	Hewlett-Packard Co.
Precision attenuator	X-382A	Hewlett-Packard Co.
Mixer	M-8.2	Scientific-Atlanta Inc.
Receiver	402C	Scientific-Atlanta Inc.
Recorder	APR/20/30	Scientific-Atlanta Inc.
Pedestal	584	. . .
Horns	Standard gain	Goodyear Aerospace

(4) Test Method

The 20-in. lenticular model was tested on the 150-ft reflectivity range under monostatic conditions (transmit and receive horns at the same point) for frequencies between 8570 and 9830 mc, to determine the effects of phasing between the edge diffraction return and the specular return. For each frequency of test, the following procedure was followed:

1. The mount, which holds a 20-in. reference sphere, was placed on the rotating pedestal.
2. The background noise level received was nulled out (to reduce errors in reflectivity patterns due to high noise level) by means of the noise cancelling network and positioning of the r-f absorber fence in front of the pedestal.
3. A pattern of received noise was then taken as

- the mount was rotated ± 90 deg to ensure that the mount noise level did not increase with mount rotation.
4. The 20-in. sphere was then placed on the mount and rotated ± 90 deg to establish a reference level pattern.
 5. The 20-in. sphere and its mount were then removed, and the mounting fixture for the lenticular model was installed.
 6. The background noise level was then rechecked and renulled, if necessary, and the mount was rotated ± 90 deg to ensure that the mount noise level did not increase with mount rotation.
 7. The lenticular model was then placed on its mount, and a reflectivity pattern was taken over ± 90 deg from nose-on.
 8. The lenticular model was then removed, and the background noise level was rechecked to ensure that there had not been an increase during the reflectivity measurement.
 9. The transmitter and receiver were then retuned to the next test frequency, and the above procedure was repeated.

Figure 120 shows relative positions of the transmit and receive horns and the lenticular model.

(5) Test Data

Test data were obtained from the monostatic reflectivity patterns taken on the lenticular model. Figures 121, 122, and 123 show representative patterns. Figure 121 shows apparent constructive interference between the edge and center spectral

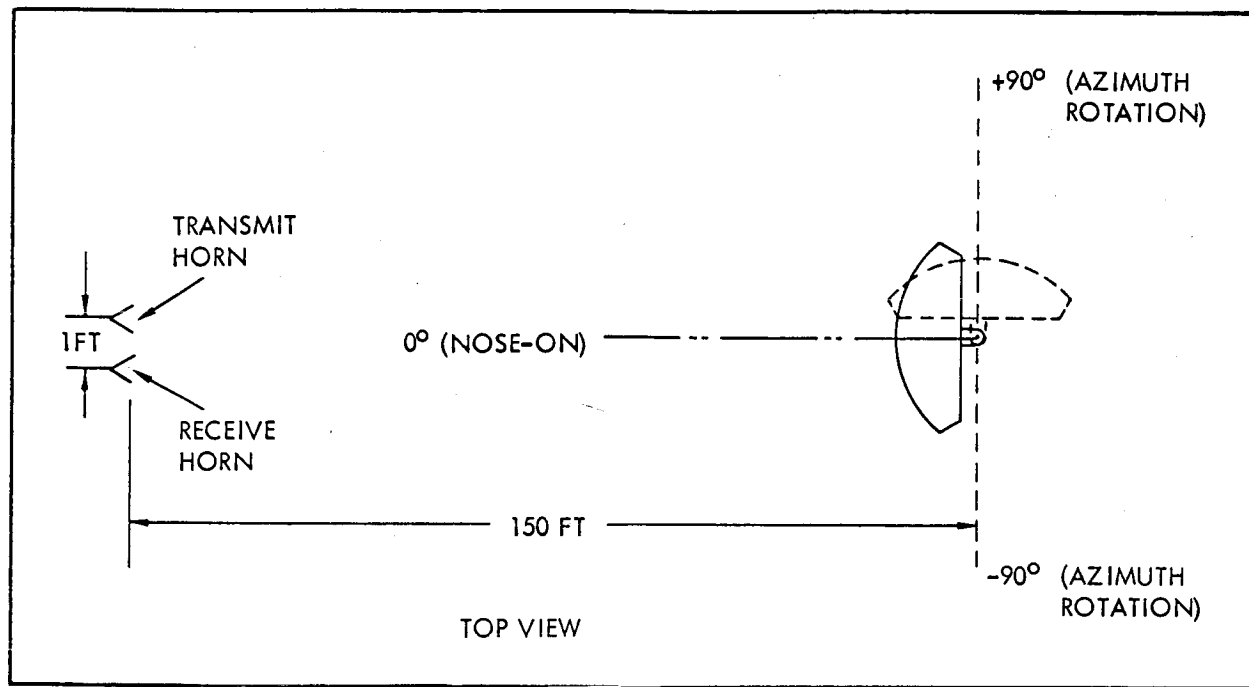


Figure 120 - Monostatic Reflectivity Measurements

returns. Figure 122 indicates apparent destructive interference (nose-on, ± 1.33 -deg region). Figure 123 shows an apparent 90-deg phase relationship between the edge and center returns.

Each reflectivity pattern contained the following:

1. Noise level of the reference sphere mount
2. The reference sphere reflectivity pattern
3. Noise level of the lenticular mount
4. The lenticular model reflectivity pattern

From the reflectivity patterns, the following items of data listed in Table XXIII were obtained:

1. Reference sphere return above noise (average)
2. Average lenticular return (over azimuth angles

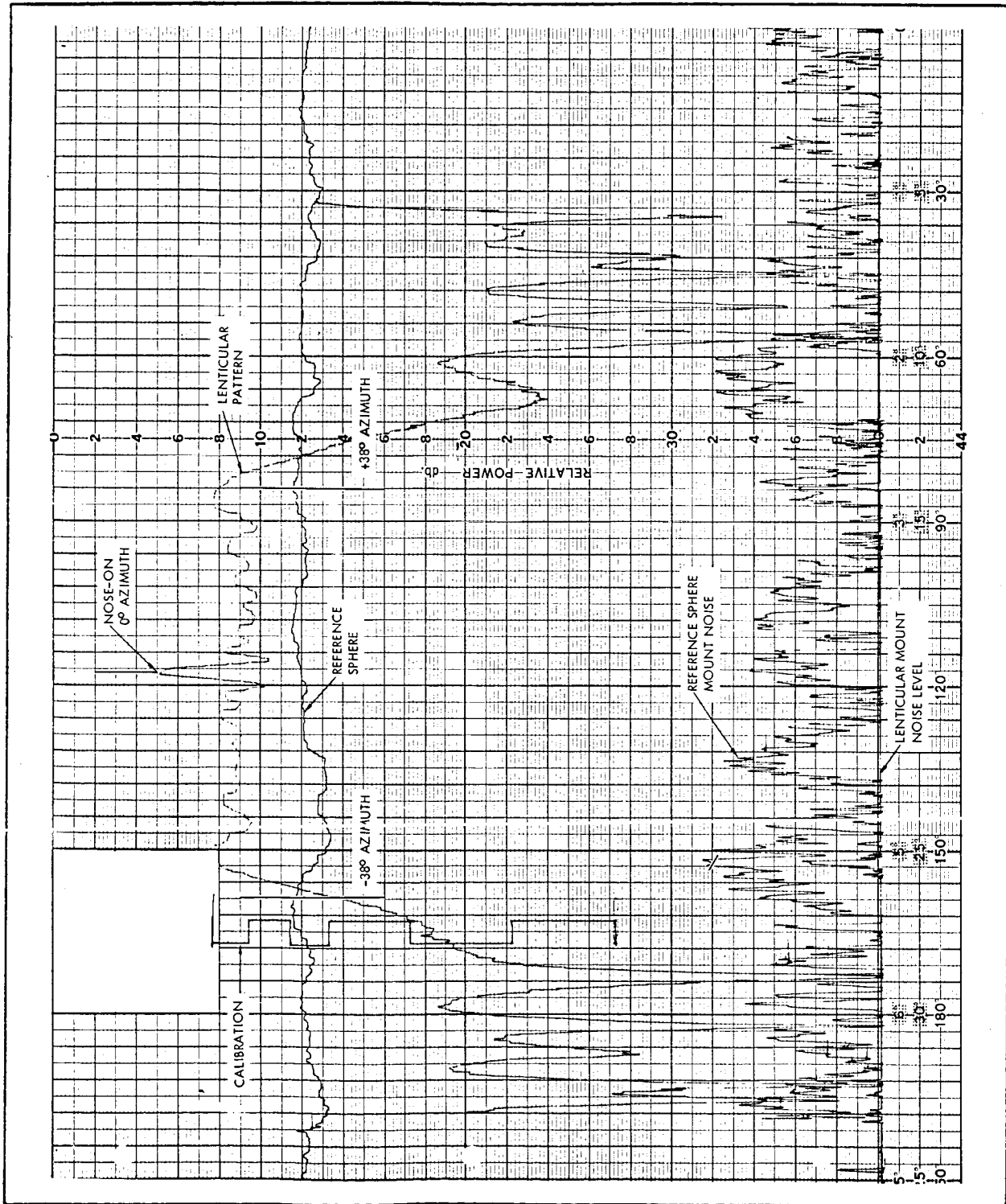


Figure 121 - Reflectivity Pattern - 9830 Mc

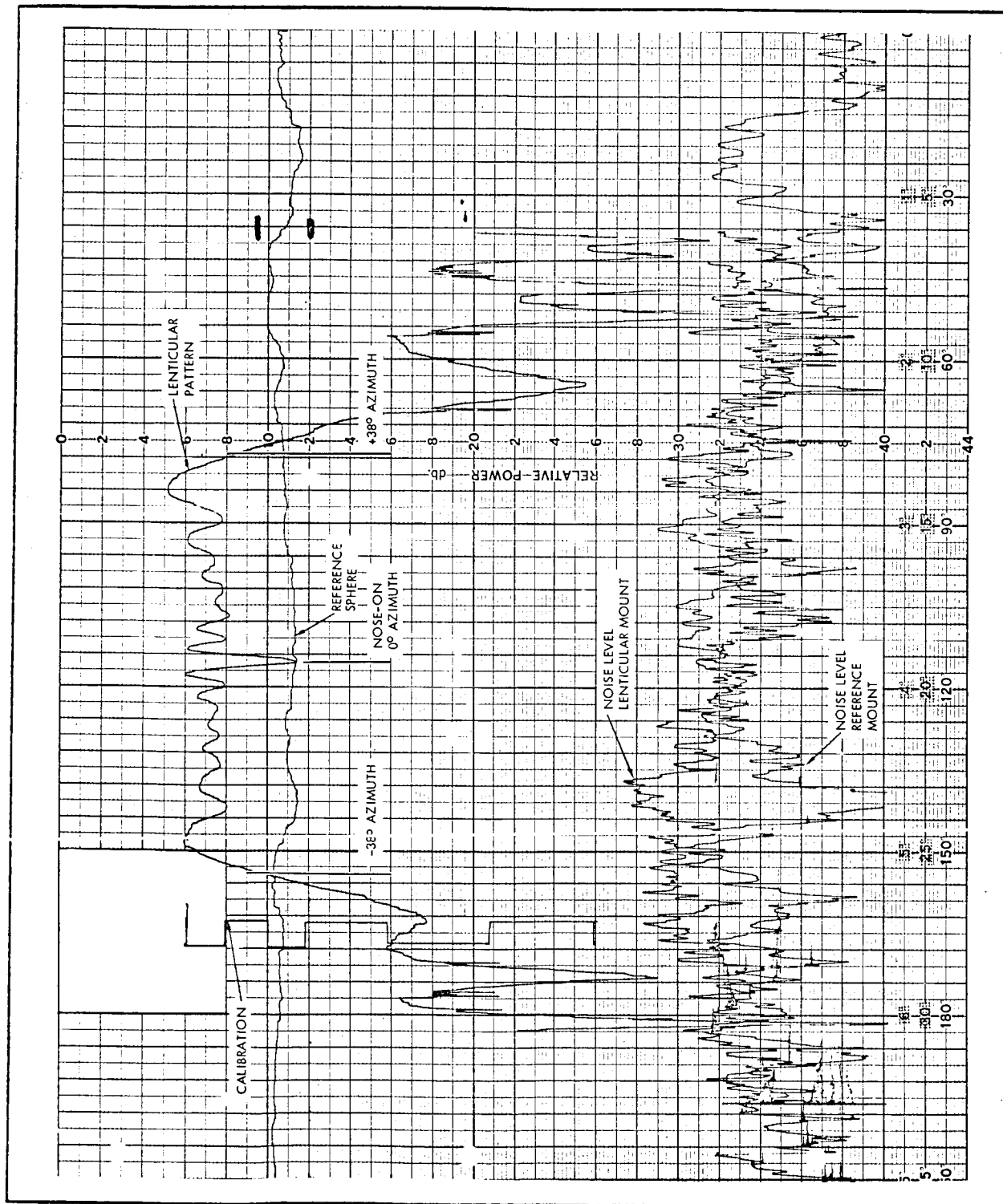


Figure 122 - Reflectivity Pattern - 9030 Mc

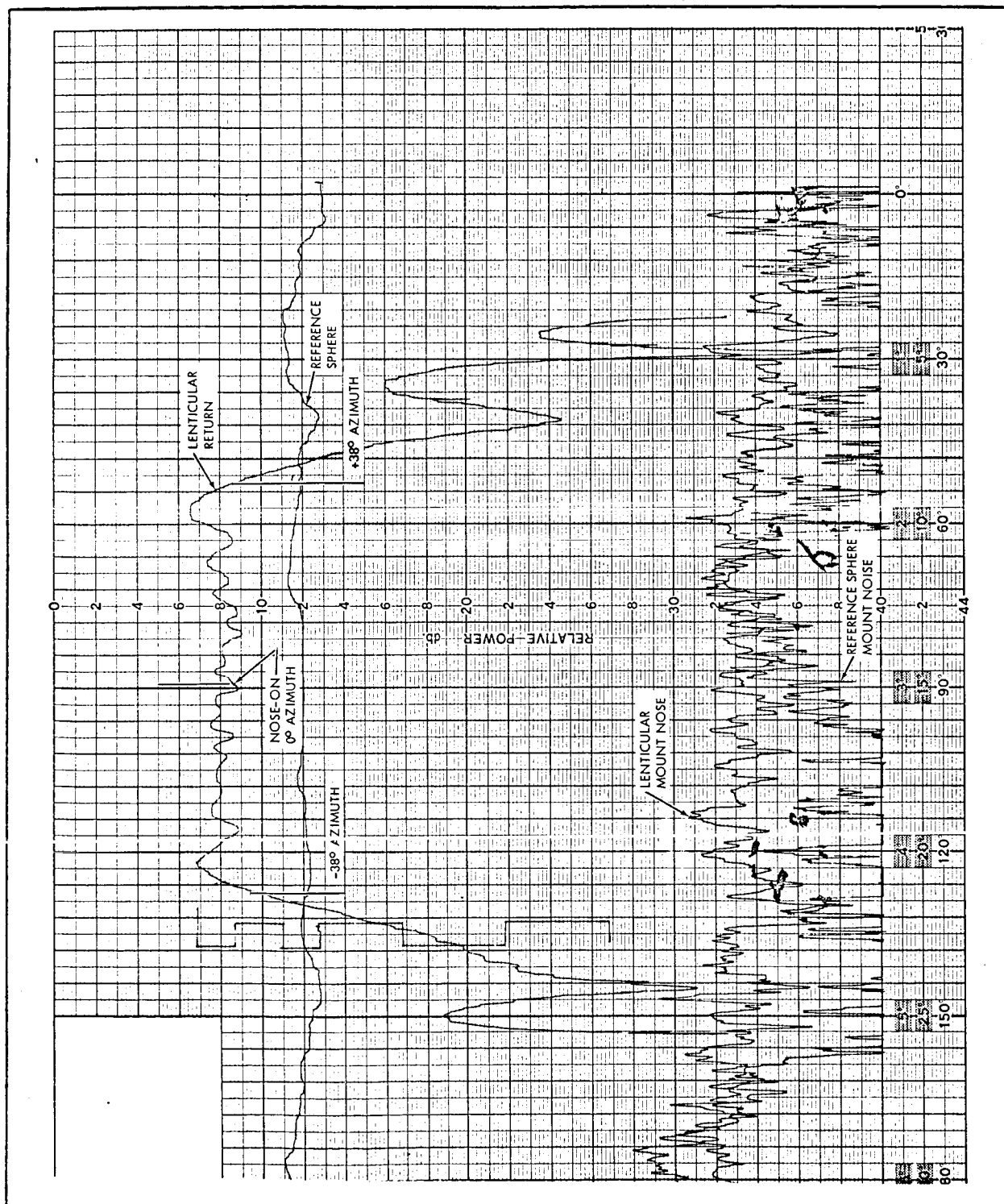


Figure 123 - Reflectivity Pattern - 9370 Mc

TABLE XXIII - DATA OBTAINED FROM REFLECTIVITY PATTERNS

Frequency (mc)	Reference sphere above noise (db)	Average lenticular return with respect to reference sphere (db)	Nose-on lenticular return with respect to average lenticular return (db)	Nose-on lenticular return with respect to average return (db)	Maximum lenticular variation (db)
9830	20	3.0	7.0	4.0	5.4
9630	15	2.0	6.4	4.4	5.0
9570	17	4.4	7.2	2.8	3.3
9430	18	2.0	3.5	1.5	2.0
9370	18	3.8	3.2	-0.6	2.2
9130	20	4.4	-0.2	-4.6	5.8
9030	19	4.0	0.0	-4.0	6.2
8970	20	2.8	3.6	0.8	3.5
8830	17	5.0	6.4	1.4	3.2
8770	15	3.6	5.8	2.2	3.8
8630	28	3.4	3.8	0.4	3.6
8570	13	3.0	3.0	0.0	2.0

of interest)^a with respect to the reference sphere return

3. Nose-on (0-deg azimuth) lenticular return with respect to the reference sphere return
4. Nose-on (0-deg azimuth) lenticular return with respect to average lenticular return (over azimuth angles of interest)
5. Maximum variation of lenticular return (over azimuth angles of interest)

Plots of the data contained in Table XXIII are given in Figures 124 through 127.

c. Test Data Analysis

In the reflectivity data analysis, it was assumed that the nose-on return of the lenticular model is the sum of two contributions, the spherical section return of the lenticular shape and the edge diffraction return. The purpose of the analysis was to determine the relative amplitude of the edge diffraction compared to the return of the spherical section.

The nose-on monostatic return is then given by two vectors, A and B (Figure 128).

The maximum power from the E vectors A and B is $(A + B)^2$, and the minimum is $(A - B)^2$. Referring to Figure 125, the maximum variation with frequency in nose-on monostatic return is 11.3 db (including ± 2 db measurement accuracy allowance). Then

^aThe lenticular model, has an included half angle of 42 deg; however, the return from the model falls off sharply at approximately 38 deg from nose-on. Data were obtained from the ± 38 deg from nose-on region.

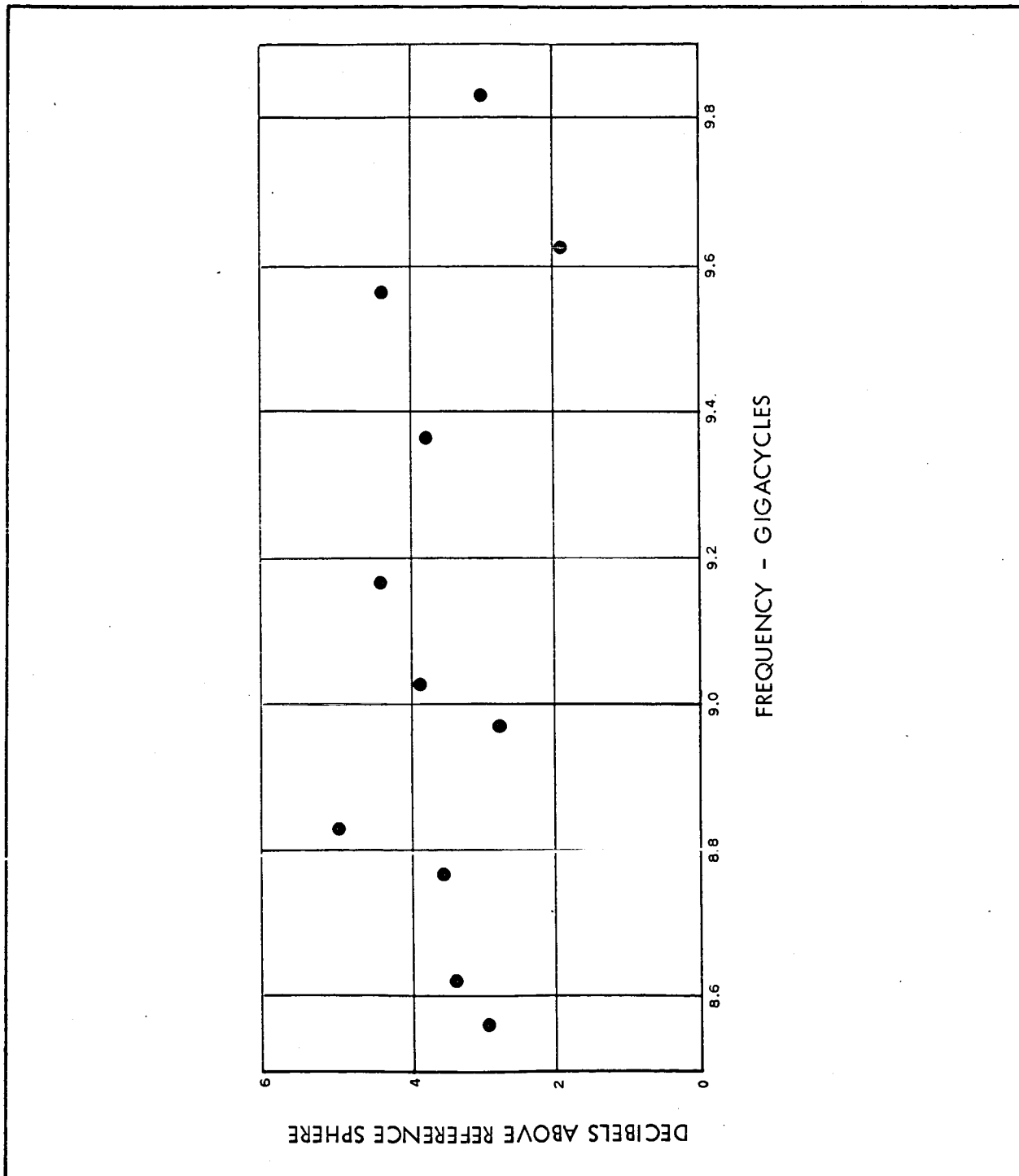


Figure 124 - Average Lenticular Return with Respect to Reference Sphere versus Frequency

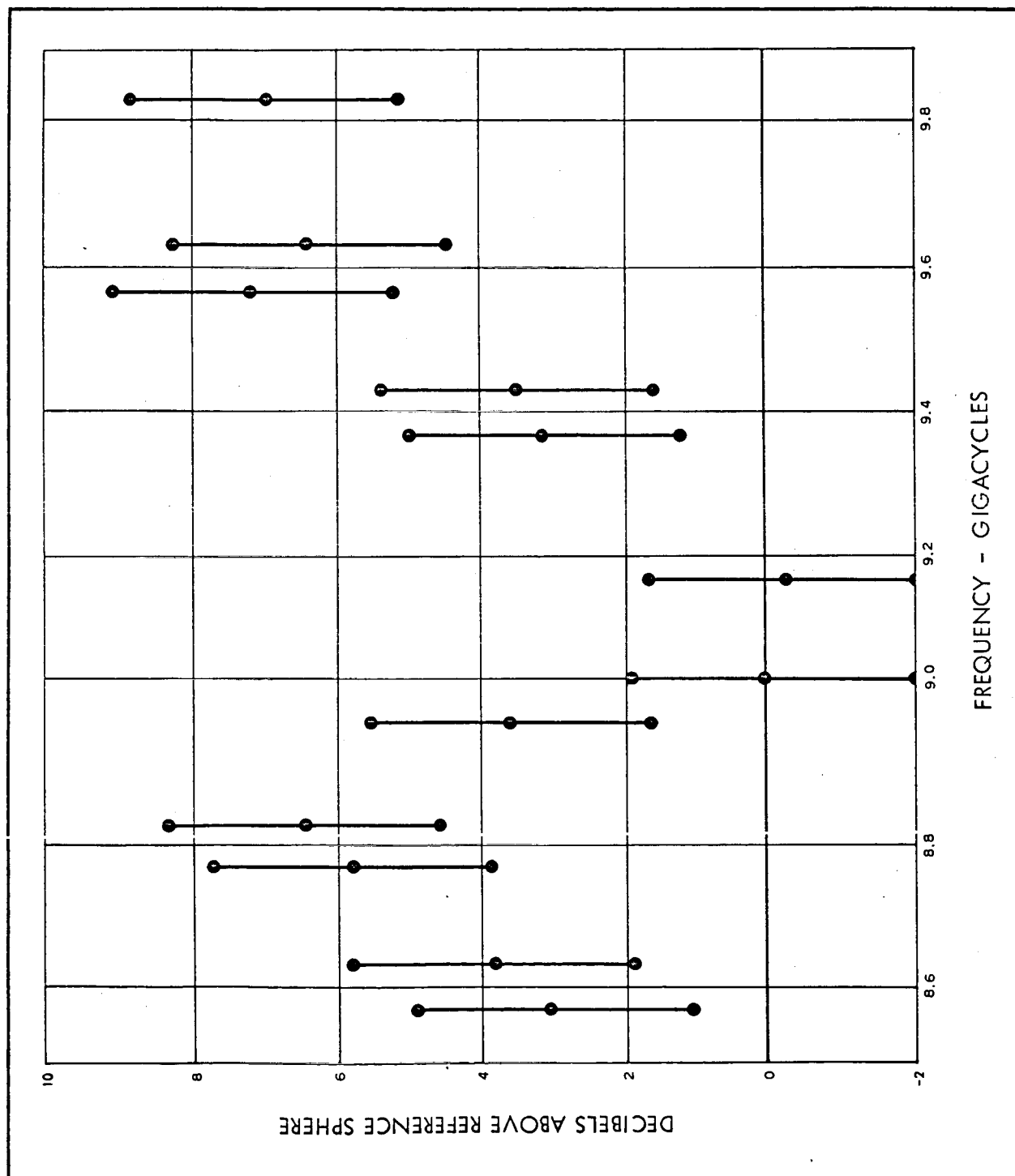


Figure 125 - Nose-On Return with Respect to Reference Sphere versus Frequency

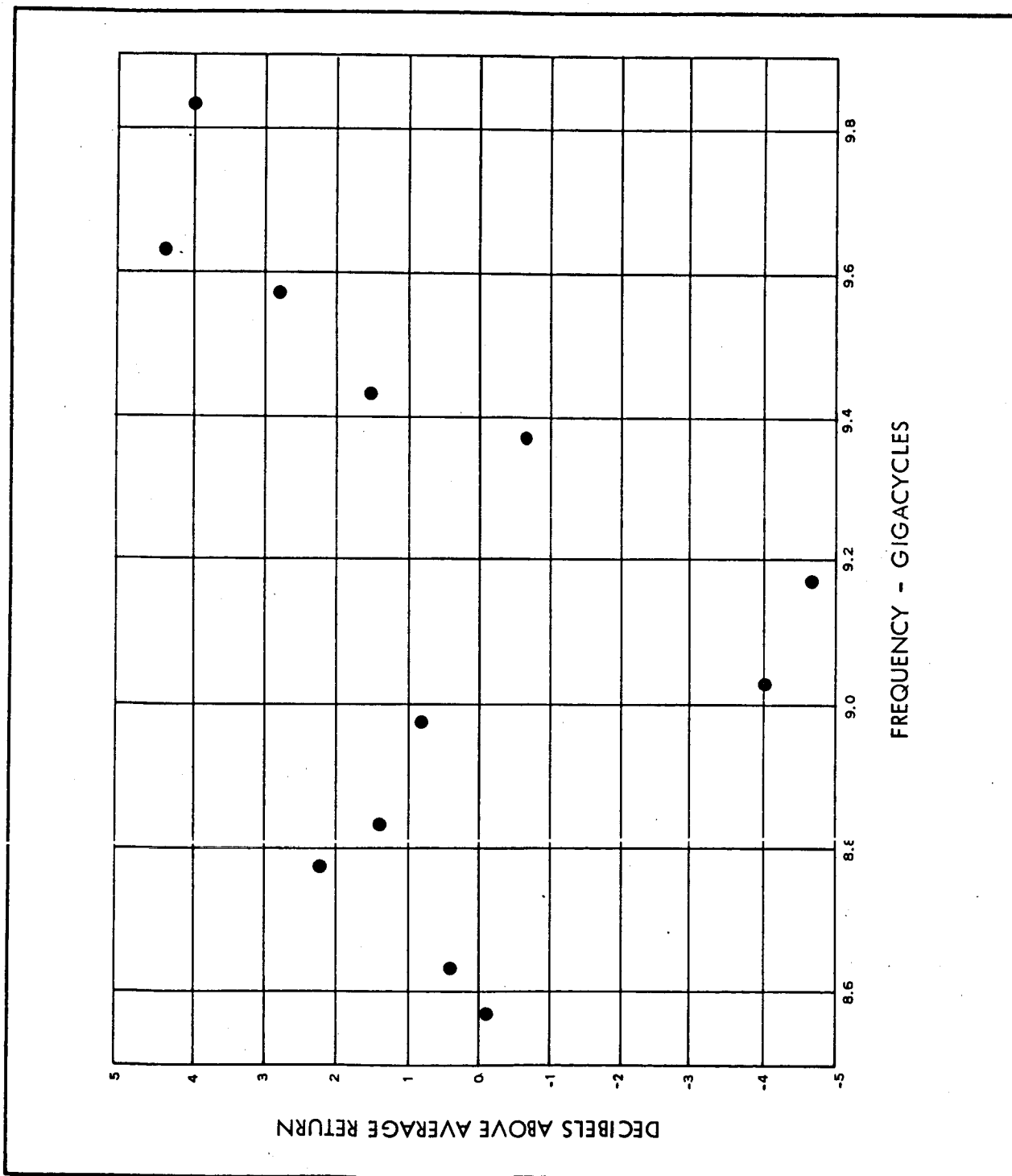


Figure 126 - Nose-On Return with Respect to Average Lenticular Return versus Frequency

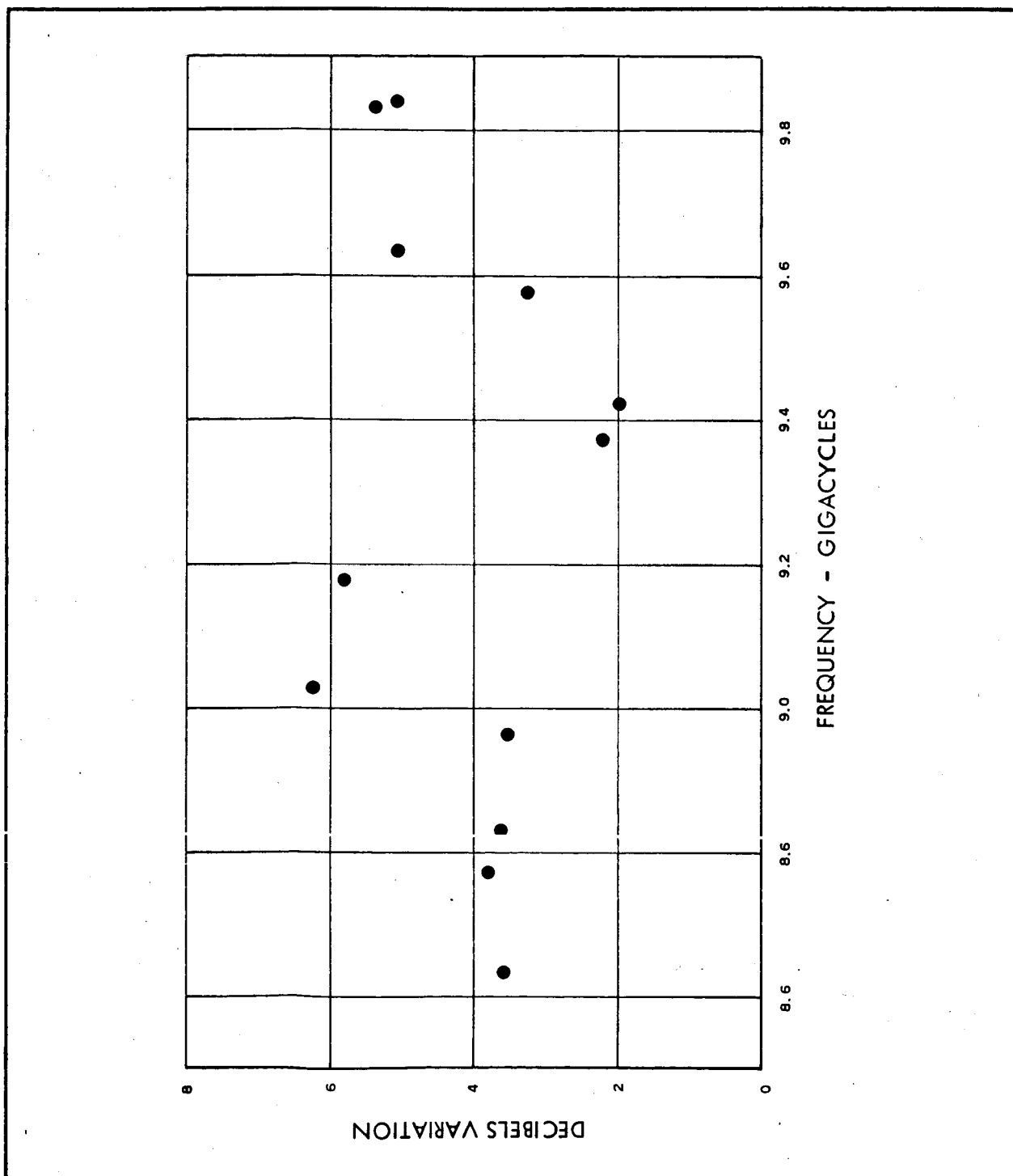


Figure 127 - Maximum Lenticular Variation of Lenticular Return versus Frequency

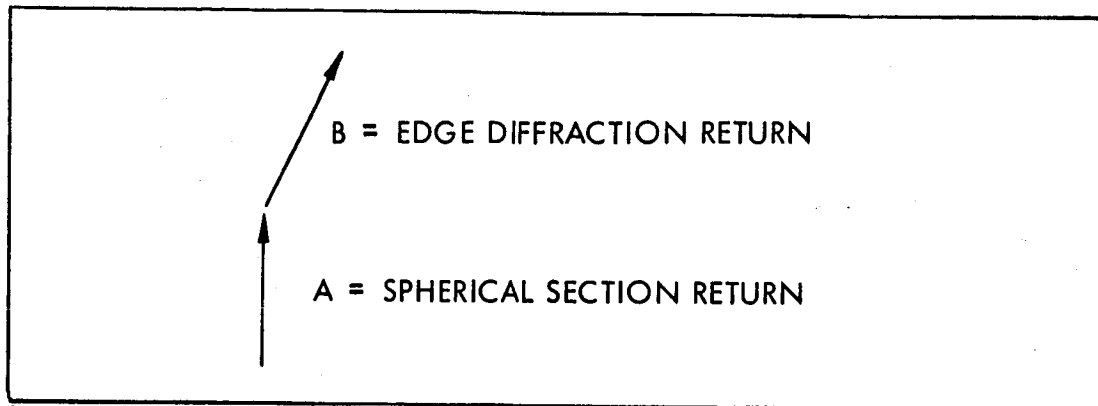


Figure 128 - Vectors A and B

$$11.3 \text{ db} = 10 \log \frac{(A + B)^2}{(A - B)^2} \quad (210)$$

and

$$11.3 \text{ db} = 20 \log \frac{1 + \frac{B}{A}}{1 - \frac{B}{A}} \quad (211)$$

Solving Equation 211 for B/A, we have

$$\begin{aligned} \frac{B}{A} &= \frac{10^{11.3/20} - 1}{10^{11.3/20} + 1} \\ &= \frac{0.572}{1} \end{aligned} \quad (212)$$

If the E vectors of the edge diffraction and the spherical section contribution are in the ratio 0.572/1, then the power ratio is 0.327/1. Theoretical calculations of Item a, above, predict a power ratio of 0.69/1.

The reflectivity patterns also indicate that the 11.3-db variations in return with frequency are only evident in the nose-on, ± 1.5 -deg region (see Figures 121 and 122) and that outside that region the return very closely approximates (± 1.5 db) the return expected from a

full sphere of the same 15-in. radius of curvature as the lenticular model. Edge effects do not appear to cause large variation in return (>4 db) outside the ± 1.5 -deg region. Since the large variations are apparently confined to this small angular range, the edge diffraction return does not pose as serious a problem as previously believed. However, the geometric configuration between the transmitter, receiver, and satellite for a typical mission should be considered to determine whether the ± 1.5 -deg region is of interest and whether the magnitude of the variations is large enough to cause significant loss of return to operational radars.

3. LENS SURFACE TOLERANCE EFFECTS

The bistatic radar cross section for a smooth, continuous, metal surface is determined by the radius of curvature of the surface at the point where the normal to the surface coincides with the bisector of the angle from the transmitter to the satellite to the receiver. The following three conditions restrict the surface so that only one normal coincides with the bisector of the scattering angle:

1. The spherical radius of curvature of the lenticular satellite will be 200 ft (± 1 percent).
2. The cord length of a spherical segment will have a diameter of no less than 50 ft.
3. Local radius of curvature will not vary by more than ± 30 percent from the design spherical radius within a 1-sq-ft section.

These conditions eliminate the possibility of an interference effect between signals from several different regions of the sphere.

The effect of a local perturbation is negligible if the local rms surface variation is less than 0.02 of the wave length (for a solid sphere).²³

Since this communication satellite is to be used at frequencies up through

X band and the maximum surface discontinuities will not be more than 0.10 in., peak-to-valley, the ratio of rms surface variation to wave length could be as large as 0.014. Although the corresponding theory for the surface variations of a wire grid sphere has not been developed, the effects of the specified maximum surface variation should also be negligible in this case.

If the satellite is fabricated to the tolerances noted above, the surface variation effect on the radar return will be insignificant.

4. BOOM AND CANISTER EFFECTS ON R-F RETURN

Boom and canister effects on the r-f return from the lenticular satellite were first analyzed by considering the radar return of the booms and canister at various aspect angles. The effects were analyzed for low dielectric material booms, one of which contained an 1/8-in. conducting wire to simulate the pressure and temperature sensor leads. The equations for the radar cross section of the booms are given in Appendix G.

Figure 129 shows the plot of radar return versus angle of incident energy to boom for polarization parallel to the boom. The return is referenced to a 200-ft radius sphere to show the effect of the boom on the over-all lenticular return. The effect of the wire is seen to be negligible except in the $90 (\pm 1)$ deg region. Outside this region the return from the wire is at least 43 db down from the spherical portion of the lenticular satellite. For this undesirable condition, $90 (\pm 1)$ deg, to exist, the satellite axis must be tilted off the vertical 8.5 deg and be illuminated at an angle $= 42$ deg to the vertical (the maximum angular range of the satellite). Also, the polarization of the incident energy must be parallel to the boom, since the radar return falls off as the $\cos^4 \phi$ (polarization angle to the boom). The return from the boom in the angular regions of interest is quite small and will have negligible effect on the lenticular return.

Since grid material was considered for rigidization of the booms, the boom return was calculated, assuming that the booms are fabricated from

NOTES: WIRE - 210 FT LONG, 1/8-IN. DIA ($\lambda = 1.18$)

WIRE GRID - 210 FT LONG, 4.1-IN. DIA ($\lambda = 5.59$)

—————

FUNCTION OF θ

σ REFERENCED TO 200-FT RADIUS SPHERE

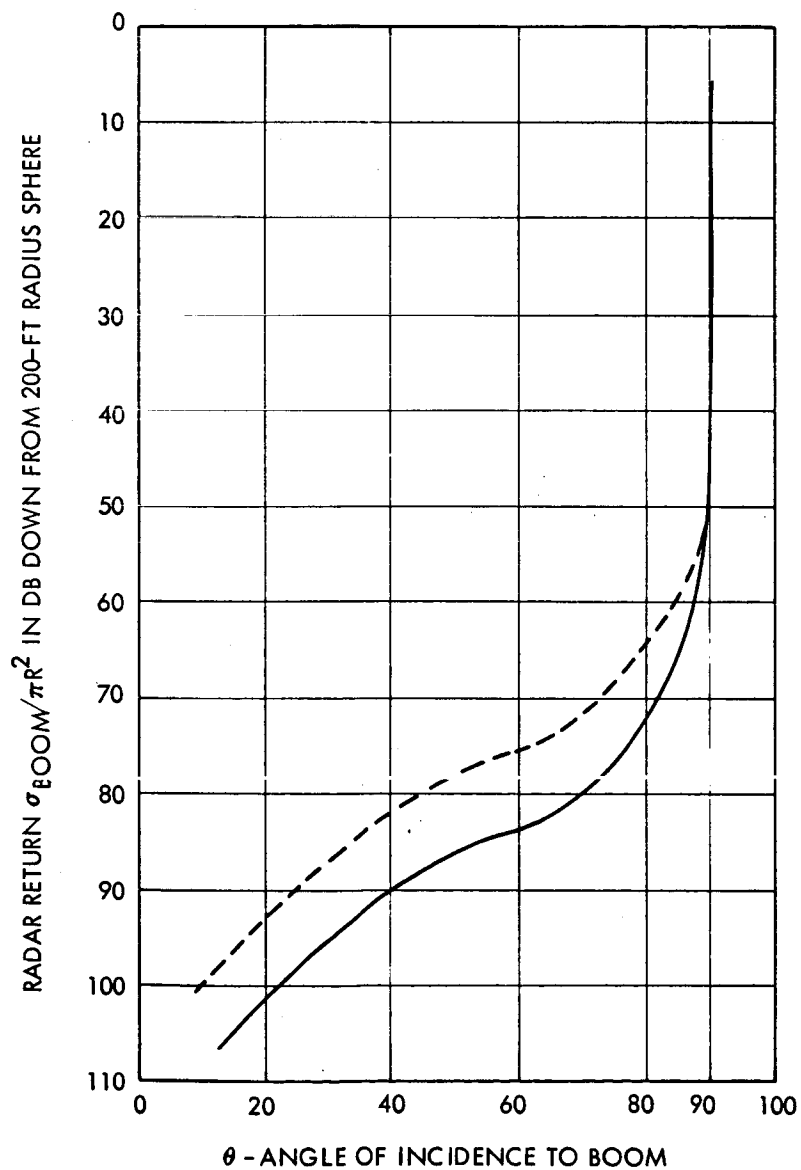


Figure 129 - Boom Radar Return versus Angle of Incidence to Boom

conducting material. The booms would then constitute cylinders 210-ft long and 4.1-in. diameter.

The wave length of incident energy would range from 1.18 to 5.59 in. It was therefore necessary to consider the boom's radar cross-section for two cases. For the high frequencies, the booms were treated as cylinders where the wave length is less than the radius of the boom ($\lambda < a$). For the low frequencies, the booms were treated as wires where the wave length is greater than the radius ($\lambda > a$).

Calculations were made at $\lambda = 1.18$ in. and $\lambda = 5.59$ in. (approximately 2 to 10 kmc frequency range). For the case of $\lambda > a$, the return due to one boom as a function of θ (angle of incidence) is shown in Figure 129. It has the same form as the return from the 1/8-in. wire considered, except that the return is approximately 8 db greater than that of the 1/8-in. wire at small θ angles and 3 db greater in the 90-deg region. The magnitude of the boom return is still quite small over the angular range of interest and has negligible effect on the lenticular return. For example, a return from the boom that is 40 db down from that of the center spherical portion of the satellite would cause only 0.18-db degradation in overall return under the worst conditions.

For the $\lambda < a$ case, the return due to one strut has the same general form as Figure 129, but has a much steeper slope near 90 deg. The detrimental effect of the conducting boom for this case is also considered negligible.

It must be concluded that if the booms were made of conducting material the effect on the satellite return would be very small, except where they are viewed exactly normal to the line of sight with the E field parallel to the boom.

The canister was considered as a sphere 56 in. in diameter. Its radar cross section at X band would be

$$\sigma_{\text{can}} = \pi R^2 = 17.2 \text{ sq ft} = 1.6 \text{ sq m.} \quad (213)$$

The radar return of the canister is down 40 db from that of the spherical portion of the satellite and would have negligible effect on the lenticular satellite return.

Boom effects computed on the basis of area blocked by the booms compared to the total reflecting surface show less than 0.2-db degradation in return.

Since the amplitude of the canister radar cross section is small compared to the theoretical lenticular radar cross section, the singular effect of the canister blocking energy on the lenticular first fresnel zone does not significantly affect the radar cross section if not more than the first fresnel zone is blocked. This results from the fact that the vector addition of the backscattered radiation from the center of the sphere and the various circular zones can be represented on the complex plane as a spiral (Figure 130). This spiral starts out approximating a circle in the first fresnel zone and slowly converges to a point at the center of the approximate circle

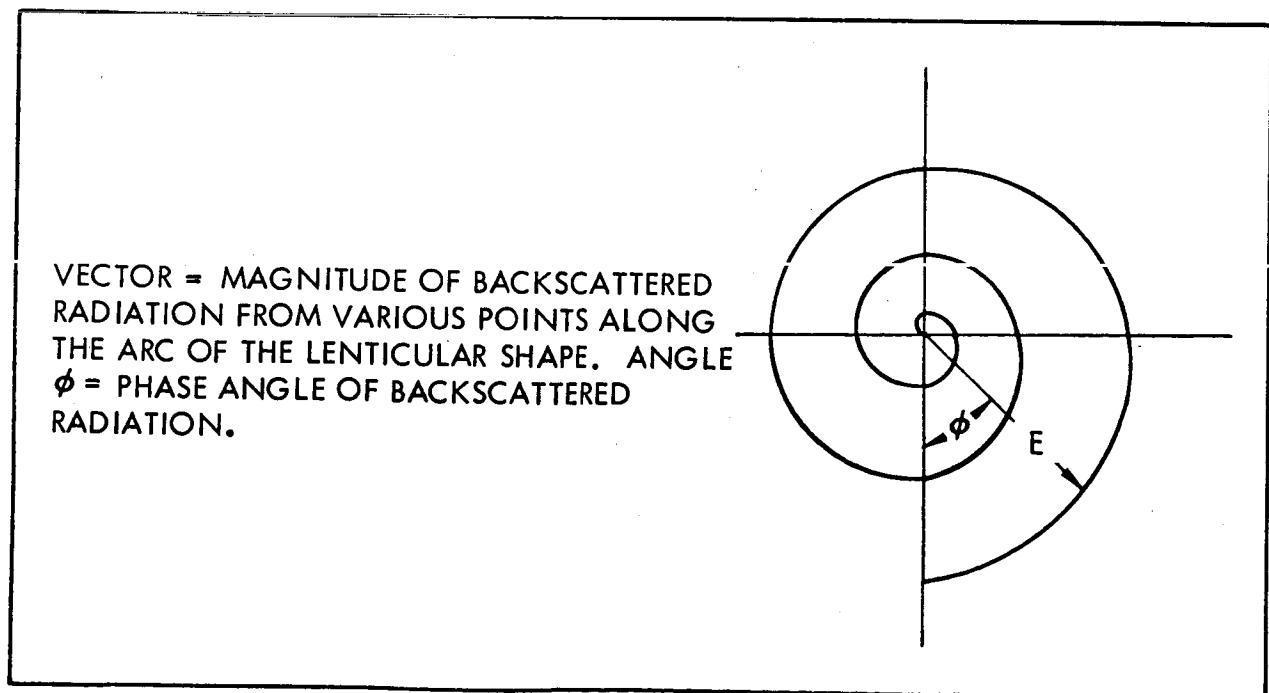


Figure 130 - Magnitude and Phase Angle of Backscattered Radiation from Lenticular Satellite

as the contributions from the zones near the shadow region are added. The total radar cross section is directly proportional to the square of the distance from the center of the spiral to the spiral position where the back-scattering first starts. Since the first fresnel zone contribution is essentially a circle, the total radar cross section would not change appreciably by blocking out less than the first fresnel zone.

5. LENS SURFACE REFLECTIVITY STUDY

The reflectivity of the 1.6- and 1.2-mil grid material was determined considering the transmission line shown in Figure 131, where jx represents the wire as a susceptive sheet. The susceptance is

$$\frac{X_a}{Z_0} = \frac{a}{\lambda} \ln \frac{a}{2\pi r} \text{ (Reference 19) ,} \quad (214)$$

where a = wire spacing (inches), and r = wire radius (inches).

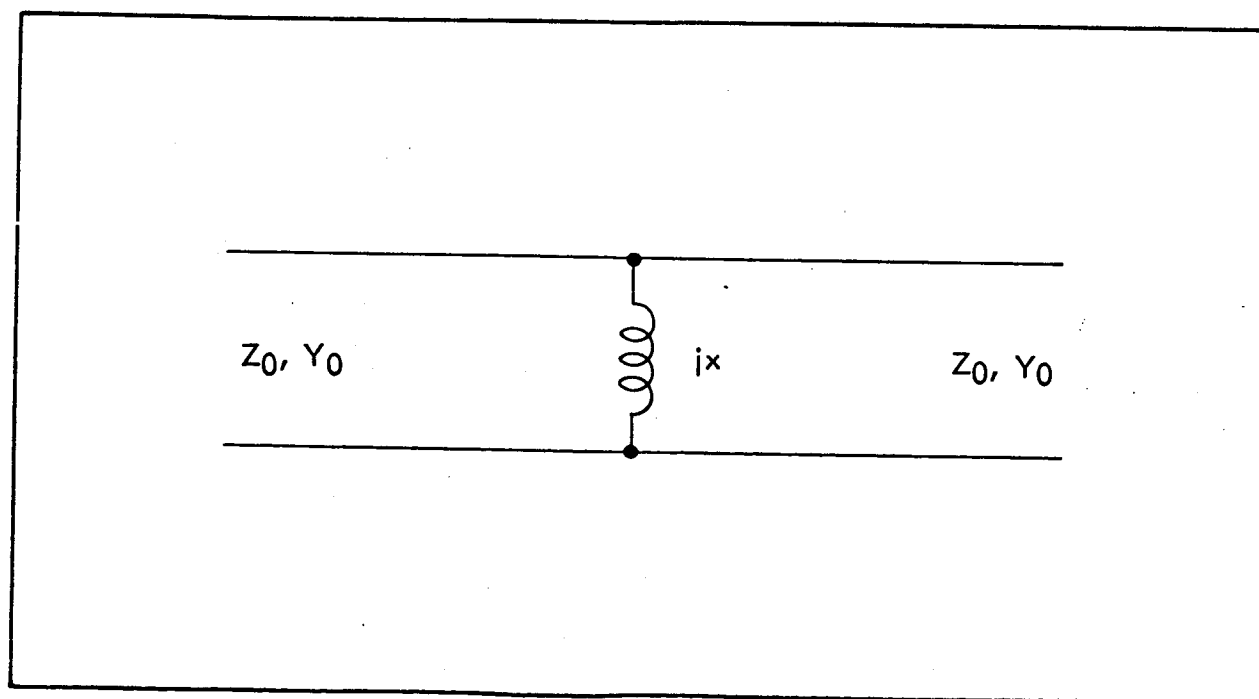


Figure 131 - Transmission Line

The reflectivity or power reflection coefficient $|r|^2$ is then given by

$$|r|^2 = \left| \frac{\frac{Y}{Y_0}}{2 + \frac{Y}{Y_0}} \right|^2 \quad (215)$$

where $Y/Y_0 = Z_0/X$.

For the cases of interest, $1.18 \text{ in.} < \lambda < 5.90$ (2 to 10 kmc operating frequency),

$$a = 1/24 \text{ in.},$$

and

(216)

$$r = 0.0008 \text{ and } 0.0006 \text{ in.}$$

The minimum reflection coefficient calculated from Equations 214 and 215 is 0.98 or 98 percent reflective. However, the exact configuration of the wire material does not give equal spacing of wires in both planes. The grid material consists of 24 wires per inch equally spaced in one plane and essentially 8 groups of 3 wires per inch in the other plane (see Figure 132).

Therefore, the reflectivity as calculated above will only hold when the polarization of the incident energy is parallel to the wires that are equally spaced 24 per inch.

Appendix H contains microwave reflectivity measurement data for the grid materials at various frequencies and parallel and perpendicular polarization.

Measurements show = 97.6 percent reflection for parallel polarization, which correlates very closely with the theoretical predictions (= 98 percent).

An exact theoretical analysis is not available for the case of perpendicular polarization, since the group of three wires may not be treated as a single conductor. However, on the basis of eight equally spaced conductors, theory predicts approximately 80 percent reflection. Microwave measurements show = 91.5 percent reflection or that the lenticular return could be

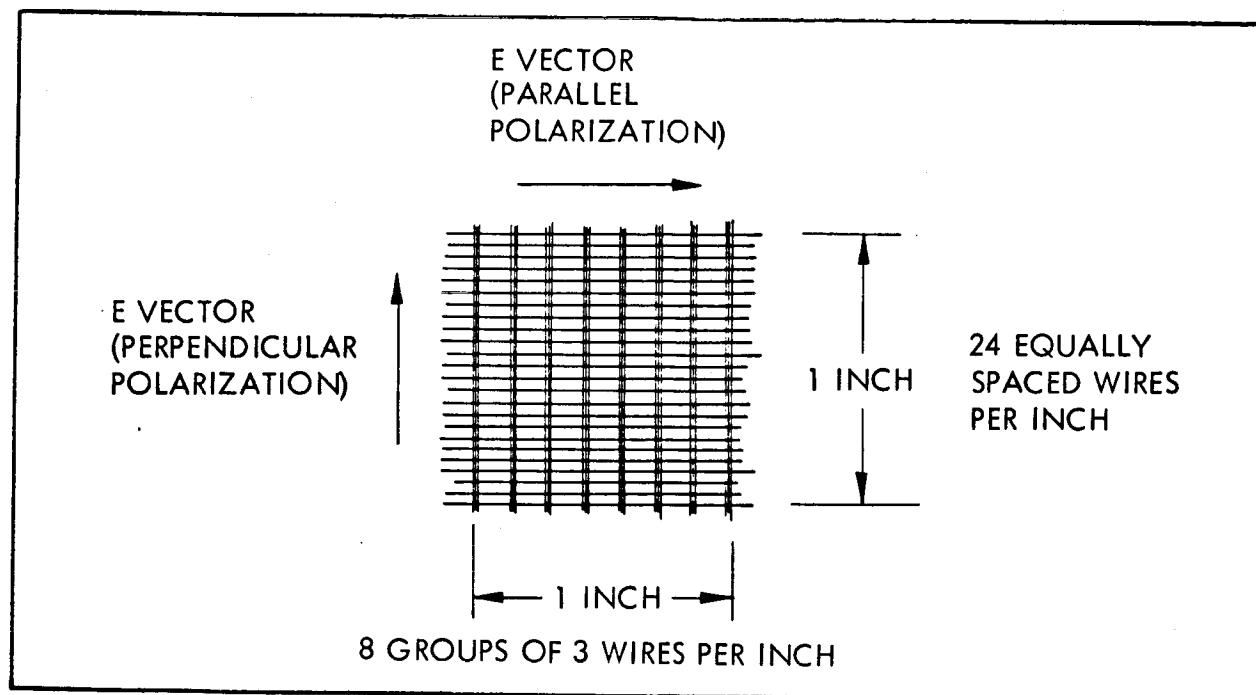


Figure 132 - Grid Material Configuration

reduced by 0.40 db by using wire-grid material instead of a solid conducting surface. These measurements were made on 1.2-mil wire at X band frequencies for the worst case polarization.

6. ELECTRICAL CONTINUITY OF LENS SURFACE

Brief theoretical consideration was given to the electrical continuity of the lens surface material. If the surface material of the satellite is continuous around the edge, the surface discontinuity will be less, thus reducing the effect of edge diffraction on the radar return. Both spherical caps of the satellite should be fabricated from conducting material to reduce the included angle at the edge of the satellite.

It is not considered necessary for adjacent gores to have conductivity as long as the spacing between seams is of sufficient length. This implies that a circular cap would be necessary where the gores become narrow near the center of the spherical surface. The approximate reflectivity

of the area near the cap as a function of cap radius is plotted in Figure 133. This cap radius was computed for the full-scale satellite. If fewer gores were used and the spacing between gores widened, a cap of smaller radius could be used.

7. PREDICTED R-F RETURN OF FULL-SCALE AND FLIGHT-TEST SATELLITES

The radar return from the full-scale (267 ft) lenticular model, predicted by theoretical considerations of the magnitude of the edge return and the phasing relationship with the center return, indicates approximately 21.5-db variation in nose-on return with changes of frequency. The period or frequency spacing at which these variations occur is approximately 10 mc for the full-scale satellite and is based on the distance, h , from the center of the lenticular shape to the edge along the line of incident energy (see Figure 134).

The period of variation for the 50-ft flight-test model would be approximately 51 mc due to the reduced h dimension; however, the theoretical magnitude of the variation would be approximately the same as that of the full-scale model (21.5-db theoretical).

The reflectivity range tests of the 20-in. model indicate that variations of approximately 11 db in nose-on monostatic return are present, but large variations are not seen outside the nose-on ± 1.5 -deg region (Figure 135). Also, for small bistatic angles the region of large variations is ± 1.5 deg from the position where the normal to the center of the spherical surface bisects the angle between the transmitter and receiver (Figure 136).

The reflectivity tests also indicate that the average return magnitude from the lenticular model very closely approximates the return magnitude to be expected from a complete sphere (πR^2) of the same radius of curvature as the lenticular model. The average radar return of the full-scale and flight-test models should therefore be equal to the return from complete spheres of their respective sizes. (The radius of curvature is

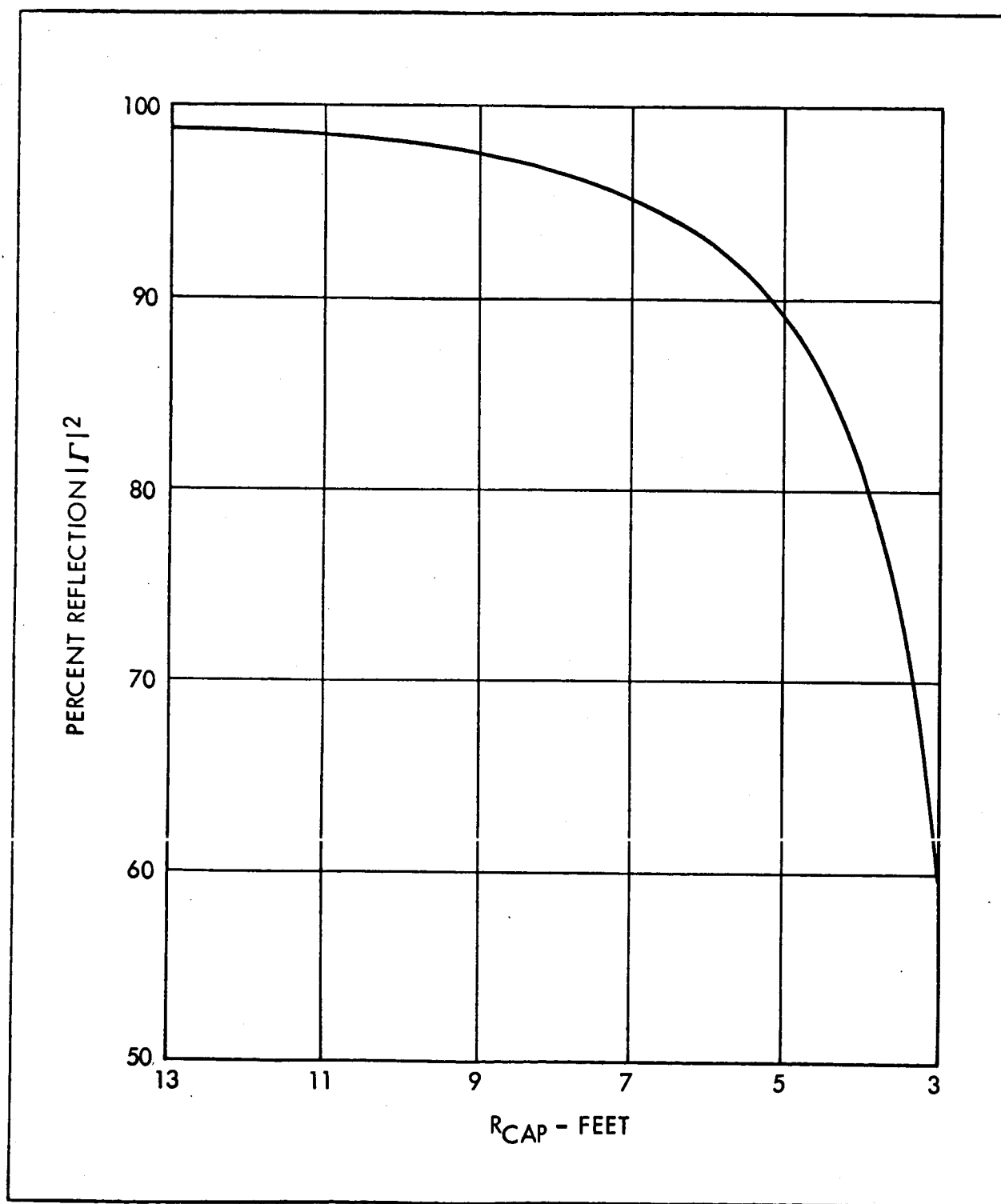


Figure 133 - Worst Case Reflectivity of Area around Cap as Function of Cap Radius

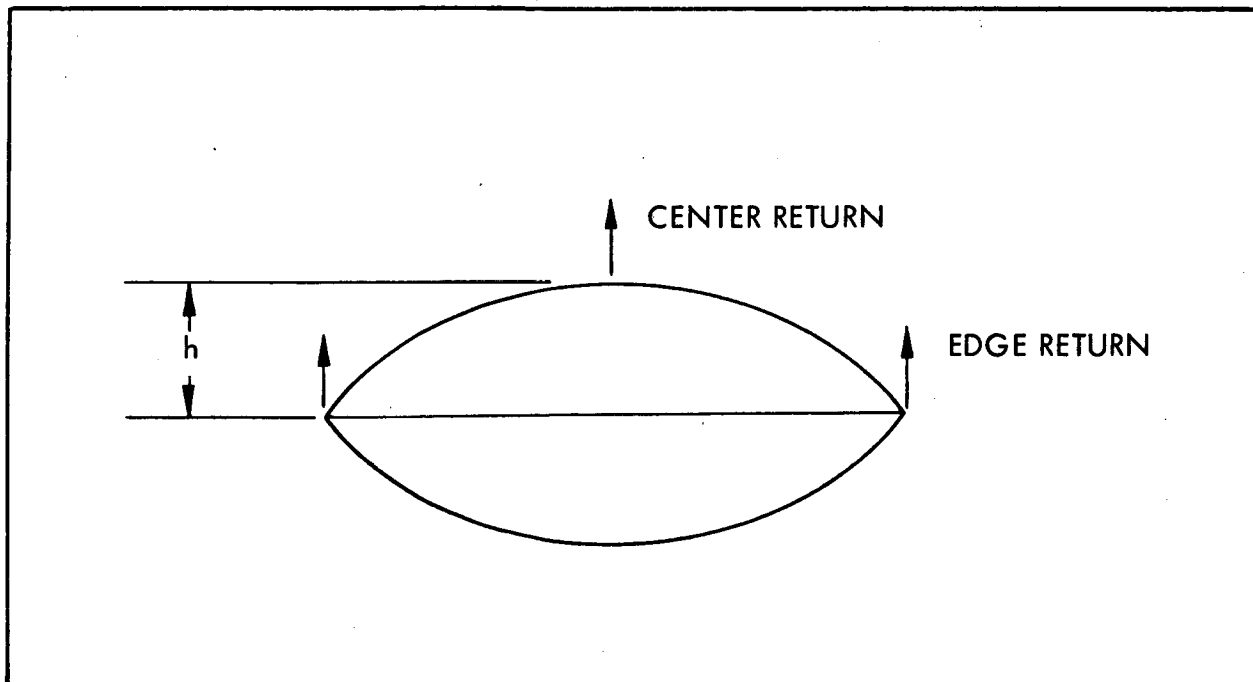


Figure 134 - Lenticular Configuration

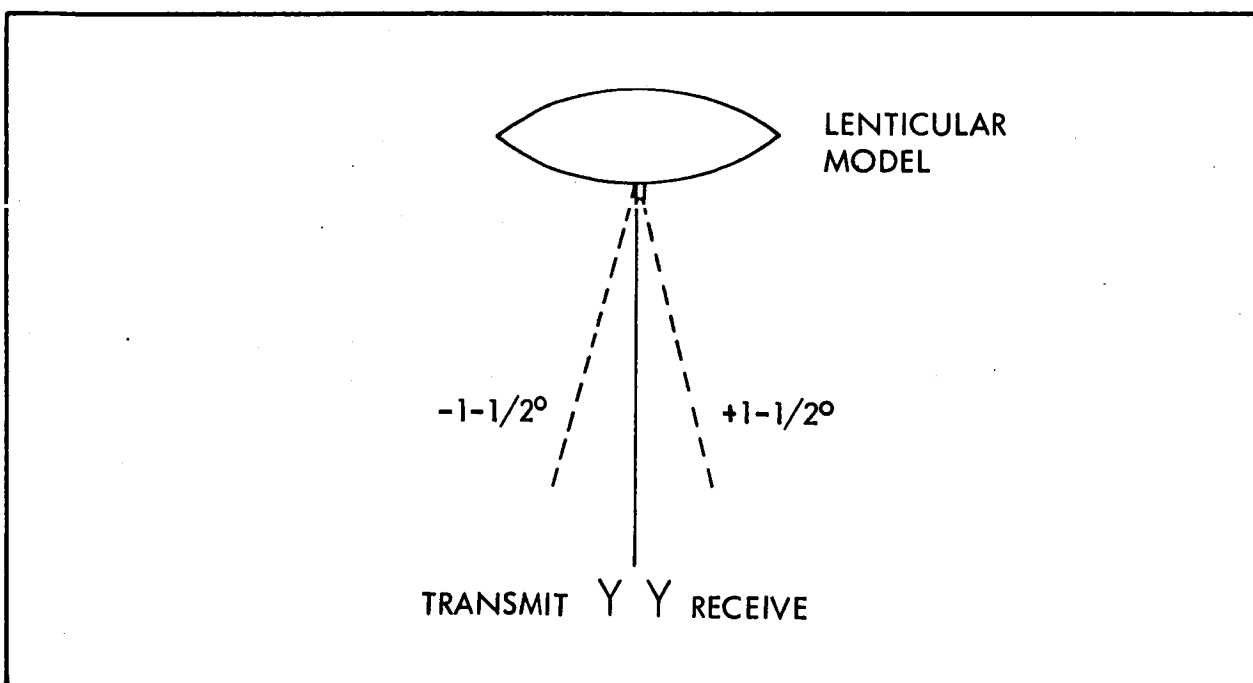


Figure 135 - Monostatic Region of Large Variations

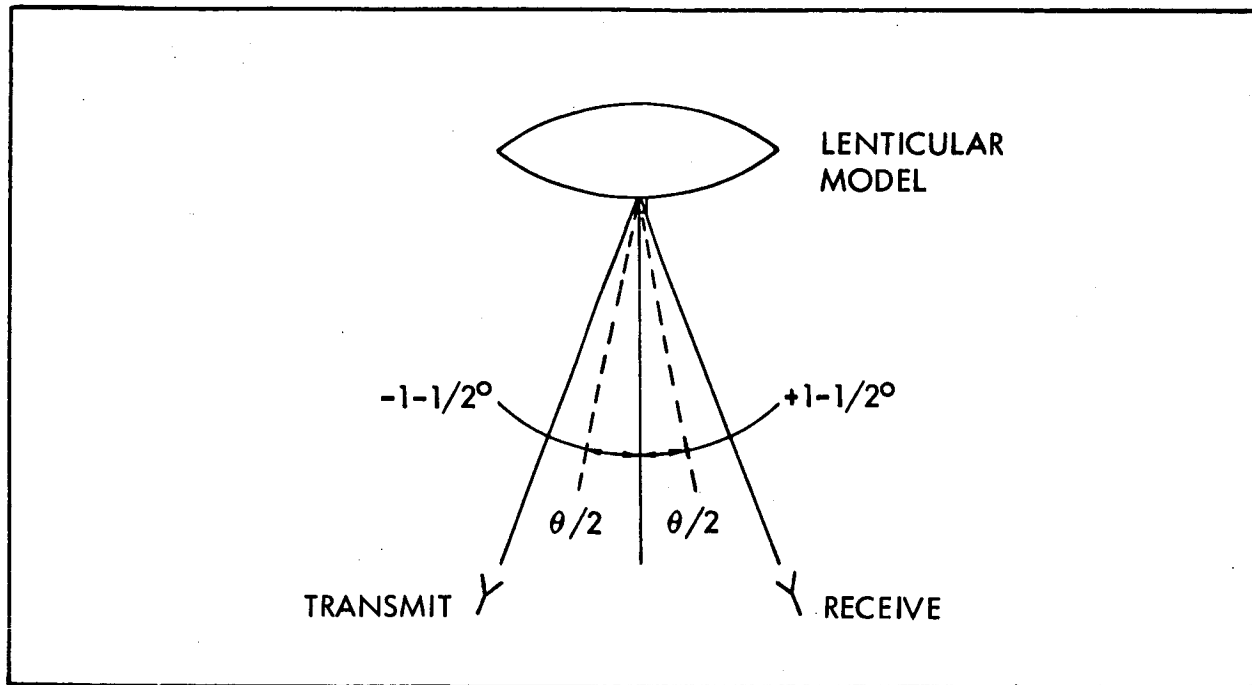


Figure 136 - Bistatic Region of Large Variations

200 ft for the full-scale model and 37.4 ft for the flight-test model.)

Since the large variation in return with changes of frequency appears to be present only in the nose-on ± 1.5 -deg region, the aspect angles of a typical operational mission must be considered. The probability of the satellite being in such a position and attitude to give a nose-on return in two planes at once is quite small, and the over-all operational capabilities of the satellite should not be critically affected. The following four cases indicate possible positions and attitudes and whether or not operation is in the critical region of variations:

Case 1 - Nose-on monostatic return in two planes (see Figure 137).

Case 2 - Bistatic operation with angle, α , between the transmitter, satellite, and receiver bisected and the satellite above the transmitter and receiver in a vertical plane (see Figure 138).

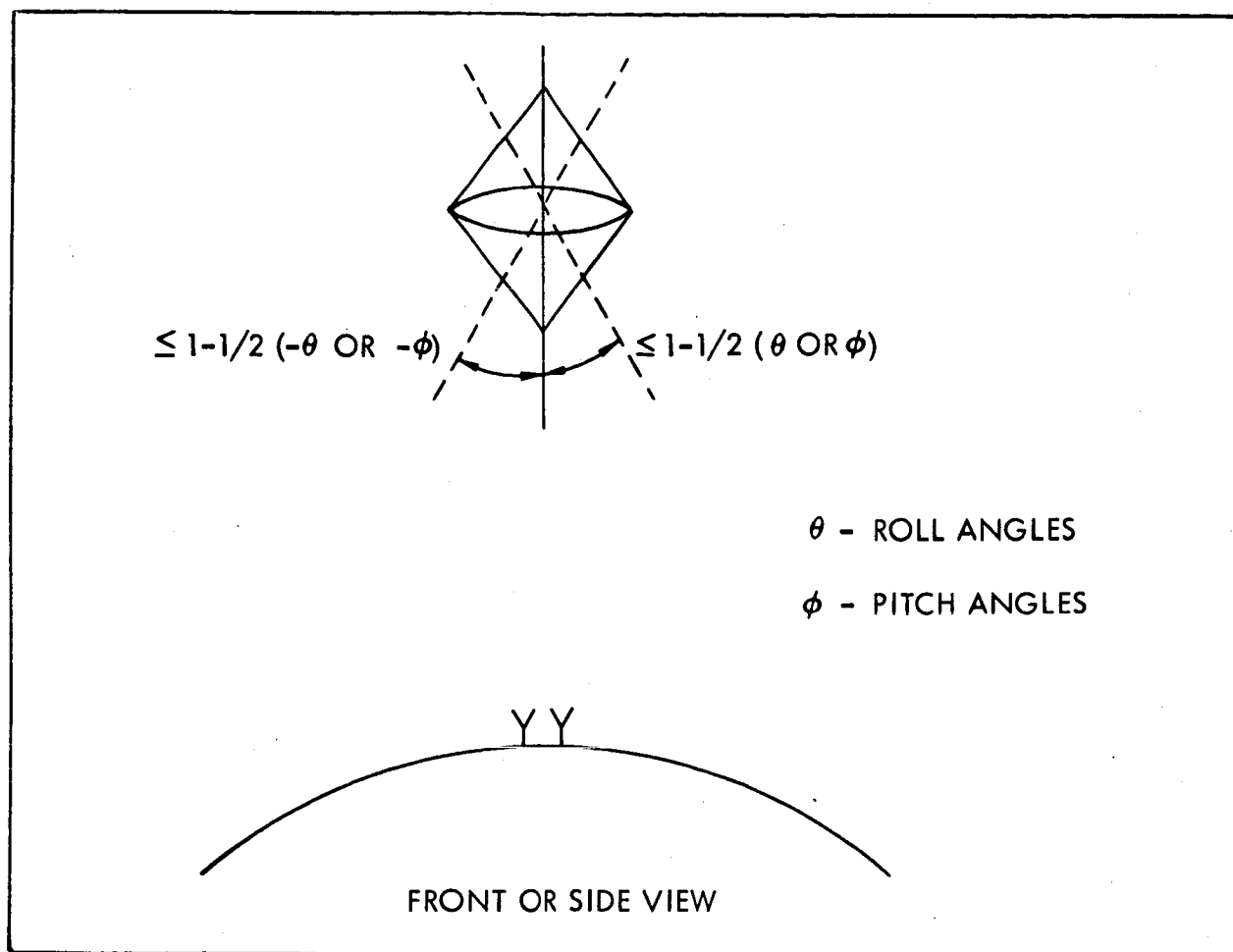


Figure 137 - Satellite Attitude and Position - Case 1

Case 3 - Bistatic operation with the satellite in a plane other than vertical above the transmitter and receiver and angle, a , between the transmitter, satellite, and receiver bisected (see Figure 139).

Case 4 - Bistatic operation with the satellite in a vertical plane above the transmitter and receiver and angle, a , between the transmitter, satellite, and receiver not bisected (see Figure 140).

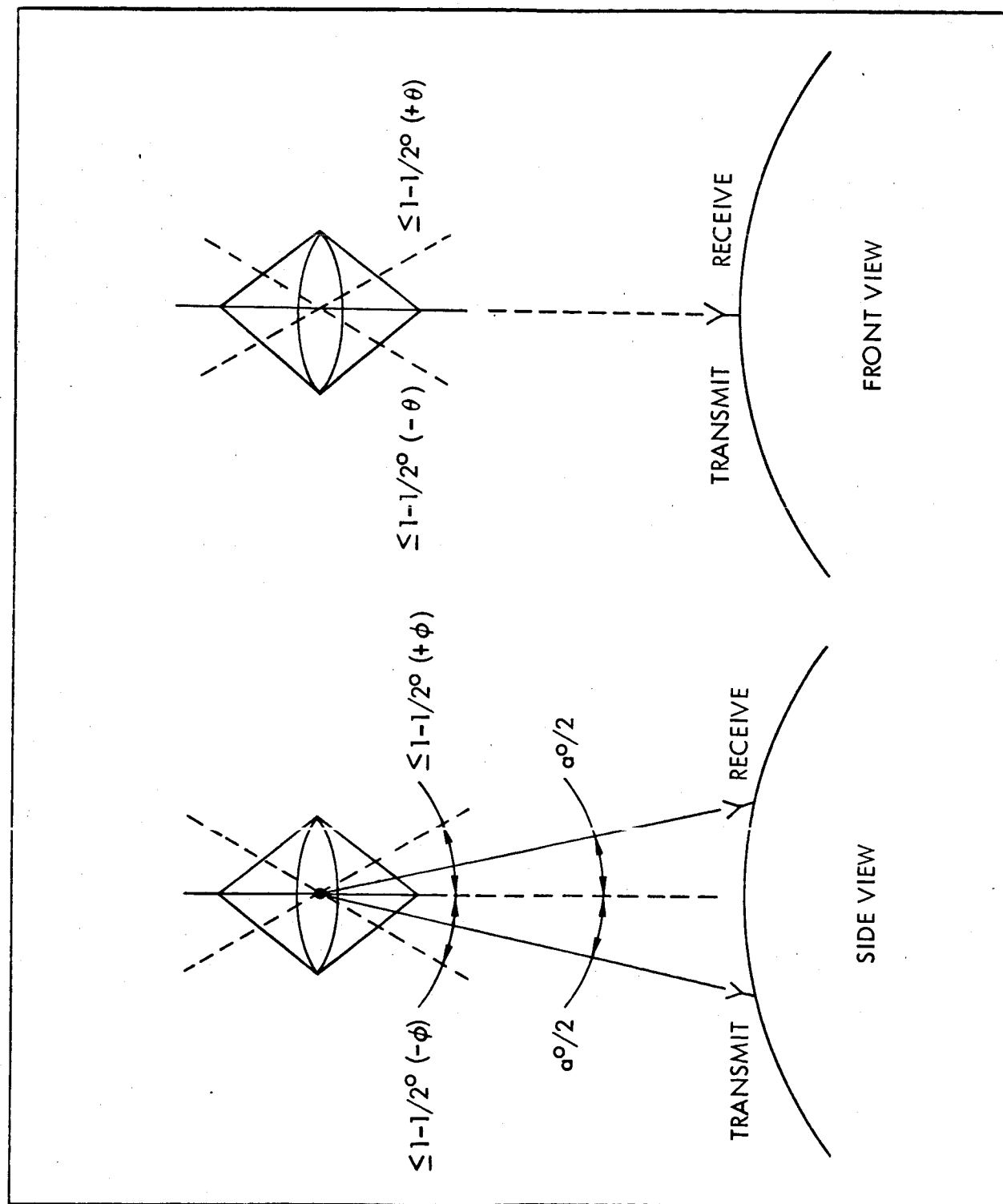


Figure 138 - Satellite Attitude and Position - Case 2

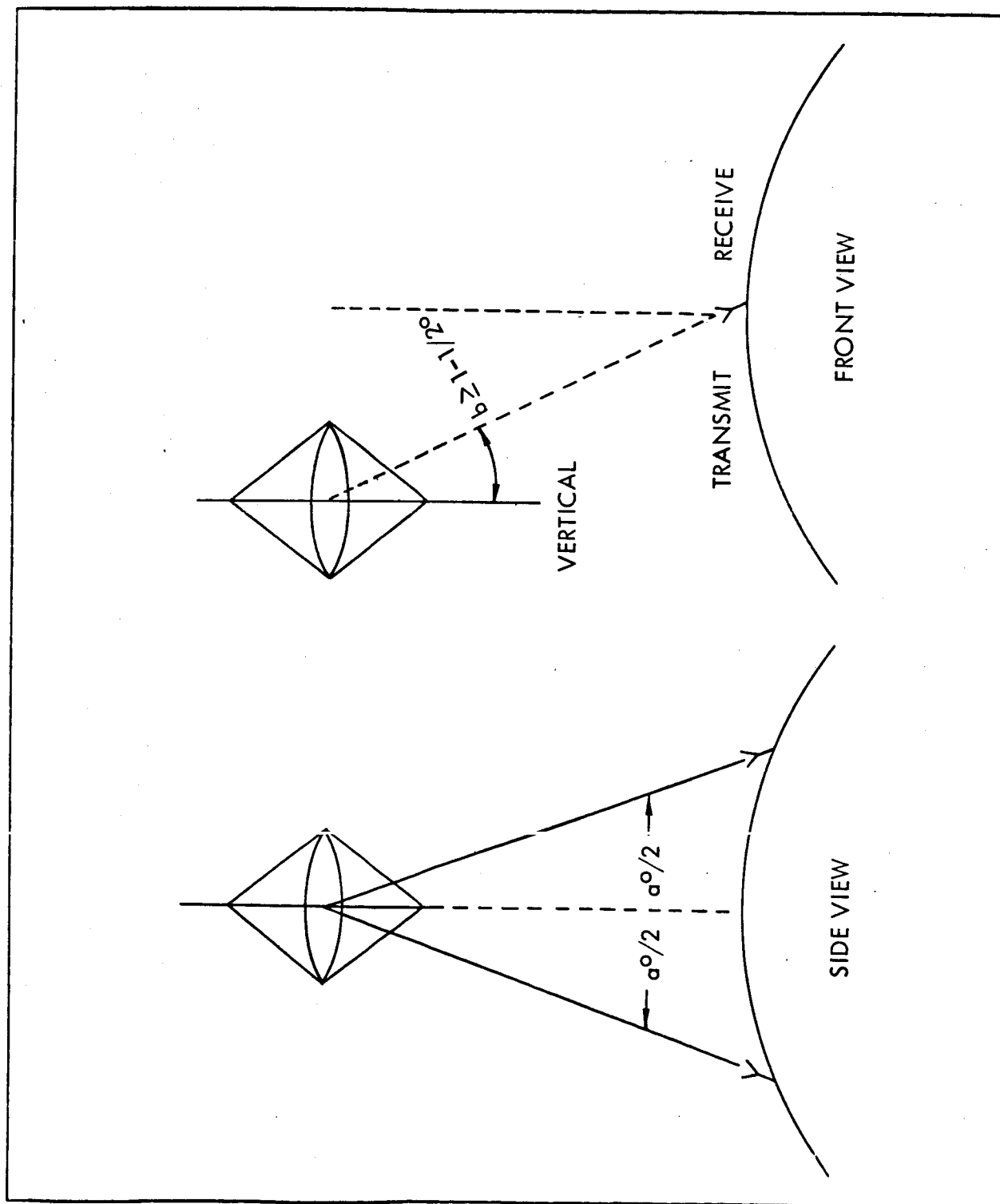


Figure 139 - Satellite Attitude and Position - Case 3

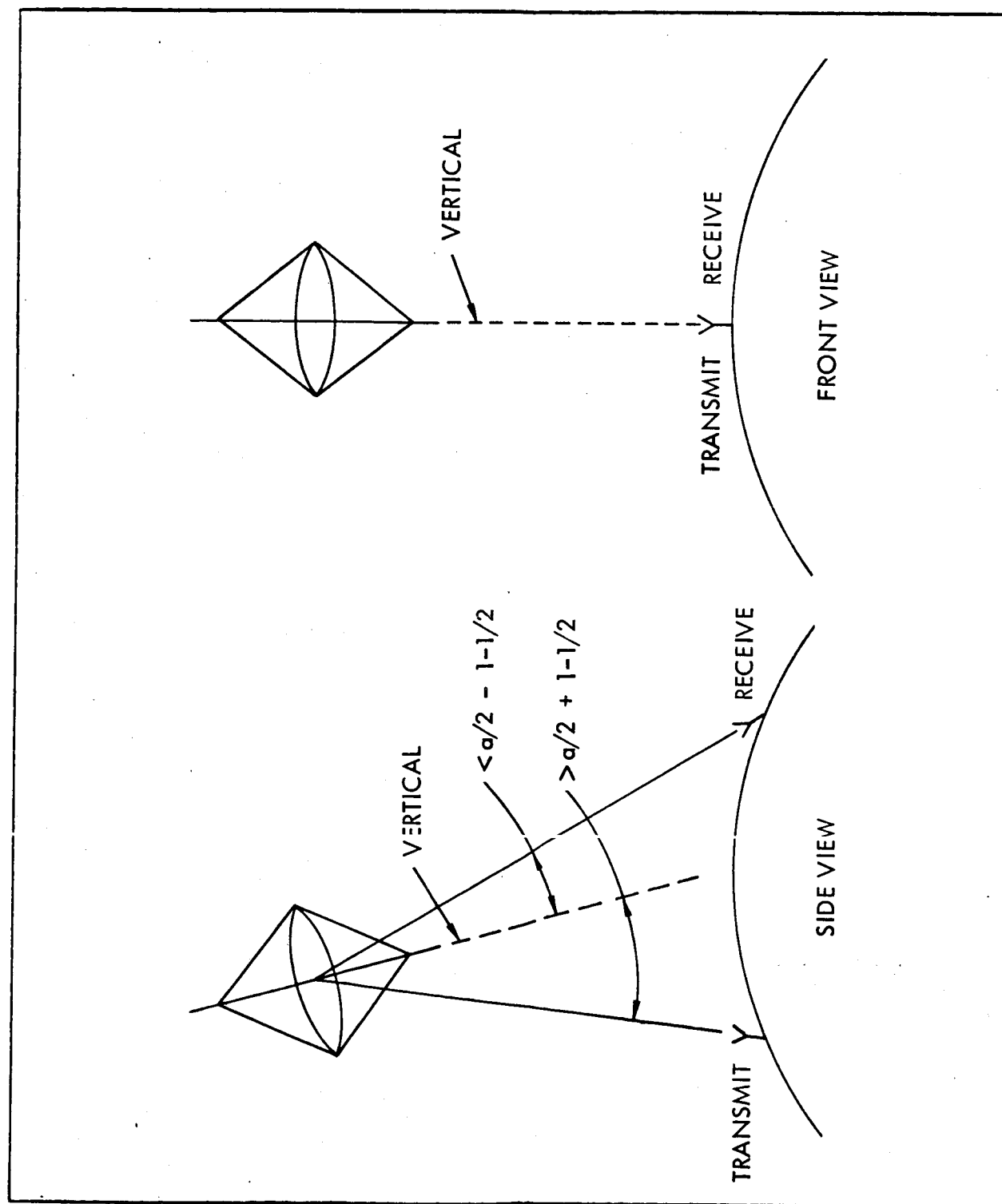


Figure 140 - Satellite Attitude and Position - Case 4

The indicated region in Case 1 (Figure 137) is a critical region of variation, but is not considered a realistic configuration for operation of a communications satellite.

If either θ or ϕ is increased beyond ± 1.5 deg, the return will be approximately that of a complete sphere ($\sigma = \pi R^2$), and large variations with frequency change will not be seen.

The region in Case 2 (Figure 138) is also one of large variations, but is a point of singularity since the angle, α , must be bisected and the satellite located in a vertical plane above the transmitter and receiver. Again, if θ or ϕ is increased beyond ± 1.5 deg, operation will not be in a region of large variations.

For the operational configuration in Case 3 (Figure 139), the return would closely approximate that expected from a complete sphere ($\sigma = \pi R^2$), and the operation should not be in a region of large variations of return with changes of frequency. This configuration is considered to be a more realistic representation of positions and attitudes to be expected in a typical mission.

The operation in the configuration in Case 4 (Figure 140) should not be in the critical region of variation with frequency, and the return should be that of a complete sphere ($\sigma = \pi R^2$).

Since Case 1 is for a monostatic operational mode, which does not appear of interest, and Case 2 is a point of singularity, Cases 3 and 4 are most representative of attitudes and aspect angles that would be encountered. The probability of being in the configuration of Case 1 or 2 is also quite small and should not greatly affect the operational capability of the satellite. The return ($\sigma = \pi R^2$) predicted for Cases 3 and 4 was based on reflectivity measurements at small bistatic angles (< 10 deg) and should therefore be qualified. Additional reflectivity measurements at large angles should be made to more accurately predict the return coverage to be expected.

8. CONCLUSIONS AND RECOMMENDATIONS

a. General

The conclusions and recommendations given below were based on the theoretical analysis and reflectivity tests of the lenticular shape.

b. Conclusions

Theoretical predictions of variation of nose-on monostatic return indicate that 21.5-db variations are to be expected compared with 11-db variations (± 2 db error assumed) shown in the reflectivity tests of the 20-in. model. The theoretical variation indicates a power ratio of 0.69/1 for the edge diffraction return to that of the center spectral return; the reflectivity measurements indicate a power ratio of 0.33/1. Although there is no close agreement between theory and tests, the indications are that considerable variations in nose-on monostatic return are to be expected. One source of possible disagreement between the theory and tests is that the frequency increments at which reflectivity patterns were taken were not sufficiently small to completely define the curve showing constructive and destructive interference between the edge and spectral return. Also, since the 20-in. test model was small compared to the full-scale satellite, an exact scaling of the edge configuration was difficult. Therefore, the edge return may not have been as large as that predicted.

Reflectivity patterns indicate that large variations (≈ 4 db) in monostatic return are not apparent outside the nose-on, ± 1.5 -deg region. Since the probability of the satellite being in such a position and attitude that a nose-on monostatic return is given in both planes is quite small, the nose-on return variation is not necessarily considered detrimental to the operational capability of the satellite. Therefore, the effect of frequency change on over-all return is not as serious as previously believed.

The average value of the lenticular monostatic return as the satellite

is rotated over its included angle very closely approximates (± 2 db) the radar return magnitude of a complete sphere of the same radius of curvature (200 ft) as the lenticular satellite.

Preliminary bistatic reflectivity tests at small bistatic angles (< 10 deg) indicate that the variations in return are approximately equal to those seen under monostatic conditions.

A moderate included angle of the lenticular configuration should be maintained since the magnitude of the edge diffraction return is an inverse function of the angle between the tangents to the two spherical caps at their point of intersection. Decreasing the included angle would increase the edge diffraction return and thus increase variations in the lenticular return.

The effect of lens surface tolerance on the radar return is considered negligible if the mechanical tolerances outlined in Item 3 are maintained.

The effects of booms and canister on the radar return are negligible even under the extreme conditions where the booms are totally conducting material.

The reflectivity of the 1.2- and 1.6-mil wire-grid material for the lens caps is sufficient. Measurements show > 91.5 percent of the worst case conditions of wire size, polarization, and frequency. Over-all lenticular return may be reduced by 0.4 db by the use of the wire grid lens instead of a totally conducting surface.

Electrical continuity between the lens caps is considered necessary to reduce the edge diffraction return. Continuity between gores is not necessary except near the center of the spherical lens where the distance between gore seams becomes small in terms of wave lengths. For this reason, a cap of grid material (13-ft radius) with electrical continuity should be used on the full-scale model.

Results have indicated that it is feasible to simulate the full-scale

satellite r-f characteristics with a 50-ft-diameter flight-test model by maintaining geometric similarity. Using prototype materials, similar r-f returns will be experienced in areas of edge diffraction, lens material reflectivity, boom blockage, and canister blockage for monostatic and bistatic attitude conditions. The r-f returns then become representative and predictable for any model size and flight altitude.

The effect of lens radius of curvature, ρ , on r-f return can readily be calculated for different size satellites through the relationship $\sigma \propto \rho^2$. The r-f return prediction, σ , for different altitudes can also be determined, since $\sigma \propto 1/S_T^2 S_R^2$ where S_T and S_R are satellite separation from transmitter and receiver respectively. On the basis of theory and ground model tests, it is possible to predict with reasonable accuracy the r-f return for any size similar satellite for known flight conditions.

c. Recommendations

Additional theoretical analysis of the edge diffraction phenomenon is recommended to better understand the effect of design parameters on the edge diffraction return. A more detailed analysis that takes into account the exact edge configuration of the satellite should be undertaken. This type of analysis would possibly provide closer correlation with the reflectivity measurements. Another area of interest would be the theoretical analysis for the bistatic operating conditions.

In conjunction with the analysis above, the theoretical prediction of the return from an additional 40-in. test model should be determined and reflectivity measurements made to substantiate this theoretical analysis.

Reflectivity range tests of the present 20-in. model and the additional 40-in. model over a complete range of bistatic angles and typical operating frequencies are considered necessary to more closely predict the operational capabilities of the lenticular configuration.

Additional effort should be made to measure the magnitude of the edge diffraction return to provide closer correlation with the theoretical analysis.

The edge of the lenticular test model should be modified and reflectivity measurements made in an effort to reduce the magnitude of the edge return and thus reduce variations in over-all return with changes of frequency.

Recent Goodyear Aerospace experience on grid materials and grid structures indicates that for a shape such as the lenticular satellite, leakage of r-f energy through the front lens may be focused and re-radiated somewhat by the rear lens and thus cause variations in the over-all satellite return due to constructive or destructive interference with the specular return. For this reason, reflectivity tests on a scale model fabricated from representative grid material are recommended. The tests would determine whether the over-all return is adversely affected by use of grid material instead of a totally reflecting lens material. The effect of spacing between lens surfaces could also be determined.

The effects of the boom and canister on r-f return were analyzed on the basis of the comparison of the magnitude of the lenticular shape return and that of the boom or canister return. Additional effort should be made to determine the effects of multiple path reflections from the booms or canister to the lenticular shape.

SECTION III - TECHNICAL DISCUSSION - PHASES I AND II

Subsection Five - Material Development

1. GENERAL

Significant advances in the development of the wire cloth-photolyzable film composite lens material were achieved during Phase II of the program. The work involved both test evaluation of previously developed composite materials and development of more refined materials. The development work was performed on (1) wire and wire cloth, (2) photolyzable film, (3) film-cloth composites, and (4) seams.

Development of wire cloth-photolyzable film materials was started by Goodyear Aerospace prior to 1 July 1963. From 1 July through 31 December 1963 GAC efforts were supplemented with funds from this contract. The materials development report⁹ for Phase II covers the combined work in this area.

The report presents the results of a wide variety of development tests. Basic stress-strain curves are given for the various wires, wire cloth, photolyzable film, and composite film-cloth materials that were investigated. Photolyzation rate curves and spectral transmission data are given for the film variations and strength and stiffness data for the various seam materials that were investigated. Also diaphragm test data to determine rigidizing and buckling characteristics of the film-cloth materials are presented. In addition the report includes data on a number of other tests such as film porosity, tear, crease resistance, impact resistance, and effects of packaging on the materials.

Because Reference 9 includes all details and data pertinent to the material development effort, this report only summarizes the work that was done.

Subsection Six includes itemized material test results together with a definition of test procedure, test facilities, and correlation of theory and experiment where applicable. Tables and figures are included to substantiate the conclusions and recommendations and to facilitate an understanding of the scope of the materials development work.

The basic lens material is a sparsely woven, fine wire cloth, coated with a photolyzable film. After deployment and inflation in space the lens will be pressurized until the material has reached its yield point. This will rigidize the wire so that the lens will remain in its inflated lenticular shape. Subsequently the film material will photolyze under the space environment of vacuum and solar radiation. The woven wire will remain as the operational satellite lens material.

Material design criteria include considerations such as (1) a low-weight material, (2) a wire-cloth material that will yield at as low an internal pressure as practical, (3) a film that will photolyze satisfactorily under space environment, (4) a film that has a low enough porosity to allow pressurization, (5) seams that will remain intact during the satellite service life, and (6) a rigidized lens that will have sufficient contour accuracy for r-f reflective characteristics.

2. WIRE AND WIRE CLOTH

Prior to the lenticular satellite program GAC had developed and produced limited quantities of two fine-wire cloths. These were:

1. Five percent phosphor bronze, 1.6-mil wire with 24 wires per inch in both warp and fill directions.
2. Stainless steel, Type 316, 1.0-mil wire with 24 wires per inch in both warp and fill directions.

During this program efforts were initiated to develop a cloth with lower yield strength. A limited quantity of cloth made of 1.2-mil copper wire

with 21 wires per inch in both warp and fill directions, was woven and weaving feasibility demonstrated. This new cloth was coated with film and a limited test evaluation performed. The resulting cloth is recommended as the prototype lens material and is described as follows.

3. PHOTOLYZABLE FILM

Prior to the lenticular satellite program GAC had initiated development of an organic photolyzable film material. This material was intended as a bladder for inflating and rigidizing large space structures. Unlike ordinary film, the photolyzable material has the desirable characteristics of disappearing in a space environment. The key to its behavior is that, under the vacuum environment of space, film chemical bonds are disrupted by combined heat and ultraviolet supplied by the sun. Once the photolysis takes place, the resulting lower molecular weight volatile fragments evaporate.

Photolysis of the film had been demonstrated in bell-jar tests under artificial ultraviolet and temperature exposure. The original film was transparent. This program was directed toward the development of colored film. With addition of dyes to the transparent film a fuller spectrum of the solar energy can be absorbed. This increases the temperature of the material in space environment and proper temperature for photolysis is achieved. Screening of dye materials resulted in the selection of Nigrosine E-8037. Weight loss tests were conducted to show that addition of the dyes did not significantly affect the photolysis process. Spectral transmission tests were conducted to show that photolysis temperatures will be achieved in the space environment.

Limited testing of the colored film material was conducted in a GAC carbon-arc solar energy simulator. This equipment closely simulates the space environment of vacuum and solar energy. The test samples are heated by absorption of energy from the solar energy simulator rather than by artificial heat that is supplied in the bell-jar tests.

4. FILM-CLOTH COMPOSITE

GAC had also previously developed a film-cloth laminating technique. The laminate consisted of a sheet of photolyzable film on each side of the cloth. The layup was cured under heat and pressure. Because the minimum practical film thickness was about 0.5-mil, a total minimum film thickness of one mil resulted.

It was considered desirable to develop a continuous laminating procedure as well as to reduce film thickness. Consequently this program initiated development of a technique to cast the liquid film resin directly onto the cloth. This resulted in a continuous belt casting process which also reduced the total film thickness to one-half mil. A schematic diagram of the continuous casting process is presented in Figure 141.

The resulting composite material, with transparent photolyzable film and both 1.6-mil phosphor bronze and 1.2-mil copper cloth, was used in test evaluations and in model fabrication.

5. SEAMS

A major effort on lens material seam development was an important part of the lenticular satellite program. Both tape-type and metal-joined-type seams were considered. Most of the work was done on tape-type seams which includes a film strap material and an adhesive for bonding to the lens material. The development effort on metal-joined seams was exploratory in nature. Some promise was shown in resistance welding and soldering of the wires together.

The seam development basically involved selecting tape material that would transfer the rigidizing loads across the seam without substantially increasing stiffness in the seam direction. Seam strength evaluations were conducted at room temperature and at 200 F. Satisfactory seams were developed to meet this requirement.

The seam stiffness evaluation involved selection of films that are applicable as the tape material. Mylar is commonly used as a tape material but

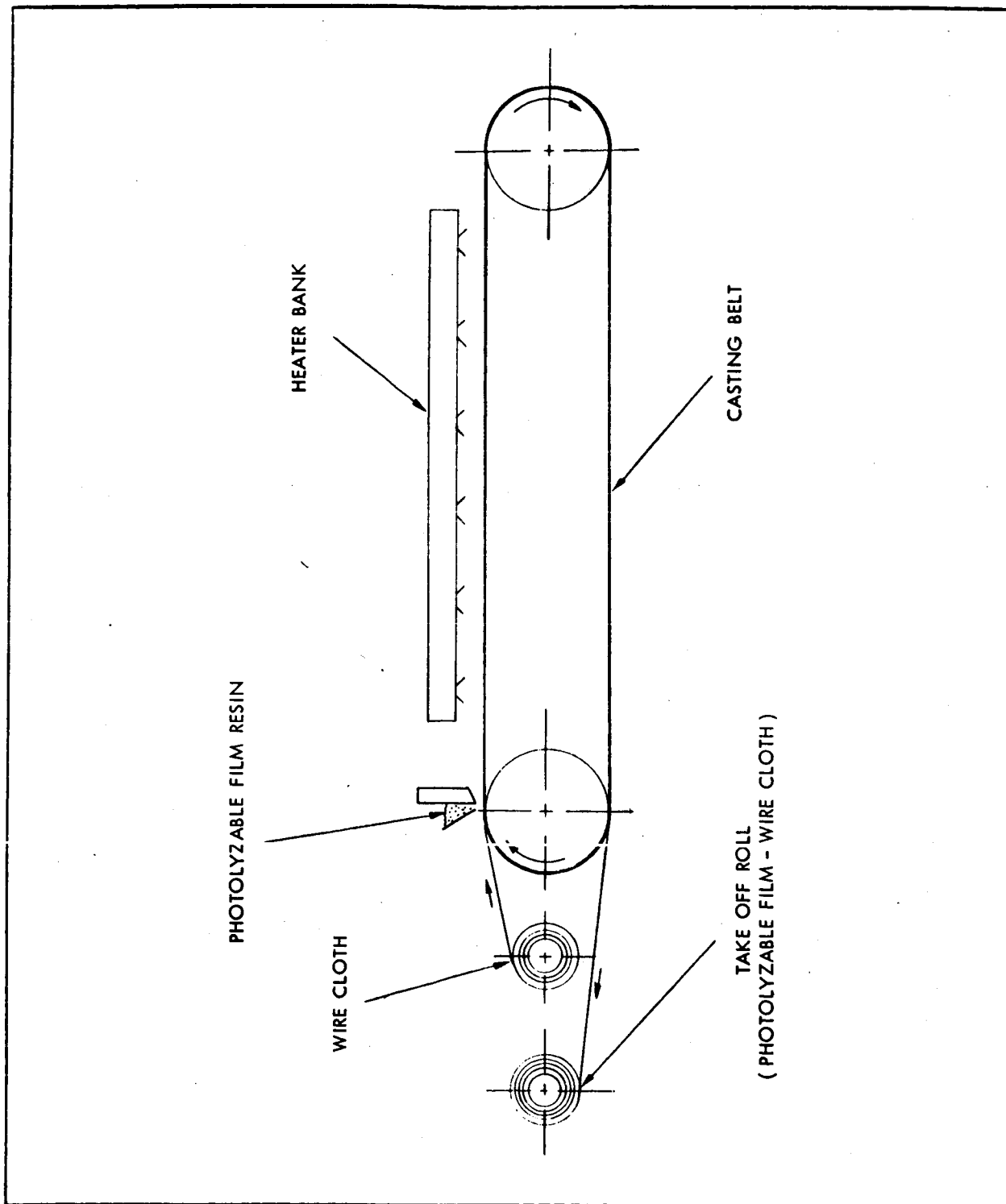


Figure 141 - The Goodyear Tire and Rubber Company Research Casting Belt

is one of the stiffer materials. Films such as Teflon and polypropylene have considerably less stiffness and are candidate tape materials. Slotting of tapes to reduce stiffness was explored and results indicated that stiffness could be greatly reduced.

All seam evaluations were performed utilizing tensile testing. Subsequent evaluation has shown a tendency for tape delamination from the film-cloth after a period of time. Test results indicate that this occurs only when certain adhesives are used on the tape. This problem area is best evaluated by peel tests.

6. CONCLUSIONS AND RECOMMENDATIONS

a. General

It is concluded that wire cloth-photolyzable film is suitable for use as the lens material. Significant advances in the development of this material were achieved on this project.

Although feasibility has been shown, continued development effort is required to assure reliability for use on flight satellites. It is therefore recommended that further development effort be authorized in the following areas:

b. Wire and Wire Cloth

Although feasibility of weaving the 1.2-mil copper wire cloth was demonstrated, additional weaving effort is recommended. This development would result in improved quality of the woven cloth which can be achieved best by actual weaving experiments.

c. Film

Continued development effort on the colored film is recommended. Photolyzation of the film has been demonstrated under controlled temperature conditions. Optical tests and thermodynamic calculations show that the film will absorb sufficient solar radiation to

achieve the required temperature in space for rapid photolyzation. Additional tests should be performed in the solar simulator facility to prove experimentally that photolyzation will take place. Screening of dye materials that can be added to improve photolyzation should be continued. Also further research on the theory of photolyzation is recommended. Although the basic principles of photolyzation are known, a thorough study is desirable. This work would be performed in conjunction with the Goodyear Tire and Rubber Company Research Laboratory.

d. Film Cloth Composite

Feasibility of the continuous process of casting the film resin directly onto the cloth was established in this program. Additional casting experiments are recommended to improve the quality of the resulting film-cloth composite. Porosity and uniformity of the material can be best established by actual casting experiments.

Additional physical property testing is also recommended to better establish the rigidizing characteristics of the composite material.

e. Seams

Development efforts in this program have established the feasibility of decreasing seam stiffness by use of softer tape materials. Slotting the tapes also decreases seam stiffness. It is recommended that continued effort be authorized on fabrication and testing of various seam materials. A thorough investigation of seam deterioration with time should be included. This would involve peel test investigations.

Protection of the seam materials from space environment is another recommended area of investigation.

f. Model Fabrication

Fabrication and testing of models is recommended particularly for

the lens material where an accurate contour is desirable. In particular this testing would evaluate seam materials for the so-called beach-ball effect. The models would range from 5-to-20-ft in diameter and would be tested at various temperatures.

SECTION III - TECHNICAL DISCUSSION - PHASES I AND II

Subsection Six - Material and Component Tests

1. MATERIAL TESTS

a. Wire and Wire Cloth

Several wire materials and sizes were obtained and tested. The data obtained included yield strength (in which 0.2 percent offset criteria were used), ultimate strength, modulus of elasticity, and percent elongation at failure. All wire materials were procured in a soft annealed condition.

The tensile tests were performed in the GAC Instron testing facility. Strain rates used were generally 10 percent per minute.

A summary of results of the wire tests is listed in Table XXIV. Typical stress-strain curves are given in Figure 142. Complete details of all tests are given in Reference 9.

Tensile tests also were performed on the bare woven cloths. The data, stress-strain, were used to compare stiffnesses of bare cloth, cloth with film applied, and an equivalent number of individual wires. Details of this testing are also given in Reference 9.

b. Photolyzable Film

The test evaluation of the film materials was subdivided into three categories:

1. Film weight-loss behavior
2. Film optical properties
3. Film physical properties

TABLE XXIV - SUMMARY OF WIRE PHYSICAL PROPERTY TESTS

Wire material	Supplier	Remarks	Wire diameter (in.)	Yield (lb)	Ultimate (lb)	Yield (psi)	Ultimate (psi)	E (psi $\times 10^6$)	Elongation (percent)
Stainless steel, type 316	A	Standard stainless steel weaving wire	0.0010	0.0795	0.1160	85,200	124,300	36.4	10.7
Phosphor bronze, 5 percent tin	B	Standard phosphor bronze weaving wire used in first portion of cloth on project	0.0016	0.0922	0.1258	48,200	65,700	16.1	33.2
Phosphor bronze, 5 percent tin	B	Standard phosphor bronze weaving wire, drawn to complete weaving	0.0016	0.0932	0.1260	41,100	55,500	16.0	34.4
Phosphor bronze	C	1-mil sample drawn as back up for copper - never woven	0.0010	0.0247	0.0428	31,500	54,600	17.5	18.2
Copper	C	Sample drawn especially for determining 1-mil copper wire feasibility	0.0010	0.0171	0.0261	23,200	35,300	15.9	13.2
Copper (tested at 200 F)	C	Same as above, tested at 200 F	0.0010	0.0166	0.0230	22,500	31,300	12.9	12.9
Copper	C	Drawn for 1-mil weaving experiment	0.0010	0.0200	0.0268	25,500	34,200	13.6	13.8
Copper	C	Drawn for 1.2-mil weaving experiment	0.0012	0.0292	0.0399	23,700	32,500	12.2	14.7

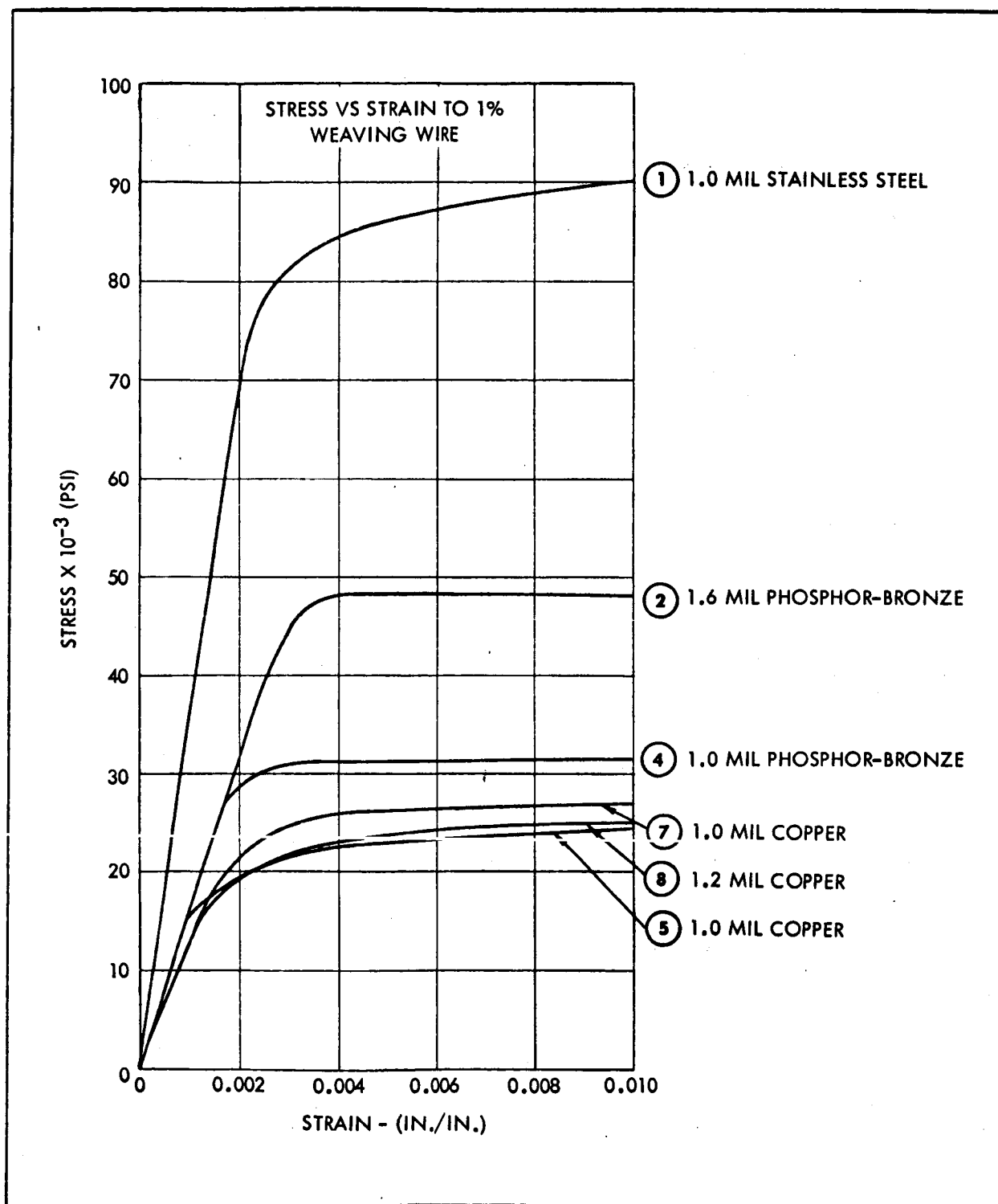


Figure 142 - Stress-Strain Curves of Various Wires

The weight-loss behavior tests involved measurements of material weight-loss per unit of time. The optical property investigation involved transmittance and reflectance measurements and subsequent calculations to obtain α/ϵ values. The physical property tests included tensile stress-strain data, Poisson's ratio data, and measurement of film material permeability.

The weight-loss tests were performed in a specially equipped bell-jar shown in Figure 143. The bell-jar system provided the vacuum while ultraviolet energy was supplied by a mercury-arc lamp mounted over the samples. The specimen mounting block was equipped with resistance heating elements to control the material temperature.

The test samples were prepared by solution casting the film directly on metal disks. The disks were then accurately weighed and clamped in the mounting block. Following vacuum, ultraviolet, and temperature exposures for specified times the test samples were removed and again accurately weighed.

Studies to determine the weight-loss characteristics of photolyzable film were directed towards the investigation of the following areas.

1. Weight-loss behavior of clear film and effect of molecular weight on behavior
2. Effect of dye concentration on the weight-loss behavior of photolyzable film. A single molecular weight resin was used for this work
3. Effect of thickness on weight-loss behavior of clear and colored film

An example of the data, which are given in full in Reference 9, is presented in Figure 144.

Exploratory photolysis tests were also conducted in the GAC carbon-arc solar energy simulator (see Reference 9 for complete

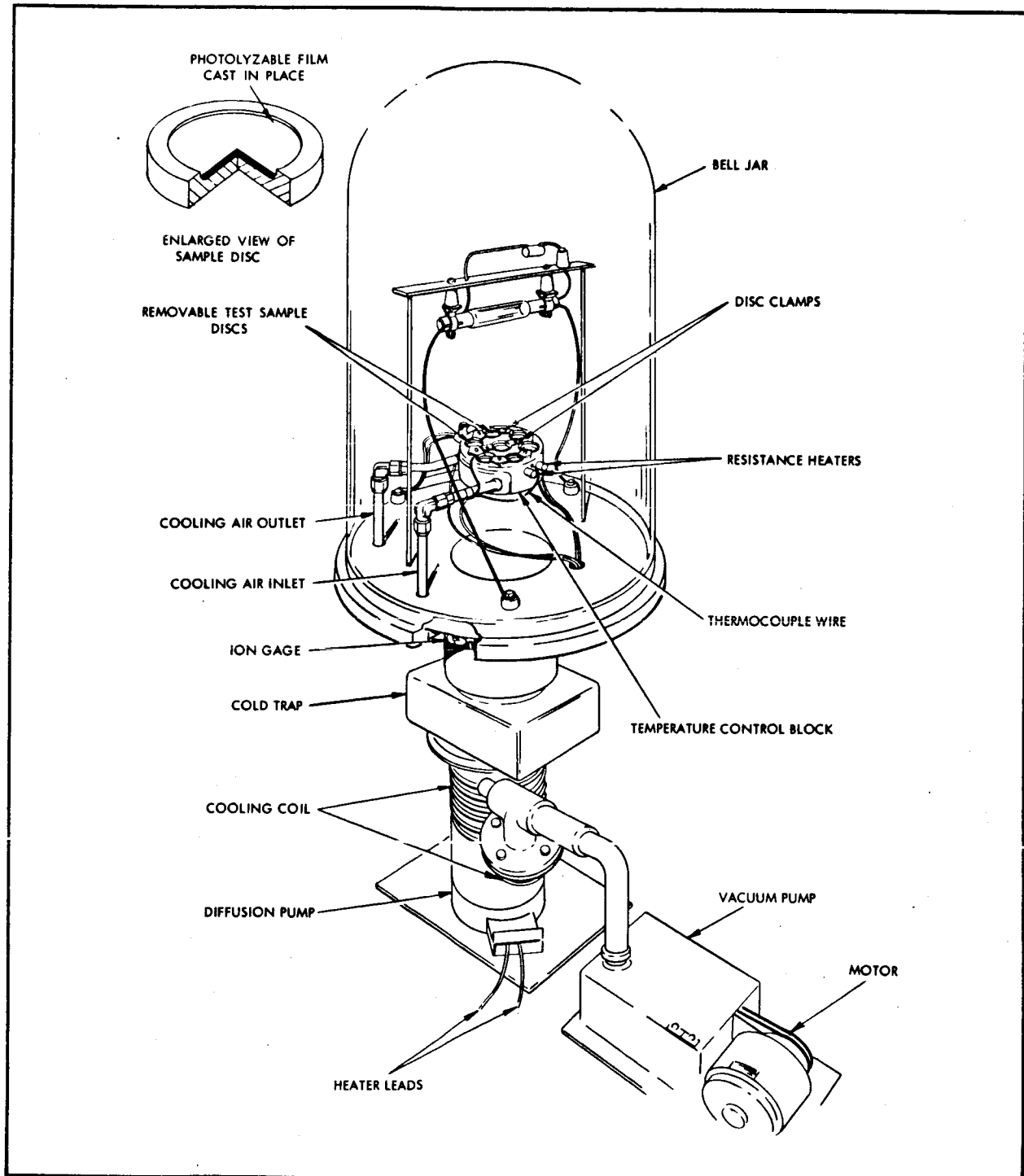


Figure 143 - Apparatus for Controlled Environment Weight-Loss
Measurements by Sample Removal Method

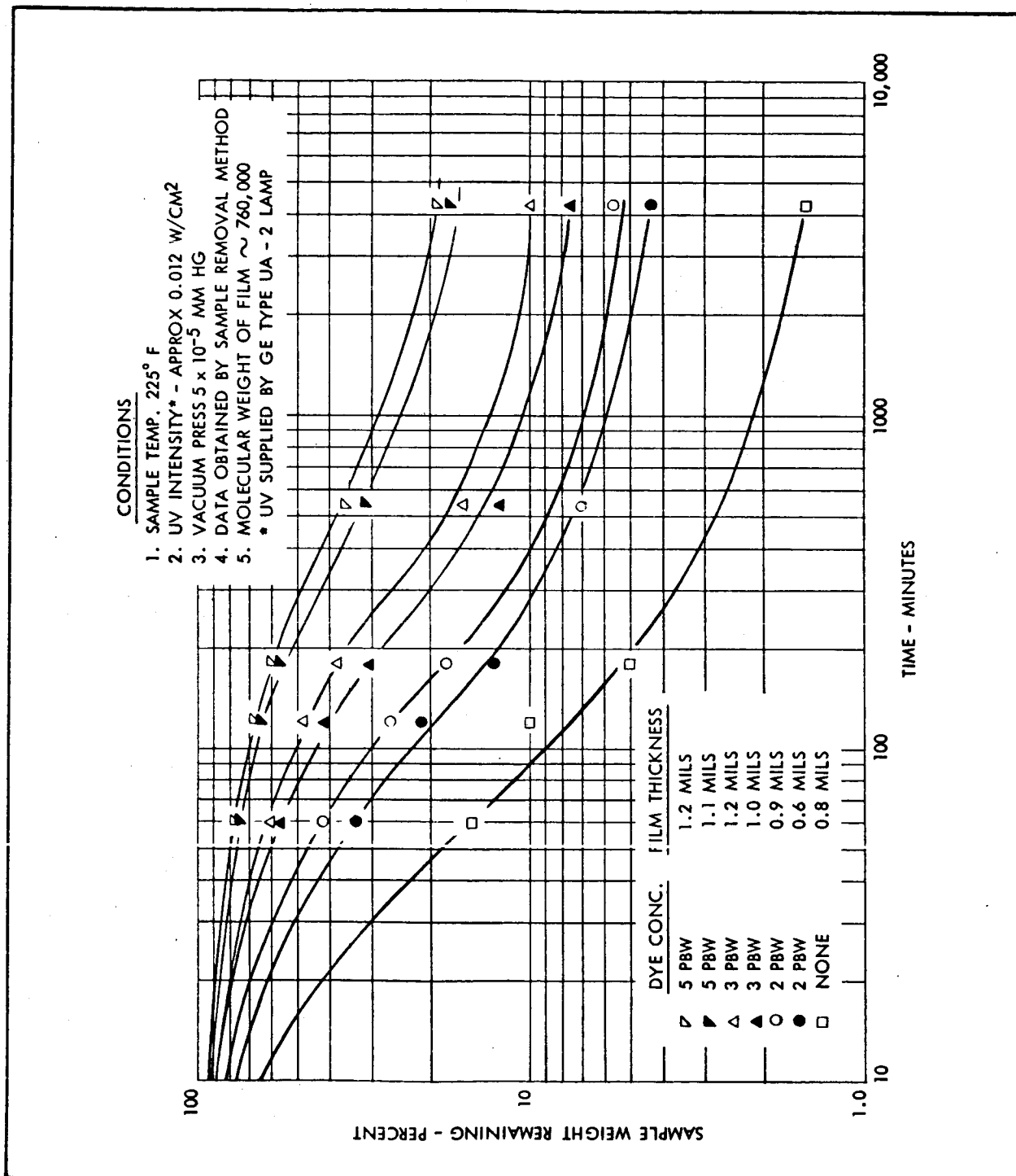


Figure 144 - Effect of Nigrosine Dye E-8037 on Weight-Loss Behavior of Photolyzable Film - Long Time Exposure

details). This type of test does not require artificial heating of the sample as do the bell-jar tests. The solar energy simulation method is extremely desirable because it provides accurate simulation of actual space conditions, including vacuum and broad-band radiant energy of the same distribution as the sun. Hence, both ultraviolet for photolyzation and longer wavelength energy for heating are supplied.

A schematic of this facility is shown in Figure 145.

Optical property measurements were made to determine solar transmittance and reflectance of the film material. These tests were performed to evaluate the solar absorptance of the material and its temperature in a spatial orbit. Variations in amount of dye material added to the film were evaluated. Typical test data are presented in Figure 146. Complete details of all tests performed are given in Reference 9.

Spectral transmittance measurements under geometrical conditions approximating normal irradiation and viewing were made using a Bausch and Lomb Model 505 spectrophotometer in the 0.200 to 0.700 micron wavelength range and a Perkin-Elmer Model 21 spectrophotometer in the 0.700 to 15 micron range.

Both instruments are double-beam-ratio recording spectrophotometers that automatically record the transmittance of a sample as a function of wavelength. Spectral reflectance measurements in the range from 0.300 to 0.700 microns were made using the integrated sphere attachment on the Bausch and Lomb instrument. With this attachment, the reflectance of a sample relative to a magnesium carbonate reference is automatically recorded. The Perkin-Elmer spectrophotometer, equipped with its specular reflectance attachment, was used for reflectance measurements in the wavelength range from 0.700 to 15 microns. With this attachment, the reflectance of a sample relative to vapor-deposited aluminum was recorded

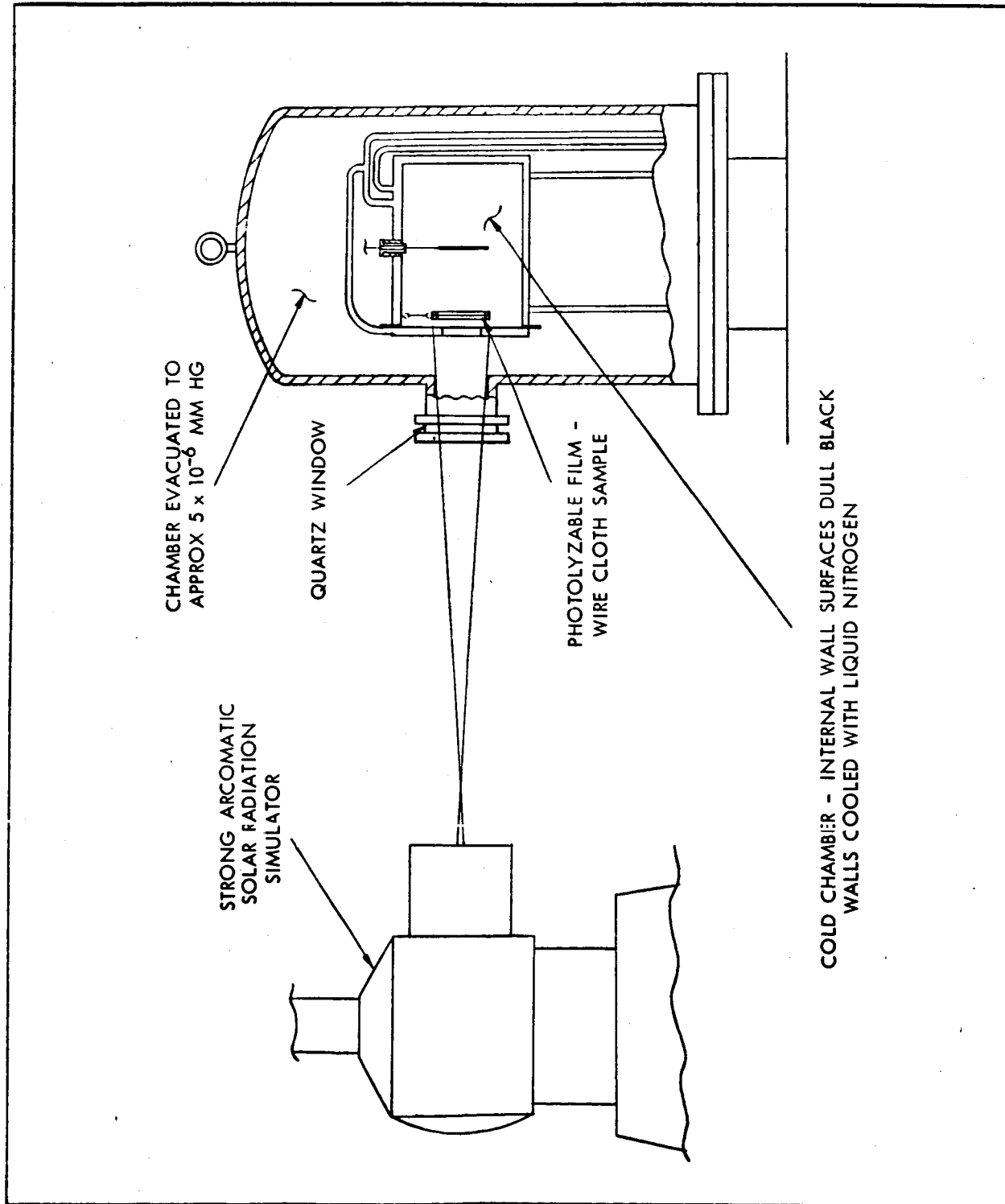


Figure 145 - Carbon-Arc Solar Radiation Simulator Test Apparatus

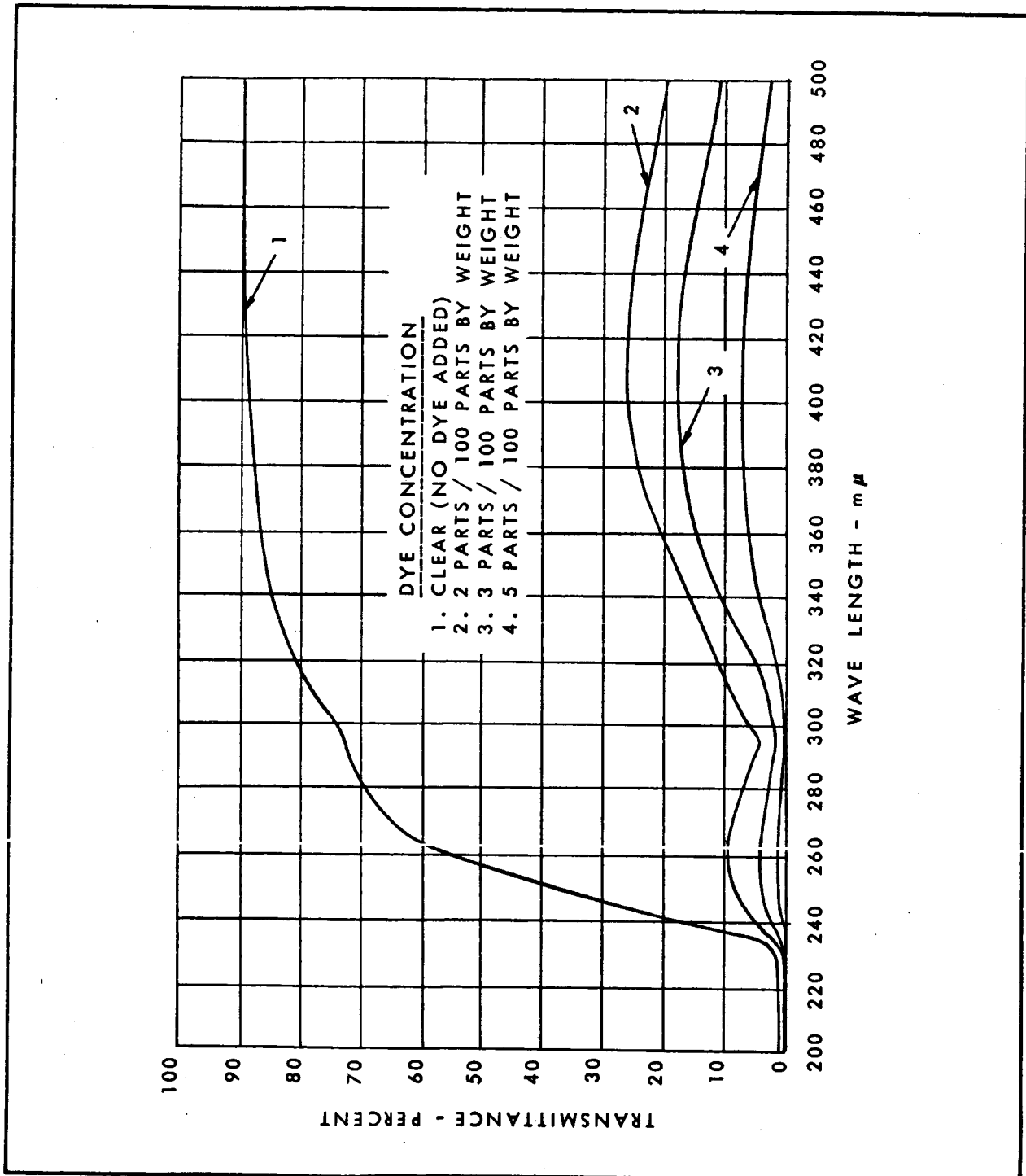


Figure 146 - Effect of Nigrosine E-8037 Dye on Ultraviolet and Visible Transmittance of 0.7-Mil Photolyzable Film

automatically. Further details of the test procedures and the test results are given in Reference 9.

c. Film-Cloth Composite

Film cloth composite strength and stiffness data were obtained at room temperature and at 200 F environments. The majority of the tests were performed on the phosphor-bronze cloth material. When the copper cloth film material became available at the latter stages of the program a limited number of tests were conducted on this material. The tests were all performed in the GAC Instron facility.

Table XXV shows the summary of tensile tests on film cloth material, and Figure 147 gives stress versus strain curves for 1.6-mil phosphor bronze wire and spreadcoat photolyzable film. The stress-strain curves compare the stiffnesses of the film cloth composite, the cloth alone, and the stiffness of an equivalent number of individual wires. Complete data are given in Reference 9.

d. Seams

A large number of screening tests on seam materials were made for this program. Reference 9 gives complete details. Most tests were performed using the 1.6-mil phosphor bronze material. The following parameters were investigated.

1. Seam width
2. Tape on rough or smooth side of the film cloth
3. Tape on one or both sides of the material
4. Types of adhesive
5. Heat sealing
6. Film-coated cloth versus uncoated cloth
7. Strap materials and thicknesses

Tensile tests were performed at room temperature and 200 F

TABLE XXV - SUMMARY OF TENSILE TESTS ON FILM CLOTH MATERIAL

Material	Wire		Film thickness (in.)	Yield		Ultimate		E ($\text{psi} \times 10^6$)	Elongation (percent)
	Diameter (in.)	Mesh (wires per inch)		(lb/in.)	(psi)	(lb/in.)	(lb/in.)		
Phosphor bronze	0.0016	24 X 24	0.0007	2.33	50,800	3.38	73,700	13.0	24.5
Phosphor bronze	0.0016	24 X 24	0.0007	2.16	47,100	3.23	70,400	11.7	22.0
Phosphor bronze at 200 F	0.0016	24 X 24	0.0007	2.28	49,700	2.82	61,600	9.3	11.9
Phosphor bronze at 200 F	0.0016	24 X 24	0.0007	1.76	38,400	2.72	59,400	7.7	26.2
Copper	0.0012	21 X 21	0.0006	0.91	35,300	1.16	45,000	6.12	2.55
Copper	0.0012	21 X 21	0.0006	0.94	36,450	1.40	54,300	5.54	7.39
Copper at 200 F	0.0012	21 X 21	0.0006	0.39	15,130	3.38	4.58
Copper at 200 F	0.0012	21 X 21	0.0006	0.56	21,700	0.72	27,950	3.77	8.49

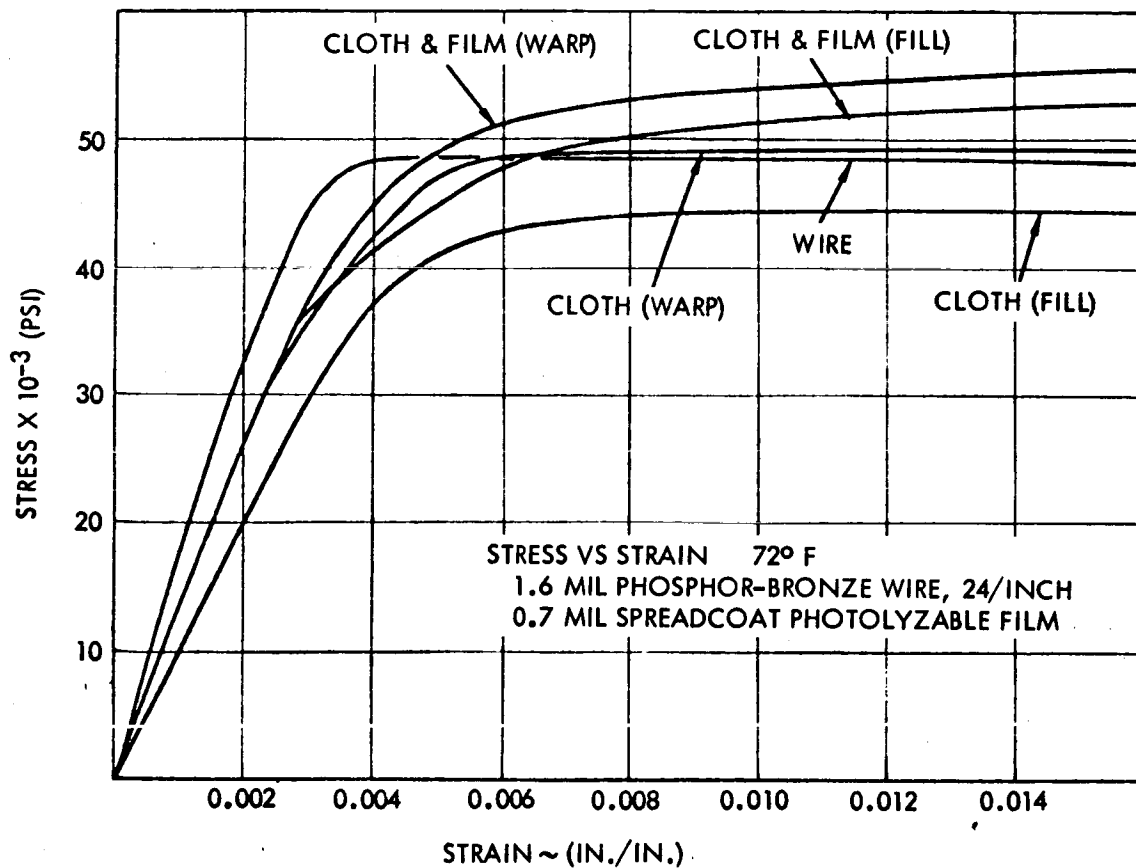


Figure 147 - Stress versus Strain, 1.6-Mil Phosphor-Bronze Wire, 24 Wires per Inch - 0.7-Mil Spreadcoat Photolyzable Film at 72 F

environments. During the latter part of the program the 1.2-mil copper material became available, and a limited number of seam tests were performed using the lighter cloth.

The seam stiffness in the seam direction was also investigated. Basic tensile stress-strain data were obtained for the seam area material and compared with the unseamed basic material. Use of seam materials of low stiffness helps to inhibit stiffness increases in the seam area.

Typical results are given in Figure 148, which shows the effective modulus of elasticity of spheres for 1.6-mil phosphor bronze cloth at room temperature and Figure 149, which shows the effective modulus of elasticity of spheres for 1.6-mil phosphor bronze cloth at 200 F.

2. COMPONENT TESTS

a. Torus

(1) Purpose

Several tests were performed on two 5-ft-diameter torus models for the determination of dimensional changes with respect to pressure, and torus stability.

(2) Test Specimens

(a) Model No. 1

Model No. 1 was a simple 5-ft-diameter torus (Figure 150) fabricated from 1-mil Mylar.

(b) Model No. 2

Model No. 2 was a 5-ft-diameter torus fabricated from 1-mil Mylar with a lens cap of 0.5-mil Mylar and a rim fabricated from 0.40-in. by 5-mil 302 stainless steel, half-hard, as shown in Figure 151.

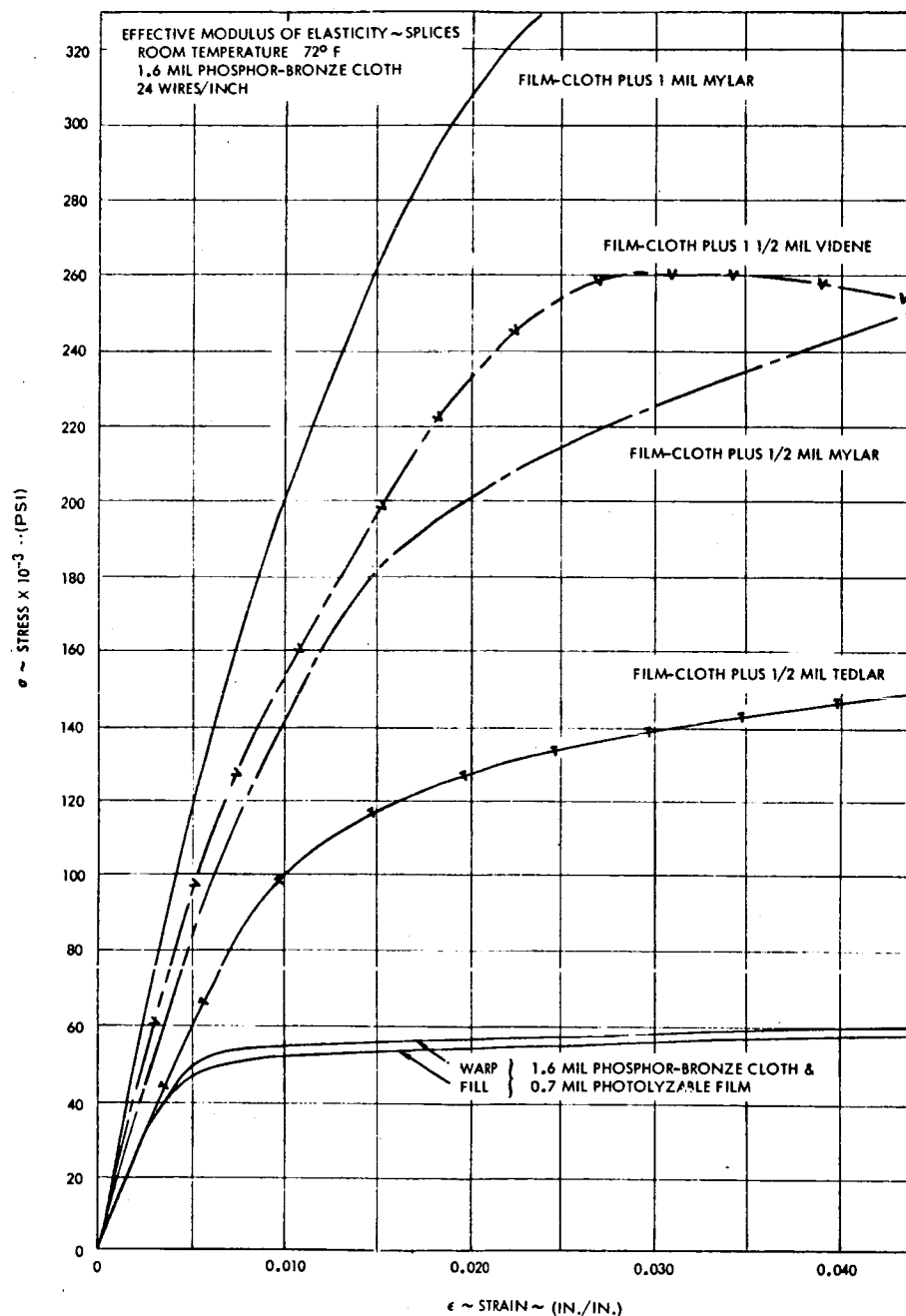


Figure 148 - Effective Modulus of Elasticity of Splices in 1.6-Mil Phosphor Bronze Cloth, 24 Wires per Inch at 72 F

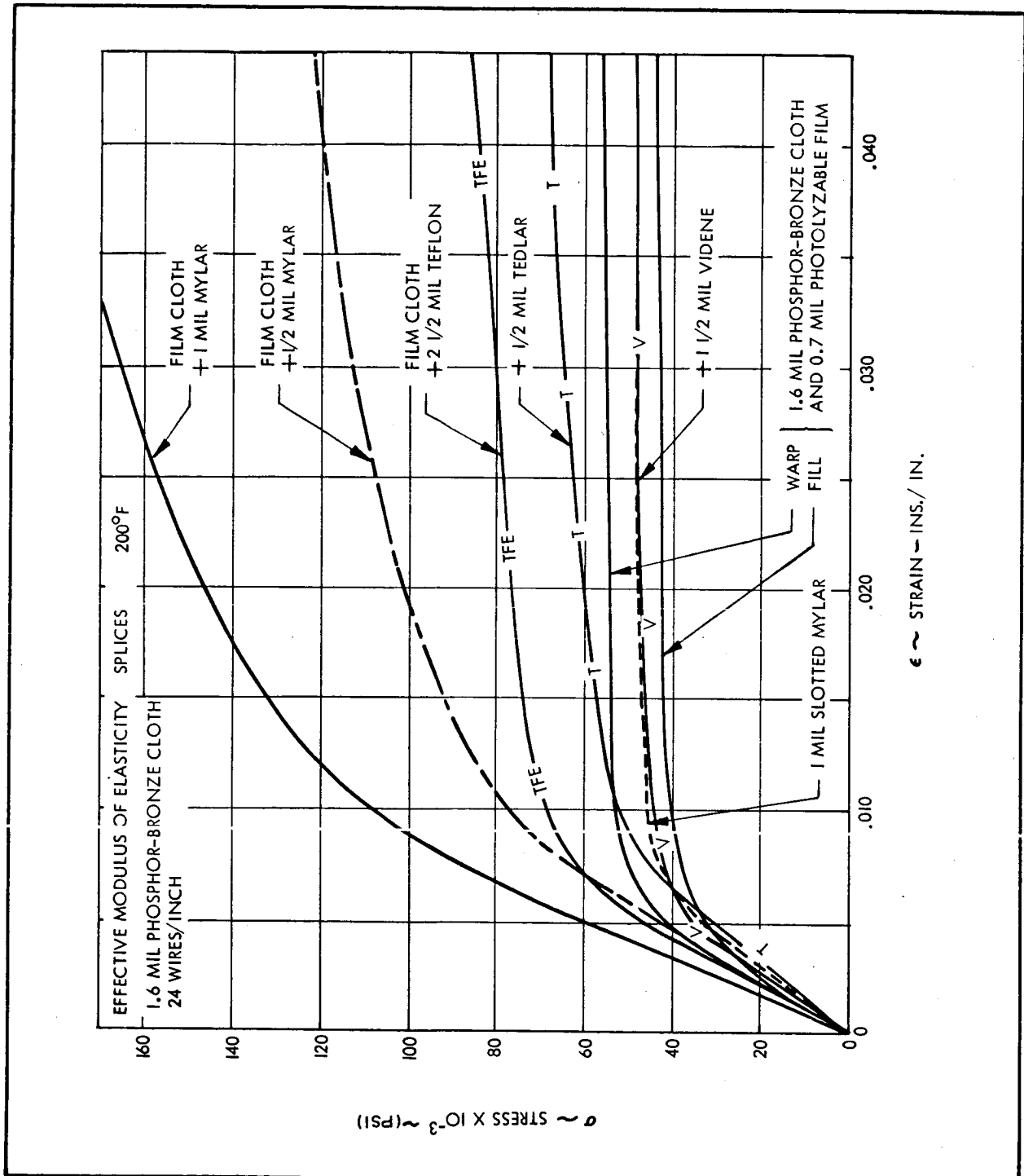


Figure 149 - Effective Modulus of Elasticity of Splices in 1.6-Mil Phosphor Bronze Cloth, 24 Wires per Inch at 200 F

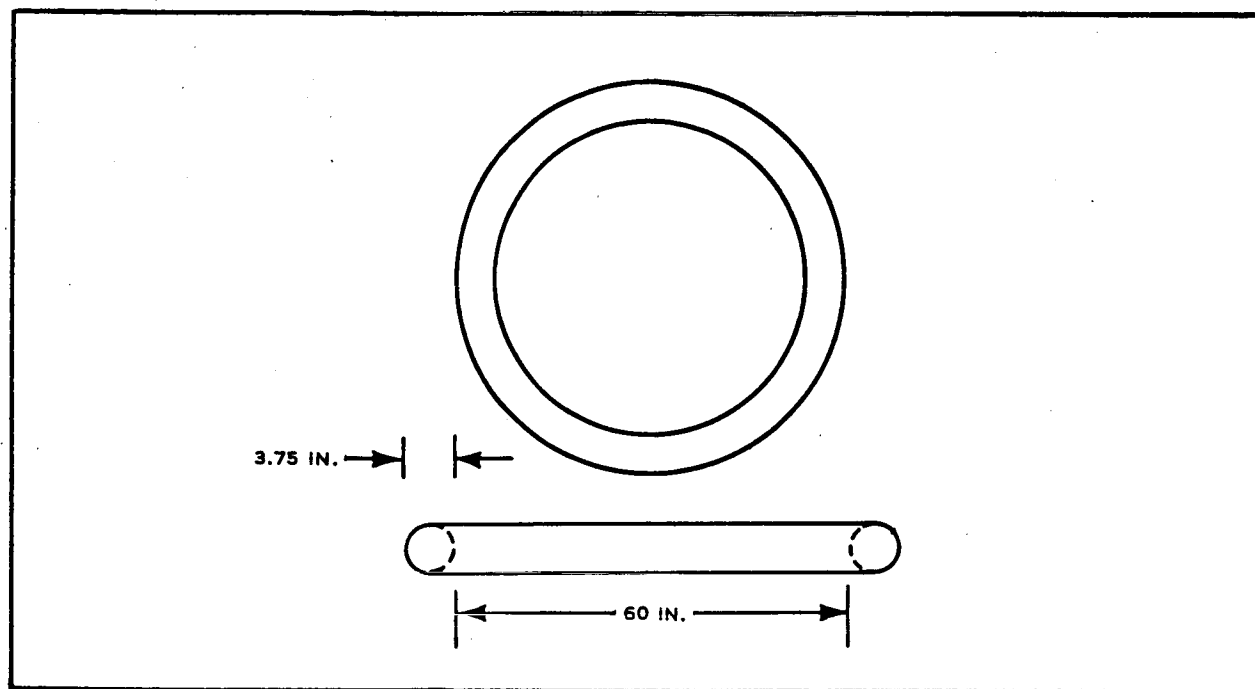


Figure 150 - Torus Model No. 1

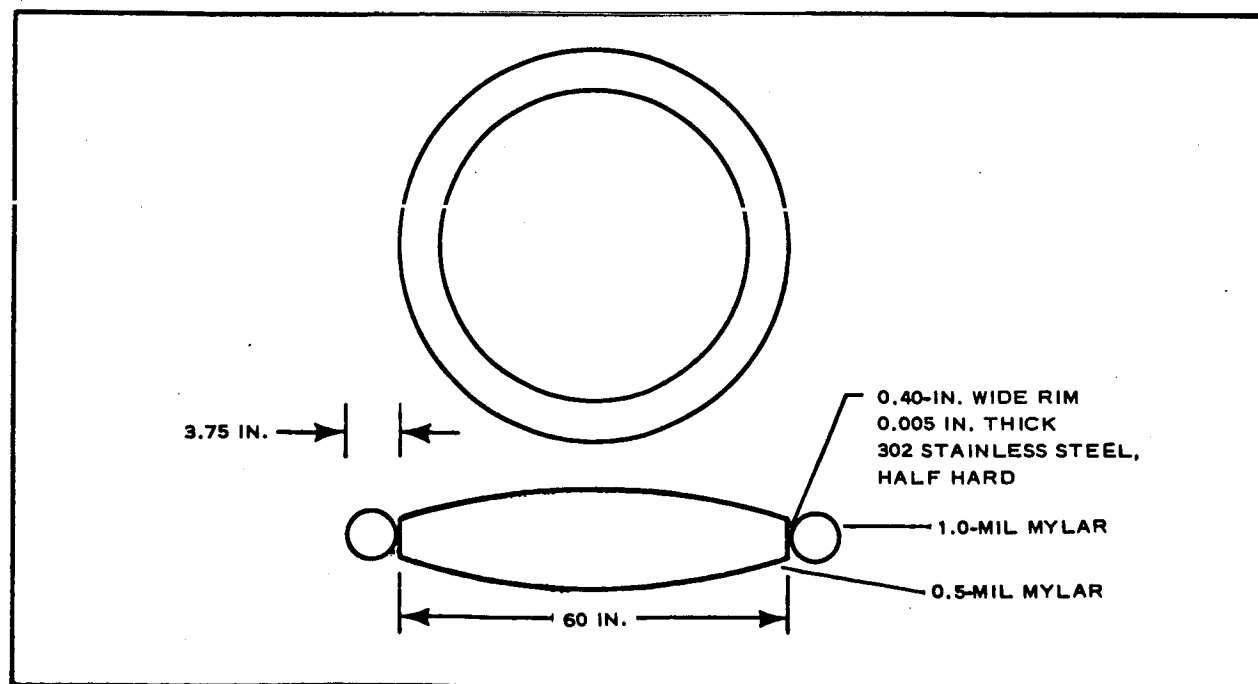


Figure 151 - Torus Model No. 2

(3) Test Setup

(a) Model No. 1

The first series of tests was conducted with the specimen lying on a flat table. To obtain diameter changes of the specimen during pressurization straight pins were cemented to the torus. Deflection scales were then placed in back of the pins and deflections measured with a level (Figures 152 and 153).

After completion of the first series of tests, a stiff ring of 3/4-in. plywood was cemented to the inside diameter of the torus as shown in Figure 154.

During the above tests pressure in the torus was measured with a dial manometer.

(b) Model No. 2

Two series of tests were conducted with the second torus

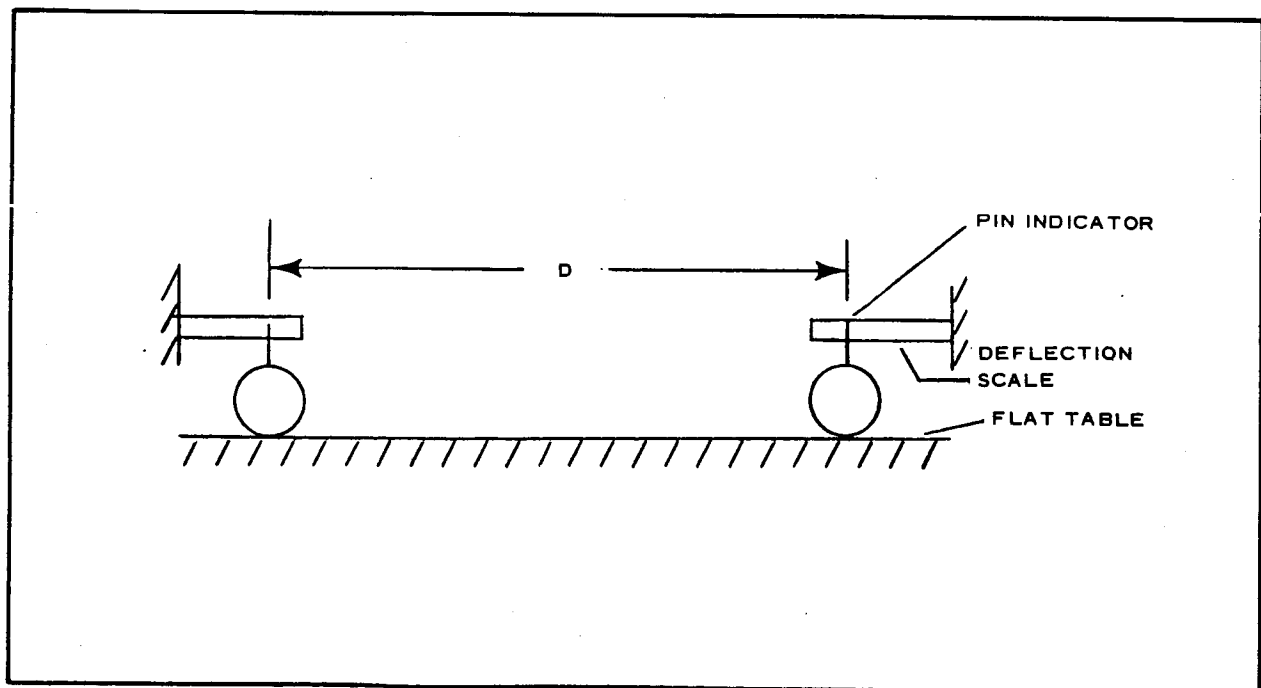


Figure 152 - Torus Model No. 1 - Schematic of Test Setup

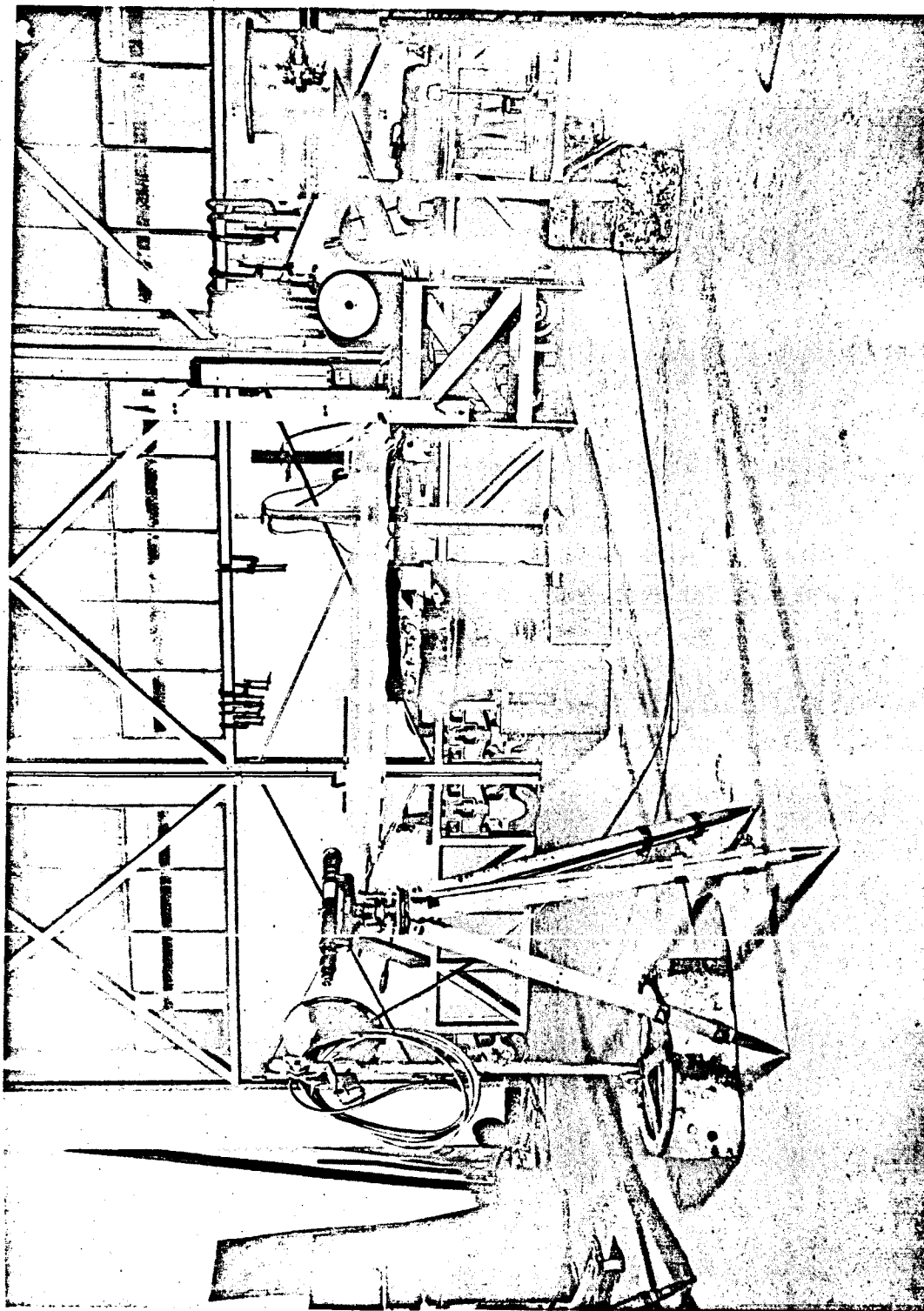


Figure 153 - Torus Model No. 1 - Test Setup

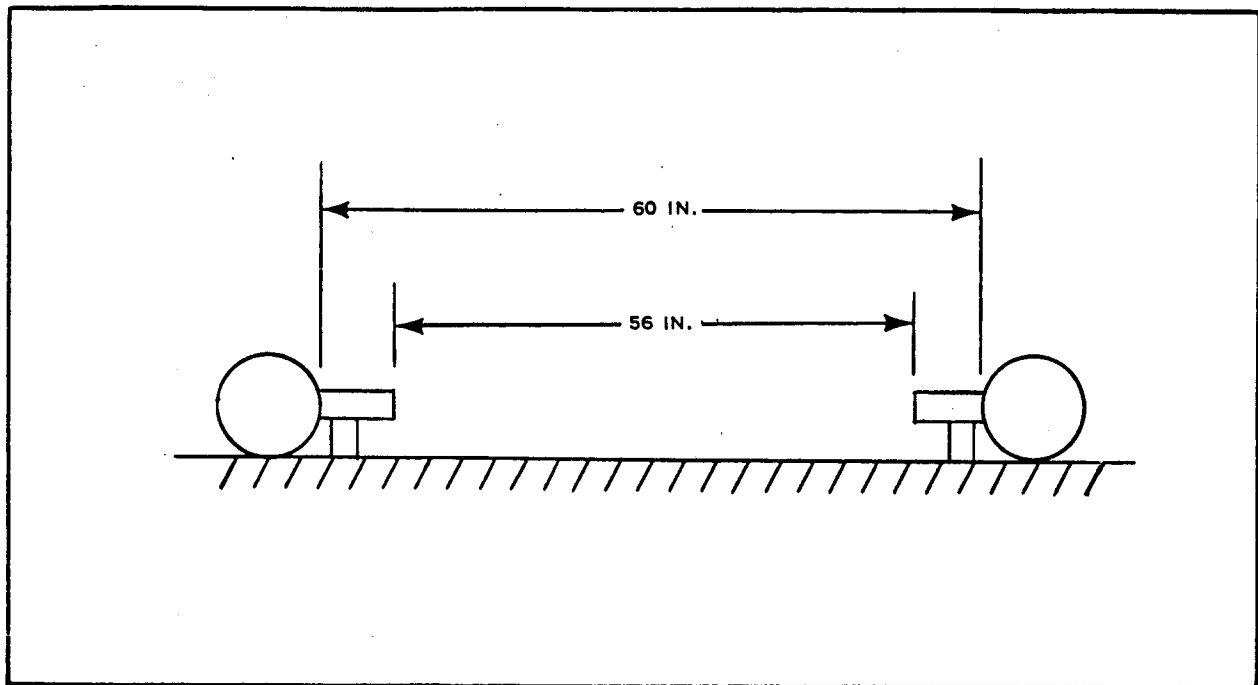


Figure 154 - Diagram of Torus Model No. 1 - Test Setup

model. During the first series of tests the model was lying on a flat table (Figure 155). Another series was conducted with the model hanging vertically (Figure 156) to check the effects of gravity during the first tests.

Deflection instrumentation during both series of tests was essentially the same and is shown in Figure 157.

A micromanometer was used to monitor pressure in the lens and a dial manometer to monitor torus pressure.

For the tests, the torus pressure was set at a specified level, the lens pressure was then increased incrementally at least one or two increments past initial wrinkling of the torus. At each level of torus pressure and lens pressure diametrical change of the torus and height change of the lens were recorded.

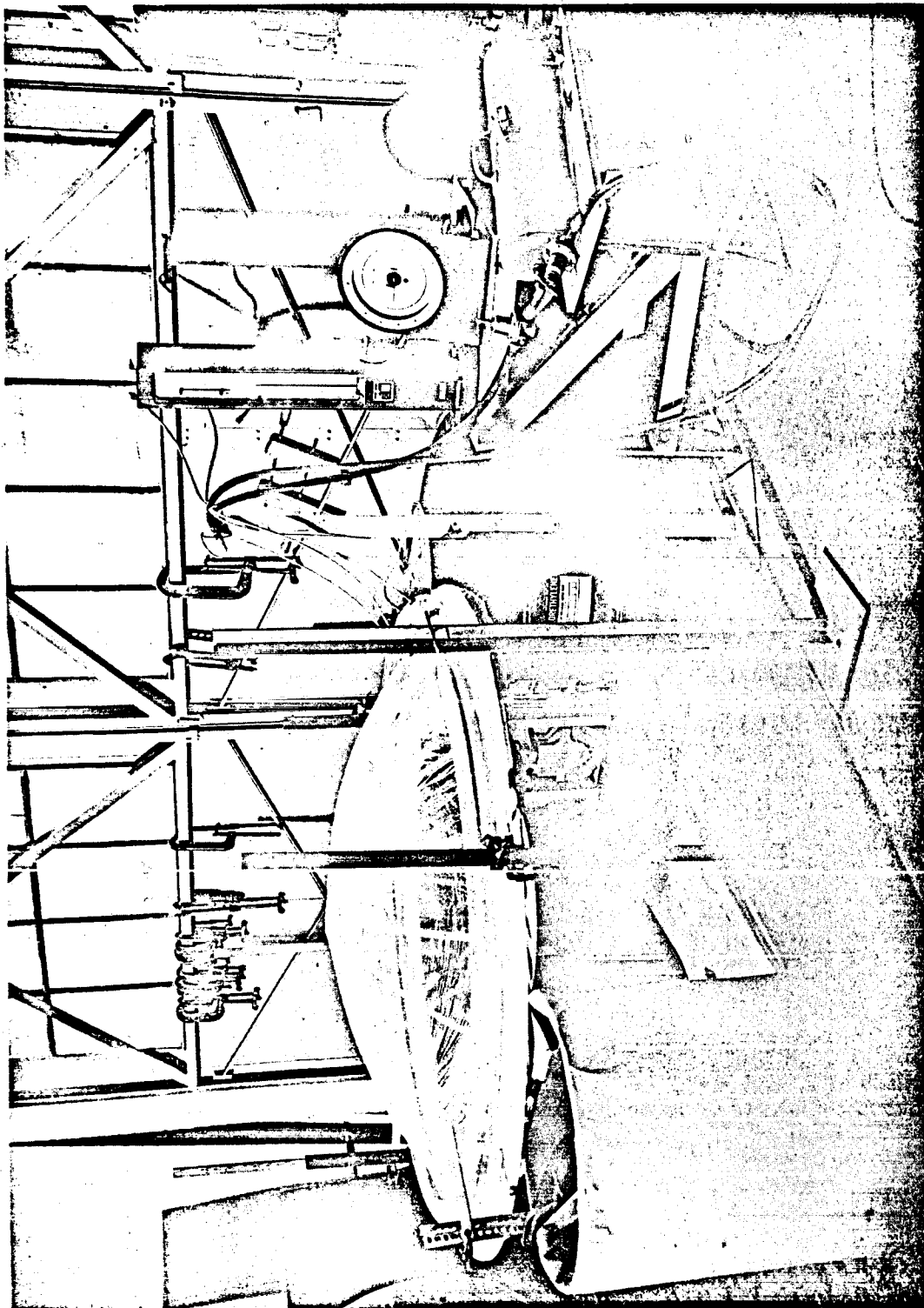


Figure 155 - Torus Model No. 2 - Test Setup on Flat Table

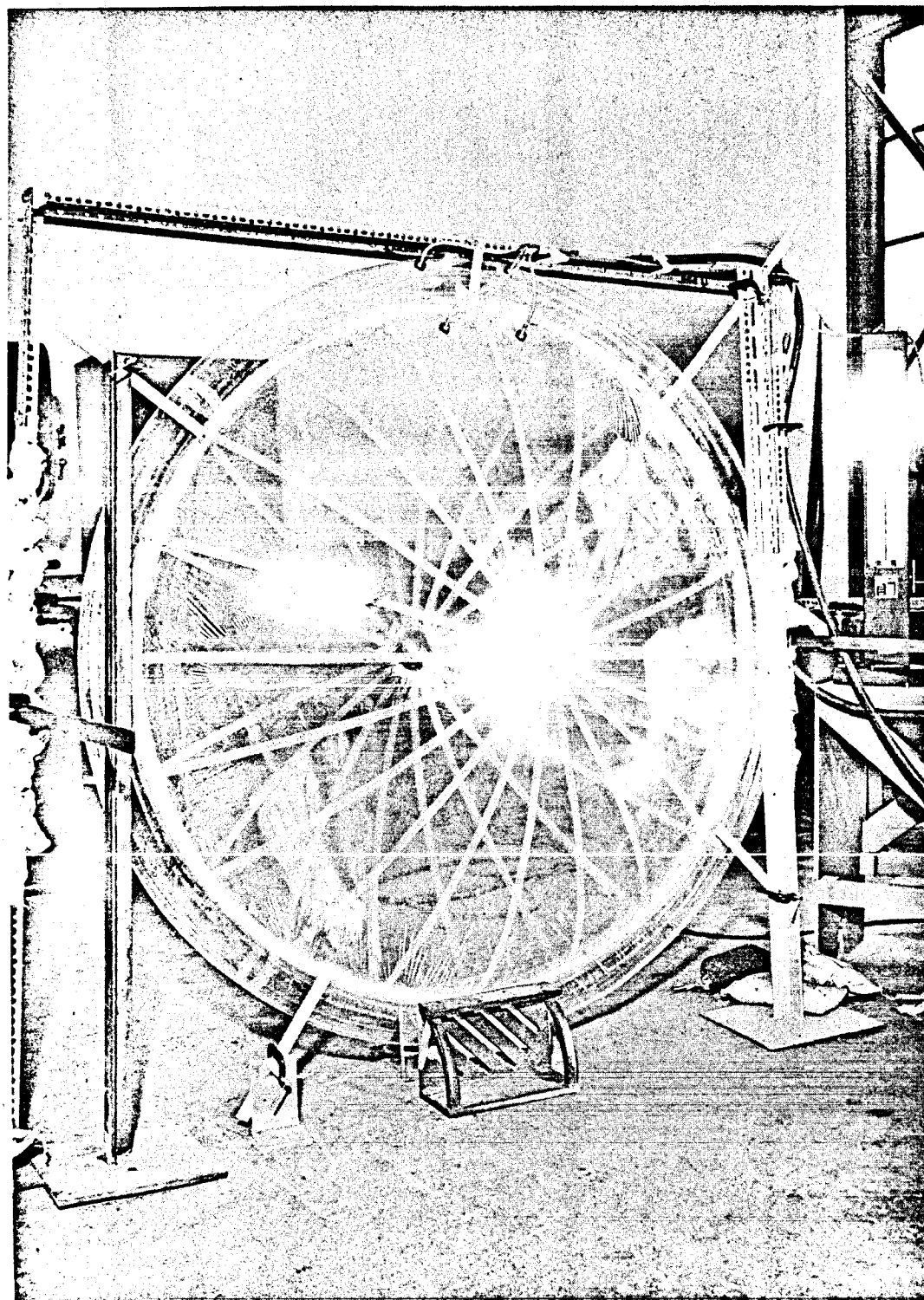


Figure 156 - Torus Model No. 2 - Test Setup Hanging Vertically

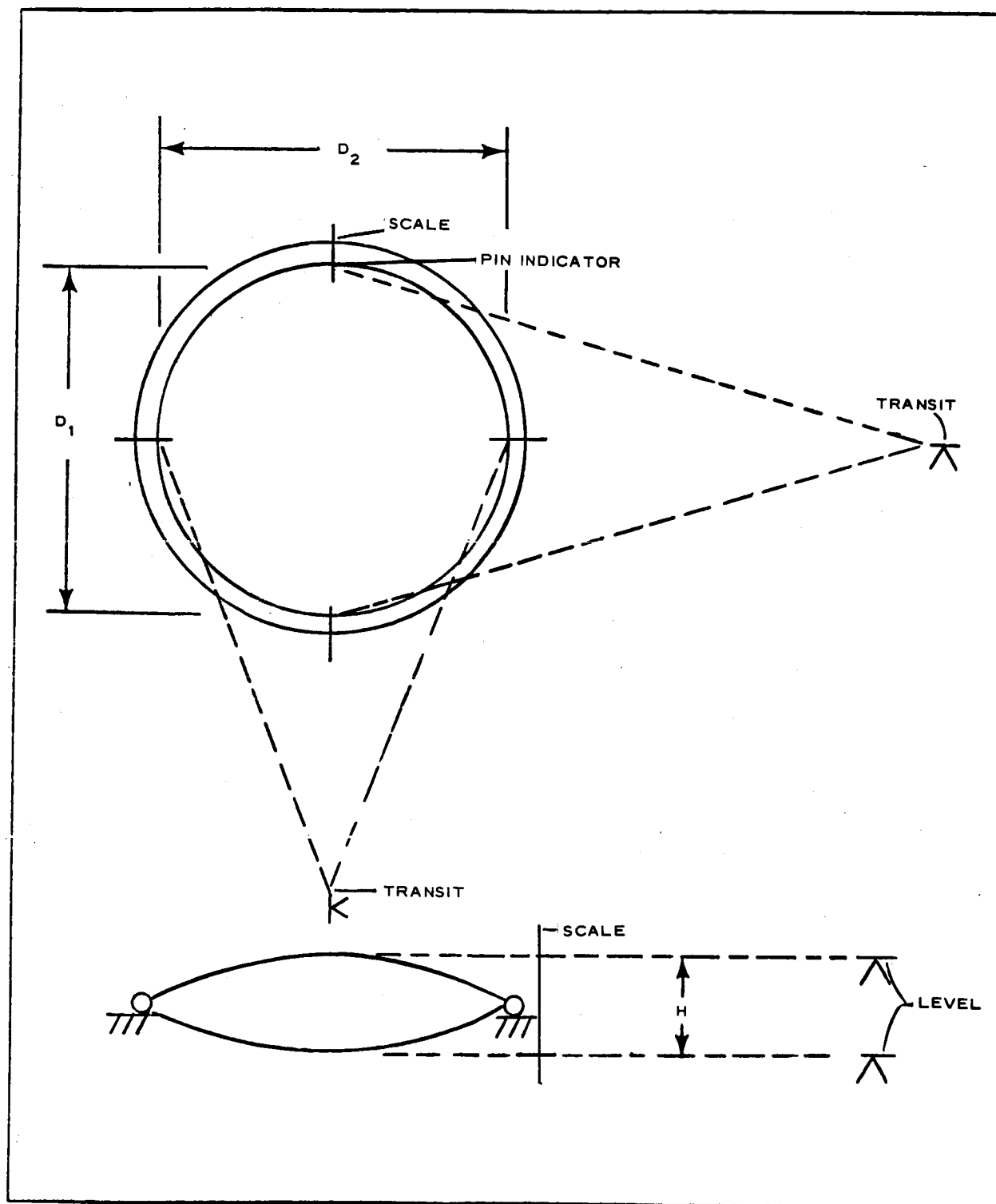


Figure 157 - Location of Deflection Points

(4) Test Results

(a) Model No. 1

The diameter changes that were measured during the first test of Model No. 1 are given in Table XXVI and plotted in Figure 158. It was observed visually during this test that the torus did not remain in a flat plane.

During the second test (with stiff ring installed) only visual observations were made. A maximum pressure of 8-in. Hg was obtained. No instability of the torus was observed.

(b) Model No. 2

The deflection data obtained in the tests of Model No. 2 are given in Tables XXVII and XXVIII, and plotted in Figures 159, 160, and 161. The δD shown is the average change in diameter obtained from D_1 and D_2 (Figure 157). Theoretical curves as established in Item (5), following, are also shown in Figures 159, 160, and 161 for convenience.

Note that the torus did not give any indications of buckling during these tests. This would indicate that the size of the torus could be decreased but that further study and testing is required to substantiate this.

(5) Theoretical Analysis of Test Specimen

(a) Torus Stability

It had been assumed in the analysis that two criteria, wrinkling and buckling, must be considered in the design of the torus. It was found as a result of the tests that the buckling requirement is not necessary and that only the wrinkling criteria must be observed.

The plots of lens pressure versus change in torus diameter revealed, in all cases tested, only a progressively increasing

TABLE XXVI - TORUS DIAMETER

CHANGE - MODEL NO. 1

Pressure (in. Hg)	δD (in.)
0.2	0.00
0.4	0.025
0.6	0.03
0.8	0.04
1.0	0.045
1.2	0.055
1.4	0.06
1.6	0.07
1.8	0.075
2.0	0.08
2.2	0.085
2.4	0.09
2.6	0.095
2.8	0.10
3.0	0.105
3.2	0.105
3.4	0.11
3.6	0.12
3.8	0.12
4.0	0.13
3.0	0.11
2.0	0.09
1.0	0.05
0.2	0.02

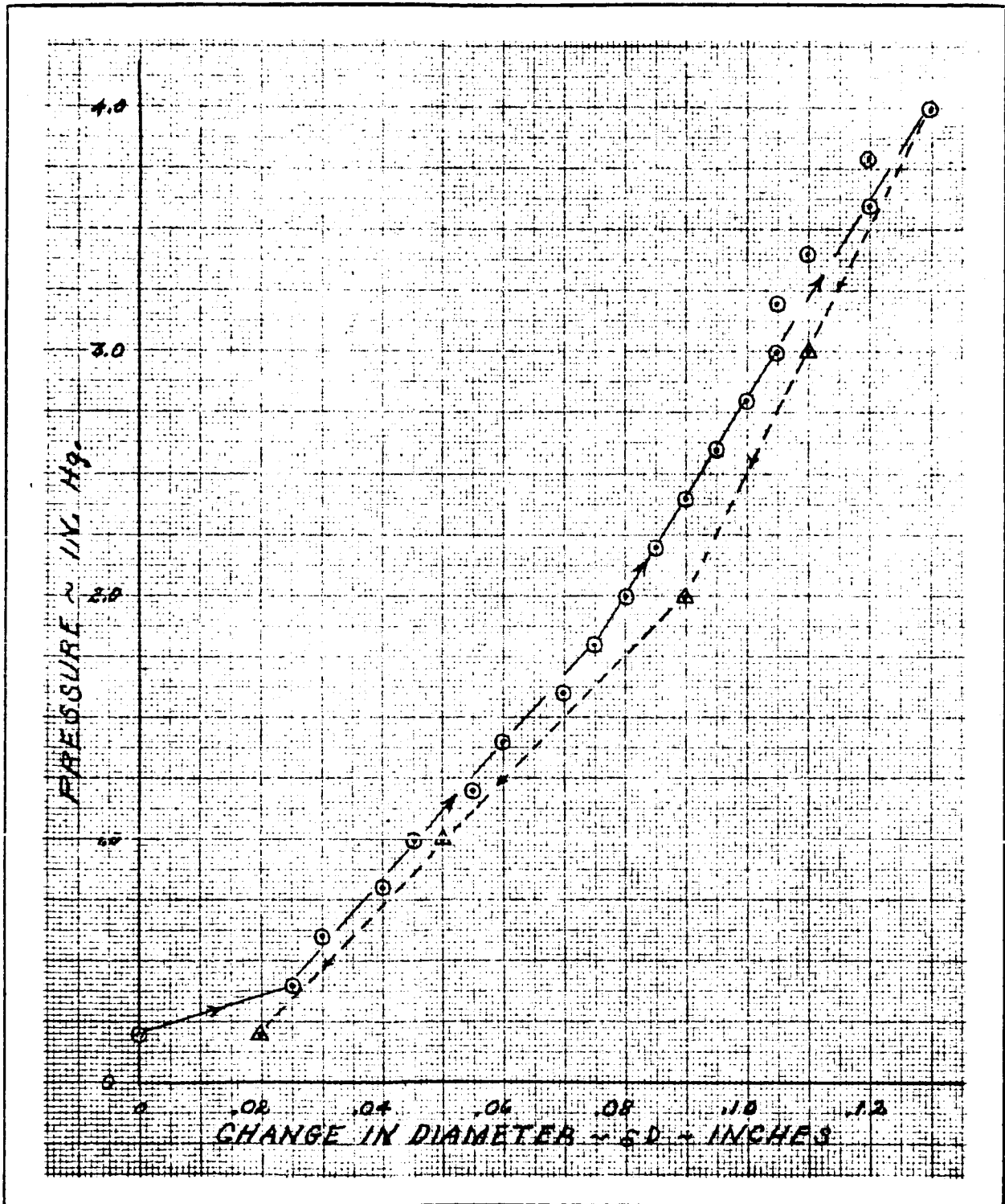


Figure 158 - Pressure versus Diameter Change, Torus Model No. 1

TABLE XXVII - RECORDED DEFLECTIONS OF MODEL NO. 2 ON
FLAT PLATE

Torus pressure (in. Hg)	Lens pressure (in. H ₂ O)	H (in.)	∂D (in.)	Torus pressure (in. Hg)	Lens pressure (in. H ₂ O)	H (in.)	∂D (in.)
0.6	0.015	22.46	0.0	3.0	0.030	22.55	0.0
	0.029	22.54	+0.010		0.120	22.71	+0.005
	0.049	22.60	0.0		0.210	22.84	+0.005
	0.075	22.70	+0.0075		0.300	22.94	-0.030
	0.100	22.80	0.0		0.380	23.00	-0.40
	0.125	22.86	-0.0025		0.450	23.08	-0.075
	0.140	22.88	-0.0225		0.520	23.13	-0.095
	0.160	22.96	-0.040		0.580	23.20	-0.130
1.0	0.012	22.44	0.0	4.0	0.620	23.30	-0.185
	0.040	22.54	+0.010		0.030	22.49	0.0
	0.080	22.70	+0.175		0.160	22.74	+0.010
	0.120	22.78	+0.0225		0.290	22.90	-0.005
	0.160	22.86	+0.010		0.420	23.00	-0.030
	0.200	22.95	-0.005		0.550	23.11	-0.070
	0.240	23.04	-0.045		0.680	23.20	-0.115
	0.260	23.14	-0.125		0.810	23.32	-0.180
2.0	0.030	22.53	0.0	5.0	0.030	22.50	0.0
	0.080	22.66	+0.015		0.190	22.78	-0.005
	0.130	22.78	0.0		0.350	22.91	-0.025
	0.180	22.86	+0.015		0.510	23.03	-0.065
	0.230	22.90	-0.010		0.680	23.13	-0.105
	0.280	22.96	-0.015		0.780	23.22	-0.145
	0.330	23.03	-0.030		0.880	23.28	-0.185
	0.380	23.10	-0.060		0.980	23.39	-0.230
	0.430	23.20	-0.115				

TABLE XXVIII - RECORDED DEFLECTIONS OF
MODEL NO. 2 HANGING VERTICALLY

Torus pressure (in. Hg)	Lens pressure (in. H ₂ O)	H (in.)	D (in.)
2.0	0.070	22.79	0.0
	0.140	22.94	0.0
	0.210	23.04	-0.020
	0.280	23.14	-0.040
	0.350	23.19	-0.125
	0.420	23.32	-0.125
	0.490	23.58	-0.300
4.0	0.070	22.74	0.0
	0.230	23.03	-0.005
	0.390	23.14	-0.035
	0.550	23.23	-0.070
	0.710	23.37	-0.100
	0.870	23.62	-0.260
5.0	0.030	22.56	0.0
	0.190	22.87	0.0
	0.350	23.04	-0.020
	0.510	23.16	-0.055
	0.680	23.27	-0.090
	0.780	23.33	-0.110
	0.880	23.39	-0.145
	0.980	23.47	-0.190
	1.080	23.66	-0.300

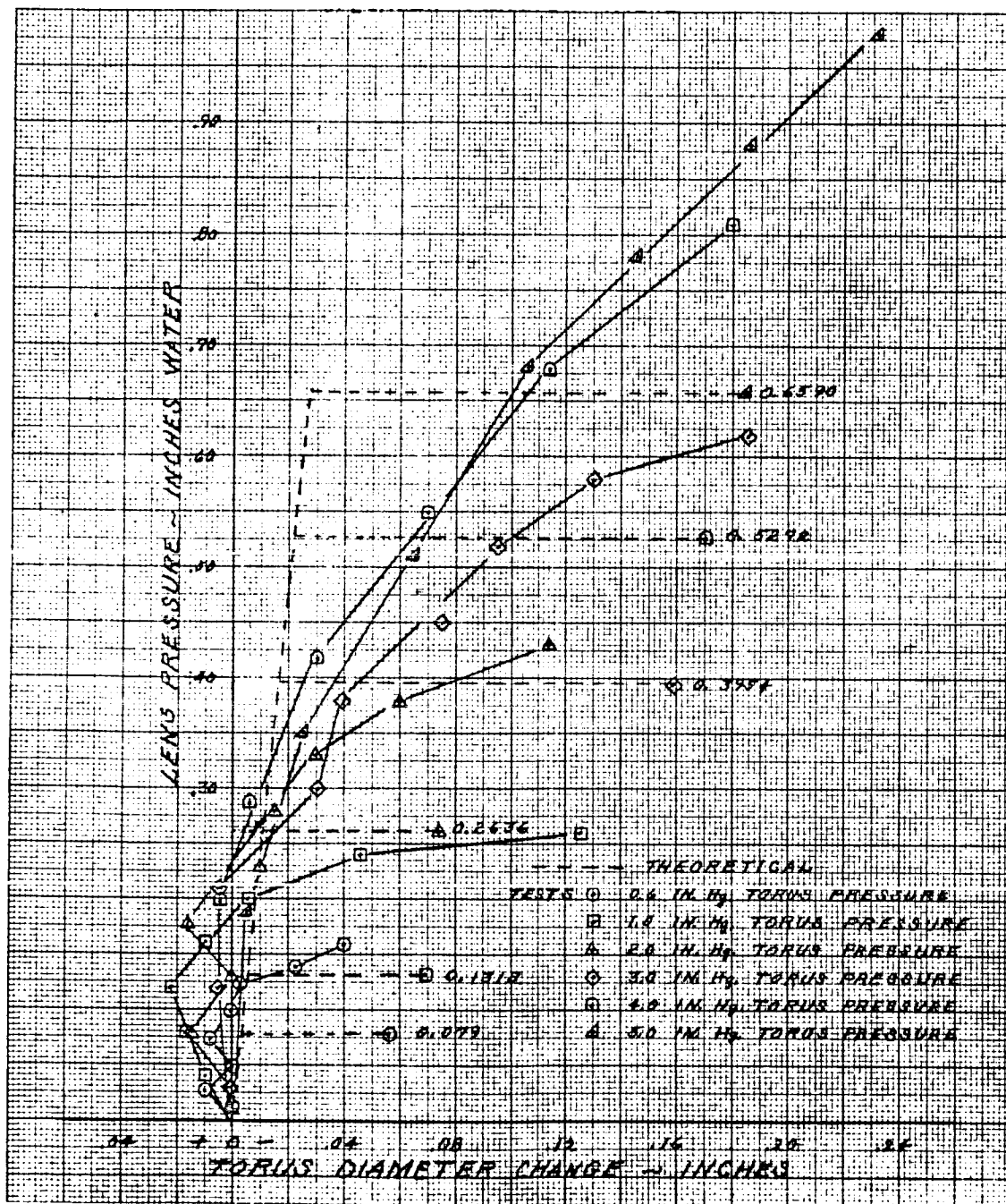


Figure 159 - Lens Pressure versus Torus Diameter, Model No. 2, Specimen on Flat Table

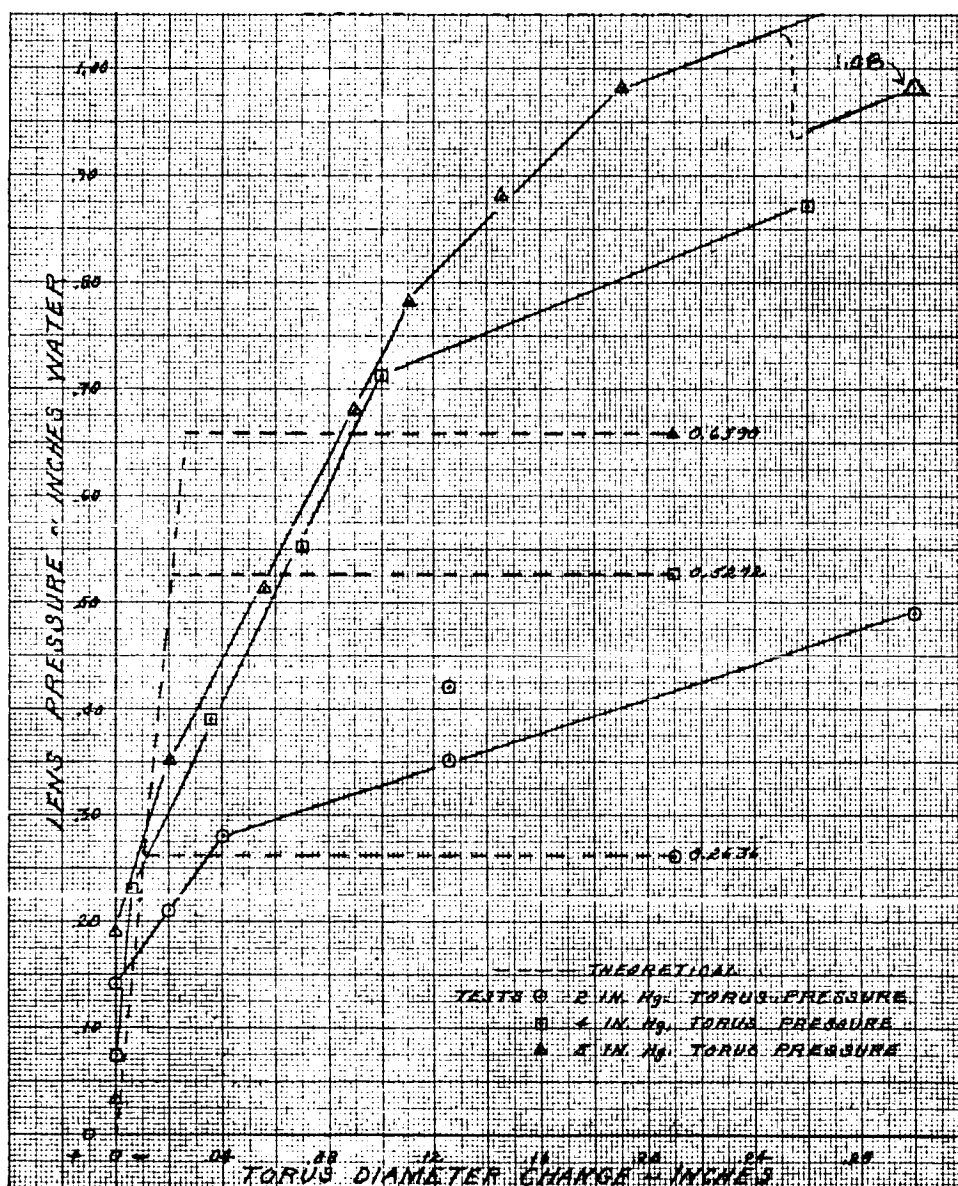


Figure 160 - Lens Pressure versus Torus Diameter, Model No. 2, Specimen Hanging Vertically

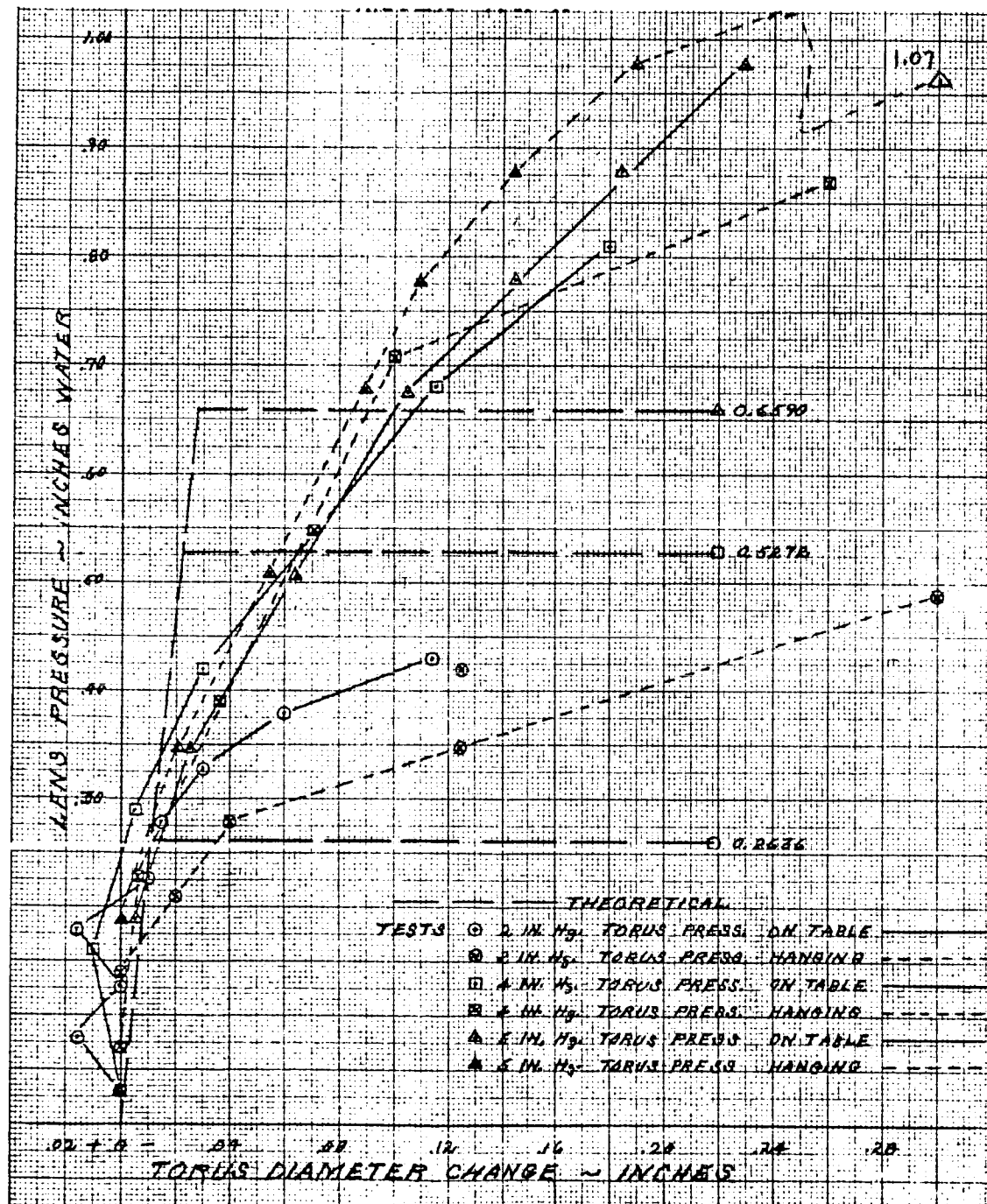


Figure 161 - Lens Pressure versus Torus Diameter, Model No. 2

change in diameter with increasing pressure, even after the wrinkling load was exceeded. In no instance was there observed a tendency for the torus to buckle out of its plane.

Figure 162 defines the terms on which the analyses for wrinkling, buckling, and effect of lens pressure in the torus inner diameter are based.

(b) Wrinkling

$$p_T \pi r^2 \geq q_{ult}(R + r) = p_L R \cot \alpha (R + r) \quad (217)$$

$$\begin{aligned} \frac{p_T}{p_L} &= \frac{\cot \alpha \left(\frac{R}{r}\right) \left[\frac{R}{r} + 1\right]}{\pi} \\ &= \frac{16 \times 17}{\pi} \cot \alpha \\ &= 86.5 \cot \alpha \end{aligned} \quad (218)$$

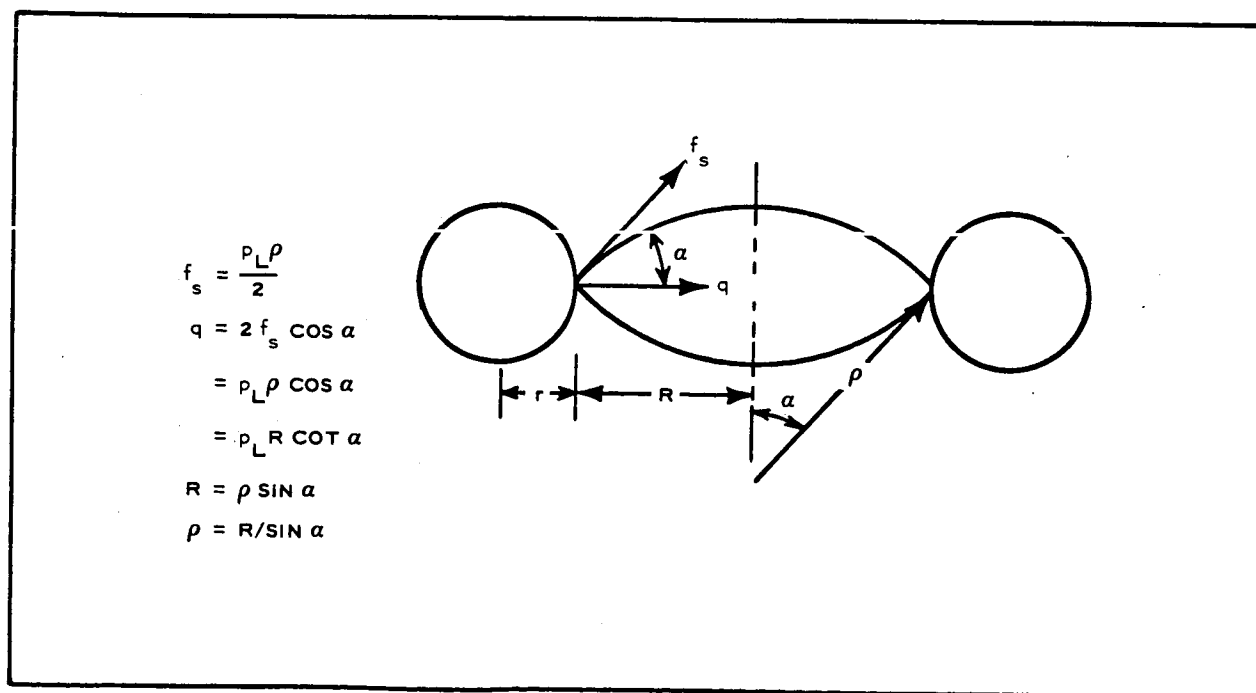


Figure 162 - Torus-Lens Axial Section

(c) Buckling

$$\begin{aligned}
 q_{\text{ult}} &= \frac{1}{(R + r)^3} \frac{12}{\frac{1}{EI} + \frac{1}{GJ}} \\
 &= \frac{12EI}{(R + r)^3} \frac{1}{\frac{EI}{GJ}} \quad (219)
 \end{aligned}$$

$$\begin{aligned}
 \frac{EI}{GJ} &= \frac{E}{\frac{E}{2(1 + \mu)}} \frac{I}{2I} \\
 &= 1 + \mu ; \quad I = \pi r^3 t \quad (220)
 \end{aligned}$$

$$\begin{aligned}
 q_{\text{ult}} &= \frac{12E\pi r^3 t}{(5 + \mu)(R + r)^3} \\
 &= \frac{12\pi}{5 + \mu} \frac{Et}{\left(\frac{R}{r} + 1\right)^3} \\
 &= 1.42 \times 10^{-3} Et \\
 &= 0.71 \text{ lb/in.} \quad (221)
 \end{aligned}$$

Values of P_L versus values of P_T for the conditions listed below are given in Table XXIX and plotted in Figure 163 for various values of the angle α .

$$R = 30 \text{ in.}$$

$$r = 1.875 \text{ in.}$$

$$\frac{R}{r} = 16$$

$$E = 0.5 \times 10^6 \text{ psi}$$

$$t = 0.001 \text{ in.}$$

TABLE XXIX - CRITICAL PRESSURE IN LENS VERSUS PRESSURE IN TORUS FOR

VARIOUS LENS ANGLES

α (deg)	$\sin \alpha$	$\cos \alpha$	ρ (in.)	q/P_L	$\cot \alpha$	P_T/P_L	P_L (buckling)	
							Psi	In. H_2O
10	0.1736	0.9848	173.0	170.5	5.6713	490	0.00417	0.116
20	0.3420	0.9397	87.8	82.5	2.7475	238	0.00861	0.239
30	0.5000	0.8660	60.0	52.0	1.7321	150	0.01365	0.379
40	0.6428	0.7660	45.6	1.1918	. . .	103	0.01985	0.551

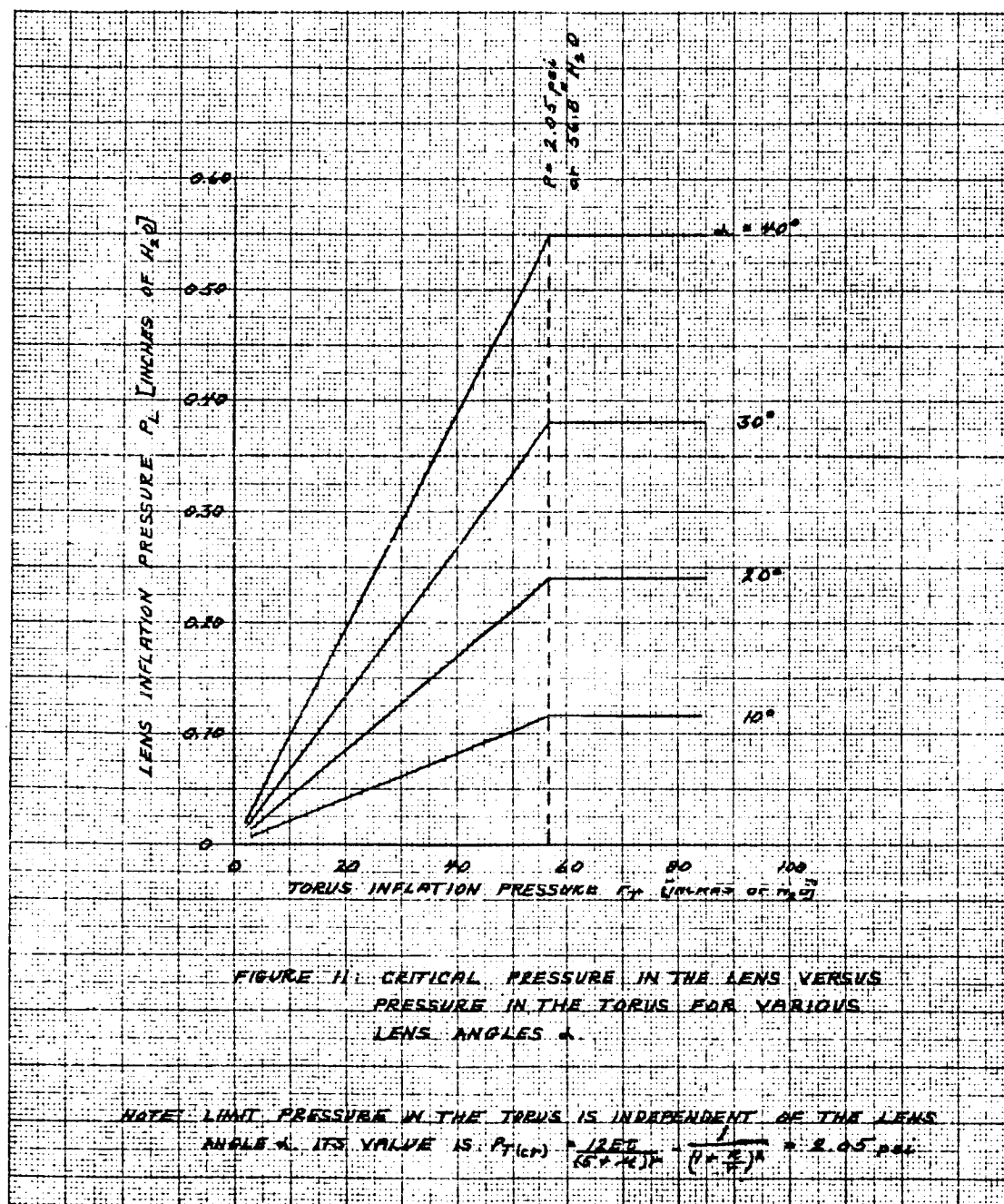


Figure 163 - Critical Pressure in the Lens versus Pressure in the Torus for Various Lens Angles α

- (d) Effect of Pressure in the Lens, P_L , on the Torus Inner Diameter

Hoop compression in the torus,

$$\begin{aligned} H &= q(R + r) \\ &= p_L R(R + r) \cot \alpha \end{aligned} \quad (222)$$

Using Hooke's law with total stiffness EA in the torus equal to the sum of the respective stiffnesses of the Mylar film and the stainless steel rim (width $b = 0.4$ in., and thickness $t' = 0.005$ in.), the total shrinkage of the torus mean diameter (midway between inner and outer equator) can be found as follows:

$$\begin{aligned} \Delta D &= \frac{1}{\pi} \frac{H 2\pi(R + r)}{2\pi r t E_M + b t' E_{ss}} \\ &= \frac{1}{\pi} \frac{R(R + r)^2 \cot \alpha}{r t E_M + \frac{b t'}{2\pi} E_{ss}} P_L \end{aligned} \quad (223)$$

The angle α remains practically constant at all lens pressures. The most representative value is 40 deg. Substituting numerical values for the letters in Equation 223 above yields,

$$\begin{aligned} \Delta D &= \frac{1}{\pi} \frac{30(31.875)^2(1.1918)}{1.875(0.001)(0.5) \times 10^6 + \frac{0.4 \times 0.005}{2\pi} \times 30 \times 10^6} P_L \\ &= \frac{36,326}{937.5\pi + 30,000} P_L \\ &= 1.1026 p_L \text{ in.} \end{aligned} \quad (224)$$

($p_L = \text{psi}$)

For p_L in inches of water the above equation becomes

$$\begin{aligned}\Delta D &= \frac{1.1026}{27.7} p_L \\ &= 0.04 p_L \text{ in.}\end{aligned}\quad (225)$$

(p_L = inches of water)

An upper limit in p_L can be determined from considerations of stability in the torus. For pressure in the torus lower than 2.05 psi this limit value in p_L is dictated by the torus wrinkling criterion, which is

$$p_L \leq \frac{P_T}{\frac{\cot \alpha \left(\frac{R}{r}\right) \left(\frac{R}{r} + 1\right)}{\pi}} \text{ psi} \quad (226)$$

For $P_T \geq 2.05$ psi however, and p_L as given by Equation 226, the torus will buckle because of insufficient bending and torsional rigidity.

Figures 159, 160, and 161 show the theoretical line with the limiting points for several torus pressures. In the same figures test curves are given for various torus pressures.

The pressure in the lens in all cases has been increased beyond the limit value. Tests were conducted with the torus lying on a horizontal plane and suspended in a vertical position. Agreement between the test results in the two positions of the torus and the theoretical values, $\Delta D = 0.04 p_L$, is generally good.

b. Rim Section

(1) Purpose

Tests were performed on a typical rim section for experimental

determination of EI and GJ values for comparison with analytical values.

(2) Test Specimen

A cross section of the rim section that was used for the tests is shown in Figure 164. The two halves of the rim were formed on a brake and then spot welded together.

(3) Test Setup and Procedure

(a) Bending Test

Bending tests were conducted with the rim section set up as a cantilever beam as shown in Figure 165. The fixed end of the rim section was held by encasing it in a block of cerrobend with a piece of string secured to the free end with tape. Dead weights were then hung on the string in increments until failure occurred. Deflection was measured by referencing a point on the end of the specimen to a deflection scale.

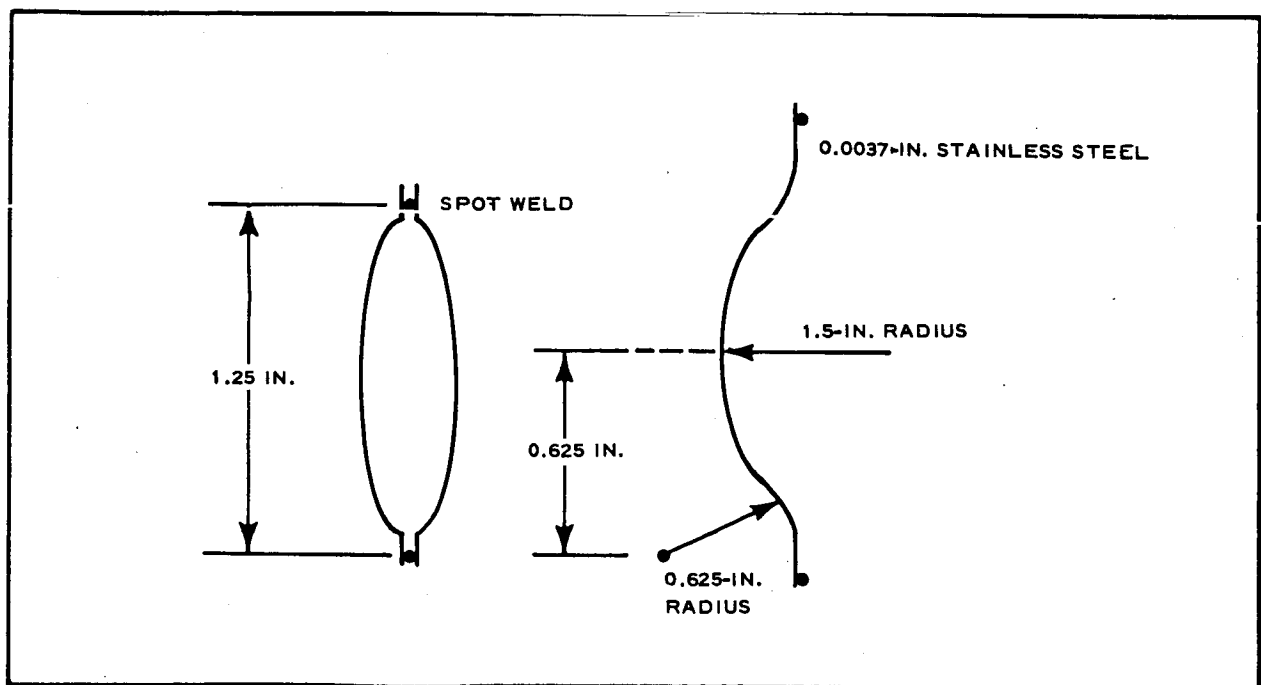


Figure 164 - Rim Cross Section

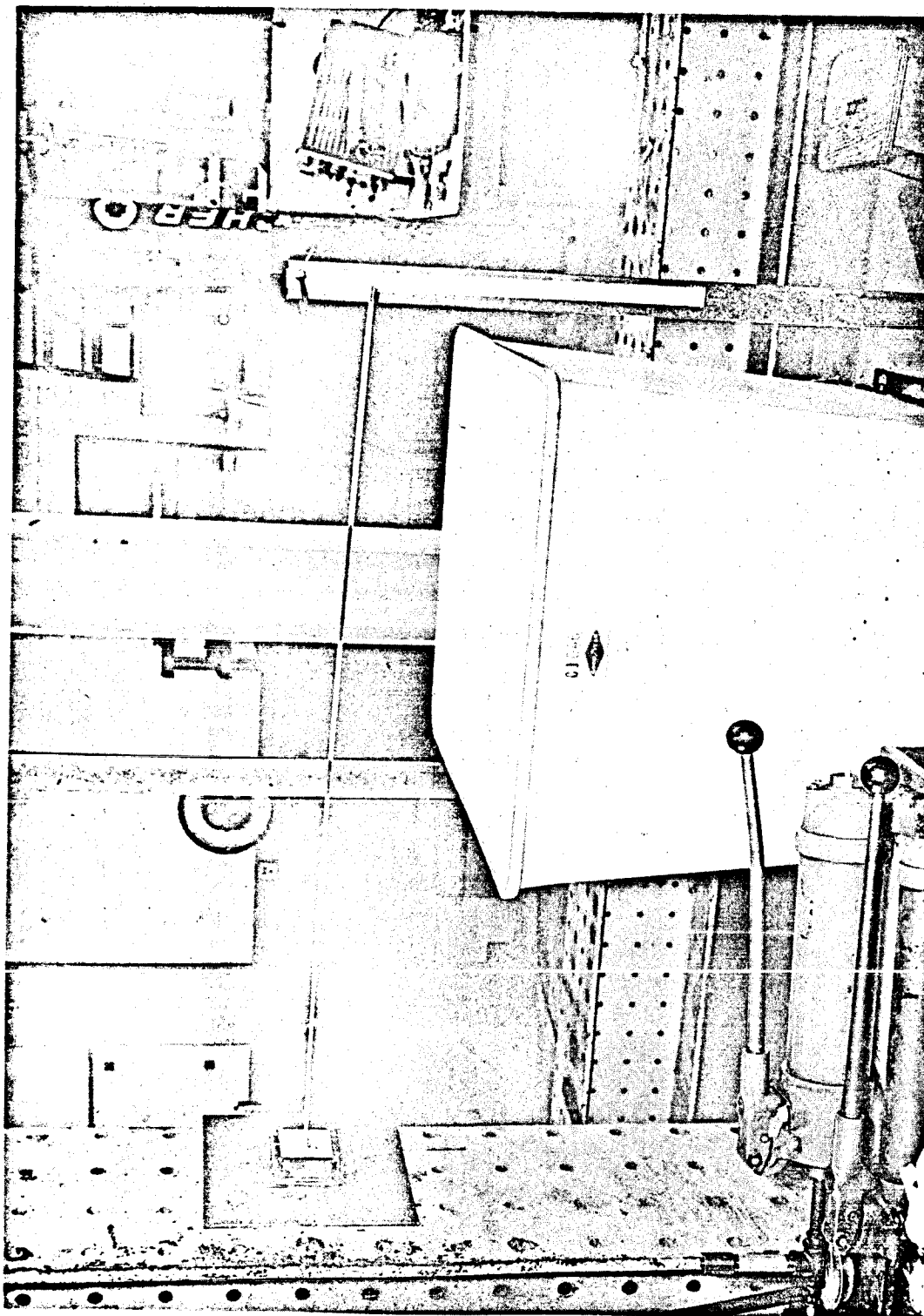


Figure 165 - Rim Section Bending Test Setup

(b) Torsion Test

For the torsion tests the specimen was secured to the fixture in the same manner as that used for the bending tests. A pulley was secured to the outboard end of the specimen (Figure 166). A fixed bolt in the bearing of the pulley held the specimen in a plane while load was applied. Rotation of the specimen was obtained from a protractor secured to the pulley.

(4) Test Results

(a) Bending Test

Two bending tests were conducted. For the first the specimen was 50 in. long and for the second, 24-3/8 in. long. The deflection data obtained during the two tests are given in Tables XXX and XXXI and plotted in Figure 167.

Specimen No. 1 failed prematurely (Figure 168). Examination of the specimen indicated that it had failed in an area that had been damaged prior to the test. Because of this, tests were conducted on a second specimen.

(b) Torsion Test

One torsion test was conducted. The data obtained during this test are given in Table XXXII and plotted in Figure 169. Figure 166 shows the failure of the specimen.

(5) Theoretical Analysis

(a) Bending and Collapse Bending of Rim Material

The rim material was tested in bending as a cantilevered beam with a concentrated tip load (see Figure 170).

Because the one-quarter cross section of the rim is unlikely to consist of two equal circular arcs of equal radii ($r_1 = r_2$)

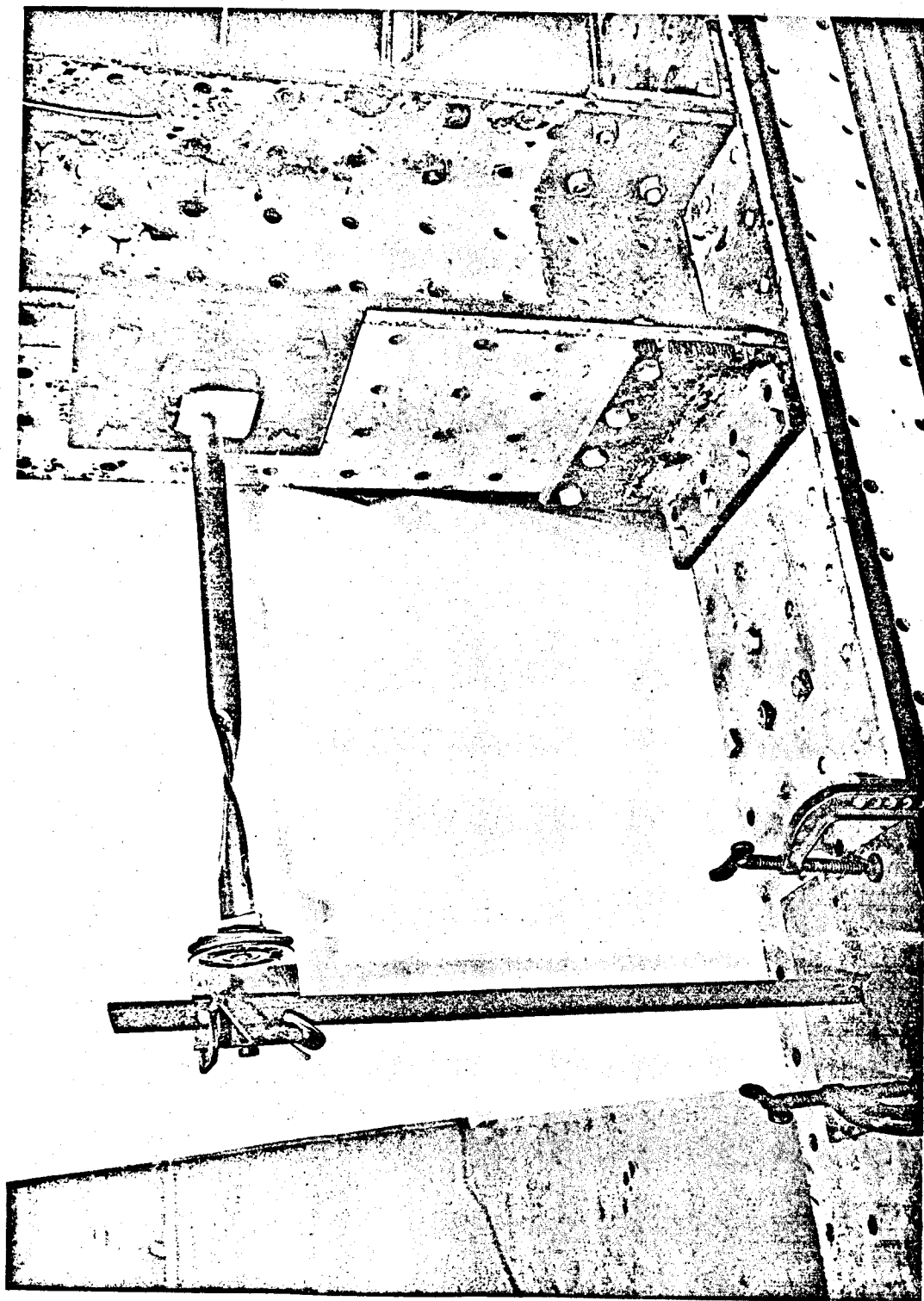


Figure 166 - Rim Section Torsion Test Setup and Failure

TABLE XXX - RIM SECTION BENDING TEST

SPECIMEN NO. 1

Load (oz)	Deflection (δ) (in.)
0.00	0.00
0.25	0.69
0.50	1.42
0.75	2.28
1.00	Failed while loading

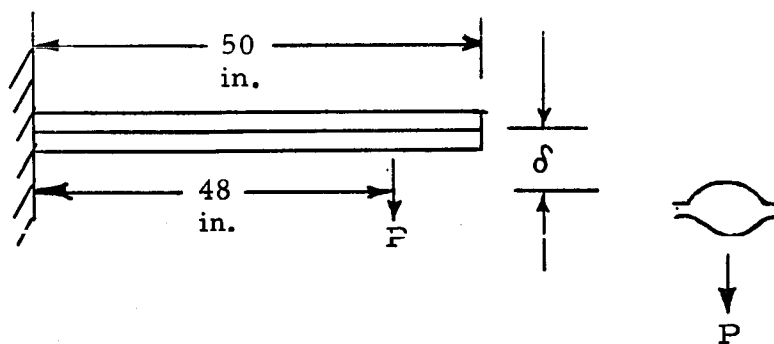
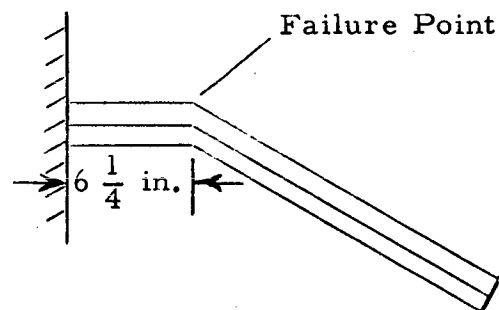
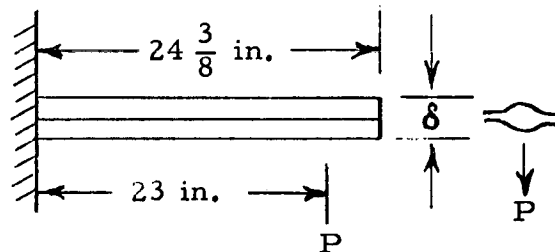


TABLE XXXI - RIM SECTION

BENDING TEST

SPECIMEN NO. 2

Load (oz)	Deflection (δ) (in.)
0.00	0.00
0.25	0.06
0.50	0.11
0.75	0.16
1.00	0.21
1.25	0.26
1.50	0.31
1.75	0.36
2.00	0.42
2.25	0.48
2.50	0.54
2.75	0.58
3.00	0.64
3.25	0.70
3.50	0.77
3.75	0.84
4.00	0.91
4.25	0.98
4.50	1.06
4.75	1.14
5.00	1.24
5.25	1.39
5.50	1.64
5.75	Failed while loading



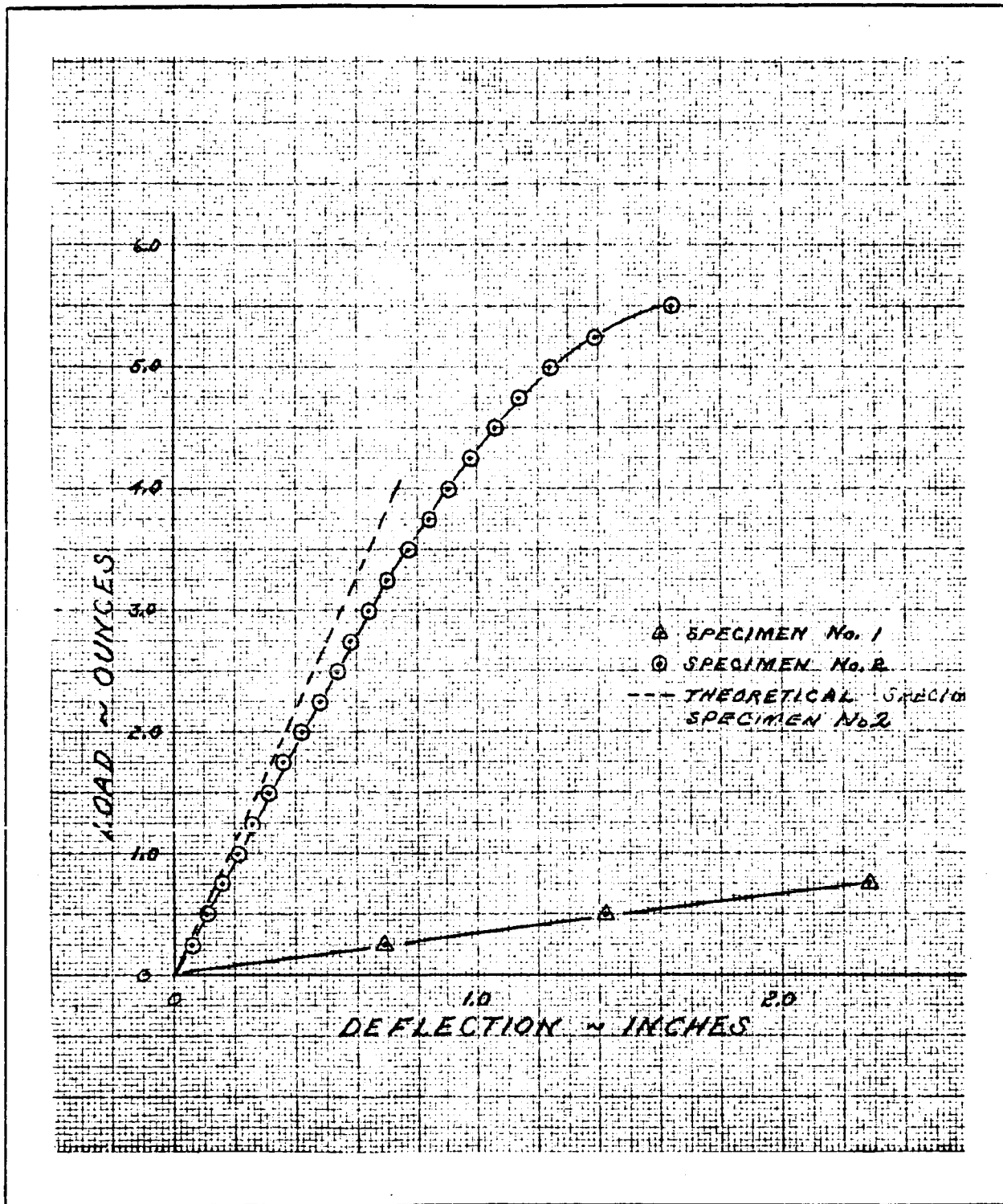


Figure 167 - Load versus Deflection, Rim Section Bending Test

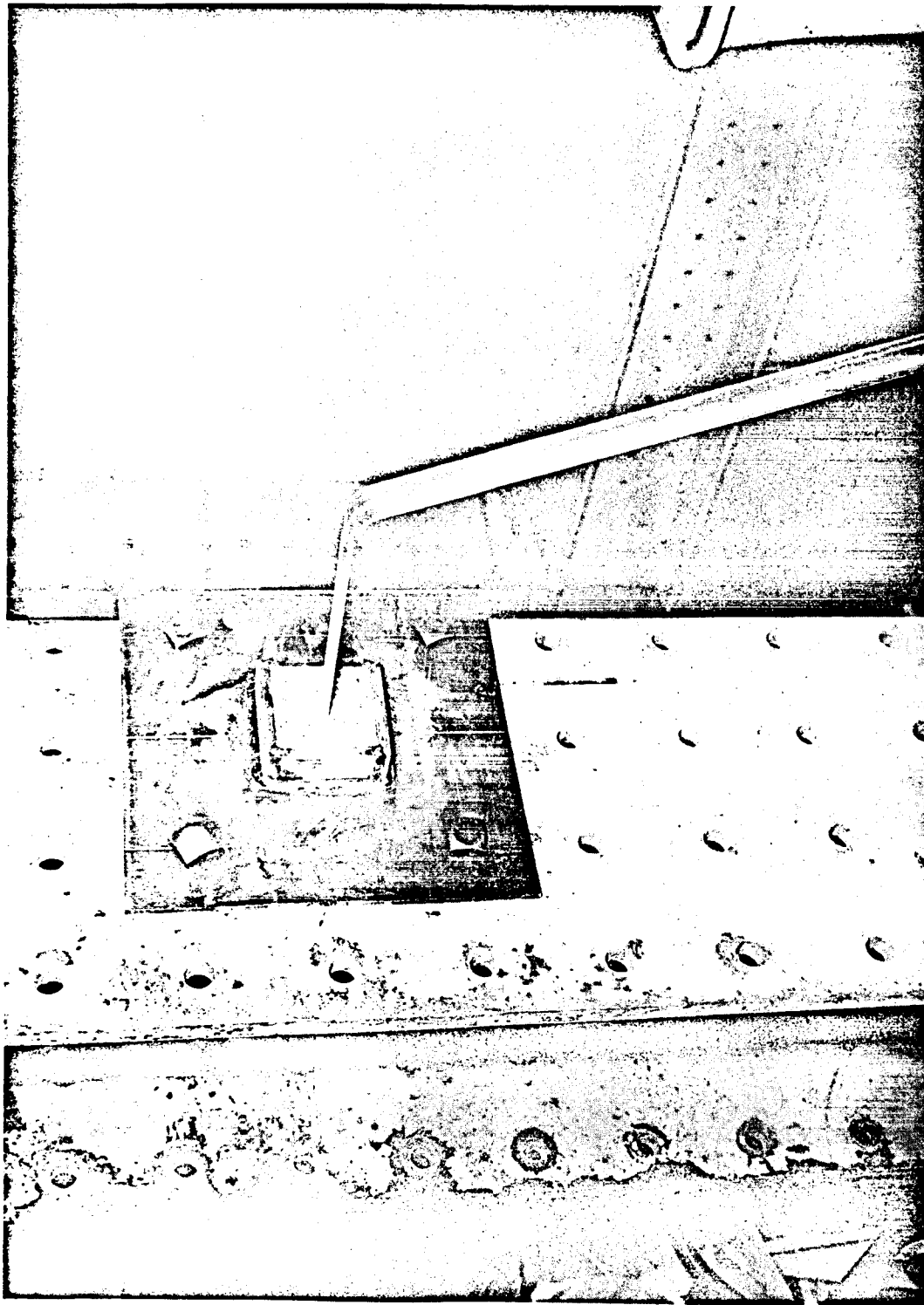
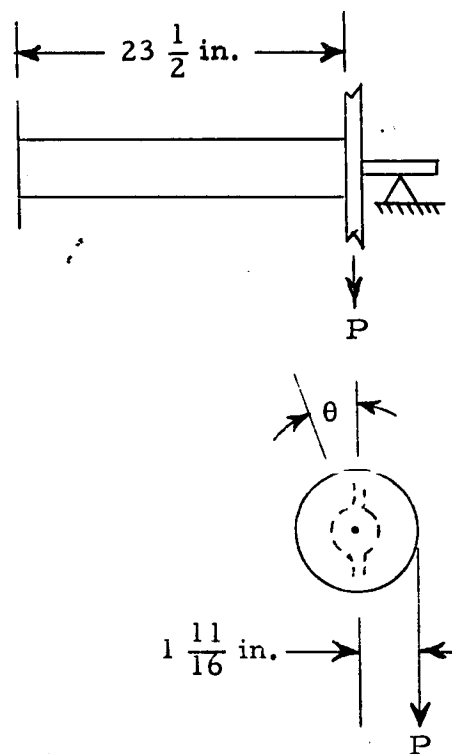


Figure 168 - Rim Section Bending Test, Specimen No. 1 Failure

TABLE XXXII - RIM SECTION
TORSION TEST

Load (lb)	Twist, θ (deg)
0.00	0.00
0.25	0.25
0.75	2.00
1.00	2.80
1.25	3.30
1.50	3.80
1.75	4.40
2.00	5.00
2.25	5.80
2.50	6.40
2.75	Failed while loading



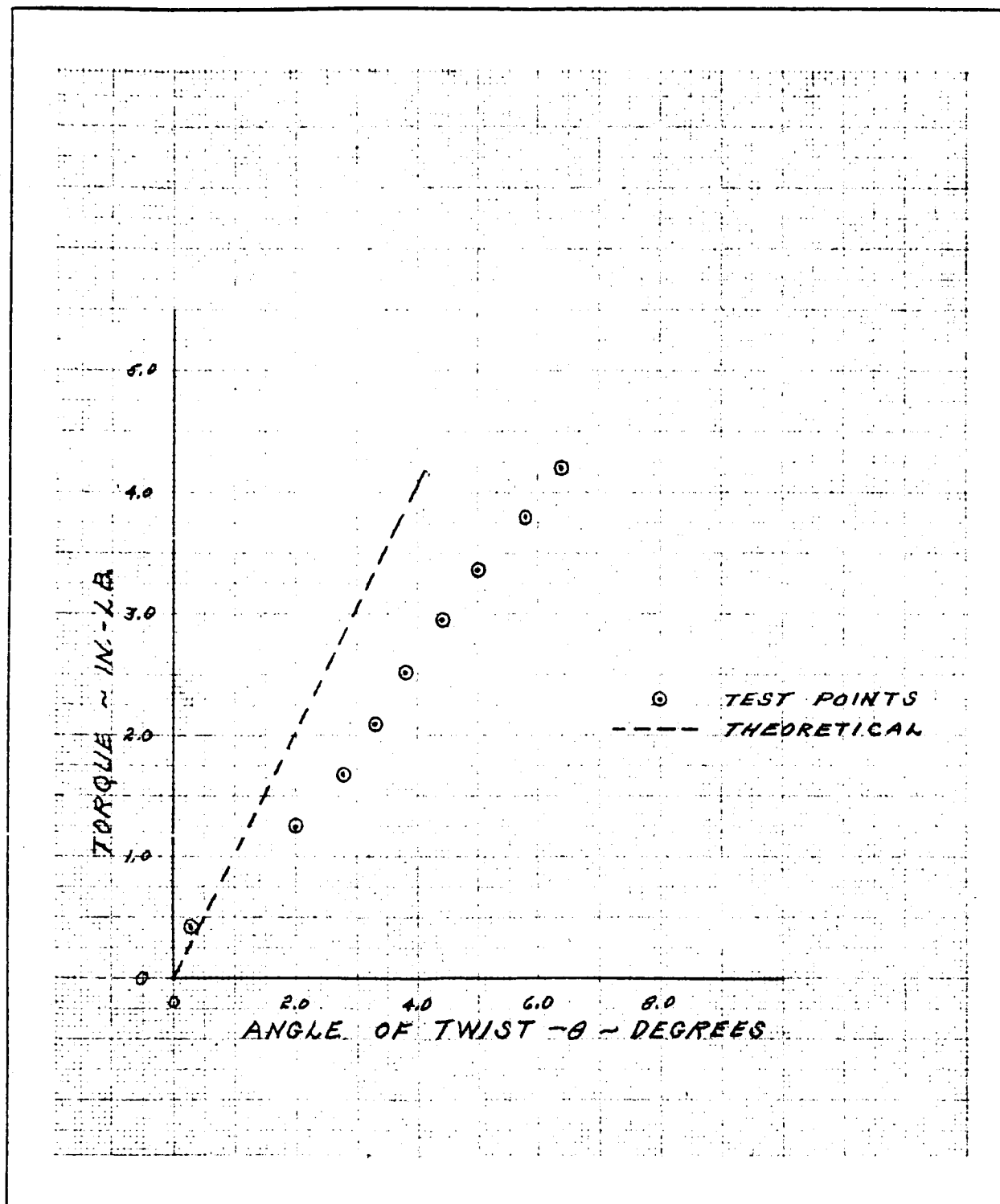


Figure 169 - Torque versus Twist Angle, Rim Section Torsion Test

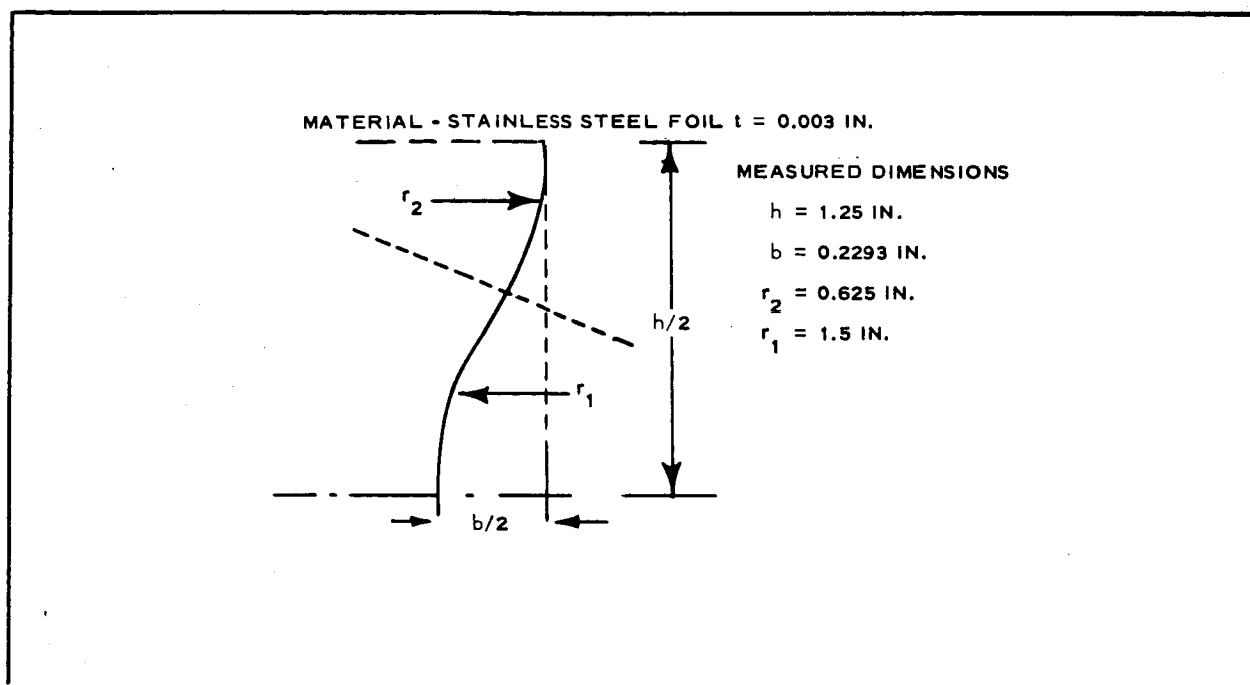


Figure 170 -One-Quarter Rim Cross Section for Bending Analysis

as was intended in manufacturing the rim, the determination of the moment of inertia I_z of the cross section has been done demi-empirically as follows:

The deflection equation is

$$\delta = \frac{PL^3}{3EI} \quad (227)$$

Using the initial straight portion of the curve ($\delta - p$) from Figure 167 the following relation between P and δ can be established,

$$\begin{aligned} P &= \delta \left(\frac{1.75 - 0.25}{0.36 - 0.06} \right) \frac{1}{16} \\ &= \frac{5}{16} \delta ; \end{aligned} \quad (228)$$

therefore, the deflection equation becomes

$$3.2 = \frac{L^3}{3EI} \quad (229)$$

from which

$$\begin{aligned} I &= \frac{L^3}{3(3.2)E} \\ &= \frac{(23)^3}{9.6 \times 30 \times 10^6} \\ &= \frac{12,167}{28.8 \times 10^7} \\ &= 42.25 \times 10^{-6} \text{ in.}^4 \end{aligned}$$

The measured dimensions h , b , r_1 , and r_2 given above are geometrically incompatible if the arc of radii r_1 and r_2 have to be tangent where they meet (inflection point). As shown in Figure 170, a geometrical construction of the rim cross section with the dimensions h , b , r_1 , and r_2 as measured would be possible only if the two arcs were not tangent. On this basis the moment of inertia I_{z-z} was calculated and found to be $46.38 \times 10^{-6} \text{ in.}^4$, that is, about 10 percent larger than the semi-empirical value 42.25×10^{-6} determined above. The calculations for the determination of the moment of inertia $I_{z-z} = 46.38 \times 10^{-6} \text{ in.}^4$, are given below (see Figure 171).

The angles θ_1 and θ_2 can be determined from equations,

$$r_1 \sin \theta_1 + r_2 \sin \theta_2 = \frac{h}{2} \quad (230)$$

and

$$r_1(1 - \cos \theta_1) + r_2(-\cos \theta_2) = \frac{b}{2} \quad (231)$$

or

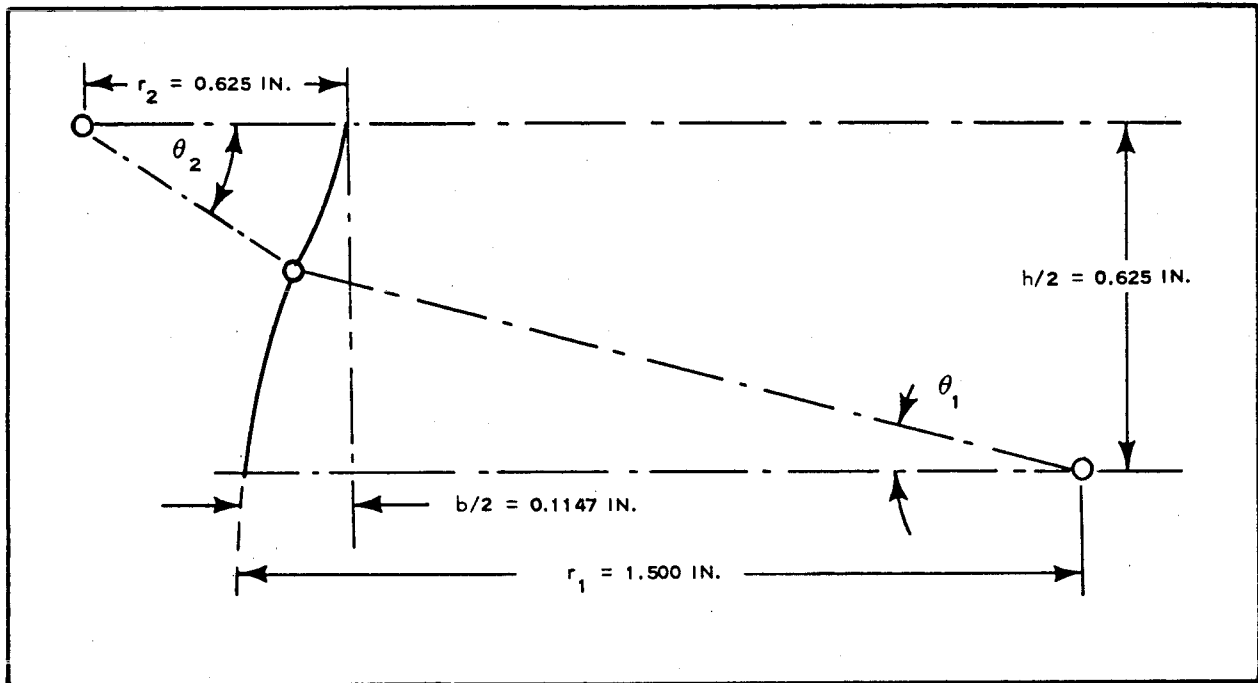


Figure 171 - Geometric Construction of One-Quarter Rim Cross-Section from Measured Dimensions

$$1.500 \sin \theta_1 + 0.625 \sin \theta_2 = 0.625$$

and

$$1.500 \cos \theta_1 + 0.625 \cos \theta_2 = 2.0103$$

Squaring both equations and adding yields $\cos(\theta_2 - \theta_1) = 0.95536 = \cos 17 \text{ deg } 11 \text{ min.}$ Then $\theta_2 = \theta_1 + 17 \text{ deg } 11 \text{ min.}$ Substituting the θ_2 value in the first of the initial equations, and letting $1.4777/16.7768 = \tan \omega = \tan 5 \text{ deg } 02 \text{ min}$ results in $\sin(\theta_1 + \omega) = 5/16.7768 \cos \omega = 0.29688 = \sin 17 \text{ deg } 16 \text{ min,}$ from which $\theta_1 = 17 \text{ deg } 16 \text{ min} - \omega = 12 \text{ deg } 14 \text{ min;}$ then $\theta_2 = 17 \text{ deg } 11 \text{ min} + 12 \text{ deg } 14 \text{ min} = 29 \text{ deg } 25 \text{ min.}$

(b) Calculation of Moment of Inertia I_{z-z}

Figure 172 shows the bending moment analysis elements.

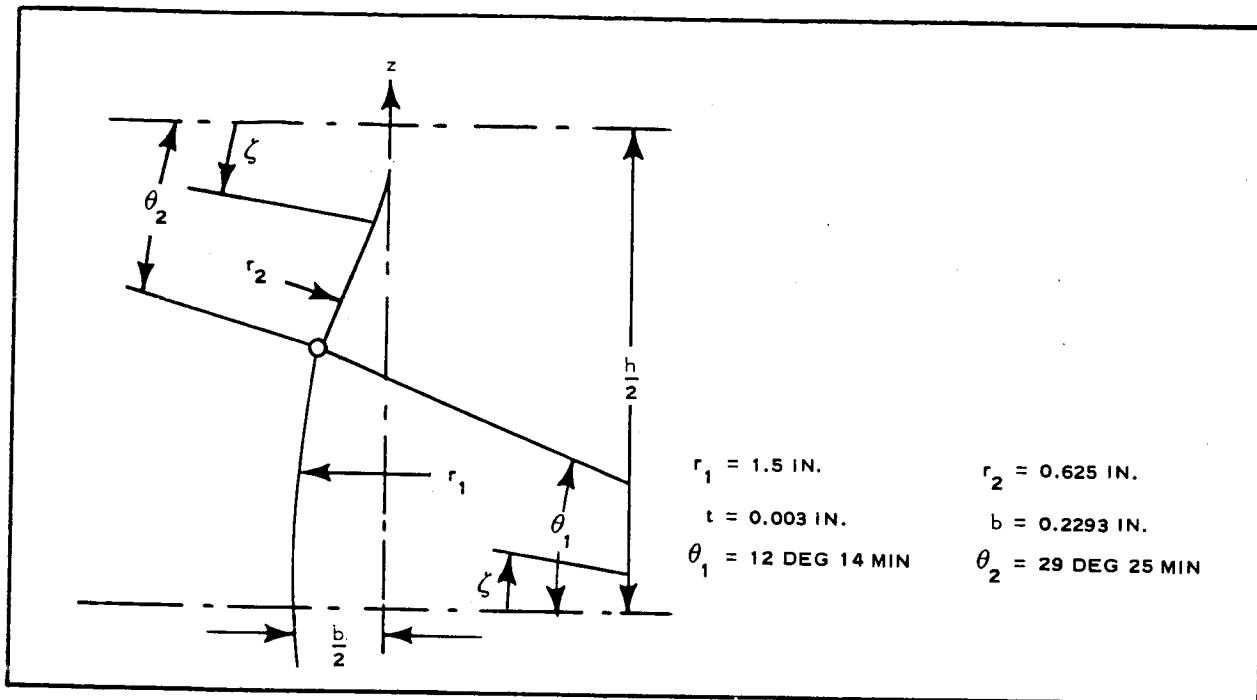


Figure 172 - One-Quarter Rim Cross Section for Moment of Inertia Analysis

$$\frac{1}{t} I_{z-z} = 4 \left[\int_0^{\theta_1} \left(r_1 \cos \xi - r_1 + \frac{b}{2} \right)^2 r_1 d\xi + \int_0^{\theta_2} r_2^2 (1 - \cos \xi)^2 r_2 d\xi \right] \quad (232)$$

$$I_{z-z} = 4tr_1^3 \left[\left(\frac{b^2}{4r_1^2} - \frac{b}{r_1} + \frac{3}{2} \right) \theta_1 + \left(\frac{b}{r_1} - 2 \right) \sin \theta_1 + \frac{\sin 2\theta_1}{4} \right] + 4tr_2^3 \left(\frac{3\theta_2}{2} - 2 \sin \theta_2 + \frac{\sin 2\theta_2}{4} \right) \quad (233)$$

For the values of r_1 , r_2 , etc. shown in Figure 172 Equation 233 becomes:

$$\begin{aligned}
I_{z-z} &= 4(0.003)\left(\frac{3}{2}\right)^3 \left[\left(\frac{0.2293^2}{9} - \frac{0.2293}{1.5} + 1.5 \right) (0.21351) + \right. \\
&\quad \left. \left(\frac{0.2293}{1.5} - 2 \right) (0.21189) + \frac{0.41416}{4} \right] + \\
&\quad 4(0.003)\left(\frac{5}{8}\right)^3 \left[1.5 \times 0.51342 - 2(0.49116) + \frac{0.85567}{4} \right] \\
&= (0.012)(3.375) \left[(0.005842 - 0.152867 + 1.5)(0.21351) - 1.847133 \times \right. \\
&\quad \left. 0.21189 + 0.10354 \right] + (0.012)(0.24414)(0.77013 - 0.98232 + 0.21392) \\
&= 0.0405 \times 0.00102 + 0.00293 \times 0.00173 \\
&= 41.31 \times 10^{-6} + 5.07 \times 10^{-6} \\
&= 46.38 \times 10^{-6} \tag{234}
\end{aligned}$$

Considering this value as the theoretical moment of inertia of the rim cross section, the tip load-to-tip deflection relation is

$$\begin{aligned}
\delta &= \frac{PL^3}{3EI} \\
&= \frac{P(23)^3}{3 \times 30 \times 10^6 \times 46.38 \times 10^{-6}} \\
&= 2.91P \text{ (P in lb)}
\end{aligned}$$

or

$$\delta = 0.182P \text{ (P in oz)} \tag{235}$$

The theoretical (P - δ) line, based on Equation 235 is shown in Figure 167 as a dotted straight line.

(c) Collapse Bending Moment

The critical stress is calculated from Equation 40 of NACA TN 3783 (August 1957),

$$\sigma_{cr} = 0.285 E \frac{t}{r} \quad (236)$$

For $E = 30 \times 10^6$, $t = 0.003$ and $r = 1.5$ in., Equation 236 yields

$$\begin{aligned} \sigma_{cr} &= 2.85 \times 30 \times 10^6 \times \frac{3}{1.5} \times 10^{-3} \\ &= 17,100 \text{ psi} \end{aligned}$$

The collapse moment can be calculated from the equation

$$\begin{aligned} M_{coll} \frac{\sigma_{cr} I}{C} &= \frac{17,100 \times 42.25 \times 10^{-6}}{0.1147} \\ &= 6.30 \text{ in.-lb.} \end{aligned} \quad (237)$$

Beam weight = 0.11328 lb per 50-in. length, or

$$\begin{aligned} W &= \frac{23}{50} \times 0.11328 \\ &= 0.05211 \text{ lb.} \end{aligned}$$

$$\begin{aligned} M_{w(max)} &= \frac{WL}{2} \\ &= \frac{0.05211}{2} \times 23 \\ &= 0.600 \text{ in.-lb.} \end{aligned} \quad (238)$$

Critical tip load, P_{cr} ,

$$P_{cr} L + 0.600 = 6.30$$

or

$$\begin{aligned}P_{cr} &= \frac{6.300 - 0.600}{23} \text{ lb} \\&= 0.2478 \text{ lb} \\&= 3.96 \text{ oz.} \quad (239)\end{aligned}$$

According to the above calculations the anticipated critical tip load, P_{cr} , is the load that causes the beam to collapse at its built-in point. The test, however, indicated that the beam collapsed 6.25 in. away from the fixed point, which is a repetition of a previously run bending test on a longer beam (50 in.). The test with the longer beam was terminated at an early stage because of permanent damage due to mishandling the specimen.

From a local stability viewpoint the beam is improved in the vicinity of the fixed end. This means that the collapse stress at the fixity and over a certain distance from it, is higher than 17,100 psi. This explains the fact that the beam collapsed at a point away from the fixed end.

According to the test, the load under which the beam collapsed was the application of an increment tip load of 0.25 oz from an existing tip load of 5.50 oz.

Let this collapse load be called 5.60 oz.

This tip load, and the beam's own weight produce a bending moment at a point 6.25 in. away from the fixity equal to

$$\begin{aligned}M &= 0.11328 \times \frac{16.5}{50} \times \frac{16.5}{2} + \frac{5.60}{16} \times 16.5 \\&= 0.308 + 5.775 \\&= 6.083 \text{ in.-lb.}\end{aligned}$$

This moment produces a maximum stress of

$$\begin{aligned}\sigma_m &= \frac{6.083 \times 0.1147}{42.25 \times 10^{-6}} \\ &= 16.510 \text{ psi ,}\end{aligned}$$

which is only

$$\frac{17,100 - 16,510}{17,100} \times 100 = 3.5 \text{ percent}$$

short of the theoretical critical stress $\sigma_{cr} = 17,100$ psi.

(d) Torsion and Collapse Torsion of Rim Material

Length of tested beam, $L = 23.5$ in.

The theoretical torque-twist relationship will be established by use of equations

$$\theta = \frac{TL}{GJ} \quad (240)$$

and

$$J = \frac{4A^2}{\int \frac{ds}{t}} \quad (241)$$

where the determination of A will be based on the cross-section geometry defined in Figure 171.

$$\begin{aligned}\frac{1}{4}A &= \frac{1}{2}r_1^2\theta_1 - \frac{1}{2}r_1^2\sin\theta_1\cos\theta_1 + r_1\sin\theta_1\left[\frac{b}{2} - r_1(1 - \cos\theta_1)\right] + \\ &\quad \frac{1}{2}r_2\sin\theta_2\left[r_2 + \frac{b}{2} - r_1(1 - \cos\theta_1)\right] - \frac{1}{2}r_2^2\theta_2 \\ &= \frac{1}{2}r_1^2\theta_1 - \frac{1}{2}r_2^2\theta_2 + \frac{1}{2}r_1^2\sin\theta_1(2 - \cos\theta_1) + \\ &\quad \frac{bh}{4} - \frac{br_2}{4}\sin\theta_2 + \frac{1}{2}r_2\sin\theta_2(r_2 - r_1 + r_1\cos\theta_1)\end{aligned} \quad (242)$$

or

$$A = 2r_1^2\theta_1 - 2r_2^2\theta_2 - 2r_1^2 \sin \theta_1(2 - \cos \theta_1) + \\ b(h - r_2 \sin \theta_2) + 2r_2 \sin \theta_2(r_2 - r_1 + r_1 \cos \theta_1) \quad (243)$$

Substituting numerical values yields

$$A = 2(1.5)^2(0.21351) - 2(0.625)^2(0.51342) - 2(1.5)^2(0.21189)(1.02271) + \\ 0.2293(1.25 - 0.625 \times 0.49116) + \\ 2(0.625)(0.49116)(0.625 - 1.50 + 1.5 \times 0.97729) \\ = 0.96080 - 0.40111 - 0.97516 + 0.21623 + 0.36279 \\ = 0.16355 \text{ in.}^2$$

$$\int \frac{ds}{t} = \frac{1}{t} \int ds \\ = \frac{4}{0.003} [0.625 \times 0.51342 + 1.500 \times 0.21351] \\ = 854.87 \quad (244)$$

Then

$$J = \frac{4A^2}{\int \frac{ds}{t}} \\ = \frac{4(0.16355)^2}{854.87} \\ = 0.0001252 \text{ in.}^4 \\ = 125.2 \times 10^{-6} \text{ in.}^4 \quad (245)$$

Therefore,

$$\begin{aligned}\theta &= \frac{TL}{GJ} \\ &= \frac{T(23.5)}{11 \times 10^6 \times 125.2 \times 10^{-6}} (57.3) \\ &= 0.976T\end{aligned}\tag{246}$$

where θ = deg and T = in. -lb.

For long and slender tubes the critical stress is

$$F_s = \frac{0.70E}{\left(\frac{D}{t}\right)^{3/2}}\tag{247}$$

regardless of the edge conditions, or

$$\begin{aligned}F_s &= \frac{0.70 \times 30 \times 10^6}{\left(\frac{3.0}{0.003}\right)^{3/2}} \\ &= 6640 \text{ psi.}\end{aligned}$$

Then

$$\begin{aligned}T_{cr} &= 2AF_s t \\ &= 2 \times 0.16355(6640)(0.003) \\ &= 6.52 \text{ in. -lb.}\end{aligned}\tag{248}$$

This value is about 40 percent larger than the test value of 4.64 in. -lb.

It should be noted that the theoretical value of the critical shear stress was found from Donnell's equation for perfectly round tubes, whereas the tested specimen was far from being a round tube. This, and some local defects in the specimen, may be the sources of discrepancy between theoretical and test values in the collapse torque.

c. Lens - 12-In. Diameter Diaphragm

(1) Purpose

Twelve-inch diaphragm tests were conducted on the lens material (1.6-mil phosphor-bronze cloth with 0.7-mil photolyzable film) for determination of rigidization and buckling. In addition, stress-strain properties of the material were also determined from these tests.

(2) Test Specimen

Test specimens were made from 1.6-mil phosphor bronze cloth with 0.7-mil photolyzable film. The specimens were cemented between two stainless steel rings (Figure 173) to prevent slipping during the tests.

(3) Test Setup and Procedure

The test specimens were installed on a pressure vessel as shown in Figures 174 and 175. To obtain deflections of the specimen, a

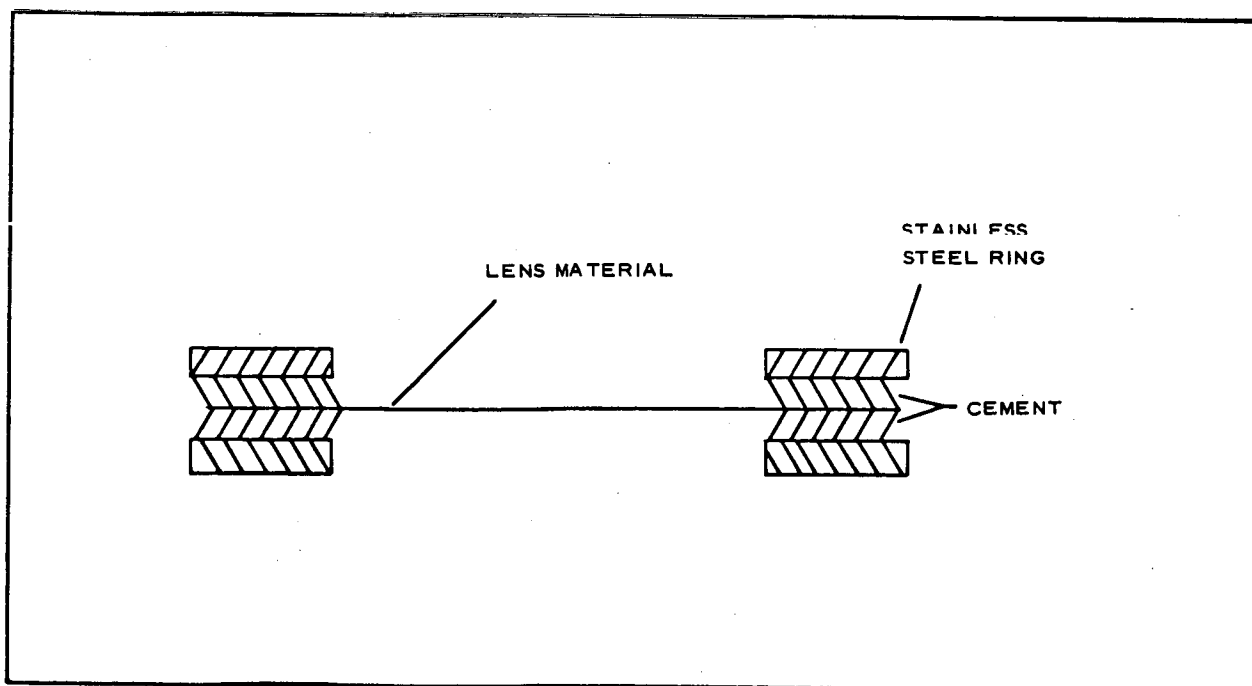


Figure 173 - Diaphragm Test Specimen

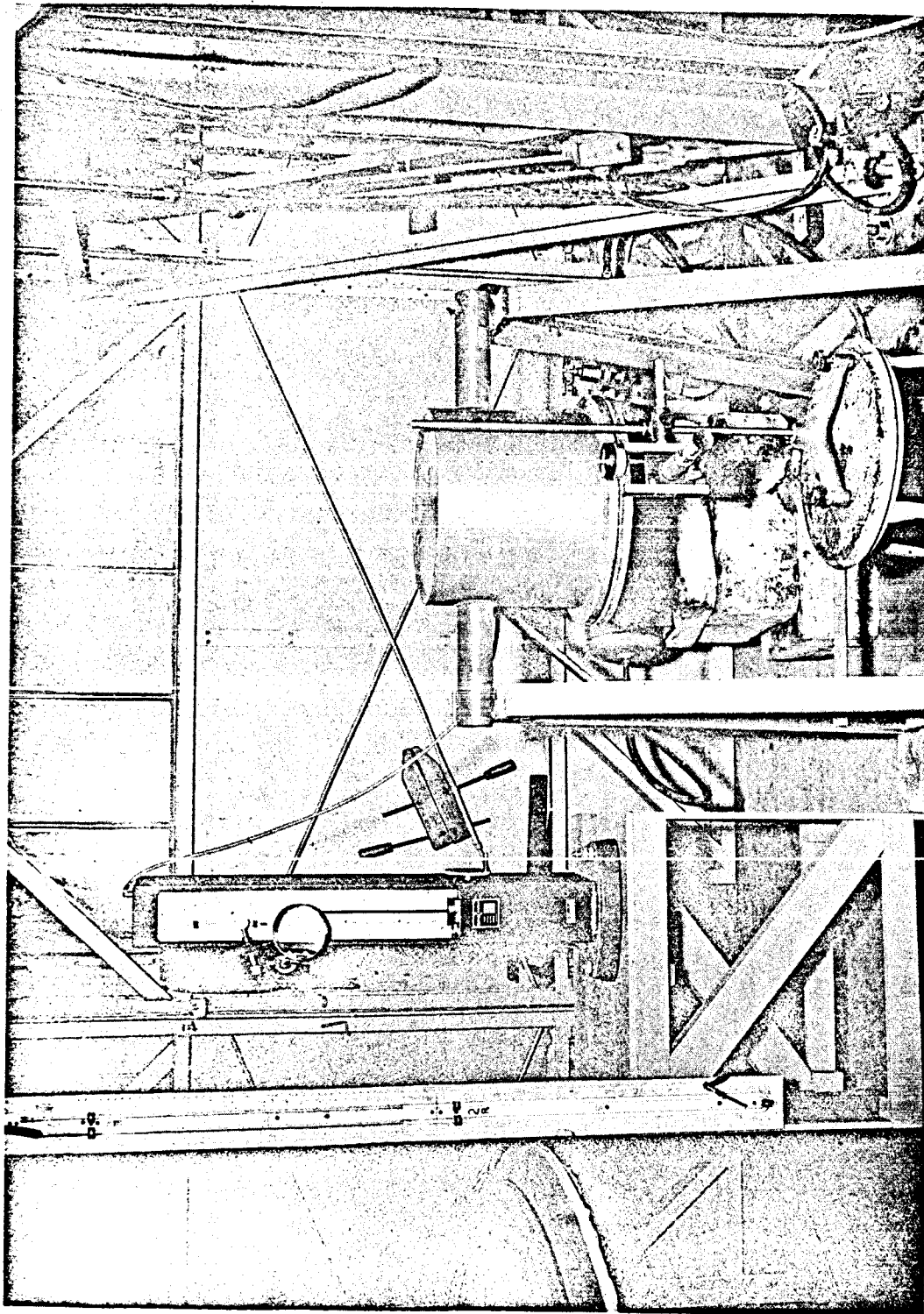


Figure 174 - Twelve-Inch Diaphragm Test Apparatus

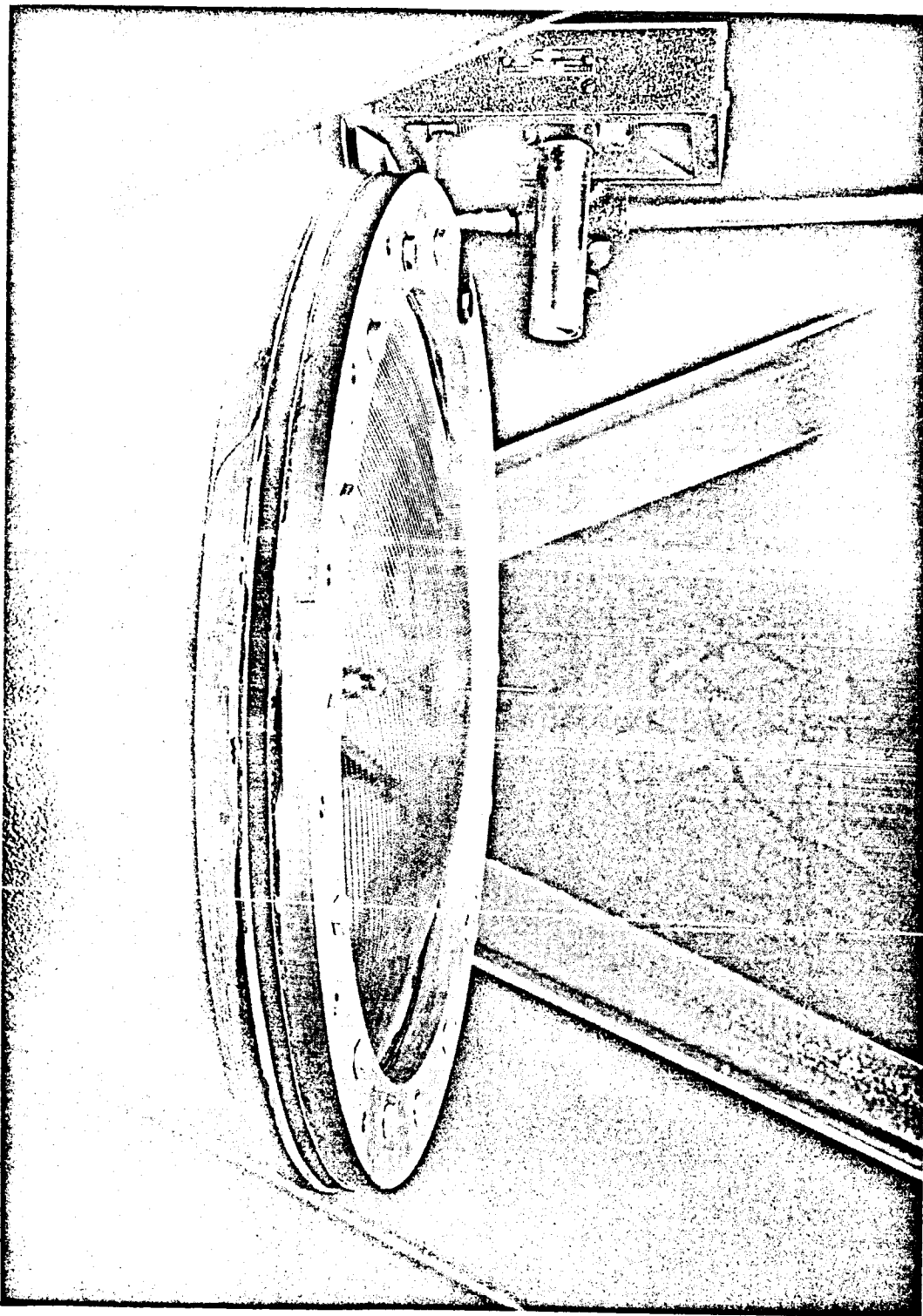


Figure 175 - Twelve-Inch Diaphragm in Fixture

straight pin was cemented to the center of the specimen (Figure 175). Movement of the tip of the pin was measured by a cathetometer.

Pressure and vacuum in the pressure vessel were measured with a micromanometer.

For conducting the tests, a reading on the pin was first obtained with the diaphragm in a flat plane using a reference built into the pressure vessel. Pressure in the vessel was then increased incrementally until a dome was formed (the lens material rigidized). On some specimens incremental pressurization was increased until failure occurred. On others, after rigidization occurred, a vacuum was applied to the vessel to obtain the buckling pressure. After buckling was obtained, the next increment of pressure was applied, followed by vacuum, etc. This was continued until failure of the specimen occurred.

The tests were conducted at room temperature and at 200 F.

(4) Test Results

The data obtained during the 12-in. diaphragm tests are given in Tables XXXIII through XLIV.

The buckling pressures obtained for specimens 4, 5, 6, and 7 are plotted in Figure 176 as a function of dome radius of curvature. The theoretical curves as determined in Item (5), following, are also included for convenience.

Stress-strain curves for specimens 1, 2, 3, 9, 10, and 11 are plotted in Figure 177.

It should be noted that at 200 F, the domes formed were of very poor quality.

SECTION III

Subsection Six - Material and Component Tests

GER-11502

TABLE XXXIII - TWELVE-INCH DIAPHRAGM,
SPECIMEN NO. 1, BELT SIDE IN

Pressure (in. H ₂ O)	Deflection, δ (in.)	$18/\delta$ (in.)	$\delta/2$ (in.)	R 1 + 2	δ^2	ϵ ($\delta^2/72$)	P (psi)	L (PR/2)
0 (flat)	0.0000
0 (G)	0.2790
0.5	0.3855	46.6926	0.1927	46.8853	0.148610	0.002064	0.01806	0.4235
0.0	0.2913							
1.0	0.4408	40.8348	0.2204	41.0552	0.194305	0.002699	0.03613	0.7417
0.0	0.3054							
1.5	0.4780	37.6569	0.2390	37.8959	0.223704	0.003107	0.05419	1.0269
0.0	0.3116							
2.0	0.5112	35.2113	0.2556	35.4669	0.261325	0.003629	0.07226	1.2811
0.0	0.3184							
2.5	0.5396	33.3580	0.2698	33.6278	0.291168	0.004044	0.09032	1.5187
0.0	0.3325							
3.0	0.5872	30.6540	0.2936	30.9476	0.344217	0.004781	0.10839	1.6772
0.0	0.4132							
3.5	0.6160	29.2208	0.3080	29.5288	0.379456	0.005270	0.12645	1.8670
0.0	0.4388							
4.0	0.6523	27.5947	0.3261	27.9208	0.425195	0.005910	0.14452	2.0175
0.0	0.4763							
4.5	0.7022	25.6337	0.3511	25.9848	0.493085	0.006848	0.16258	2.1123
0.0	0.5375							
5.0	0.7549	23.8442	0.3774	24.2216	0.569874	0.007915	0.18065	2.1878
0.0	0.6080							
5.5	0.8038	22.3936	0.4019	22.7955	0.646094	0.008974	0.19871	2.2648
0.0	0.6691							
6.0	0.8670	20.7612	0.4335	21.1947	0.751689	0.010440	0.21676	2.2729
0.0	0.7359							
6.5	0.9357	19.2369	0.4678	19.7047	0.875534	0.012160	0.23484	2.3138
0.0*	0.8159							
7.0	0.9869	18.2389	0.4934	18.7323	0.973972	0.013527	0.25291	2.3688
0.0†	0.8805							
7.5	1.0594	16.9891	0.5297	17.5188	1.122328	0.015588	0.27097	2.3735
0.0‡	0.9633							
8.0	1.1235	16.0214	0.5617	16.5831	1.262252	0.017531	0.28904	2.3966
0.0	1.0347							
8.5	1.2133	14.8356	0.6066	15.4422	1.472097	0.020446	0.307105	2.3712
0.0	1.1316							

* Good dome formed except for a few spots.

† Dome a little better.

‡ Dome further improved.

TABLE XXXIV - TWELVE-INCH DIAPHRAGM,
SPECIMEN NO. 2, BELT SIDE IN

Pressure (in. H ₂ O)	Deflection, δ (in.)	$18/\delta$ (in.)	$\delta/2$ (in.)	R 1 + 2	δ^2	$(\delta^2/72)$	P (psi)	L (PR/2)
0 (flat)	0.0000
0 (G)	0.1216
0.5	0.3073	58.5747	0.1536	58.7283	0.094433	0.001316	0.01806	0.5303
0.0	0.1662							
1.0	0.3859	46.6442	0.1929	46.8371	0.148919	0.002068	0.03613	0.8461
0.0	0.2093							
1.5	0.4297	41.8897	0.2148	42.1045	0.184642	0.002564	0.05419	1.1408
0.0	0.2266							
2.0	0.4653	38.6847	0.2326	38.9173	0.216504	0.003007	0.07226	1.4061
0.0	0.2427							
2.5	0.5051	35.6365	0.2525	35.8890	0.255126	0.003543	0.09032	1.6207
0.0	0.2752							
3.0	0.5396	33.3580	0.2698	33.6278	0.291168	0.004044	0.10839	1.8224
0.0	0.3145							
3.5	0.5860	30.7167	0.2930	31.0097	0.343296	0.004769	0.12645	1.9606
0.0	0.3799							
4.0	0.6333	28.4225	0.3166	28.7391	0.401069	0.005570	0.14452	2.0767
0.0	0.4509							
4.5	0.6951	25.8956	0.3475	26.2431	0.483164	0.006711	0.16258	2.1333
0.0	0.5349							
5.0	0.7645	23.5448	0.3822	23.9270	0.584460	0.008118	0.18065	2.1612
0.0*	0.6267							
5.5	0.8298	21.6920	0.4149	22.1069	0.688568	0.009563	0.19871	2.1964
0.0†	0.7038							
6.0	0.8858	20.3206	0.4429	20.7635	0.784642	0.010898	0.21678	2.2505
0.0	0.7776							
6.5	0.9606	18.7383	0.4803	19.2186	0.922752	0.012816	0.23484	2.2566
0.0‡	0.8634							
7.0	1.0290	17.4927	0.5145	18.0072	1.058841	0.014706	0.25291	2.2771
0.0	0.9420							
7.5	1.0986	16.3845	0.5493	16.9338	1.206922	0.016763	0.27097	2.2943
0.0	1.0159							
8.0	1.1740	15.3322	0.5870	15.9192	1.378276	0.019143	0.28904	2.3006
0.0	1.1008							
8.5	1.2663	14.2146	0.6331	14.8477	1.603516	0.022271	0.30710	2.2799
0.0	1.1912							
9.0	1.3274	13.5603	0.6637	14.2240	1.761991	0.024472	0.32517	2.3126
0.0	1.2567							
9.5	1.4001	12.8562	0.7000	13.5562	1.960280	0.027226	0.34323	2.3264
0.0	1.3356							
10.0	1.4784	12.1753	0.7392	12.9145	2.185667	0.030356	0.36130	2.3330
0.0	1.4097							

* Fair dome formed.

† A little better.

‡ Good dome.

TABLE XXXV - TWELVE-INCH DIAPHRAGM,
SPECIMEN NO. 3, BELT SIDE IN

Pressure (in. H ₂ O)	Deflection, δ (in.)	$18/\delta$ (in.)	$\delta/2$ (in.)	R 1 + 2	δ^2	$(\delta^2/72)$	P (psi)	L (PR/2)
0 (flat)	0.0000
0 (G)	0.1793
0.5	0.3342	53.8600	0.1671	54.0271	0.111690	0.001551	0.01806	0.4879
0.0	0.2227							
1.0	0.4009	44.8990	0.2004	45.0994	0.160721	0.002232	0.03613	0.8147
0.0	0.2491							
1.5	0.4527	39.7614	0.2263	39.9877	0.204937	0.002846	0.05419	1.0834
0.0	0.2698							
2.0	0.4818	37.3599	0.2409	37.6008	0.232131	0.003224	0.07226	1.3585
0.0	0.2883							
2.5	0.5213	34.5291	0.2606	34.7897	0.271754	0.003774	0.09032	1.5711
0.0	0.3299							
3.0	0.5604	32.1199	0.2802	32.4001	0.314048	0.004362	0.10839	1.7559
0.0	0.3713							
3.5	0.6098	29.5179	0.3049	29.8228	0.371856	0.005165	0.12645	1.8855
0.0	0.4378							
4.0	0.6586	27.3307	0.3293	27.6600	0.433754	0.006024	0.14452	1.9987
0.0	0.4977							
4.5	0.7084	25.4094	0.3542	25.7636	0.501831	0.006970	0.16258	2.0943
0.0	0.5561							
5.0	0.7715	23.3312	0.3857	23.7169	0.595212	0.008267	0.18065	2.1422
0.0	0.6358							
5.5	0.8275	21.7523	0.4137	22.1660	0.684756	0.009511	0.19871	2.2023
0.0*	0.7064							
6.0	0.8997	20.0067	0.4498	20.4565	0.809460	0.011242	0.21678	2.2172
0.0+	0.7915							
6.5	0.9702	18.5529	0.4851	19.0380	0.941288	0.013073	0.23484	2.2554
0.0*	0.8617							
7.0	1.0438	17.2447	0.5219	17.7666	1.089518	0.015132	0.25291	2.2467
0.0	0.9489							
7.5	1.1237	16.0185	0.5618	16.5803	1.262702	0.017538	0.27097	2.2463
0.0	1.0402							
8.0	1.1970	15.0376	0.5985	15.6361	1.432809	0.019900	0.28904	2.2597
0.0	1.1200							
8.5	1.2732	14.1376	0.6366	14.7742	1.621038	0.022514	0.30710	2.2686
0.0	1.1964							
9.0	1.3440	13.3928	0.6720	14.0648	1.806336	0.025088	0.32517	2.2867
0.0	1.2703							
9.5	1.4313	12.5760	0.7156	13.2916	2.048620	0.028453	0.34323	2.2810
0.0	1.3683							

* Fair dome formed.

+ Better.

* Good.

SECTION III

Subsection Six - Material and Component Tests

GER-11502

TABLE XXXVI - TWELVE-INCH DIAPHRAGM,
SPECIMEN NO. 4, BELT SIDE IN

Pressure (in. H ₂ O)	Deflection, δ (in.)	$18/\delta$ (in.)	$\delta/2$ (in.)	R 1 + 2	δ^2	δ^2/ϵ ($\delta^2/72$)	P (psi)	L (PR/2)
0.0	0.0000							
1.0	0.4205	42.8062	0.2102	43.0164	0.176820	0.002456	0.07226	1.5542
0.0	0.2315							
3.0	0.5091	35.3565	0.2545	35.6110	0.259183	0.003600	0.10839	1.9299
0.0								
4.0	0.6063	29.6883	0.3031	29.9914	0.367600	0.005106	0.14452	2.1672
0.0	0.4888							
5.0	0.7366	24.4366	0.3683	24.8049	0.542580	0.007536	0.18065	2.2405
0.0	0.6149							
6.0	0.8555	21.0403	0.4277	21.4680	0.731880	0.010165	0.21678	2.3269
0.0	0.7648							
6.5	0.9504	18.9394	0.4752	19.4146	0.903260	0.012545	0.23484	2.2797
0.0								
0.008*								
7.0	1.0173	17.6939	0.5086	18.2026	1.03490	0.014374	0.25291	2.3018
0.0								
0.026*								
7.5	1.0698	16.8256	0.5349	17.3605	1.14447	0.015895	0.27097	2.3521
0.0	1.0129							
0.011*								
8.0	1.1439	15.7356	0.5719	16.3075	1.30851	0.018174	0.28904	2.3568
0.0	1.0913							
0.020*								
8.5	1.2329	14.5997	0.6164	15.2161	1.52004	0.021112	0.30710	2.3364
0.0	1.2309							
0.012*								
9.0	1.3213	13.6229	0.6606	14.2835	1.74583	0.024248	0.32517	2.3223
0.0	1.2593							
0.011*								

* Vacuum buckling occurred.

TABLE XXXVII - TWELVE-INCH DIAPHRAGM,
SPECIMEN NO. 5, BELT SIDE OUT

Pressure (in. H ₂ O)	Deflection, δ (in.)	$18/\delta$ (in.)	$\delta/2$ (in.)	R 1 + 2	δ^2	$(\delta^2/72)$	P (psi)	L (PR/2)
0.0	0.0000							
4.0	0.5640	31.9148	0.2820	32.1968	0.318096	0.004418	0.14452	2.3267
0.0	0.4198							
5.0	0.6939	25.9403	0.3469	26.2872	0.481497	0.006687	0.18065	2.3749
0.0	0.5463							
5.5	0.7401	24.3210	0.3700	24.6910	0.547748	0.007608	0.19871	2.4532
0.0	0.5927							
6.0	0.8178	22.0103	0.4089	22.4192	0.668797	0.009289	0.21678	2.4300
0.0	0.6931							
6.5	0.8791	20.4755	0.4395	20.9150	0.772817	0.010734	0.23484	2.4558
0.0	0.7681							
0.0205*								
7.0	0.9608	18.7344	0.4804	19.2148	0.923137	0.012821	0.25291	2.4298
0.0	0.8555							
0.015*								
7.5	1.0511	17.1249	0.5255	17.6504	1.104811	0.015345	0.27097	2.3914
0.0	0.9578							
0.0005*								
8.0	1.1147	16.1478	0.5573	16.7051	1.242556	0.017258	0.28904	2.4142
0.0	1.0403							
0.013*								
8.5	1.2223	14.7263	0.6111	15.3374	1.494017	0.020750	0.30710	2.3551
0.0	1.1866							
0.024*								
9.0	1.2906	13.9470	0.6453	14.5923	1.665648	0.023134	0.32517	2.3725
0.0	1.2598							
0.018*								
9.5	1.3889	12.9599	0.6944	13.6543	1.929043	0.026792	0.34323	2.3433
0.0	1.3563							
0.015*								
10.0	1.4531	12.3873	0.7265	13.1138	2.111500	0.029326	0.36130	2.3690
0.0	1.4111							
0.022*								
10.5	1.4991	12.0072	0.7495	12.7567	2.247301	0.031213	0.37936	2.4197
0.0	1.4723							
0.037*								
11.0	1.6465	10.9323	0.8232	11.7555	2.710962	0.037652	0.39743	2.3360
0.0	1.6161							
0.024*								
11.5	1.7258	10.4299	0.8629	11.2928	2.978386	0.041367	0.41548	2.3460
0.0	1.6856							
0.014*								

* Vacuum buckling occurred.

TABLE XXXVIII - TWELVE-INCH DIAPHRAGM, SPECIMEN NO. 6,
BELT SIDE OUT

Pressure (in. H ₂ O)	Deflection, δ (in.)	$18/\delta$ (in.)	$\delta/2$ (in.)	R 1 + 2	δ^2	$\frac{\delta^3}{72}$	P (psi)	L (PR/2)
0.0	0.0000							
4.0	0.6344	28.3733	0.3172	28.6905	0.402463	0.005590	0.14452	2.0732
0.0	0.5164							
5.0	0.7243	24.8516	0.3621	25.2137	0.524610	0.007286	0.18065	2.2774
0.0	0.6271							
5.5	0.7967	22.5932	0.3483	22.9415	0.634731	0.008816	0.19871	2.2794
0.0	0.7071							
0.022*								
6.0	0.8755	20.5597	0.4377	20.9974	0.766500	0.010646	0.21678	2.2759
0.0	0.8015							
0.016*								
6.5	0.9374	19.2020	0.4687	19.6707	0.878719	0.012204	0.23484	2.3097
0.0								
0.0275*								
7.0	1.0054	17.9033	0.5027	18.4060	1.010829	0.014039	0.25291	2.3275
0.0	0.9636							
0.031*								
7.5	1.1061	16.2734	0.5530	16.8264	1.223457	0.016992	0.27097	2.2797
0.0	1.0488							
0.022*								
8.0	1.1729	15.3466	0.5864	15.9330	1.375694	0.019107	0.28904	2.3026
0.0	1.1270							
0.020*								
8.5	1.2459	14.4474	0.6229	15.0703	1.552267	0.021559	0.30710	2.3140
0.0	1.2223							
0.022*								
9.0	1.3323	13.5105	0.6661	14.1766	1.775023	0.024653	0.32517	2.3049
0.0	1.2976							
0.026*								
9.5	1.3849	12.9973	0.6924	13.6897	1.917948	0.026638	0.34323	2.3494
0.0	1.3517							
0.023*								
10.0	1.4790	12.1704	0.7395	12.9099	2.187441	0.030381	0.36130	2.3322
0.0	1.4454							
0.008*								
10.5	1.5532	11.5889	0.7766	12.3655	2.412430	0.033506	0.37936	2.3455
0.0	1.5154							
0.012*								

* Vacuum.

SECTION III

Subsection Six - Material and Component Tests

GER-11502

TABLE XXXIX - TWELVE-INCH DIAPHRAGM,
SPECIMEN NO. 7, BELT SIDE IN

Pressure (in. H ₂ O)	Deflection, δ (in.)	$18/\delta$ (in.)	$\delta/2$ (in.)	R 1 + 2	δ^2	$(\delta^2 f/72)$	P (psi)	L (PR/2)
0.0	0.0000							
4.0	0.6346	28.3643	0.3173	28.6816	0.40272	0.005593	0.14452	2.0725
0.0	0.5294							
5.0	0.7537	23.882	0.3768	24.2590	0.56806	0.007890	0.18065	2.1912
0.0	0.6700							
6.0	0.8935	20.1455	0.4467	20.5922	0.79834	0.011088	0.21678	2.2320
0.0	0.8307							
0.015*								
6.5	0.9683	18.5893	0.4841	19.0734	0.93760	0.013022	0.23484	2.2396
0.0	0.9243							
0.018*								
7.0	1.0510	17.1265	0.5255	17.6520	1.10460	0.015342	0.25291	2.2322
0.0	1.0015							
0.017*								
7.5	1.1262	15.9630	0.5631	16.5461	1.26833	0.017616	0.27097	2.2417
0.0	1.0847							
0.012*								
8.0	1.1955	15.0565	0.5977	15.6542	1.42922	0.019850	0.28904	2.2623
0.0	1.1624							
0.018*								
8.5	1.2861	13.9958	0.6430	14.6388	1.65405	0.022973	0.30710	2.2478
0.0	1.2499							
0.024*								
9.0	1.3596	13.2392	0.6798	13.9190	1.84851	0.025674	0.32517	2.2630
0.0	1.3334							
0.024*								
9.5	1.4610	12.3203	0.7305	13.0508	2.13452	0.29646	0.34323	2.2397
0.0	1.4231							
0.021*								
10.0	1.5093	11.9261	0.7546	12.6807	2.27799	0.031639	0.36130	2.2908
0.0	1.4908							
0.0245*								
10.5	1.5774	11.4112	0.7887	12.1999	2.48819	0.034558	0.37936	2.3141
0.0	1.5752							
0.030*								
11.0	1.6775	10.7303	0.8387	11.5690	2.81401	0.039084	0.39743	2.2989
0.0	1.6671							
0.0345*								
11.5	1.7460	10.3093	0.8730	11.1823	3.04852	0.042341	0.41548	2.3230
0.0	1.7533							
0.044*								
12.0	1.8220	9.8793	0.9110	10.7903	3.31968	0.046107	0.43355	2.3391
0.0	1.8263							
0.031*								

* Vacuum.

TABLE XL - TWELVE-INCH DIAPHRAGM, SPECIMEN NO. 8
AT 200 F, BELT SIDE OUT

Pressure (in. H ₂ O)	Deflection, δ (in.)	$18/\delta$	$\delta/2$	R $1+2$	δ^2	ϵ $\delta^2/72$	P (psi)	L (PR/2)
0.0	0.0000							
0.5	0.2525	71.2871	0.1262	71.4133	0.063756	0.000886	0.01806	0.6450
0.0	0.0037							
1.0	0.3348	53.7634	0.1674	53.9308	0.112091	0.001557	0.03613	0.9742
0.0	0.0056							
1.5	0.3823	47.0834	0.1911	47.2745	0.146153	0.002030	0.05419	1.2809
0.0	0.0054							
2.0	0.4216	42.6945	0.2108	42.9053	0.177746	0.002469	0.07226	1.5501
0.0	0.0037							
2.5	0.4746	37.9267	0.2373	38.1640	0.225245	0.003128	0.09032	1.7235
0.0	0.0043							
3.0	0.5074	35.4750	0.2537	35.7287	0.257455	0.003576	0.10839	1.9363
0.0	0.0090							
3.5	0.5530	32.5497	0.2765	32.8262	0.305809	0.004247	0.12645	2.0754
0.0	0.0081							
4.0	0.5998	30.0100	0.2999	30.3099	0.359760	0.004997	0.14452	2.1902
0.0	0.0115							
4.5	0.6518	27.6158	0.3259	27.9417	0.424843	0.005901	0.16258	2.2714
0.0	0.0084							
5.0	0.7144	25.1960	0.3572	25.5532	0.510367	0.007088	0.18065	2.3081
0.0	0.0125							
5.5	0.7688	23.4131	0.3844	23.7975	0.591053	0.008209	0.19671	2.3644
0.0	0.0139							
6.0	0.8379	21.4823	0.4189	21.9012	0.702076	0.009751	0.21678	2.3738
0.0	0.0136							
6.5	0.8959	20.0915	0.4479	20.5394	0.802637	0.011148	0.23484	2.4117
0.0	0.7560							
7.0	0.9730	18.4995	0.4865	18.9860	0.946729	0.013149	0.25291	2.4009
0.0	0.8310							
7.5	1.0386	17.3310	0.5193	17.8503	1.078690	0.014982	0.27097	2.4184
0.0	0.9203							
8.0	1.1181	16.0987	0.5590	16.6577	1.250148	0.017363	0.28904	2.4073
0.0	0.9852							
8.5	Failure							

SECTION III

Subsection Six - Material and Component Tests

GER-11502

TABLE XLI - TWELVE-INCH DIAPHRAGM, SPECIMEN NO. 9

AT 200 F, BELT SIDE IN

Pressure (in. H ₂ O)	Deflection, δ (in.)	$18/\delta$	$\delta/2$	R 1 + 2	δ^2	δ^2/γ_2	P (psi)	L (PR/2)
0.0								
0.5	0.3141	57.3066	0.1570	57.4636	0.098659	0.001370	0.01806	0.5189
0.0	0.2234							
1.0	0.3643	49.4098	0.1821	49.5919	0.132714	0.001843	0.03613	0.8959
0.0	0.2502							
1.5	0.4044	44.5104	0.2022	44.7126	0.163539	0.002271	0.05419	1.2115
0.0	0.2632							
2.0	0.4448	40.4676	0.2224	40.6900	0.197847	0.002748	0.07226	1.4701
0.0	0.2822							
2.5	0.4737	37.9987	0.2368	38.2355	0.224392	0.003117	0.09032	1.7267
0.0	0.3065							
3.0	0.5121	35.1494	0.2560	35.4054	0.262246	0.003642	0.10839	1.9188
0.0	0.3441							
3.5	0.5528	32.5615	0.2764	32.8379	0.305588	0.004244	0.12645	2.0761
0.0	0.3845							
4.0	0.6080	29.6053	0.3040	29.9093	0.369664	0.005134	0.14452	2.1612
0.0	0.4591							
4.5	0.6726	26.7618	0.3363	27.0981	0.452391	0.006283	0.16258	2.2028
0.0	0.5340							
5.0	0.7276	24.7389	0.3638	25.1027	0.529402	0.007353	0.18065	2.2674
0.0	0.6135							
5.5	0.8090	22.2497	0.4045	22.6542	0.654481	0.009090	0.19871	2.2508
0.0	0.7183							
6.0	0.8716	20.6517	0.4358	21.0875	0.759687	1.055120	0.21678	2.2857
0.0	0.7948							
6.5	0.9599	18.7520	0.4800	19.2320	0.921408	1.279733	0.23484	2.2582
0.0	0.8954							
7.0	1.0213	17.6246	0.5106	18.1362	1.043054	1.448686	0.25291	2.2932
0.0	0.9632							
7.5	1.0901	16.5122	0.5450	17.0572	1.188318	1.650442	0.27097	2.3109
0.0	1.0321							
8.0	1.1864	15.1719	0.5932	15.7651	1.407545	1.954924	0.28904	2.2783
0.0	1.1329							

TABLE XLII - TWELVE-INCH DIAPHRAGM, SPECIMEN NO. 10
AT 200 F, BELT SIDE IN

Pressure (in. H ₂ O)	Deflection, δ (in.)	$18/\delta$	$\delta/2$	R $1 + 2$	δ^2	$\frac{\epsilon}{\delta^2/72}$	P (psi)	L (PR/2)
0.0 (flat)	0.0							
1.0	0.3212	56.0399	0.1606	56.2005	0.103169	0.001432	0.03613	1.0152
0.0	0.1261							
2.0	0.4048	44.6640	0.2024	44.8664	0.163863	0.002276	0.07226	1.6210
0.0	0.2767							
3.0	0.4975	36.1809	0.2487	36.4296	0.247506	0.003438	0.10839	1.9743
0.0	0.4031							
4.0	0.6057	29.7177	0.3029	30.0206	0.366872	0.005095	0.14452	2.1692
0.0	0.5003							
-0.005	Buckle							
5.0	0.7431	24.2229	0.3765	24.5994	0.552198	0.007669	0.18065	2.2219
0.0	0.6832							
-0.007	Buckle							
6.0	0.9104	19.7715	0.4552	20.2267	0.828828	0.011512	0.21678	2.1923
0.0	0.8964							
-0.0015	Buckle							
7.0	1.0748	16.7473	0.5374	17.2847	1.155195	0.016044	0.25291	2.1857
0.0	1.0673							
-0.007	Buckle							
8.0	1.2471	14.4335	0.6235	15.0570	1.555258	0.021601	0.28904	2.1760
0.0	1.2443							
-0.006	Buckle							
9.0	1.4285	12.6006	0.7142	13.3148	2.040612	0.028341	0.32517	2.1647
0.0	1.4431							
-0.007	Buckle							
10.0	1.5822	11.3766	0.7911	12.1677	2.503357	0.034769	0.36130	2.1980
0.0	1.6240							
-0.003	Buckle							

TABLE XLIII - TWELVE-INCH DIAPHRAGM, SPECIMEN NO. 11 AT 200 F, BELT SIDE IN

Pressure (in. H ₂ O)	Deflection, δ (in.)	18/ δ	$\delta/2$	R 1 + 2	δ^2	$\delta^2 \epsilon / 72$	P (psi)	L (PR/2)
0.0	0.0							
1.0	0.3631	49.5731	0.1815	49.7546	0.131842	0.001831	0.03613	0.8955
0.0	0.1607							
2.0	0.4531	39.7263	0.2265	39.9528	0.205300	0.002851	0.07226	1.4435
0.0	0.2939							
3.0	0.5257	34.2401	0.2628	34.5029	0.276360	0.003838	0.10839	1.8699
0.0	0.3540							
4.0	0.6009	29.9551	0.3004	30.2555	0.361081	0.005015	0.14452	2.1863
0.0	0.4485							
5.0	0.7211	24.9619	0.3605	25.3224	0.519985	0.007222	0.18065	2.2872
0.0	0.6151							
6.0	0.8483	21.2189	0.4241	21.6430	0.804443	0.011173	0.21678	2.3459
0.0	0.7688							
7.0	0.9884	18.2113	0.4942	18.7055	0.976935	0.013568	0.25291	2.3654
0.0	0.9456							
8.0	1.1246	16.0357	0.5623	16.5680	1.264725	0.017566	0.28904	2.3944
0.0	1.0982							
0.010	Vacuum							
9.0	1.5189	11.8507	0.7594	12.6101	2.307057	0.032042	0.32517	2.0502
0.0	1.5189							
0.004	Vacuum							

SECTION III

Subsection Six - Material and Component Tests

GER-11502

TABLE XLIV - TWELVE-INCH DIAPHRAGM, SPECIMEN NO. 12 AT

200 F, BELT SIDE OUT

Pressure (in. H ₂ O)	Deflection, δ (in.)	$18/\delta$	$\delta/2$	R $1 + \frac{\delta}{2}$	δ^2	$\frac{\epsilon}{\delta^2/72}$	P (psi)	L (PR/2)
0.0	0.0							
1.0	0.3512	51.2528	0.1756	51.4234	0.123341	0.001713	0.03613	0.9291
0.0	0.1897							
2.0	0.4317	41.6956	0.2158	41.9114	0.186365	0.002588	0.07226	1.5143
0.0	0.2817							
3.0	0.5091	35.3565	0.2545	35.6110	0.259183	0.003600	0.10839	1.9299
0.0	0.3577							
4.0	0.5886	30.5810	0.2943	30.8753	0.346450	0.004812	0.14452	2.2310
0.0	0.4607							
0.045								
5.0	0.7068	25.4669	0.3534	25.8203	0.499566	0.006938	0.18065	2.3322
0.0	0.6129							
0.014								
6.0	0.8452	21.2967	0.4226	21.7193	0.714363	0.009922	0.21678	2.3542
0.0	0.7769							
0.025								
7.0	0.9853	18.2685	0.4926	18.7611	0.970816	0.013484	0.25291	2.3724
0.0	0.9490							
0.005	Vacuum							
8.0	1.1235	16.0214	0.5617	16.5831	1.26225	0.017531	0.28904	2.3966
0.0	1.0948							
0.0005	Vacuum							
8.5	Failure							

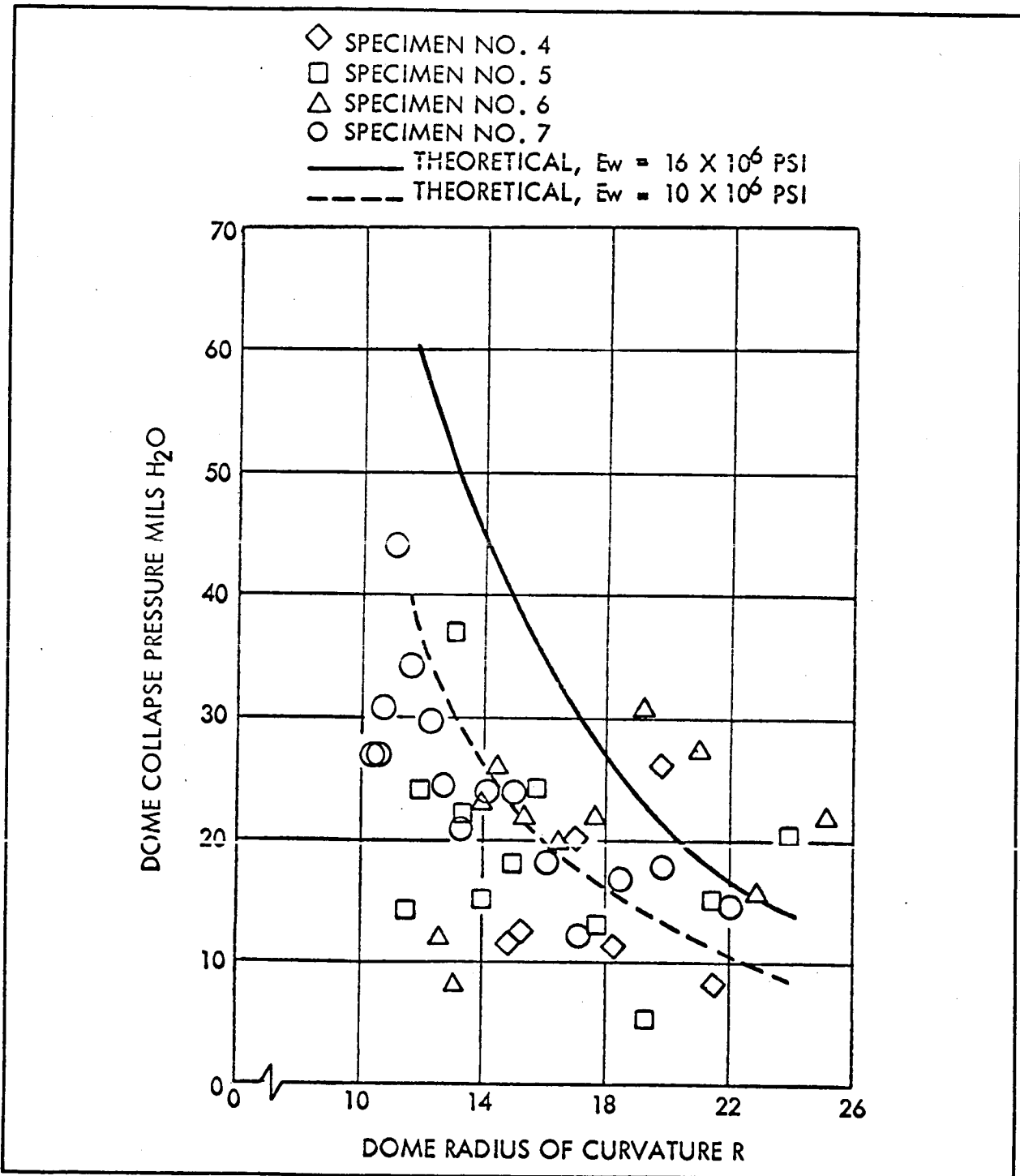


Figure 176 - Diaphragm Collapse Pressure versus Radius of Curvature of Diaphragm

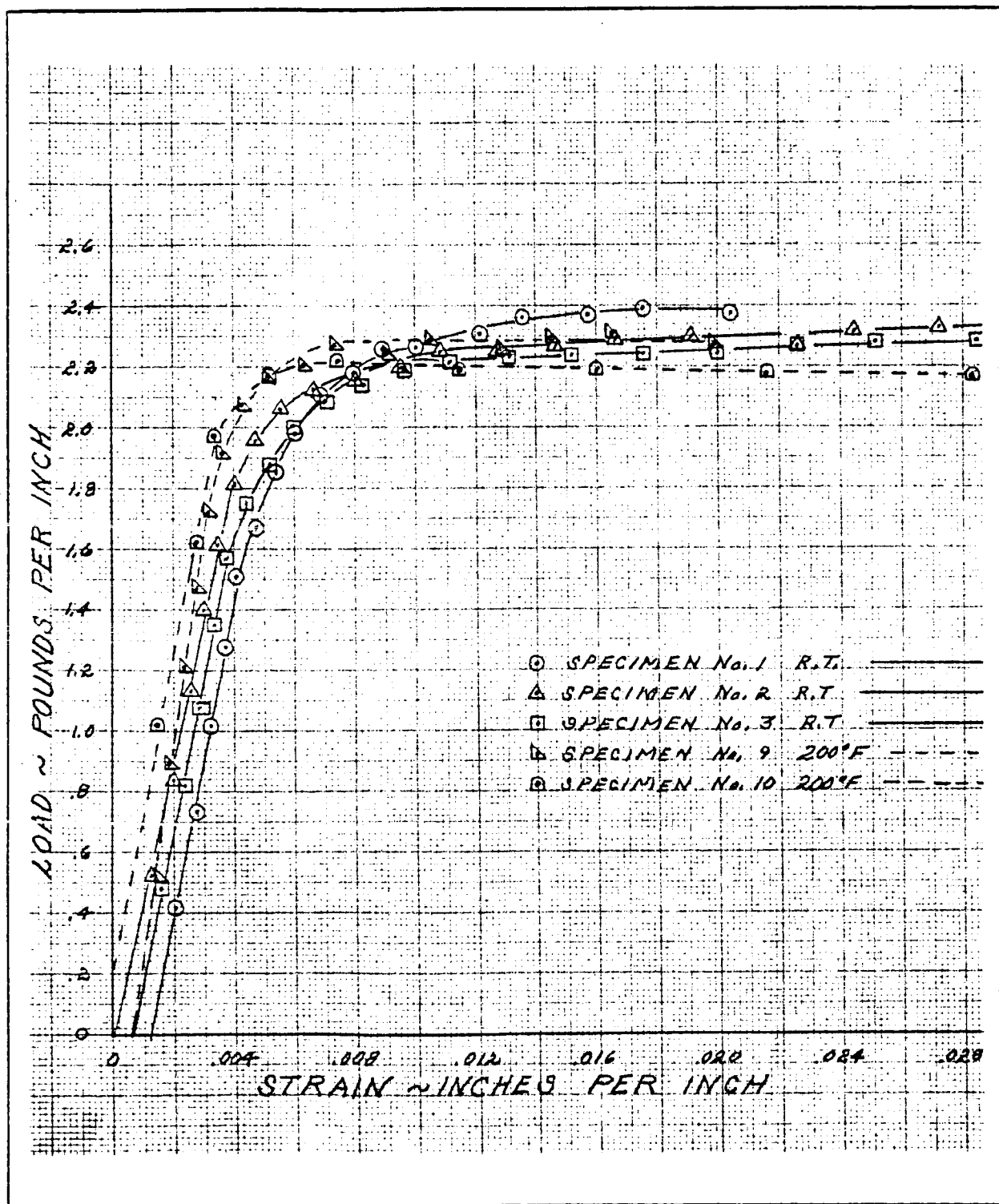


Figure 177 - Load versus Strain, 12-In. Diaphragm Test

(5) Theoretical Analysis

(a) Lens Material

The important characteristics of the lens material insofar as rigidization is concerned are the yield stress and the initial modulus of elasticity. These are given in Table XLV.

It is apparent that:

1. Weaving the cloth does not affect the yield strength but does reduce the modulus.
2. A temperature of 200 F reduces both yield stress and modulus
3. The addition of 0.7 mil of photolyzable film has little effect on the properties
4. The diaphragm test shows a reduction of both properties compared to the Instron tests. Inasmuch as the stress and strain are both derived from pressure and deflection data, it is recommended that the Instron values be used for determining stress-strain characteristics

(b) Critical Buckling Pressure

The critical buckling pressure was obtained by pressurizing a flat diaphragm to form a shallow dome, then reversing the pressure to obtain the buckling pressure. By using successively higher pressures, several domes could be formed with increasingly smaller curvature.

This method has two features that tend to give low values of buckling pressure. The first is that at low pressures the

TABLE XLV - LENS MATERIAL DATA, 1.6-MIL
PHOSPHOR BRONZE WIRE

Test material	Temperature (F)	$F_{TY} \times 10^{-3}$	$E \times 10^{-6}$
Wire	Room	48.2	15.6
Cloth warp	Room	48.2	13.2
Cloth fill	Room	47.0	12.2
Cloth warp	200	40.5	9.5
Cloth fill	200	40.9	9.2
Wire film
Wire warp	Room	51.1	13.8
Wire fill	Room	46.5	11.9
Diaphragm	Room	43.8	10.0

domes that are formed have visual imperfections. The second is that at higher pressures restoring moments become large due to the clamped edges.

It is concluded therefore that the design criteria for buckling that have been used in the structural analysis are satisfactory.

The critical buckling pressure of a spherical dome is given by equation

$$p_{cr} = 0.191 E_w \frac{d^3}{SR^2}, \quad (249)$$

where

E_w = modulus of elasticity of phosphor
bronze wires = 16×10^6

d = wire diameter = 1.6 mil

s = wire spacing = $1/24$ in. = 0.04167 in.

R = radius of dome (variable).

Then

$$\begin{aligned} p_{cr} &= 0.191 \times 16 \times 10^6 \frac{(0.0016)^3}{\frac{1}{24} R^3} \\ &= \frac{0.191 \times 16 \times 24 \times 4096 \times 10^{-6}}{R^3} \\ &= \frac{0.3004}{R^2} \text{ psi } (R = \text{inches}). \end{aligned}$$

The radius of curvature of the spherical zone of the dome (see Figure 178) can be found from the equation,

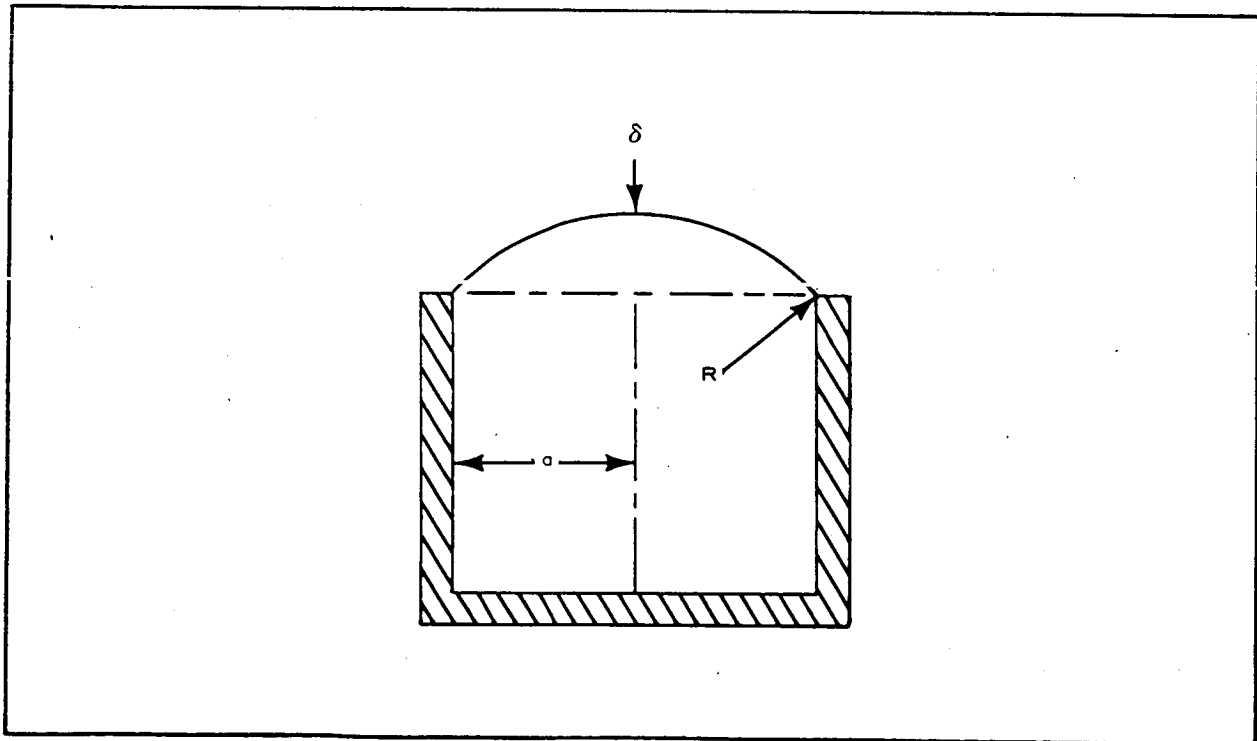


Figure 178 - Twelve-Inch Diaphragm Attached at End of Rigid Cylinder

$$a^2 = \delta(2R - \delta)$$

or

$$R = \frac{a^2 + \delta^2}{2\delta} \quad (250)$$

for

$$a = 6 \text{ in. , and}$$

$$R = \frac{18}{\delta} + \frac{\delta}{2} \text{ in.}$$

where δ is measured in inches.

Theoretical curves for $E_w = 16 \times 10^6$ psi and $E_w = 10 \times 10^6$ psi are plotted in Figure 176, together with test points for four tested specimens (designated as specimens 4, 5, 6, and 7). Comparison between theory and tests is fairly good, especially for the low modulus value.

3. LENS SPHERICITY

a. Purpose

Tests were conducted on a six-foot-diameter diaphragm to obtain preliminary information with regard to determination of sphericity versus pressure, rigidization, and buckling. The results of the tests were to be used also for planning additional elevated temperature tests.

b. Test Specimen

The test specimen was a diaphragm, six feet in diameter, fabricated from 1.2-mil copper cloth, 21 X 21 weave, with 0.6-mil photolyzable film. The diaphragm was made with 24 gores as shown in Figure 179. Seams were butt joints secured with 1-mil X 1-in. wide Mylar tape. Selection of specimen size was based on data of Appendix I.

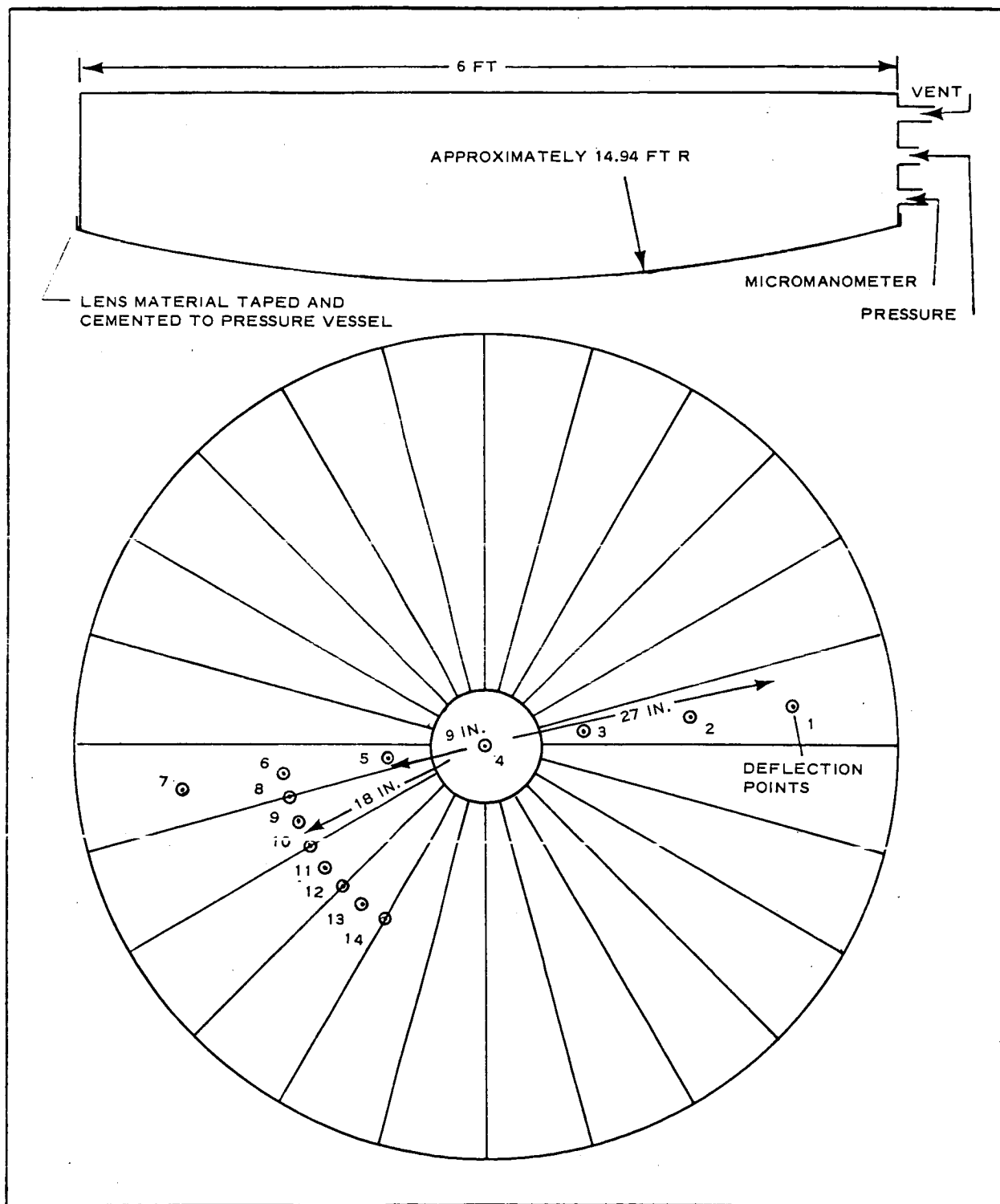


Figure 179 - Lens Sphericity Test Setup

c. Test Setup and Procedure

The test specimen was cemented and taped to a pressure vessel as shown in Figures 179 and 180. Pins, used as deflection indicators, were cemented to the diaphragm with contact cement at the locations shown in Figure 179. Deflections were obtained by sighting the tip of the pin with transits, with reference to fixed deflection scales.

Zero deflection readings were obtained and recorded with no pressure on the diaphragm. The pressure vessel was then pressurized in increments of 0.04-in. water. At each increment of load, deflection readings were recorded and the pressure then returned to zero, deflections again recorded and a visual inspection of the diaphragm was made. Pressurization was continued in this manner until failure of the diaphragm occurred.

d. Test Results

The data obtained during the test are listed in Table XLVI. Figures 180 through 183 show the appearance of the diaphragm under pressure and at zero return. During the test there was no visible indication of diaphragm rigidization.

This test pointed out several problem areas, as follows:

1. A more accurate method of obtaining deflections is required.
2. It appeared that scalloping of the diaphragm occurred nearer the outside edges; therefore, deflections should be obtained along an arc 27 in. from the center as well as the quarter point.
3. Softer and narrower seams are required.
4. Care must be used in seaming the center cap to eliminate double and triple seams in that area.

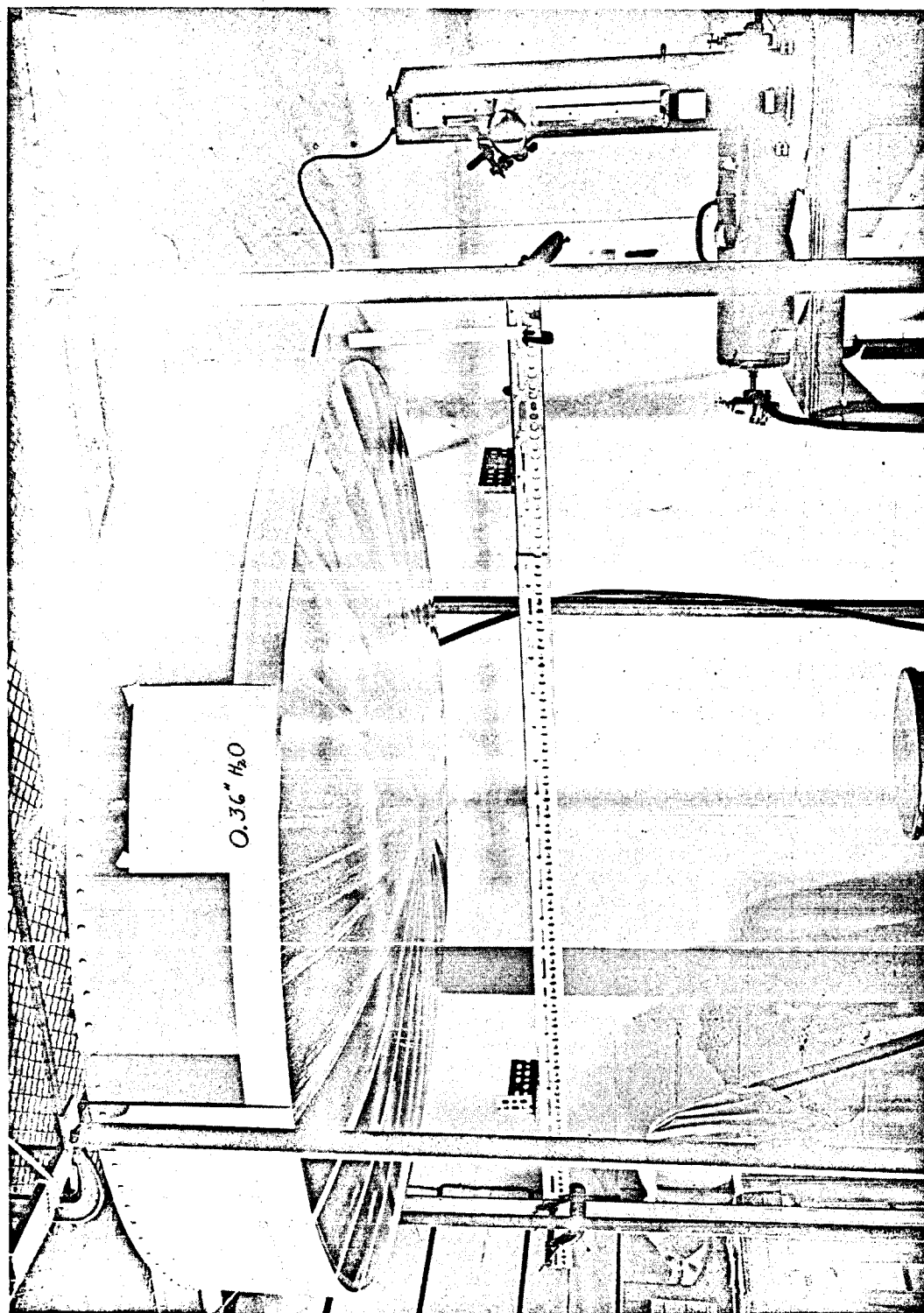


Figure 180 - Large Diaphragm, 0.36-In. H_2O Pressure

TABLE XLVI - RECORDED DEFLECTIONS, SIX-FOOT DIAPHRAGM

Pressure (in. H ₂ O)	Deflection at point number (see Figure 179) (in.)													
	Point number													
	1	2	3	4	5	6	7	8	9	10	11	12	13	14
0.00	0.00	0.00	0.00	0.00	0.00	0.00	0.00	0.00	0.00	0.00	0.00	0.00	0.00	0.00
0.04	0.56	0.98	1.32	1.46	1.12	0.97	0.59	1.02	1.06	1.06	1.12	1.15	1.12	1.11
0.00	0.06	0.08	0.03	0.05	0.07	0.10	0.09	0.07	0.06	0.02	0.04	0.04	0.04	0.05
0.08	0.87	1.48	1.81	1.85	1.50	1.24	0.80	1.33	1.35	1.50	1.44	1.50	1.48	1.49
0.00	1.12	0.18	0.13	0.11	0.12	0.14	0.16	0.11	0.11	0.06	0.05	0.06	0.07	0.05
0.12	1.00	1.77	2.19	2.15	1.86	1.53	0.94	1.60	1.62	1.77	1.72	1.78	1.75	1.76
0.00	0.16	0.24	0.18	0.14	0.16	0.21	0.19	0.15	0.17	0.08	0.08	0.08	0.10	0.06
0.16	1.14	1.96	2.44	2.35	2.02	1.74	1.07	1.81	1.83	1.99	1.95	2.01	1.98	1.99
0.00	0.21	0.35	0.26	0.20	0.23	0.28	0.27	0.22	0.22	0.11	0.14	0.12	0.17	0.12
0.20	1.26	2.15	2.66	2.54	2.22	1.91	1.17	1.98	2.01	2.19	2.14	2.19	2.16	2.16
0.00														
0.24	1.27	2.16	2.78	2.05	2.31	1.92	1.14	2.02	2.05	2.36	2.25	2.36	2.25	2.34
0.00	0.27	0.34	0.27	0.18	0.23	0.31	0.24	0.22	0.21	0.16	0.12	0.15	0.11	0.16
0.28	1.33	2.30	2.93	2.18	2.46	2.04	1.24	2.13	2.14	2.49	2.36	2.51	2.37	2.46
0.00	0.33	0.45	0.40	0.28	0.33	0.37	0.31	0.31	0.29	0.23	0.18	0.20	0.20	0.24
0.32		2.44	3.10	2.32	2.62	2.17	1.33	2.30	2.34	2.64	2.53	2.65	2.52	2.62
0.00	0.43	0.56	0.54	0.40	0.44	0.48	0.38	0.43	0.39	0.32	0.27	0.30	0.28	0.34
0.36	1.30	2.22	2.36	2.03	2.57	2.08	1.20	2.23	2.24	2.62	2.53	2.66	2.51	2.60
0.00	0.36	0.50	0.36	0.41	0.37	0.39	0.26	0.32	0.30	0.25	0.24	0.24	0.06	0.25
0.40	1.39	2.38	2.53	2.52	2.72	2.23	1.30	2.36	2.39	2.79	2.69	2.84	2.66	2.70
0.00	0.49	0.67	0.54	0.61	0.57	0.57	0.38	0.50	0.46	0.42	0.40	0.40	0.38	0.40
0.44*	1.49	2.54	2.68	2.73	2.91	2.40	1.43	2.55	2.58	2.96	2.85	3.00	2.83	2.91

* Center cap failing.

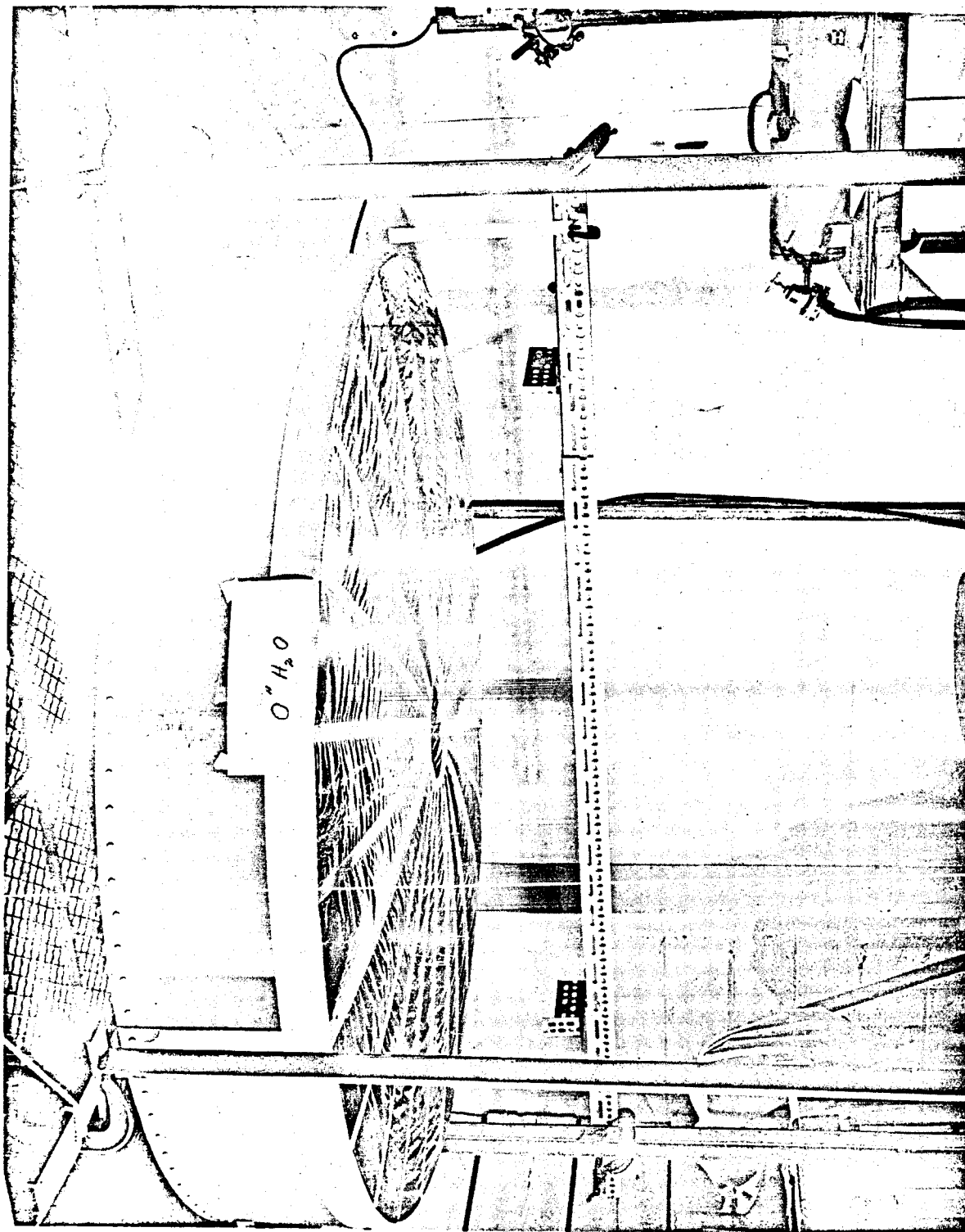


Figure 181 - Large Diaphragm, Zero Return after 0.36-In. H₂O Pressure

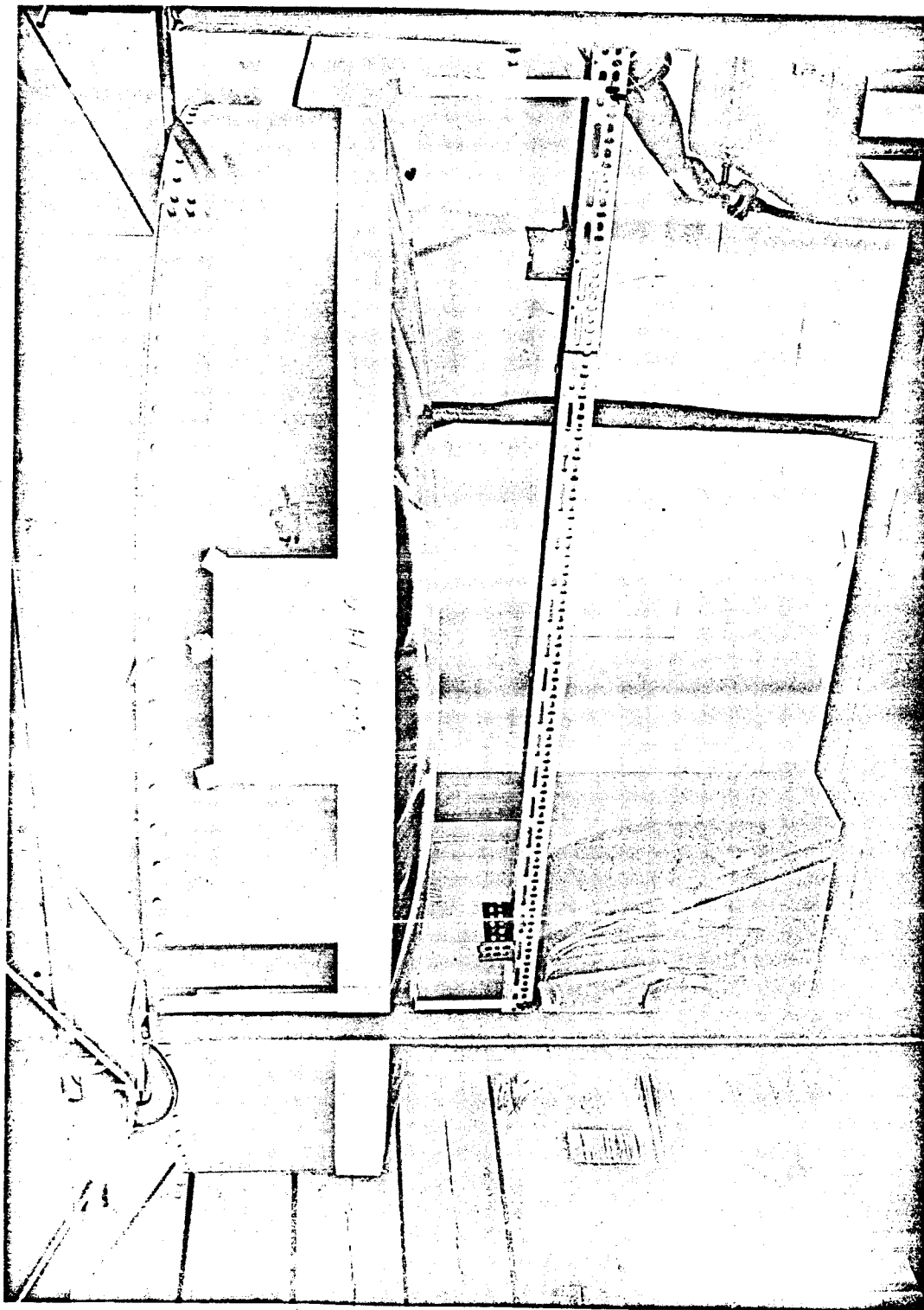


Figure 182 - Large Diaphragm, 0.40-In. H_2O Pressure

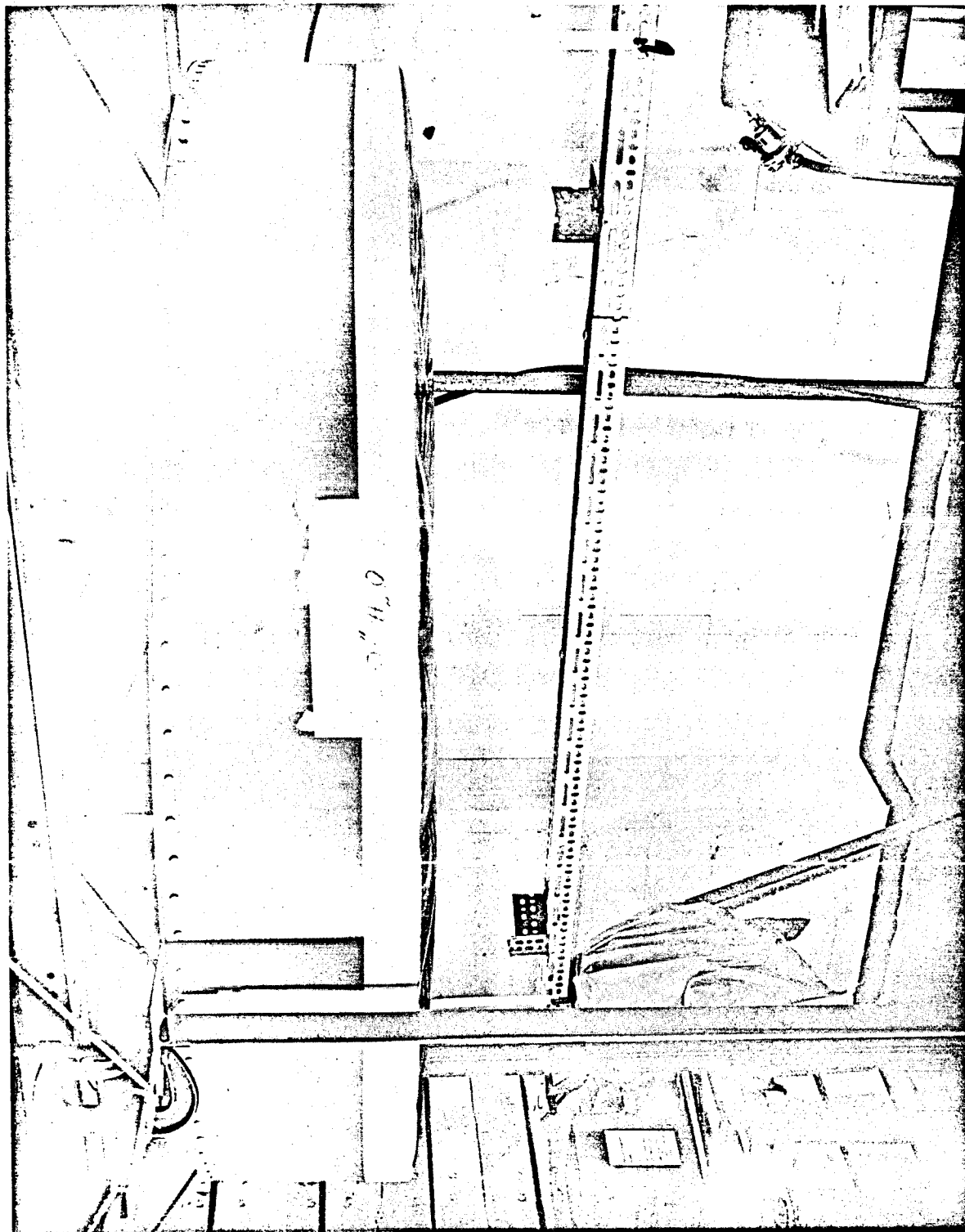


Figure 183 - Large Diaphragm, Zero Return After 0.40-In. H₂O Pressure

SECTION III - TECHNICAL DISCUSSION - PHASES I AND II

Subsection Seven - Instrumentation and Control Parameters

1. GENERAL

The instrumentation and control systems considered herein include both those for the full-scale satellite and the 50-ft flight-test vehicle.

Because the two satellites have differences in their systems it will be necessary, when applicable, to indicate which satellite the system is used on.

The instrumentation and systems include the command and sequence control system, the inflation and rigidization system, data acquisition and sensors, storage and transmission, power regulation and some of the necessary electronics. For block diagrams of the respective systems see Figures 184 and 185. Power requirements, sizes, and weights of instrumentation system components of the two systems are given in Tables XLVII and XLVIII.

2. SEQUENCE CONTROL SYSTEM

a. Canister Pressure Equalization

Immediately prior to sequence control in both satellites there is a function that must occur sometime after the vehicle has obtained an altitude of 100,000 ft or greater. The precise time is not critical.

This function is the canister pressure equalization. Prior to launch the canister will be pumped down to a pressure as closely oriented with the orbital environment as possible.

In the 50-ft test vehicle this function can be commanded to start with deployment of the heat shield of the launch vehicle.

Depending on the launch vehicle, the full-scale orbital satellite will have to have a time control of so many minutes from launch or a sequencing similar to that for the 50-ft model to command this function.

This pressure equalization will result from opening a squib-actuated valve in the canister wall. Escaping air will flow into a diffusion mechanism to eliminate any thrust effect on the satellite. Equalization of the canister pressure will continue to occur until canister separation.

b. Canister Separation from Launch Vehicle

The sequence of events and controls described in this item and Items c and d below applies to the 50-ft test vehicle only.

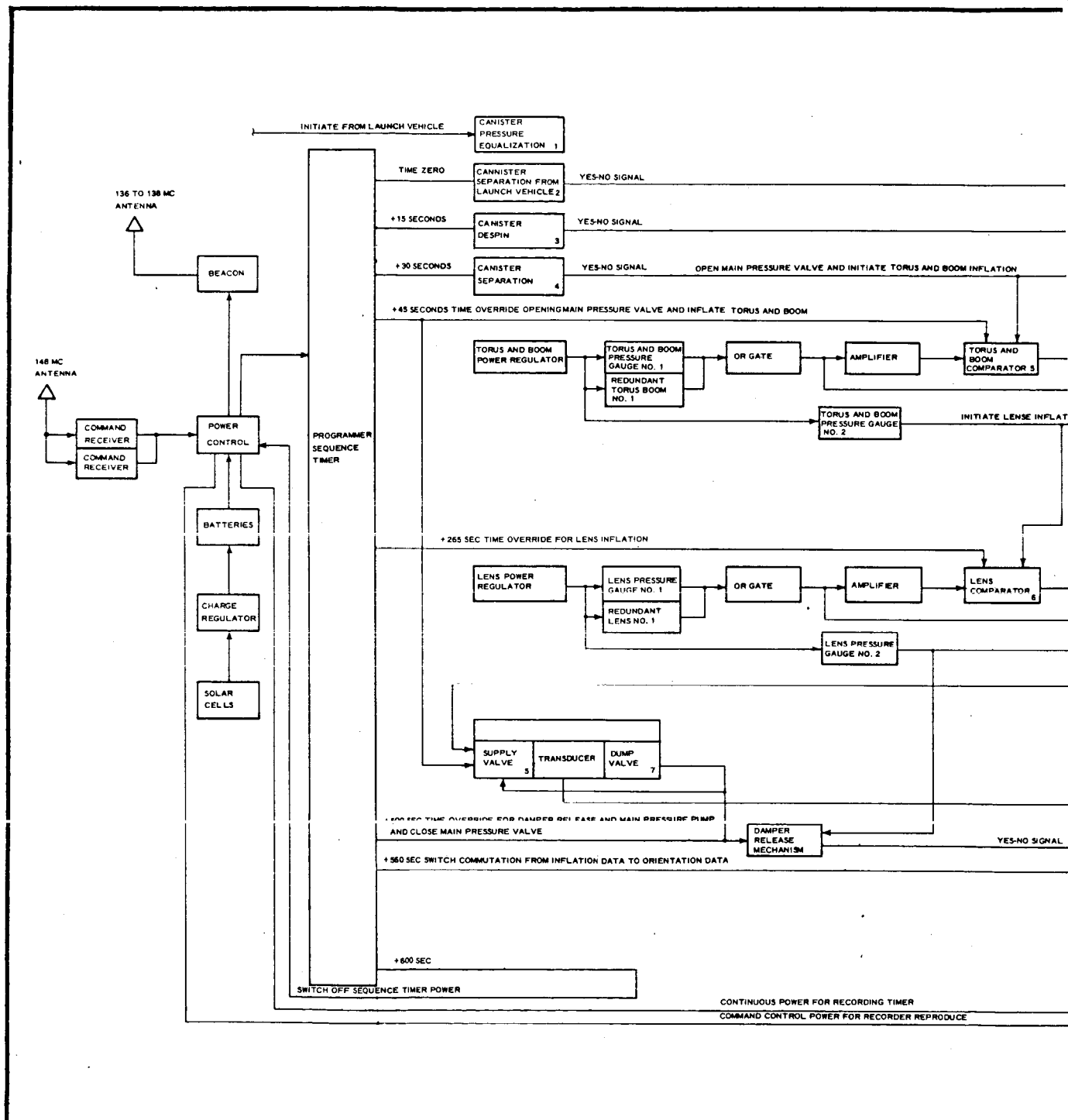
Upon command from the control system (see Item 5, a) the sequence timer will begin to function. The start will be identified as time zero for the remaining functions. At the same time the canister will be separated from the launch vehicle by means of explosive squibs and a spring mechanism. Upon separation a switch-closure type mechanism will send a signal to the signal conditioning and commutator electronics for storage in the tape recorder.

c. Canister Despin

At time 0 + 15 sec the despin mechanism will be released. This mechanism is comprised of a series of weights and straps attached to the canister. The weights are spring loaded and attached by explosive bolts. The release system will fire the bolts and allow the system to function. When the entire system is free of the canister a switch-closure type signal will be sent to the commutator for storage.

d. Canister Separation

At time 0 + 30 sec the sequence timer will signal for the canister halves to be separated by squib operated shaped charges. After the shaped charges have blown, the canister halves will be separated by



SECTION III
Subsection Seven - Instrumentation and Control Parameters

GER-11502

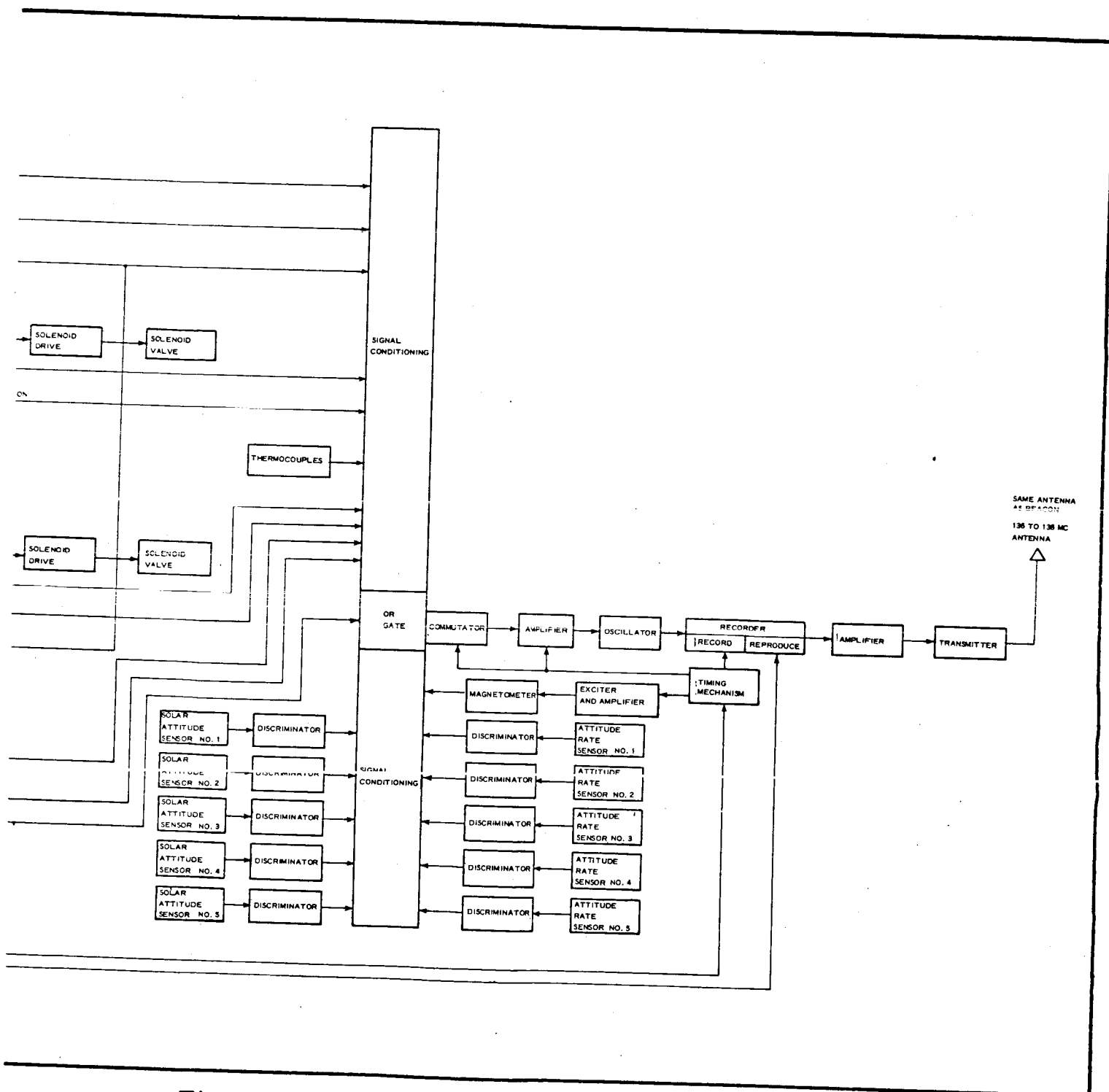


Figure 184 - Telemetry and Programming Systems Block Diagram for 50-Ft Flight-Test Satellite

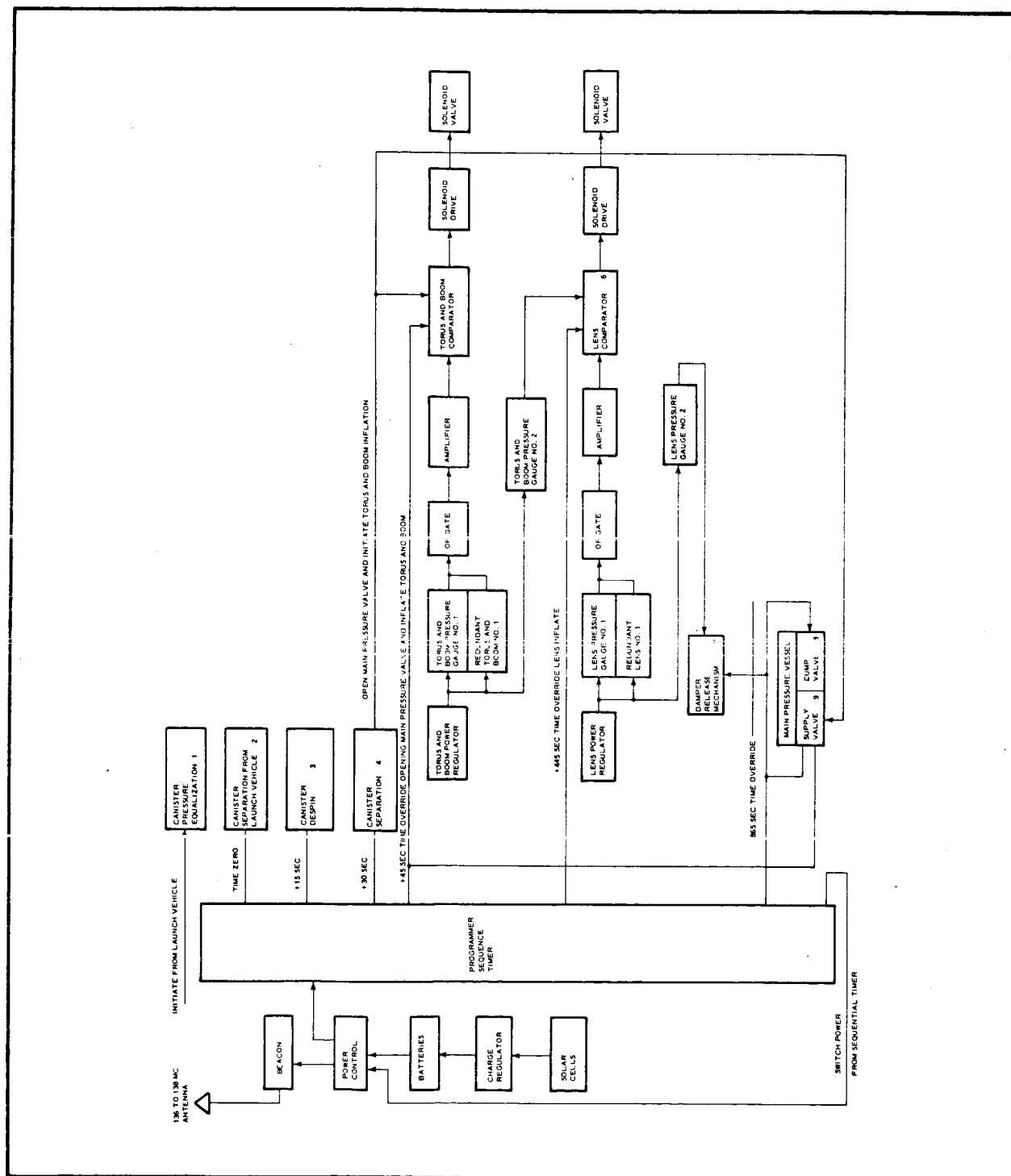


Figure 185 - Sequence and Control System Block Diagram for Full-Scale Satellite

SECTION III

Subsection Seven - Instrumentation and Control Parameters

GER-11502

TABLE XLVII - INSTRUMENTATION DETAILS FOR 50-FT
FLIGHT-TEST SATELLITE

Item	Current at 28 v dc (amps)	Volume (cu in.)	Weight (oz)
Command receiver 148 mc range (2)	0.030	100.0	40.0
Radio beacon, 136 to 138 mc	0.016	22.0	10.5
Recorder reproducer (1 w record - 2 w reproduce)	0.250	69.0	80.0
Transmitter, 136 to 138 mc	0.040	19.0	20.0
Program sequence timer	0.200	26.5	20.0
Commutator	0.100	12.0	16.0
Signal conditioning circuits	0.100	24.0	16.0
Voltage-control oscillator	0.040	19.0	20.0
Amplifier	0.040	12.0	10.0
Recorder timing mechanism	0.020	14.0	10.0
Main pressure solenoid valve	0.400	22.0	10.4
Main pressure dump valve	0.400	12.0	6.4
Torus and boom solenoid valve	0.400	12.0	6.4
Torus and boom pressure gauge tube	0.150	0.5	6.0
Torus and boom power regulation system	0.040	10.0	4.0
Lens solenoid valve	0.400	12.0	6.4
Lens pressure gauge tube	0.150	0.5	6.0
Lens power regulation system	0.040	10.0	4.0
Thermocouples	...	3.0	6.0
Magnetometer	0.010	126.0	48.0
Solar attitude sensors	...	30.0	12.0
Solar rate sensors	...	30.0	12.0
Canister separation from launch vehicle (3 explosive bolts with 2 squibs each)	136,080 ergs
Canister despin release mechanism*	136,080 ergs
Canister halves separation	45,360 ergs
Batteries, solar cells, and charge regulation	...	100.0	40.0
Antennas	...	33.0	10.0
Wire	48.0

*If canister despin mechanism is used.

SECTION III

Subsection Seven - Instrumentation and Control Parameters

GER-11502

TABLE XLVIII - INSTRUMENTATION DETAILS FOR
FULL-SCALE SATELLITE

Item	Current at 28 v dc (amps)	Volume (cu in.)	Weight (oz)
Beacon, 136 to 138 mc	0.016	22.0	10.5
Program sequence timer	0.2	26.5	20.0
Main pressure solenoid valve	0.4	22.0	10.4
Main pressure solenoid dump valve	0.4	12.0	6.4
Torus and boom solenoid valve	0.4	12.0	6.4
Torus and boom gauge pressure tube (3)	0.15	0.5	6.0
Torus and boom power regula- tion system	0.04	10.0	6.0
Lens solenoid valve	0.4	12.0	6.4
Lens gauge pressure tube (3)	0.15	0.5	6.0
Lens power regulation system	0.04	10.0	6.0
Canister separation from launch vehicle (3 explosive bolts with 2 squibs each)	136,080 ergs
Canister despin release mecha- nism*	136,080 ergs
Canister separation	45,360 ergs
Batteries, solar cells and charge regulation antenna, wire, etc.	12.75 lb

*If canister despin mechanism is used.

a spring mechanism. A switch closure signal will indicate that the halves have been separated by sending a signal to the recorder for signal storage.

This signal, however, will have a multiple function because it also will go to the inflation system to initiate the inflation sequence (see Item 3, a).

The same or a similar system will be used on the full-scale satellite, depending on the launch vehicle. The initiation of the sequence timer will have to be commanded from the launch vehicle because the full-scale satellite will not have a command receiver. The separation from the launch vehicle will be the same. Despin might not be required, depending on whether or not the launch vehicle will despin itself prior to orbit or not at all. The canister halves will be separated the same as for the 50-ft test vehicle. All switch-closure signals will be eliminated except for the inflation initiation because there will be no data storage or instrumentation on the full-scale model.

The sequence timer intended at this time will be a ten-channel mechanical switch, with time settings of 2 to 40 min for the full cycle. It will have a temperature range from -55 to +71 C and will withstand 150 g for 11 msec.

Table XLIX and L are complete listings of the sequence of events, times, and type of signal for the functional sequences of the two satellites.

3. INFLATION SYSTEM

a. Torus and Boom Inflation

The inflation system for the full-scale satellite and the 50-ft test vehicle will be the same except for adjustment of the comparators. This difference will be required to compensate for different pressures.

SECTION III

Subsection Seven - Instrumentation and Control Parameters

GER-11502

TABLE XLIX - FUNCTIONAL SEQUENCE FOR 50-FT TEST VEHICLE

Number	Item	Function start after 0 sec (sec)	Elapsed time for function (sec)	Type of signal
1	Canister pressure equalization	...	Continuous	None
2	Canister separate from launch vehicle	0	3.0	Yes-no
3	Canister despin mechanism release *	+15	0.5	Yes-no
4	Canister halves separate	+30	1.0	Yes-no
5a	Main pressure valve open	Yes signal from 4	0.5	Pressure
	Function override	+45		
5b	Torus and boom inflation	Yes signal from 4	120.0	Pressure
	Function override	+45		
6	Lens inflation	Yes signal from 5	120.0	Pressure
	Function override	+265		
7	Damper mechanism release	Yes signal from 6	0.5	Yes-no
	Function override	+500		
8	Close main pressure vessel and open dump valve	+500	0.5	Pressure
9	Switch functions off commutator	+560	0.1	None
	Switch orientation function on commutator	+560	0.1	None
	Switch all power from program sequence time	+600	0.1	None
10	Switch power to orientation data timer	+600	0.1	None

* If canister despin is used.

TABLE L - FUNCTIONAL SEQUENCE FOR FULL-SCALE VEHICLE

Number	Item	Function start after 0 sec (sec)	Elapsed time for function (sec)
1	Canister pressure equalization	. . .	Continuous
2	Canister separate from launch vehicle	0	3.0
3	Canister despin mechanism release*	+15	0.5
4	Canister halves separate	+30	1.0
5a	Main pressure valve open	Yes signal from 4	0.5
	Function override	+45	
5b	Torus and boom inflation	Yes signal from 4	300.0
	Function override	+45	
6	Lens inflation	Yes signal from 5	300.0
	Function override	+445	
7	Damper release	Yes signal from 6	0.5
	Function override	+865	0.5
8	Close main pressure valve and open dump valve	+865	0.5
9	Switch all power from program sequence and functions	+985	0.1

* If canister despin is used.

The full-scale satellite will have the torus and booms inflated to 0.1678 psia and the lens inflated to 0.000316 psia. The 50-ft test vehicle will have a torus and boom pressure of 1.047 psia and a lens pressure of 0.002437 psia. This can all be compensated for in electronics and pressure gauge ranges.

The signal initiated by the separation of the canister halves will start the inflation system by operating the solenoid-operated main pressure valve in the pressure cylinder and advising the torus and boom comparator to start inflating the torus and boom. The high pressure gas, at 3000 psi, will then flow to a pressure reduction valve that will drop the pressure to 5 psia. All pressure inflation systems are fed from this pressure reducer.

If for some reason or other, the canister half separation signal does not initiate the main pressure vessel and the comparator, an override signal from the sequence timer will cause both to function at time 0 + 45 sec.

A pressure gauge in the main pressure line will signal the commutator, and this signal will be recorded until such time as it is switched off the commutator.

The pressure gauge tube in the inflation system will operate on the heated thermopile principle. By passing an alternating current through the thermopile heater elements, a direct current output will be generated which will vary according to the amount of gas passing over the heater elements and the thermopile. This direct current output will be sent to the comparator to be compared by means of known resistance with known voltages for specific pressures. The amount of gas fed to the torus and boom will be controlled by a solenoid-operated valve, which, in turn, will be controlled by the comparator to open and close continually until a predetermined pressure is reached and maintained in the torus and booms. To assure accurate measurements of pressure, this system will have its own power

regulation. Therefore, known voltages will be maintained at all times. The signal from the pressure tube also will go to the commutator of the recording system to be kept as a data item for playback.

A redundant pressure tube tied in with that described above will operate through an or-gate so that either gauge will function in the system.

A third pressure tube located in the fourth segment of the torus will initiate a signal to the comparator of the lens system for lens inflation to start when the torus is completely inflated.

Present thinking indicates that this should occur at approximately 0 + 165 sec for the 50-ft test vehicle and at 0 + 345 sec for the full-scale satellite. If for some reason no signal is received for the lens to begin inflation, the sequence timer override will give the signal for inflation at 265 sec for the 50-ft test vehicle and 445 sec for the full-scale vehicle.

b. Lens Inflation

The system for lens inflation will be the same system as for the torus and booms except for pressures involved in the comparator and the volume of gas that will be used. All pressure tubes and solenoid switches will operate on the same principle. The inflation time for the lens will be 2 min for the 50-ft test vehicle and 5 min for the full-scale satellite.

The third pressure tube in the lens system will give a signal to release the damping mechanism. This will probably be a squib-operated latch-type device containing the damper weight.

If for some reason this does not occur when the lens is inflated, the sequence timer will override this function at 0 + 500 sec for the 50-ft test vehicle and at 0 + 865 sec for the full-scale satellite. This override signal also will close the main pressure valve of the pressure tank, and open a squib-actuated valve in the tank to dump the remaining gas through a diffusion mechanism.

On the full-scale satellite all power will be switched off the program sequence timer at 0 + 985 sec.

For the 50-ft test vehicle, the next function at 0 + 560 sec will switch all sequencing and inflation functions off the commutator and recording system and switch the commutator to the orbital orientation functions. At 0 + 600 sec all power will be switched off the program sequence and its functions, and be applied to the orbital orientation data timing mechanism.

4. ORBITAL ORIENTATION DATA ACQUISITION

a. General

Accurate knowledge of the satellite's orientation to earth while in orbit will be a prime factor in this program to ascertain the true results of the damping system and to predict the results of the satellite as a reflective surface.

All sensors used for orbital orientation will apply strictly to the 50-ft test vehicle. It is not intended to acquire orientation data on the full-scale satellite.

b. Temperature Profile

A temperature profile of the vehicle will be established by placing thermistors at key positions. These sensors will be located at all pressure pickups, at the main pressure vessel, at the instrumentation compartment, and at other strategic points on the lens and torus. All temperature data will be commutated and recorded during the inflation and rigidization sequence as well as during all the remaining orbits. Chromel-constantan thermocouples will be used to monitor the temperature anticipated to range from -100 to +300 F.

c. Pressure Sensors

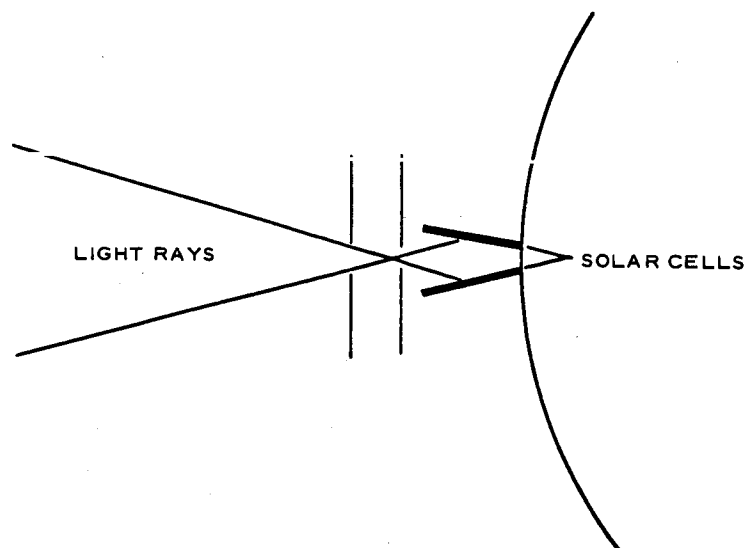
The pressure sensors will be the Hastings-Roydest thermopile-type transducers. Two ranges will be used for the different pressures

being monitored. For a thorough description of the transducers see Item 3, a.

d. Attitude Sensing

The attitude sensing system will contain a three-axis earth-field magnetometer. The magnetometer will provide complete 4π steradian coverage for measuring the earth-field components at all points in the satellite orbit, not limited by tumbling considerations. This magnetometer will be considered as a rough sensing device for all portions of the orbit except when the satellite is in the earth shadow. At this time it will be the only means of obtaining orientation data.

Obtaining a fine degree of accuracy in orientation will have to be accomplished with an array of solar cells strategically located around the periphery of the canister. These solar cells can be mounted in pairs that nearly parallel each other and are shaded by a mechanical aperture to precisely indicate angle of light. The sketch below shows a



typical arrangement of solar cells. The solar cells will also be shaded from reflected earth light. With the indicated arrangement, the amount of sunlight impinging on the cells will tend to cause the least amount of degradation. Solar cells are simple and reliable, have no moving parts, and require no power inputs. Because of the closeness to the instrumentation in the canister, there will be a minimum of line losses. There will be periods of inoperation when the earth or vehicle structure will block the view of the sun, and also when the sun line is aligned with the spin axis. The effects of shading by the vehicle structure can be countered with redundant devices. Although nothing can be done directly about earth shading, the resulting periods of inoperation will be short compared with total time, during which magnetometer readings will indicate any drastic change of attitude.

All data from the solar cells and magnetometers will be commutated and recorded during the second periods programmed into the system for recording approximately one minute out of every ten during an orbit for playback upon command. The system will be capable of numerous orbits of recording without playback.

e. Attitude Rate Sensors

Some attitude rate data can be obtained from the attitude sensors. Their prime function, however, is for accurate orientation. Therefore additional spin-rate measuring devices will be used. These will consist of an array of solar cells mounted behind an array of parallel slots in a cylinder. As the satellite rotates, sunlight will impinge on the cells periodically and the electrical outputs of the cells can be counted to give a measure of component spin along an axis parallel to the slots.

The solar cells will be mounted in pairs inside a housing as shown in Figure 186A. Internal shielding will ensure that each cell will respond to the light passing through one end only. Four such housings

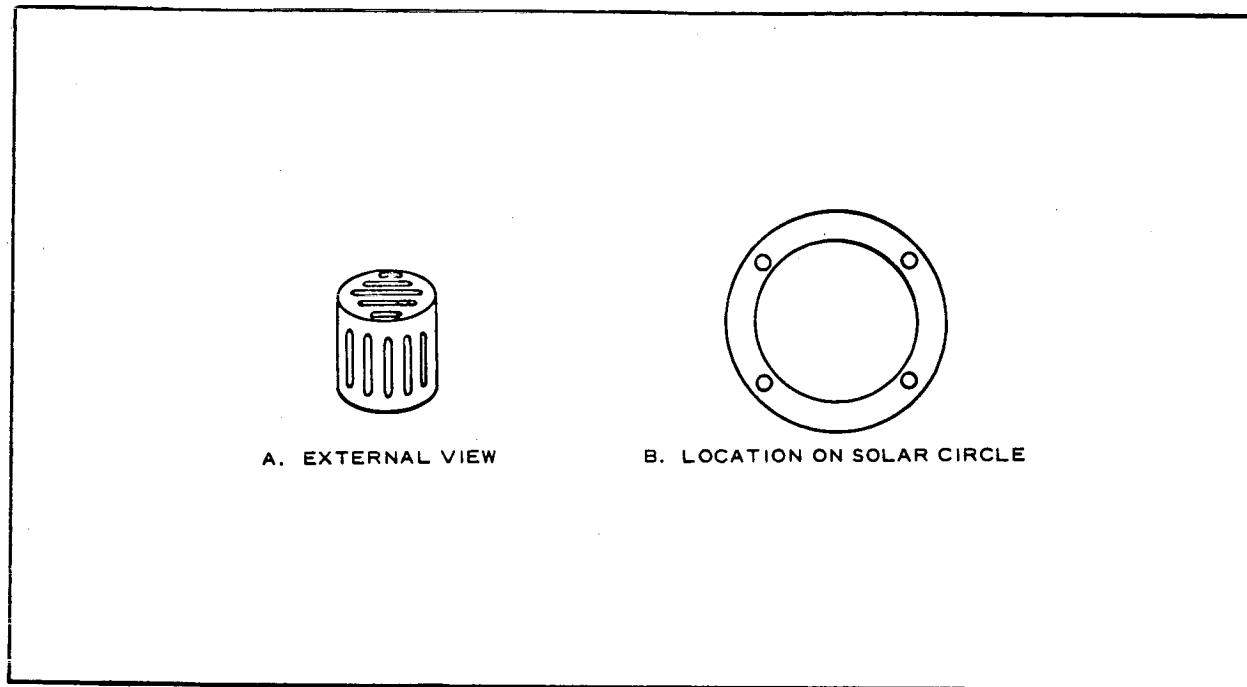


Figure 186 - Spin-Rate Sensor Housing

will be spaced equidistant around the solar circle (see Figure 186B) to provide coverage of the three principal axes of the vehicle with some redundancy to counter at least partially the effect of structural shielding. The output of each cell will be telemetered to a ground station for data reduction.

5. DATA LINK

a. General

The data link comprised of all communications to and from the satellite and the flow of information through the satellite pertains strictly to the 50-ft flight test vehicle except for the beacon system. There will be a beacon system as described in Item c below in operation on the full-scale vehicle.

b. Command Control System

The command control receiver basically will control all functions

through a power control system rather than a direct tie to the function or system. A redundant command receiver will be used to ensure positive operation of all critical functions and systems. The command control receiver will operate on a frequency of 148 mc. The command receiver intended for use on the flight-test satellite is flight-proved hardware that has been flown on the Tiros satellite.

c. Beacon System

The beacon tracking system will be in continuous operation, except for the short periods of data transmission. The interlock between the beacon on-off and the data transmission will be the power control switch system. This power control system in turn will be controlled by the command control receiver. The beacon tracking system will operate in the 136 to 138 mc frequency range. The beacon presently intended for use on this satellite is flight-proved hardware that has been used successfully on the Tiros IV. This beacon will be the only part of the data link used on the full-scale satellite as well as on the 50-ft test vehicle.

d. Commutation and Signal Conditioning

All deployment and inflation data items such as switch closures and pressure will be fed through a switch-type conditioning to the commutator. Temperature readings will be fed direct to the commutator. All of these signals will then be amplified and recorded. After 560 sec the switch-closure and pressure signals will be switched off the commutator. These same signals will then be replaced by orientation signals from solar cells in the attitude and attitude rate sensors and the magnetometers. The temperature readings will remain on the commutator in the same position. All signals in both portions of commutation will be low-level-type signals and will have to be amplified to be recorded. The commutation rate from all sensors will be in the order of two samples per second. This rate should be sufficient because the information rate of all data items will not be very rapid.

e. Recording and Reproducing

The events that comprise satellite inflation and rigidization are such that sufficient time is not available for complete data transmission of the whole sequence, using a single ground station. Therefore a minimum of two overlapping ground stations, with recording and command control capabilities, will be required. The requirements for the more important function of orbital orientation are even more complex. A series of orbital points will be required to accurately plot the satellite, earth orbit, and orientation. The number of ground stations that would be required and their locations make this an impossible situation. Hence it was decided to use a record, reproduce system.

To plot a satisfactory curve of orbital orientation it will be desirable to have data from at least 10 to 15 points in each orbit. The length of time for data pickup at each point will be dependent on the orbit of the satellite. By using an endless tape loop, and varying the record and reproduce speeds, sufficient data can be accumulated so that playback will only have to occur over a single ground station. Data from solar attitude sensors will not be effective while the satellite is in the earth's shadow, but magnetometer readings through this period will be valid. Hence valid curves can be drawn to show orientation through the earth's shadow.

The record periods will be programmed to the recorder by means of a sequence timer. Playback will be controlled by the command control system, with an automatic return to recording after reproducing. The recorder can be made compatible with a transmission system of 136 to 138 mc.

f. Telemetry

Prelaunch acquisition of data for all systems will be required. How this is obtained will depend considerably on the launch vehicle. It probably will be obtained by means of an umbilical cable. After

SECTION III

Subsection Seven - Instrumentation and Control Parameters

GER-11502

launch there will be no signal from this portion of the satellite until the canister is unshielded and the beacon signals begin. This in turn will be the only signal until the transmitter is commanded to transmit data.

Because of the quantity of information that will be monitored and recorded and then reproduced for transmission, a simple fm/fm telemetry system will be used. Telemetry transmitter power requirements have been determined on the basis of the following data link parameters:

- | | |
|---|----------|
| 1. Transmitter antenna gain | -3 db |
| 2. Receiving antenna gain (based on 85-ft parabolic dish at 136 mc) | 28 db |
| 3. Minitrack receiver sensitivity (based on 100-cps channel) | -150 dbm |
| 4. Signal-to-noise ratio | 15 db |
| 5. Path loss (based on maximum 2500 naut mi range and 136 mc) | 150 db |
| 6. Miscellaneous losses | 10 db |

With these parameters, a transmitter power of 1 mw is indicated. However, an 0.1-w transmitter is being considered to remain conservative in the first analysis. Thus, a transmitter operating at 136 to 138 mc with a rating of 0.1 w output into a 50-ohm antenna is used for the later calculations.

A single voltage-controlled subcarrier oscillator will be provided to monitor the output signals from the sensors. However, recorder reproduce may require additional amplification prior to transmission.

Power requirements will be dictated partially by the peak load of total on-time required per orbit by the transmitter. Because of the availability of space-proved electronic components and the low power levels,

the maintaining of the proper thermal balance in the satellite canister is not expected to be a serious problem.

g. Antenna System

Two payload antennas will be required to provide the data link functions. One antenna will operate in the 136 to 138 mc range for the tracking beacon and telemetry; the second will be compatible with the command control link at 148 mc.

Coverage requirements for the antenna system are based on the geometry in Figure 187; for the worst case, the electronics payload can be tipped up 90 deg from vertical and required to communicate with a ground station at 55 deg (800-mi orbit, line of sight) in the other direction off normal.

Thus, to obtain adequate coverage, the antenna field intensity for both systems should be constant over a 300 deg segment of a sphere, symmetrical with the long axis of the vehicle.

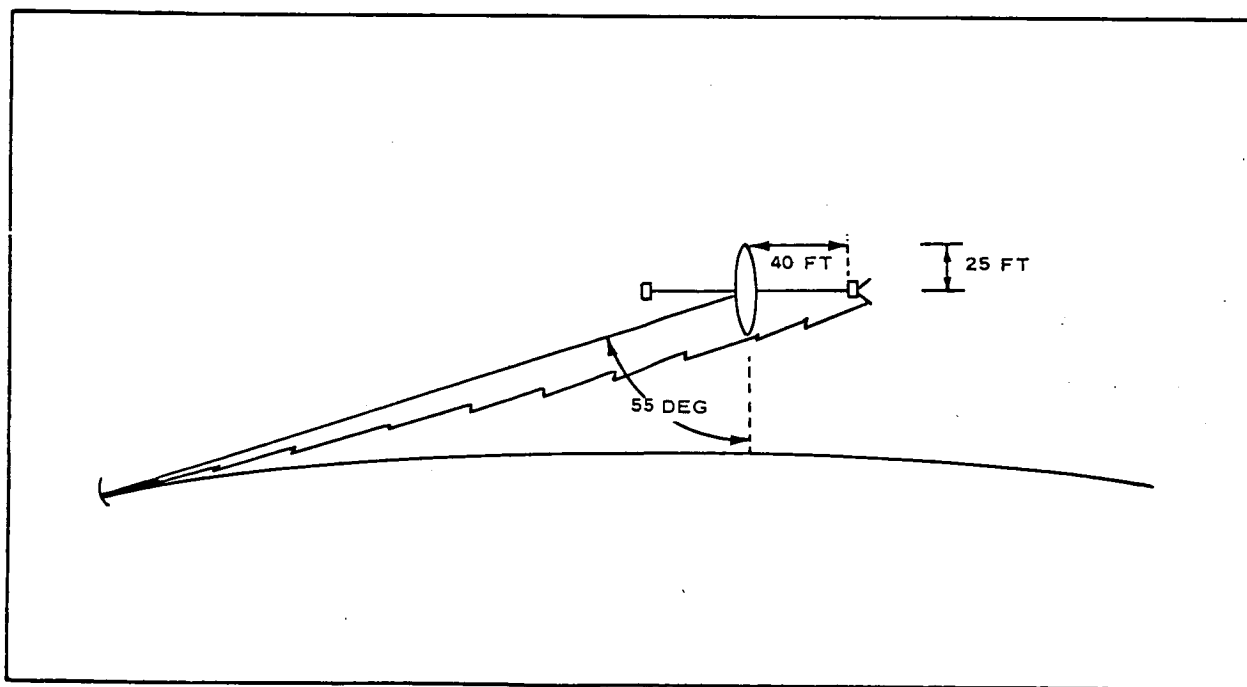


Figure 187 - Antenna Tipped 90 Deg (Worst Case) to Determine Coverage Requirements

This coverage can be achieved by locating the antenna system at the extremity of the mast mounted to the payload canister cover. This location also allows for use of the antennas before deployment of the satellite.

Each antenna system will consist of two orthogonal half-wave-length dipole elements, oriented horizontally and vertically with respect to the surface of the vehicle (see Figure 188A). An alternate antenna system will consist of a symmetric array of four parallel elements bent radially from the center axis by an angle of 45 deg. The spacing between diametrically opposed elements will be on the order of a half wave length (see Figure 188B).

6. POWER SUPPLY

To support the experiment in orbit, a limited amount of continuous power will be required to operate the beacon, the command receiver, the recorder, and the recorder timer. The peak power loads will occur upon

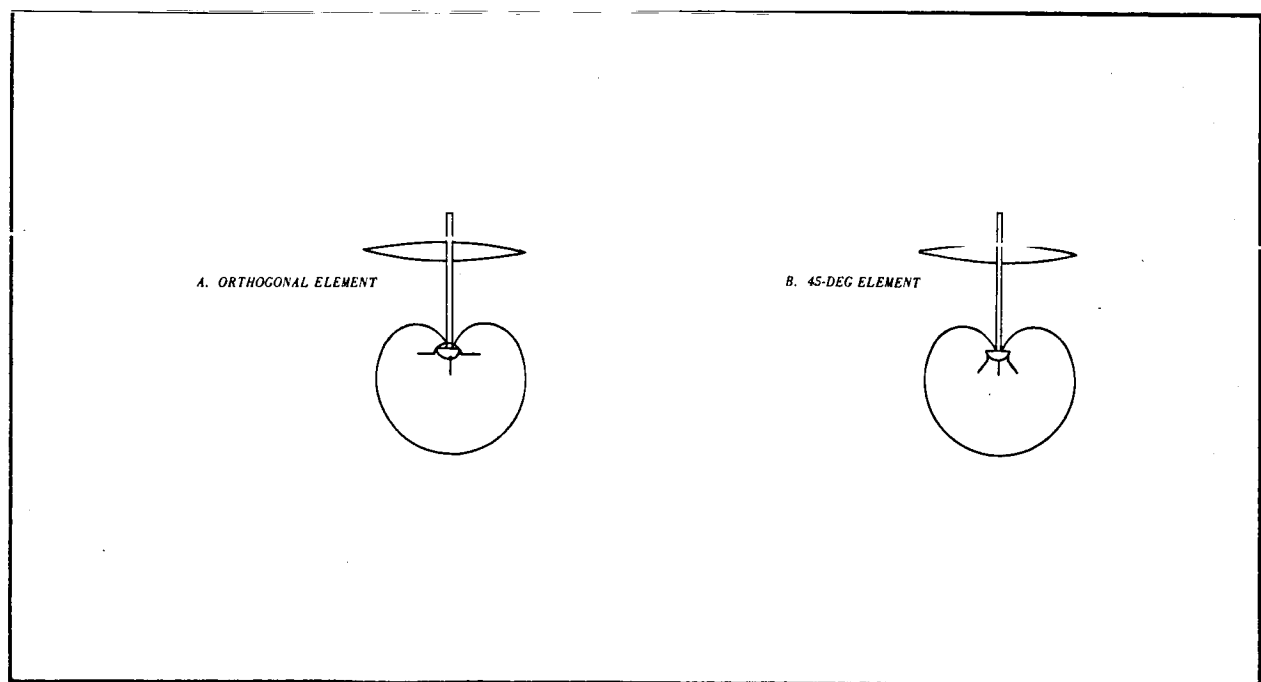


Figure 188 - Antenna Pattern

command for the recorder to reproduce and transmit to the ground station.

The satellite orbit altitude of 800 mi indicates an orbital period of approximately 115 min. If the satellite is launched into this orbit from Wallops Island (approximately 37 deg N latitude), the sunlight and shadow time of the orbit will be approximately 85 and 35 min, respectively. The electrical loads are established to be 1.2 w continuous and standby power, and 11.5 w peak during telemetry transmission. A long-time telemetry readout time of 10 min maximum once per orbit will be used. A rechargeable battery and solar cell power supply will be used during the telemetry readout and during the shadow portion of the orbit. The same batteries will be used to power the deployment and inflation portion of the flight.

With perfect earth orientation, the array will be shadowed by the lenticular shape for approximately 21 min of each orbit. Therefore, the solar array will be illuminated for 64 min of each orbit. Due to the orientation of the satellite, the center line of the cylindrical array will not always be normal to the solar incidence; the average angle of incidence is estimated to be 28 deg. Based on the total power requirements, the area of solar array required to keep the batteries charged is about 3.9 sq ft. Although perfect orientation is not practical, it is assumed that the rate of change in satellite attitude with respect to earth will be low in relation to the orbit period. Therefore, the average time the solar array is illuminated and the average angle of incidence will be nearly the same for all orbits.

7. GROUND ENVIRONMENT AND PROCESSING

The proposed telemetry data flow is shown in Figure 189. Telemetry signals will be received from the satellite at Minitrack stations along the orbital ground path. Since the flight instrumentation system will be comprised of a single transmitter frequency-modulated by a voltage-controlled subcarrier oscillator, only a modest amount of f-m/f-m ground station equipment will be required for data acquisition. Adequate equipment should be available at the tracking stations.

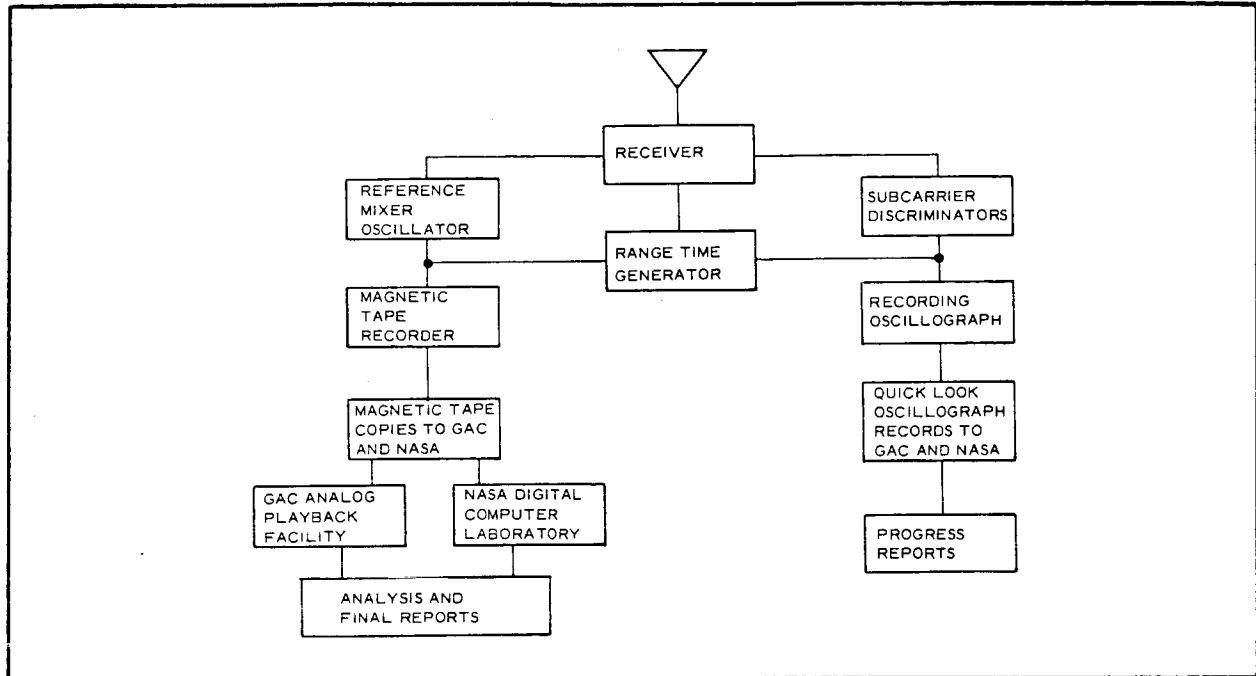


Figure 189 - Telemetry Data Acquisition and Reduction

The satellite signals will be detected by a receiver and demodulated by subcarrier discriminators. The discriminator outputs will be recorded on a pen or heated stylus oscillograph. The receiver output will also be mixed with a reference signal and recorded on magnetic tape. A range time generator will provide timing signals and chronological reference for the tape and oscillograph recordings. The real time oscillograph records will provide monitoring information for the receiving station operators and project representatives.

The formal data reduction for analysis and final report will be accomplished from playbacks of the magnetic tape recordings. If there are sufficient data to justify machine and programming expense, Government-furnished data-reduction facilities will be required.

Analog data traces are easily scaled, identified, and reduced to report format by procedures presently in use at GAC. Since the commutated

data consist essentially of housekeeping steady-state pressure, temperature, and slowly changing attitude data, only a modest number of data points per channel will need to be reduced for each reception period.

8. HARDWARE SUMMARY

A summary of the instrumentation hardware requirements, power, weight, and size is given in Tables XLVII and XLVIII.

The sequence of events and times involved in deployment and inflation is shown in Tables XLIX and L.

The block diagrams depicting the full systems are shown in Figures 184 and 185.

SECTION III - TECHNICAL DISCUSSION - PHASES I AND II

Subsection Eight - Reliability Considerations

1. GENERAL

An important consideration in the lenticular satellite investigation was the reliable deployment and operation of the communication satellite. In order to ensure a reliable system, GAC was required to perform preliminary reliability studies and statistical analyses and establish reliability requirements and goals for the satellite system. Emphasis was placed on minimizing complexity, maximizing the use of design state-of-the-art, and the incorporation of redundancy where needed.

As part of its research activity for 1963 GAC initiated a program to evaluate existing reliability methodology as it applies to space systems utilizing expandable structure. Data from the communication satellite project were used as a basis for these developmental studies. The results obtained therefrom which are considered of importance to the lenticular satellite project are incorporated herein, along with the results of the contractually funded effort.

2. OVER-ALL PROGRAM PLAN

A reliability program contains a series of specific steps aimed at achieving inherent reliability in design and maintaining it during fabrication and operation. In order to facilitate measurement of progress toward this objective a series of monitoring points or milestones are established within the program.

Figure 190 shows the over-all reliability program plan prepared for the lenticular satellite project. Milestones are blocked off and their associated efforts delineated directly underneath. Reference is also made to the

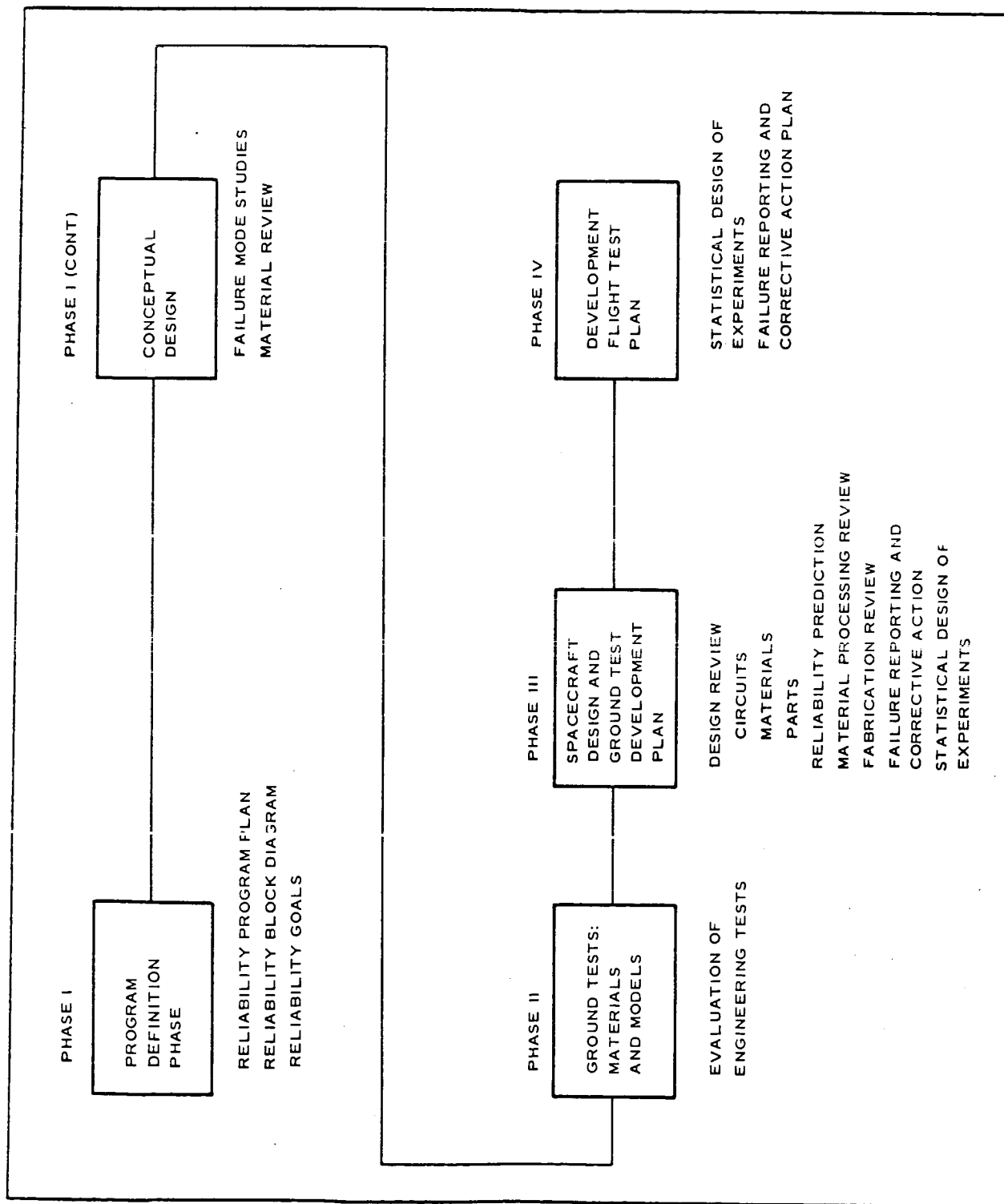


Figure 190 - Over-all Plan for Reliability Program

four phases as noted in the NASA Statement of Work, L-3308 of 17 April 1963. It will be noted that Phase I, Design Studies, has been broken down into two steps, program definition and conceptual design.

During the program definition phase, the function block diagram supplied by Design was converted to a reliability block diagram and preliminary calculations were made to determine a feasible reliability goal.

As conceptual design proceeded in the latter part of Phase I, failure mode studies were made along with a review of potential material problems.

In Phase II the reliability effort consisted primarily of the evaluation of functional engineering tests, because hardware had not been developed to the point where reliability tests were appropriate.

Figure 190 also shows the steps considered mandatory during Phases III and IV for achievement of the system reliability goal.

3. PROGRAM DEFINITION PHASE

a. Reliability Block Diagram

After completing the over-all reliability program plan, the preliminary functional block diagram prepared by Design was converted to the reliability block diagrams shown in Figures 191, 192, 193, and 194.

Figure 191 is the reliability block diagram for the lenticular satellite system and the monitoring system. In constructing this diagram the following ground rules were used, giving separate consideration to the satellite system and the monitoring systems:

1. The deployment system components were considered to operate one cycle or one hour, whichever was applicable.
2. The operational period for the test satellite was considered 200 hr

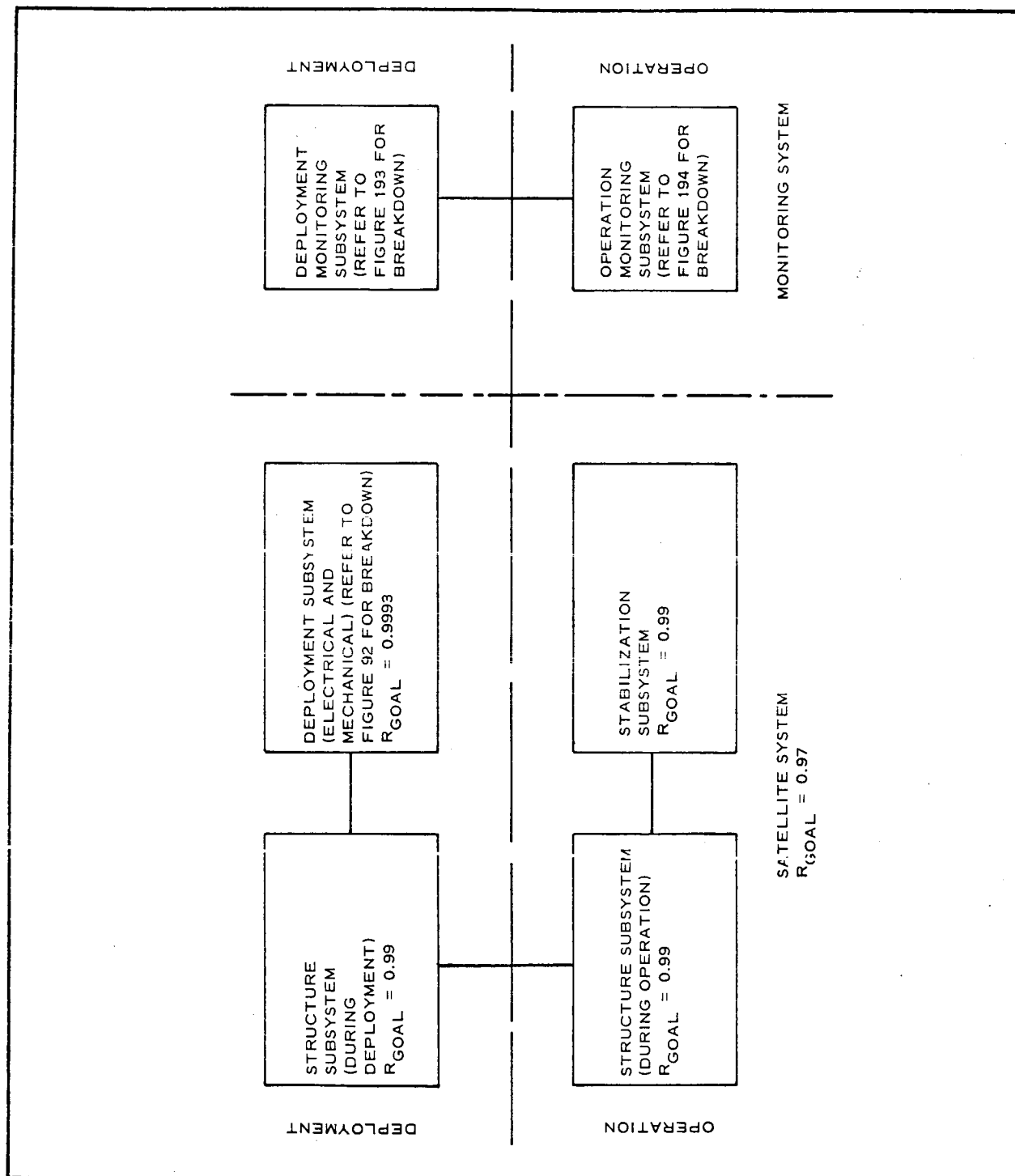
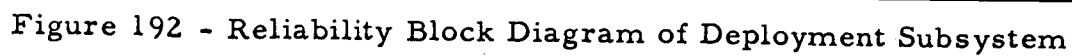
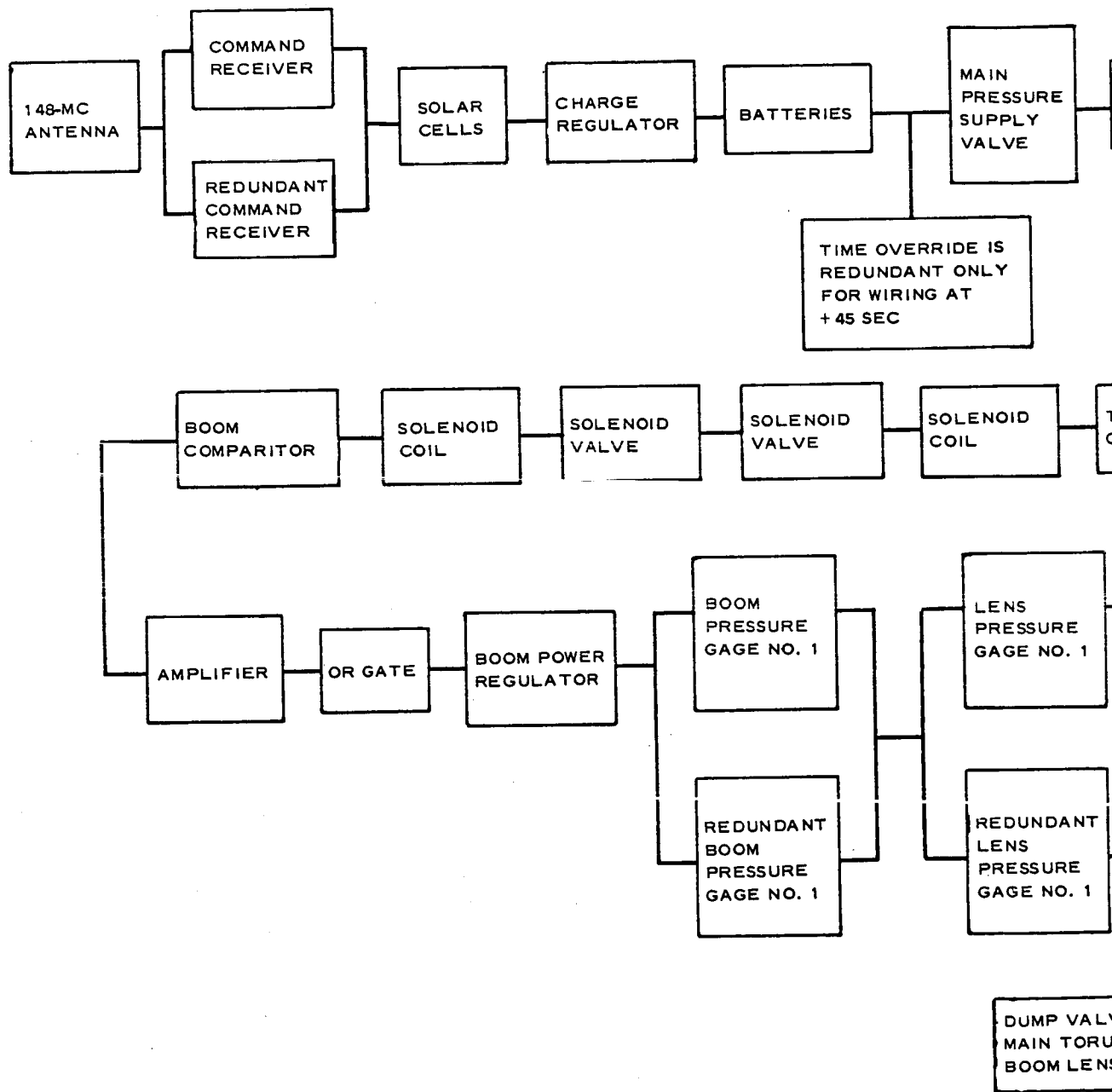


Figure 191 - Reliability Block Diagram for Gravity-Gradient-Stabilized Lenticular Satellite System and Monitoring System

GER-11502





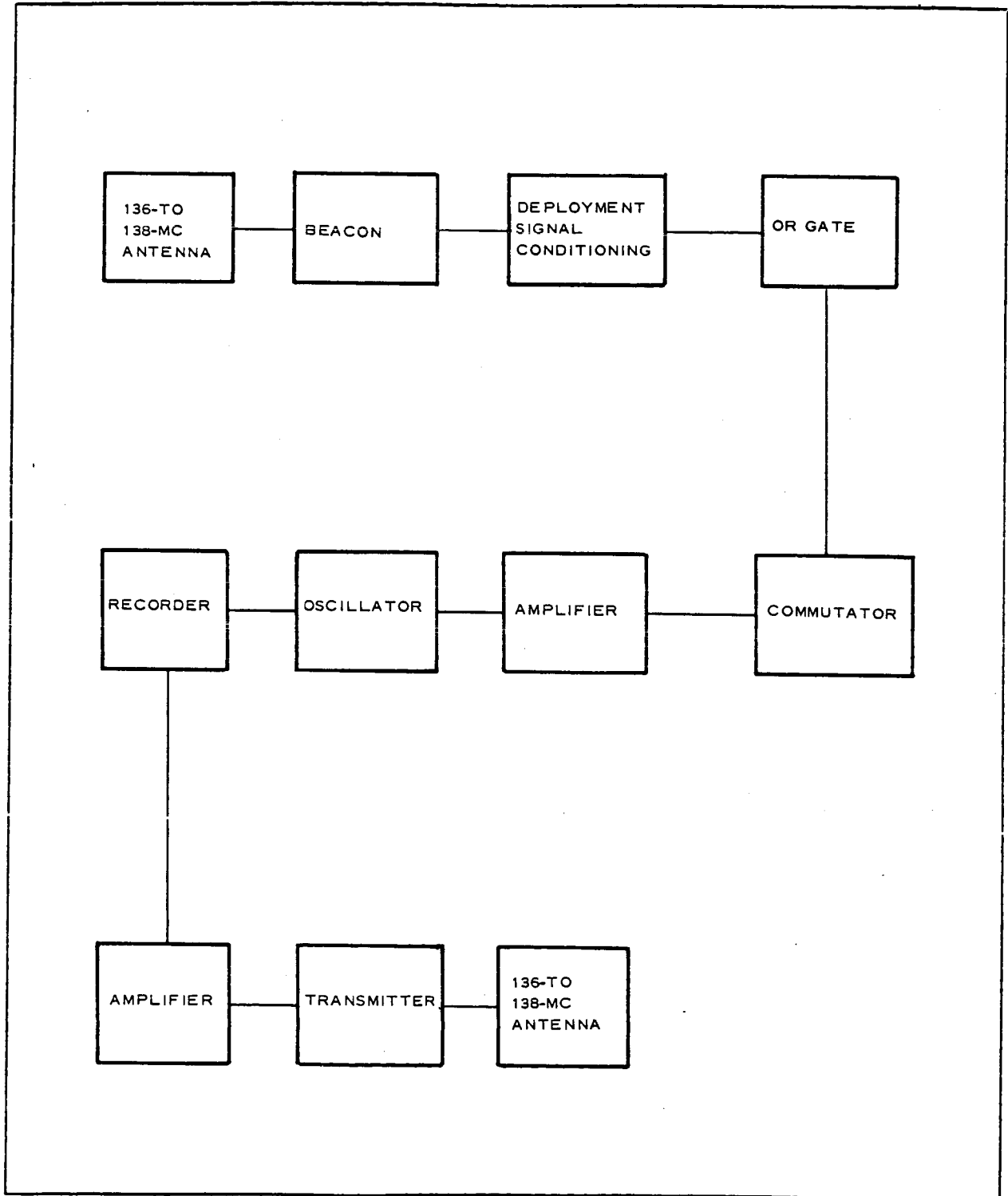


Figure 193 - Reliability Block Diagram for Deployment Monitoring Subsystem

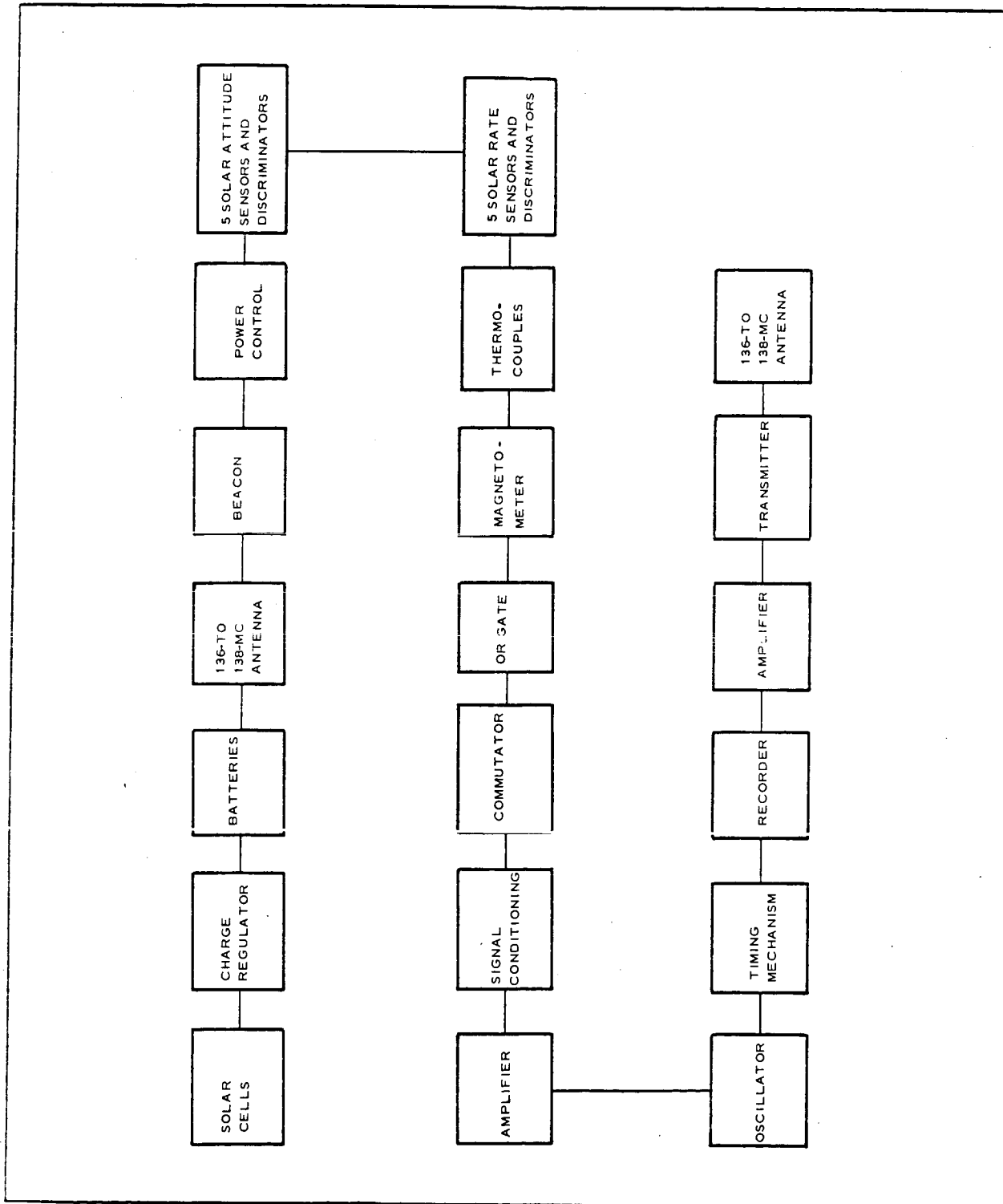


Figure 194 - Reliability Block Diagram for Operation Monitoring Subsystem

These mission times were selected to enable reliability estimates to be made and may be modified by program requirements.

Neither the reliability of the equipment used to monitor deployment nor the reliability of the equipment used to monitor operation were considered as part of the satellite reliability.

Figure 192 is the reliability block diagram for the deployment subsystem. With the exception of the redundancies shown, the components are considered to be in series. That is, if any component fails, the system fails. The command receivers are redundant as are the No. 1 pressure gages in the torus, boom, and lens. Time overrides in the programmer sequence timer are considered to be redundant with the No. 2 pressure gages in the torus and lens.

Figure 193 shows the deployment monitoring subsystem, and Figure 194 shows the operation monitoring subsystem.

A failure of any sensor or other part of the monitoring subsystem was considered to result in a subsystem failure. It is expected that this definition of operation monitoring subsystem failure might be changed later in the satellite program when the data feedback requirements are defined in more detail.

b. Reliability Goals

Because the work statement does not specify a numerical reliability requirement or goal for the lenticular satellite, the next step was to attempt to calculate this factor on a preliminary basis using known or assumed reliability values for each functional block. The resulting factor, $R = 0.97$, is considered an objective for the satellite system that might require adjustment as the program progresses, since there are several components and subsystems for which there are no reliability performance data at present.

The monitoring and the deployment subsystems consisted basically of hardware for which failure rate data were available. An exponential

failure law and independent component failure probabilities were assumed to be applicable for this equipment, and preliminary reliability predictions were made (see Appendix J). Because the failure rates used in these predictions were considered pessimistic, goals for these equipments were established by doubling the predicted mean-time-to-failure.

It is apparent from the system reliability block diagram, Figure 191, that the satellite reliability goal has been established primarily by the assignment of goals for the structural equipment, and that the influence of the deployment system prediction on the final goal is relatively small.

c. Structural Reliability

In order to establish a reliability goal for the over-all project, reliability goals of 99 percent were assigned to the stabilization system and to the satellite structure. This implies a 1 percent probability of random failure of structure due to material or fabrication defects, excessive overload or deterioration as a result of prolonged exposure to environmental extremes.

4. CONCEPTUAL DESIGN PHASE

a. General

During the conceptual design phase, preliminary sketches were prepared for fabrication of structural working models. Since the purpose of these models was primarily to accomplish functional testing, the design data were not sufficiently detailed to permit complete design review. The information did serve as a basis for failure mode studies and material reviews.

b. Failure Mode Studies

Lists of failure modes during deployment (Appendix K) and during operation (Appendix L) were generated. Analyses of three of the more critical failure modes were made.

Disturbing torque caused by nonuniform gas leakage might be so great that the satellite could not be stabilized. A single example of adverse pressure distribution was shown (refer to Appendix M) to produce a disturbing torque of the same order of magnitude as the maximum value of gravity-gradient restoring torque. This indicates that the leakage and diffusion must be controlled by controlling hole location during or after fabrication.

c. Material Review

A summary was made of areas wherein problems might occur in the manufacture of photolyzable film-wire cloth material, as follows:

1. Polymer Resin Preparation

- a. Monomer - Monomer is supplied by an outside vendor and consistent quality would have to be assured.
- b. Polymerization - Process control is extremely important at this point. All polymerization has been done on laboratory scale thus far. This area is being looked into by Goodyear Tire Research.
- c. Incorporation of Dye in Polymer - Dye is added to the polymer to increase absorption of solar radiation and thus increase the temperature of the film in space. The dye would be obtained from an outside vendor and would have to be checked carefully to ensure that it contained no impurities that would inhibit photolyzation. Proper blending of the resin and dye will have to be

made to obtain the desired α_s/ϵ characteristics. Process control in this area is very important.

2. Wire Drawing and Weaving

- a. Material for Wire - Composition of the basic material to be drawn into wire would have to be carefully checked to ensure that it did not contain any undesirable impurities.
- b. Wire Drawing - Stress-strain properties of the wire must be checked. Also, inspections must be made to determine whether defects appear along the wire and whether cross-sectional shape is maintained.
- c. Wire Weaving - Many problems can and do occur in the weaving of this fine wire. Techniques or equipment design for weaving such fine-wire open-mesh cloth as required for this application are not well established or defined. Present materials have been produced on experimental equipment. For large quantities, looms would have to be modified. Wire is easily damaged in the "take-off" process, thus making it important to look at this area also.

3. Resin-Wire Cloth Combining

In this step two approved items, the resin and the wire cloth, are combined into one item.

Casting of the film on the wire cloth has proved to be a satisfactory method. Present materials have been cast on Goodyear experimental equipment. Larger quantities would have to be made on larger Goodyear equipment. Some problems might occur in making this change-over. Final checks would have to be made at many points along the roll to determine whether optical properties (α_s/ϵ), photolytic behavior, stress-strain, pin hole count, etc. meet established requirements.

5. GROUND TESTS: MATERIALS AND MODELS

Phase II material tests were of a development nature and generally did not provide data that could be used to measure reliability.

The model deployment tests, although qualitative in nature and performed without complete environmental simulation, were considered significant from a reliability viewpoint. Seven tests were observed. Five of these tests were with the torus only and two with the torus and lens. Six of the seven tests were considered successful. During the seventh test there was a deployment difficulty in which the lens tangled, preventing complete deployment. However, this difficulty was considered to be the result of friction and gravity restraints that would not be present in orbit. It appears that the space deployment system will be satisfactory. (Refer to Appendix N.)

6. CONCLUSIONS

Insufficient data are available to provide a measurement of the reliability of the proposed structure or stabilization system.

In the absence of a firm reliability factor for the structure and stabilization system, a reliability prediction would not be meaningful at this time.

Using assumed conservative figures for the structures and stabilization system, a reliability goal of 97 percent appears feasible for the system.

Because the remaining components (electrical, electronic, mechanical, pyrotechnic, etc.) are currently available from known suppliers, normal reliability surveillance in selection, application, and quality control should provide satisfactory reliability.

The most critical area, from a reliability viewpoint, will be the control of raw material and processing in the fabrication of structures.

7. RECOMMENDATIONS

In continuing phases of the subject program, it is recommended that reliability be treated as a goal rather than a requirement.

It is also recommended that additional effort be expended for reducing material variabilities and for improving control of processes and fabrication techniques. Investigation of step-by-step procedures during the manufacturing operation from receipt of raw material to the finished product would be the initial activity.

SECTION IV - TECHNICAL DISCUSSION - PHASES III AND IV

1. PRELIMINARY SPACECRAFT DESIGN

a. General

The flight-test satellite is designed to be launched with the Scout vehicle. The design effort for this phase of the program required definition of the interface and separation of the payload from the vehicle, a despin system for the payload, and the payload canister separation arrangement. Figure 195 is a general arrangement layout of these items.

b. Interface and Separation

The interface and separation system is basically the same as defined by Chance Vought Corporation Drawing No. 399-00882, Sheets 1 and 2. The E section assembly will require the addition of tapped holes to accommodate the interface connection between the payload and fourth-stage vehicle. The payload can be housed in the standard 34-in. diameter heat shield and attached to the vehicle by the standard separation clamp shown with the E section assembly. At a predetermined signal, separation will take place at Station 35.11. Six ejection springs will separate the payload from the fourth-stage Scout. A microswitch-type device attached to the payload will start the satellite sequence programmer in operation at time of separation.

c. Despin System

The despin system is a two-stage system, the sequence of operation being the same for each step. The first-stage despin weights (yo-yo's) will be deployed immediately after separation of the payload from the vehicle. The despin weights will be on the ends of lines wrapped around the payload canister. Cable cutters will release the

despin weights and lines which will unwind from the canister by centrifugal force. When the weights and lines reach the proper position on the canister, the lines will slip out of a slot, at which time the second stage of the despin system will be initiated. At the conclusion of second-stage despin, the payload will be ready for deployment.

d. Canister Separation

The canister separation system used will be similar to the Echo I system. Canister sealing will be accomplished by O ring. The two halves will be laced together with Dacron line. A shaped charge will cut the Dacron line, thus releasing the canister halves. This charge will be designed so that separation forces are not imposed on the canister halves.

2. PROGRAM PLANNING

a. General

The go-ahead date for the following master plan assumes that prototype material technology has advanced beyond the state-of-the-art at the conclusion of Phase II, Contract NAS 1-3114.

In addition, the satellite basic design concept was taken as defined in this report at the start of the master plan. The over-all format of the charts and text is based on GAC's experience and assuming that GAC will be the follow-on contractor for convenience.

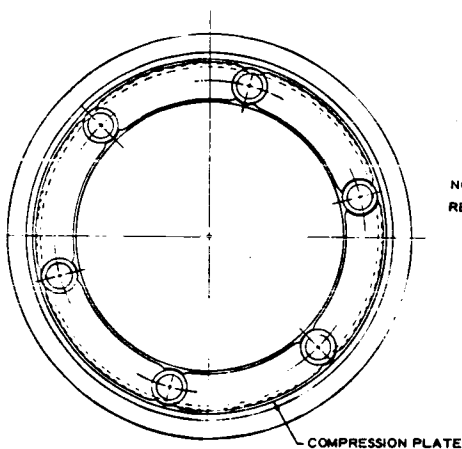
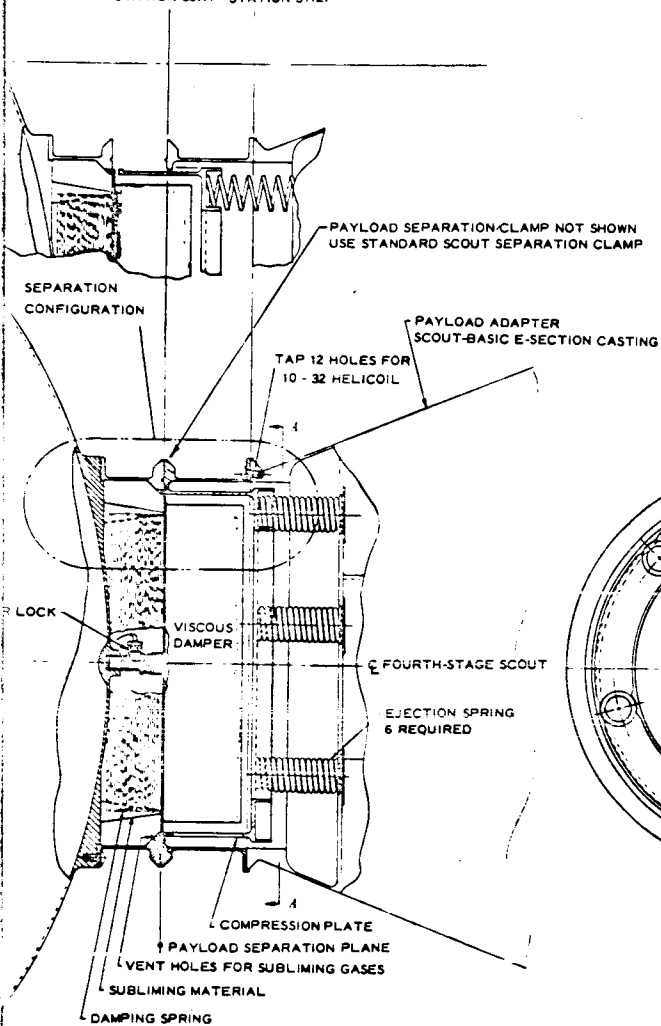
The information on these charts can be used effectively for future cost estimating of the flight test program and its major parts.

b. Master Plan

(1) General

The master plan for the design, development, and flight test of the gravity-gradient-stabilized satellite is shown on Figure 196. This plan calls for an orbital launch twenty-two months

STATION 35.11 STATION 37.27



A-A

NO. 2B CABLE-
RELEASE SLOT

SECOND STAGE, 3-OZ WEIGHT

NO. 2A

FIRST STAGE, 2-OZ WEIGHT

NO. 1A

FIRST STAGE
FIRST STAGE
SECOND STA
SECOND STA

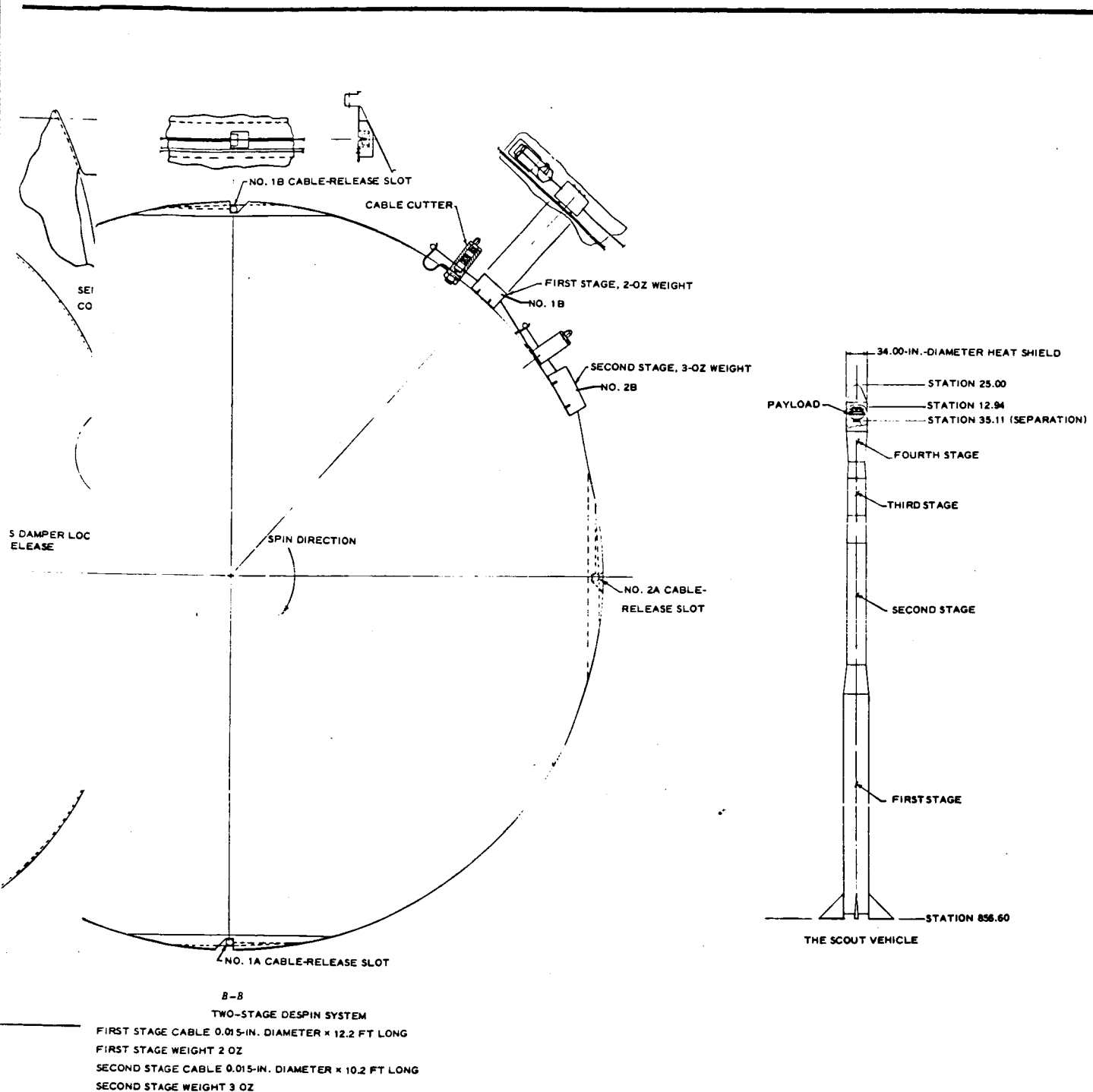


Figure 195 - Payload Separation and Despin System

STATION 4.20

STATION 12.94

STATION 23.78

STA

30.00-IN.
DIAMETER

COMMAND RECEIVER

RECORDER

TRANSMITTER

BEACON

COMMAND RECEIVER

INFLATION SYSTEM
(PROGRAMMER,
INFLATION VALVES)

BATTERIES

TOROIDAL GAS CONTAINER

DACRON LINE

NO. 1A

NO. 2B

NO. 2A

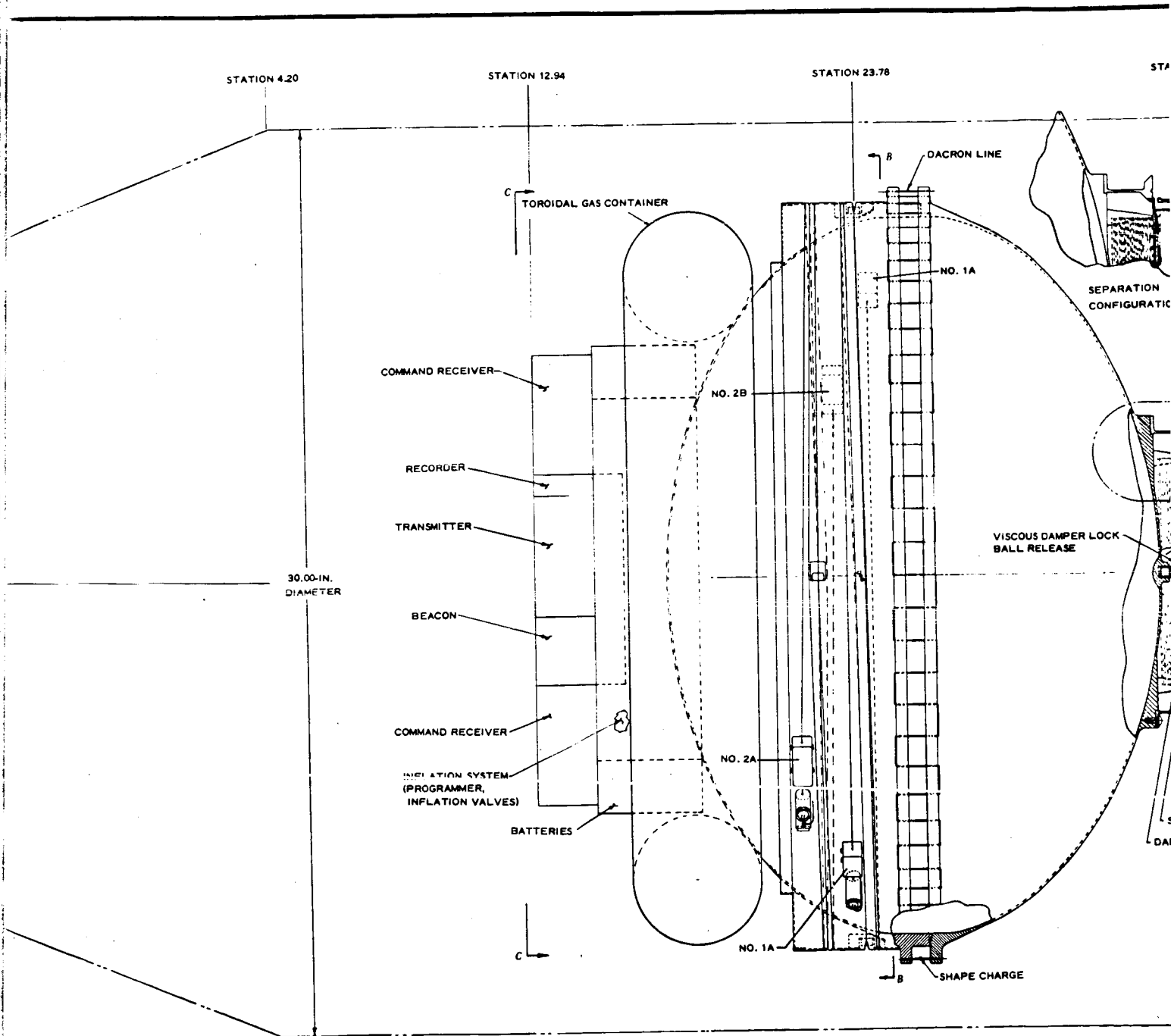
NO. 1A

VISCOUS DAMPER LOCK
BALL RELEASE

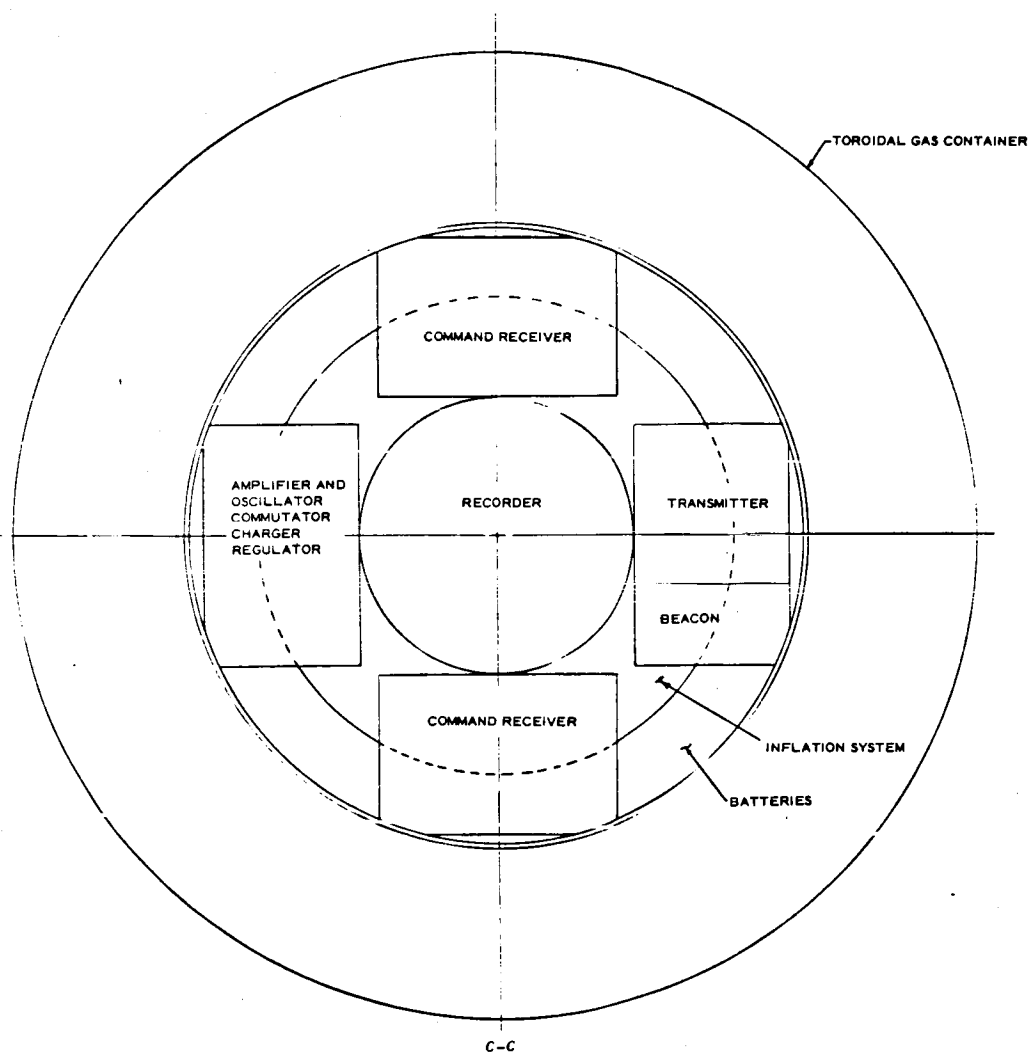
SEPARATION
CONFIGURATIC

SHAPE CHARGE

5
DAN



STATION 11.00



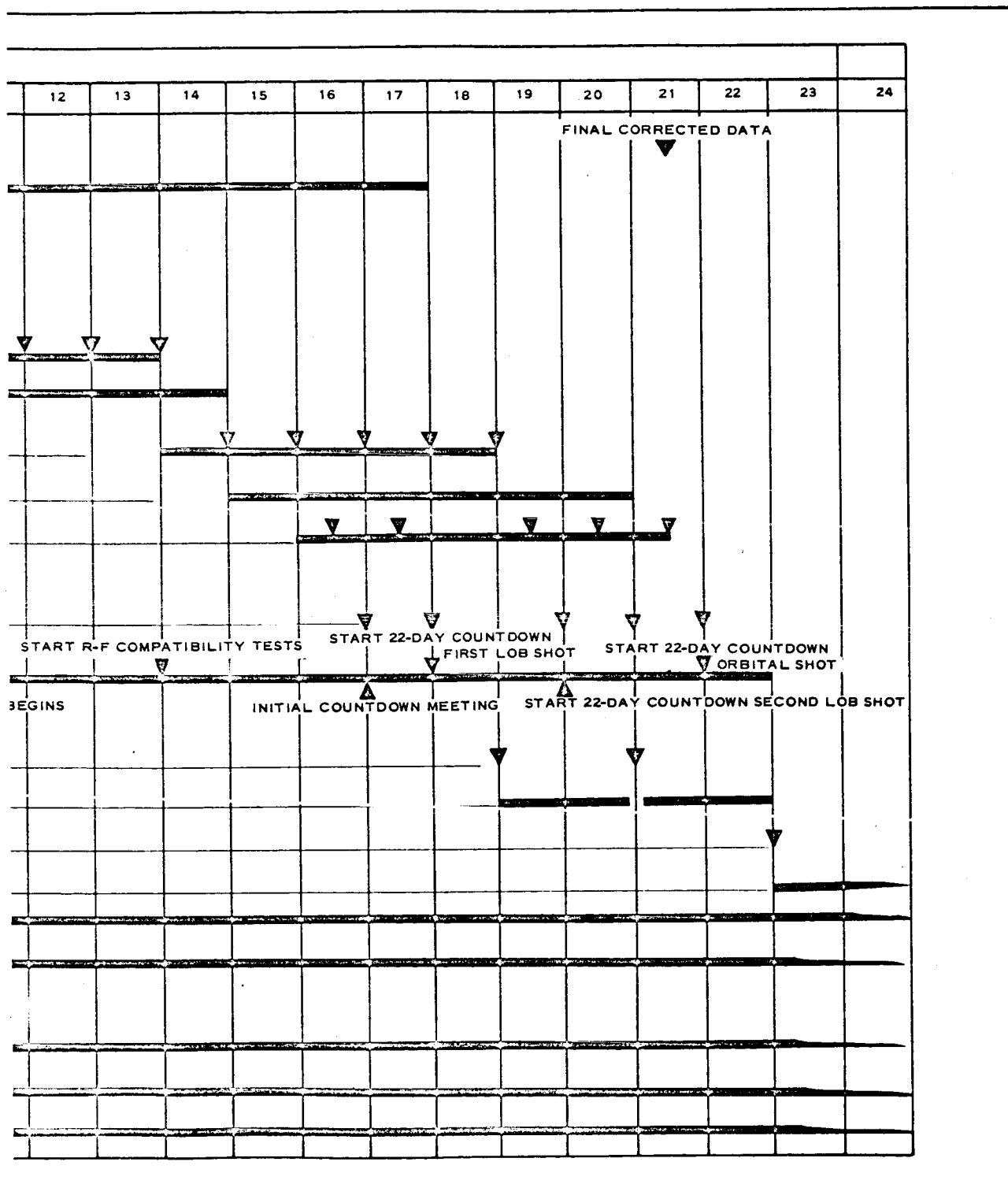
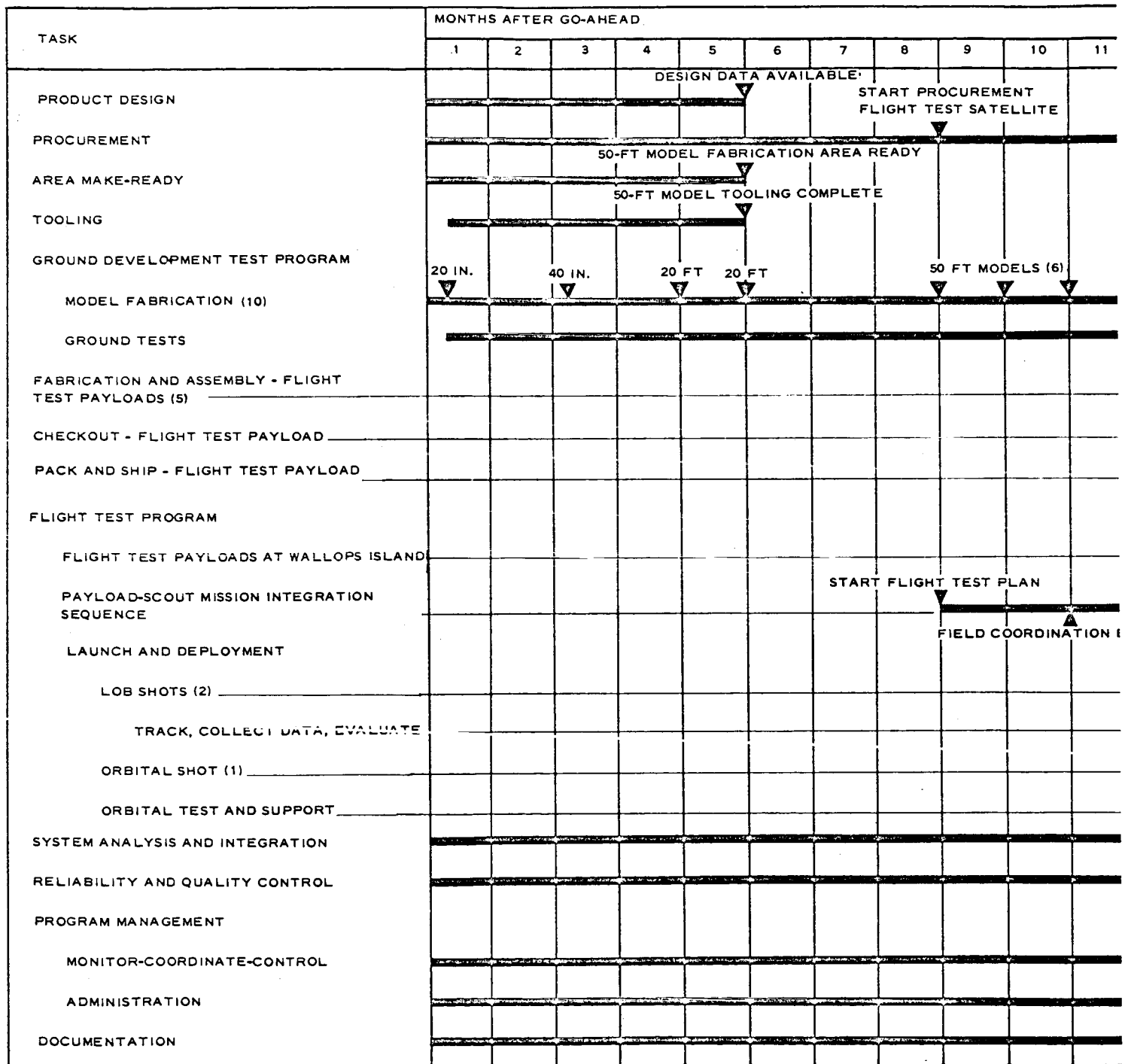


Figure 196 - Master Program Plan



after go-ahead and that orbital tests, including tracking, data collection, data evaluation, and reporting will continue after launch.

Altogether, the plan utilizes fifteen models ranging in size from the 20-in. microwave range test model to the 50-ft flight-test satellites. Of the fifteen models, ten are scheduled for the ground test effort, and five will be shipped to Wallops Island for the flight test program.

The schedule calls for the availability of all design information, tooling, and a completed assembly area at the end of five months.. It is anticipated that procurement will extend over a seventeen-month period. Ordering of flight-test satellite materials will start during the ninth month.

Ground tests will commence almost immediately in the program, as GAC already has a thorough knowledge of the requirements. Ground tests will continue through the fourteenth month. The significance of these tests is fully recognized - a conclusive ground test program being absolutely essential to a successful flight test program.

Fabrication, assembly, and checkout of the five flight test payloads are scheduled to overlap. Checkout will be completed at the end of the twentieth month.

Starting at the ninth month, and paralleling the development effort at GAC, the payload-Scout mission integration sequence will begin exactly eight months prior to the first of the two proposed lob shots (launcher). The need for good communications between GAC, LRC, and the Wallops Island personnel is of paramount importance to minimize possible error in mating the vehicle and payload systems. Both the lob shot payloads and the orbital shot payload will have standbys. These standbys

will be available at the start of each twenty-two day countdown. The lob shots will provide the final design development support data. A design freeze is scheduled midway through the twenty-first month.

Orbital test data will be thoroughly analyzed. Once good analyses are available, a critique of the entire program is recommended, with an emphasis on future application.

Program management, documentation, administration, and associated support activities will be continuous.

(2) Product Design Plan

The design effort is presented in detail on Figure 197. Initial drawing releases will be made by the end of the first month. Subsystem design is scheduled to be complete the middle of the fifth month. System design integration begins the third month and continues through the sixth month. All design data will be available at this point.

Design liaison and coordination will support both the ground test effort and the flight test effort up to orbital launch. Final corrective data are scheduled due the middle of the twenty-first month, or 1/2 month prior to orbital launch.

(3) Manufacturing Plan

The manufacturing plan (see Figure 198) is based on a continuous receipt of the necessary materials and as great a degree of flexibility and cohesion as can be achieved between Engineering and the Development Shop.

It utilizes a task-force-type team that will include all the elements necessary to discharge the manufacturing responsibilities. These responsibilities are divided among the appropriate departments: Engineering, Development Shop, Materials, and

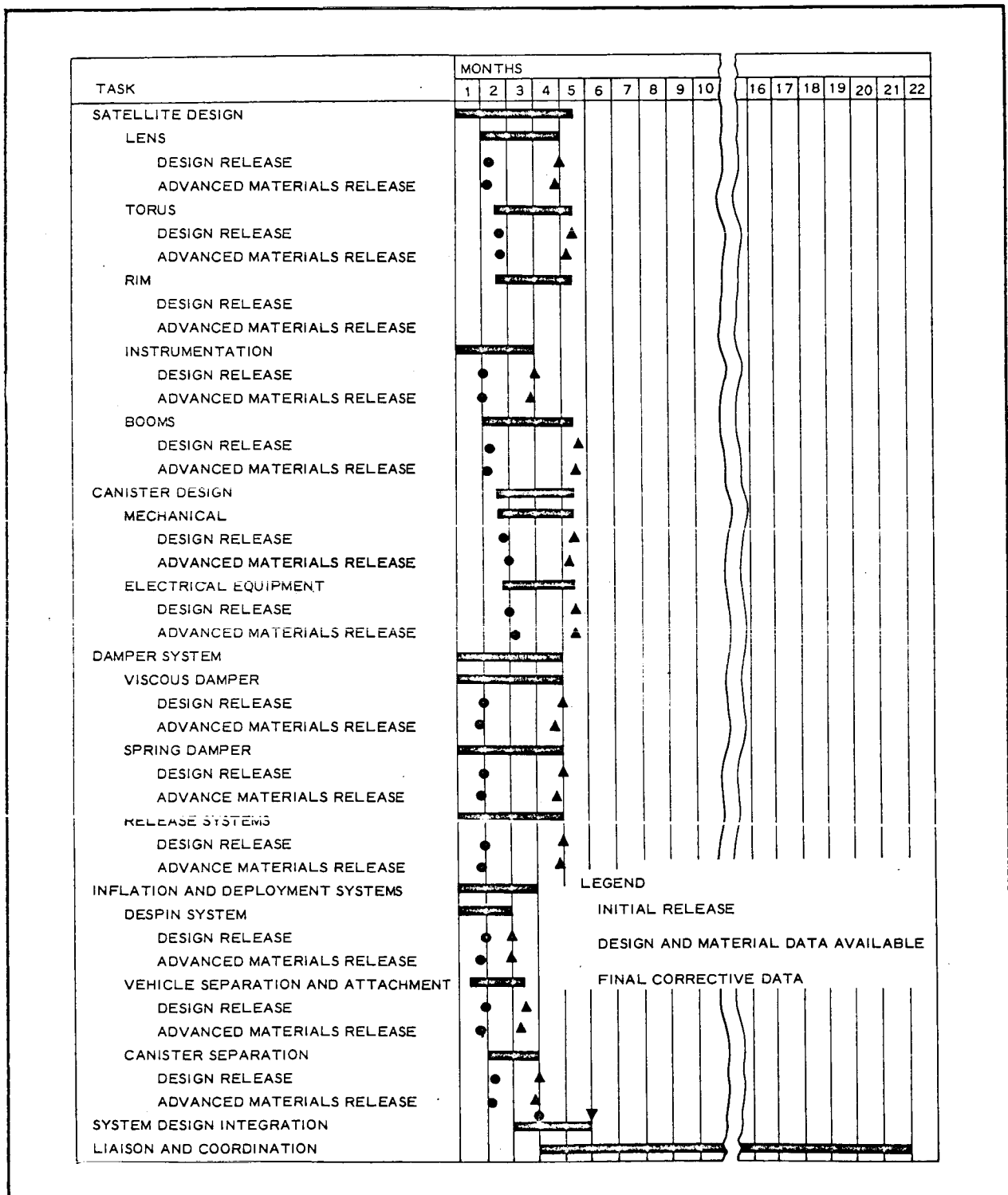


Figure 197 - Product Design Plan

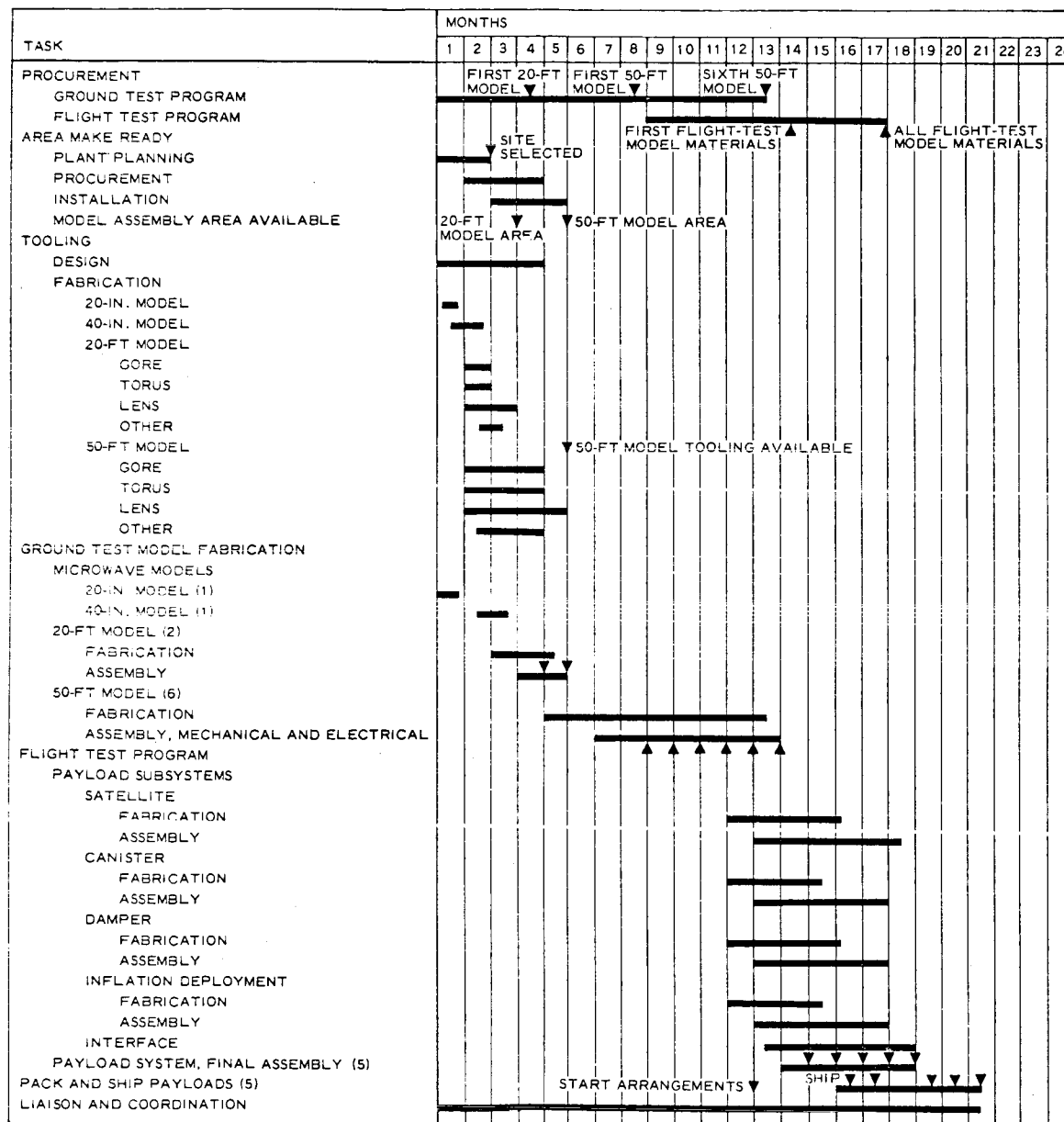


Figure 198 - Manufacturing Plan

Plant Engineering. All fabrication and assembly work will be done by the Development Shop, which is a part of the Engineering Organization. The entire Manufacturing team will be under the direction of an Assistant Project Engineer.

The plan utilizes all of GAC's standard systems and procedures. Control methods have been reduced to a minimum with respect to cost and time consumed. Yet the plan contains all the procedures that are necessary for proper control of costs, quality, and schedule.

Tasks have been planned to be overlapped, such as simultaneous assembly area make-ready, tooling fabrication, and fabrication and assembly of the two 20-ft ground test models. Standard or like parts will be released to the Development Shop by Engineering early in the program in order to complete the various models in the shortest possible time and to keep manpower peaking to a minimum.

Finally, a coordinator will be assigned to the floor to monitor daily progress in all areas to the manufacturing schedule. The coordinator will be responsible for proper man loading by production, acquisition of materials or parts, direction of flow of work, and general schedule maintenance in all manufacturing areas.

(4) Program Management Plan

The program management plan is shown on Figure 199. It is recognized that effective management is possible only when a system exists to balance time, cost, and technical performance. This plan is designed to maintain maximum cognizance and control over the program by a thorough coverage of these same areas from a planning standpoint. The techniques used are based on GAC's experiences gained over the years in the following areas:

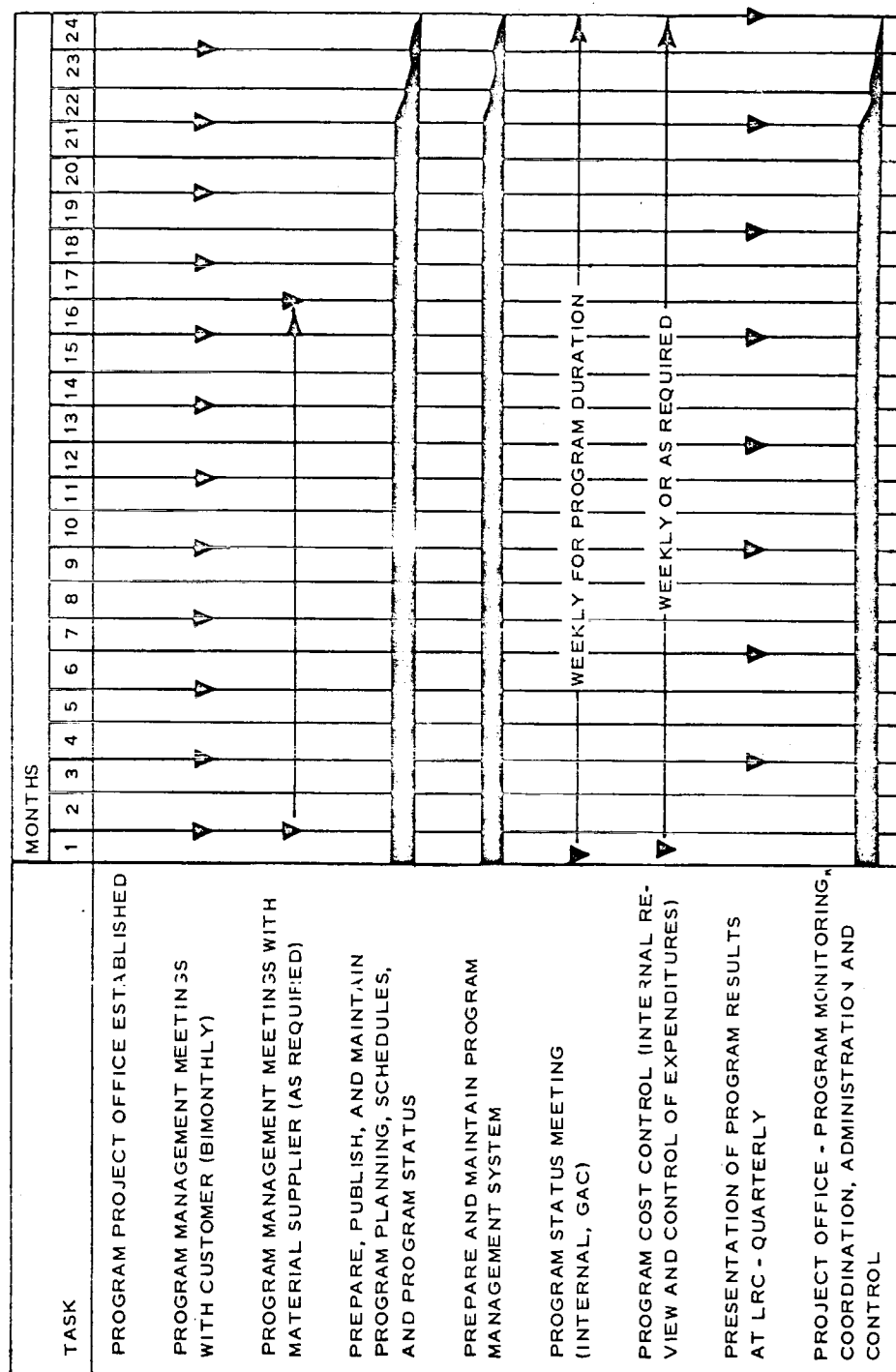


Figure 199 - Program Management Plan

1. Communication systems - 8 years
2. Missiles weapon systems - 13 years
3. Airborne guidance systems - 12 years
4. Expandable structures - 5 years
5. Airborne radar - 12 years
6. Ground radar antennas - 15 years
7. Rocket motor cases - 6 years
8. Plastics - 12 years
9. Radomes - 10 years
10. Airframes and major components of aircraft - 18 years
11. Electronic and mechanical ground support equipment - 20 years
12. Simulator and training devices - 11 years
13. Computing devices - 13 years
14. Airships - 20 years

The assigned project engineer will be responsible for effective management controls. Program monitoring techniques will be used to anticipate and evaluate indications of program schedule slippages or cost overruns. Specific plans and reports that will be used for effective management controls include (1) items-of-work - versus - time bar charts with appropriate milestones, (2) engineering experimental shop release schedule, (3) purchase parts status report, (4) manpower utilization and distribution curves, (5) subcontractor performance reports, (6) projected cost to complete, and (7) program summary reports.

GAC suggests that LRC and the contractor schedule and hold both bi-monthly and quarterly meetings. The bi-monthly meetings would be held to review technical progress and to discuss specific technical and administrative problems encountered and resolved. During the quarterly meetings the program would be reviewed at management level with an emphasis on the big picture. It is suggested LRC be the location of all quarterly meetings.

In addition to the above meetings, the contractor will conduct, under the program manager's direction, weekly coordination meetings to be attended by key personnel.

For internal use at Goodyear Aerospace, a program management system (PERT or Line-of-Balance) will be initiated and maintained throughout the program as the major planning tool. It will be designed to optimize, in schedule and cost, the development of the orbital hardware.

(5) Documentation Plan

Additional liaison and program visibility will be provided through periodic cost and technical progress reports. These reports, issued by the project office, will provide program status in depth to permit assessment of status and progress, isolation of problem areas, and coordination of corrective action. The proposed documentation and reporting plan is shown in Figure 200.

3. GROUND TEST DEVELOPMENT PLAN

a. Introduction

The ground testing of the spacecraft and its components will be conducted in four phases as outlined in Table LI and Figure 201. Table LI is a summary of Ground Test Requirements in a condensed form for quick reference. It lists the components or system to be

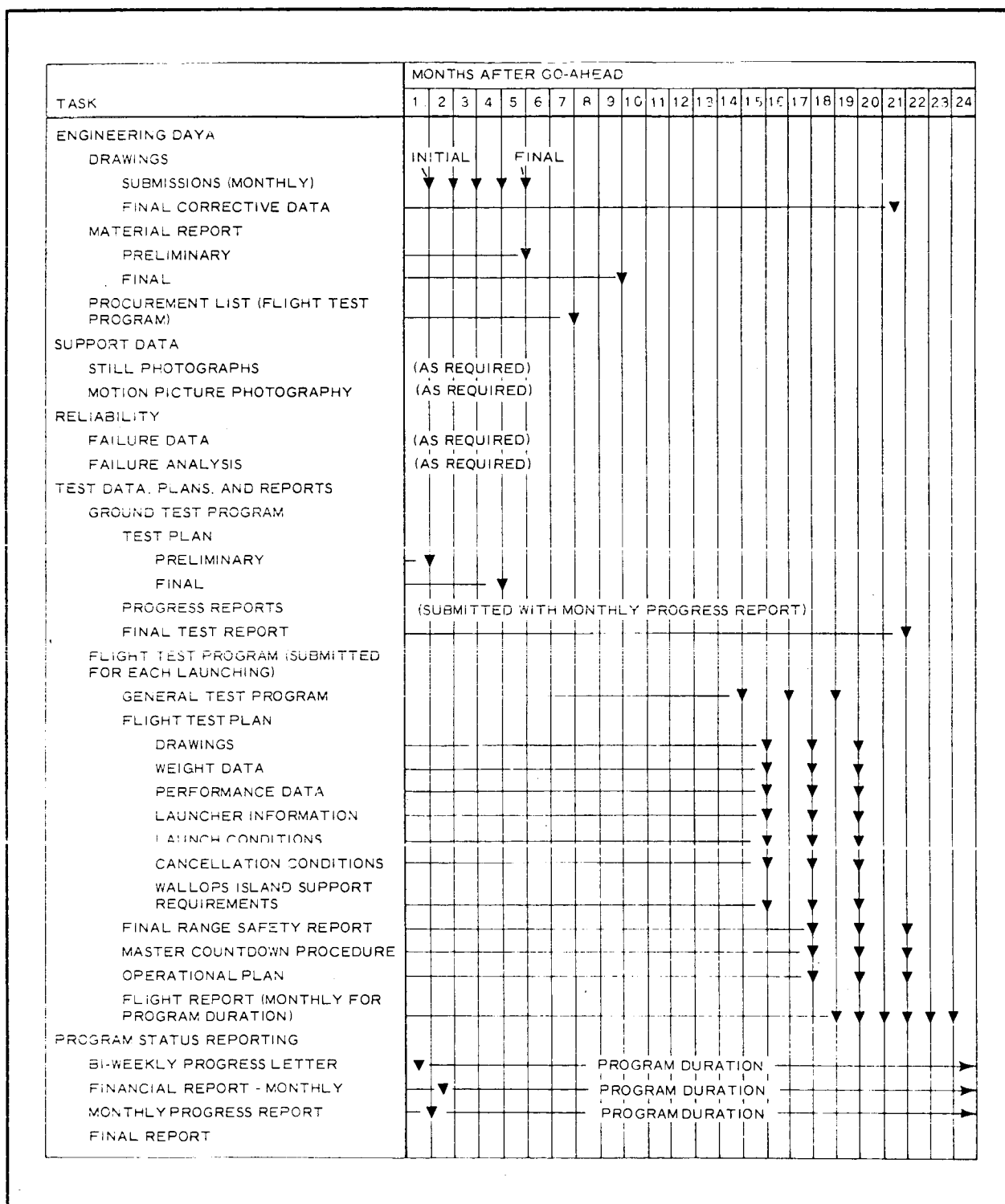


Figure 200 - Documentation Plan

TABLE LI - SUMMARY OF GROUND TEST REQUIREMENTS

Item	Type of test	Number of models	Purpose of tests	Test data	Test facility	Location
Development						
Material						
Lens	Material verification	As necessary	To study the material characteristics and verify data previously obtained in materials studies	Photolysis rate, stress-strain, porosity	Advanced Material Laboratory	GAC
Boom	Material verification					
Torus	Material verification					
Fabrication techniques	Frame, joints, attachments - tensile tests					
10-ft-diameter micropack	Contour measurements - seam etc. tests	5	To study various means of joining the inflatable portions and to determine the strength characteristics of these joints	Tensile strength	Advanced Material Laboratory	GAC
20-ft-diameter satellite model	Packaging, deployment, inflation, deflation, contour	2	To study various characteristics of the satellite configuration on scale model		Static Test Laboratory	
50-ft-diameter models						
Torus	Inflation, deployment, contour check, deflation	1	To study and refine various inflation, deployment, and packaging techniques. To determine contour stresses and inflation repeatability. To study deployment characteristics after being subjected to certain environmental conditions	Contour, pressure versus deflection, load versus deflection, modes of deployment	Static Test Laboratory	GAC
Boom	Structural, deployment (or release)	2				
Boom and torus	Deployment and stabilization, contour check and deflation, packaging	1		Contour change versus pressure		
Boom	Structural, inflation, deployment, contour check and deflation	1				
Satellite (complete)	Inflation, packaging, contour check	1		Packaged size, packaging sequence		
Satellite package*	Moment of inertia and center of gravity, environmental (vibration), separation, deployment, inflation, contour	3		Photos and movies	80- and 100-ft-diameter vacuum chambers	LRC
Canister*	Structural, leak test, separation	3	To study design features and functional characteristics	Stress-strain, leak rate, photos	Static Test Laboratory	GAC
Inflation system	Flow characteristics, pressure regulation and response, environmental (aircraft fuel)	2	To verify design parameters and to study inflation system characteristics	Flow rate, pressure drop, pressure response time		
Stabilization system*	Sublimation rate, deployment and response, release, environmental, spring rate, spring fatigue	10	To study various sublimation materials and confirm design configuration and operation under environmental conditions	Sublimation rate	Vacuum chamber, Environmental Test Laboratory	GAC
Despin system*	Despin rate, cable release, system activation, environmental	1	To study and confirm design parameters and operating sequence	Despin versus time, photos	Static Test Laboratory	GAC
Instrumentation	All components and systems to be subjected to launch environment	4	To confirm design philosophy and determine functional characteristics	Functional characteristics	Electronic Development Laboratory	GAC
Engine control	Response and control, environmental		To confirm vendor specifications			
Data acquisition						
Recorder	Power required, noise, interference, tape speeds (record and play) signal input and output					
Sensors	Signal input, noise, interference, frequency limit, power required					
Computers	Signal input and output, power requirements, noise level, interference, inflation speed					
Amplifier	Power requirements, signal output and input, noise, interference					
Subcarrier oscillator	Signal input and output, frequency and amplitude, noise level, power requirements					
Signal conditioner	Power requirements, noise level					
Data link						
Command receivers	Power requirements, frequency and band width, noise level, channel discrimination					
Heaven and signal transmitters	Power required, frequency and band width, noise level, power output level					
Antennas	Wave length, power loss					
Power supply						
Power controller	Response time, power requirements, noise level					
Batteries	Shelf life, charge and discharge rates, power capacity					
Solar cells	Power output capacity, degradation study					
Charge regulator	Power limitations test					
R-F tests (microwave)						
20-in.-diameter model tests	Edge diffraction, monostatic and bistatic tests					
40-in.-diameter model tests	Monostatic and bistatic tests, boom and canister blockage test					
Material reflectivity	Reflectivity					
Rear surface interference	Surface tolerance effects					
50-ft model	Packaging effects					
50-ft model	Environmental and functional					
Functional tests						
Inflation system		1	To demonstrate the functional characteristics of all systems and components	Functional		GAC
Stabilization system		1				
Despin system		1				
Sequence control system		1				
Data acquisition system		1				
Data link system		1				
Power supply system		1				
Canister separation system		2				
Payload separation system		2				
50-ft-diameter satellite (complete packaged system)		2				
Reliability tests						
Despin system	Functional and statistical		Statistical analysis			
Stabilization system						
Canister separation						
50-ft satellite (complete package)						
Checkout flight models	Electrical and mechanical checkout		Preshipment check	Electrical continuity		GAC

*Reliability test models have been included in starred items

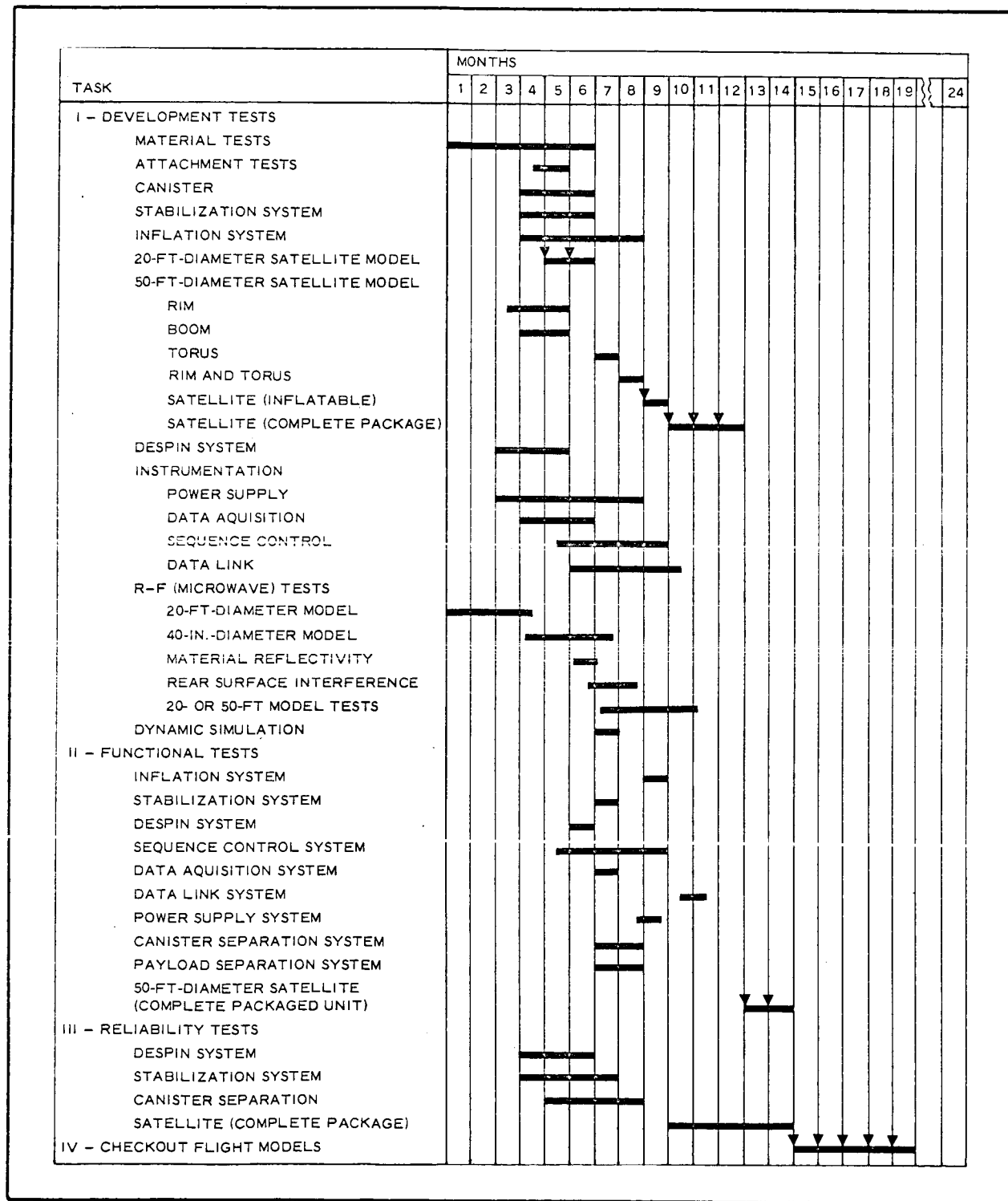


Figure 201 - Ground Test Schedule

tested, the types of tests to which each will be subjected, the purpose of the tests, the test data that will be obtained, the number of models (of each system or component) to be tested, and the test facility and its location.

Figure 201 predicts when the various tests will be conducted prior to the flight test phase of the program.

Development testing will commence at the outset of the program and will extend through to delivery of the orbital payloads. The testing involved in this phase will begin with material tests and will end with studies of the design operating characteristics of the entire system incorporated into a development satellite. During the development program all components, systems, and subsystems will be exhaustively tested and their characteristics analyzed.

Functional testing of prototype components, systems, and subsystems will start as soon as development tests have proved design concepts and design modifications have been incorporated. The functional testing will be culminated by the incorporation of all satellite systems into a packaged spacecraft and then tested under conditions simulating as nearly as possible orbital deployment of the satellite.

Reliability testing of components and systems will be accomplished throughout the life of the program.

Checkout of the flight payloads prior to delivery will be accomplished at GAC. All flight models will be completely checked during assembly and readied for preflight checks at the launch site.

b. Development Tests

(1) Material Tests

(a) Objectives

The objectives of the material test program will be to:

1. Confirm the stress-strain characteristics of the boom, torus and rim material, and the wire, wire cloth, and wire cloth-photolyzable film composite material that will be used in the fabrication of the satellite lens.
2. Confirm the quality of the composite lens material.
3. Confirm the porosity and photolyzation characteristics of the film-cloth material (1.2-mil copper wire cloth with 0.6-mil photolyzable film).
4. Confirm and establish fabrication techniques of the lens, including all seaming.
5. Demonstrate the ability of the seams to perform satisfactorily for long periods of time under a spatial environment.
6. Confirm rigidizing and buckling characteristics of the lens material, using 12-in. diameter diaphragm test samples.

(b) Procedures

Specimens of the wire, wire cloth, film cloth, torus, boom, and rim materials will be tested for stress-strain characteristics with the Instron testing machine.

Samples of the composite material will be subjected to porosity tests, using the permeability testing machine. Photolyzation tests will be conducted in spatially simulated environment of temperature pressure and radiation (sun simulation) to establish film photolyzation rates.

Sample seams to be used in the fabrication of the lens, torus, and booms will be tested, to determine their tensile

strength and peel characteristics after being subjected to the applicable environment. These tests will be conducted using the Instron testing machine.

The rigidizing pressure and the buckling characteristics of the lens material will be determined by conducting tests utilizing 12-in.-diameter diaphragms. Thus tests will be conducted with a specially fabricated pressure vessel inside a vacuum chamber, at pressures and temperatures simulating an orbital environment. Deflection measurements of the diaphragm will be made remotely.

(c) Expected Results

It is anticipated that these tests will qualify the material chosen for the fabrication of the lens, torus, rim, and boom of the lenticular satellite.

(2) Six-Foot-Diameter Diaphragm Tests

(a) Objective

The objective of the diaphragm tests will be to determine the lens sphericity and the buckling characteristics of the lens material. Also to investigate the effects of seams on the contour accuracy under rigidized conditions at various temperatures.

(b) Procedure

A specially fabricated 6-ft-diameter pressure vessel will be utilized for this test. The material diaphragms will be installed on the vessel and the vessel pressurized to rigidize the material. Contour measurements will be made using Allied Research Associates, dynamic deflection transducers, Model 1013.

These tests will be conducted under atmospheric conditions of temperature and pressure and finally orbital environmental conditions.

(c) Expected Results

The 6-ft-diameter diaphragm tests are expected to prove the contour and buckling characteristics of the lens, including the effects of seams, and the effects of environmental conditions of temperature and pressure.

(3) Twenty-Foot-Diameter Satellite Model

(a) Objective

The objective of the 20-ft-model tests will be to establish preliminary techniques of packaging, deployment, and inflation, for application to the 50-ft-diameter satellite. Also to study material dimensional stability by conducting contour measurements, and to establish material fabrication tolerances.

(b) Procedure

The deployment tests of the 20-ft satellite will be conducted by utilizing a water table, to allow free inflation of the satellite without subjecting it to undue forces due to gravity and friction. Motion and still pictures of the deployment will be taken during the tests.

The contour measurement of the 20-ft satellite will be conducted at ambient conditions (temperature and pressure) in a manner that will minimize the effects of gravity as shown in Figure 202. The satellite will be mounted on supports located around the periphery of the lens at the junctions of the lens and torus. Measurements of both the top and bottom contours will be made. The satellite will

then be inverted and the same measurements recorded.

(c) Expected Results

The above described tests are expected to provide information relative to the packaging, deployment, and inflation, necessary for establishing methods for the 50-ft-diameter satellite. They should also establish the dimensional control necessary during fabrication to maintain the design inflated contour.

(4) Fifty-Foot-Diameter Models

(a) Torus

Objective - The test objective will be to determine the deployment and inflation characteristics of the torus. Also to determine the structural characteristics of the torus at various inflation pressures and to measure its deflection. The contour will be measured to determine fabrication tolerances.

Procedure - The torus will be packaged and deployed on a water table. The deployment will be photographed with motion picture camera to allow a more detailed analysis of the deployment motion.

The torus will be placed in a special jig similar to that shown in Figure 202, and the contour will be measured to determine if it is within design tolerances.

The structural characteristics will be determined by inflating the torus to test pressure and applying loads. The deflection and contour change will be measured.

Expected Results - The results of this test will demonstrate the functional characteristics of the torus and its dimensional stability under inflated conditions.

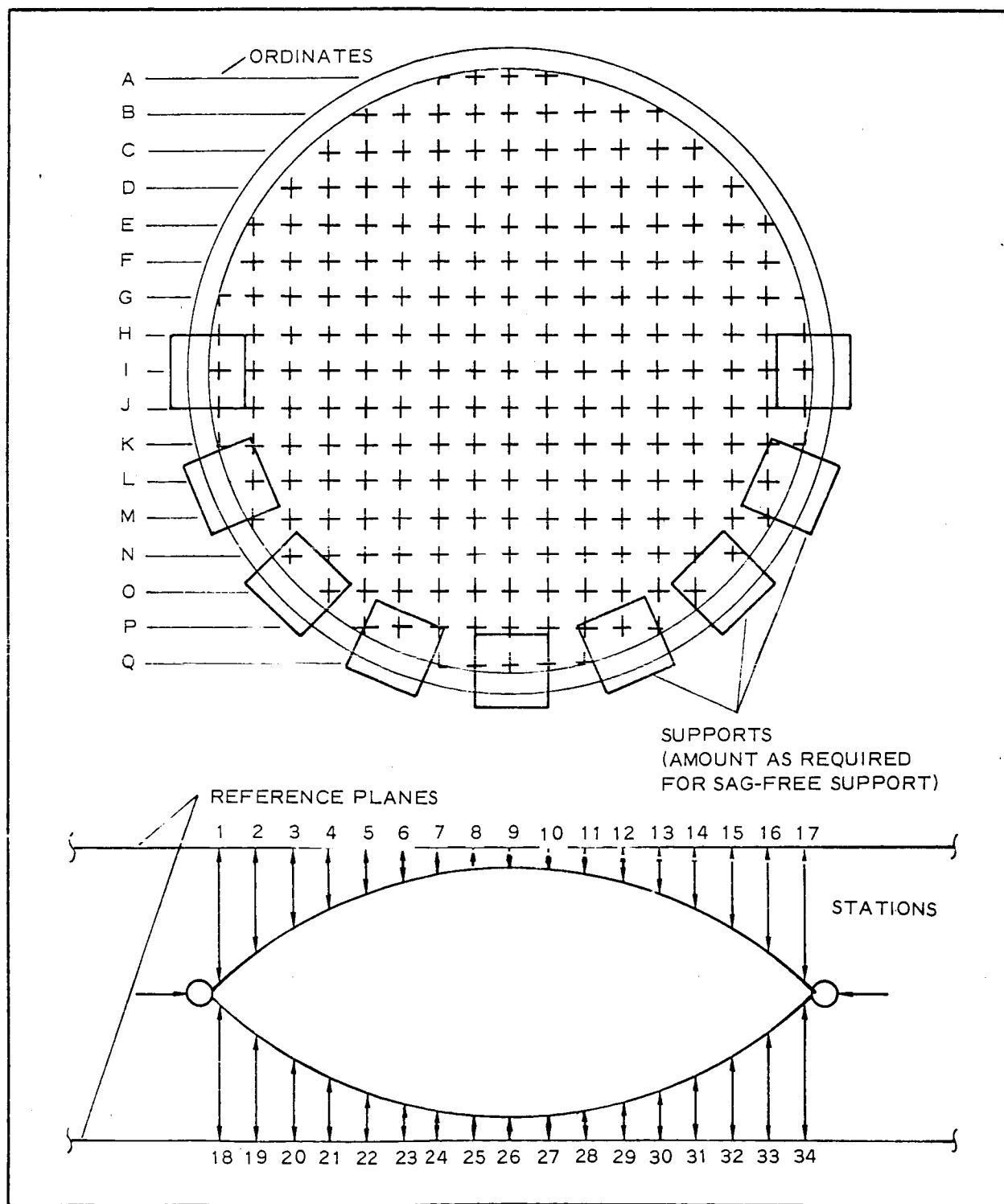


Figure 202 - Setup for Satellite Model Contour Measurement

(b) Rim

Objectives - The rim tests will determine the torsional structural characteristics of rim segments in the deployed condition. They will verify the ability of the rim to be successfully packaged and released. A further objective will be to measure the expanded contours (diameter) to determine the creep strength characteristics of the rim material.

Procedure - Segments of the rim will be tested for torsional rigidity and buckling, and deflection measurements will be recorded. The rim will be packaged and allowed to release. Release will be observed and stability will be noted. The rim will again be packaged and stored in the packaged condition for a specified period of time, then released. The release will be observed and the creep stress effects noted. Motion pictures will be taken for detailed analysis of the deployment.

Expected Results - It is expected that these tests will verify the structural characteristics of the rim section and its ability to be packaged and released and also show the creep strength characteristics of the rim material.

(c) Rim and Torus

Objectives - The objectives of the rim and torus tests will be to determine the packaging, deployment, and inflation characteristics of the rim and torus combination. Also to determine the dimensional stability of the combination by conducting contour measurements and deflection tests and to determine the efficiency of the attachment method.

Procedure - The deployment and inflation test will be conducted on a water table. The test will be observed

and the deployment time will be measured. Also motion pictures will be taken for detailed analysis of the deployment sequence.

The contour check and deflection test will be conducted on a special test fixture, fabricated for this test. Optical measurements will be made where possible to improve accuracy. Where deflection is too great for optical measurement, a mechanical means of measuring will be incorporated.

Expected Results - The above described tests should show the packaging and deployment characteristics of the rim and torus and also verify the inflated dimensional stability of the rim-torus combination.

(d) Complete 50-Ft-Diameter Satellite

Objective - The objective of the test of the complete 50-ft satellite will be to determine the most effective method of packaging the satellite with regard to method and packaging sizes and to determine the effects of repeated packaging on the inflation characteristics and on the contour of the lens.

Procedure - The satellite will be packaged and inflated (on the water table) a sufficient number of times to determine the most efficient packaging method and optimum package size. A contour check will be made before the satellite is first packaged and again after it has been packaged and deployed.

Expected Result - This test will provide qualitative information with regard to the effects of repeated packaging and inflation on the life of the satellite materials, and the dimensional changes due to buckling and wrinkling of these materials.

(e) Complete 50-Ft-Diameter Satellite Payload Tests

Objectives - The primary objective of the payload test will be to determine the functional characteristics of the development satellite with regard to canister separation, deployment, and inflation. A further objective will be to determine the effects of environmental conditions of shock and vibration (launch conditions of the Scout) on the functioning of the development systems.

Another objective will be to determine the accuracy of the satellite contour construction.

Procedure - The satellite will be packaged and installed in the canister and all residual air will be removed. The payload will be installed in the test fixture at GAC and the deployment sequences initiated. Figure 14 shows a typical canister separation and deployment sequence.

Motion pictures will be obtained, for detailed study of the sequence. Sequence time, and torus, boom, and lens pressures will be recorded during the test.

The satellite payload will then be repackaged and residual air removed and assembled into the canister, with all systems aboard. The payload will then be installed on a vibration test machine and subjected to the vibration spectrum of the launch cycle of the Scout rocket, which is given in Appendix O.

After the vibration test of the package has been completed, it will be reinstalled in the test fixture on the water table and the deployment sequence will again be initiated.

Motion pictures, pressures, and deployment time will be obtained during the test.

Similar tests will be conducted on other models in the 60- or 100-ft-diameter vacuum chamber at NASA - Langley Research Center. In these tests the satellite will be deployed in a plastic sheet installed inside the vacuum chamber. Three models of the satellite will be used to conduct these tests. Each model will be subjected to tests, some of which will be the same or similar.

Expected Results - The initial deployment tests will indicate the functional characteristics of the developmental payload separation system, the canister separation system, and the inflation system. Post-vibration functional tests will prove the ability of the system to function after having been exposed to simulated launch conditions.

(5) Canister Tests

(a) Objectives

The objectives of the canister tests will be to verify the design concepts for the separation of the canister, to determine the structural characteristics of the canister and its attachments, and to prove the pressure integrity of the canister and its connections.

(b) Procedure

The canister will be subjected to loads that will simulate flight loading (not vibrations). Strain and deflection measurements will be obtained during the test.

Separation tests will be conducted in which the canister halves will be separated using the explosive bolts. Separation velocity will be recorded and high speed motion pictures will be taken to determine the stability of the canister halves during and immediately after separation.

This test will be designed to minimize the effects of gravity.

The canister will be subjected to vacuum tests to determine its ability to maintain a specified pressure for a given time. The pressure rise and time will be recorded in order that the leak rate can be established.

(c) Expected Results

The above tests are expected to prove the design concepts of the canister with respect to separation mechanism, separation stability, and structural and vacuum integrity.

(6) Inflation System

(a) Objective

The inflation system tests will be conducted to prove the functioning concept of the pressure regulating valves and sensors and to prove the adequacy of the pressure vessel. They will also determine the flow rate of the inflation system and the effect of the flight environment (shock, vibration, and temperature) on the components and on the system.

(b) Procedures

The test of the inflation system will be conducted on a special test setup inside a vacuum chamber. The response of the sensors and pressure regulators will be recorded, as well as the pressure of each system.

The inflation system (with all components) will be subjected to the Scout launch environment of shock and vibration. The system will then be retested as above

to determine the effects of the launch environment on the functioning of the systems and components.

(c) Expected Results

The inflation system tests should expose any design deficiencies in the operation of the inflation systems and its components and indicate desired corrective measures. They also will show the effect of the launch environment on the functioning of the system.

(7) Stabilization System

(a) Objective

The stabilization system tests will investigate the sublimation rates of various materials for possible application to the stabilization system and the spring rates of various materials and wire sizes. The tests also will determine the release rate of the spring, and subliming material configurations chosen for the stabilization system. The environmental effects of radiation on the damper fluid and the effects of launch environment of shock and vibration on the assembled system will also be investigated.

(b) Procedure

Various subliming materials will be subjected to environmental conditions of temperature and pressure. The sublimation rate as a function of temperature and pressure will be determined for each material.

Spring rate tests of various materials and wire sizes will be conducted to determine the optimum spring material and configuration.

The design configuration of spring and sublimation material will be subjected to environmental conditions of temperature and pressure (vacuum) to determine the spring release rate.

The assembled stabilization system will be subjected to launch conditions of shock and vibration to determine what, if any, detrimental effects occur on either the spring or sublimation material.

The damper fluid will be subjected to simulated solar radiation, and the effects of this environment will be noted for several types of fluid.

All tests of the stabilization system will be designed so that the effect of gravity will be kept to a minimum.

(c) Expected Results

The results of this investigation will provide assurance of the design possibility of the stabilization system.

(8) Despin System

(a) Objective

The design capability of the despin mechanism, release mechanism, and actuating mechanism will be demonstrated. Also the effect of launch environment (shock and vibration) on the functioning of the despin system will be determined.

(b) Procedure

The despin mechanism will be installed on a dummy mock-up of the payload (with the same weight, moment of inertia, and cg as the real satellite). The mockup will be installed on a rotational test fixture. The payload will then be spun up to test rpm and the despin mechanism released. The despin rate, initial rpm, and final rpm will be recorded.

The mock payload with the despin mechanism will be subjected to launch environmental conditions of shock and vibration as outlined in Appendix O and retested to determine the effect of launch environment on the functioning of the system.

(c) Expected Results

It is expected that the foregoing tests will prove the design concept of the despin mechanism and determine the effects, if any, of launch condition of shock and vibration on the functioning of the system and its components.

(9) Instrumentation

(a) Sequence Control

Objectives - In testing the sequence control system there are several objectives to work for. These are (1) to ensure functioning and compliance with specifications of components in response time, repeatability, noise level, and power requirements and (2) to assure compatibility of all components functioning as a unit, or system.

Procedure - All components will be tested individually and assembled into a system. The system will then be checked for function and continuity. High and low voltage inputs will be used to ascertain limits. Normal sequence functioning will be run and each override function will be operated. Electrical noise levels and interference will be checked. The system will be vibrated at Scout launch spectrums and then checked again.

Expected Results - The results of these tests will indicate the compatibility of the sequence times in the overall system and establish repeatability of time versus

function curves. Noise interference levels will have been ascertained and compensated for. Compliance with specifications will be ascertained.

(b) Data Acquisition

Objectives - The objectives in the data acquisition test will involve the data sensors - to ascertain their compliance with specifications in both environmental and functional qualities.

Procedure - All components will be tested for signal output with both high and low voltage inputs. Functioning speed and rates will be established and noise interference levels will be checked. Repeatability and response times will be tabulated and component calibrations will be established.

Expected Results - The results of these tests will indicate the compatibility of the sensors with their systems. Sensor output calibration curves will be established. Response time and operating speeds will be determined. Noise levels will have been ascertained and compensated for. Compliance with specifications will be ascertained.

(c) Data Link

Objectives - The data link tests will entail objectives such as the functioning of component parts with respect to required specifications and the capability of all components to function as a system.

Procedure - All components, both receiving and transmitting, will be checked with varied power supply to ascertain an operating power range. These components will be tested for power consumption, signal strength, noise interference, and functionability with other

SECTION IV - TECHNICAL DISCUSSION - PHASES III AND IV GER-11502

components and as a system. Antenna patterns will be checked. All systems will be functionally checked after vibration test of the system.

Expected Results - The results of these tests will indicate the compatibility of the units to operate as a system. The design specifications of the components and the system will be established. Noise interference levels will be established and compensated for. Signal strength and antenna wave patterns will be confirmed.

(d) Power Supply

Objectives - Objectives of the power supply test will be to determine component compliance with specifications and compatibility with the requirements of all systems.

Procedure - Tests will be conducted to ascertain battery shelf life, charge rates, discharge rates, and power output. Solar cell charge rates will be tabulated. Functional test of charge regulation systems and peak power requirements will be checked.

Expected Results - These tests will prove the power supply capability of maintaining all systems. It will ascertain the charge rate of the system. The compliance of components to design specifications will be ascertained.

(10) R-F Ground Test Program

(a) General

The several elements of the radio-frequency ground test program are outlined in Figure 203 and described in Items (b) through (i), below.

(b) Model Tests (20-In. -Diameter)

Objective - The 20-in. diameter model tests will determine the magnitude of the edge diffraction return with

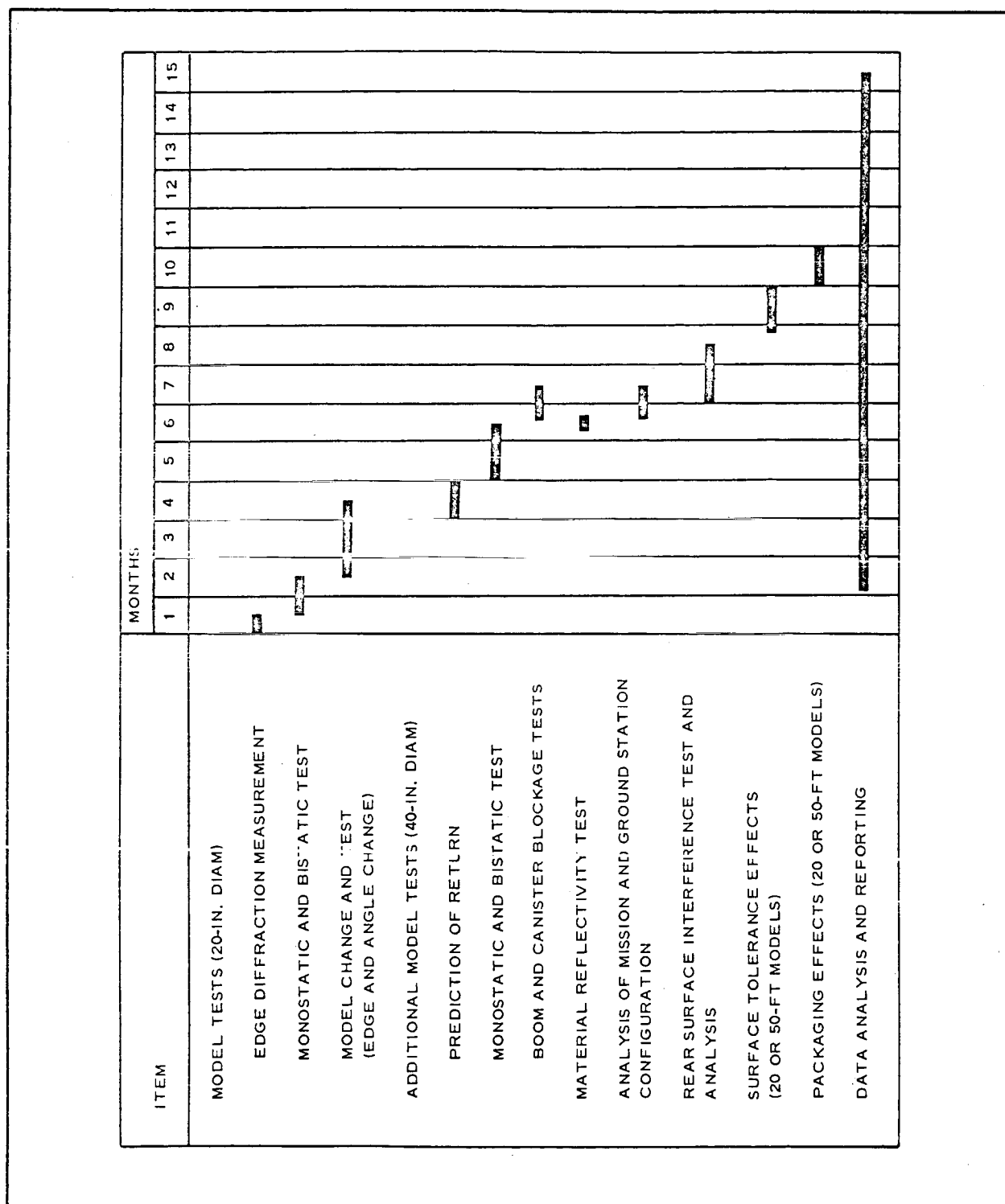


Figure 203 - Radio Frequency Ground-Test Schedule

respect to that of the center spectral return. Another objective will be to predict the radar return coverage and operational capabilities of the lenticular satellite configuration and to determine the effect of edge configuration on the magnitude of the edge diffraction return.

Procedure - Edge diffraction measurements on the 20-in. model will consist of reflectivity measurement on the 150-ft range at X-band frequencies. Microwave absorbing material will be placed between the model and the transmitting horn in such a manner as to intercept energy incident upon the center portion of the model. Thus, as the model is rotated behind the absorber, the resultant reflection pattern will be that of the edge diffraction return (see Figure 204). Four sizes of absorber material will be used to determine the effect of varying degrees of edge exposure.

Monostatic and bistatic reflectivity tests also will be performed on the 150-ft reflectivity range for various X-band frequencies and tilt angles on the model (Figure 205).

The edge configuration of the model will be changed in various ways and reflectivity patterns taken. These patterns will then be compared to the reflectivity patterns of the present configuration to determine the effect on edge diffraction return. Figure 206 indicates edge modifications to be made.

Results Expected - It is anticipated that the measured value of the edge diffraction return will more closely correlate with the return predicted by theory and that the over-all lenticular return coverage can be more closely predicted at various bistatic aspect angles. It

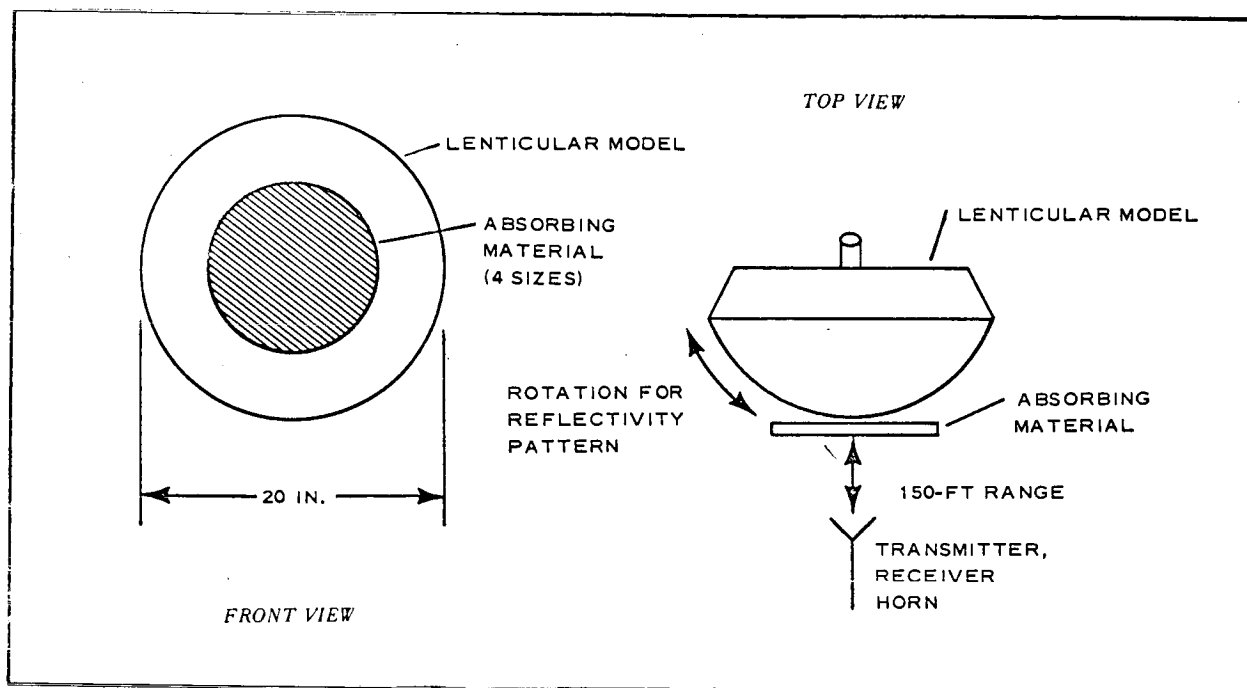


Figure 204 - Edge Diffraction Returns

is expected that increased radius of curvature of the edge configuration or addition of absorbing material at the lenticular edge will significantly reduce the magnitude of the edge diffraction return.

(c) Additional Model Tests (40-In. Diameter)

Objective - The objective of these tests will be to predict the radar return of the additional 40-in. test model from data analysis of the 20-in. test model measurements and thus provide further knowledge of the return expected from the full-scale lenticular satellite. To measure the radar return coverage and capabilities of the 40-in. model for comparison with the 20-in. model measurements and to determine the boom and canister blockage and multiple path effects on the lenticular return will be additional objectives.

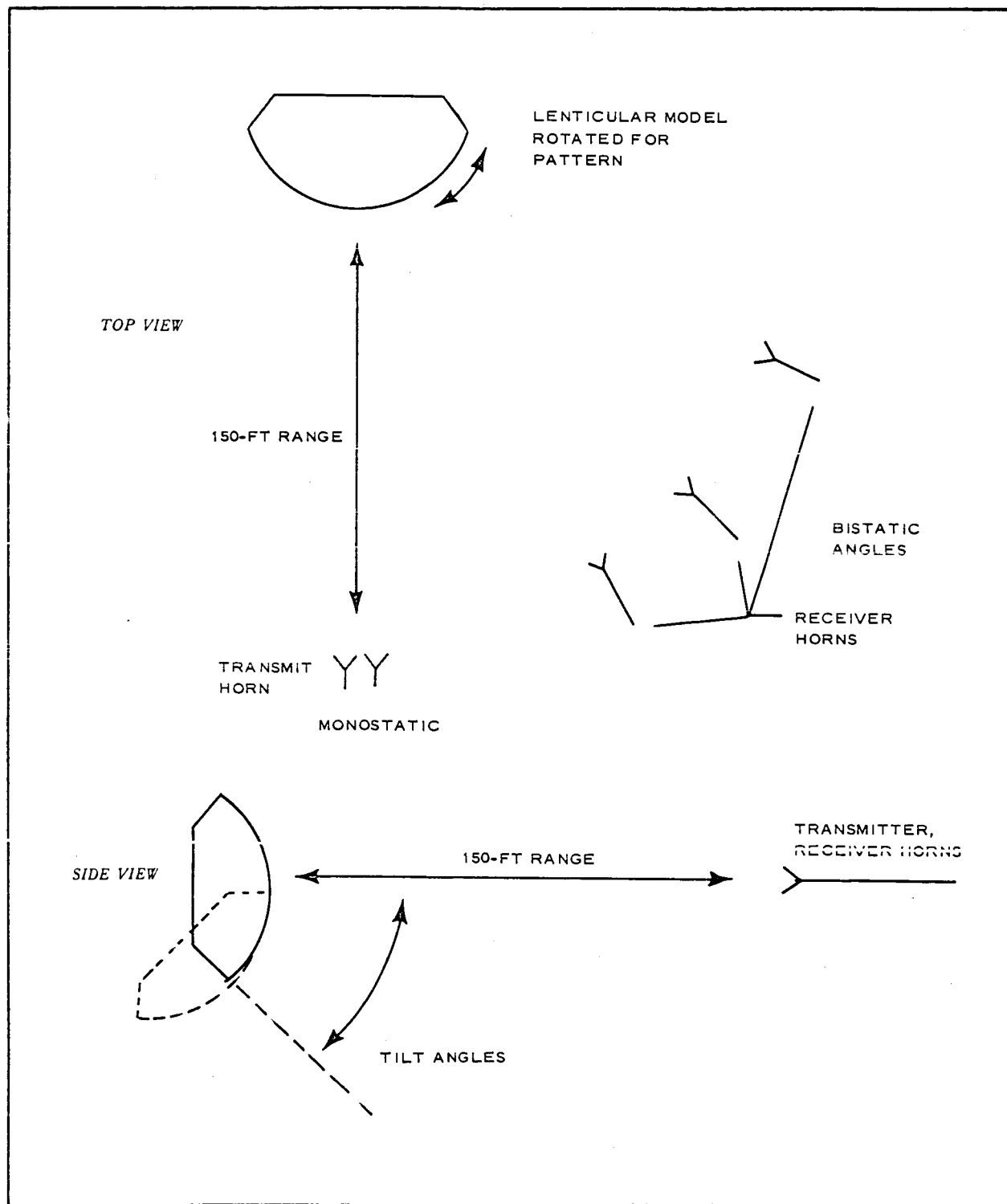


Figure 205 - Diagram of Monostatic and Bistatic Reflectivity Tests

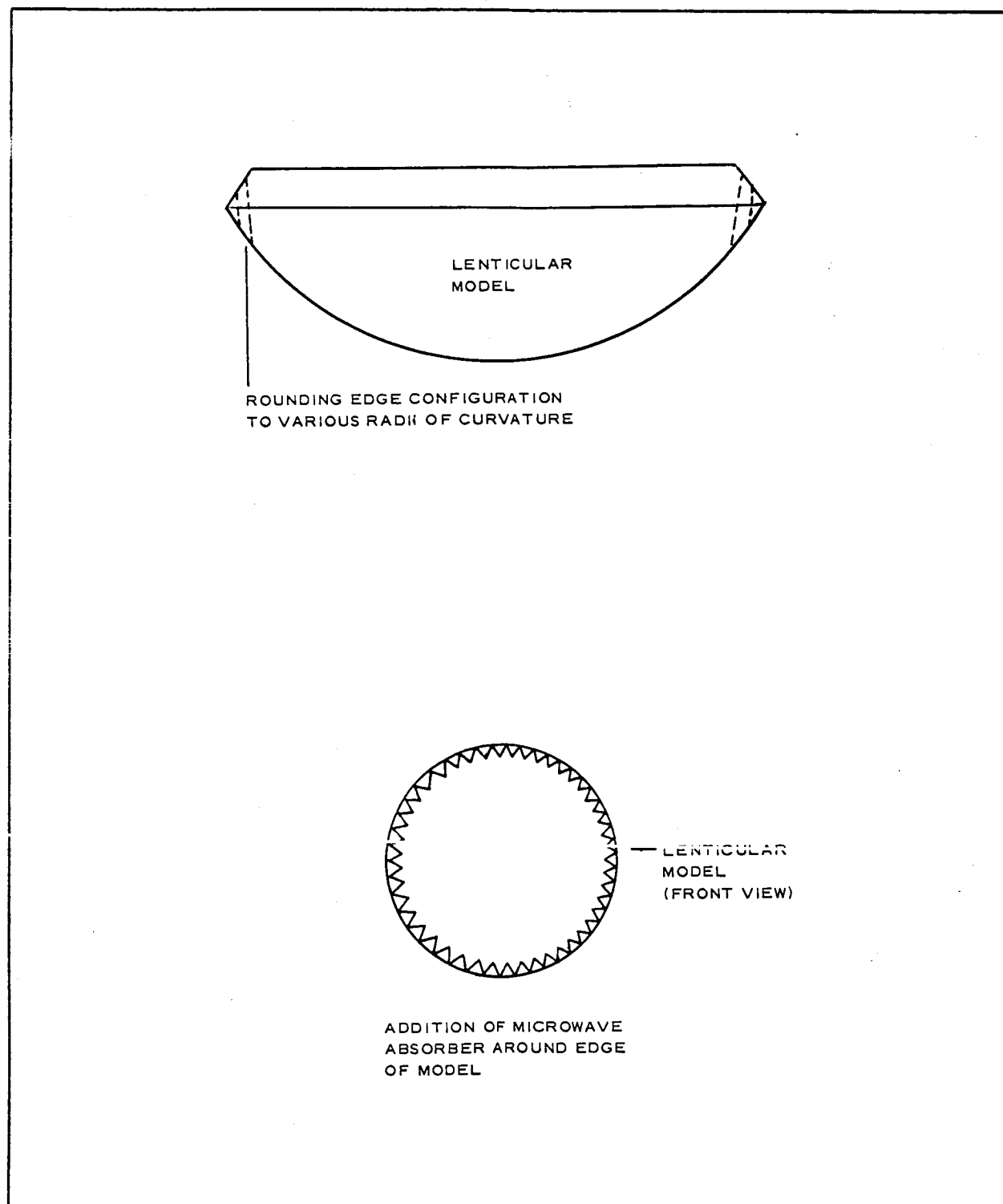


Figure 206 - Edge Modifications

Procedure - Prediction of the expected 40-in. test model return will be made on the basis of the reflectivity patterns taken on the 20-in. model and also considering the dimension changes that affect the characteristics of the radar return.

Monostatic and bistatic reflectivity measurements will be made in the same manner as on the 20-in. model. The 40-in. model will, however, require a 240-ft. range due to its larger diameter. This range length is required to provide uniform illumination over the model aperture.

Boom and canister blockage and multipath effects will be measured by making reflectivity patterns of the 40-in. model fitted with sealed models of the booms and canister. These reflectivity patterns will then be compared to the reflectivity patterns of the 40-in. model without booms and canister.

Expected Results - It is anticipated that the radar return of the 40-in. model can be predicted from those measurements made on the 20-in. model. Also that the angular region of variation of return with changes of frequency will be reduced by the larger model size and that the period of constructive and destructive interference between the spectral and edge diffraction return will be reduced due to the increased h dimension of the model (Figure 207). It is expected that the monostatic and bistatic reflectivity test data will provide additional design parameter information and determine the effect of parameter variation on the full-scale satellite return. That the effect of boom and canister on the radar return is negligible should also be ascertained from these tests.

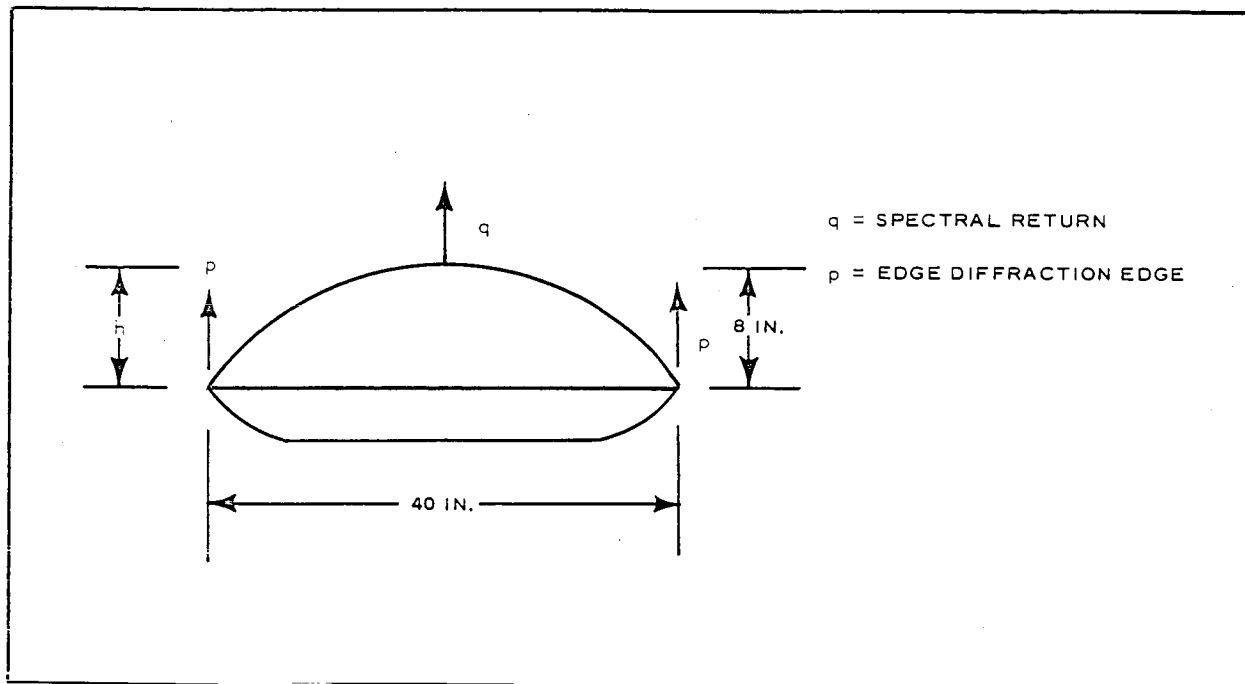


Figure 207 - Effect of Increased h Dimension

(d) Material Reflectivity Tests

Objective - The material reflectivity tests will measure the reflectivity of representative lens grid materials and determine their efficiency as a microwave reflector.

Procedure - Measurements will be performed on an interferometer set-up where a sample of the grid material is placed between a transmitting and receiving horn and the power leakage through the grid material is measured. The percentage of reflectivity can then be calculated from the leakage power measured.

Expected Results - The material reflectivity tests should show that wire mesh of proper wire size and spacing will act as a totally conductive reflecting plate.

(e) Analysis of Mission and Ground Station Configuration

Objective - The analysis should determine the capability of the lenticular configuration to provide a communications link between representative ground stations and for a typical orbit.

Procedure - The radar return magnitude of the full-scale model can be predicted for various aspect angles from the previous reflectivity model tests. The range of aspect angles over which the lenticular satellite would be required to provide a return could then be determined for proposed ground stations and a typical orbit. The communications capabilities can then be analyzed, taking into consideration the power level transmitted, the range of return magnitude over the aspect angles of interest, and the sensitivity of the ground station receiver.

Expected Results - The limitations of the lenticular satellite for providing a communications link will be determined. Also the maximum aspect angles and ranges from ground stations that can be used will be established.

(f) Rear Lens Surface Interference Test and Analysis

Objective - This analysis will determine the effect on the lenticular radar return of energy leakage through the front lens surface and focused and reradiated by the rear lens surface. It should also determine the lens grid material reflectivity required to reduce the effect of this reradiated energy to acceptable limits.

Procedure - A 40-in. test model will be fabricated from representative wire grid material. Reflectivity patterns of this model will then be obtained and compared to the patterns of the solid 40-in. model. Interference due to the rear lens

surface return can then be measured. If the interference variation between the reflections from the front and rear lens surface is not acceptable, additional models fabricated from grid materials with larger wire diameter or closer wire spacing will be tested and a suitable material chosen.

Expected Results - It is anticipated that the magnitude of the lenticular return variation due to lens interference effects will be determined and that a minimum wire grid size and spacing will be found to reduce the interference effect to acceptable limits.

(g) Surface Tolerance Effects

Objective - These tests will determine the degradation of the lenticular radar return due to surface irregularities and departure from a true spherical shape.

Procedure - A 20-ft model or the 50-ft flight-test model will be inflated and a mechanical contour check made on the surface. A one-horn interferometer setup will then be used to illuminate small areas of the model and to measure return from various areas. The magnitude of the radar return from the various areas will indicate the effect of surface tolerance on return.

Expected Results - It is expected that a measurement of the degradation of the lenticular return for known surface irregularities will be found and that maximum values on surface irregularities will be set to limit the degradation of the radar return.

(h) Packaging Effects

Objective - The degradation of the lenticular radar return due to additional surface irregularities caused by packaging of the model in the canister should be ascertained in these tests.

Procedure - A 20-ft model or the 50-ft flight test model will be packaged in a manner simulating the actual packaging procedure that will be used on the full-scale satellites. The model will then be inflated and mechanical and electrical measurements as outlined in Item (f) above will be made.

The magnitude of the radar return variation from the various areas of the model will again indicate the effect of surface irregularities.

Expected Results - The additional mechanical and electrical measurements after packaging compared to the previous surface tolerance measurements will show the surface irregularities caused by the packaging and provide additional data on radar return degradation. The tests will determine whether or not packaging causes surface variations which are within acceptable limits.

(i) Data Analysis and Reporting

Objective - The analysis will determine the effect of design parameters on the performance of the lenticular satellite as a communications relay and establish configuration and material requirements to assure adequate performance.

Procedure - Data analysis will be performed by comparison of the expected theoretical return characteristics with those characteristics obtained from reflectivity measurements. Use of consultants and state-of-the-art theoretical considerations will be made. Data will also be analyzed by comparison of the reflectivity patterns of the various phases of the ground checkout program. These reflectivity measurements are designed to isolate individual radar return characteristics and provide additional information about the effect of design parameters on these characteristics.

Expected Results - Configuration and material requirements that will assure adequate performance of the lenticular satellite will be established. An accurate prediction of the operational capabilities of the full-scale satellite is also anticipated.

c. Functional Testing

(1) Objectives

The objectives of the functional tests will be to prove the operational characteristics of the prototype and flight systems and components of the satellite package, in both ambient and spatial environments.

Also they should prove that launch environmental conditions of shock and vibration will have no effect on the functional operation. The environmental tests will be conducted in the large (80-ft diameter) vacuum chambers at LRC and the ambient tests at GAC.

(2) Procedure

Each system will be functionally checked after fabrication at ambient and spatial environment to determine that it will function properly according to the design specification.

The systems will then be subjected to Scout launch environment of shock, vibration, and temperature as outlined in Appendix O and retested.

A complete packaged satellite with all systems integrated as for flight will then undergo a complete functional sequence test, including payload separation, canister separation, deployment, and inflation.

The satellite will be repackaged and the complete assembly subjected to Scout launch environmental conditions, after which the sequence test will be repeated.

(3) Expected Results

The functional test is designed to prove that individual systems and components as well as the integrated satellite package will function properly and that the satellite will perform its assigned tasks after being placed into orbit.

d. Checkout of Flight Payloads

(1) Objectives

These tests will check out the circuitry of all electrical systems, including an electrical deployment sequence operation, to determine that all systems are functioning properly.

(2) Procedure

The three spacecraft to be used for lob shots and the two for orbiting will undergo a complete electrical continuity checkout and visual inspection during assembly. The electrical checkout will be so designed that all electrical deployment sequences can be checked for operation.

(3) Expected Results

The payload checkout tests will ensure that the spacecraft is electrically capable of functioning as designed, when lob tests and orbital shots are conducted.

e. Reliability Tests

(1) General

The following items will be tested in the reliability ground test program:

1. Despin system
2. Stabilization system components
3. Canister separation
4. Satellite deployment subsystem (complete package)

The objectives, procedures, and expected results of the tests are described below.

(2) Despin System

Objective - The objective of the despin test will be to determine experimentally the effect of variations of dimensions and masses on the residual spin of the packaged satellite.

Procedure - One despin mechanism with provision for rotation will be required. The test will be conducted in vacuum.

Values of I , m , r , L , defined below, will be measured before tests.

- I = Spin moment of inertia of canister
- m_1 = Mass of despin weights
- m_2 = Mass of cables
- r = Radius of coiled cables
- L = Length of cables

Test will be designed statistically so that effects of controlled variations in dimensions of the elements defined above on final or residual spin speed can be determined.

Expected Results - The probability of obtaining the required final spin speed will be determined.

(3) Stabilization System Components

(a) Damper

Objective - This component test will determine whether the damper will operate satisfactorily in orbital environment for its required life after exposure to the launch environment.

Procedure - Launch environment vibration and acceleration will be simulated (and overtested) followed by life test (20-yr life).

Orbital radiation will be simulated (either complete damper or fluid. If fluid is tested separately, the testing agency will report the effect on viscosity).

Test equipment will be specified.

One sample will be required (20-yr life test).

Expected Results - Failure of damping fluid to resist radiation is expected to be exposed by this test. Also mechanical failures induced by the launch vibration are expected to be exposed.

(b) Damper Spring

Objective - The object of this test is to determine that the spring material can continue to function after cyclic loading for the required satellite life.

Procedure - Simulation of launch environment will be covered in a damper spring deployment device test.

Statistically designed torsional fatigue tests will be made on a large number of relatively short lengths of spring wire. Results of fatigue tests will be analyzed using extreme value distribution.

Samples will be made available any time in the program.

Expected Results - This test is expected to yield a function for the probability of successfully completing a given number of cycles at a given stress and a given probability.

(c) Damper Spring Deployment Device

Objective - This test will determine the design characteristics of the subliming material for design purposes

and observe the initial design behavior for failure modes.

Procedure - Test will be planned to determine effect of temperature and pressure and subliming shape on ultimate strength and sublimation rate of subliming material used in device (early in the design program).

Five devices of initial design will be tested, applying constant load magnitude, varying direction, (simulating deployment force on spring) under the conditions of vacuum and pressure expected. Tests will require constant observation for failure modes, and satisfactory operation of all samples.

If results of tests indicate the need for design changes, then the design changes will be retested.

This testing will begin early in the design phase and will probably extend to the end of it.

Expected Results - The data on subliming rates and strength required for design and the possible failure modes of the design are expected to be acquired.

(d) Canister Separation

Objective - The canister separation tests will be run to observe possible failure modes.

Procedure - The test is to be conducted in vacuum and observed for modes of failure after exposure to launch vibration, shock and acceleration environment.

Three samples will be required.

Expected Results - Failure modes will be observed and reported.

(e) Satellite Deployment Sybsystem (Complete Package)

Objective - These tests will overtest the deployment subsystem during the inflation and deflation sequence to expose weak areas in the design.

Procedure - This will be an overtest program. The primary concern will be to establish what components, if any, are likely to fail in the launch environment.

Three completely packaged satellites will be needed early in the design cycle so that corrective actions can be made if required.

The test sequence will be:

1. Functional test
2. Launch environmental simulation of thermal and vibration conditions at Level 1
3. Functional test
4. Launch environmental simulation of thermal and vibration conditions at Level 2
5. Functional test
6. Launch environmental simulation of thermal and vibration conditions at Level 3.

Corrective action will be required on any component failing at Level 1.

After corrective action has been incorporated in components failing in Level 1, the component will be required to pass overtest designed statistically and conducted with environment based on records made during Level 1 test.

Expected Results - Corrective action will be taken based on this overtest program.

4. FLIGHT TEST DEVELOPMENT

a. General

The following flight test program plan encompasses the essential prelaunch and post-launch activities associated with the orbital flight test of the 50-ft lenticular satellite.

The plan will also be applicable for lob shots with the exception that the Minitrack tracking facilities would not be required.

The test program can be divided into the following two major efforts:

1. Prelaunch activities
2. Orbital test and support

Prelaunch activities would normally begin at T minus eight months and continue through countdown to liftoff. The orbital test and support will begin immediately upon liftoff and continue for the duration of the experiment. A flight test plan and schedule of events are shown in Figures 208, 209, and 210.

The information in this section is considered to be compatible with the requirements established in the Scout Handbook (Ref 1) and in the Wallops Station Handbook (Ref 2).

b. Prelaunch Activities

(1) General

Prelaunch activities are divided into the following three areas:

1. Flight test preparation
2. Test site operation
3. Launch pad operation

(2) Flight Test Preparation

(a) General

Preparation for the test flight will begin approximately

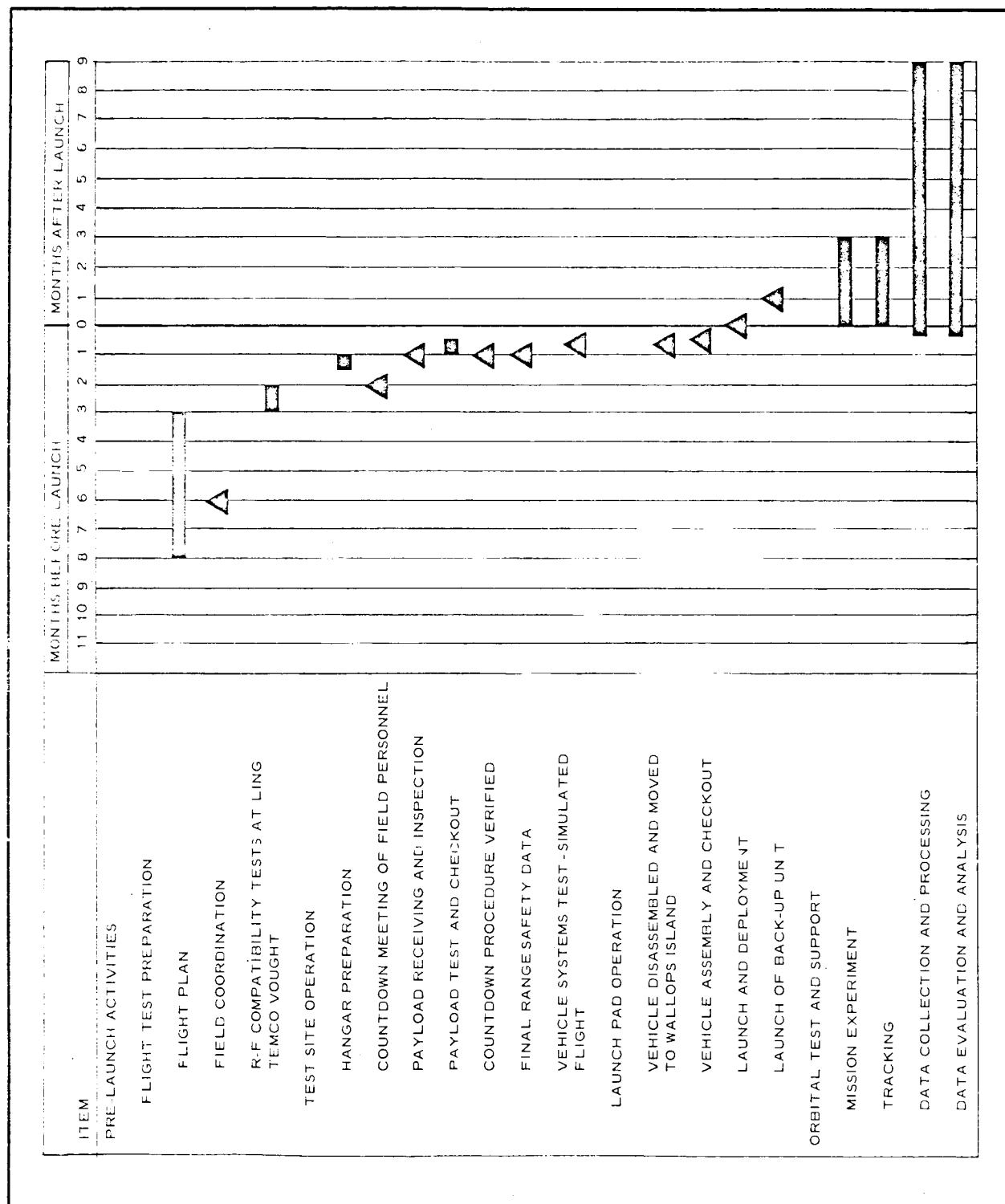


Figure 208 - Flight Test Plan and Schedule - Months Before and After Launch

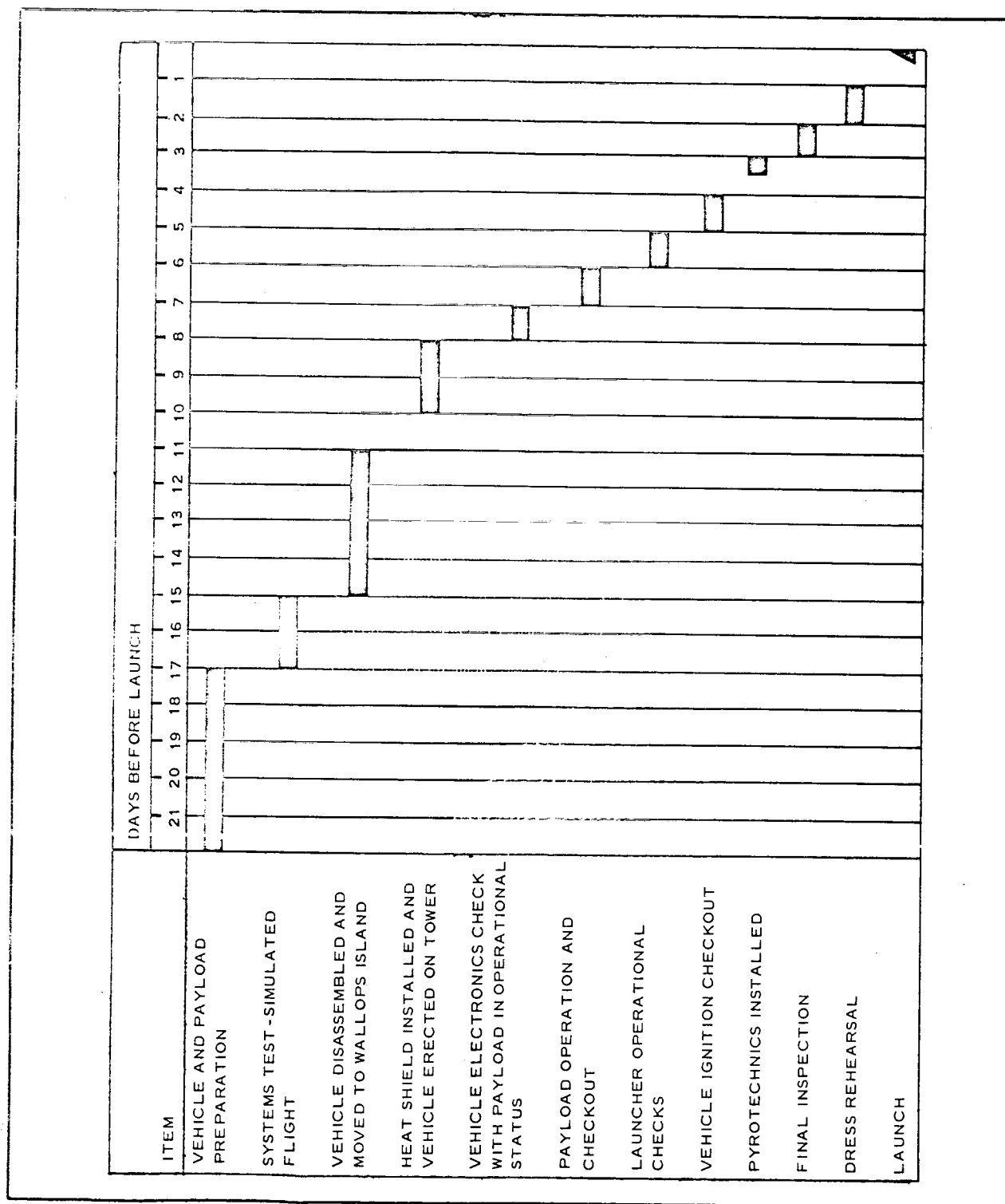


Figure 209 - Flight Test Plan and Schedule - Days Before Launch

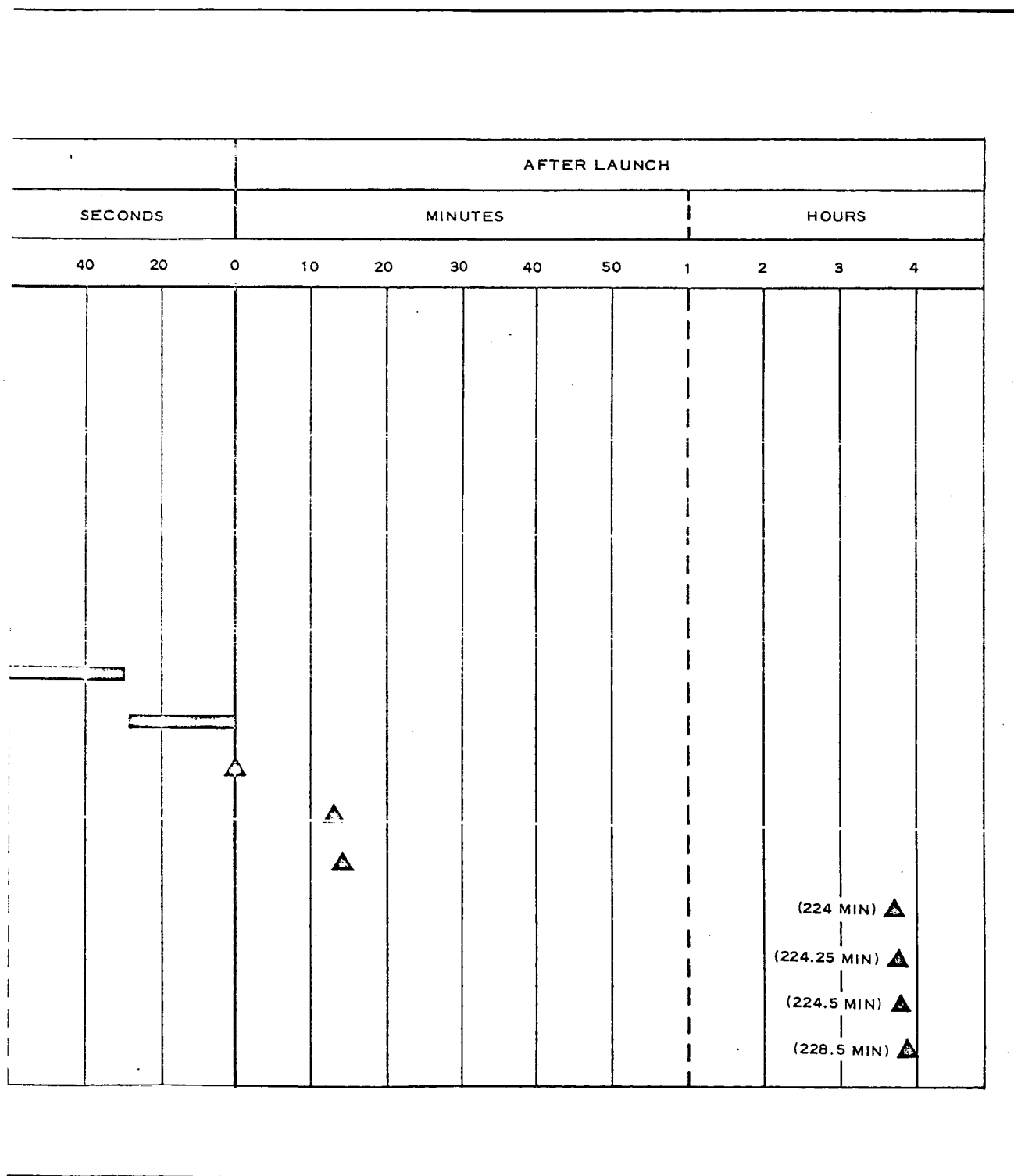


Figure 210 - Flight Test Plan and Schedule - Launch Day

[illegible]

eight months prior to the scheduled launch date. This activity includes (1) preparation and documentation of a detailed flight plan, (2) field coordination, and (3) r-f compatibility tests at LTV.

(b) Flight Plan

Administrative, technical, and operational data will be prepared and submitted to LRC, for approval, three months prior to the scheduled launch date.

The administrative data will include information relative to project designation, classification levels, project officers, and a complete description of the mission, including launch window, orbit inclination, ground tracking requirements, go no-go criteria for the payload, launch angle in azimuth and elevation, and ascent trajectory constraints.

Technical data will include payload dimensions and weights, electrical details including schematics and drawings, operational sequence of payload, spin rate at fourth-stage burn-out, details of the separation system, and details of the heat shield. In addition, tower environmental data relative to payload requirements will be submitted as well as complete requirements for tracking and data acquisition from liftoff through termination of the experiment. Tentative tracking and data acquisition requirements are presented in a subsequent section of this report.

Operational data to be included in the flight plan will include personnel, space, and support requirements. Personnel will be assigned to the project by both the contractor and Langley Research Center. These assignments cover engineering personnel, mechanical services personnel,

and downrange personnel. Support equipment requirements include an area for mechanical assembly and handling of live rocket motors, dynamic balancing facility for vertical balancing of the payload, a facility for determining weights, cg, and moments of inertias. A work area will also be required for instrumentation checkout.

In addition to the above information, a detailed plan of operation will be prepared as outlined in Figure 209 and Figure 210.

(c) Field Coordination

General - Field coordination will be required with the Project Office at Langley Research Center and with the Wallops Island project engineer assigned to the program by the Wallops test director. This activity will start six months prior to the date of launch and continue throughout the program.

All preliminary discussions relative to the test program will be carried on between the Wallops Project Engineer (WPE) and the Contractor's Project Engineer (CPE). The WPE will be responsible for coordinating the requirements of the contractor with the Wallops Station Flight Test Division and other range activities during prelaunch activities and countdown operations.

At approximately four months from launch a general test program description will be submitted to the Director, Wallops Station, and will contain the following information: (1) test description, (2) test vehicle description, (3) payload description, and (4) safety information.

Long-Range Planning and Scheduling - Once the above preliminary information has been submitted, the contractor must prepare and submit his long-range planning and

scheduling data. This document will be submitted three months prior to the scheduled test date and will include the following information:

1. Drawings - The drawings will give all details necessary for proper assembly of the vehicle, schematics, and wiring diagrams of all pyrotechnic circuits and umbilical connections.
2. Weight Data - The weight data will include launch weight, weight versus time curve, and weights of additional parts, such as heat shields, fairings, nozzle extension, etc.
3. Performance Data - Performance data requirements include all trajectory information for normal conditions and for all possible abnormal conditions. Plots will be required showing altitude versus range to impact for each stage, altitude versus time, velocity versus time for each stage, acceleration versus time for each stage, and drag curves versus mach number for each stage during burning and nonburning. In addition, the ignition and burnout times of each stage are required along with a preliminary dispersion analysis of impact areas in terms of 1, 2, and 3 sigma curves.
4. Launcher Information - Launcher information will include type of launcher required and any special launcher requirements relative to special pad preparation or work platforms.

5. Launch Conditions - The elevation and azimuth angles must be determined along with allowable adjustments for purposes of range safety. In addition, all information relative to the launch window must be presented.
6. Cancellation Conditions - All conditions that would require postponement or cancellation of the launch other than equipment malfunctions must be stated. These may include such items as maximum wind, clouds and visibility, temperature extremes, precipitation, humidity, etc.
7. Wallops Support Requirements - This section of the planning document will contain information concerning the amount of support required from Wallops Station and includes the services of the standards laboratory, meteorological section, instrumentation and range control systems, vehicle preparation, and launching services, data reduction, photographic section, and down-range instrumentation. Other support items, such as office and work space, furniture, etc., should also be listed.

Instrumentation requirements include skin and beacon tracking, telemetry data, command control, range time, and communications.

Master Countdown Document - A master countdown document will be prepared and submitted to the Director, Wallops Station, at least 30 days before the scheduled test

date. This document will contain detailed procedures to be followed during countdown operations and include the following:

1. Electronic systems - This section of the master countdown document will include a precountdown check list that will outline station manning requirements, vehicle check items, blockhouse check list, and range and communications check lists. In addition, procedures will be established for the checkout of the vehicle and payload instrumentation systems, command destruct, guidance, guidance-ignition programmer, and an over-all systems close-out procedure.
2. Nitrogen and hydrogen peroxide servicing - This section of the master countdown will include procedures for off-site preparation, servicing, topping off, hydrogen peroxide system test and monitor, and abort. In addition, detailed procedures will be developed for the servicing crew.
3. Vehicle launcher securing - Procedures for vehicle shakedown inspection and securing, tower heating, and air-conditioning equipment, and vehicle tower securing will be presented in this section.
4. Arming countdown - Arming countdown procedures will be prepared to perform open circuit voltage checks, ohm meter calibration, ground resistance measurements, ignition timer checks, and resistance measurements.

5. Terminal countdown - Terminal countdown will begin at T-30 min and continue through liftoff. In addition to listing conditions at start of countdown, a detailed procedure depicting sequence of events as a function of time will be outlined. These events will include the following: Energize ignition battery heaters, open tower platform, record ambient temperatures, remote torquing check, uncage system-operational test, instrumentation test-vehicle and P/2, confirmation of ignition battery heater cycling, confirmation that N_2 pressures are satisfactory, confirmation of range readiness, confirmation of payload readiness, Wallops station check, warmup burps, arming, ignition battery tests, activation of ignition key, no-load voltage checks, load check, burp test, activation of P/L power, launch console check, start of sequencer, instrumentation check using internal power, activation of guidance internal power, launch vehicle to proper launch angle, starting of recorders, uncaging of pitch, roll, and yaw gyros, release of range programmer, reset of command, removal of umbilical cables, voice countdown.
6. Emergency procedures - Emergency procedures will be established and presented in a separate section of the master countdown document. These procedures are established in the event that it becomes necessary to troubleshoot or otherwise defer the countdown.

7. Recovery period procedure - The recovery period is defined as the time between dress rehearsal and operational countdown. Procedures for this operation will be included as part of the master countdown document and involve retraction of the vehicle to the vertical position, recovery, and reinstallation of all umbilical and flyaways, connection of tower environmental control equipment, reconnect to external power, verify installation of mechanical safety pins, etc., for each section.

(d) R-F Compatibility Tests

Radio-frequency interference tests will be conducted in accordance with Specifications MIL-I-6181D and MIL-I-26600. These tests will be conducted using the facilities at LTV approximately three months prior to the scheduled test date.

(3) Test Site Operation

(a) General

At approximately two months before the scheduled test date, control of the program will be transferred to the field working group. Action will be initiated by a meeting between the contractor's field personnel and the Wallops Station project engineer. During this meeting a complete project review will be made and all parameters for the mission will be verified.

(b) Hangar Preparation and Ground-Support Equipment

Part of the support services required for the program includes adequate work area for preparation and preflight

tests of the payload and vehicle. The area should also be approved for handling and storing live rocket motors and equipped with overhead hoist. An air-pressure supply should also be available for operation of air-driven drill motors.

Other support facilities that will be required include the following:

1. Dynamic balancing facility for vertical balancing of payload
2. Facility for determining center-of-gravity, moments of inertias, and payload weight. This facility should include a swing ring, transit, calibrated weight scales, and an overhead hoist.
3. Instrumentation checkout and work area equipped with 50-amp, 115-v, 60-cps service for operation of test and ground checkout equipment. The area should be relatively dust free and reasonably air conditioned.
4. Vacuum facility consisting of an oil diffusion pumping system will be required to maintain internal pressure of the payload canister at 20 u or less.
5. Safety equipment such as hard hats and insect repellent will be required.
6. An office area near the blockhouse is required for payload administrative personnel. This area should be equipped with at least three desks and two phones, one of which can

be used to make long-distance calls after normal working hours. An intercom connected to the Wallops network should also be available.

Transportation services will be required to transport the payload between facilities.

(c) Countdown Meeting of Field Personnel

A meeting will be held two months before the scheduled launch date to finalize the information to be included in the master countdown operations plan.

(d) Payload Receiving and Inspection

The payload should arrive at Wallops Station no later than one calendar month before the scheduled test date. Upon arrival at the test site, the payload will be uncrated and given a thorough visual check to make sure that it arrived in an undamaged condition. Following the visual check, a functional test will be made of the electronic systems to determine whether or not damage was sustained during delivery from the factory.

(e) Payload Test and Checkout

With the assumption that preliminary checks mentioned in the preceding paragraphs reveal no damage or cause for corrective action, a complete test and checkout of the payload will be accomplished in accordance with established test procedures. The main base telemetering station will be required periodically during the instrumentation checkout. The various stages of the Scout vehicle will undergo test and checkout concurrently with the above tests on the payload. These tests are expected to consume approximately five working days.

(f) Countdown Procedure Verified

At approximately one month prior to the test date a countdown meeting will be held to verify and/or finalize the master countdown procedures to be followed during operations at the launch pad. This meeting will be attended by the contractor's project engineer, Wallops project engineer, and section heads of the various support sections designated by the Wallops Project Engineer.

(g) Final Range-Safety Data

A range safety plan that will delineate procedures to be followed by all personnel involved in preparation of the payload and vehicle prior to and during launch will be prepared by the range safety section. The plan will include the following data:

1. Responsibility for implementation of safety requirements
2. A description of the vehicle motor, igniters, squib characteristics, and method of actuation. Minimum and recommended firing currents and squib resistance are also required
3. Description of auxiliary pyrotechnic devices
4. Description of the destruct system
5. Pyrotechnic checkout, staging, and precautions procedures at the launch area
6. Abort and recovery procedures
7. Area definitions relative to the launch area, launch pad, hazard area, etc.
8. Times of caution and/or danger during countdown or preparations for countdown.

9. R-f energy requirements and/or restrictions
10. Use of warning systems
11. Requirements and/or restrictions relative to types of tests to be conducted

(h) Systems Test

Upon completion of subsystems test and checkout, the payload will be mounted to the fourth stage and together they will be given a complete dynamic balance. The center of gravity and moments of inertia will be determined during this operation. After satisfactory completion of the systems test, the vehicle and payload will be disassembled and moved to Wallops Island for reassembly on the launch pad.

(4) Launch Pad Operations

(a) Vehicle Assembly and Checkout

General - After delivery of the payload and vehicle to the launch pad, these units will be assembled into the final flight configuration and undergo a complete test and checkout as an operating system. Four days are allocated for the complete operation of disassembly at the test site, transporting all units to the launch pad, and reassembly. Two days will be required, starting at T minus 10 working days, to install the heat shield and erect the vehicle on the tower.

Vehicle Checkout - The vehicle electronics system will be tested with the payload in an operational status. The purpose of this test is to ensure r-f compatibility between the payload and Scout vehicle. This test will be performed during the seventh day prior to launch.

Payload Operation and Checkout - The payload will be given its final checkout prior to start of countdown during the sixth working day prior to launch. During this time, telemetry and beacon checks will be made along with the instrumentation, power supplies, and the command control receiver. Services of Wallops main base telemetry station will be required during the above tests.

Launcher Operational Checks - Launcher operational checks will begin five days before launch. These checks will include, but will not be limited to the following: (1) installation of lanyards and flyaways, (2) tower heating and air-conditioning systems, (3) electrical verification tests, (4) inspection and conditioning of all mechanical interface connections, and (5) simulated flight test to prove combined vehicle, payload, range, and procedural compatibility. R-f compatibility checks will also become a part of these tests.

Vehicle Ignition Checkout - Priority will be established for checkout of the vehicle ignition system during the fourth day before launch. These tests will include ground and continuity checks of ignition switches and monitoring circuits for each stage. No payload checks will be made during this time.

Pyrotechnics Installed - The flight pyrotechnics will be installed during the third working day prior to the scheduled launch day. Bridge wire resistance measurements will be made and the firing circuits and shields will be tested for continuity. An orderly procedure will be provided for the performance and documentation of each check. All readings will be compared with reference values to verify that resistance of the pyrotechnics has

not changed and that an open circuit does not exist due to improper connections or wire breakage.

Final Inspection - Final inspection of the vehicle and payload will be made to verify complete readiness of the vehicle and all systems for launch. This activity will occur two days before the scheduled launch day.

Dress Rehearsal - A complete dress rehearsal for launching the test vehicle will be made the day before the scheduled launch day. Procedure for the dress rehearsal will be the same as those outlined in the master countdown document. This will include an electronics system, nitrogen and hydrogen servicing, vehicle/launcher securing procedure, arming, terminal countdown, and a recovery period procedure.

(b) Launch

Countdown for launching the vehicle will begin approximately six hours before launch time. A time schedule of the various events is presented in Figure 210. Actual countdown will begin with electronic systems checkout starting at T-5.75 hr. Details of the complete countdown procedure will be contained in the master countdown document.

(c) Backup Unit

A backup payload and vehicle will be available at the test site in the event of catastrophic malfunctions detected prior to actual launch or in the event that the flight must be aborted subsequent to launch.

c. Orbital Test and Support

(1) General

Orbit test and support activities include mission experiment, tracking, data collection and processing, and data evaluation

and analysis. Operation plans for each area are discussed in subsequent paragraphs.

(2) Stabilization System

It has been estimated that oscillations in the roll axis will be on the order of 2 cycles per orbit, and in the pitch axis approximately $\sqrt{3}$ or 1.7 cycles per orbit. Therefore, a minimum of four measurements must be made during each orbit to evaluate the stabilization system.

(3) R-F Reflectivity Measurements

All the parameters for conducting the r-f experiment have not as yet been established. However, in general, it can be concluded that bistatic reflectivity measurements will be made during the time when the ground path of the satellite's orbit is within the continental limits of the United States. The frequency of the signal and type of modulation will be determined from results obtained during ground tests.

(4) Mission Experiment

The primary objective of the experiment is to prove the feasibility of using gravity-gradient stabilization techniques for large passive communications satellites. Secondary objectives are to evaluate r-f reflectivity characteristics of the lenticular shape and to prove feasibility of using the proposed deployment and inflation techniques for the full-scale model. To accomplish these objectives, an instrumentation system will be designed and installed as part of the payload.

The onboard instrumentation system will be used for the measurement, storage, and transmission of test data. Basically, the system consists of a commutator, a voltage-controlled oscillator, tape recorder, command control receiver, beacon, programmer, sensors, and signal conditioners. Functions of

the sequence and control system, and the inflation and rigidization system will be monitored throughout deployment of the satellite. Once deployment is complete, power will be switched to the orbital orientation functions for monitoring attitude and temperatures for the duration of the mission experiment. The commutator is employed to sample the output sequentially from each sensor at a rate of two samples per second. The resulting pulse train is then used to modulate the voltage-controlled oscillator. The modulated output from the oscillator is then recorded on magnetic tape for storage, and subsequent playback upon command from one of the ground receiving stations. The command receiver will also have a channel to permit real-time monitoring of the data when the satellite is within range of a receiving station. The command receiver will operate at an assigned frequency in the 148-mc band, and interrogation signals will be provided by the Collins 242G-2 vhf transmitter installed at the receiving sites.

A beacon transmitter will be provided to perform two functions. The first of these is to generate the signal necessary for tracking by the ground receiving stations and the second is to telemeter the data obtained by the instrumentation system. The beacon will be a pulsed system and will operate in the 136- to 138-mc frequency band. This system was selected because of its compatibility with the Minitrack tracking network.

(5) Tracking

During liftoff and ascent to orbital injection, the tracking facilities of Wallops Island, Wallops telemetry ship, and Bermuda will be required. In addition, the Minitrack station located at Fort Myers, Florida, may be used to provide backup data.

A list of equipment required during this portion of the flight is presented in Table LII and includes radar optics, telemetry, command destruct, and communications.

TABLE LII - TRACKING STATION AND EQUIPMENT REQUIREMENTS DURING
ASCENT AND ORBIT INJECTION

Equipment	Model	Purpose	Equipment Location				Wallops telemetry ship
			Wallops Station	GSFC	LRC	Bermuda	
Radar	FPS-16	Beacon and skin track	x			x	
	M. I. T.	Skin track	x				
	SCR584	Skin track	x				
	MOD II	Skin track	x				
	SPANDAR	Skin track	x				
Optical	VERLORT	Long-range skin track				x	
	IGOR	Document performance and sequence of events	x				
	RT-2	Document performance and sequence of events	x				
	FASTEX	Vehicle performance at liftoff	x				
	BC-4	Position and velocity				x	
	RC-5	Position				x	
	KC-24	Position wide coverage				x	
Telemeter	K-24	Position secondary				x	
	PE610	High magnification for event study				x	
	FM	Data acquisition and readout	x	x	x	x	x
	FRW-3	Safety	x			x	
	SCAMA	Communications	x			x	
Radio	General	Communications	x	x	x		
	SSB		x			x	x

During the remainder of the orbital flight and throughout mission life of the experiment, the tracking and data acquisition functions will be performed by facilities of the Minitrack tracking network. The stations along with their geodetic locations and the orbits during which their tracking services will be required are presented in Tables LIII²⁶ and LIV, respectively.

Note that an instrument ship will have to be provided for tracking and command functions during the deployment sequence, since these events will occur during a time when the satellite is out of r-f range with a Minitrack tracking station.

Assuming that the satellite's orbit is circular at an altitude of 800 naut mi, the period would be approximately 115 min, and during the thirteenth orbit, the ground path of the first orbit would essentially be repeated. Also, with the satellite at 800 naut mi the r-f line-of-sight from horizon to horizon will be approximately 5000 naut mi. A plot showing earth's ground path for the first 12 orbits is presented in Figure 211. The envelope of the composite r-f coverage of the Minitrack network is also plotted. In addition to the above plot, the length of time that the satellite will be in view from each station during the first 13 orbits was determined. These data are presented in Figure 212.

(6) Data Collection and Processing

The acquisition of test data from onboard instrumentation will be obtained from each tracking station in accordance with a schedule to be outlined in the operations plan. In general, however, the received telemetry signal will be demodulated and the video output from the receiver will be recorded on magnetic tape along with a reference frequency that can be used for compensation of data error due to wow and flutter characteristics of different tape recorders. The output from

a binary time code generator and voice commentary will also be recorded on separate tracks of the magnetic tape. These tapes will then be sent to Wallops Station for further processing and data evaluation.

(7) Data Evaluation and Analysis

Evaluation and analysis of the telemetered data will be performed jointly by personnel assigned to the program by Langley Research Center and by the payload contractor. Results from the analysis will then be published in progress reports and subsequently in a final report.

TABLE LIII - GEODETIC LOCATION OF MINITRACK STATIONS

Station location	East Longitude	Latitude	Elevation (ft)
Blossom Point, Md.	282-54-48.170	N-38-25-49.718	15
St. Johns, Newfoundland	307-16-43.240	N-47-44-29.049	400
Fort Meyers, Fla.	278-08-03.887	N-26-32-53.516	11.56
East Grand Forks, Minn.	262-59-21.556	N-48-01-20.668	823
Esselen Park, South Africa	028-14-28.376	S-26-01-56.845	5370
Woomera, Australia	136-46-59.52	S-31-06-09.49	510
Goldstone Lake, Calif.	243-06-02.776	N-35-19-48.525	3044
Quito, Ecuador	281-25-14.77	S-00-37-21.751	11703
Fairbanks, Alaska	212-09-47.387	N-64-52-18.591	527
Lima, Peru	282-50-58.184	S-11-46-36.492	161
Antofagasta, Chile	289-43-36.838	S-23-37-15.993	1703
Santiago, Chile	289-19-51.283	S-33-08-58.106	2280
Winkfield, England	359-18-14.615	N-51-26-44.122	215
Instrument Ship*	150-00-00	N-15-00-00	0

* Due to mobility of the instrument ship, location is approximated.

TABLE LIV - MINITRACK FACILITIES REQUIRED FOR TRACKING AND

DATA ACQUISITION

Tracking Station	Orbit											
	1	2	3	4	5	6	7	8	9	10	11	12
Blossom Point, Md.	x	x	x	x						x	x	x
St. Johns, Newfoundland*	x	x								x	x	x
Fort Meyers, Fla.	x	x	x	x						x	x	x
East Grand Forks, Minn.*	x	x	x	x								x
Esselen Park, South Africa	x	x	x	x	x							
Woomera, Australia	x	x				x			x	x	x	x
Quito, Ecuador*		x	x	x	x	x		x	x	x	x	x
Fairbanks, Alaska		x	x									
Lima, Peru			x	x	x	x	x	x	x	x	x	
Antofagasta, Chile*				x	x	x	x	x	x	x		
Santiago, Chile*				x	x	x	x	x	x	x		
Winkfield, England								x	x	x	x	x
Goldstone Lake, Calif.	x	x	x	x	x							x
Instrument Ship	x	x										x

*These stations could be relieved from tracking duties since area coverage can be supplied by other facilities.

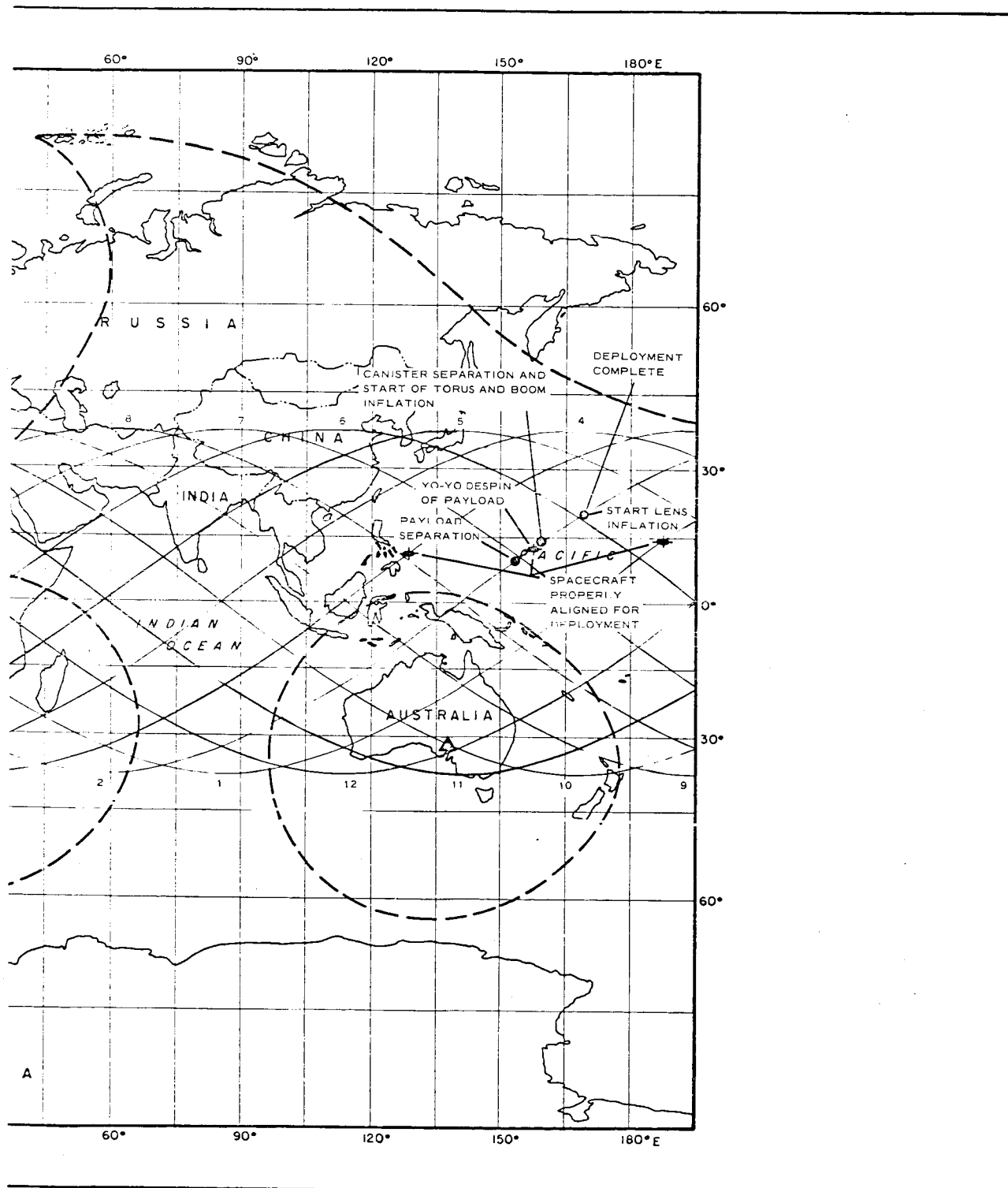
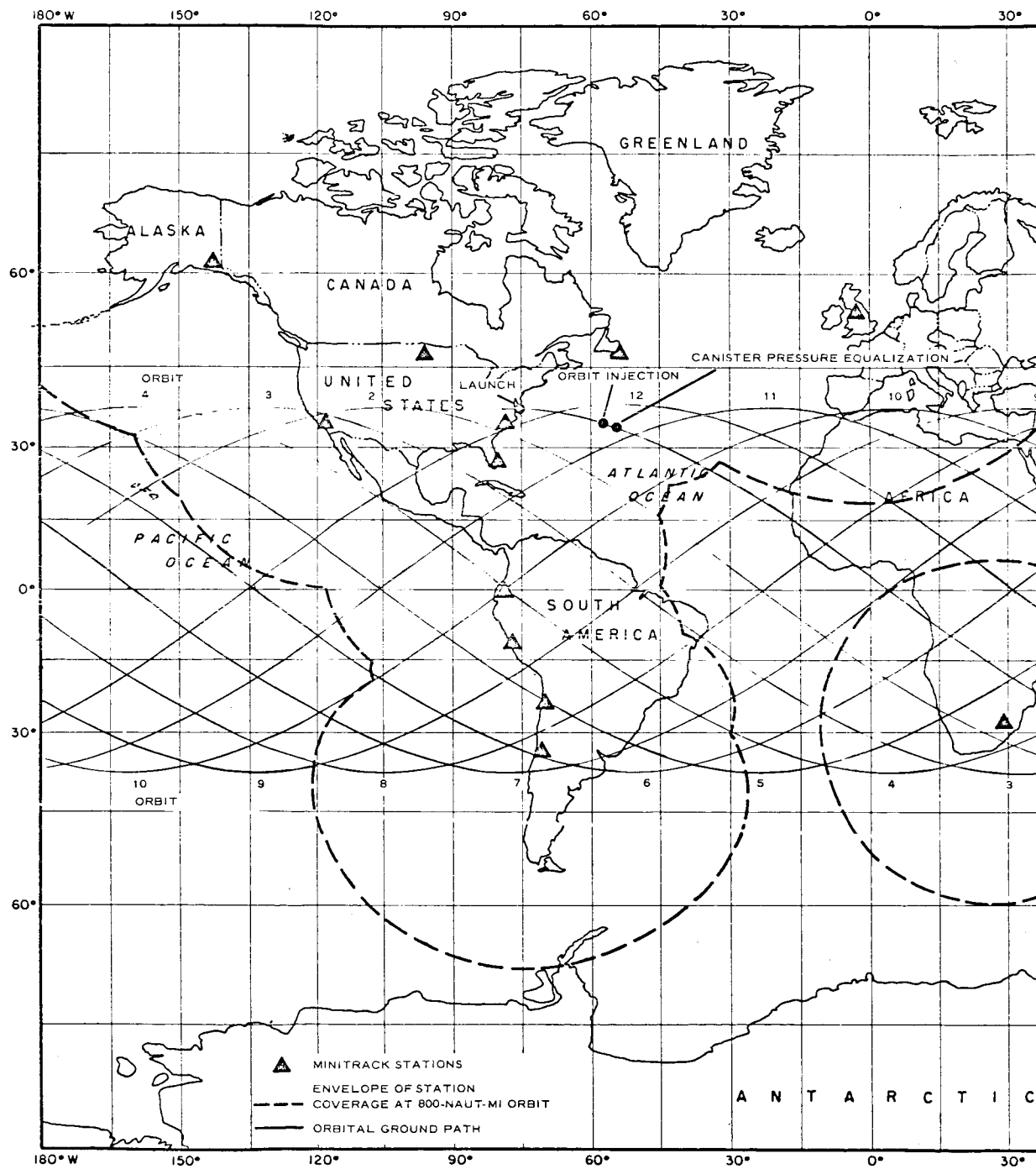


Figure 211 - Flight Test Orbits and Operational Sequences for 800-Mile Orbit



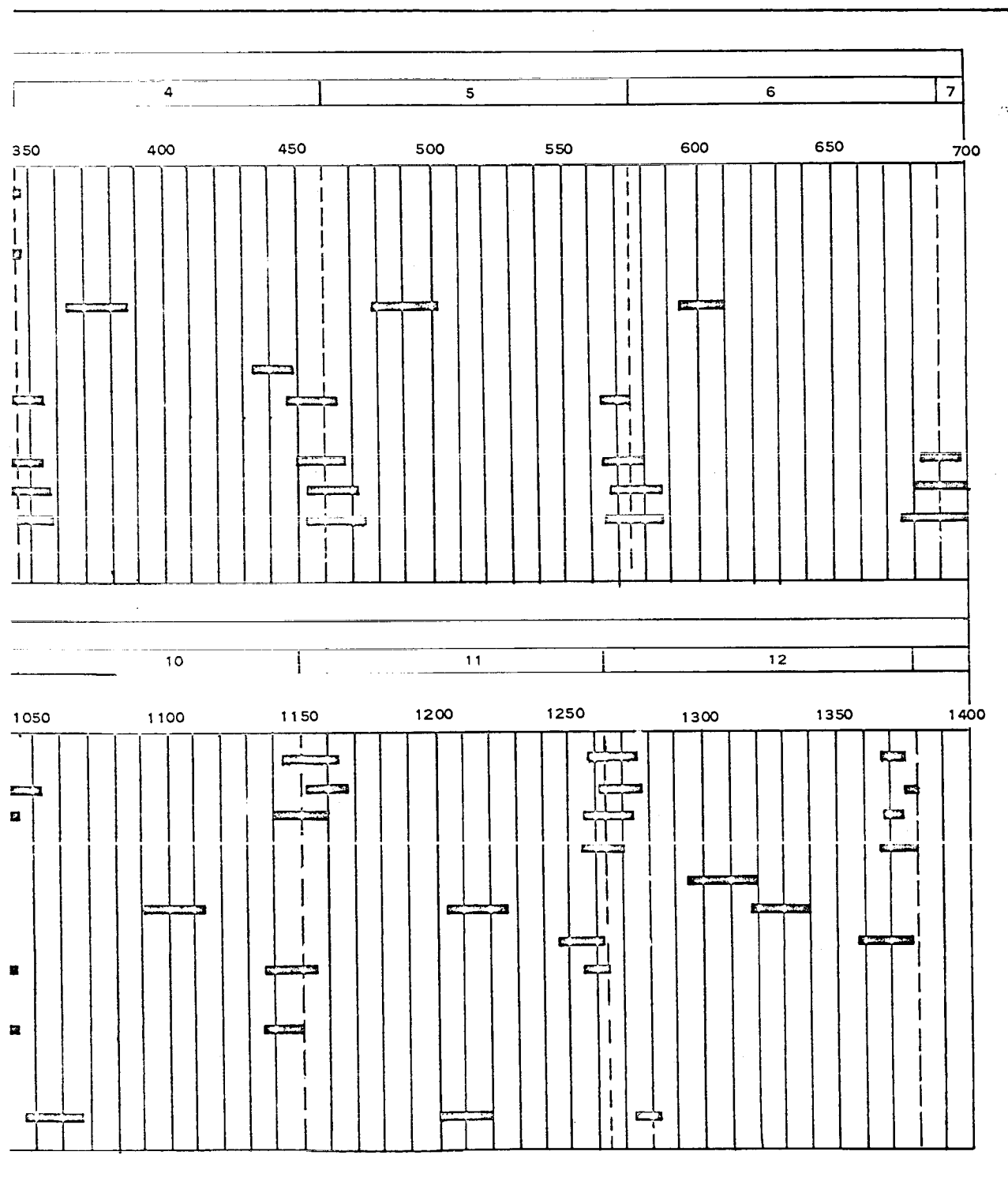


Figure 212 - Ground Station Acquisition Times

SECTION V - LENTICULAR SATELLITE TRADE-OFF STUDIES

1. GENERAL

GAC research and development funded system studies were conducted to complement the lenticular satellite development program and to aid future planning in terms of potential capability and best application. This effort involved communication system considerations and parametric trades. Certain significant aspects are summarized below.

2. REVIEW OF LENTICULAR CONCEPT AND GEOMETRY

Because of the ground station and satellite orbit geometry, only a small portion of a spherical satellite, such as Echo, is required for radio reflection between two points on the earth at any particular time. The lenticular concept (see Figure 213) takes advantage of this situation by using the material that would have comprised a sphere to form a lenticular shape with a larger radius of curvature, ρ , and hence a much larger reflection cross-section, σ , which is proportional to ρ^2 for a given weight. A lenticular shape is defined as the spherical cap formed by the intersection of a sphere and a plane. The lenticular angle is defined by a cone extending from the center of curvature to the sphere-plane intersection.

For a single-relay satellite communication system, the required lenticular angle, θ , is a function of orbital altitude and can be defined simply as the angle from the satellite that subtends the earth's horizon. As the orbital height, H , increases, the lenticular angle decreases, which gives a lenticular advantage with altitude. Plots of the lenticular angle and the lenticular advantage over an equivalent-weight sphere in the form of σ/ρ_0 for a reference altitude of 1700 naut mi are plotted versus orbital altitude in Figure 214. The values are also given in Table LV.

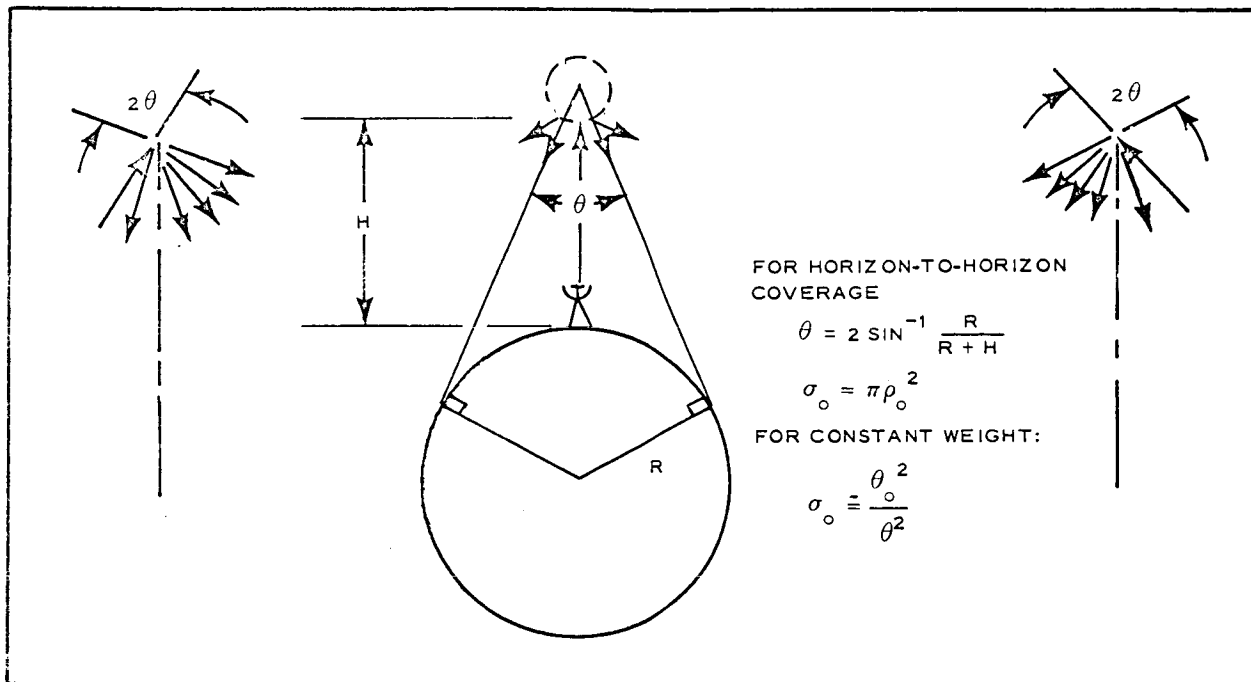


Figure 213 - Lenticular Geometry

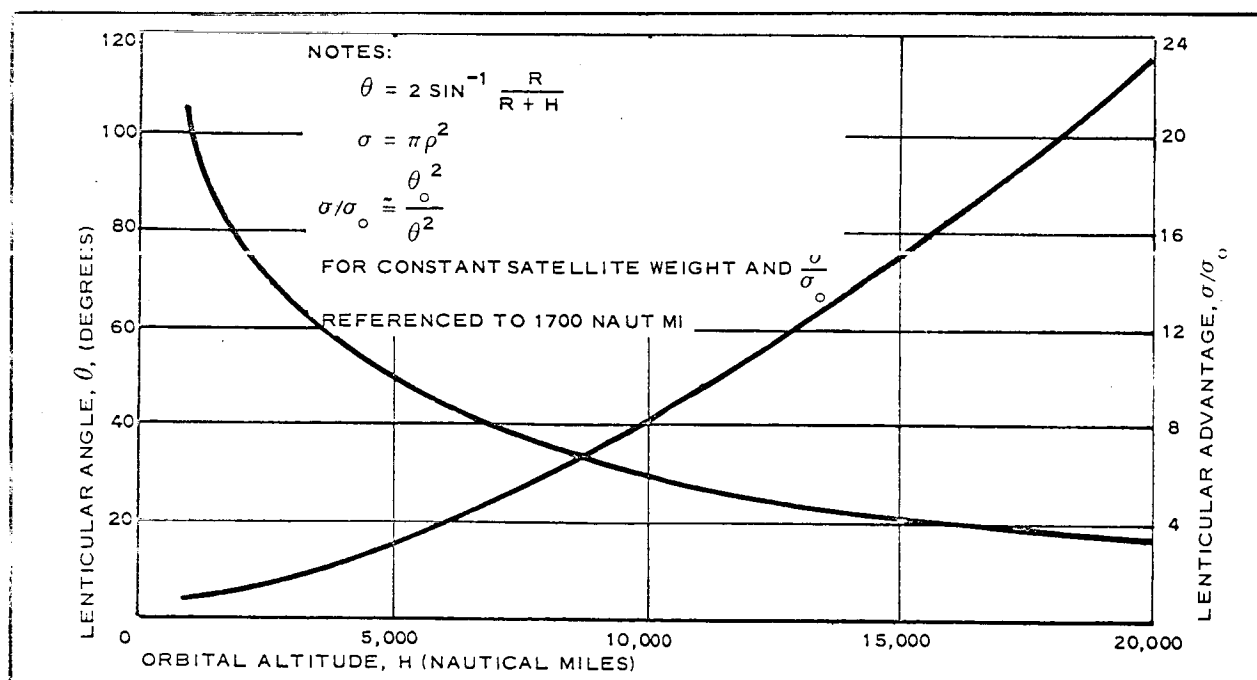


Figure 214 - Lenticular Angle and Lenticular Advantage

TABLE LV - LENTICULAR ANGLE AND LENTICULAR
ADVANTAGE FOR VARIOUS ORBITAL ALTITUDES

H (naut mi)	θ (deg)	σ/σ_o
1,000	101.6	0.5
2,000	78.4	1.1
3,000	64.6	1.7
5,000	48.0	3.1
10,000	59.6	8.1
20,313	17.4	23.3

The possibility of employing a lenticular angle reduced from the simple criterion above to yield a further advantage in weight or reflection cross-section is discussed in Item 6, "Lenticular Angle Criteria and Coverage," below.

The lenticular concept employs an oriented reflecting surface and, as such, incorporates a stabilization and damping system.

3. LENTICULAR PHYSICAL CHARACTERISTICS AND WEIGHT SCALING

The present full-scale lenticular design weighs about 1250 lb, including canister and deployment equipment and material. It has a radius of curvature of 200 ft, a lenticular angle of 84 deg, and a diameter of 267 ft. Plots of scaled weight, W , versus lenticular angle for several curvatures and versus satellite diameter, D , are shown in Figure 215, based upon the following scaling relationship:

$$\begin{aligned}
 W &= W_0 \left(\frac{\rho}{\rho_0} \right)^2 \left(\frac{\theta}{\theta_0} \right)^2 \\
 &= W_0 \left(\frac{D}{D_0} \right)^2 .
 \end{aligned}$$

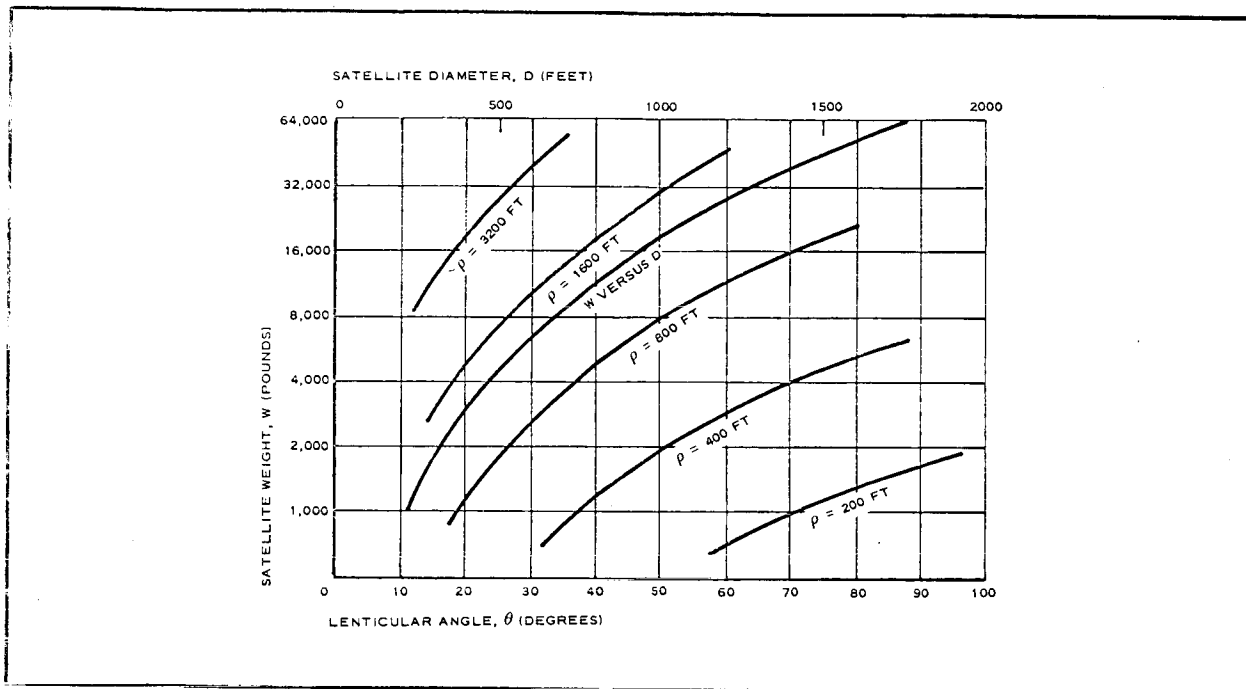


Figure 215 - Satellite Weight versus Lenticular Angle and Diameter

4. MICROWAVE COMMUNICATION PARAMETERS

A passive satellite relay communication system involves the propagation of signals through large distances with resulting attenuation effects. System considerations involve the parametric trades that can be made. A system of satellites is assumed here, sufficient to provide a single-relay satellite within the common region of the fields of view of two ground stations. The conditions for its achievement are discussed in Item 6, "Lenticular Angle Criteria and Coverage," below.

Power is generated in a transmitter, radiated from an antenna, propagated to the reflecting satellite, reradiated, propagated back to a receiving antenna, detected, and processed. The information is encoded by the technique of modulation. The amount of information achievable is related to the band width and noise level. Band width (B) is related to power, carrier-to-noise ratio (C/N), and a reception characteristic customarily expressed as the receiver noise temperature (T_R).

If the transmitting antenna has an actual gain of G_T and radiates power of P_T watts, the power density at a distance L_1 will be $G_T P_T / 4\pi L_1^2$. The microwave reflection cross section of a lenticular section is the same as that of a sphere and is $\sigma = \pi \rho^2$. This can be illustrated simply in a monostatic case. The amount of power intercepted by a lenticular section axially illuminated is equal to the product of the power density and the projected area $\pi \rho^2 \sin^2 \theta / 2$. The lenticular section radiates this energy into a solid angle of $2\pi(1 - \cos\theta)$. The reradiated power density at a distance L_2 will then be $(G_T P_T / 4\pi L_1^2)(\pi \rho^2 / 4\pi L_2^2)$, an expression identical to that for a spherical satellite of isotropically scattering cross section $\sigma = \pi \rho^2$. Thus, the effective lenticular area is $\pi \rho^2$. The amount of power (P_R) received by an antenna is equal to the product of the power density and the effective collecting area (A_R). Since isotropic gain is $4\pi A / \lambda^2$, an expression for free-space path loss (L) results upon rearranging in the customary form

$$L = \frac{P_R}{P_T}$$

$$= \frac{G_T G_R G_S \lambda^4}{(4\pi)^4 L_1^2 L_2^2},$$

and band width is

$$B = \frac{P_R}{\frac{C}{N} K T_R}$$

$$= \frac{P_T G_T G_R G_S \lambda^4}{\frac{C}{N} K T_R (4\pi)^4 L_1^2 L_2^2},$$

expressed in terms of ground station and relay gain (or area if converted directly through the relationship between gain and area as a function of wave length or frequency).

It is customary in communication engineering to perform calculations in the convenient form of decibels. The band width equation becomes:

$$B = P_T + G_T - \alpha_1 + G_S - \alpha_2 + G_R + KT_R - \frac{C}{N},$$

with isotropic path loss

$$\alpha = 38 + 20 \log L_1 + 20 \log f.$$

It can be seen that band width is directly proportional to P_T , G_T , G_R , ρ^2 (A_T , A_R , f^2) and inversely proportional to C/N , T_R , λ^2 , L_1^2 , and L_2^2 .

5. LENTICULAR COMSAT COMMUNICATION SYSTEM CAPABILITY

Communication capability can be illustrated through parametric band-width considerations. Consideration of existing ground terminals, such as Telstar, Comsat, and Syncom II, indicates that a reference ground terminal condition might be P_T of 10 kw, D_R of 85 ft, T_R of 58 K, f of 8000 mc, and C/N of 40. A P_T of 100 kw would also be a reasonable condition.

In Figure 216 equivalent reflected power is plotted versus slant range for parametric values of lenticular curvature and transmitter power. It can be seen that sizable numbers of watts of equivalent reflected power as defined by the equation can be achieved with the lenticular satellite.

The communication band width achievable with the lenticular satellite in a moderately low orbit of 2000 naut mi is shown in Figure 217 as a function of receiving antenna diameter for typical parametric conditions of lenticular cross section, main terminal transmitting power, and receiver noise temperature. The chart is equally applicable to communication back from the remote to the main terminal if the values of transmitting power shown are reduced by the ratio of receiver noise temperature. A few teletype or voice channels are achievable with very small receiving antennas, and broadcast capability is possible.

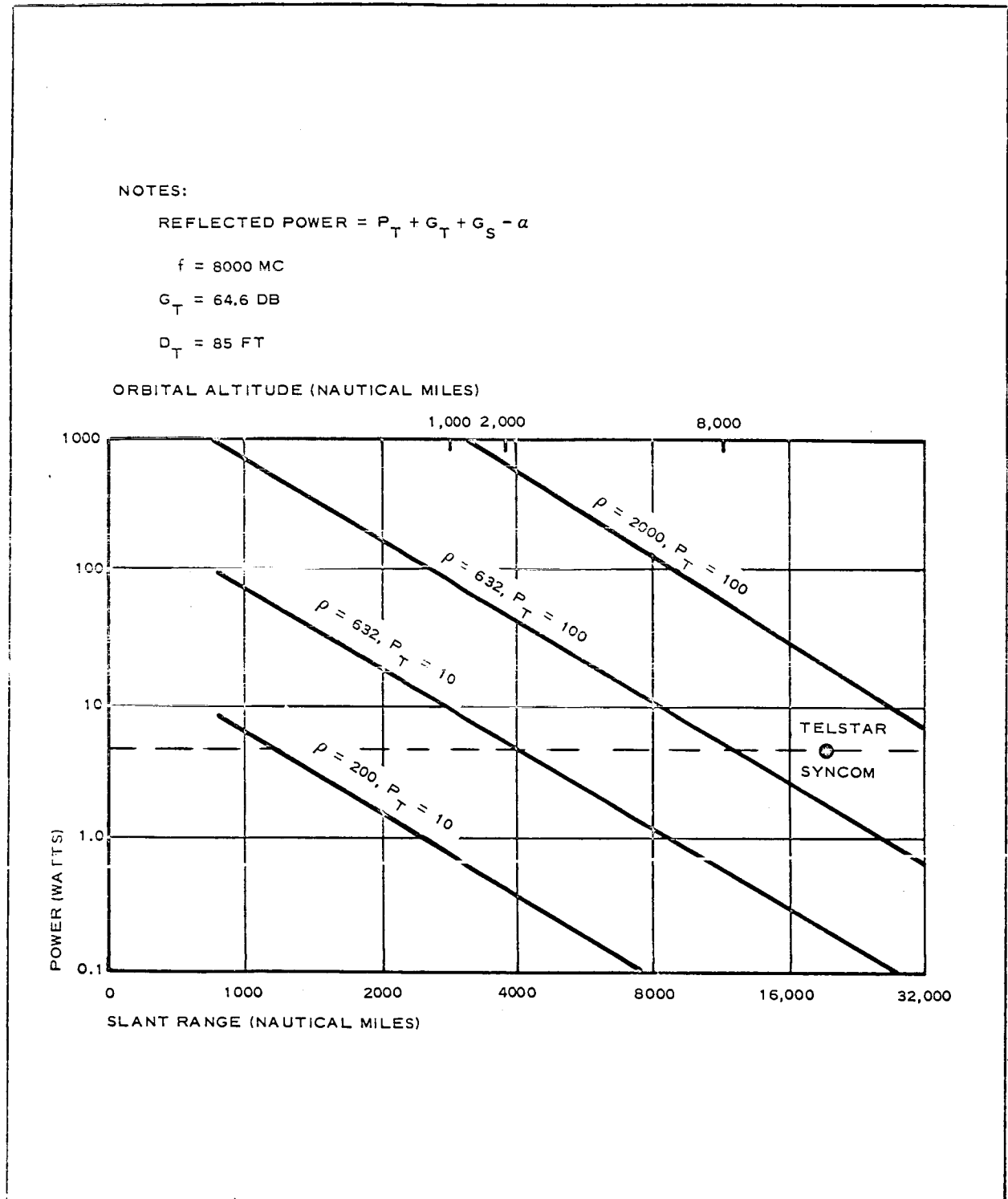


Figure 216 - Equivalent Reflected Power versus Slant Range

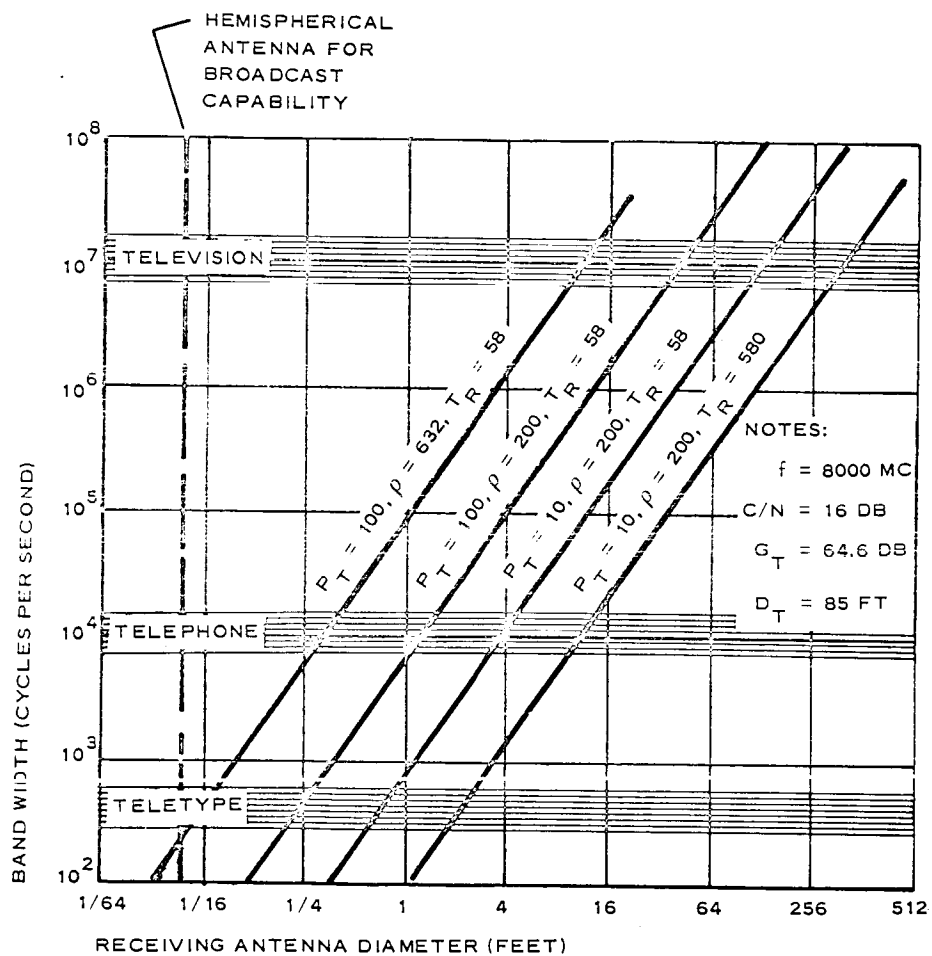


Figure 217 - Band Width versus Receiving Antenna Diameter for 2000-Naut-Mi Orbit

The weight of an Echo-type passive satellite scaled to synchronous orbit becomes prohibitive because of the large diameter required to balance the square law isotropic path loss. However, the lenticular concept provides a weight advantage with altitude, which effectively cancels the one-way path loss at higher altitudes. Hence, the situation becomes somewhat analogous to that of active systems, and the capability of a few satellites to provide continuous service without handover at synchronous orbit warrants their consideration for lenticular passive satellite applications. However, station keeping and gravity-gradient stabilization of synchronous systems are problems requiring further consideration. Figure 218 plots band width versus satellite diameter at synchronous orbit for several ground environments. Values of satellite weight and radius of curvature are also shown on the abscissa. A lenticular angle of 20 deg was assumed, with weight and radius of curvature scaled from the current lenticular design.

6. LENTICULAR ANGLE CRITERIA AND COVERAGE CONSIDERATIONS

It was shown earlier that the lenticular configuration possesses a radio reflection cross section-to-weight advantage over a sphere. Preliminary study results indicate that a further advantage in weight or reflection cross section can be achieved through the use of smaller lenticular angles than specified by the simple horizon subtending criterion described previously and used in the present preliminary design. An improvement of between 5 to 10 db is achievable. However, the number of satellites and handover frequency to provide a desired service continuity are increased. Several considerations are involved.

First, ground terminal coverage down to the horizon is impractical for both the transmitter and receiver. The minimum value of usable antenna beam elevation angle (ϵ) is typically between 5 to 10 deg above the horizon.

Second, for two ground terminals separated a distance S , a limiting condition exists for mutual visibility of a satellite orbiting at altitude H . The

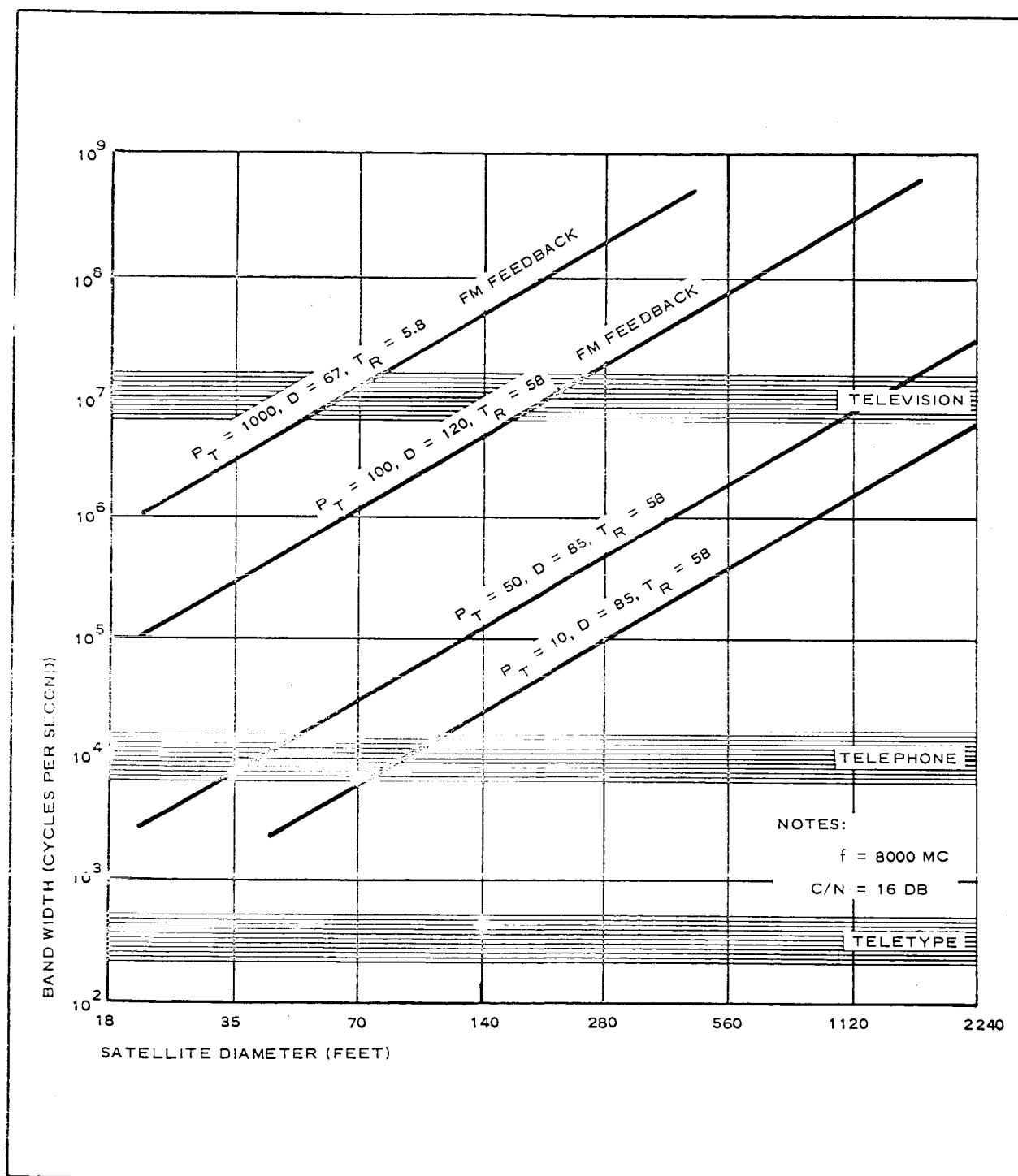


Figure 218 - Band Width versus Satellite Diameter for Synchronous Orbit

lenticular angle required is specified at the maximum extension of the mutual visibility region and becomes smaller at greater station separation.

Third, lenticular angles smaller than required for use throughout the mutual visibility region can be employed. The lenticular mutual communication region is then smaller, which requires a greater number of satellites to provide a desired relay service probability. However, increased band width or reduced weight in orbit results.

In all cases, because the lenticular satellite is an oriented configuration, the usable angle is smaller than the configurational value due to stabilization and damping error.

The lenticular angle required for relay communication throughout the mutual visibility region of two ground terminals (sphere equivalent coverage) is given in Table LVI and shown in Figure 219 as a function of orbital altitude for typical parametric conditions of terminal separations and minimum usable elevation angle (ξ).

TABLE LVI - LENTICULAR ANGLE AS FUNCTION OF
COMMUNICATION LINKS

H (naut mi)	θ S = 0, $\xi = 0$ (deg)	θ S = 0, $\xi = 10$ (deg)	θ S = 2000, $\xi = 5$ (deg)	θ S = 3000, $\xi = 5$ (deg)	θ S = 4000, $\xi = 5$ (deg)
1,000	101.6	99.4	92.5	77.8	33.1
2,000	78.4	77.0	73.2	66.5	54.9
3,000	64.6	63.4	61.8	57.0	49.6
4,000	55.1	54.1	52.0	48.2	42.7
6,000	42.7	42.0
8,000	35.0	34.4	33.0	31.1	28.4
10,000	29.6	29.1

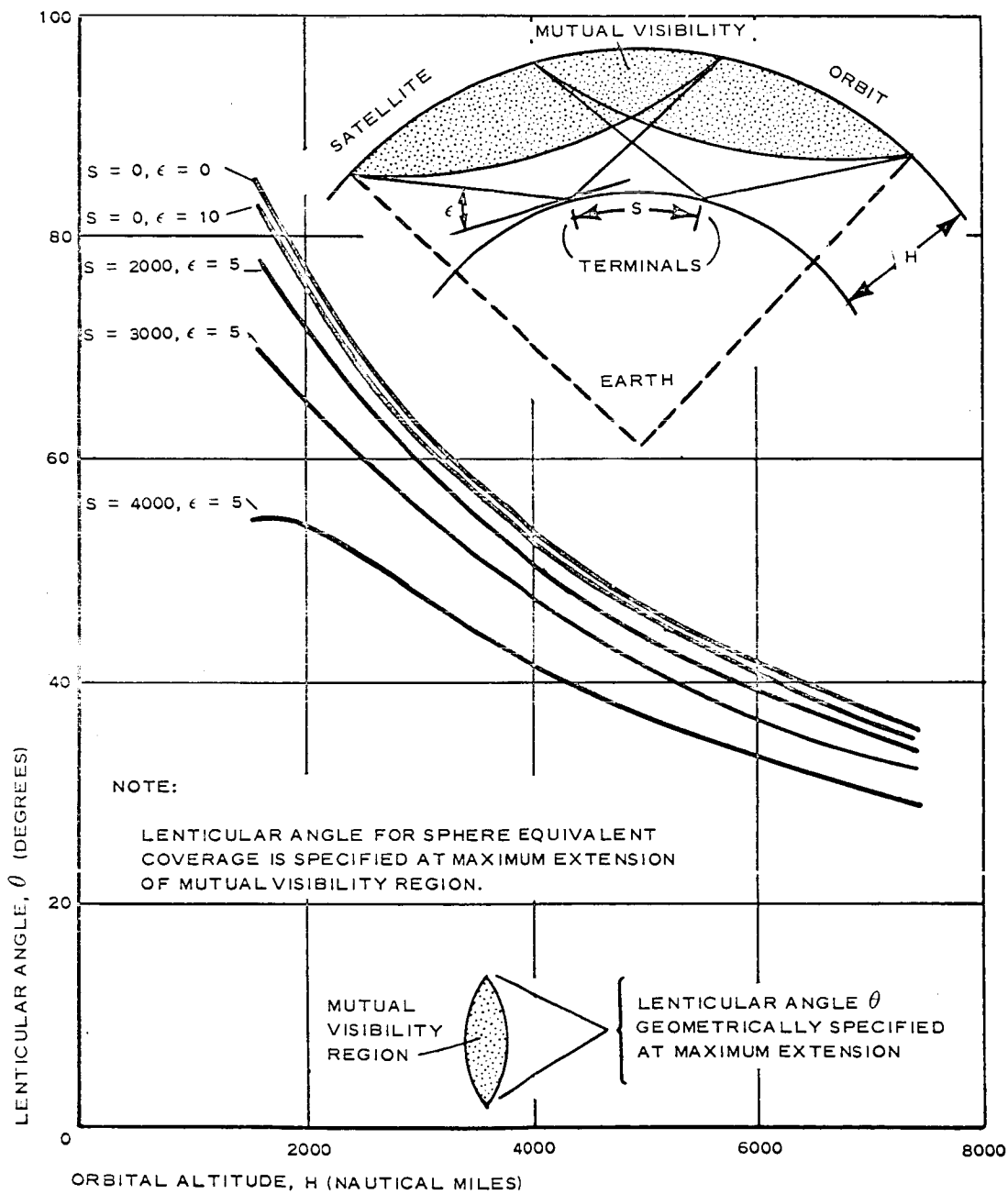
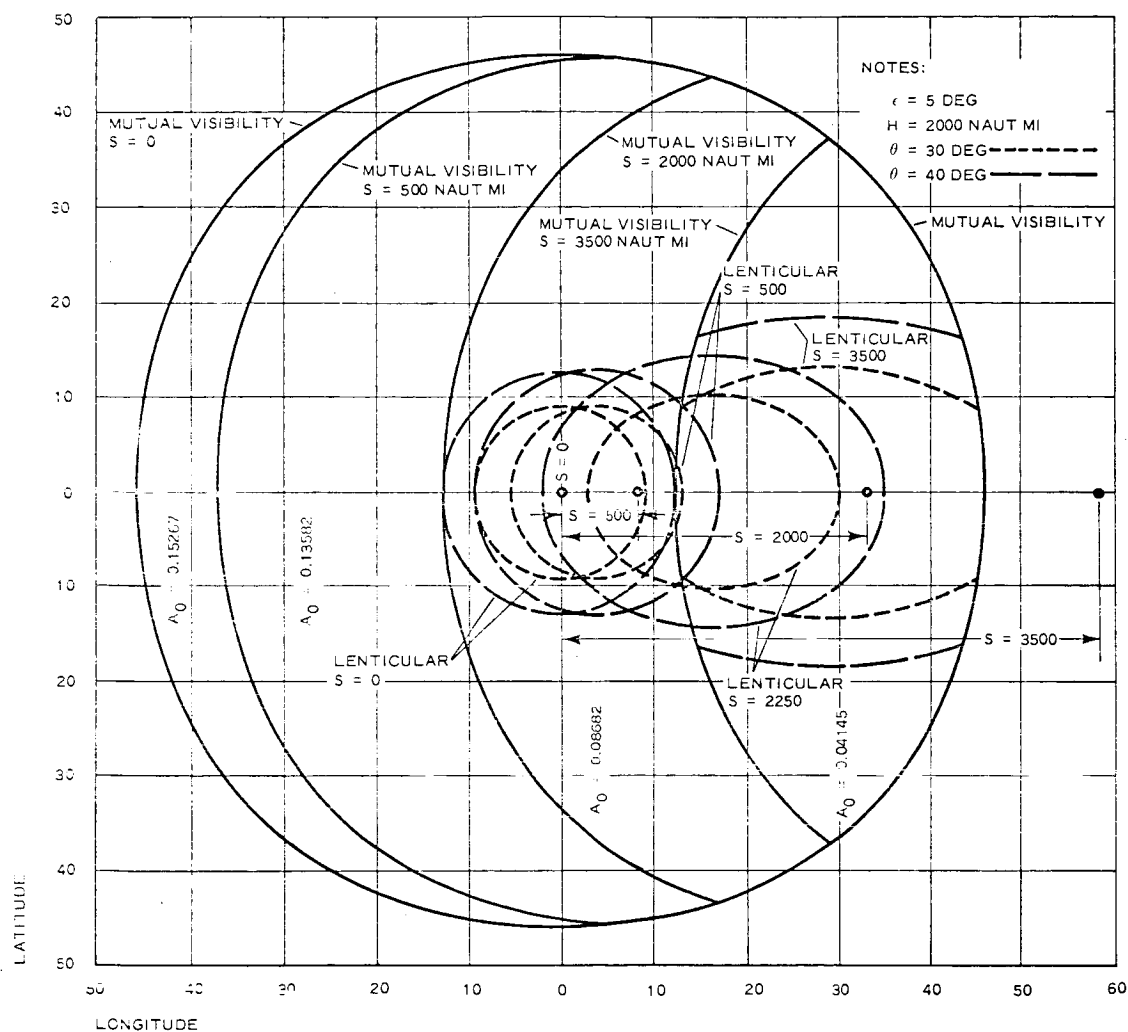


Figure 219 - Lenticular Angle versus Orbital Altitude

Figure 220 shows the mutual visibility region and the lenticular coverage regions of 30- and 40-deg lenticular satellites in a 2000-naut-mi circular orbit for a 5-deg minimum elevation and several station separations at zero latitude. It can be seen that the mutual visibility region of two ground terminals is of a somewhat lenticular shape with the major axis normal to a line connecting the two stations. The lenticular satellite mutual communication region is of somewhat elliptical shape with the major axis aligned with the terminals, modified in some cases by the elevation limit. As the lenticular angle is reduced below that value just providing full coverage of the mutual visibility region, the area of the mutual communication region is reduced. Hence, more satellites are required, and their individual duration of use per pass is reduced. However, their individual weight is less, and the communication path loss is reduced since the slant range is less. A net advantage in communication band width, or weight in orbit, results for reduced lenticular angle. The expression shown in Figure 220 gives an approximate constant circuit probability relationship with lenticular angle of band width for constant weight in orbit and orbital weight for constant band width for a worldwide random system. Area ratios and communication band width or orbital weight advantages are tabulated. The coverage regions shown are for illustration only, and the values of advantage or improvement given are referenced to sphere equivalent coverage. The advantage would be greater if referenced to the present preliminary design employing a lenticular angle of 84 deg. Terminals actually on the equator could of course employ an equatorial orbit with the number of satellites dependent on the longitude width of the coverage region.

Figure 221 presents a polar stereographic plot of the mutual visibility and lenticular coverage zones for a typical link from Eastern United States to Western Europe. Two terminals are spaced 3000 naut mi at 45 deg north latitude. Orbital altitude is 2000 naut mi. Lenticular angles are 66.5, 40, and 30 deg. Probabilities of communication relay for a single satellite



FOR CONSTANT CIRCUIT PROBABILITY,

$$\left(\frac{B}{B_0}\right)_{W \text{ CONSTANT}} = \frac{A}{A_0} \left(\frac{W_0}{W}\right)^2 \frac{(L_1 L_2)_0^2}{(L_1 L_2)^2} = \left(\frac{W_0}{W}\right)_{B \text{ CONSTANT}}$$

S (NAUT MI)	θ (DEG)	AREA RATIO		B OR W ADVANTAGE (DB)	
		30 DEG	40 DEG	30 DEG	40 DEG
0	78.2	0.042	0.081	5.3	4.3
500	77.8	0.049	0.094	5.6	5.1
2000	73.2	0.124	0.233	6.6	6.0
3500	61.6	0.454	0.648	7.0	5.3

Figure 220 - Mutual Coverage, Example A

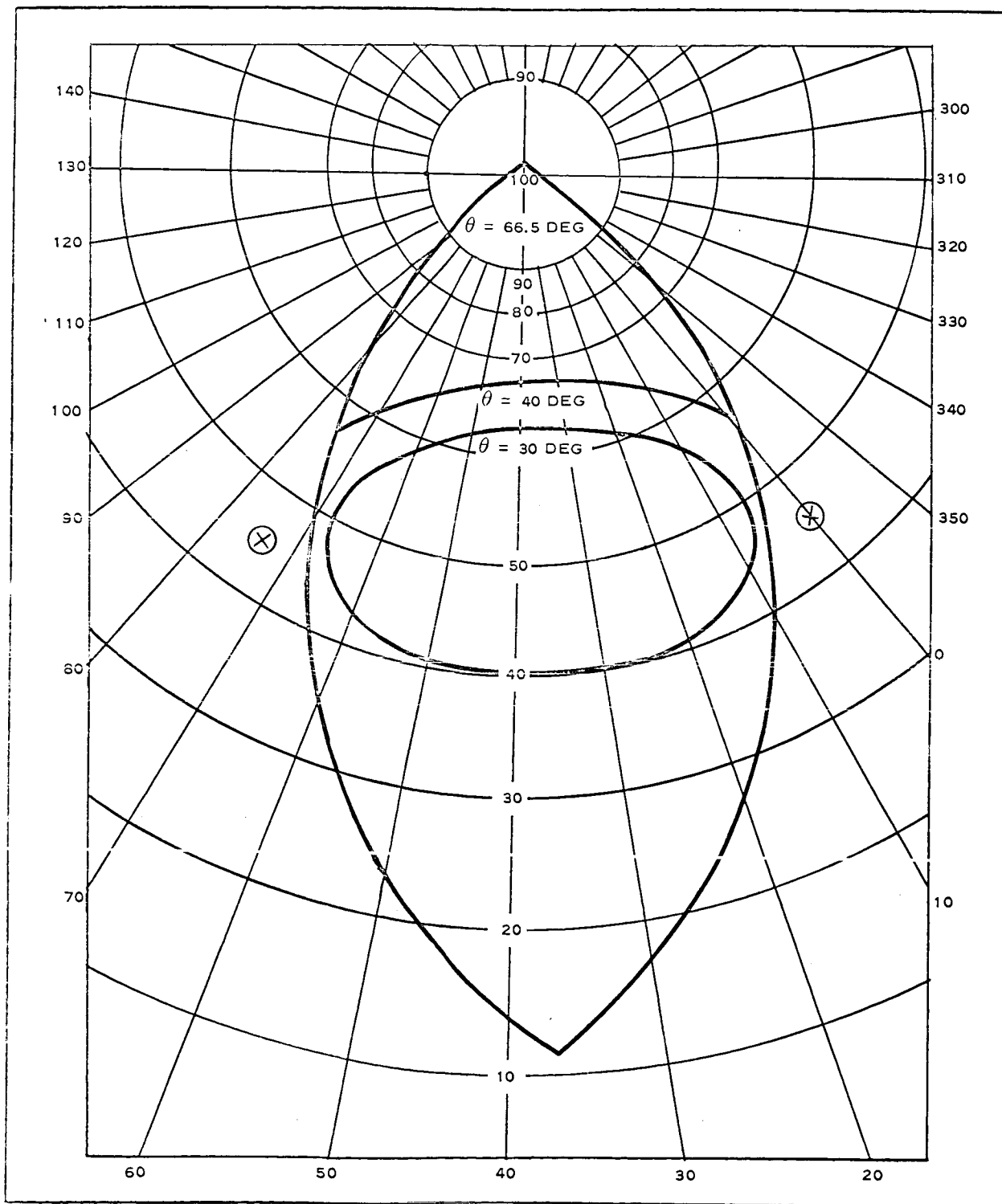


Figure 221 - Mutual Coverage, Example B

are 0.089, 0.045, and 0.031 for optimum orbit inclinations of 90, 62, and 59 deg, respectively. The number of satellites required for 90-percent service in a random system would be 25, 50, and 73, and twice these numbers for 99-percent service.

The conditions to achieve satellite relay continuity for a network of ground terminals is a complex consideration not within the scope of the present contract. Typical considerations include ground station location, satellite visibility and duration, orbital elements, random and spaced systems, number of satellites, outages, handover, and multiple access. Economic optimization further involves launch propulsion and ground terminal characteristics. Figure 222 shows general information for the number of satellites versus orbital altitude with parametric conditions of service probability and station separation. Conditions are worldwide two-station relay from a circular orbit random satellite system with a five-degree minimum usable elevation angle. The number of satellites can be reduced by optimum orbit selection for specific station locations and by station keeping in spaced systems. The number of satellites will increase for reduced lenticular angles and for multiple access between several stations.

7. ADVANCED LENTICULAR CONCEPT FOR SYNCHRONOUS ORBIT

An important result of the system trade-off studies is the disclosure of the lenticular satellite potential for a synchronous orbit system. Isotropically reflecting passive satellites, such as Echo, have not been considered seriously for synchronous orbit because of the fourth-power communication relay path loss with distance to the satellite. However, the lenticular advantage over a sphere, described in Item 2, and the lenticular weight scaling relationship, shown in Item 3, yield an effective path loss, described in Item 4, which for constant weight varies approximately as the second power of distance, as described in Item 5, and results in sizable band-width potential, as also shown in Item 5.

The further application of such recent space system developments as

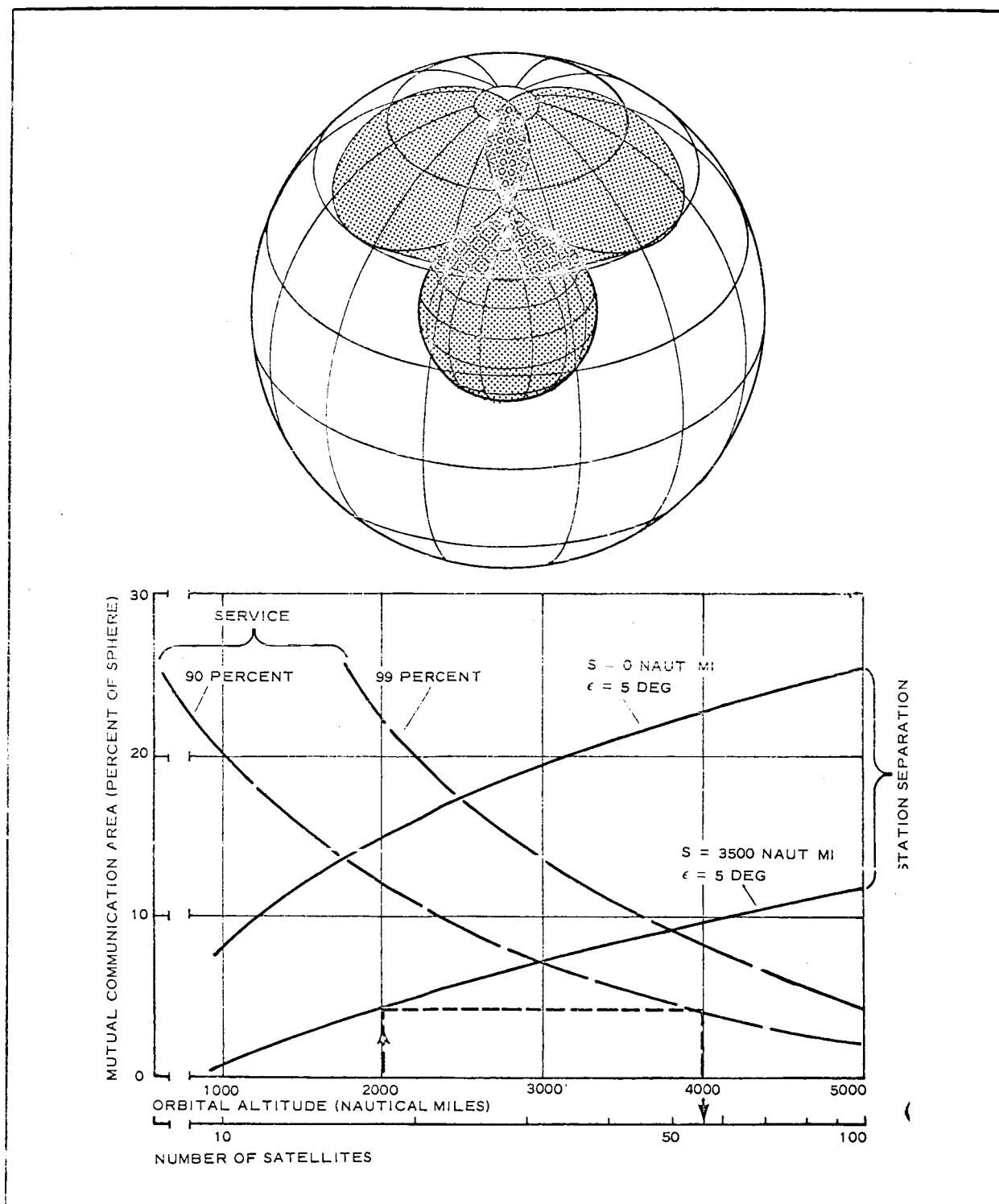


Figure 222 - Number of Satellites for Worldwide Random System

improvement in ground transmitting, receiving, and antenna systems, large payload launch vehicles, orbital placement and station keeping through solar sailing, improved space structures and materials, and improved gravity-gradient stabilization and damping systems, could allow a synchronous lenticular communication satellite system that provides thousands of megacycles of band width at signal levels adequate for mobile station and television broadcast applications. Figure 223 shows the communication capability possible. The synchronous system trades increased launch cost per satellite and increased ground transmitter cost for reduction in cost or complexity of many parameters. Sizable benefits of the synchronous system occur in such areas as multiple access, number of satellites, tracking equipment, satellite assignment bookkeeping, receiver noise temperature, and signal variation from path loss.

A more detailed discussion of this advanced lenticular concept for synchronous orbit is given in Appendix P.

8. CONCLUSIONS AND RECOMMENDATIONS

Studies to date indicate a large potential capability for lenticular satellite communication systems. Lenticular satellite system development should be continued to further advance the technology and to prove lenticular capability.

Further work is recommended in the areas of stabilization, materials, microwave, configuration, solar sailing, reliability, models, tests, and system studies of both 2000- to 6000-mi and synchronous-orbit systems. The system studies should incorporate advances in space systems and communication technology and should consider advanced concepts for both commercial and military applications.

A high pay-off area is the search for a self-deploying satellite design.

A large increase in radio reflection area-to-mass ratio would result from elimination of the film bladder and its supporting inflation equipment of

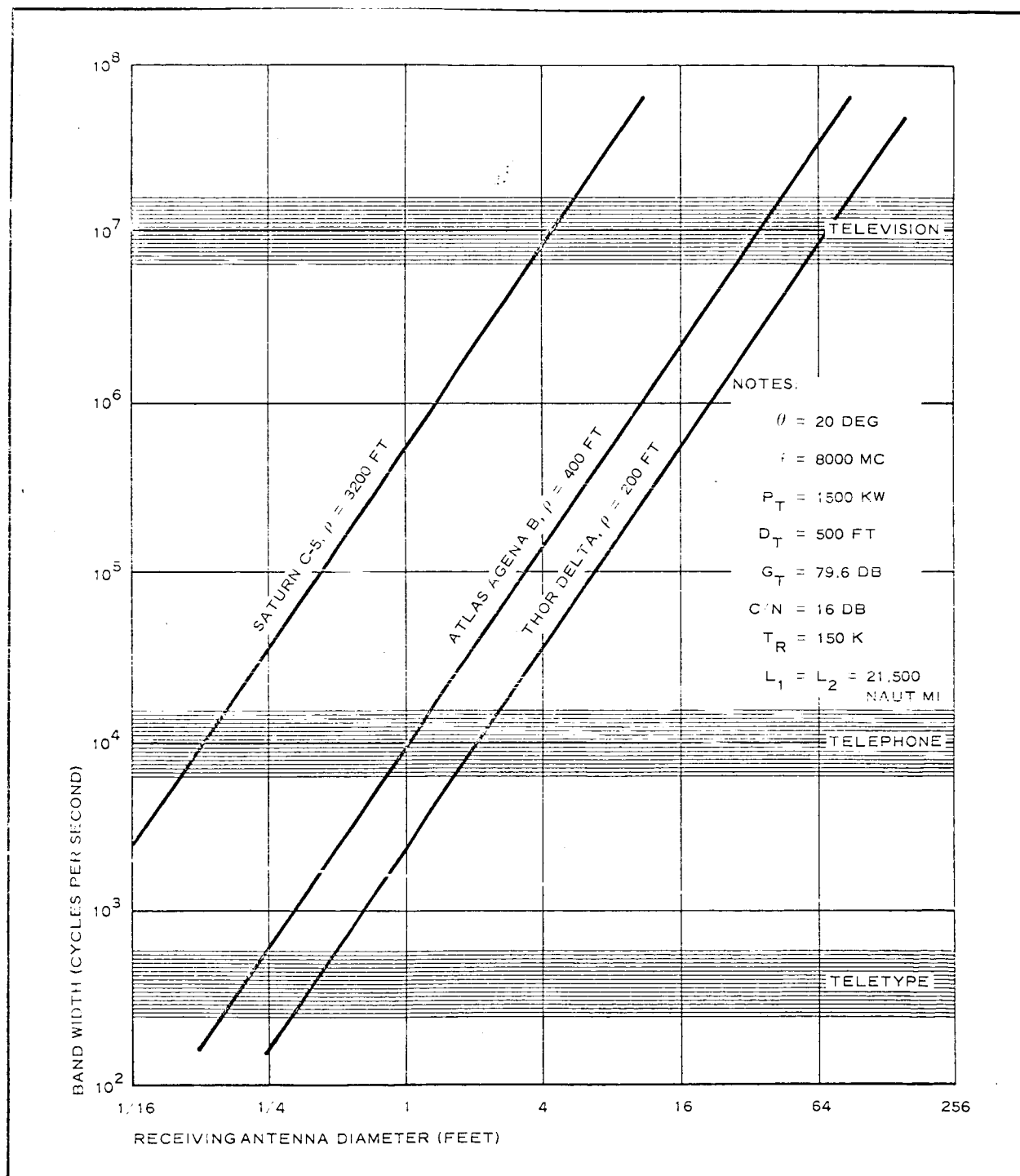


Figure 223 - Advanced Lenticular Concept Communication Capability:
Band Width versus Receiving Antenna Diameter

the present design. Accomplishment might be through configuration, structure, materials, or application of physical principles in new concepts. For illustration, consider a grid of small fiberglass type threads that retains structural memory and that packages without yielding or creeping. This type of lens material together with the present torus rim and auxiliary deployment aids might result in an appreciable weight reduction.

The following technological advances point to synchronous orbit application of lenticular satellites: efficient gravity gradient dampers, possibility of long lightweight booms and potential of gravity-gradient stabilization at higher altitudes, potential of grid structures for equalizing solar perturbation torques, better understanding of space environment effects, and such orbital perturbations as the solar pressure effect on Echo, advances in communication ground equipment, and large payload launch vehicles. Suggested development areas include the following.

1. Design study for satellites using smaller lenticular angles
2. Study of solar sailing to determine benefits and to establish practical requirements
3. Study of gravity-gradient stabilization and damping at higher altitudes to establish practicability and to determine design considerations
4. Study of satellite magnetic torquing to establish practicability and to determine design considerations. Uniformity of the earth's magnetic field for synchronous orbit simplifies the problem.
5. Investigation of solar sail materials, including control of reflection-transmission characteristics through electrostatic potential

6. System study to expose promising considerations and applications from a total comsat system aspect and to expose problem areas and potential solutions.

As shown in Figure 223 and Appendix P, a very significant communication capability can be achieved with a synchronous lenticular satellite system orbited by the Thor Delta. It is recommended that a design program be implemented incorporating the above studies to develop a synchronous lenticular design meeting Thor Delta payload requirements.

SECTION VI - CONCLUSIONS AND RECOMMENDATIONS

1. CONCLUSIONS

The results of this research and development program clearly indicate that the gravity-gradient-stabilized lenticular satellite is feasible and that significant performance data for a communications system evaluation can be obtained from a 50-ft flight-test satellite. Theoretical and experimental investigations resulted in similar lenticular satellite designs for the 267-ft-diameter full-scale unit and the 50-ft-diameter flight-test unit. Maintaining geometric similarity between satellite models will give the best indication of full-scale satellite performance.

The proposed satellite design is essentially within the state of the art as far as materials, structural analyses, fabrication, packaging, deployment, inflation, and rigidization techniques are concerned. It is feasible to meet the over-all system requirements with the full-scale satellite proposed herein. A further reduction in weight is possible by design refinements and development of improved materials. Comparative studies have shown that the lenticular design has several advantages over other types of passive communication satellites. Based on a limited reliability analysis, the satellite and spacecraft designs chosen appear satisfactory and no unusual problems should be experienced with a prototype system.

Significant advances in the development of the wire cloth-photolyzable film were achieved on this program. This material appears suitable for satellite lens application. Continued development and refinement might be advisable to improve its physical characteristics and enhance over-all satellite reliability.

R-f theory and experiment verified the existence of edge diffraction phenomena for nose-on monostatic return caused by the sharp edge of the

lenticular lens. Reflectivity patterns indicate that large variations in monostatic return are not apparent outside the nose-on region. From an operational standpoint the nose-on monostatic condition has limited value and therefore the r-f characteristics of the satellite seem in general to be satisfactory. The effect of lens surface tolerance, tripod, booms, and canister on the radar return of the lens was determined to be negligible under the most adverse design conditions.

The gravity-gradient-stabilization studies indicate that large lenticular satellites can be stabilized with satisfactory accuracy if a good damping system is provided. Based on published literature, satellite dampers currently flight tested do not provide adequate damping. However, GAC's second-generation damper, the Rice-Wilberforce, appears to be very adequate for this application. Therefore the gravity-gradient stabilization principle can be utilized.

Review of the detailed ground test development and the flight test plans has indicated that immediate initiation is possible of a development program of the proposed prototype satellite system. The test methods and equipments required are within the state of the art and no particular schedule difficulties should be encountered.

2. RECOMMENDATIONS

It is recommended that a flight-test model lenticular satellite program be initiated to demonstrate and to obtain information regarding packaging, deployment, rigidization, r-f characteristics, and orbital behavior. This will increase confidence in the basic concept and improve the design of the full-scale satellite.

In the interim, however, it might be advantageous to initiate the following efforts to expedite a future flight-test program:

1. Fabrication and ground testing of additional small-scale satellite models and primary components to

enhance satellite reliability and improve understanding of the associated phenomena.

2. Evaluation of the Rice-Wilberforce libration damper for the transient and steady-state conditions to determine compatibility with stabilization accuracy requirements. (Hardware studies should be made to verify optimum tuning theory of the damper and pinpoint physical characteristics of the helical spring and damping fluid.)
3. Additional theoretical and experimental investigations on the edge diffraction phenomena of the proposed lenticular satellite design. (Additional r-f model tests and theoretical investigations should be conducted within the required bistatic operating conditions for better evaluation of the satellite's mission capabilities. Testing of several small-sized models will allow correlation with theory and enhance prediction of r-f characteristics of the flight test and prototype lenticular satellites.)

The proposed lenticular satellite design makes a very attractive passive communication satellite system. It would appear advisable, however, to conduct studies of system and configurization optimization in parallel with the model flight test program which could include (1) parametric trades on the lenticular angle to maximize the microwave relay performance versus system cost for various orbits, (2) incorporation of station-keeping capability into the satellite, and (3) review of alternate configurations. Therefore, additional system studies are recommended to make the lenticular satellites even more effective.

LIST OF REFERENCES

1. GAP-2066: Feasibility Study and Preliminary Design of Gravity-Gradient-Stabilized Lenticular Test Satellite. Akron, Ohio, Goodyear Aircraft Corporation, 8 May 1963.
2. Contract NAS 1-3114: Feasibility Study and Preliminary Design of a Gravity-Gradient-Stabilized Lenticular Test Satellite. Hampton, Va., National Aeronautics and Space Administration, Langley Research Center, 26 June 1963.
3. GER-11189 through GER-11189S10: Monthly Progress Reports for Feasibility Study and Preliminary Design of a Gravity-Gradient-Stabilized Lenticular Test Satellite. Akron, Ohio, Goodyear Aerospace Corporation, 5 August 1963 through 5 June 1964.
4. Den Hartog, J. P.: Advanced Strength of Materials. New York, McGraw-Hill Book Co., Inc., 1952.
5. Rottmayer, E.; and Mandel, J. A.: Design of Cylinders and Spheres of Wire Film Materials. GER-11201, Akron, Ohio, Goodyear Aerospace Corporation, 19 August 1963.
6. Timoshenko, S. P.: Theory of Elastic Stability. 2nd ed. New York, McGraw-Hill Book Co., Inc., 1962.
7. Rottmayer, E.; and Marketos, J. D.: Study of Orbital Design Conditions for a Gravity-Gradient-Stabilized Lenticular Satellite. GER-11277, Akron, Ohio, Goodyear Aerospace Corporation, 14 October 1963.
8. Eckert, E. R. G.; and Drake, R. M. Jr.: Heat and Mass Transfer. 2nd ed. New York, McGraw-Hill Book Co., Inc., 1959.
9. GER-11452: Materials Development Report - Phase II for Feasibility Study and Preliminary Design of a Gravity-Gradient-Stabilized Lenticular Test Satellite. Akron, Ohio, Goodyear Aerospace Corporation, 1 February 1964.
10. Timoshenko, S. P.: Strength of Materials. 2nd ed. New York, D. Van Nostrand Co., Inc., 1940.
11. TG-502: Dynamic Analysis of Gravity-Gradient Satellite with Passive Damping. The Johns Hopkins University, Applied Physics Laboratory, June 1963.

12. Chenyshev, N. A.: Nonlinear Theory of Elastic Deformation of Cylindrically Wound Springs. Governmental Scientific Technical Publications on Machine Construction, Moscow, 1958.
13. GER-11539: Digital Computer Solution of Gravity-Gradient Stabilized Lenticular Satellite. Akron, Ohio, Goodyear Aerospace Corporation, 17 April 1964.
14. Fondriat, E.; and Hannah, M.: Moments Due to Solar Radiation Acting on a Lenticular Satellite. Hampton, Va., National Aeronautics and Space Administration, Langley Research Center (preliminary data, unpublished).
15. Woodling, C. H.; Elliott, J. R.; and Stull, T. G.: Orbital Error Analysis of Scout Research Vehicle. NASA TND-1639, May 1963.
16. Anon: International, The Scout. Fort Worth, Texas, Astronautics Division, Chance Vought Corporation, Revision October 1962.
17. AST/AVC-3-52(20-62-72): Fort Worth, Texas, Astronautics Division, Chance Vought Corporation, 6 December 1962.
18. Fedor, J. V.: Theory and Design Curves for a Yo-Yo Despin Mechanism for Satellites. NASA TND-708.
19. Crispen, W., Jr.; Goodrich, R. F.; and Seigel, K. M.: A Theoretical Method for the Calculation of Radar Cross-Section of Aircraft and Missiles. Report 2591-1-H. University of Michigan, Ann Arbor, Mich., July 1959.
20. Kennough, E. M.; and Cosguff, R. L.: "Microwave Theory and Techniques," IRE National Convention Record, Antenna Laboratory, Ohio State University, Columbus, Ohio, March 1958.
21. Keller, J. B.: "Backscatter from a Finite Cone," PGAP, March 1960.
22. Kennough, E. M.: Use of Impulse Response in Electromagnetic Scattering Problems. Antenna Laboratory, Ohio State University, Columbus, Ohio.
23. Hiat, R. E.; Semor, T. B. A.; and Weston, V. H.: "A Study of Surface Roughness," Proceedings of IRE, Vol 48, December 1960.
24. Anon: Scout Handbook. Revision October, 1962, Dallas, Texas, Astronautics Division, Chance Vought Corporation.

25. Anon: Wallops Station Handbook; Volume I - General Information. Volume II - Flight Test and Support Service Facilities. Volume III - Range Users Information. Wallops Station, Va.
26. Anon: Satellite Instrumentation Network Facilities Report. Operations and Support Division of Goddard Space Flight Center, Greenbelt, Md.

APPENDIX A - ORBITAL DESIGN CONDITIONS FOR COMPONENTS OF
GRAVITY-GRADIENT-STABILIZED LENTICULAR SATELLITE

1. LOADING CONDITIONS

Let \bar{i} , \bar{j} , and \bar{k} be unit vectors normal to the orbital plane, tangent to the orbit, and along the earth radius at a point respectively, and x , y , and z centroidal axes of the satellite that coincide with \bar{i} , \bar{j} , and \bar{k} respectively, when the satellite is in normal position. The various components of the satellite have been analyzed structurally for the most critical of the following four conditions.

1. Condition I - This is defined as the condition for which the z axis of the satellite makes an angle α with the unit vector \bar{k} , while the x axis coincides with the vector \bar{i} and the angular velocity of the satellite about \bar{i} at this instant is zero.
2. Condition II - If the satellite is displaced an amount α_0 as defined in Condition I, the gravity gradient produces a restoring moment about the vector \bar{i} , which will be a maximum when α becomes zero. Condition II consists of the gravity gradient forces at $\alpha = 0$ plus the centrifugal forces associated with the angular velocity $\dot{\alpha}_{\max}$.
3. Condition III - This condition is similar to Condition I except that the satellite is displaced out of the plane of the orbit by the angle β while the y axis coincides with the unit vector \bar{j} .
4. Condition IV - This condition is similar to Condition II except that it is related to the satellite displacement out of the orbital plane.

2. CRITICAL LOADS IN THE TRIPOD BOOMS

Table A-I gives the axial loads in the tripod booms for all four loading conditions. Configurations A and B designate the orientation of the tripod relative to the coordinate system (xyz), as shown by the sketches in Table A-I.

Distributed loads on the booms, which come from gravity gradient, inertia loads, and solar pressure can be found readily for the critical conditions. For the analysis of the booms the critical conditions are those that produce compression in the booms.

3. CRITICAL LOADS FOR THE RIM

There are two kinds of rim loads, in-plane rim loads and out-of-plane rim loads. The in-plane loads are either the radial components of the tripod axial loads or distributed loads produced by gravity gradient and inertia loads on the rim mass.

Let M and S be the satellite configurations when the booms meet the rim at the same points or they are staggered respectively. If A and B represent two critical orientations of the tripods relative to the coordinate axes, there are four combinations that might cause critical loading on the rim. These combinations are given schematically in Figure A-1.

Rim radial loads, Q , are given in Table A-II for loads P_x , P_y , and P_z at the top of the tripods for all four configurations shown in Figure A-1. The values of Table A-II are combined with actual gravity gradient and inertia loads P_x , P_y , and P_z corresponding to the critical Conditions I through IV as described above, and the results are summarized in Table A-III.

The out-of-plane loads for all configurations of Figure A-1 and the loading Conditions I through IV as described above are summarized in Tables A-IV and A-V.

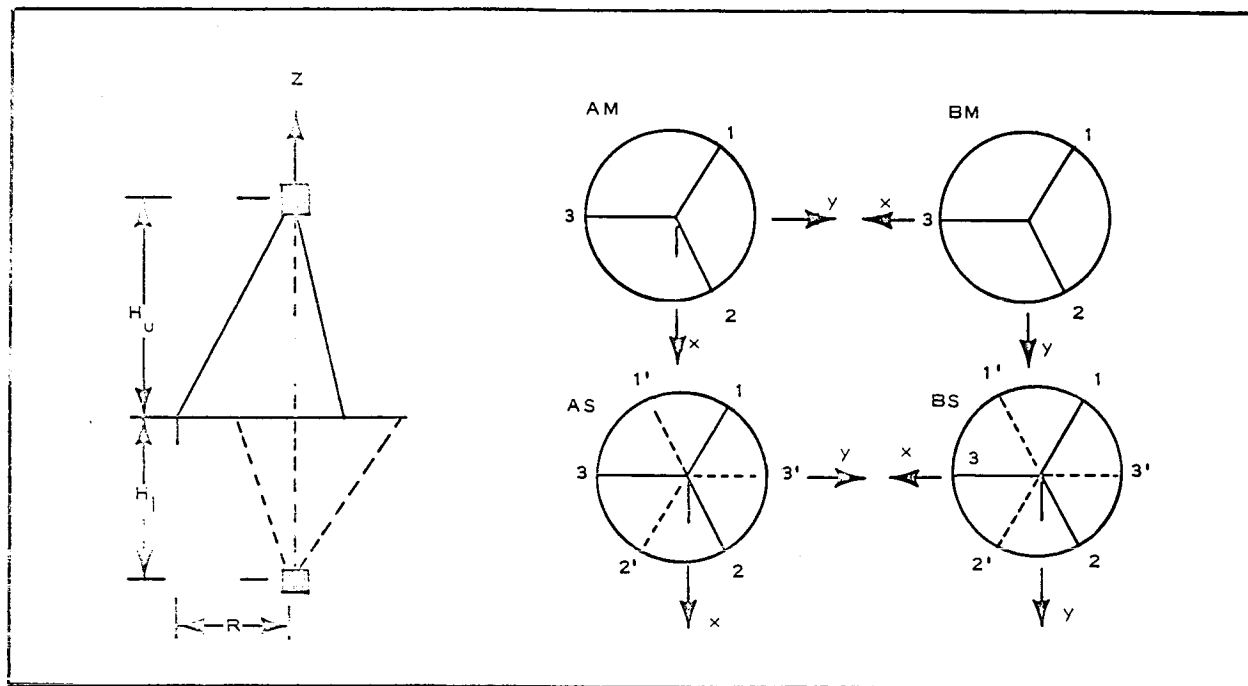


Figure A-1 - Satellite Configurations M and S Combined with Orientations A and B of Tripods Relative to Coordinate Axes

TABLE A-1 - AXIAL LOADS IN TRIPOD BOOMS UNDER ALL BASIC LOADING CONDITIONS

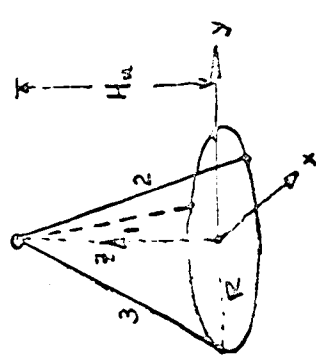
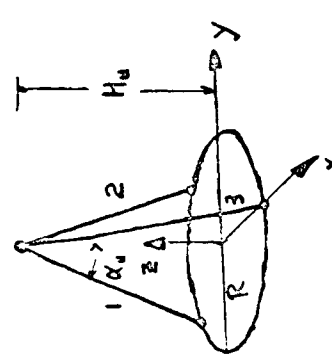
LOADING CONDITION & SINGULARITY ORIENTATION	LOADING CONDITION	BOOM AXIAL LOAD
<p>A.</p> 	A	$M_u H_u \omega^2 \cos \alpha_u \left[\frac{\cos \alpha_u}{\cos \alpha_u} + (1-\lambda) \frac{\sin \alpha_u}{\sin \alpha_u} \right]$ Same as L1A
	B	$M_u H_u \omega^2 \cos \alpha_u \left[\frac{\cos \alpha_u}{\cos \alpha_u} - 2(1-\lambda) \frac{\sin \alpha_u}{\sin \alpha_u} \right]$ $M_u H_u \omega^2 \cos \alpha_u \left[\frac{\cos \alpha_u}{\cos \alpha_u} - 2\sqrt{3}(1-\lambda) \frac{\sin \alpha_u}{\sin \alpha_u} \right]$ $M_u H_u \omega^2 \cos \alpha_u \left[\frac{\cos \alpha_u}{\cos \alpha_u} + 2\sqrt{3}(1-\lambda) \frac{\sin \alpha_u}{\sin \alpha_u} \right]$
	A	All Equal $\left\{ M_u H_u \omega^2 (1-\lambda \sin^2 \alpha_u) / \cos \alpha_u \right\}$
	B	Same as A of this condition.
	A	$M_u H_u \omega^2 \left[\frac{4 \cos^3 \beta - 1}{3 \cos \alpha_u} + \frac{2}{3} (1-\lambda) \frac{\sin 2\beta}{\sin \alpha_u} \right]$ Same as L1A
	B	$M_u H_u \omega^2 \left[\frac{4 \cos^3 \beta - 1}{3 \cos \alpha_u} - \frac{4}{3} (1-\lambda) \frac{\sin 2\beta}{\sin \alpha_u} \right]$ $M_u H_u \omega^2 \left[\frac{4 \cos^3 \beta - 1}{3 \cos \alpha_u} - \frac{4}{3} (1-\lambda) \frac{\sin 2\beta}{\sin \alpha_u} \right]$ $M_u H_u \omega^2 \left[\frac{4 \cos^3 \beta - 1}{3 \cos \alpha_u} + \frac{4}{3} (1-\lambda) \frac{\sin 2\beta}{\sin \alpha_u} \right]$ $M_u H_u \omega^2 \left[\frac{4 \cos^3 \beta - 1}{3 \cos \alpha_u} + \frac{4}{3} (1-\lambda) \frac{\sin 2\beta}{\sin \alpha_u} \right]$
<p>B.</p>  <p> $\tan \alpha_u = \frac{R}{H_u}$ </p>	A	All Equal $\left\{ M_u H_u \omega^2 \left(1 + \frac{4}{3} \lambda \sin^2 \beta_0 \right) / \cos \alpha_u \right\}$
	B	Same as A of this condition
	A	
	B	
	A	
	B	

TABLE A-II - IN-PLANE RIM LOADS DUE TO CONCENTRATED LOADS AT ENDS OF TRIPODS

LOAD	CONFIGURATION	RIM RADIAL LOAD						
		Q_1	Q_2	Q_3	$Q_{1'}$	$Q_{1'}$	$Q_{1'}$	$Q_{3'}$
P_{ux}	AM	—	—	—	—	—	—	—
	BM	—	—	—	—	—	—	—
	AS	$-\frac{1}{\sqrt{3}} P_{ux}$	$+\frac{1}{\sqrt{3}} P_{ux}$	0	$+\frac{1}{\sqrt{3}} P_{ux}$	$-\frac{1}{\sqrt{3}} P_{ux}$	0	0
	BS	$-\frac{1}{3} P_{ux}$	$-\frac{1}{3} P_{ux}$	$+\frac{2}{3} P_{ux}$	$-\frac{1}{3} P_{ux}$	$-\frac{1}{3} P_{ux}$	$+\frac{2}{3} P_{ux}$	—
P_{uy}	AM	—	—	—	—	—	—	—
	BM	—	—	—	—	—	—	—
	AS	$+\frac{1}{3} P_{uy}$	$+\frac{1}{3} P_{uy}$	$-\frac{2}{3} P_{uy}$	$+\frac{1}{3} P_{uy}$	$+\frac{1}{3} P_{uy}$	$-\frac{2}{3} P_{uy}$	—
	BS	$-\frac{1}{\sqrt{3}} P_{uy}$	$+\frac{1}{\sqrt{3}} P_{uy}$	0	$+\frac{1}{\sqrt{3}} P_{uy}$	$-\frac{1}{\sqrt{3}} P_{uy}$	0	—
P_{uz}	AM	$-\frac{1}{3} P_{uz}(\tan \alpha_1 + \tan \alpha_2)$	Same as Q_1	Same as Q_1	0	0	0	0
	BM	$-\frac{1}{3} P_{uz}(\tan \alpha_1 + \tan \alpha_2)$	Same as Q_1	Same as Q_1	0	0	0	0
	AS	$-\frac{1}{3} P_{uz} \tan \alpha_1$	Same as Q_1	Same as Q_1	$-\frac{1}{3} P_{uz} \tan \alpha_2$	Same as $Q_{1'}$	Same as $Q_{1'}$	Same as $Q_{1'}$
	BS	Same as AS	Same as AS	Same as AS	Same as AS	Same as AS	Same as AS	Same as AS

TABLE A-III - IN-PLANE RIM LOADS FOR SATELLITE
LOADING CONDITIONS I TO IV

LOAD	SATELLITE LOADING CONDITIONS			
	I ($\alpha \neq 0$)	II ($\alpha = 0$)	III ($\beta \neq 0$)	IV ($\beta = 0$)
P_{ux}	0	0	$-2M_u H_u \omega^2 (1-\lambda) \sin 2\beta$	0
P_{uy}	$-\frac{3}{2} M_u H_u \omega^2 (1-\lambda) \sin 2\alpha$	0	0	0
P_{uz}	$3M_u H_u \omega^2 \cos^2 \alpha$	$3M_u H_u \omega^2 (1+\lambda \sin^2 \alpha_0)$	$-M_u H_u \omega^2 (1-4 \cos^2 \beta)$	$M_u H_u \omega^2 (3+4 \lambda \sin^2 \beta_0)$
q_{rx}	$R m_r \omega^2 \sin \phi$	$R m_r \omega^2 \sin \phi$	$R m_r \omega^2 (1-4 \sin^2 \beta) \sin \phi$	$R m_r \omega^2 (1-4 \lambda \sin^2 \beta_0) \sin \phi$
q_{ry}	$3 R m_r \omega^2 \cos \phi \sin^2 \alpha$	$3 R m_r \lambda \omega^2 \sin \alpha_0 \cos \phi$	0	0

LOADS $Q_1, Q_2, \dots, Q_2', Q_3'$, AND DISTRIBUTED LOADS q FOR THE FOUR BASIC LOADING CONDITIONS.

I	AM	$Q_1 = Q_2 = Q_3 = -\frac{1}{3} P_{uz} (\tan \alpha_u + \tan \alpha_\ell); Q_1' = Q_2' = Q_3' = 0; q_{rx}, q_{ry}$
	BM	$Q_1 = Q_2 = Q_3 = -\frac{1}{3} P_{uz} (\tan \alpha_u + \tan \alpha_\ell); Q_1' = Q_2' = Q_3' = 0; q_{rx}, q_{ry}$
	AS	$Q_1 = Q_2 = \frac{1}{3} (P_{uy} - P_{uz} \tan \alpha_u), Q_3 = -\frac{1}{3} (2P_{uy} + P_{uz} \tan \alpha_u)$ $Q_1' = Q_2' = \frac{1}{3} (P_{uy} - P_{uz} \tan \alpha_\ell), Q_3' = -\frac{1}{3} (2P_{uy} + P_{uz} \tan \alpha_\ell); q_{rx}, q_{ry}$
	BS	$Q_1 = -\frac{1}{3} (\sqrt{3} P_{uy} + P_{uz} \tan \alpha_u); Q_2 = \frac{1}{3} (\sqrt{3} P_{uy} - P_{uz} \tan \alpha_u); Q_3 = -\frac{1}{3} P_{uz} \tan \alpha_u$ $Q_1' = \frac{1}{3} (\sqrt{3} P_{uy} - P_{uz} \tan \alpha_\ell); Q_2' = -\frac{1}{3} (\sqrt{3} P_{uy} + P_{uz} \tan \alpha_\ell); Q_3' = -\frac{1}{3} P_{uz} \tan \alpha_\ell; q_{rx}, q_{ry}$
II	AM	$Q_1 = Q_2 = Q_3 = -\frac{1}{3} P_{uz} (\tan \alpha_u + \tan \alpha_\ell); Q_1' = Q_2' = Q_3' = 0; q_{rx}, q_{ry}$
	BM	SAME AS AM
	AS	$Q_1 = Q_2 = Q_3 = -\frac{1}{3} P_{uz} \tan \alpha_u; Q_1' = Q_2' = Q_3' = -\frac{1}{3} P_{uz} \tan \alpha_\ell; q_{rx}, q_{ry}$
	BS	SAME AS CONFIGURATION AS
III	AM	$Q_1 = Q_2 = Q_3 = -\frac{1}{3} P_{uz} (\tan \alpha_u + \tan \alpha_\ell); Q_1' = Q_2' = Q_3' = 0; q_{rx}.$
	BM	SAME AS AM
	AS	$Q_1 = -\frac{1}{3} (\sqrt{3} P_{ux} + P_{uz} \tan \alpha_u); Q_2 = \frac{1}{3} (\sqrt{3} P_{ux} - P_{uz} \tan \alpha_u); Q_3 = -\frac{1}{3} P_{uz} \tan \alpha_u$ $Q_1' = \frac{1}{3} (\sqrt{3} P_{ux} - P_{uz} \tan \alpha_\ell); Q_2' = -\frac{1}{3} (\sqrt{3} P_{ux} + P_{uz} \tan \alpha_\ell); Q_3' = -\frac{1}{3} P_{uz} \tan \alpha_\ell; q_{rx}$
	BS	$Q_1 = Q_2 = -\frac{1}{3} (P_{ux} + P_{uz} \tan \alpha_u); Q_3 = +\frac{1}{3} (2P_{ux} - P_{uz} \tan \alpha_u);$ $Q_1' = Q_2' = -\frac{1}{3} (P_{ux} + P_{uz} \tan \alpha_\ell); Q_3' = +\frac{1}{3} (2P_{ux} - P_{uz} \tan \alpha_\ell); q_{rx}$
IV	AM	$Q_1 = Q_2 = Q_3 = -\frac{1}{3} P_{uz} (\tan \alpha_u + \tan \alpha_\ell); Q_1' = Q_2' = Q_3' = 0; q_{rx}$
	BM	SAME AS AM
	AS	$Q_1 = Q_2 = Q_3 = -\frac{1}{3} P_{uz} \tan \alpha_u; Q_1' = Q_2' = Q_3' = -\frac{1}{3} P_{uz} \tan \alpha_\ell; q_{rx}$
	BS	SAME AS CONFIGURATION AS.

TABLE A-IV - OUT-OF-PLANE RIM LOADS DUE TO CONCENTRATED LOADS AT

ENDS OF TRIPON

LOAD	CONFI- GURATION	RIM OUT-OF-PLANE LOADS					
		F_1	F_2	F_3	F_1'	F_2'	F_3'
P_{ux}	AM	$+\frac{P_{ux}}{\sqrt{3}}(\cot\alpha_u + \cot\alpha_\ell)$	$-\frac{P_{ux}}{\sqrt{3}}(\cot\alpha_u + \cot\alpha_\ell)$	0	—	—	—
	BM	$+\frac{1}{3}P_{ux}(\cot\alpha_u + \cot\alpha_\ell)$	$+\frac{1}{3}P_{ux}(\cot\alpha_u + \cot\alpha_\ell) - \frac{2}{3}P_{ux}(\cot\alpha_u + \cot\alpha_\ell)$	—	—	—	—
	AS	$+\frac{P_{ux}}{\sqrt{3}}\cot\alpha_u$	$-\frac{P_{ux}}{\sqrt{3}}\cot\alpha_u$	0	$+\frac{P_{ux}}{\sqrt{3}}\cot\alpha_\ell$	$-\frac{P_{ux}}{\sqrt{3}}\cot\alpha_\ell$	0
	BS	$+\frac{1}{3}P_{ux}\cot\alpha_u$	$+\frac{1}{3}P_{ux}\cot\alpha_u$	$-\frac{2}{3}P_{ux}\cot\alpha_u$	$-\frac{1}{3}P_{ux}\cot\alpha_\ell$	$-\frac{1}{3}P_{ux}\cot\alpha_\ell$	$+\frac{2}{3}P_{ux}\cot\alpha_\ell$
P_{uy}	AM	$-\frac{1}{3}P_{uy}(\cot\alpha_u + \cot\alpha_\ell)$	$-\frac{1}{3}P_{uy}(\cot\alpha_u + \cot\alpha_\ell)$	$+\frac{2}{3}P_{uy}(\cot\alpha_u + \cot\alpha_\ell)$	—	—	—
	BM	$+\frac{P_{uy}}{\sqrt{3}}(\cot\alpha_u + \cot\alpha_\ell)$	$-\frac{P_{uy}}{\sqrt{3}}(\cot\alpha_u + \cot\alpha_\ell)$	0	—	—	—
	AS	$-\frac{1}{3}P_{uy}\cot\alpha_u$	$-\frac{1}{3}P_{uy}\cot\alpha_u$	$+\frac{2}{3}P_{uy}\cot\alpha_u$	$+\frac{1}{3}P_{uy}\cot\alpha_\ell$	$+\frac{1}{3}P_{uy}\cot\alpha_\ell$	$-\frac{2}{3}P_{uy}\cot\alpha_\ell$
	BS	$+\frac{P_{uy}}{\sqrt{3}}\cot\alpha_u$	$-\frac{P_{uy}}{\sqrt{3}}\cot\alpha_u$	0	$+\frac{P_{uy}}{\sqrt{3}}\cot\alpha_\ell$	$-\frac{P_{uy}}{\sqrt{3}}\cot\alpha_\ell$	0
P_{uz}	AM	—	—	—	—	—	—
	BM	—	—	—	—	—	—
	AS	$\frac{1}{3}P_{uz}$	$\frac{1}{3}P_{uz}$	$\frac{1}{3}P_{uz}$	$-\frac{1}{3}P_{uz}$	$-\frac{1}{3}P_{uz}$	$-\frac{1}{3}P_{uz}$
	BS	$\frac{1}{3}P_{uz}$	$\frac{1}{3}P_{uz}$	$\frac{1}{3}P_{uz}$	$-\frac{1}{3}P_{uz}$	$-\frac{1}{3}P_{uz}$	$-\frac{1}{3}P_{uz}$

TABLE A-V - OUT-OF-PLANE RIM LOADS FOR SATELLITE
LOADING CONDITIONS I TO IV

LOAD	SATELLITE LOADING CONDITIONS			
	I ($\alpha \neq 0$)	II ($\alpha = 0$)	III ($\beta \neq 0$)	IV ($\beta = 0$)
P_{ux}	0	0	$-2M_u H_u \omega^2 (1-\lambda) \sin 2\beta$	0
P_{uy}	$-\frac{2}{3} M_u H_u \omega^2 (1-\lambda) \sin 2\alpha$	0	0	0
P_{uz}	$3M_u H_u \omega^2 \cos^2 \alpha$	$3M_u H_u \omega^2 (1+\lambda \sin^2 \alpha_0)$	$-M_u H_u \omega^2 (1-4 \cos^2 \beta)$	$M_u H_u \omega^2 (3+4\lambda \sin^2 \beta_0)$
q_{rz}	$-\frac{2}{3} R m_r \omega^2 (1+\lambda) \cos \beta \sin 2\alpha$	0	$2R m_r \omega^2 (1+\lambda) \sin \beta \sin 2\beta$	0

LOADS $F_1, F_2, F_3, F_1', F_2', F_3'$, AND DISTRIBUTED LOAD q_{rz} FOR THE FOUR BASIC LOADING CONDITIONS.

I	AM	$F_1 = F_2 = -\frac{1}{2} F_3 = -\frac{1}{3} P_{uy} (\cot \alpha_u + \cot \alpha_\ell)$; $F_1' = F_2' = F_3' = 0$; q_{rz} .
	BM	$F_1 = -F_2 = \frac{1}{3} P_{uy} (\cot \alpha_u + \cot \alpha_\ell)$; $F_3 = 0$; $F_1' = F_2' = F_3' = 0$; q_{rz} .
	AS	$F_1 = F_2 = \frac{1}{3} (P_{uz} - P_{uy} \cot \alpha_u)$; $F_3 = \frac{1}{3} (P_{uz} + 2 P_{uy} \cot \alpha_u)$ $F_1' = F_2' = -\frac{1}{3} (P_{uz} - P_{uy} \cot \alpha_\ell)$; $F_3' = -\frac{1}{3} (P_{uz} + 2 P_{uy} \cot \alpha_\ell)$; q_{rz} .
	BS	$F_1 = \frac{1}{3} (P_{uz} + \sqrt{3} P_{uy} \cot \alpha_u)$; $F_2 = \frac{1}{3} (P_{uz} - \sqrt{3} P_{uy} \cot \alpha_u)$; $F_3 = \frac{1}{3} P_{uz}$. $F_1' = -\frac{1}{3} (P_{uz} - \sqrt{3} P_{uy} \cot \alpha_\ell)$; $F_2' = -\frac{1}{3} (P_{uz} + \sqrt{3} P_{uy} \cot \alpha_\ell)$; $F_3' = -\frac{1}{3} P_{uz}$; q_{rz} .
II	AM	NO LOADING
	BM	NO LOADING
	AS	$F_1 = F_2 = F_3 = \frac{1}{3} P_{uz}$; $F_1' = F_2' = F_3' = -\frac{1}{3} P_{uz}$; $q_{rz} = 0$
	BS	SAME AS CONFIGURATION AS
III	AM	$F_1 = -F_2 = \frac{P_{ux}}{\sqrt{3}} (\cot \alpha_u + \cot \alpha_\ell)$; $F_3 = 0$; $F_1' = F_2' = F_3' = 0$; q_{rz} .
	BM	$F_1 = F_2 = -\frac{1}{2} F_3 = \frac{1}{3} P_{ux} (\cot \alpha_u + \cot \alpha_\ell)$; $F_1' = F_2' = F_3' = 0$; q_{rz} .
	AS	$F_1 = \frac{1}{3} (P_{uz} + \sqrt{3} P_{ux} \cot \alpha_u)$; $F_2 = \frac{1}{3} (P_{uz} - \sqrt{3} P_{ux} \cot \alpha_u)$; $F_3 = \frac{1}{3} P_{uz}$ $F_1' = -\frac{1}{3} (P_{uz} - \sqrt{3} P_{ux} \cot \alpha_\ell)$; $F_2' = -\frac{1}{3} (P_{uz} + \sqrt{3} P_{ux} \cot \alpha_\ell)$; $F_3' = -\frac{1}{3} P_{uz}$; q_{rz} .
	BS	$F_1 = F_2 = \frac{1}{3} (P_{uz} + P_{ux} \cot \alpha_u)$; $F_3 = \frac{1}{3} (P_{uz} - 2 P_{ux} \cot \alpha_u)$; $F_1' = F_2' = -\frac{1}{3} (P_{uz} + P_{ux} \cot \alpha_\ell)$; $F_3' = -\frac{1}{3} (P_{uz} - 2 P_{ux} \cot \alpha_\ell)$; q_{rz} .
IV	AM	NO LOADING
	BM	NO LOADING
	AS	$F_1 = F_2 = F_3 = \frac{1}{3} P_{uz}$; $F_1' = F_2' = F_3' = -\frac{1}{3} P_{uz}$; $q_{rz} = 0$
	BS	SAME AS CONFIGURATION AS.

APPENDIX B - LENTICULAR SATELLITE
PRESSURIZATION STUDY REPORT

1. INTRODUCTION

This appendix demonstrates the feasibility of the pressurization concept for a full-scale lenticular satellite. The analysis is made assuming a set of system parameters consistent with the present design concept. The major conclusions are the following.

1. The amount of pressurizing gas (helium) required is reasonable.
2. The pressure differential required between torus and lens to prevent collapse of the structure can be controlled satisfactorily by passive means during the pressure decay phase.
3. The rate of pressure decay after inflation may require a programmed venting system to prevent uncontrolled escape of residual gases through random holes that will appear in the photolyzable film.

The method of analysis used herein will be employed during the optimization phase of the program.

2. ASSUMED SYSTEM PARAMETERS

The assumed system parameters are the following.

1. The torus has a volume of 268,000 cu ft and a surface area of 55,000 sq ft. Two 0.020-in.-diameter holes are located in each square foot of surface area to allow depressurization. Design pressure is 0.0388 psi absolute.

2. The lens has a volume of 3,060,000 cu ft and a surface area of 129,000 sq ft. The ratio of exhaust hole area to volume is the same for the lens as for the torus, so that the equivalent of 9.737 holes with 0.020-in. diameters are located in each square foot of lens surface area. Design pressure is 0.00036 psi absolute.
3. The pressurizing or inflating gas is helium stored at 3000 psi. This gas passes through a pressure regulator set for 5 psi absolute and then through individual flow-limiting orifices before entering the lens and torus. On-off valves and pressure sensors prevent the pressures from exceeding design values, or maintain these pressures as required.
4. The sequence of events is to allow five minutes for pressurization of the torus to design values immediately followed by five minutes for pressurization of the lens to design values, two and four additional minutes at the design pressures for the lens and torus respectively, and then shut-off of the pressurization system with pressure decay resulting.

3. ANALYSIS

The type of flow through the torus and lens exhaust holes must be established by comparing the mean free molecular path with the hole diameters. Using relationships from the book, Procedures in Experimental Physics:^a

$$\lambda = \frac{1.77 \times 10^{-23} T}{P \sigma^2} \quad (B-1)$$

^aStrong, John D.: Procedures in Experimental Physics. New York, Prentice-Hall, Inc., 1938.

For helium at room temperature (529 R) with a mean free path of 0.020 in., the computed pressure is 0.0063 psi. It is observed that the flow from the lens is free molecular; the flow from the torus is primarily transitional becoming free molecular at the extremes of the pressurization and depressurization periods; and the flow through the supply orifices is continuum. For simplicity the flow from the torus is assumed to be free molecular during this analysis; during the optimization phase of the program this assumption will be refined.

Again using Procedures in Experimental Physics, the expression for flow through an orifice in free molecular flow in terms of upstream pressure is:

$$\frac{W\sqrt{T}}{PA} = \frac{135.7}{\sqrt{R}} \quad (B-2)$$

For continuum flow the velocity in an orifice is sonic if the downstream pressure is less than approximately half the upstream pressure. Since this condition is met, the gas velocity in the orifice is:

$$U = 340.3 \sqrt{KRT_S} \quad (B-3)$$

The equation for flow in the orifice is:

$$\rho UAC_D = 144 W, \quad (B-4)$$

or, substituting Equation B-3 and the perfect gas law,

$$\frac{W\sqrt{T_S}}{P_S A} = 340.3 C_D \sqrt{\frac{K}{R}} \quad (B-5)$$

For sonic velocity the relationship between static and total temperatures is:

$$\frac{T}{T_S} = \frac{K+1}{2}; \quad (B-6)$$

and for static and total pressures,

$$\frac{P}{P_S} = \left(\frac{K+1}{2} \right)^{\frac{K}{K-1}}. \quad (B-7)$$

Equation B-5 in terms of total temperature and pressure, which correspond to upstream conditions, is:

$$\frac{W\sqrt{T}}{PA} = 340.3 C_D \sqrt{\frac{K}{R} \left(\frac{2}{K+1} \right)^{\frac{K+1}{K-1}}}. \quad (B-8)$$

The stored gas temperature is presumed to be 529 R (69 F), and if no heat energy is exchanged with the containers, lines, etc., the total temperature throughout the system will also be 529 R. The gas actually loses some heat energy to the lens and torus material during inflation, but this heat energy raises the temperature of the lens and torus material with subsequent heat transfer back to the gas. All total temperatures, therefore, will be presumed as 529 R.

During the inflation process of either torus or lens, helium is supplied at the rate W_{IN} . Helium is also exhausted through the holes in the fabric at the rate W_{OUT} ; therefore:

$$\frac{dw}{d\theta} = W_{IN} - W_{OUT}. \quad (B-9)$$

The mass of the contained gas (w) is expressed by:

$$144PV = wRT \quad (B-10)$$

the differential form of which is

$$\frac{dw}{d\theta} = \frac{144V}{RT} \frac{dP}{d\theta}. \quad (B-11)$$

The incoming flow (W_{IN}) is defined by Equation B-8 and, since the upstream pressure of 5 psi is constant, W_{IN} is constant. The outgoing flow (W_{OUT}) is defined by Equation B-2, and varies with time. Equation B-9 now can be written:

$$\frac{144V}{RT} \frac{dP}{d\theta} = W_{IN} - (135.7 \frac{A}{\sqrt{RT}})P, \quad (B-12)$$

or, upon integrating, where θ is time from start of pressurization,

$$P = 0.007369 \frac{\sqrt{RT}}{A} W_{IN} (1 - e^{-0.9424 \sqrt{RT} \frac{A}{V} \theta}). \quad (B-13)$$

For the torus, Equation B-13 becomes:

$$P = 0.09639 W_{IN} (1 - e^{-0.05493 \theta}). \quad (B-14)$$

For the lens, Equation B-13 becomes:

$$P = 0.00844 W_{IN} (1 - e^{-0.05493 \theta}). \quad (B-15)$$

For the specified design pressure at five minutes, Equations B-14 and B-15 yield values of W_{IN} of 1.6761 and 0.17761 lb per minute for the torus and lens, respectively. The supply orifice can be computed from Equation B-8 if the discharge coefficient (C_D) is established. C_D depends on the ratio of orifice diameter to duct diameter; a value of 0.8 is assumed to obtain approximate orifice sizes. Computed orifice areas are 0.767 and 0.0813 sq in. for the torus and lens, respectively, while the respective orifice diameters are 0.988 and 0.322 in.

For the period in which the design pressures are maintained, Equation B-9 becomes:

$$W_{IN} = W_{OUT}. \quad (B-16)$$

The outgoing flow (W_{OUT}) can be computed from Equation B-2, and is 0.4026 and 0.04265 lb per minute for the torus and lens, respectively.

For the depressurization process, Equation B-9 becomes:

$$-\frac{dw}{d\theta} = W_{OUT}. \quad (B-17)$$

By use of Equations B-2 and B-11, Equation B-17 becomes:

$$-\frac{144V}{RT} \frac{dP}{d\theta} = 135.7 \frac{A}{\sqrt{RT}} P, \quad (B-18)$$

the integral form of which is, for θ measured from start of depressurization,

$$\frac{P}{P_o} = e^{-0.9424 \sqrt{RT} \frac{A}{V} \theta}. \quad (B-19)$$

For the torus, Equation B-19 becomes:

$$P = 0.0388 e^{-0.05493 \theta}. \quad (B-20)$$

For the lens, Equation B-19 becomes:

$$P = 0.00036 e^{-0.05493 \theta}. \quad (B-21)$$

Required gas quantities can be computed from the above values of incoming flow and the respective times. The pressurization process requires 8.38 and 0.89 lb of helium for the torus and lens, respectively. The torus requires an additional 3.62 lb of helium for the nine-minute period of maintained design pressure, while the lens requires an additional 0.09 lb of helium for the two-minute period of maintained design pressure. Total helium requirements are 12.98 lb or 6.14 cu ft when stored at 3000 psi.

4. SUMMARY

For the specified design, the pressurization system must supply 12.98 lb of helium, exclusive of safety margins or residual gas in the storage tank. If the above mass is stored at 3000 psi, the volume is 6.14 cu ft.

The supply orifice sizes should be approximately 0.767 sq in. for the torus and 0.0813 sq in. for the lens. The respective diameters are 0.988 and 0.322 in. These figures should be refined when the duct sizes are established.

The predicted pressure-time curves are shown in Figures B-1 and B-2 and represent Equations B-14, B-15, B-20, and B-21 with the specified conditions.

5. DEFINITION OF SYMBOLS

Symbols

A	=	orifice area, sq in.
C_D	=	coefficient of discharge
K	=	ratio of specific heats (1.66 for He)
P	=	total pressure in torus, lens, or duct, lb_f/in^2
P_S	=	static pressure, lb_f/in^2
R	=	gas constant (386.2 for He) $\text{ft}\cdot\text{lb}_f/\text{lb}_m\cdot\text{deg R}$
T	=	total temperature in torus, lens, or duct, R
T_S	=	static temperature, R
U	=	sonic velocity, fpm
V	=	volume of gas in torus or lens, cu ft
W	=	mass flow rate, lb_m/min
t	=	time, min
λ	=	mean free molecular path, in.
ρ	=	gas density, lb_m/ft^3
σ	=	molecular diameter (0.86×10^{-8} for He), in.
w	=	mas of gas in torus or lens, lb_m

Subscripts

IN	=	into torus or lens
OUT	=	from torus or lens
o	=	initial

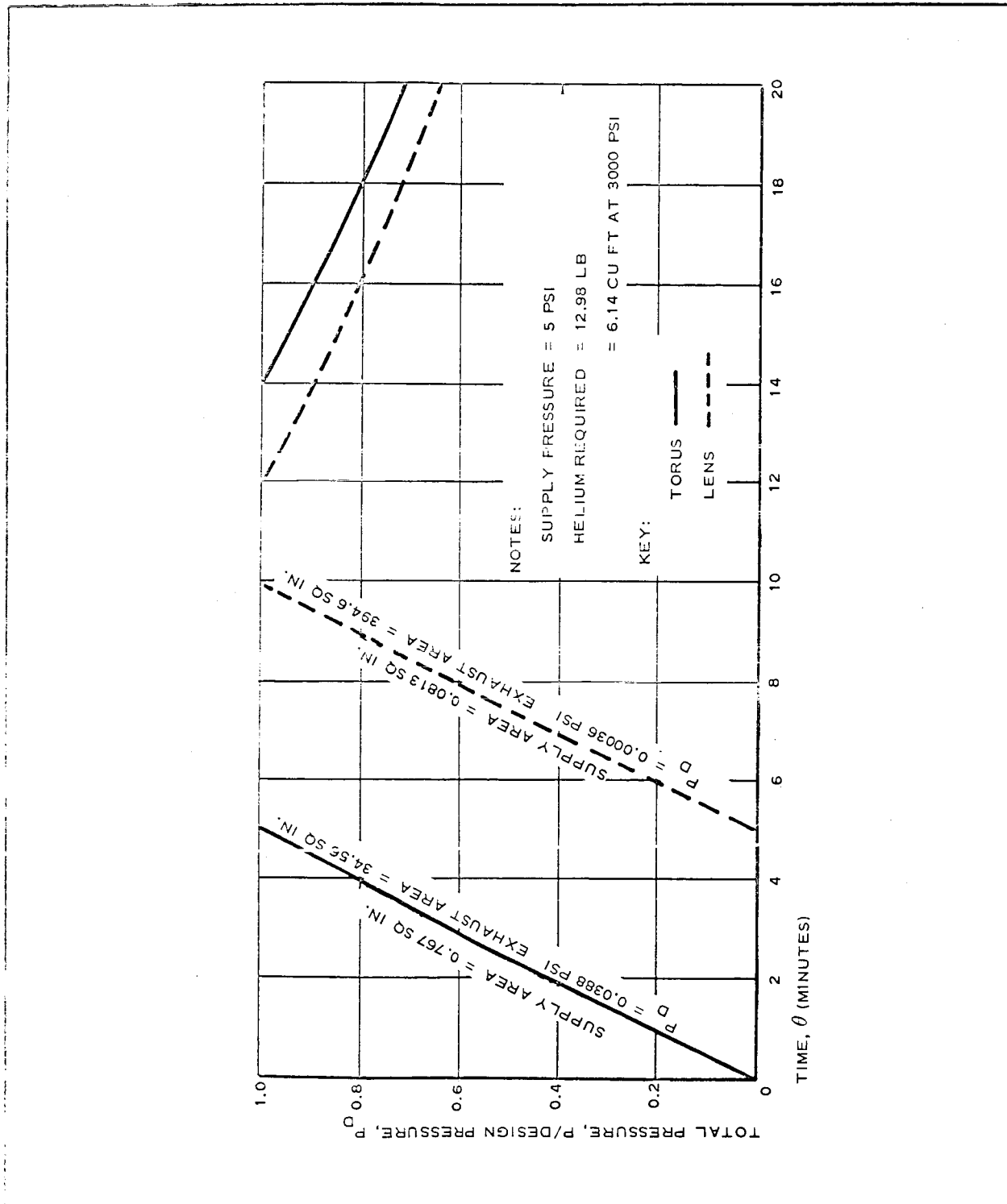


Figure B-1 - Linear Plot of Lenticular Satellite Pressure versus Time

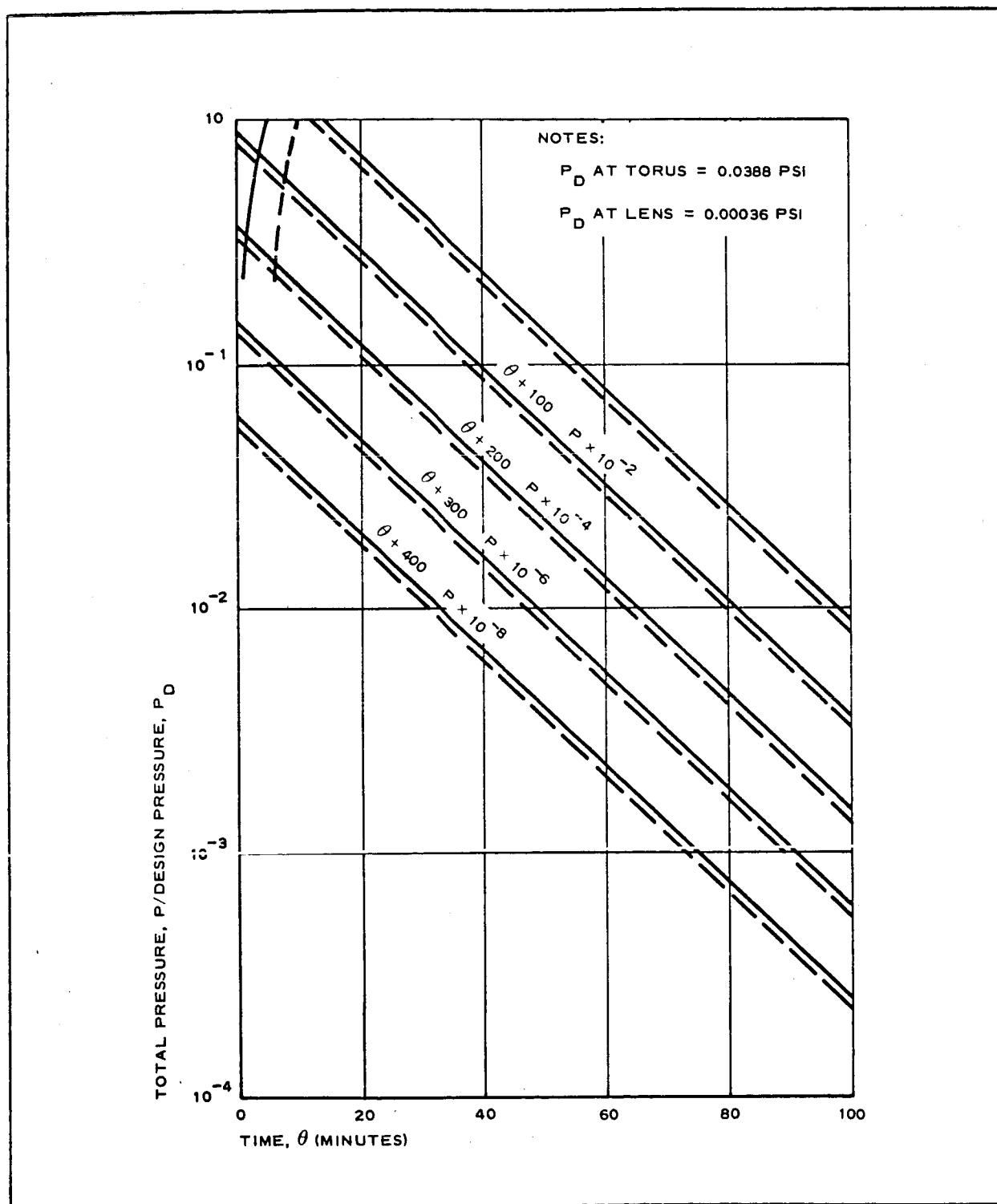


Figure B-2 - Semilog Plot of Lenticular Satellite Pressure versus Time

APPENDIX C - TORUS PRESSURIZATION STUDY

1. INTRODUCTION

The objective of this study is to investigate analytically the effects of compartmentization on the lenticular satellite torus pressurization and to determine flow control orifice sizes for the bulkheads of the 20-ft deployment model. This study supplements a test program on a 5-ft test model conducted by Astronautics Design.

The major conclusions are:

1. The compartmentization concept is feasible. The compartments should allow an orderly inflation and deployment sequence with negligible pressure differentials between compartments when fully inflated.
2. An inflation test at room pressure is significantly different from a test in vacuum. The pressurization response curves, optimum flow control orifice sizes, and gas supply rates for the two conditions have little resemblance.

2. ASSUMED SYSTEM PARAMETERS

The 20-ft deployment model torus shown in Figure 27 has a total volume of 256 cu ft, is divided into four compartments, and has a surface area of 720.9 cu ft. The surface is perforated with two 0.020-in. -diameter holes per square foot to facilitate packaging and deflation. Bulkheads are located at 45 deg, 90 deg, 120 deg, and 180 deg from the gas inlet port clockwise around the torus; only the first three contain flow control orifices. The torus material is 0.0015-in. -thick Mylar, which weighs 0.000075 psi.

The torus is inflated with air supplied at a constant flow rate until the first chamber attains the design pressure of 0.317 psia or psig as appropriate; the flow rate is then regulated to maintain the pressure at 0.317 psia or psig.

3. ANALYSIS (VACUUM)

In the vacuum condition resistance to inflation is provided by the inertia, friction, and kinks of the fabric and steel rim, as well as the weight of the fabric. It is noted that the fabric weight and sliding friction with the supporting medium exist for a test in a vacuum chamber but not for an orbital condition. Of the above items only kinks and sliding friction are significant, but unfortunately these items are not amenable to analysis.

This analysis therefore neglects these items and relies upon test programs to establish their influence.

In view of the above discussion, each torus chamber or compartment inflates with the first finite surge of gas to the affected chamber with subsequent buildup of pressure. From the viewpoint of compartment pressures the situation is analogous to the torus being fully inflated initially with pressures of essentially zero.

Let the chambers be numbered in sequence from the gas inlet port as 1, 2, 3, etc. Let the subscripts n and a refer to these chamber numbers and to ambient, respectively. The conservation of mass equation for chamber one during pressure buildup can be written as:

$$60 \frac{dw_1}{d\theta} = W_{SI} - W_{1-2} - W_{1-a} \quad (C-1)$$

After design pressure is attained, Equation D-1 becomes:

$$0 = W_S - W_{1-2} - W_{1-a} \quad (C-2)$$

Note that W_{SI} is constant while W_S is a variable.

For chambers 2 or greater:

$$60 \frac{dw_n}{d\theta} = W_{(n-1) - n} - W_{n - (n+1)} - W_{n - a} \quad (C-3)$$

For the last chamber, note that $W_{n - (n+1)}$ is zero.

The perfect gas law for each chamber is:

$$144 P_n V_n = w_n RT \quad (C-4)$$

Assuming a constant temperature, the differential form of Equation C-4 is:

$$\frac{dw_n}{d\theta} = \frac{144 V_n}{RT} \frac{dP_n}{d\theta} \quad (C-5)$$

The flow rates may be expressed as:

$$w_{n-m} = \frac{A_{n-m}}{\sqrt{T}} f_{n-m}(P_n, P_m, C, R, K) \quad (C-6)$$

The flow is basically continuum and the gas is air, but the flow may be sonic or subsonic. The value of coefficient of discharge (C) goes from approximately 0.6 for low velocities to 0.9 for sonic flow in such a manner that the parameter f_{n-m} may be approximated by two equations. If $0 \leq P_m/P_n \leq 0.4718$:

$$f_{n-m} = 28.73 P_n \quad (C-7)$$

If $0.4718 < P_m/P_n \leq 1$:

$$f_{n-m} = 39.53 \sqrt{P_n (P_n - P_m)} \quad (C-8)$$

Substituting Equations C-5 and C-6 into Equations C-1, C-2, and C-3, for pressure buildup of chamber 1,

$$\frac{dP_1}{d\theta} = 0.006175 \frac{\sqrt{T}}{V_1} \left(\sqrt{T} W_{SI} - A_{1-2} f_{1-2} - A_{1-a} f_{1-a} \right) \quad (C-9)$$

For chamber 1 after pressure buildup:

$$W_S = \frac{A_1 - 2}{\sqrt{T}} f_1 - 2 + \frac{A_1 - a}{\sqrt{T}} f_1 - a \quad (C-10)$$

and

$$P_1 = P_D \quad (C-11)$$

For chambers 2 or greater:

$$\frac{dP_n}{d\theta} = 0.006175 \frac{\sqrt{T}}{V_n} \left[A_{(n-1)} - n^{f(n-1)} - n - A_n - (n+1)^{f(n+1)} - A_n - a^{f(n-a)} \right] \quad (C-12)$$

By use of Equations C-7, C-8, C-9, C-10, and C-12 the pressure versus time relationship for each chamber may be obtained. GAC computer program El030 was written to solve these equations by use of a finite difference technique. Utilizing the specified system parameters and assuming a temperature of 69 F, the pressures are a function of the flow control orifice sizes and supply flow rate (W_{SI}) as well as time. By manipulation of these remaining variables the pressure-time curves are obtained.

A test program on a 5-ft test model indicated that rapid inflation minimizes the effects of kinks on inflation. Somewhat arbitrarily assuming a supply flow rate (W_{SI}) of 1.3 lb per minute and bulkhead flow control orifice sizes of 1-5/16, 31/32, and 5/8 in. diameters, respectively (one orifice per bulkhead), Figure C-2 was obtained.

4. ANALYSIS (ATMOSPHERIC)

In the atmospheric condition, resistance to inflation is provided by atmospheric pressure as well as the items discussed for the vacuum case. Again neglecting kinks, friction, and inertia, the pressure within a partially inflated chamber is atmospheric pressure plus the weight of fabric supported

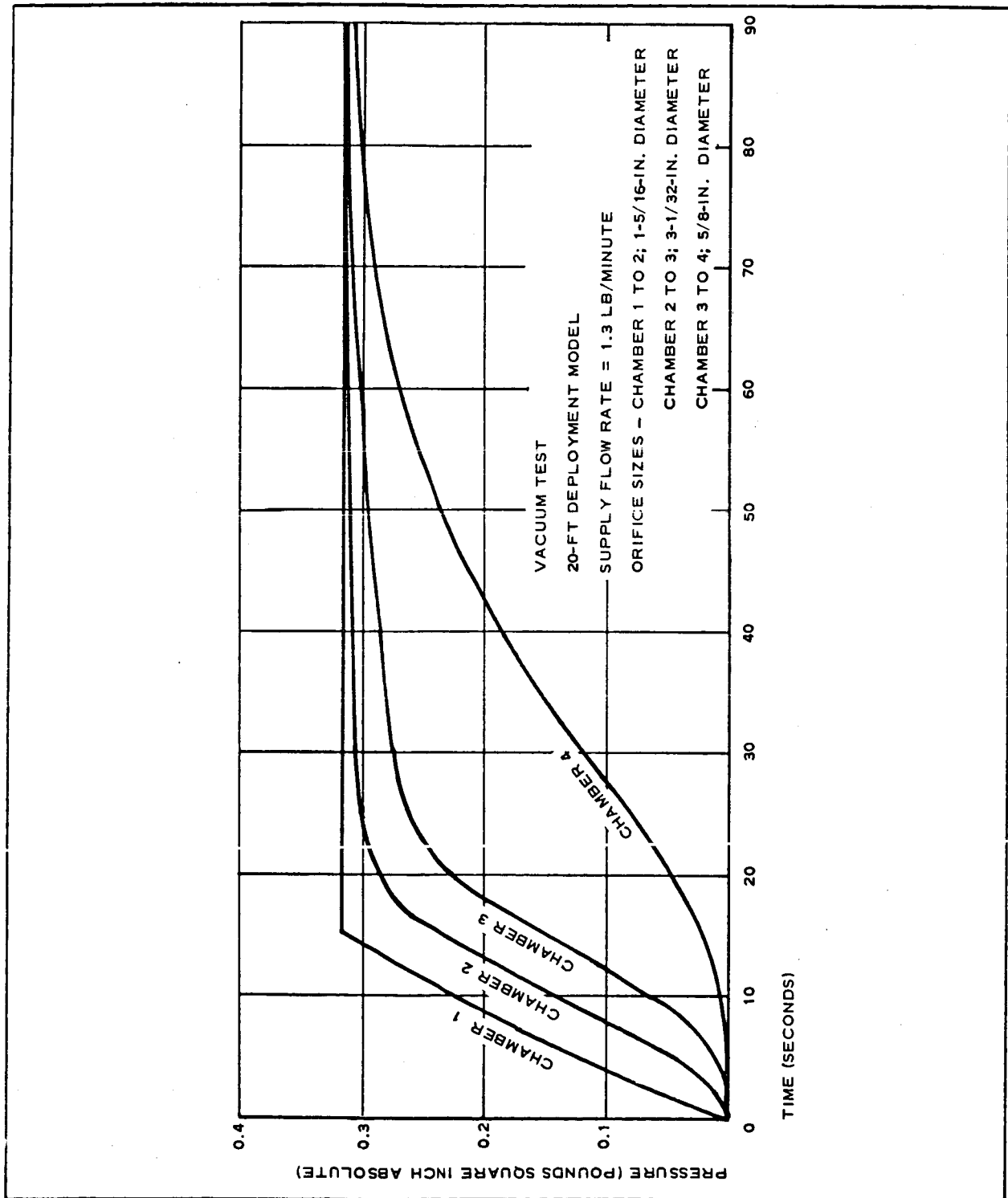


Figure C-1 - Torus Pressures versus Time

by the gas within the chamber. This latter term (weight of fabric) varies somewhat due to varying curvature of the fabric, but in any event is small when compared with design pressure (e. g., 0.000075 psi versus 0.317 psi). As air is supplied to a chamber the volume will increase while the pressure remains essentially constant at slightly above atmospheric until the chamber is inflated; the volume is then constant while the pressure increases toward design pressure. For simplicity the pressures during inflation are presumed to be atmospheric.

The conservation of mass equation for chamber 1 during volume or pressure buildup is again:

$$60 \frac{dw_1}{d\theta} = W_{SI} - W_{1-2} - W_{1-a} \quad (C-1)$$

After design pressure is attained:

$$0 = W_S - W_{1-2} - W_{1-a} \quad (C-2)$$

For chambers 2 or greater:

$$60 \frac{dw_n}{d\theta} = W_{(n-1)-n} - W_{n-(n+1)} - W_{n-a} \quad (C-3)$$

For each chamber, let V_n denote the volume when fully inflated and V_{nt} the actual volume at any time. The perfect gas law is then:

$$144 P_n V_{nt} = W_n RT \quad (C-13)$$

Again, assuming constant temperature, the differential form of Equation C-13 is one of two possible forms. If $0 \leq V_{nt} < V_n$:

$$\frac{dw_n}{d\theta} = \frac{144 P_a}{RT} \frac{dV_{nt}}{d\theta} \quad (C-14)$$

If $V_{nt} = V_n$,

$$\frac{dw_n}{d\theta} = \frac{144V_n}{RT} \frac{dP_n}{d\theta} \quad (C-5)$$

The flow rates are again:

$$W_{n-m} = \frac{A_{n-m}}{\sqrt{T}} f_{n-m}(P_n, P_m, C, R, K) \quad (C-6)$$

Since the flow is always subsonic,

$$f_{n-m} = 39.53 \sqrt{P_n(P_n - P_m)} \quad (C-8)$$

Equation C-6 then becomes:

$$W_{n-m} = \frac{39.53A_{n-m}}{\sqrt{T}} \sqrt{P_n(P_n - P_m)} \quad (C-15)$$

Substituting Equations C-14, C-5, and C-15 into Equations C-1, C-2, and C-3, if $0 \leq V_{1t} < V_1$:

$$\frac{dV_1}{d\theta} = 0.006175 \frac{T}{P_a} W_{SI} \quad (C-16)$$

and

$$P_1 = P_a \quad (C-17)$$

If $V_{1t} = V_1$ and $P_a \leq P_1 < P_D$,

$$\frac{dP_1}{d\theta} =$$

$$0.006175 \frac{\sqrt{T}}{V_1} \left[\sqrt{T} W_{SI} - 39.53A_1 - a \sqrt{P_1(P_1 - P_a)} - 39.53A_1 - 2 P_1(P_1 - P_2) \right] \quad (C-18)$$

If $V_{1t} = V_1$ and $P_1 = P_D$

$$W_S = \frac{39.53}{\sqrt{T}} \left[A_1 - a\sqrt{P_D(P_D - P_a)} + A_1 - 2\sqrt{P_D(P_D - P_2)} \right] \quad (C-19)$$

For chambers 2 or greater, if $0 \leq V_{nt} < V_n$:

$$\frac{dV_n}{d\theta} = 0.006175 \frac{\sqrt{T}}{P_a} \left[39.53A_{(n-1)} - n\sqrt{P_{n-1}(P_{n-1} - P_a)} \right] \quad (C-20)$$

and

$$P_n = P_a \quad (C-21)$$

If $V_{nt} = V_n$

$$\begin{aligned} \frac{dP_n}{d\theta} = 0.006175 \times 39.53 \frac{\sqrt{T}}{V_n} & \left[A_{(n-1)} - n\sqrt{P_{n-1}(P_{n-1} - P_n)} - \right. \\ & \left. A_n - (n+1)\sqrt{P_n(P_n - P_{n+1})} - A_n - a\sqrt{P_n(P_n - P_a)} \right] \quad (C-22) \end{aligned}$$

By use of Equations C-16, C-17, C-18, C-20, C-21, and C-22 the pressure and volume versus time curves for each chamber may be obtained. GAC computer program El030 also solves these equations. Again, assuming a temperature of 69 F, making all bulkhead orifice sizes equal, and per Astronautics Design test trends, presuming the optimum inflation times of chambers 1 and 4 to be approximately 35 and 60 sec, respectively, the supply flow rate (W_{SI}) and flow control orifice sizes were found by trial and error substitution in the above equations. The values are 19.93 lb per minute for the supply flow rate and 3-in. diameter for the flow control orifice sizes (one orifice per bulkhead). Figure C-2 presents the corresponding plots of pressures and volumes versus time.

5. ANALYSIS (SUPPLY FLOW RATES)

The desired supply flow rates, before flow regulation, may be obtained by a judicious selection of supply pressure and inlet port orifice size. Since

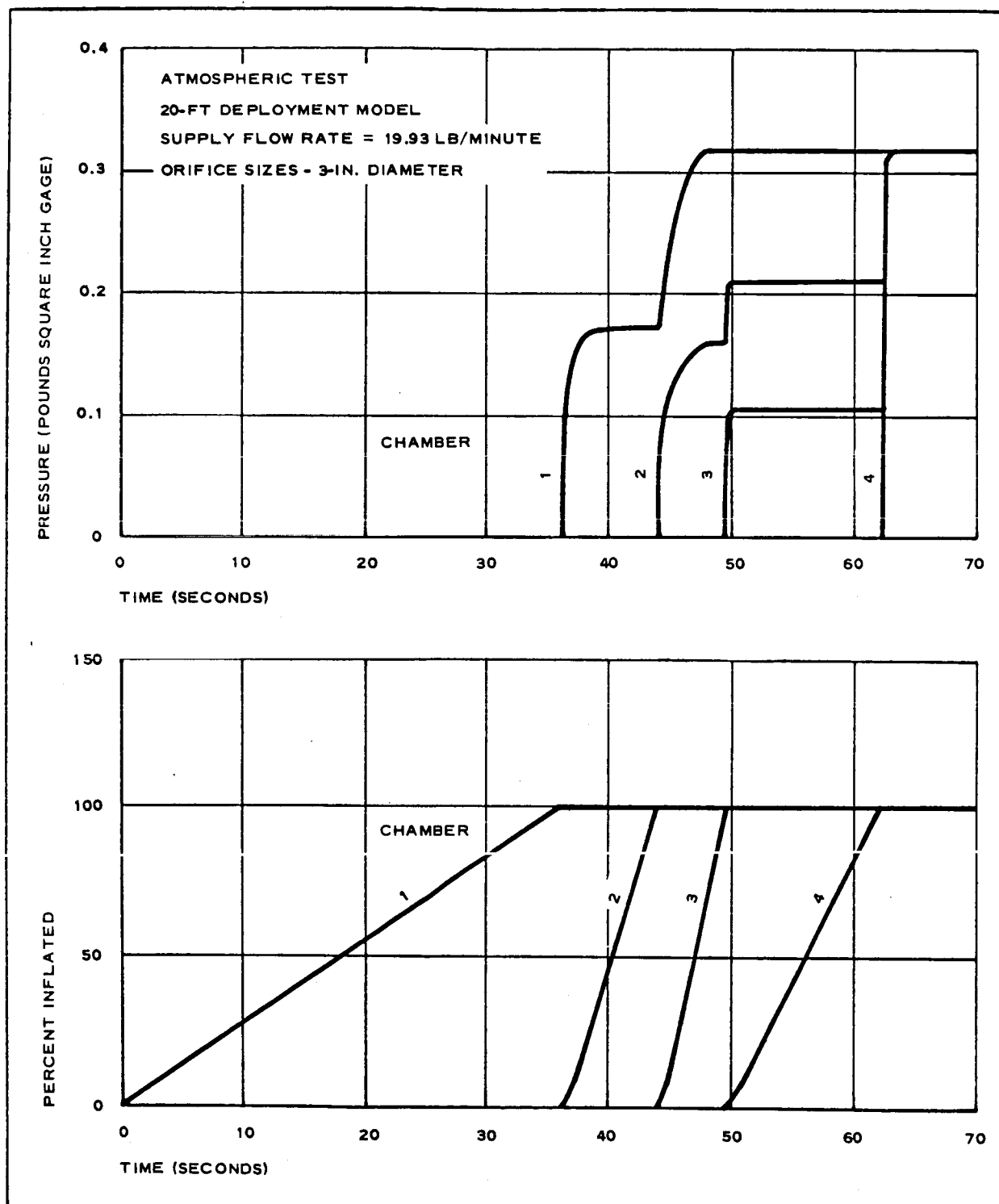


Figure C-2 - Torus Pressures and Volumes versus Time

plant air supply is to be used for the testing programs on the 20-ft deployment model, the supply pressure may easily be maintained in excess of twice the absolute design pressure, thereby assuring sonic flow through the inlet port orifice and constant flow rate. The flow equation is then:

$$W_{SI} = 31.92 \frac{P_{SI} A_{SI} C}{\sqrt{T}} \quad (C-23)$$

Under this condition the coefficient of discharge (C) is approximately 0.85. Again assuming a temperature of 69 F:

$$P_{SI} A_{SI} = 0.8477 W_{SI} \quad (C-24)$$

For any value of flow rate (W_{SI}), the supply pressure (P_{SI}) and port orifice size may be balanced as desired within limits. For the specified flow rate of 1.3 lb per minute for vacuum tests, a possible combination is a supply pressure of 89.8 psia or 75.1 psig and a port orifice diameter of 1/8 in. For the specified flow rate of 19.93 lb per minute for atmospheric tests, a possible combination is a supply pressure of 86.0 psia or 71.3 psig and a port orifice diameter of 1/2 in.

6. SUMMARY

The three bulkhead flow control orifices for the 20 ft-deployment model should be 3 in. in diameter for atmospheric testing and 1-5/16, 31/32, and 5/8 in. in diameter, respectively, for vacuum testing. Initial supply air flow rates (nonregulated) should be 19.93 lb per minute for atmospheric testing and 1.3 lb per minute for vacuum testing. Since the above analysis of necessity disregarded kinks in the fabric and steel rim, with only gross approximations on optimum inflation times, the above values are approximate and may be refined by a rigorous test program.

The above initial supply flow rates may be obtained by 1/8-in. and 1/2-in. diameter inlet port orifices and supply pressures of 89.8 psia (75.1 psig) and 86.0 psia (71.3 psig) for the vacuum and atmospheric tests, respectively.

The techniques and computer program described herein may be used for any size torus divided into any number of compartments.

7. DEFINITION OF TERMS

Symbol

A = orifice area(s), sq in.

C = coefficient of discharge

f = function, $\text{lb}_m - R^{0.5}/\text{min-in.}^2$

K = ratio of specific heat

P = pressure, $\text{lb}_f/\text{in.}^2(\text{abs})$

R = gas constant, $\text{ft-lb}_f/\text{lb}_m - R$

T = temperature, R

V_n = volume when inflated, cu ft

V_{nt} = volume at any time, cu ft

W = mass flow rate, lb_m/min

w = mass of gas, lb_m

θ = time, sec

Subscripts

a = ambient

D = design value

m = chamber number or ambient (generalized)

n = chamber number (generalized)

1, 2, 3, etc. = chamber number (particular)

S = supply (variable)

SI = supply (constant)

APPENDIX D - ERROR ANALYSIS FOR LENS OF LENTICULAR SATELLITE

1. INTRODUCTION

The lens of the lenticular satellite is a segment of a sphere. There are four quantities available to define the lens. These are shown in Figure D-1 and are: included angle, θ ; radius, ρ ; chord, D ; and arc length, S . Any two of these quantities may be used to define the spherical segment.

From a microwave viewpoint the quantities directly of interest are ρ and θ . Physically the lens shape depends upon S and D , neither of which can be precisely controlled. The arc length, S , depends upon manufacturing tolerances and the amount of net strain of the lens material obtained during the rigidizing process. The chord length, D , also depends upon manufacturing tolerances and will vary with time due to the perturbing forces.

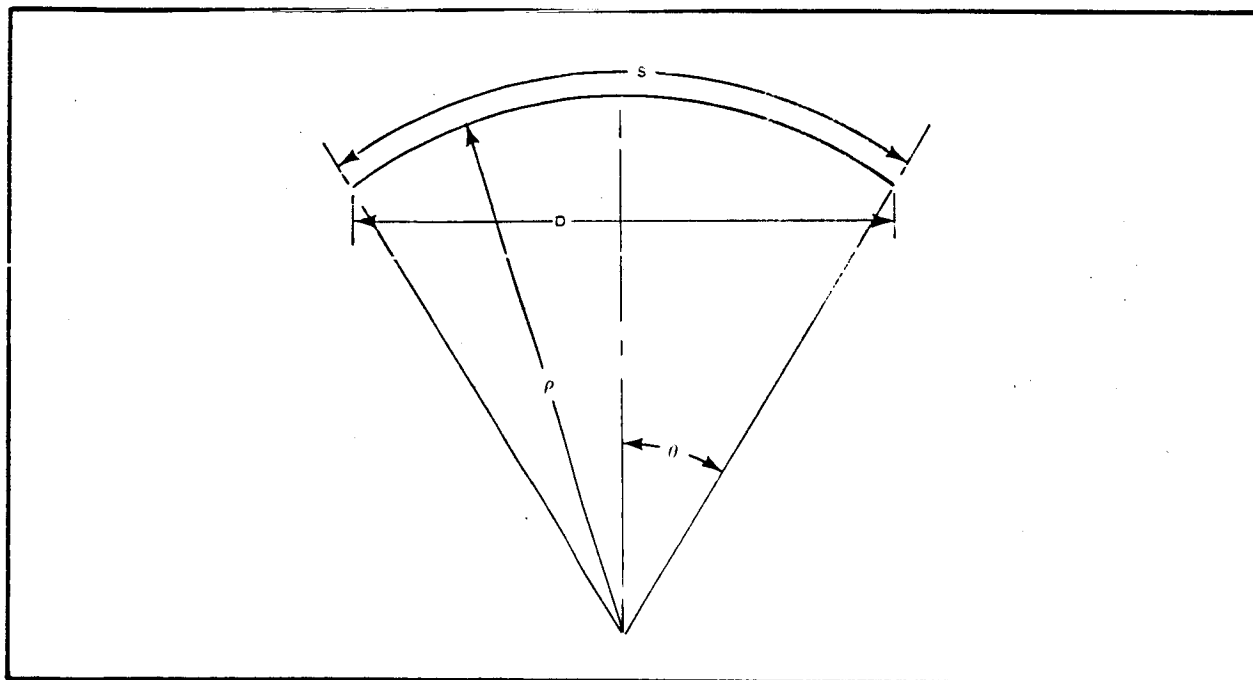


Figure D-1 - Lens Geometry

The specification of ρ , tolerance on ρ , and θ imposes a set of constraints on the system design that might affect seriously the final cost and weight. A convenient method of evaluating these constraints is desirable. The object of this study is to provide such a method.

2. ANALYSIS

From geometry it is apparent (see Figure D-1) that the following two relate the four variables.

$$\rho\theta = \frac{S}{2} \quad (D-1)$$

$$\rho \sin \theta = \frac{D}{2} \quad (D-2)$$

The above can be written

$$\theta = \frac{S}{2\rho} \quad (D-3)$$

$$\sin \theta = \frac{D}{2\rho} \quad (D-4)$$

Let ρ_o , θ_o , S_o , and D_o be a set of initial conditions; then for small variations in S and D the new radius is given by:

$$\rho = \rho_o + \left. \frac{\partial \rho}{\partial S} \right|_o (\Delta S) + \left. \frac{\partial \rho}{\partial D} \right|_o (\Delta D) \quad (D-5)$$

The coefficients ΔS and ΔD are designated herein as error coefficients. They are found by using Equations D-2 and D-3 to obtain

$$\begin{aligned} F &= \rho' \sin \frac{S}{2\rho} - \frac{D}{2} \\ &= 0 \end{aligned} \quad (D-6)$$

From the advanced calculus, then

$$\begin{aligned}
 \frac{\partial \rho}{\partial S} &= - \frac{\frac{\partial F}{\partial S}}{\frac{\partial F}{\partial \rho}} \\
 &= \frac{-\rho \left(\frac{1}{2\phi}\right) \cos\left(\frac{S}{\partial \rho}\right)}{\sin\left(\frac{S}{\partial \rho}\right) + \rho \left(-\frac{S}{2\rho^2}\right) \cos\left(\frac{S}{2\rho}\right)} \\
 &= \frac{-\cos\left(\frac{S}{\partial \rho}\right)}{2 \left[\sin\left(\frac{S}{2\rho}\right) - \left(\frac{S}{\phi\phi}\right) \cos\left(\frac{S}{\partial \rho}\right) \right]} \quad (D-7)
 \end{aligned}$$

$$\begin{aligned}
 \frac{\partial \rho}{\partial D} &= - \frac{\frac{\partial F}{\partial D}}{\frac{\partial F}{\partial \rho}} \\
 &= \frac{1}{2 \left[\sin\left(\frac{S}{\partial \rho}\right) - \left(\frac{S}{\partial \rho}\right) \cos\left(\frac{S}{\partial \rho}\right) \right]} \quad (D-8)
 \end{aligned}$$

Making use of Equation D-3, the above can be written

$$\frac{\partial \rho}{\partial S} = \frac{-\cos \theta}{2(\sin \theta - \theta \cos \theta)} \quad (D-9)$$

$$\frac{\partial \rho}{\partial D} = \frac{1}{2(\sin \theta - \theta \cos \theta)} \quad (D-10)$$

From small angles a more convenient expression is obtained by expanding in series form the denominator of the above equations.

$$\begin{aligned}\sin \theta - \theta \cos \theta &= \theta - \frac{\theta^3}{3!} + \frac{\theta^5}{5!} - \frac{\theta^7}{7!} - \theta \left(1 - \frac{\theta^2}{2!} + \frac{\theta^4}{4!} - \frac{\theta^6}{6!} \text{ etc.} \right) \\ &= \frac{\theta^3}{3} - \frac{\theta^5}{30} + \frac{\theta^7}{840} + \text{H. O. T.}\end{aligned}\quad (\text{D-11})$$

If only the first term in the expansion is retained then Equations D-9 and D-10 can be written

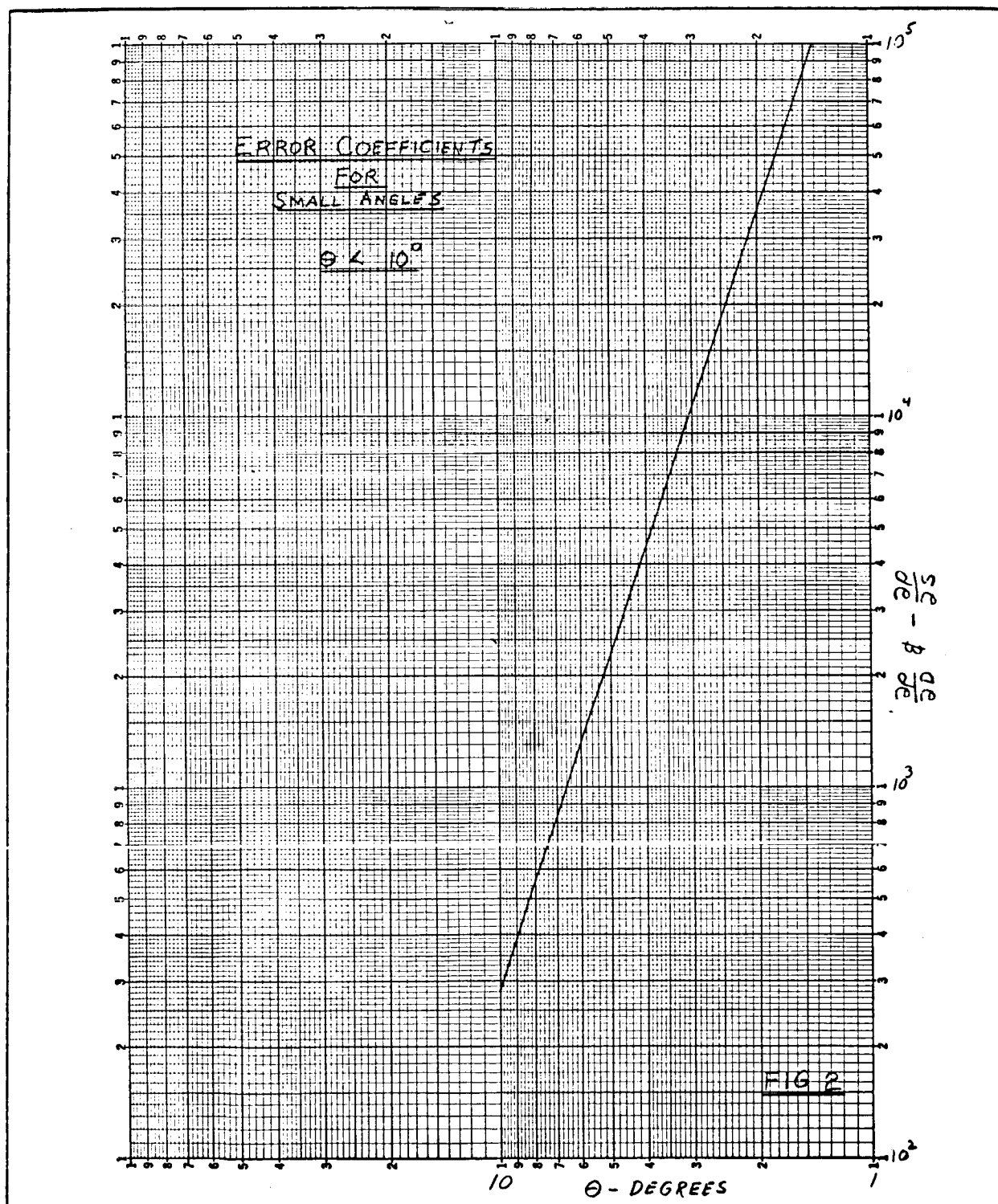
$$\begin{aligned}\frac{\partial \rho}{\partial D} &\approx -\frac{\partial \rho}{\partial S} = \frac{3}{2\theta^3} \text{ in radians} \\ &= \frac{282,200}{\theta^3} \text{ in degrees.}\end{aligned}\quad (\text{D-12})$$

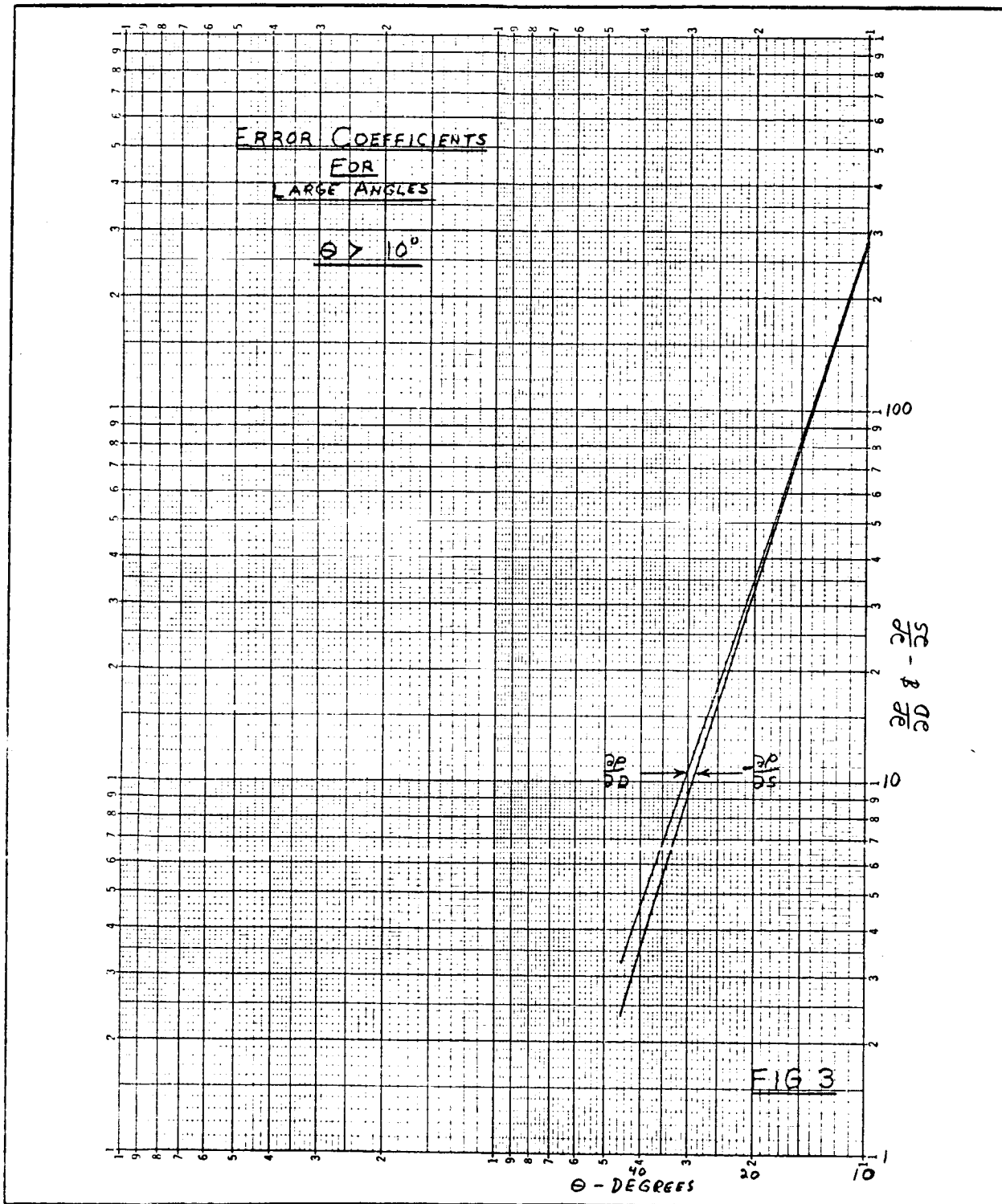
Values of $\partial \rho / \partial D$ and $\partial \rho / \partial S$, using Equations D-9 and D-10, were computed at 5-deg intervals through the range of 10 to 45 deg. These computations are shown in Table D-1. For convenience they have been plotted in Figure D-2. For angles under 10 deg, Equation D-12 is plotted in Figure D-3.

The final radius, ρ , can be found by Equation D-5 and Figures D-2 or D-3 to obtain the error coefficients. Once ρ is determined the final angle, θ , can be found from Equations D-1 and D-2.

TABLE D-1 - COMPUTATIONS FOR EQUATIONS D-9 AND D-10

θ°	$\theta \text{ rad}$	$\cos \theta$	$\sin \theta$	$\theta \cos \theta$	$\theta - \theta \cos \theta$	$\partial \rho / \partial D$	$-\partial \rho / \partial S$
10	0.174533	0.98481	0.17365	0.17188	0.00177	282.5	278.2
15	0.261799	0.96593	0.25882	0.25288	0.00594	84.18	81.31
20	0.349066	0.93969	0.34202	0.32801	0.01401	35.69	33.54
25	0.436332	0.90631	0.42262	0.39545	0.02717	18.40	16.68
30	0.523599	0.86603	0.50000	0.45345	0.04655	10.74	9.302
35	0.610865	0.81915	0.57358	0.50039	0.07319	6.832	5.596
40	0.698132	0.76604	0.64279	0.53480	0.10799	4.630	3.547
45	0.785398	0.70711	0.70711	0.55536	0.15175	3.295	2.330

Figure D-2 - Error Coefficients for Small Angles ($\theta < 10$ Deg)

Figure D-3 - Error Coefficients for Large Angles ($\theta > 10$ Deg)

3. DISCUSSION

Equations D-1 and D-2 plus a knowledge of the variations in S and D are sufficient to make an error analysis. In fact, they must be used if large variations are permitted. For small variations the method derived herein simplifies the calculations and provides greater insight into the problem.

An examination of Figures D-2 and D-3 immediately reveals the powerful influence of the angle θ on the error coefficients. Without further knowledge of ΔS and ΔD it is apparent that small θ imposes a very severe constraint upon the system design.

The weight and cost of the system can be affected seriously by the restrictions imposed on ΔS and ΔD by the microwave requirements. The major considerations are:

1. Manufacturing tolerances on S and D .
2. Rigidization - The final arc length, S , is dependent upon the accuracy with which the permanent set of the wire film material can be controlled. The ΔS permitted therefore dictates the accuracy of the inflation system required.
3. Orbital Loads - These produce time varying loads and deflections on the rim. The in-plane deflections are changes in the diameter, D ; hence the rim stiffness and weight are a function of ΔD . Further, since rim weight is the principal contributor to the polar moment of inertia and fixed ratio of inertia is desired, the entire system weight is affected.

APPENDIX E - PROPERTIES OF THE SATELLITE COMPONENTS

The main components of the lenticular satellite, exclusive of the concentrated masses at the ends of the tripods, are:

1. The faces of the lens (two spherical zones)
2. The metal rim, which constitutes the bounding edge of the satellite
3. The torus which is used to stabilize the lenticular shape during the rigidization phase

Table E-I gives the surface area, volume, and moments of inertia of the main components of the lenticular satellite shown in Figure E-1. The centroidal mass moment of inertia, $I_{x-x(\text{lens})}$, of the lens about the x-axis can be found from equation

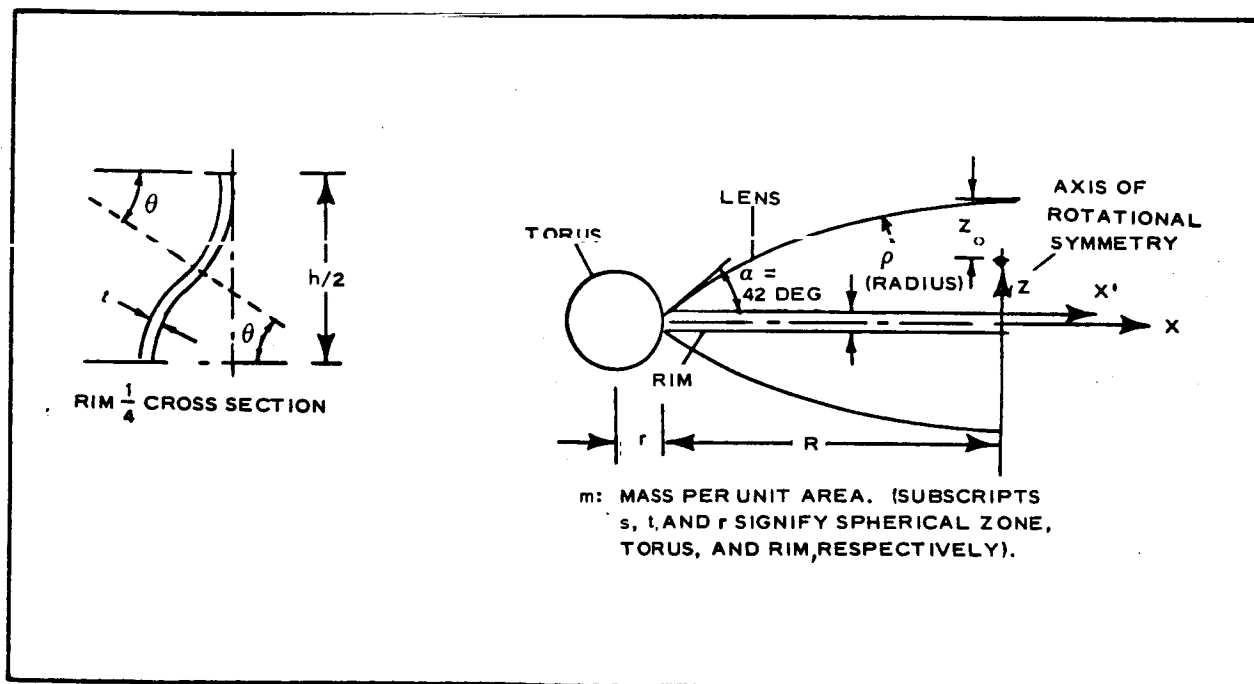
$$\begin{aligned}
 I_{x-x(\text{lens})} &= 2I_{x'-x'} - 2Am_s Z_o^2 + 2Am_s \left(Z_o + \frac{h}{2}\right)^2 \\
 &= 2I_{x'-x'} + \frac{Am_s h}{2} (4Z_o + h) \\
 &\approx 2I_{x'-x'} + 2Am_s h Z_o .
 \end{aligned}$$

Substituting values for $I_{x'-x'}$, A , and Z_o from Table E-I and simplifying yields

$$I_{x-x(\text{lens})} = 2\pi p^4 m_s (1 - \cos \alpha)^2 \left(\frac{4}{3} - \frac{1}{3} \cos \alpha + \frac{h}{\rho} \right) .$$

**TABLE E-I - PROPERTIES OF MAIN COMPONENTS OF
LENTICULAR SATELLITE**

Property	Lens (only one spherical zone)	Torus	Equatorial rim
Surface area, A	$2\pi p^2(1 - \cos \alpha)$	$4\pi^{\omega} r(R + r)$	Actual foil area (two wavy cylindrical surfaces) $4\pi rh \left(\frac{\theta}{\sin \theta} \right)$
Volume	Bounded by top spherical zone and coordinate plane x'y' $\frac{1}{3} \pi p^3 (1 - \cos \alpha)^2 (2 + \cos \alpha)$	$2\pi^2 r^2 (R + r)$	Actual material volume $4\pi Rht \left(\frac{\theta}{\sin \theta} \right)$
Polar moment of inertia (about z-axis)	$\frac{2}{3} \pi p^4 m_s (\cos^3 \alpha + 2 - 3 \cos \alpha)$	$4\pi^2 r^3 m_t (R + r) \left[\left(\frac{R}{r} + 1 \right)^2 + \frac{3}{2} \right]$	$4\pi R^3 h m_r \left(\frac{\theta}{\sin \theta} \right)$
Moment of inertia about x-axis	...	$2\pi^2 r^3 (R + r) m_t \left[\left(\frac{R}{r} + 1 \right)^2 + \frac{5}{2} \right]$	$2\pi R^3 h m_r \left(\frac{\theta}{\sin \theta} \right)$
Moment of inertia about x'-axis	$\frac{1}{3} \pi p^4 m_s (1 - \cos \alpha)^2 (4 - \cos \alpha)$
CG location	$Z_o = \frac{p}{2} (1 - \cos \alpha)$



APPENDIX F - LENTICULAR RETURN VERSUS $2\pi R/\lambda$ AND FREQUENCY

Graphs of nose-on monostatic return from the lenticular shape and radar return for various frequency regions of interest are discussed in this appendix. Figure F-1 shows the following:

1. First order of approximation to Rayleigh scattering
2. Points indicating peaks and nulls of power reflection
3. Curves indicating envelope of maximum and minimum values

Frequencies are indicated on the upper axis. $2\pi R/\lambda$ is indicated on the lower axis. Note that the power return curve is approximately $\sin^2 2\pi R/(\lambda/4)$ and oscillates to the extent that it could not be shown effectively on the graph paper used (a complete cycle of variations occurs with a 10-mc frequency change).

Test model $2\pi R/\lambda = 90$ (X band)

50-foot test model $2\pi R/\lambda = 2170$ (X band)

These values ($2\pi R/\lambda$ for the test model and the 50-foot model) are indicated in Figure F-1 and show the region of operation if these models were tested at X band (10 kmc).

The graph of lenticular return was obtained from a computer analysis of Equation F-1:

$$\frac{\sigma}{\pi R^2} = \frac{4}{R^2} \left\{ \left(-q + p \cos \omega a + \frac{c}{4\omega} \sin \omega a \right)^2 + \frac{c}{4\omega} \left[(\cos \omega a - 1) - p \sin \omega a \right]^2 \right\}, \quad (F-1)$$

where

σ = radar cross section,
 R = radius of curvature,

- q = center spectral return,
- p = edge diffraction return,
- c = velocity of propagation,
- a = distance between center and edge return, and
- $\omega = 2\pi f$.

The resultant curves indicate constructive and destructive interference between the center spectral return and the edge diffraction. The variation in return due to this interference is shown to be 21.5 db.

The radar return versus $2\pi R/\lambda$ and frequency for three frequency regions of interest are shown in Figures F-2 through F-5.

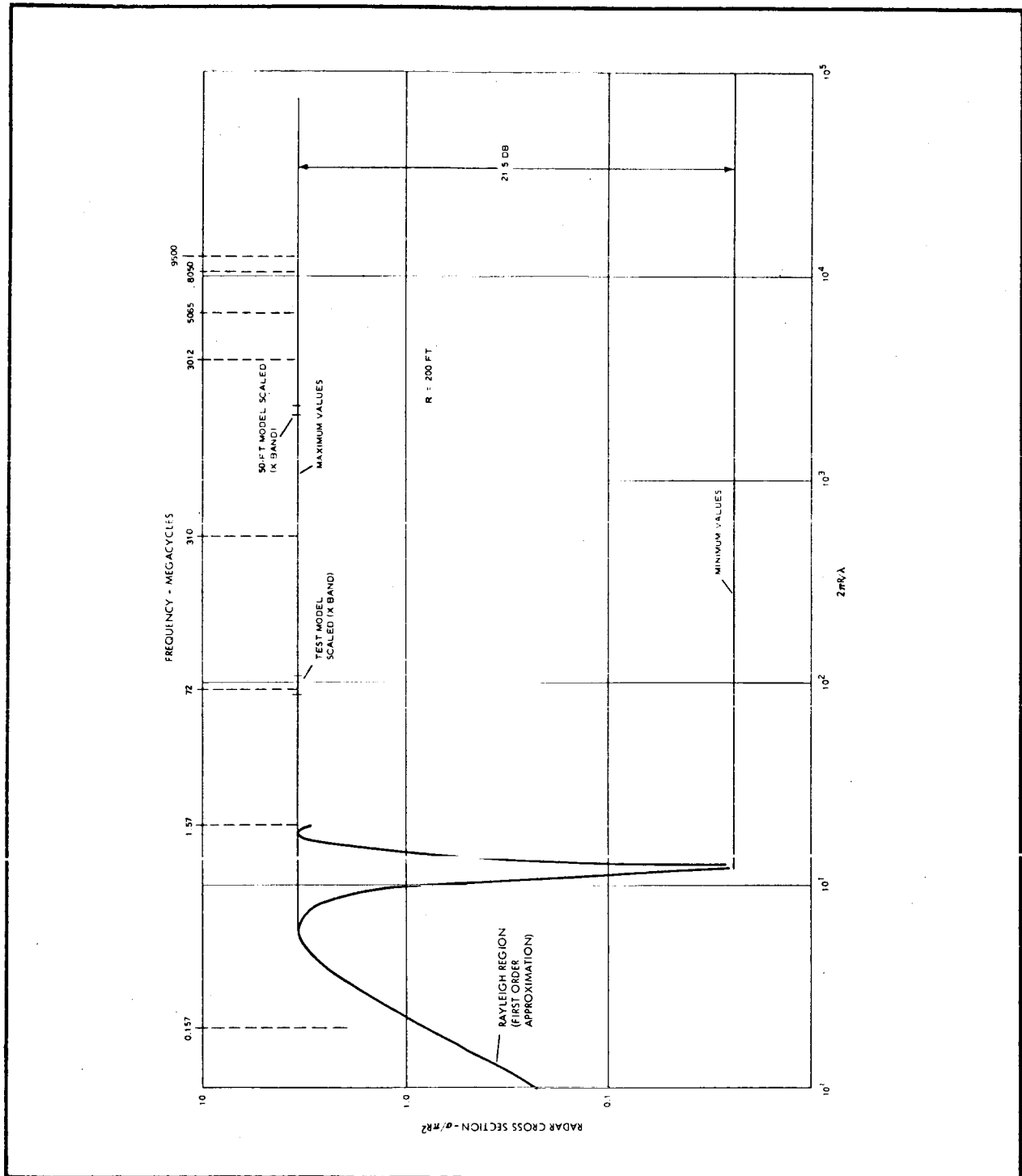


Figure F-1 - Theoretical Return of Full-Scale Lenticular Satellite versus $2\pi R/\lambda$ and Frequency

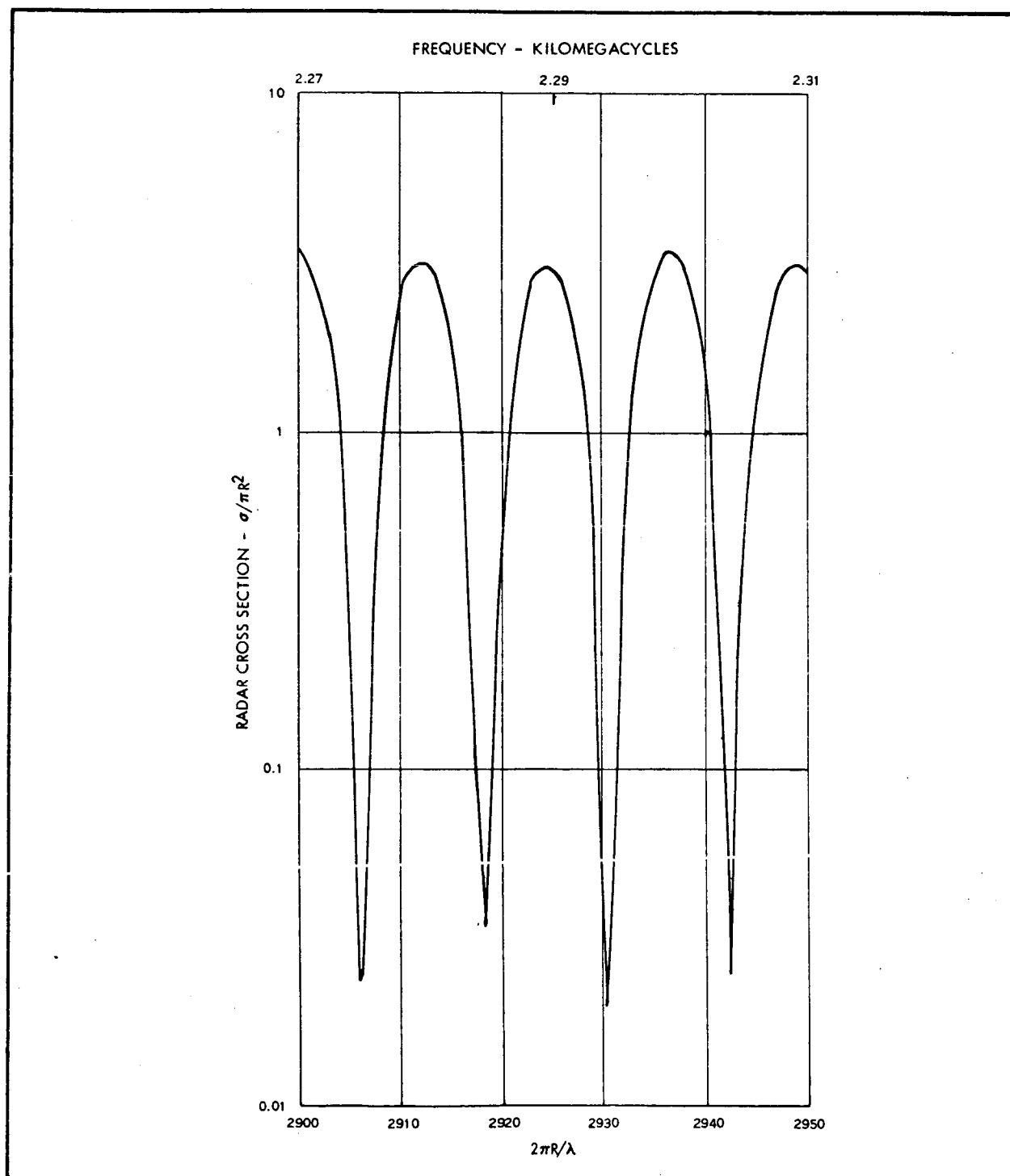


Figure F-2 - Lenticular Return versus $2\pi R/\lambda$ and Frequency (2.27 to 2.31 KMC)

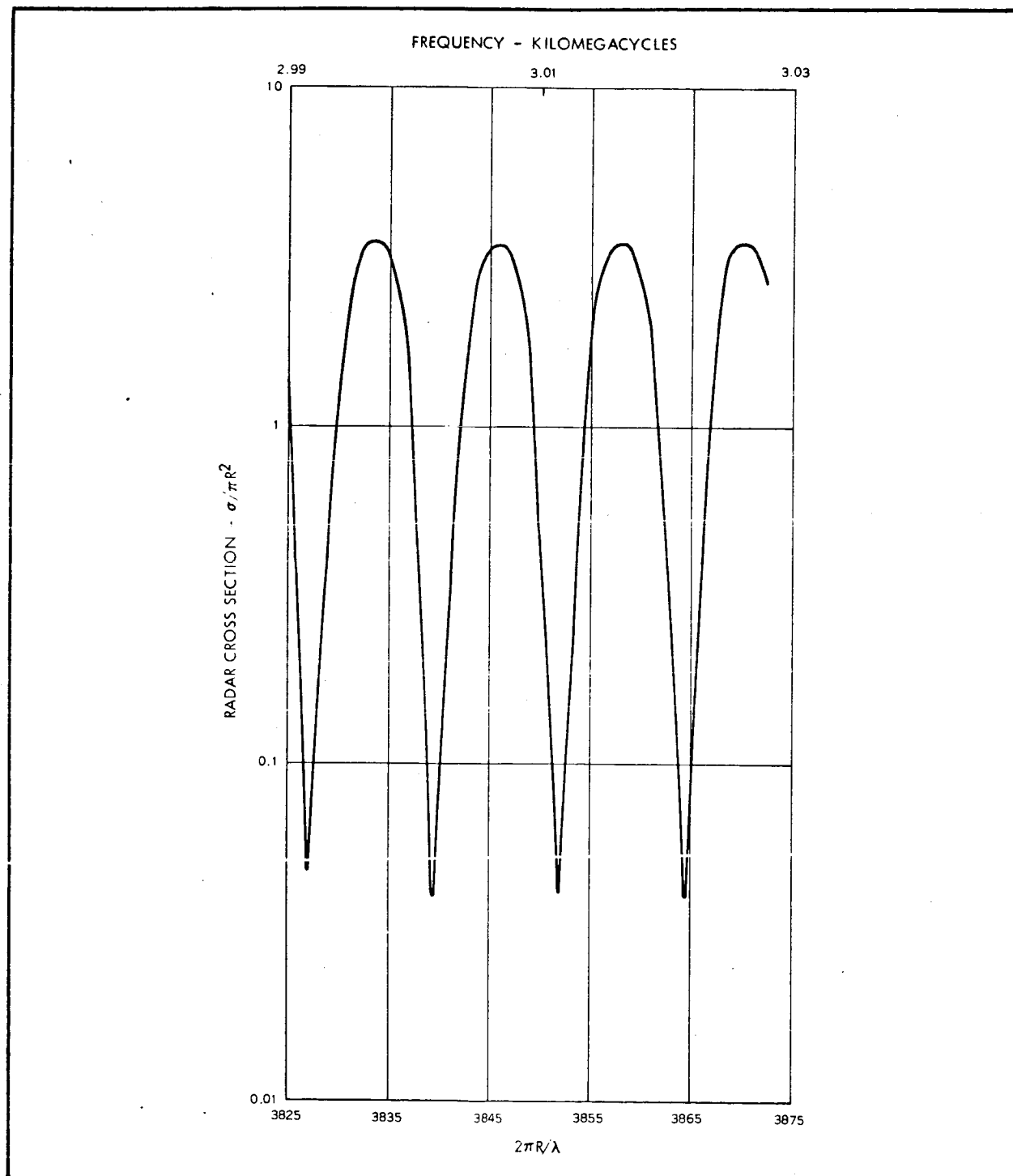


Figure F-3 - Lenticular Return versus $2\pi R/\lambda$ and Frequency (2.99 to 3.03 KMC)

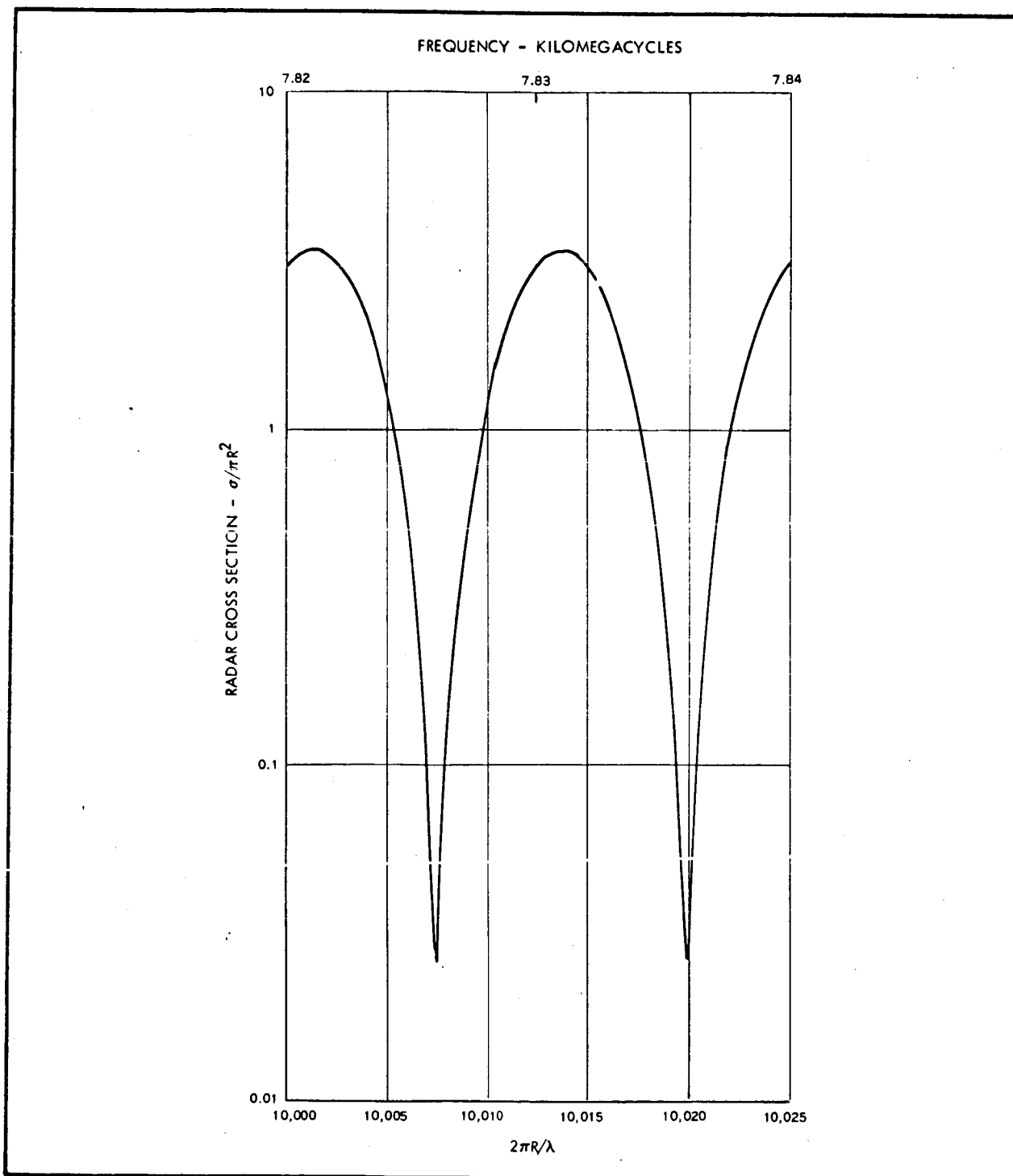


Figure F-4 - Lenticular Return versus $2\pi R/\lambda$ and Frequency (7.82 to 7.84 KMC)

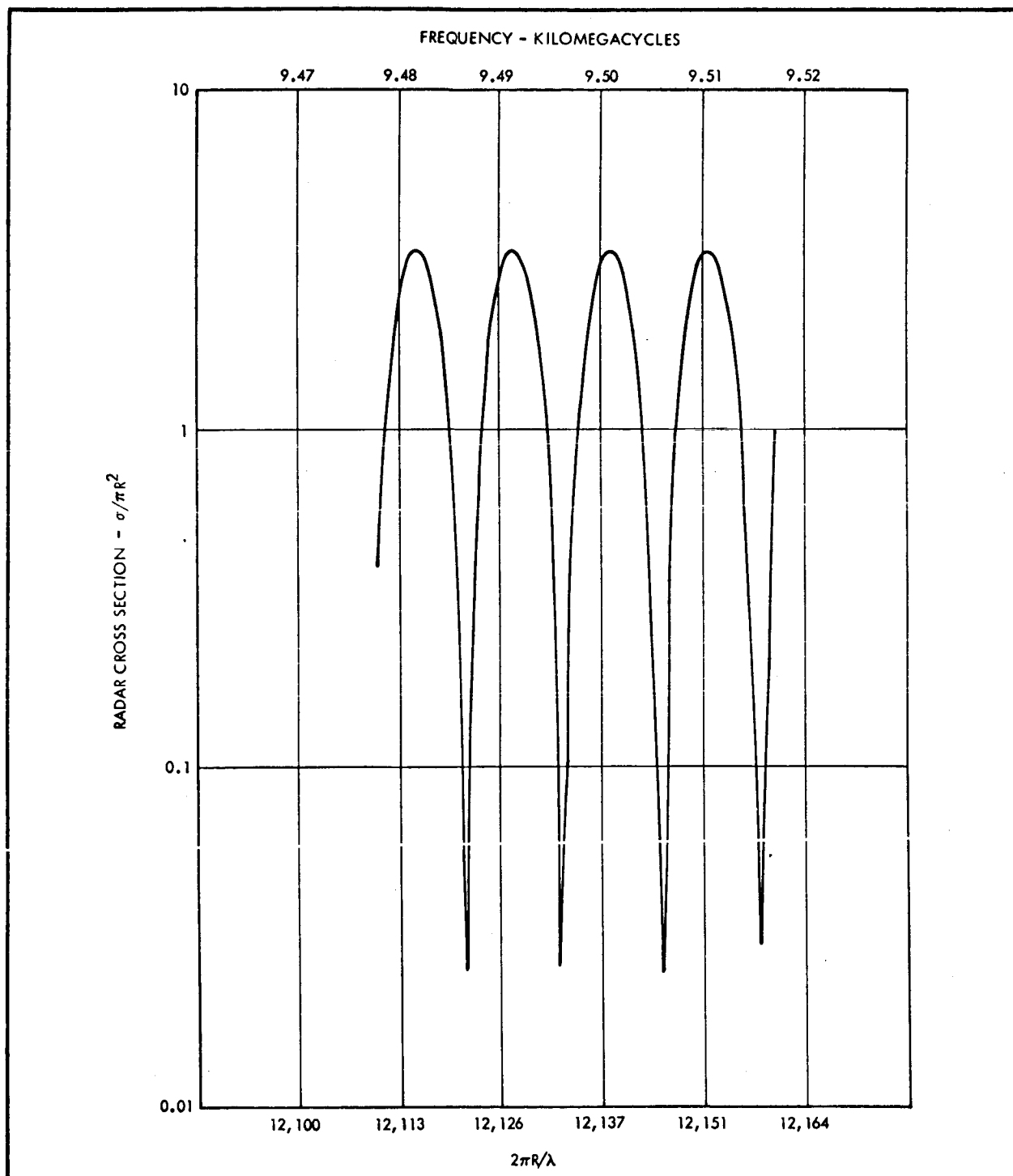


Figure F-5 - Lenticular Return versus $2\pi R/\lambda$ and Frequency (9.47 to 9.52 KMC)

APPENDIX G - CALCULATION OF BOOM RETURN

The equations for the calculation of the radar return from a thin wire are used to calculate the return from the lenticular satellite booms.^a

$$\sigma = \frac{\pi L^2 \sin^2 \theta \left[\frac{\sin\left(\frac{2\pi L}{\lambda} \cos \theta\right)}{\frac{2\pi L}{\lambda} \cos \theta} \right]^2}{\left(\frac{\pi}{2}\right)^2 + \left(\ln \frac{\lambda}{\gamma \pi a \sin \theta}\right)^2} \cos^4 \phi. \quad (G-1)$$

For

$\theta = \frac{\pi}{2}$, Equation G-1 reduces to

$$\sigma = \frac{\pi L^2}{\left(\frac{\pi}{2}\right)^2 + \left(\ln \frac{\lambda}{\gamma \pi a}\right)^2} \cos^4 \phi, \quad (G-2)$$

where

L = length of boom (ft),

a = radius of wire (inches).

$\gamma = 1.78$,

θ = angle between axis of boom and incident energy, and

ϕ = angle between polarization and plane of wire and line of incident energy.

The equations were evaluated for the following cases of interest:

^aCrispen, W. Jr.: Goodrich, R. F.; and Seigel, K. M.: A Theoretical Method for the Calculation of Radar Cross-Section of Aircraft and Missiles. Report 2591-1-H. Ann Arbor, Mich., University of Michigan, July 1959.

Case 1

$$L = 210 \text{ ft}$$

$$\lambda = 1.97 \text{ in. (6 kmc)}$$

$$a = 0.0625 \text{ in. (1/8-inch wire in boom)}$$

$$\phi = 0 \text{ deg (polarization parallel with wire)}$$

Case 2

$$L = 210 \text{ ft}$$

$$\lambda = 1.18 \text{ in. (10 kmc)}$$

$$a = 4.1 \text{ in. (wire grid boom)}$$

$$\phi = 0 \text{ deg (polarization parallel with boom)}$$

Case 3

$$L = 210 \text{ ft}$$

$$\lambda = 5.59 \text{ in. (2 kmc)}$$

$$a = 4.1 \text{ in. (wire grid boom)}$$

$$\phi = 0 \text{ deg (polarization parallel with boom)}$$

Due to the magnitude of $\frac{2\pi L}{\lambda} \cos \theta$ for angle $< \pi/2$, the following approximation was made:

$$\sin\left(\frac{2\pi L}{\lambda} \cos \theta\right) = 1 \text{ (worst case);} \quad (\text{G-3})$$

then Equation G-1 becomes

$$\sigma \approx \frac{\lambda^2}{4\pi} \frac{\tan^2 \theta}{\left(\frac{\pi}{2}\right)^2 + \left(\ln \frac{\lambda}{\gamma \pi a \sin \theta}\right)^2} . \quad (\text{G-4})$$

Equation G-4 in effect eliminates the side lobes in the wire pattern given by the factor

$$\frac{\sin\left(\frac{2\pi L}{\lambda} \cos \theta\right)}{\frac{2\pi L}{\lambda} \cos \theta} . \quad (\text{G-5})$$

APPENDIX H - MICROWAVE REFLECTIVITY MEASUREMENT DATA

A free-space transmission test was performed to determine the reflection coefficient of the photolyzable grid panel at four frequencies. The test compares the received power level between a transmitting and receiving horn with and without the panel inserted between them. The panel is oriented normal to the beam of the transmitting horn. The two horns are collimated with respect to one another.

The decibel difference in reading is measured five consecutive times at both maximum and minimum transmission values, which are obtained by transversely positioning the transmitter horn. These values are converted to power ratios, and the maximum-minimum values corresponding to each of the five positions are averaged. These five values obtained are again averaged to give one final transmission value. (See Tables H-I and H-II.)

The reflection coefficient is found from the relationship

$$T^2 + \Gamma^2 = 1,$$

where

T = transmission voltage

Γ = reflection voltage

TABLE H-I - REFLECTIVITY MEASUREMENTS DATA OF GAC
1.6-MIL WIRE GRID PHOTOLYZABLE FILM MATERIAL

Test Frequency	Position	DB Difference		Power Ratio		Avg	Total Avg T^2	Reflection Coefficient $\Gamma = \sqrt{1 - T^2}$
		Max	Min	Max	Min			
5000 mc, parallel polarization	1	21.41	22.44	0.007228	0.005702	0.006465	0.005863	0.997
	2	21.83	23.57	0.006561	0.004395	0.005478		
	3	22.33	22.75	0.005848	0.005309	0.005579		
	4	21.50	22.86	0.007079	0.005176	0.006128		
	5	22.02	22.80	0.006281	0.005248	0.005765		
5000 mc, perpendicular polarization	1	15.26	16.64	0.02979	0.02168	0.02574	0.02747	0.986
	2	15.25	16.60	0.02985	0.02188	0.02587		
	3	15.40	16.48	0.02884	0.02249	0.02567		
	4	14.50	15.91	0.03548	0.02564	0.03056		
	5	14.74	15.95	0.03357	0.02541	0.02949		
4875 mc, parallel polarization	1	20.93	21.42	0.008072	0.007211	0.007642	0.006910	0.996
	2	21.50	22.10	0.007079	0.006166	0.006623		
	3	21.24	21.45	0.007516	0.007161	0.007339		
	4	21.52	21.97	0.007046	0.006353	0.006700		
	5	22.00	22.09	0.006310	0.006180	0.006245		
4875 mc, perpendicular polarization	1	14.90	15.55	0.03236	0.02786	0.03011	0.02831	0.985
	2	14.77	15.36	0.03334	0.02911	0.03123		
	3	14.74	15.04	0.03357	0.03133	0.03245		
	4	15.93	16.75	0.02553	0.02113	0.02333		
	5	15.80	16.47	0.02630	0.02254	0.02442		
9373 mc, perpendicular polarization	1	9.70	12.12	0.1072	0.06138	0.0843	0.0890	0.954
	2	9.67	12.13	0.1079	0.06124	0.0846		
	3	9.38	12.03	0.1153	0.06266	0.0890		
	4	9.34	11.82	0.1164	0.06577	0.0911		
	5	9.17	11.52	0.1211	0.07047	0.0958		
9373 mc, parallel polarization	1	15.66	18.28	0.02716	0.01486	0.02101	0.01962	0.990
	2	15.95	18.60	0.02541	0.01380	0.01961		
	3	15.97	18.65	0.02529	0.01365	0.01947		
	4	15.95	18.62	0.02541	0.01374	0.01958		
	5	15.98	18.67	0.02523	0.01358	0.01941		
8600 mc, perpendicular polarization	1	9.36	11.87	0.1159	0.06501	0.0905	0.0919	0.953
	2	9.30	11.75	0.1175	0.06683	0.0922		
	3	9.28	11.72	0.1180	0.06730	0.0927		
	4	9.20	11.60	0.1202	0.06918	0.0947		
	5	9.58	11.63	0.1102	0.06871	0.0895		
8600 mc, parallel polarization	1	15.55	18.27	0.02786	0.01489	0.02138	0.02110	0.989
	2	15.59	18.28	0.02761	0.01486	0.02124		
	3	15.67	18.20	0.02710	0.01514	0.02112		
	4	15.79	18.20	0.02636	0.01514	0.02075		
	5	15.71	18.20	0.02685	0.01514	0.02100		

TABLE H-II - REFLECTIVITY MEASUREMENTS DATA OF GAC
1.2-MIL WIRE GRID PHOTOLYZABLE FILM MATERIAL

Test Frequency	Position	DB Difference		Power Ratio		Avg	Total Avg T ²	Reflection Coefficient $\Gamma = \sqrt{1 - T^2}$
		Max	Min	Max	Min			
9373 mc, perpendicular polarization	1	8.56	10.02	0.1393	0.0995	0.1194	0.1155	0.941
	2	8.90	10.25	0.1288	0.0944	0.1116		
	3	8.90	10.34	0.1288	0.0925	0.1107		
	4	8.86	10.30	0.1300	0.0933	0.1117		
	5	8.21	10.12	0.1510	0.0973	0.1242		
9373 mc, parallel polarization	1	13.20	14.05	0.0479	0.0394	0.0442	0.0434	0.978
	2	13.20	14.05	0.0479	0.0394	0.0437		
	3	13.34	14.05	0.0483	0.0394	0.0429		
	4	13.29	14.05	0.0463	0.0394	0.0429		
	5	13.41	14.02	0.0456	0.0396	0.0431		
8600 mc, perpendicular polarization	1	6.98	9.70	0.2004	0.1072	0.1538	0.1631	0.915
	2	6.70	9.52	0.2138	0.1117	0.1628		
	3	6.91	9.52	0.2037	0.1117	0.1577		
	4	6.57	9.37	0.2203	0.1156	0.1680		
	5	6.46	9.18	0.2259	0.1208	0.1734		
8600 mc, parallel polarization	1	12.03	15.41	0.0627	0.0288	0.0458	0.0466	0.976
	2	11.88	15.55	0.0649	0.0279	0.0464		
	3	11.88	15.55	0.0649	0.0279	0.0464		
	4	11.78	15.50	0.0664	0.0282	0.0473		
	5	11.78	15.56	0.0664	0.0278	0.0471		

APPENDIX I - SELECTION OF LARGE DIAPHRAGM TEST SPECIMEN

1. INTRODUCTION

Paragraph 5.3.5 of the Statement of Work^a states the requirements for structural tests. Included in these tests are diaphragm tests to check rigidization, buckling, and model sphericity. The general philosophy of these tests has been discussed a number of times and agreement was reached during the Technical Review at LRC on 11-12 September 1963. The agreements reached are presented on page 241 of GER-11189S2.^b On the basis of these ground rules a large size diaphragm test has been selected. The object of this appendix is to present information pertinent to the selection of the specimen size and method of testing.

2. FACTORS AFFECTING SELECTION

a. Gravity

The weight of the cloth during a test on earth must be considered as an effective pressure. The final selection of the material has not been made at this time but should be very close to the proposed material insofar as weight is concerned. The proposed material is 1-mil-diameter copper wire spaced 24 to the inch with a 1/2 mil of photolyzable film. The weight of this material is

^a Statement of Work for Feasibility Study and Preliminary Design of a Gravity Gradient Stabilized Lenticular Test Satellite. NASA-LRC, 10 June 1963.

^b GER-11189S2: Feasibility Study and Preliminary Design of Gravity-Gradient-Stabilized Lenticular Test Satellite. Monthly Progress Report No. 3, September 1963. Akron, Ohio, Goodyear Aerospace Corporation, 5 October 1963.

$$\text{Wire weight} = \frac{2 \times 24 \times (0.001)^2 \times 0.324}{4} = 0.0000122 \text{ psi}$$

$$\text{Film weight} = 0.0005 \times 0.038 = 0.0000190$$

$$\text{Total weight} = p_w = 0.0000312 \text{ psi}$$

b. Buckling

The buckling strength of the material is an important factor. This is given by

$$p_{cr} = 0.680 E_w \frac{d^3}{SR^2} \text{ (from GER-11201}^a \text{)}.$$

For the proposed material this equation is plotted in Figure I-1..

c. Vacuum

A vacuum is not a consideration from a photolyzation standpoint, but is advisable from a consideration of the static pressure that may be caused by currents in the earth's atmosphere. The magnitude of these depend upon the velocity of the currents and is given by

$$\begin{aligned} p_{S.L.} &= \frac{1}{2} \rho V^2 \\ &= 0.001188 V^2 \text{ psf} \\ &= 0.00000825 V^2 \text{ psi,} \end{aligned}$$

where V is in fps.

This can be reduced by operating at a partial vacuum. At 60,000-ft altitude, the density ratio is 0.09413. Therefore, the effect of stray currents can be reduced by an order of magnitude, or

^aGER-11201: Design of Cylinders and Spheres of Wire-Film Material. Akron, Ohio, Goodyear Aerospace Corporation.

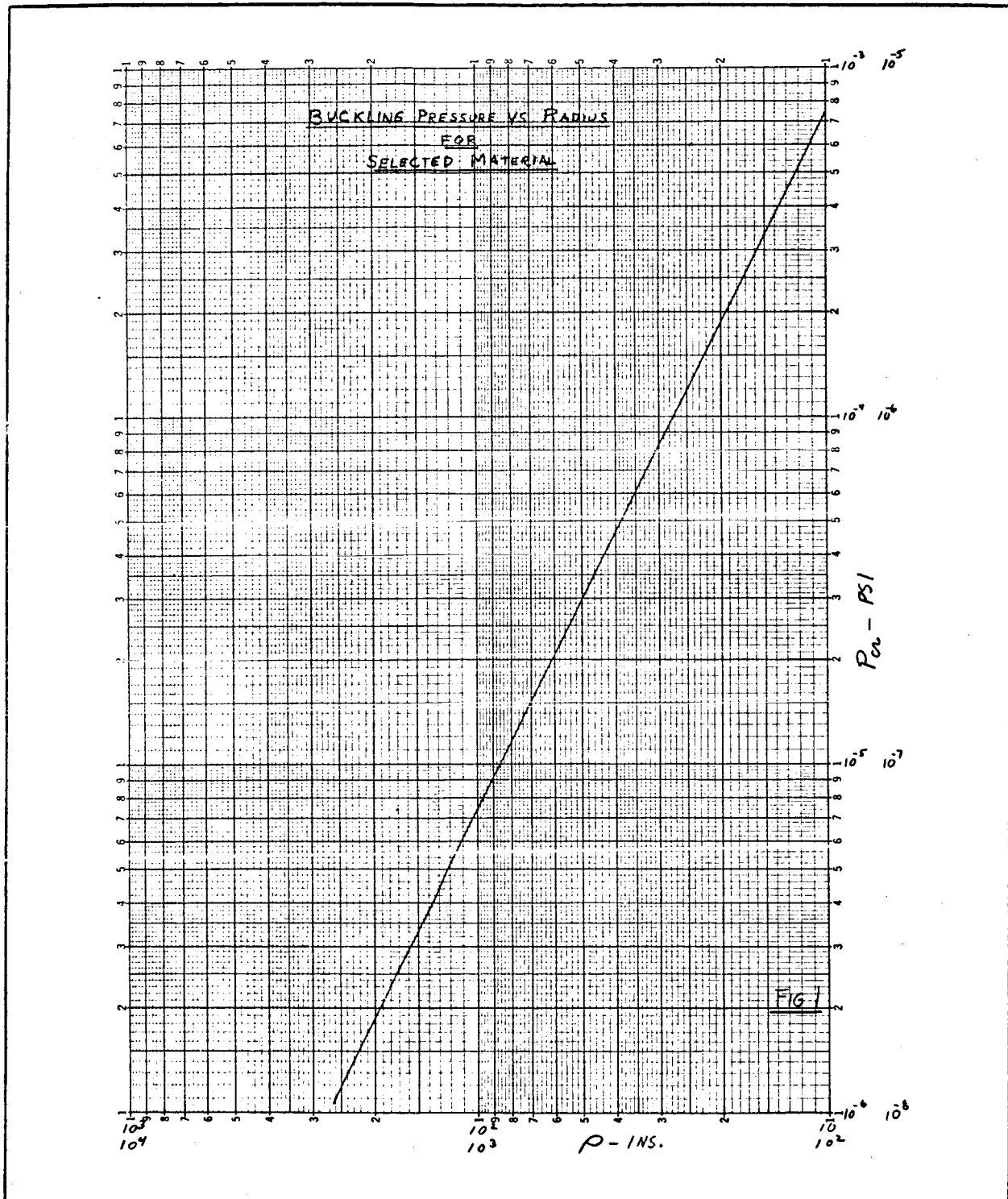


Figure I-1 - Buckling Pressure versus Radius for Selected Material

$$p_a = 0.000000777V^2 \text{ psi.}$$

d. Temperature

Rigidization of wire-film material is dependent upon the stress-strain characteristics of both the wire and the film.^a The stress-strain characteristics of photolyzable film are highly dependent upon temperature (see Figure 4 of GER-11251).^b Therefore, the tests should be conducted at elevated temperature.

e. Accuracy of Pressure Differential Measurements

The best equipment available is a micromanometer that is accurate to one thousandth of an inch of water. The pressure measuring accuracy is then

$$p_M = 0.000036 \text{ psi.}$$

f. Maximum Pressure Required

It is estimated that the maximum membrane load level that must be developed during the test is approximately 0.4 lb per inch. For a 180-in. radius this corresponds to a pressure of

$$\begin{aligned} p_R &= \frac{2 \times 0.4}{180} \\ &= 0.0044 \text{ psi.} \end{aligned}$$

3. DISCUSSION OF PROPOSED TEST

The desirability of performing the tests at elevated temperature and reduced atmospheric density is the reason for proposing to conduct the large diaphragm test in the Tenny walk-in chamber. With this equipment the

^aGER-11117: Rigidization Analysis of Wire-Film Materials. Akron, Ohio, Goodyear Aerospace Corporation.

^bGER-11251: Weight Loss Behavior of Type I Photolyzable Film Under Simulated Space Conditions. Akron, Ohio, Goodyear Aerospace Corporation.

60,000-ft altitude and temperature of 200 F can be obtained. This chamber is 7-ft wide, which will limit the diameter of the specimen to approximately 6 ft.

The radius of curvature selected was approximately 15 ft or 180 in. This radius was selected so that the tooling for the 20-ft deployment model could be used. This will then have an included half angle of

$$\begin{aligned}\sin \theta &= \frac{3}{15} \\ &= 0.02 \\ \theta &= 11-1/2 \text{ deg.}\end{aligned}$$

This radius and diameter combination is so that it will be necessary to tailor gores, and thus the manufacturing techniques employed will be representative of the full-scale satellite.

The radius selected is also satisfactory from the magnitude of the loads involved. These are summarized below:

<u>Source</u>	<u>Symbol</u>	<u>Magnitude</u>
Gravity	P_W	$31.2 \times 10^{-6} \text{ psi}$
Buckling	P_{cr}	$2.6 \times 10^{-6} \text{ psi}$
Stray currents	P_a	0.777×10^{-6}
Accuracy	P_M	36×10^{-6}
Estimate maximum required	P_R	4400×10^{-6}

It is evident from the above that buckling can not be demonstrated. The buckling pressure is small compared with accuracy of the pressure-measuring instrument. Even if more sensitive instrumentation were used the effects of gravity, which are over 10 times the buckling pressure would mask the results.

The measuring accuracy is about one percent of the maximum pressure anticipated and from this standpoint should be satisfactory.

The most difficult item to evaluate is the effect of stray currents. These can only be minimized by reducing density and attempting to exclude currents by testing in a closed chamber. It is desirable to have the buckling pressure high compared with the stray current pressures that may occur. The only way to increase P_{cr} is to reduce the radius of curvature, which is contrary to the test objective.

4. CONCLUSIONS

It is concluded that the specimen geometry and test environment selected is the best compromise that can be made consistent with the objective of the test.

APPENDIX J - RELIABILITY PREDICTION

1. GENERAL

This appendix contains the preliminary reliability predictions that are pertinent to the definition of the system reliability goal and the assessment of the over-all satellite reliability. Predictions of monitoring equipment and deployment subsystem reliabilities were made. Structure and stabilization reliabilities have not been included, since the data necessary for a prediction is inadequate.

The system reliability model defined for this assessment is shown in Figure J-1. Two phases of operation have been specified in the establishment of the model - the deployment phase and the orbit-operational phase.

The mission profile in time has been defined to consist of one hour of operation in the deployment phase and 200 hr of operation in orbit. Components that experienced one cycle, redundant, and continuous modes of operation, respectively, were considered separately within the deployment subsystem.

Reliability predictions for the monitoring equipment used within each phase are treated separately since the monitoring function does not affect the satellite reliability goal as presently defined.

2. ASSUMPTIONS

The following assumptions were made in obtaining the predictions:

1. The exponential failure law is valid for the continuous operating equipment listed in the ensuing tables, that is, the reliability, R , can be expressed as

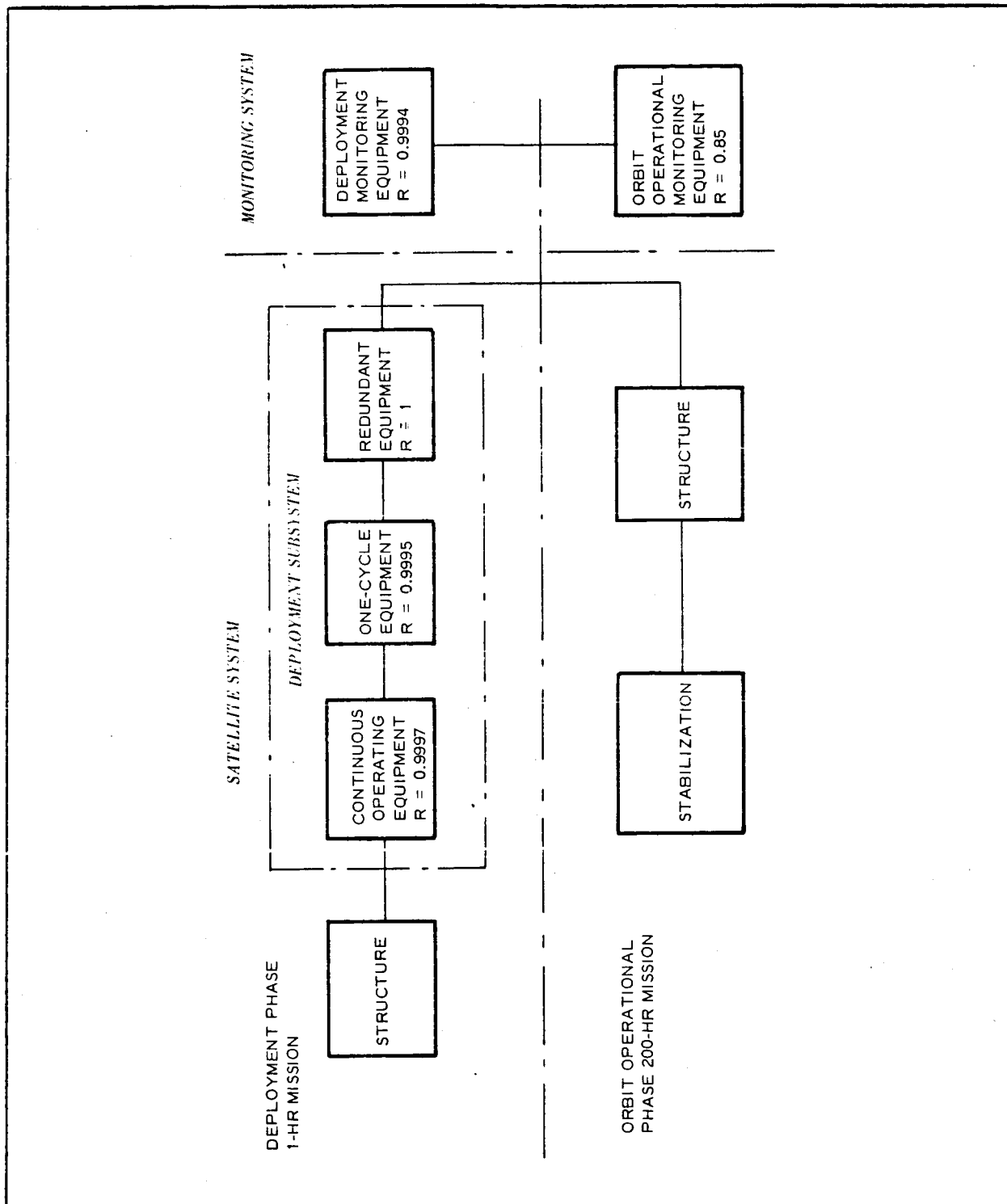


Figure J-1 - Reliability Model

$$R = e^{-\lambda t},$$

where λ is the failure rate per hour, t is the mission time in hours, and MTBF (mean time between failure) $= 1/\lambda$.

2. The product rule is applicable, that is, individual component failure probabilities are independent, and the total failure rate λ_T can be calculated by

$$\lambda_T = \sum_{i=1}^N \lambda_i.$$

3. Redundant portions of the system operate continuously and the reliability, R , can be predicted by

$$R = [1 - (1 - R_1)(1 - R_2)],$$

where R_1 and R_2 are the reliabilities of the respective redundant components for a specified mission time.

4. A failure of any component, excluding redundancy, results in failure of the system.

3. FAILURE RATE DATA

The failure rate data listed in Table J-I were used as the basic source for the predictions herein. Secondary sources were the Bureau of Naval Weapons Data Handbook (Farada) and the Avco Corporation's Reliability Data Series publication on failure rates.

4. PREDICTIONS

The following tables show the procedure used to obtain the reliability predictions and list the components used within the respective equipment blocks shown in Figure J-1.

TABLE J-I - OBSERVED COMPONENT -PART FAILURE
 RATES FROM SATELLITE ORBITAL DATA*

Component part	Failures/ 10^6 hr
Capacitor - general purpose	0.6
Capacitor - tantalum	5.0
Choke - filter	7.5
Choke - r-f	3.0
Coil - r-f	2.0
Crystal - quartz	2.0
Diode	
Signal	1.7
Power	3.5
Zener	2.2
Magnetic amp	16.0
Motor	
AC	88.0
DC	88.0
Potentiometer	15.0
Relay - general purpose	20.0
Resistor	0.5
Solenoid	36.0
Switch/commutator	1.5
Transformer - power	12.0
Transformer - i.f., signal	4.0
Transistor	
Signal	6.0
Power	40.0
Photomultiplier	16.0

* Component Reliability in Orbiting Satellites, Proceedings of 1962 Electronic Components Conference, May, 1962

TABLE J-II - DEPLOYMENT SUBSYSTEM
(CONTINUOUS OPERATING EQUIPMENT)

Component	Failures/ 10^6 hr *
3 Coils	6.00
1 Antenna	5.00
Solar cells	2.00
1 Charge regulator	8.82
Batteries	1.40
8 Valves	40.00
1 Program sequence timer	1.20
1 Power control	20.00
3 Power regulators	26.46
3 Or gates	10.95
3 Amplifiers	134.70
3 Comparators	<u>64.50</u>
	321.03

*Results:

$$\sum \lambda = \lambda_c = 321 \times 10^{-6}$$

$$R = e^{-\lambda_c t} = e^{-(321 \times 10^{-6})(1)}$$

$$R = 0.9997$$

A goal was obtained by doubling the mtbf.

$$R_{\text{goal}} = e^{-(160 \times 10^{-6})(1)}$$

$$R_{\text{goal}} = 0.9998$$

TABLE J-III - DEPLOYMENT SUBSYSTEM
(ONE-CYCLE EQUIPMENT)

Function	Estimated reliability*
Canister separation	0.9999
Canister despin	0.9998
Canister separation, 4th stage	0.9999
Pressure equalization	0.9999

*R = probability of no function failure =
0.9995

TABLE J-IV - DEPLOYMENT SUBSYSTEM
(REDUNDANT EQUIPMENT)

Component	Component failure rate per hour	Success probability of redundant combination for one-hour mission *
Receiver	250×10^{-6}	1.0
Torus pressure gage No. 1	2×10^{-6}	1.0
Torus pressure gage No. 2 and time override	2×10^{-6}	1.0
Boom pressure gage No. 1	0.12×10^{-6}	
Lens pressure gage No. 1	2×10^{-6}	1.0
Lens pressure gage No. 2 and time override	2×10^{-6}	1.0
	0.12×10^{-6}	1.0

*Probability of successful redundant equipment operation, $R \cong 1$.

TABLE J-V - DEPLOYMENT MONITORING SUBSYSTEM
(CONTINUOUS OPERATING EQUIPMENT)

Component	Failures/ 10^6 hr *
1 Beacon	4.00
1 Or gate	3.65
2 Antennas	10.00
Signal conditioning	76.00
1 Commutator	1.50
1 Oscillator	8.80
1 Recorder	88.00
1 Transmitter	300.00
2 Amplifiers	<u>89.80</u>
	581.75

* Results:

$$\sum \lambda = \lambda_m = 582 \times 10^{-6}$$

$$R = e^{-\lambda_m t} = e^{-(582 \times 10^{-6}) (1)}$$

$$R = 0.9994$$

TABLE J-VI - OPERATION MONITORING SUBSYSTEM
(MISSION TIME = 200 HR)

Component	Failures/ 10^6 hr *
Solar cells	2.00
1 Charge regulator	8.82
Batteries	1.40
2 Antennas	10.00
1 Beacon	4.00
1 Power, control	20.00

TABLE J-VI - OPERATION MONITORING SUBSYSTEM

(MISSION TIME = 200 HR) (Continued)

Component	Failures/ 10^6 hr *
Solar attitude and rate sensors	180.00
Thermocouples	16.00
1 Magnetometer	10.00
1 Or gate	3.65
1 Commutator	1.50
Signal conditioning	76.00
2 Amplifiers	89.80
1 Oscillator	8.80
1 Timing mechanism	1.20
1 Recorder	88.00
1 Transmitter	<u>300.00</u>
	821.17

*Results:

$$R = e^{-(821 \times 10^{-6}) (200)} = e^{-0.164}$$

$$R = 0.85$$

APPENDIX K - SEQUENCE OF OPERATIONS AND FAILURE MODES
DURING DEPLOYMENT

Event no.	Event and time (after launching)	Failure mode no.	Failure mode	Subsystem in which failure occurred
1	Equalize pressure in canister 13 min	1	Squib-operated valve doesn't operate	Deployment
		2	Lead wire broken	Deployment
		3	Squib doesn't fire	Deployment
		4	Dirt in valve	Deployment
		5	Blocking of air flow within structure could cause blowout	Structure
		23	Orbit disturbed by exploding device	Unknown until detail design available
2	Ejection of payload from 4th stage - 224 min	2	See 2 above	
		3	See above	
		6	Payload ejection system* doesn't work	Scout, payload ejection system
		26	Satellite and 4th stage may not stay separated - might be caused by improper spring action at release. May interfere with radar reflection.	Deployment
3	Despin (Yo-yo) 224 min - 15 sec	7	Yo-yo weight release timing* off	Deployment
		8	Yo-yo cable release timing* off	Deployment
4	Separation of canister - 224 min 30 sec	2	See above	
		3	See above	

* Additional analysis is required.

Event no.	Event and time (after launching)	Failure mode no.	Failure mode	Subsystem in which failure occurred
5	Open main gas supply valve 224 min - 31 sec	2	See above	Deployment
		4	See above	
		9	Failure of programmer*	
		10	Failure of valve*	
6	Open torus and boom inflation valve - 224 min 32 sec	2	See above	Deployment
		4	See above	
7	Open lens inflation valves - 227 min 45 sec	5	See above	Structural
		9	See above	
		10	See above	
		11	Rim fails to remain in a plane and buckles	
		12	Excessive diffusion or leakage of gas causes disturbing torque from which satellite cannot recover	
		13	When canister separates it may pull boom off torus	
		14	Pressure sensor may give signal at too low a pressure, resulting in incomplete rigidization or at too high a pressure causing blowout of structure, including damage due to vibration during launch	
		25	Final position of satellite after deployment prevents stabilization	Deployment

* Additional analysis is required.

Event no.	Event and time (after launching)	Failure mode no.	Failure mode	Subsystem in which failure occurred
-----------	----------------------------------	------------------	--------------	-------------------------------------

The following failure modes are all associated with the materials

		15	Local yield strength higher than test samples, resulting in incomplete rigidization, possibly at seam	Structural
		16	Local ultimate strength lower than test samples, resulting in blowout, possibly at seam	Structural
		17	Failure at bond between boom and rim	Structural
		18	Sticking together of photolyzable material	Structural
		19	Temperature extremes and temperature cycling may cause blowout	Structural
		20	Excessive creasing caused by either launch vibration or prelaunch storage of structure may result in blowout	Structural
		21	Pressure buildup may be too rapid, causing blowout	Structural
		22	High pressure surge through valve at opening may cause damage	Structural
8	Open dump valves 230 min, 45 sec	2, 4, 5, 9, 10	See above	
9	Deploy damper and spring 230 min, 45 sec	24	Tangling of spring during deployment	Stabilization
6 and 7	Open inflation valves	27	Hang-up of structure during deployment	Structural

APPENDIX L - FAILURE MODES DURING OPERATION

Failure mode	Subsystem in which failure occurred
Wear of damper may cause degradation of damping	Stabilization
Degradation of damping properties of cadmium-plated spring	Stabilization
Low-cycle fatigue failure of BeCu spring	Stabilization
Local variations may give signals in phase when it should be out and vice versa	Structure
More general (less localized) variation of the lens radius across the seams which may affect the r-f return energy	Structure
Low-cycle fatigue of rigidized structure	Structure
Thermal fatigue of structure	Structure
Failure due to micrometeoroid damage	Structure

APPENDIX M - EXAMINATION OF DISTURBING TORQUE ON FULL-SCALE
SATELLITE CAUSED BY NONUNIFORM GAS LEAKAGE

1. ABSTRACT

Initial data have been reduced to a form showing the reaction pressure per square inch of material (see Table M-I).

An example of adverse distribution of porosity has been shown, resulting in a disturbing torque of 0.189 ft-lb.

The maximum value of gravity-gradient restoring torque is shown to be 0.737 ft-lb. This indicates that leakage and diffusion must be controlled and that the maximum allowable disturbing torque should be determined.

TABLE M-I - DATA FROM DIFFUSION TESTS*

Material measured	Diffusion (liters per square meter per 24 hr)	$\Delta V/\Delta t$ (in. per sec)
Wire cloth and film	3000	1.368×10^{-3}
	2400	1.094×10^{-3}
	3000	1.368×10^{-3}
Film only	1200	0.547×10^{-3}
	400	0.182×10^{-3}
	800	0.364×10^{-3}

*Accuracy of data is questionable.

Caution should be exercised in the use of this analysis for the following reasons:

1. The film tested was an early sample.
2. The diffusion was greater than the measuring equipment was designed for; therefore, the accuracy is questionable.

2. DISCUSSION

Tests were run with a pressure differential of 3 cm of water and helium gas (density of helium = 6.45×10^{-6} lb per cubic inch; 3 cm of H_2O = 42.75×10^{-3} psi).

Using Equation M-6, below:

$$P_R = 1 \times \frac{\Delta V}{\Delta t} \left(\frac{\text{inches}}{\text{seconds}} \right) \sqrt{\frac{42.75 \times 10^{-3} \times 6.45 \times 10^{-6} \left(\frac{\text{lb}}{\text{sq in.}} \times \frac{\text{lb}}{\text{cu in.}} \right)}{2 \times 32.2 \times 12 \left(\frac{\text{inches}}{\text{sec}^2} \right)}}$$

$$= 1.891 \frac{\Delta V}{\Delta t} \times 10^{-5} \text{ lb per square inch.} \quad (\text{M-1})$$

$\frac{\Delta V}{\Delta t}$	1.368×10^{-3}	1.094×10^{-3}	0.547×10^{-3}	0.364×10^{-3}	0.182×10^{-3}
P_R lb per square inch	2.58×10^{-8}	2.07×10^{-8}	1.035×10^{-8}	0.689×10^{-8}	0.344×10^{-8}

Let v = velocity of discharge through orifice. Then,

$$v = \frac{2gp}{\rho}, \quad (\text{M-2})$$

where

g = acceleration due to gravity, feet per second squared;

p = internal pressure, lb per square inch; and

ρ = density of gas, lb per cubic inch.

The diffusion data represent a discharge per second $\Delta V/\Delta t$ per square inch of cloth, and

$$\frac{\Delta V}{\Delta t} = v A_A, \quad (M-3)$$

where A_A is the apparent area through which gas escapes per square inch of cloth and film.

$$A_A = \frac{\frac{\Delta V}{\Delta t}}{\sqrt{\frac{2gp}{\rho}}}, \quad (M-4)$$

and A_A can be calculated for each item of data from the diffusion tests.

The thrust reaction from the escaping gas is

$$F = C p A_A, \quad (M-5)$$

where C is an unknown orifice coefficient, and p and A_A have been defined previously. Now A_A is defined as the apparent escape area per square inch of cloth and film. Therefore, F is the thrust reaction per square inch of cloth and film, so F can be called the reaction pressure, P_R .

$$P_R = C \frac{\Delta V}{\Delta t} \sqrt{\frac{p\rho}{2g}}. \quad (M-6)$$

The following is an example of adverse porosity distribution. (No attempt has been made to show the probability of occurrence of this distribution.) Assuming that the area of the crosshatched section is one-third of the pie section shown in Figure M-1, and that there is an extremely high reaction pressure in this area and a uniformly low pressure in all other areas, the reaction torque will be

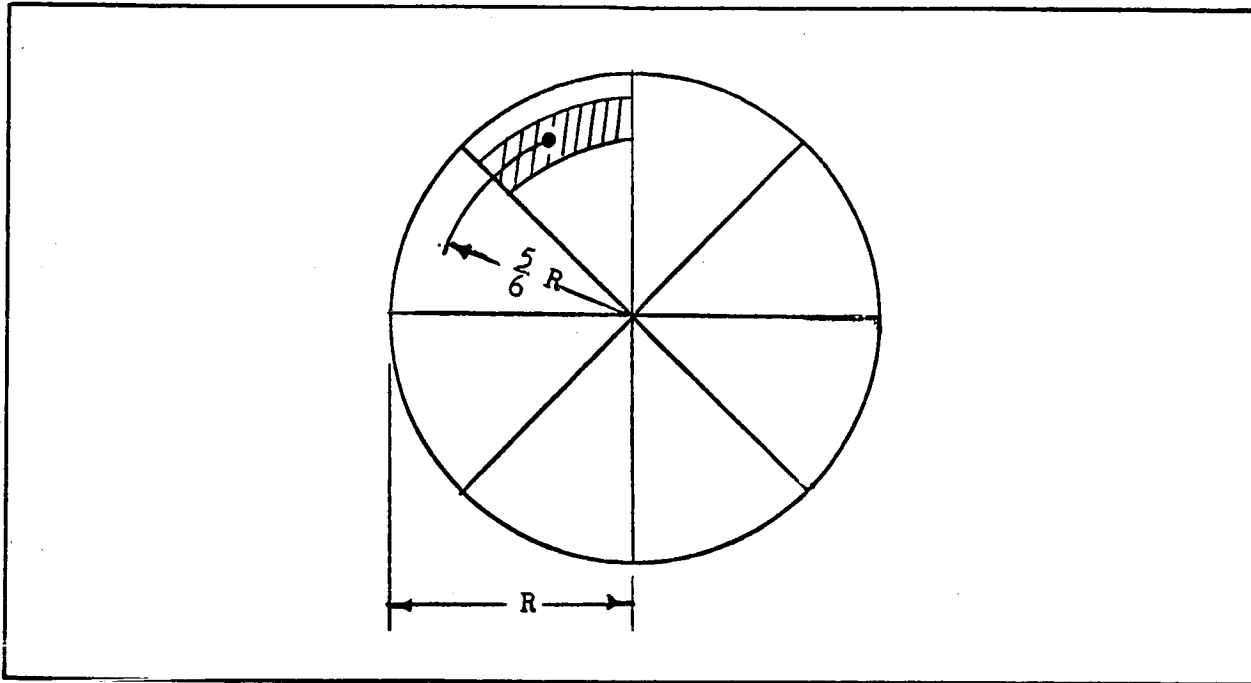


Figure M-1 - Example of Adverse Porosity Distribution

$$\Delta P_R A \times \frac{5}{6} R = T, \quad (M-7)$$

where

$$\Delta P_R = P_{\max} - P_{\min},$$

$$A = \frac{1}{3} \times \frac{1}{8} \times \pi R^2, \text{ and}$$

$$\begin{aligned} T &= 73 \times \frac{\pi}{24} \times \frac{5}{6} (133.5)^3 \times 10^{-8} \\ &= 0.189 \text{ ft-lb.} \end{aligned}$$

If

$$R = \frac{267 \text{ ft}}{2} = 133.5 \text{ ft},$$

$$\begin{aligned} P_{\max} - P_{\min} &= (2.58 - 2.07) \times 10^{-8} \\ &= 0.51 \times 10^{-8} \text{ lb per square inch} \\ &= 73 \times 10^{-8} \text{ lb per square foot.} \end{aligned}$$

The gravity-gradient restoring torque about the pitch axis is

$$T_g = -\frac{3}{2} \omega_o^2 (I_x - I_z) \sin 2\theta . \quad (M-8)$$

This restoring torque will be a maximum when $\theta = 45$ deg; then,

$$\begin{aligned} T_g &= -\frac{3}{2} \omega_o^2 (I_x - I_z) \\ &= -\frac{3}{2} (8.7 \times 10^{-4}) (649 \times 10^3) \\ &= 73,700 \times 10^{-5} \text{ ft-lb} \\ &= 0.737 \text{ ft-lb.} \end{aligned}$$

$$I_x = 1,026,173 \text{ lb-ft-sec}^2 ,$$

$$I_z = 377,529 \text{ lb-ft-sec}^2 ,$$

$$I_x - I_z = 648,644 \text{ lb-ft-sec}^2 ,$$

$$\omega_o \leq 8.7 \times 10^{-4} \text{ rad per second .}$$

This represents the maximum value of restoring torque, which will vary sinusoidally with θ .

APPENDIX N - ESTIMATED FLIGHT ENVIRONMENT OF THE
SCOUT LAUNCH VEHICLE

1. GENERAL FLIGHT ENVIRONMENT

a. Temperature

The nose-cone heat shield around the fourth-stage motor and payload is of fiberglass and is jettisoned just prior to third-stage ignition. The surface temperature of the inside surface of the heat shield will experience a temperature rise varying from 350 F on the conical section to 210 F on the cylindrical section during the approximately 128 sec of burning time. The temperature rise of the payload will be a function of its proximity, its surface emissivity, and the amount of insulation placed between it and the heat shield.

b. Pressure

The minimum pressure will be approximately 10^{-9} mm of mercury.

c. Acceleration

The average value of the maximum acceleration imposed on the payload is 23 g for approximately 30 sec. This loading occurs during fourth-stage burning.

d. Shock

Shock impulses of 30 g with durations of 11 ± 1 msec (all axes) will occur.

e. Spin

Maximum spin will be 180 rpm.

f. Vibration

Table N-I indicates the general nature of the vibration environment

to be expected. These levels represent the input to the payload support structure in the thrust axis.

TABLE N-1 - EXPECTED VIBRATION ENVIRONMENT

Duration per axis (min)	Frequency (cps)		Acceleration		Power spectral density (g ² /cps)
			Sine log sweep (±g)	Random (g rms)	
	Lower	Upper			
0.35	20	50	1
0.80	50	500	4
0.50	500	2000	8
2.00	20	2000	. . .	7.7	0.03
0.20	50	70	2

2. RECOMMENDED MECHANICAL ENVIRONMENTS

a. Test Levels

The following paragraphs are a summary of minimum basic test requirements and recommended test levels for the environmental testing of prototype and flight models to be launched by Scout vehicles. They cover only the mechanical environment during flight ascent through spacecraft separation, but apply to the complete spacecraft assembly. These basic requirements are considered to be a minimum for the demonstration of the structural, mechanical, and electronic integrity of the spacecraft during flight ascent.

b. Dynamic Balance

The spacecraft in its fourth-stage spin-up configuration and with systems nonoperating will be balanced statically and dynamically, prior to the other tests, within the following limits:

1. Maximum static unbalance - 12 oz-in.
2. Maximum dynamic unbalance - 200 oz-in.²

The prototype will be balanced dynamically at 1-1/4 times the maximum flight spin rate. Flight hardware will be balanced dynamically at the maximum flight spin rate (maximum flight spin rate = 180 rpm).

c. Acceleration

The prototype spacecraft will be operating during the acceleration tests in each of three axes. Acceleration applied along the thrust axis should be 1-1/2 times the maximum calculated level for the spacecraft weight and center of gravity (cg) for a duration of 3 min. Acceleration applied in each of the transverse axes should be at 3 g for a duration of 1 min. Acceleration gradient from the cg should not be over ± 10 percent. The acceleration test will be performed on the prototype spacecraft only, unless deemed otherwise necessary (average maximum acceleration achieved is 23 g).

d. Shock

The spacecraft in the fourth-stage ignition configuration will be operating during exposure to the shock tests in the thrust axis. The prototype spacecraft will be subjected to three 1/2-sine pulses of 30-g peak amplitude and 10 to 15 msec total duration. The flight spacecraft shall be subjected to a 1/2-sine pulse of 20-g peak amplitude and 10 to 15 msec total duration.

e. Vibration

(1) General

The spacecraft (including the support and separation assembly structure which attaches the payload to the fourth-stage motor) should be operating during exposure to the vibration test. The test levels apply at the interface of the forward motor shoulder of the fourth-stage motor. The tests should be performed with a structurally and dynamically similar separation assembly installed. The sinusoidal vibration test will be conducted by

sweeping at a logarithmic rate from the lowest to the highest frequency once for each range specified. The random vibration test will be of random peak accelerations over the frequency ranges specified. The peak accelerations that exceed the g rms value by more than three times will be clipped and not be imposed on the spacecraft.

(2) Prototype Spacecraft

(a) Sinusoidal Vibration Test

Apply one sweep in each of three axes at a logarithmic sweep rate not greater than two octaves per minute (see Table N-II).

TABLE N-II - SINUSOIDAL VIBRATION TEST -
PROTOTYPE SPACECRAFT

Frequency range (cps)	Acceleration (\pm g)	
	Thrust axis	Transverse axes
5 to 10	0.4 in DA	0.2 in DA
10 to 50	2.0	1.0*
50 to 500	6.0	1.5*
500 to 2000	12.0	2.5

* The acceleration at the spacecraft cg will be limited to ± 3 g from $1/2$ the first resonant frequency of the spacecraft to $1-1/2$ the frequency when vibrated in either of the transverse axes.

(b) Special Sinusoidal Vibration Test

Apply one sweep of frequency range 50 to 70 cps for 24 sec at ± 3 g in thrust axis only.

(c) Random Vibration Test

Apply Gaussian random for 4 min in each of three axes (see Table N-III).

TABLE N-III - RANDOM VIBRATION TEST -
PROTOTYPE SPACECRAFT

Axis	Frequency range (cps)	Acceleration (g rms)	Power spectral density reference (g^2/cps)
Thrust	20 to 2000	11.5	0.07
Transverse (2)	20 to 2000	6.3	0.02

(3) Flight Spacecraft (Flight Acceptance Tests)

(a) Sinusoidal Vibration Test

Apply one sweep in each of three axes at a logarithmic sweep rate not greater than 4 octaves per minute (see Table N-IV).

TABLE N-IV - SINUSOIDAL VIBRATION TEST -
FLIGHT SPACECRAFT

Frequency range (cps)	Acceleration ($\pm g$)	
	Thrust axis	Transverse axes
20 to 50	1	0.6*
50 to 500	4	0.8*
500 to 2000	8	1.6

* The acceleration at the spacecraft cg will be limited to $\pm 3 g$ from $1/2$ the first resonant frequency of the spacecraft to $1-1/2$ the frequency when vibrated in either of the transverse axes.

(b) Special Sinusoidal Vibration Test

Apply one sweep of frequency range 50 to 70 cps for 12-sec duration at ± 2 g in thrust axis only.

(c) Random Vibration Test

Apply Gaussian random in each of three axes for 2-min duration for thrust axis and 1-min duration for each of the transverse axes (see Table N-V).

TABLE N-V - RANDOM VIBRATION TEST -
FLIGHT SPACECRAFT

Axis	Frequency range (cps)	Acceleration (g rms)	Power spectral density reference (g^2/cps)
Thrust	20 to 2000	7.7	0.03
Transverse (2)	20 to 2000	4.4	0.01

APPENDIX O - POTENTIAL PASSIVE SATELLITE
COMMUNICATION SYSTEM FOR ALL NATIONS

This appendix is a paper to be presented by Mr. C. M. Kelly of GAC's Astronautics Systems Department at the XVth International Astronautical Congress, September 1964, Warsaw, Poland.

SECTION I - INTRODUCTION

1. GENERAL

This paper provides data to show the promise of a lenticular gravity-gradient stabilized passive communication satellite system to provide scores of global broadcast type audio and television channels as well as tens of thousands of voice telephone circuits. It is expected that the system could fulfill most of the satellite communication requirements on this planet for the remainder of the century.

The system presented exploits recent advances in space technology and the many natural capabilities of lenticular satellites such as:

1. Wide communications bandwidth
2. Terminal sharing - i.e., ability to permit small inexpensive ground terminals to receive signals from and transmit into the satellite communication network. This is accomplished by receiving the strong signal reflected from the satellite via a high powered transmitter and a large antenna of a master terminal. Transmitting into the system from a small inexpensive terminal with a low power transmitter is practicable because of the large antenna and sensitive receiver of the master terminal.
3. A satellite radio reflection cross-section-to-mass ratio improvement with respect to Echo II of more than 100 for higher orbit satellites.
4. Launch vehicle payloads up to 100,000 lb by using vehicles that are developed on the manned space flight program.

5. Useful satellite life of tens of years
6. Satellites that are immune to radiation damage
7. Accomplishment of minor orbital adjustments by solar sailing, i. e., adding ancillary structures or surface coatings, and actuating provisions on the satellite to permit orbital positioning with the forces generated from solar radiation pressure
8. Improvements in ground transmitters, receivers, and antenna technology

2. LENTICULAR SATELLITE BACKGROUND

Like its antecedents Echo I and II, the lenticular gravity-gradient stabilized passive communication satellite is a technical offspring of Langley Research Center of the National Aeronautics and Space Administration (NASA).

The objectives of Echo I were to demonstrate the feasibility of large inflatable spheres as communication reflectors and to study the behavior of large, lightweight erectible structures in space environment.^{1, a}

Many communication experiments were carried out via Echo I including the establishment of teletype, facsimile, two-way voice and television circuits, using various types of modulation techniques. No deviations from propagation theory were observed, and the returned signal strength from Echo I was within 1 db during the two weeks that the satellite was pressurized.

Echo II was developed to permit further investigation of inflation, rigidization, surface contouring, thermal control, structural techniques, fabrication techniques, microwave wave reflectivity characteristics, and communication system characteristics of large lightweight space structures.

Echo I and II have contributed significantly to the understanding of the space environment and the nature of orbital perturbations. Echo satellites have demonstrated that high area to mass structures are very

^aSuperior numbers in the text refer to items in the List of References.

sensitive to solar radiation pressure and have provided experimental background for the solar sailing station keeping techniques discussed in this paper.

Early in 1963 NASA awarded study contracts to improve passive satellites in general and to determine the feasibility of (1) stabilizing a lenticular satellite by means of the earth's gravity gradient field^a and (2) applying solar radiation pressure to provide the necessary mobility for initial orbital placement and orbit position control.^b Other goals of this program include: (1) improving the satellite radio reflectivity to weight ratio; (2) developing oriented spherical lenticular segment type satellites; (3) applying solar sailing, orbital placement, and station keeping techniques; (4) applying advanced materials and structures; and (5) satellite improvement by any other practicable method.

A configuration was selected, based on preliminary studies, which offered structural advantages over other designs considered.

This configuration is illustrated in Figure 1 and forms the basis of the subject paper. It is discussed in greater detail in the subsequent paragraphs.

3. LENTICULAR CONCEPT

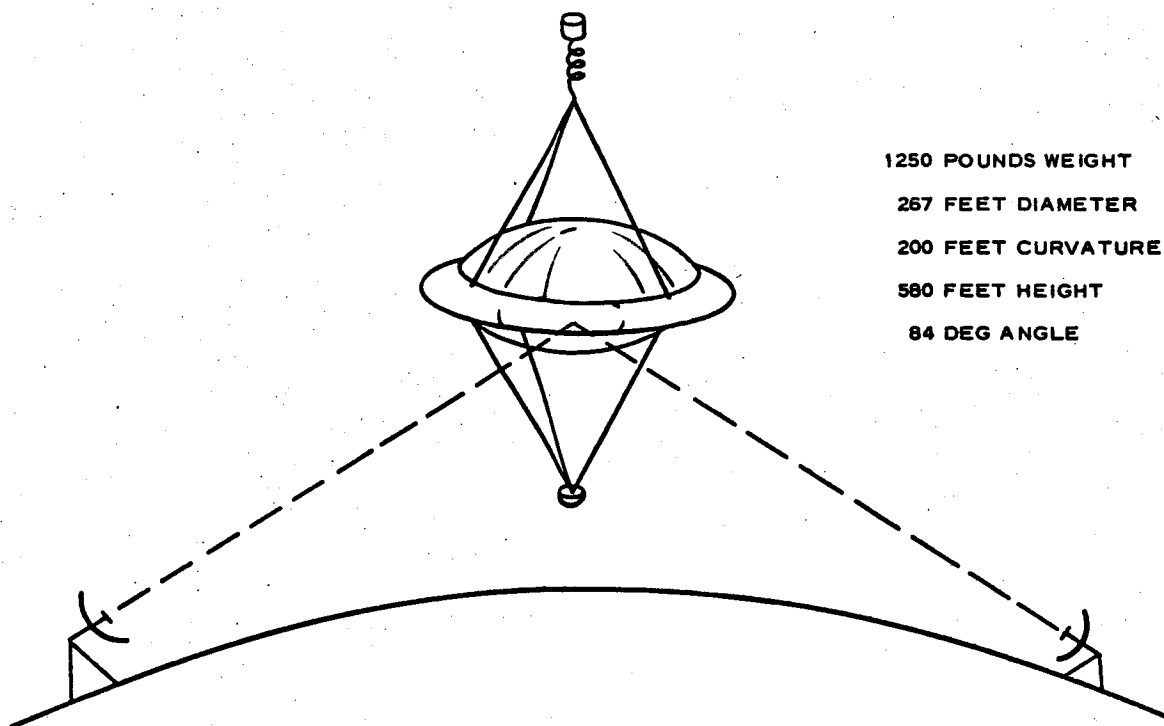
A lenticular shape is defined as the spherical cap formed by the intersection of a sphere and a plane. The lenticular angle (θ) is formed by the lines extending from the center of curvature to the sphere-plane intersection.

Because of the ground station and satellite orbit system geometry (see Figure 2), only a small portion of an Echo spherical type structure is required for radio reflection to the earth at any particular time.

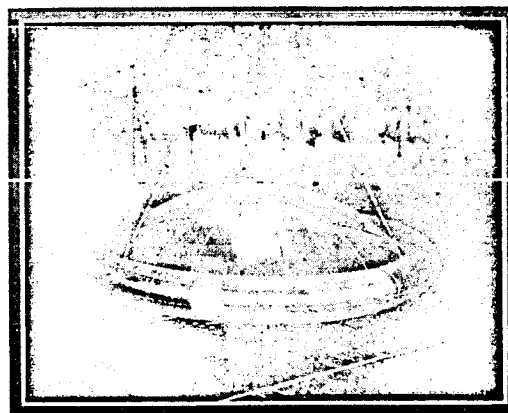
The lenticular satellite concept takes advantage of this situation by using the material that would have comprised a sphere to form a lenticular shape with a larger radius of curvature (ρ), and hence a much larger radio reflection cross section (σ), for a given weight, particularly at the

^aGoodyear Aerospace Corporation, Akron 15, Ohio.

^bWestinghouse, Baltimore, Maryland.



20-FOOT MODEL



VACUUM CHAMBER TEST

Figure 1 - Lenticular Comsat.

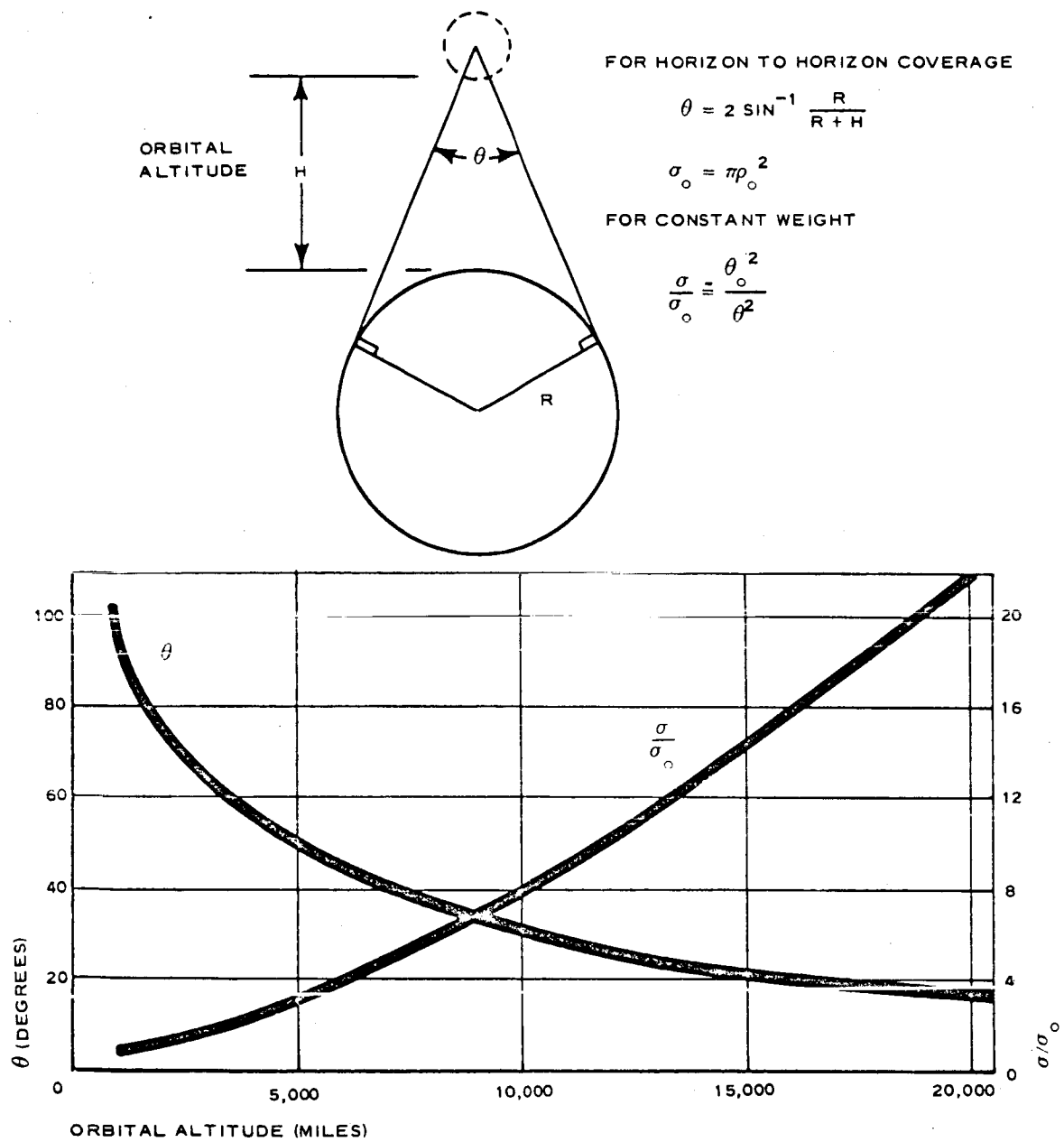


Figure 2 - Lenticular System Geometry

higher orbit altitudes. For a sphere or a lenticular satellite the radar reflection cross section is equal to $\sigma_s = \pi r^2$.

4. SCOPE OF PAPER

This paper describes the communication capabilities that could be realized using a lenticular gravity-gradient stabilized passived satellite communication system. Both the low-orbit (2000 naut mi) and the synchronous-orbit applications are discussed. The terminal sharing and wide bandwidth capabilities inherent in a spherical segment-type passive satellite system are presented. The low orbit system shows near future capabilities and the synchronous orbit system typifies the significant capabilities that might be realized in the more distant future.

This paper also describes a technique for passive satellite orbital placement and station keeping. This may be accomplished by adding or removing energy from the satellite orbit via solar radiation pressure reacting on the passive satellite structure, while sailing away or toward the sun respectively.

SECTION II - SATELLITE

1. GENERAL

The primary research and development of this past year has been centered around the 267 ft, 1250 lb satellite illustrated at the top of Figure 1. Also shown is a 20-ft model, successfully deployed in the NASA-Langley 60-ft space chamber. Configuration, deployment and packaging characteristics of a lenticular satellite are shown in Figures 3 and 4.

The satellite consists of two low-curvature, radar-reflective, wire grid spherical segments joined back-to-back. The reflective surface is typically 1 mil wire screen with $1/21$ in. apertures. A $1/4$ -mil photolyzable film bladder deploys and contours the lenticular wire grid lens in space by gas inflation. After deployment the film slowly evaporates or photolyzes due to exposure to the solar radiation spectrum. This provides a wire grid that is essentially transparent to the solar radiation spectrum but reflective to microwaves. Characteristics of Type-Z photolyzable film are shown in Figure 5.

The satellite lens is bounded by a peripheral rim, a torus, and two displaced masses that are each supported from the rim by a series of boom structures. The inflation of the entire system elongates the surface to the yield point region of the material to rigidize the lenticular surfaces.

The two spherical segments are interconnected through a solid rim of collapsible cross section. The rim might be fabricated of beryllium copper hollow flexible tape and includes two hinged joints 180 deg apart to permit proper packaging of the system. The rim also provides the structural attachment for the booms supporting the gravity-gradient masses and perhaps the solar sails.

The lenticular lens and metal rim are encircled by a torus section. The torus is inflated first, thereby unfurling the packaged lens surfaces, and is maintained under a relatively high pressure to support the erection

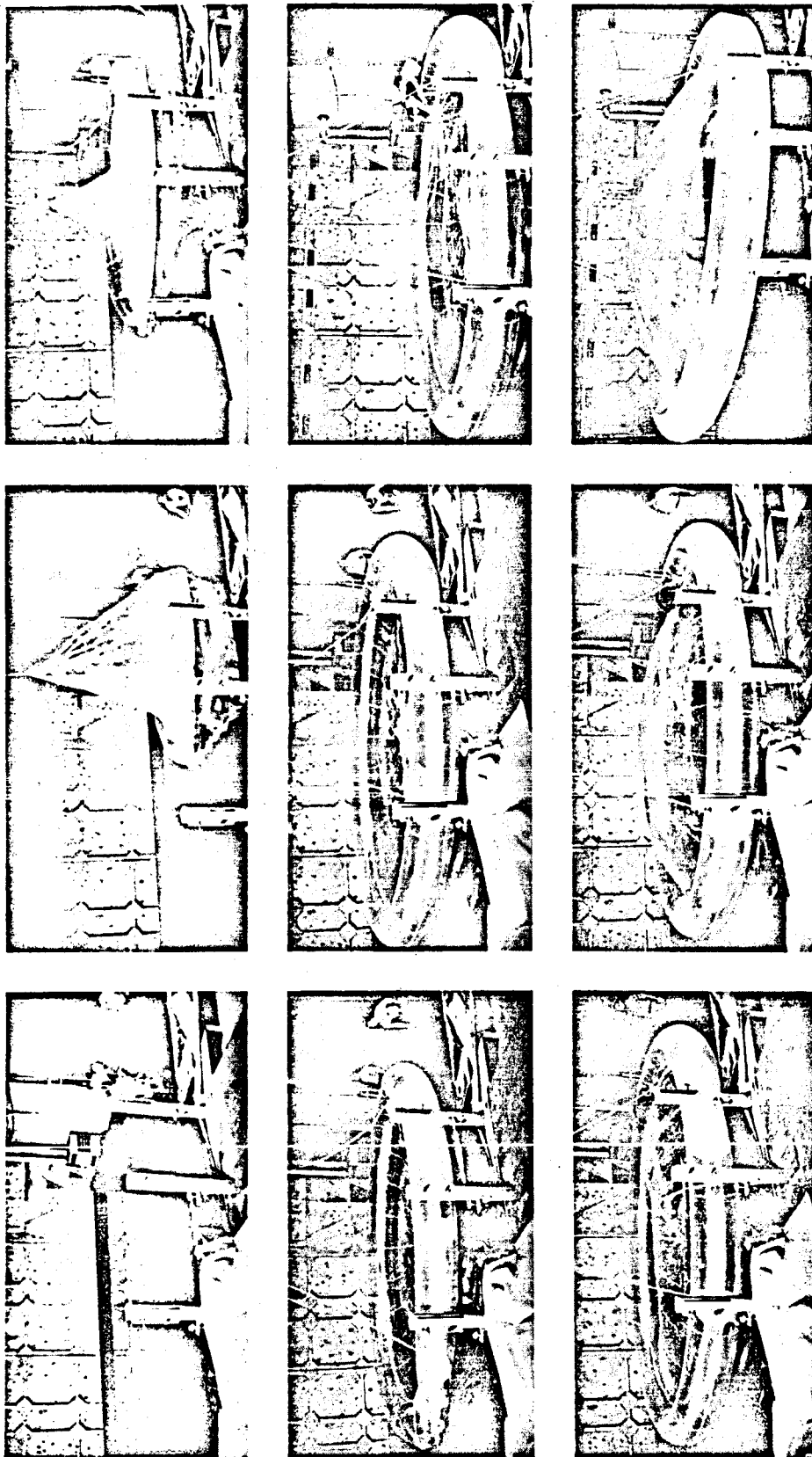


Figure 3 - Deployment Sequence, 20-Foot Lenticular Satellite Model

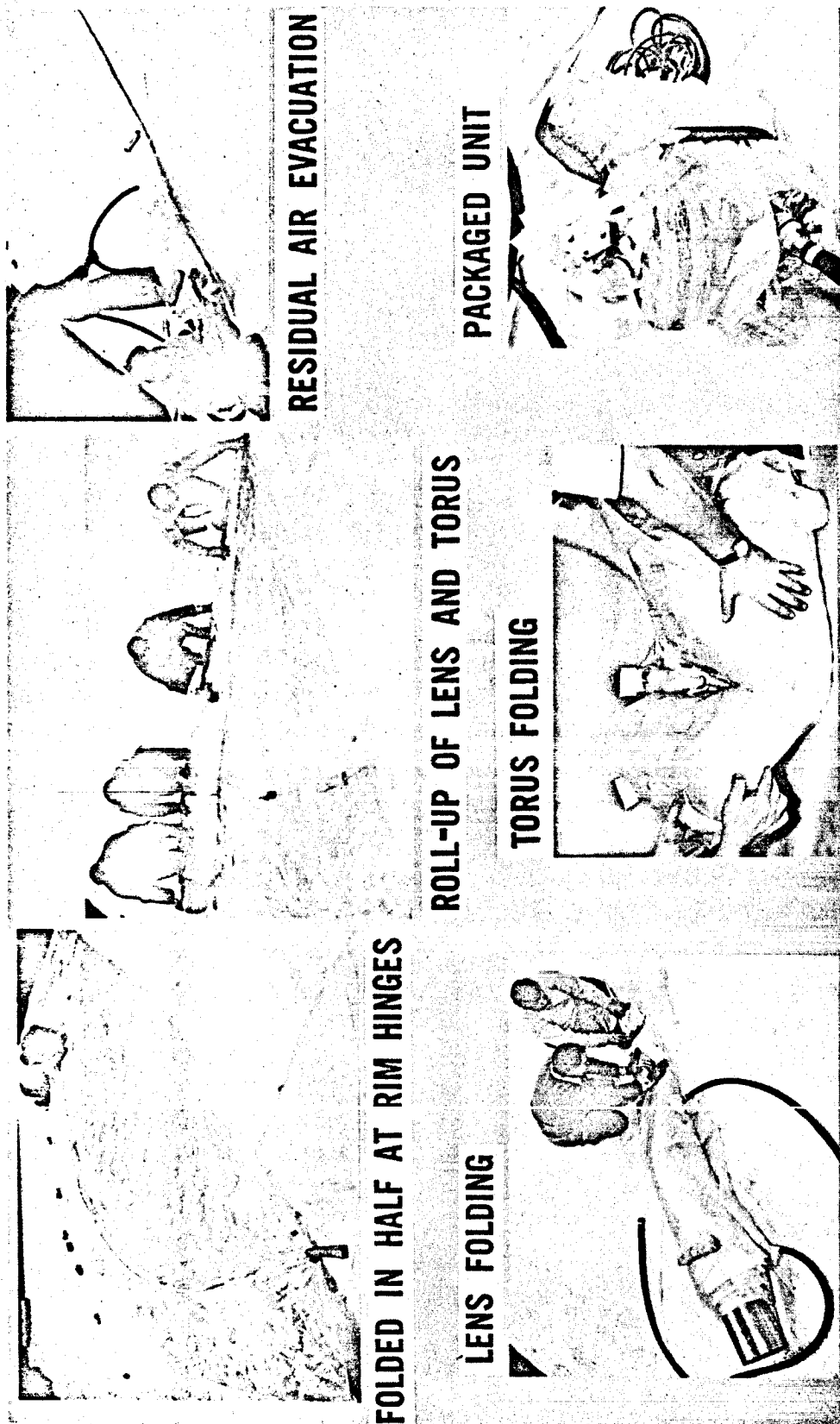
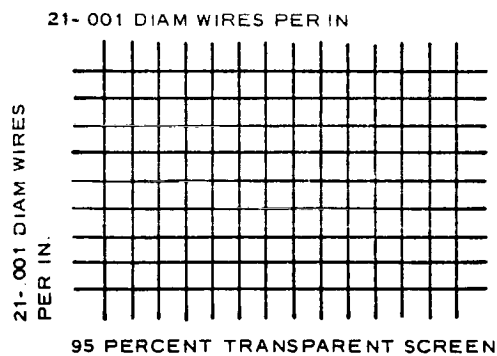
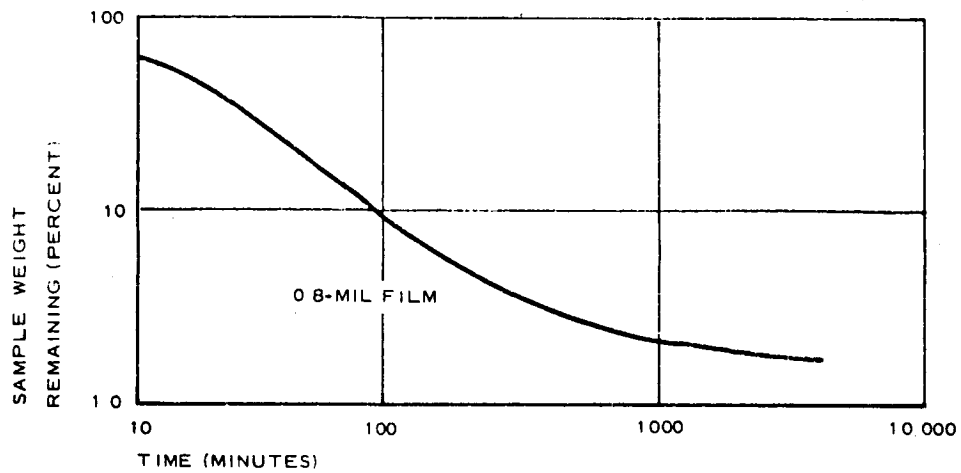


Figure 4 - Packaging Sequence - 20-Foot Lenticular Satellite Model



**STABILIZATION SYSTEM REQUIREMENTS ARE REDUCED
BECAUSE OF SATELLITE TRANSPARENCY**

Figure 5 - Photolyzable Film - Wire Grid Characteristics

loads imposed by pressure contouring of the lens surfaces.

Two masses, one on each side of the lenticular shape, are supported at the apex of the booms. These masses, which provide the required longitudinal to transverse inertia ratio for gravity-gradient stabilization torques, consist of the packaging canister halves and fixed equipments, such as inflation system and damping system. The inflatable elements of the satellite are packaged in the canister, which, at deployment, separates at its equator.

The earth-side canister half of the stabilized configuration provides the mounting interface of the inflation system and the electrical system components. The opposite canister half provides the mounting interface for the damping system.

2. GRAVITY-GRADIENT STABILIZATION AND ORIENTATION SYSTEM

The purpose of the stabilization system is to keep the lenticular satellite oriented to the local earth vertical within a nominal accuracy of ± 3 deg. To do so the stabilization system must ensure: (1) that initial attitude errors are damped out within a reasonable time limit; and (2) that steady-state perturbing torques on the satellite, such as those due to orbital frequency, solar pressure and orbital eccentricity, are prevented from building up attitude errors in excess of the nominal accuracy. The gravity-gradient stabilization system consists of gravity-gradient booms with attached canister masses and a libration damping device. Figure 6 presents a schematic of the system. For gravity stabilization purposes, the important considerations are the moments of inertia of the principal axes of the satellite, including the contribution of the gravity-gradient booms and their associated canister masses, and the energy dissipation capability of the damping device.³

On the basis of studies made so far, it appears that the orientation system does not require any active attitude control jets or magnetic torquing coils.

Studies of the gravity-gradient stabilization system have considered both transient and steady-state disturbance conditions. Figure 6 presents a sketch of the dual-mode lossy spring and fluid damper as applied to the lenticular satellite. This form of the damper is a very efficient as a

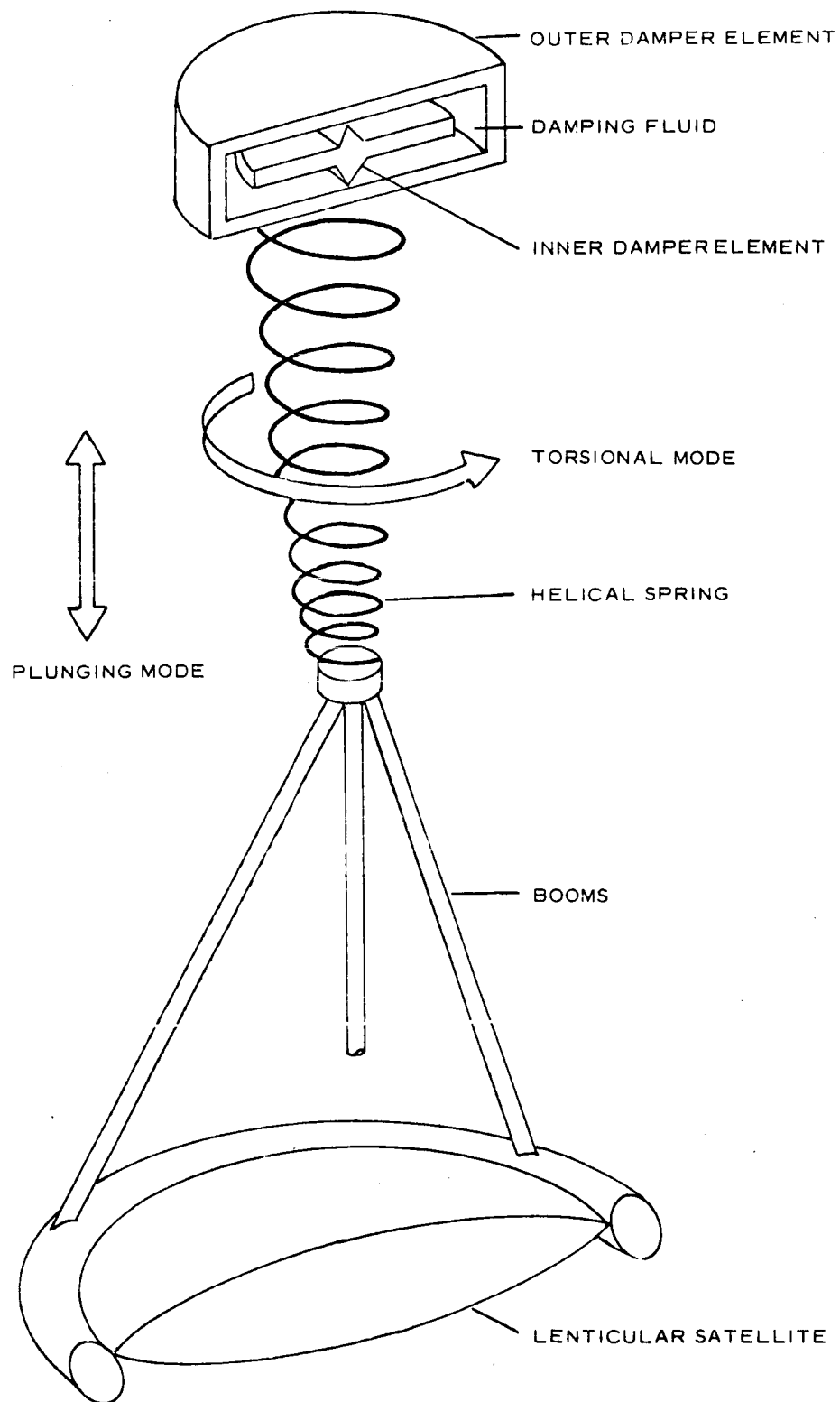


Figure 6 - Rice/Wilberforce Damper Applied to Lenticular Satellite

gravity-gradient stabilizer device, and provides damping time constants in both pitch and roll axes of the order of 1-1/2 orbits as indicated in Figure 7 and has no steady bias or hang-off errors. However, further studies must be made to assess the full effect of cross coupling in the equations of motion. Present results are therefore somewhat tentative, but very encouraging.

3. SATELLITE SIZE AND WEIGHT CHARACTERISTICS

Physical characteristics and a weight scaling relationship are shown for the current lenticular design (Figure 8). The satellite without a sail weighs about 1250 lb, including canister and deployment equipment and material. It has a radius of curvature of 200 ft, with a lenticular angle for several curvatures and versus satellite diameter are presented.

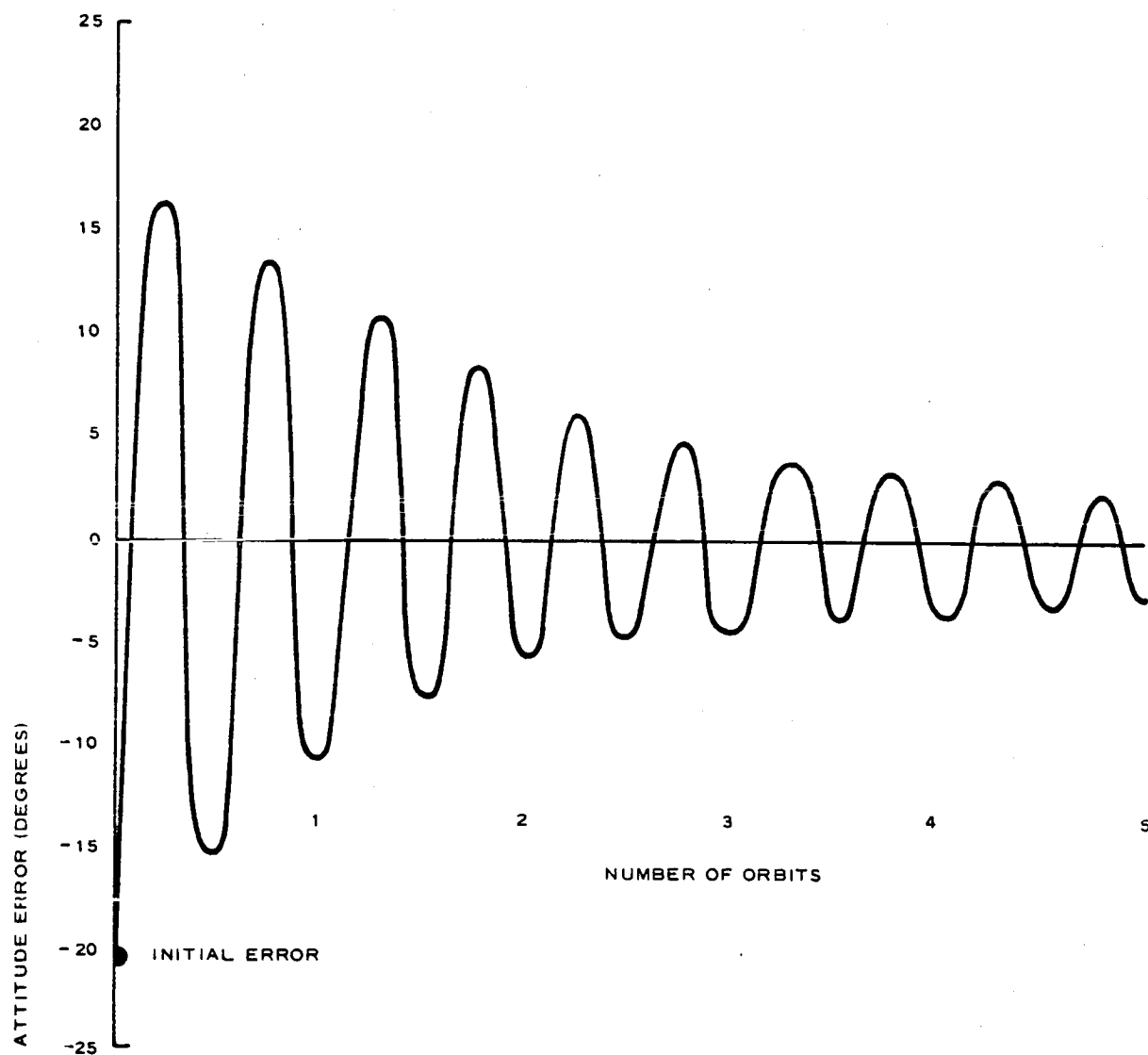


Figure 7 - Damper Performance on Lenticular Passive Communication Satellite

CURRENT DESIGN FOR 1700 NAUTICAL MILE ORBIT

$W = 1250$ POUNDS

$\theta = 84$ DEG

$\rho = 200$ FEET

$D = 267$ FEET

WEIGHT SCALING

$$W \cong W_o \left(\frac{\rho}{\rho_o} \right)^2 \left(\frac{\theta}{\theta_o} \right)^2 \cong W_o \left(\frac{D}{D_o} \right)^2$$

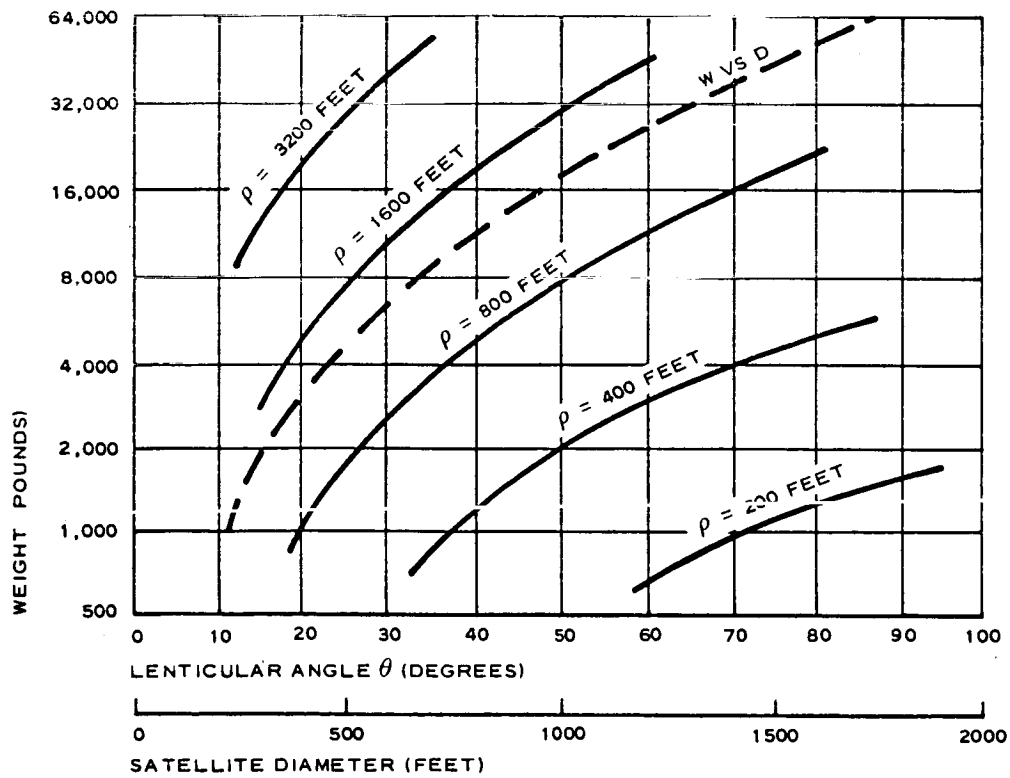
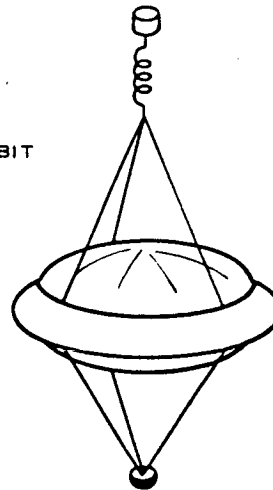


Figure 8 - Lenticular Satellite

SECTION III - COMMUNICATION SYSTEM PERFORMANCE

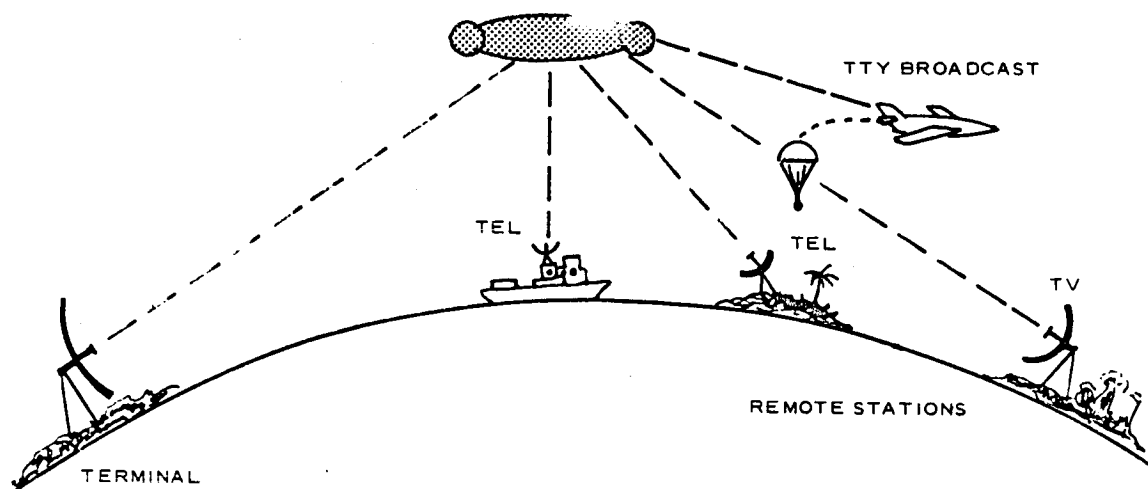
The flexibility of a passive lenticular communications satellite system is shown by transferring ground terminal capability into a master terminal, and simultaneous communications is possible with a variety of remote stations of lesser capability. The remote power required to communicate back is reduced by the ratio of the receiver capabilities, a feature not realized with active communication satellite systems.

Equivalent reflected power is plotted versus slant range in Figure 10 for sample values of lenticular curvature and transmitter power. It can be seen that sizable numbers of watts of equivalent reflected power as defined by the equation can be achieved with the lenticular satellite. P_T , G_T , G_S and α are the radiated power, transmitter antenna gain, satellite gain, and path loss with reference to an isotrope, respectively.

An example calculation for a low-orbit lenticular communication link is shown in Figure 11. A bandwidth of 7 mc is shown for typical ground terminals and a relatively long link. Trade examples illustrate the larger bandwidth available with a shorter link distance or reduced lenticular curvature and smaller bandwidth for a smaller receiving dish.

The equation shown for system bandwidth (B) illustrates one of the most important aspects for realizing the economic design of a passive communication satellite system. That is, the appropriate trades available for realizing the link parameters of transmitter power (P_T), antenna gains (G_T and G_R), satellite gain (G_S), receiver noise temperature (T_R), and link frequency (f). As shown by the bandwidth equation, P_T , G_T , G_R , and G_S are linearly related and may be directly traded. The receiver noise temperature (T_R) trades inversely, and the frequency (f) trades on a second power basis for bandwidth.

One of the most common ways of making a passive comsat system appear



- SERVICE
 - TELETYPE - CW
 - TELEPHONE
 - TELEVISION
 - BROADCAST
- SIMULTANEOUS OPERATIONS

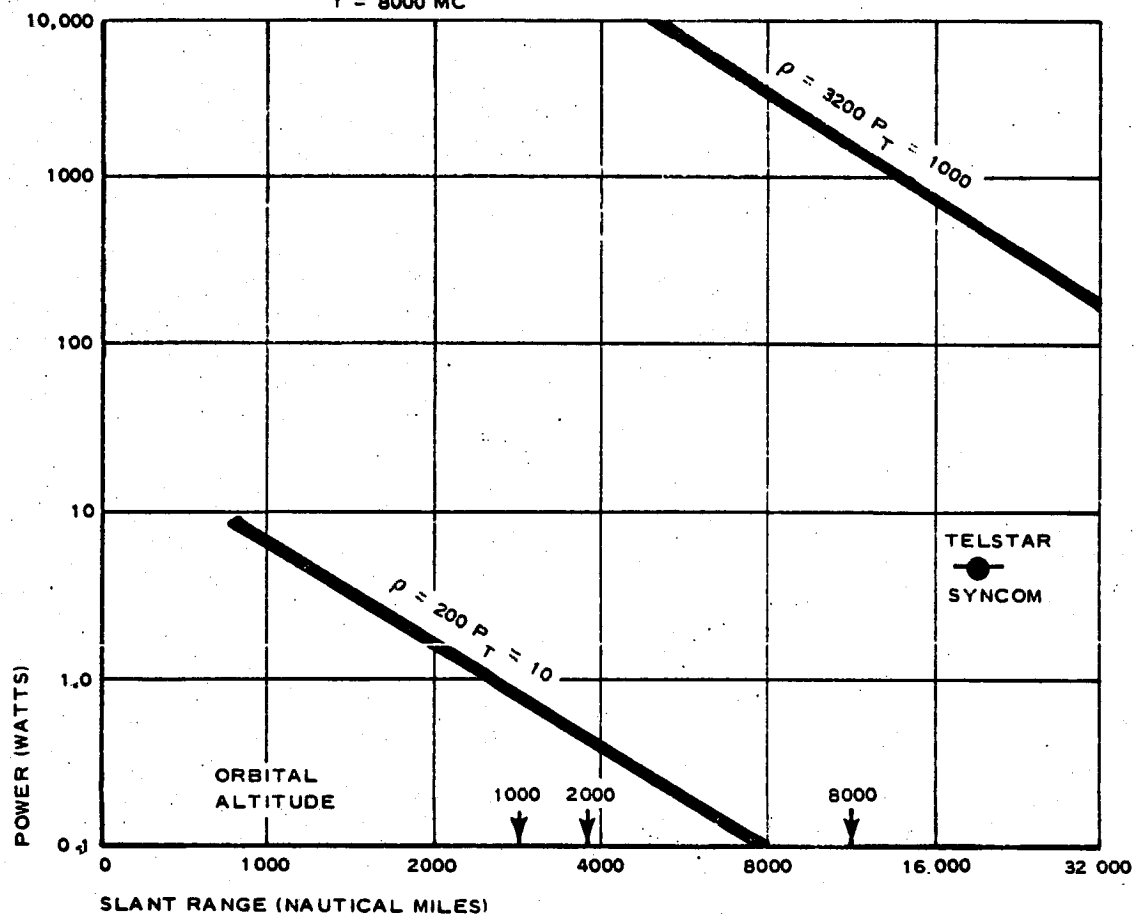
Figure 9 - Lenticular System Flexibility

$$G_S = \frac{\pi (3200)^2}{4 \times 11}$$

$$\text{REFLECTED POWER} = P_T + G_T + G_S - \alpha$$

$$G_T = 64.6 \text{ DB} \quad D_T = 85 \text{ FT}$$

$$f = 8000 \text{ MC}$$



$$38 + 20 \log 8000 + 20 \log 16,000.$$

$$38 + 20(3.903) + 20(4.204)$$

$$38 + 78 + 84 = 200$$

Figure 10 - Lenticular Equivalent Reflected Power

$$\frac{\pi \rho^2}{4\pi} = 9$$

$f = 8000 \text{ MC}$

$C/N = 16 \text{ DB}$

$P_T = 10 \text{ KW} = 40 \text{ DB}$

$G_T = 64.6 \text{ DB}$

$D_T = 85 \text{ FT}$

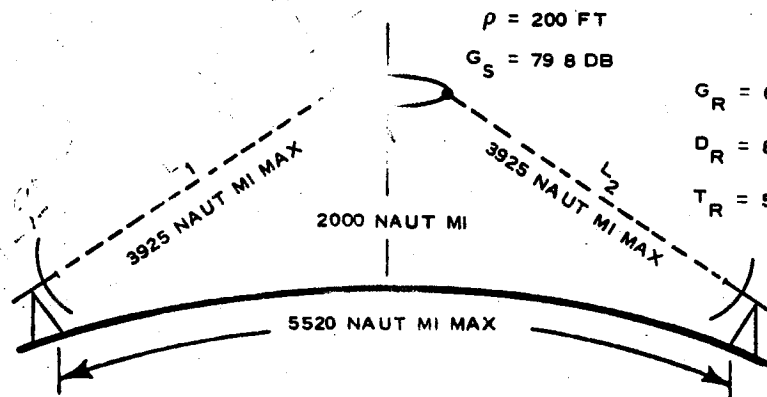
$\rho = 200 \text{ FT}$

$G_S = 79.8 \text{ DB}$

$G_R = 64.6 \text{ DB}$

$D_R = 85 \text{ FT}$

$T_R = 58 \text{ DEG K}$



$$\begin{aligned} B &= -16 + P_T + G_T + G_S - \alpha_1 - \alpha_2 + G_R + K T_R \\ &= -16 + 40 + 64.6 + 79.8 - 187.8 - 187.8 + 64.6 + 211 \\ &= 68.4 \text{ DBC} \\ &= 7 \text{ MC} \end{aligned}$$

TRADE EXAMPLES

MAKE $L_1 = L_2 = 2000 \text{ NAUT MI}$ THEN $B = 100 \text{ MC}$

OR

MAKE $D_R = 10 \text{ FT}$ THEN $B = 95 \text{ KC}$

OR

MAKE $\rho = 648 \text{ FT}$ THEN $B = 70 \text{ MC}$

$\alpha_1 =$

$F \cdot T \cdot H \cdot (MC)$

$\alpha_1 = \frac{36}{36} + 20 \log f + 20 \log D_1$

$8000 \cdot (202.1)$

$n. mi$

Figure 11 - Lenticular Typical System

impracticable is to attempt to provide too large a portion of the link capability with the G_S parameter rather than by choosing an economic balance among all available parameters.

The bandwidth achievable in the previous example is presented in Figure 12 as a function of vehicle antenna diameter for typical parametric conditions of lenticular cross-section, main terminal transmitting power and receiver noise temperature. Satellite altitude is 2000 naut mi. The chart is equally applicable to communication back from the vehicle to the main terminal if the values of transmitting power shown are reduced by the ratio of receiver noise temperatures.

This chart shows how trades can be made between the two terminal environments and how for given terminal environments bandwidth is proportional to the lenticular cross-section. Limited bandwidth communication can be accomplished with a very small vehicle antenna.

Figures 13 and 14 tabulate example values for the various classes of communication service, terminal to remote and remote back to main terminal.

In Figure 15 satellite weight scaled from the current lenticular design (no solar sail) is shown versus slant range and orbital altitude for a bandwidth of 8 mc achieved from three different ground environments.

The table below gives the salient characteristics of candidate passive satellite systems.

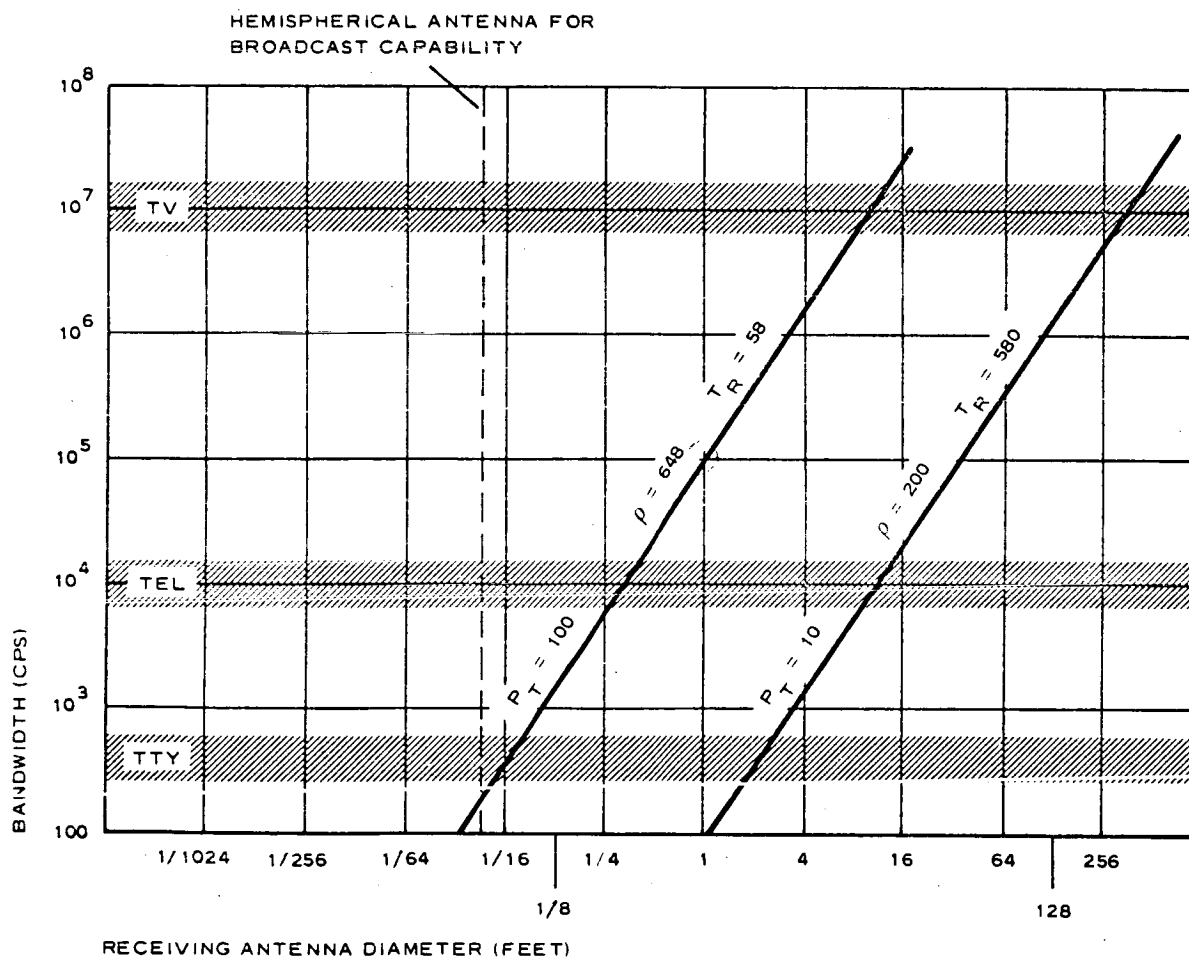
TABLE I - EXAMPLE SYSTEMS - 2000 NAUT MI ORBIT

Characteristics	Atlas Agena-D	Titan	Saturn C-5
Number of satellites	24	120	80
Launch vehicles (min)	3	3	2
Satellites per vehicle	8	40	40
Orbital planes	3 at 120 deg apart	3	2
Radius of curvature (ft)	200	200	648
Lenticular angle (deg)	40	40	40
Satellite weight (lb)	325	325	3000
Station keeping	Some	Consider	Consider
Payload (lb)	2600	12, 000	120, 000

$f = 8000 \text{ MC}$
 $C/N = 16 \text{ DB}$

$G_T = 64.6 \text{ DB}$
 $D_T = 85 \text{ FT}$

2000 NAUT MI ORBIT
 $L_1 = L_2 = 3925 \text{ NAUT MI}$



$$G_R = \frac{4\pi^2 C^2}{4.0000} \cdot (9.869)(10)(1)$$

$$= 3.10 \cdot 5.045$$

$$= 38.36$$

Figure 12 - Lenticular Low-Altitude System - Bandwidth versus Receiving Antenna Diameter

TERMINAL P_T (KW)	ρ (FT)	REMOTE D_R (FT)	REMOTE T_R (DEG K)	B (KC)	SERVICE
10	200	4	580	1.5	TTY
		10		10	TEL
		85	58	7000	TV
100		27		7000	TV
	648	0.07		0.4	TTY BROADCAST

$f = 8000 \text{ MC}$ $G_T = 64.6 \text{ DB}$ 2000 NAUT MI ORBIT
 $C/N = 16 \text{ DB}$ $D_T = 85 \text{ FT}$ $L_1 = L_2 = 3925 \text{ NAUT MI}$

Figure 13 - Typical System - Terminal to Remote Communication

REMOTE P_T	ρ	REMOTE D_T	TERMINAL T_R	B	SERVICE
(KW)	(FT)	(FT)	(DEG K)	(KC)	
1	200	4	58	1.5	TTY
		10		10	TEL
10		85		7000	TV

FOR EQUIVALENT BANDWIDTH:

$$\text{REMOTE } P_T = \frac{\text{TERMINAL } T_R}{\text{REMOTE } T_R} \text{ TERMINAL } P_T$$

Figure 14 - Typical System - Remote to Terminal Communication

$f = 8000 \text{ MC}$
 $C/N = 16 \text{ DB}$

$D_T = D_R = 85 \text{ FT}$
 $G_T = G_R = 64.6 \text{ DB}$

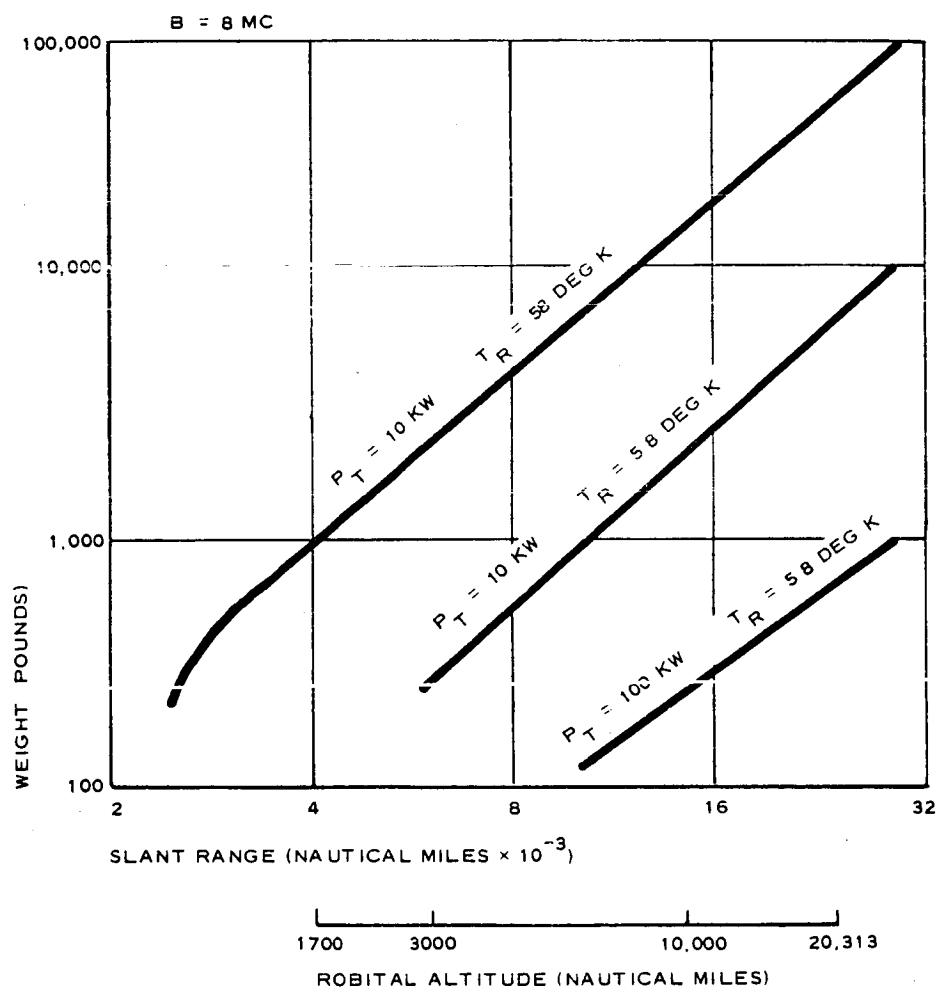


Figure 15 - Lenticular Weight versus Slant Range

Figure 16 shows that equivalent reflected power is essentially constant for a fixed weight lenticular satellite (without sail) provided that the lenticular angle is scaled as indicated in Figure 1.

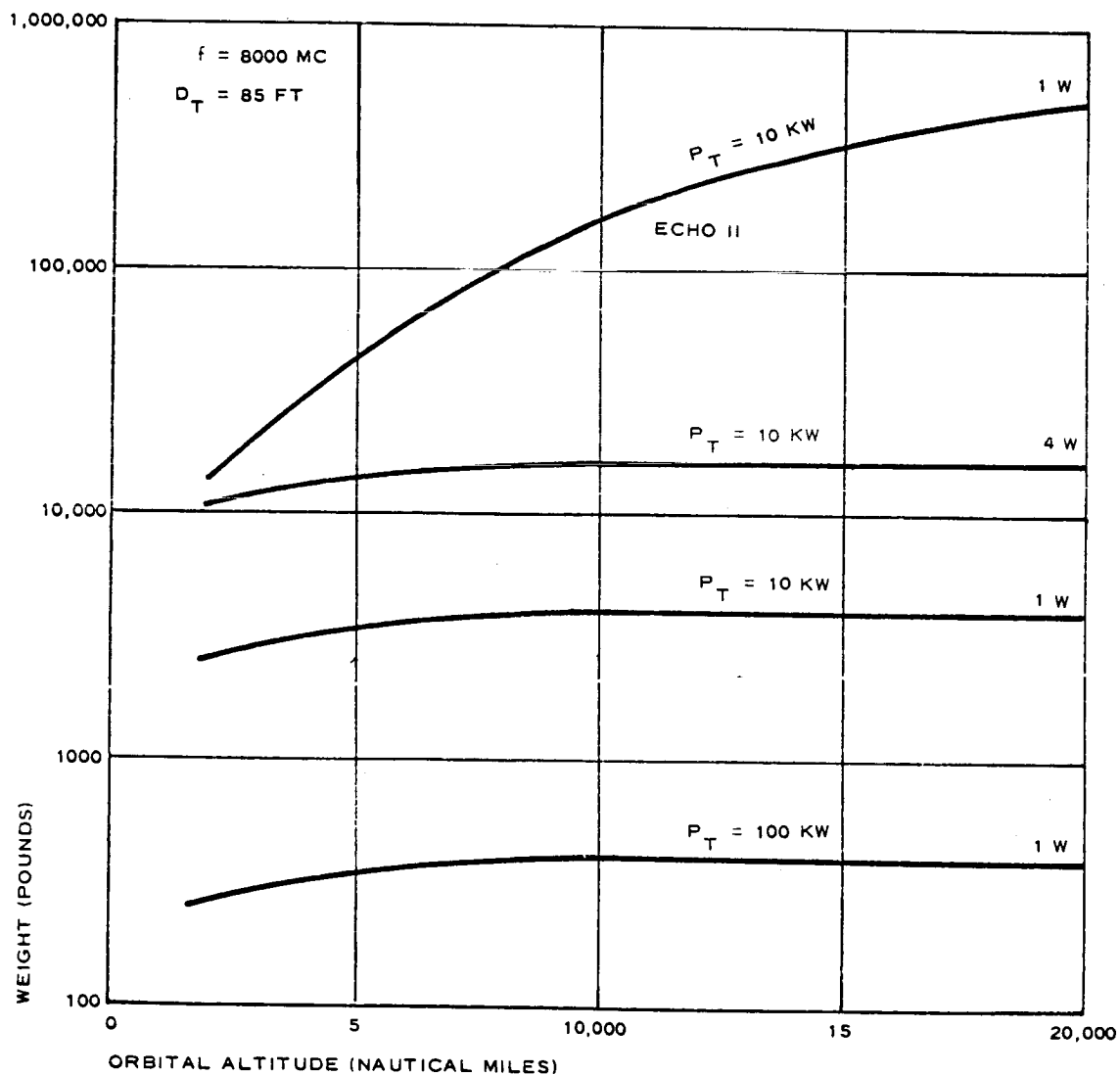


Figure 16 - Lenticular Satellite Weight versus Orbital Altitude for Constant Equivalent Reflected Power

SECTION IV - ADVANCED SYSTEMS CONCEPT FOR SYNCHRONOUS ORBIT

1. GENERAL

Isotropically reflecting passive communication satellites, such as Echo I and Echo II, have not been considered seriously for synchronous orbit altitudes because the associated communication system suffers a fourth power transmission loss with respect to path distance to the satellite.

However, for a fixed-weight lenticular satellite the effective over-all system path loss reduces in effect to that of approximately the square of the distance to the satellite. This is because the satellite's lenticular angle is selected to illuminate only the region near the earth rather than reflecting isotropically like a complete sphere. This fact can also be deduced from Figure 16 by noting that the equivalent reflected power is essentially independent of orbital altitude for higher-altitude orbits.

Synchronous orbit passive communication satellite systems capable of providing point-to-point facilities, as well as voice and television broadcast capabilities, are discussed in the following paragraphs to show the great potential of future lenticular passive satellite communication systems.

2. POINT-TO-POINT COMMUNICATIONS

Figure 17 shows the point-to-point communication capabilities expected from solar sail-equipped synchronous-orbit lenticular gravity-gradient stabilized satellites. Table II gives satellite characteristics for a few typical launch vehicle systems.

From Figure 17 and Table II it can be deduced that such capabilities as point-to-point television circuits or hundreds of voice channels can be established with (1) a 70-ft lenticular satellite launched by a Thor-Delta,

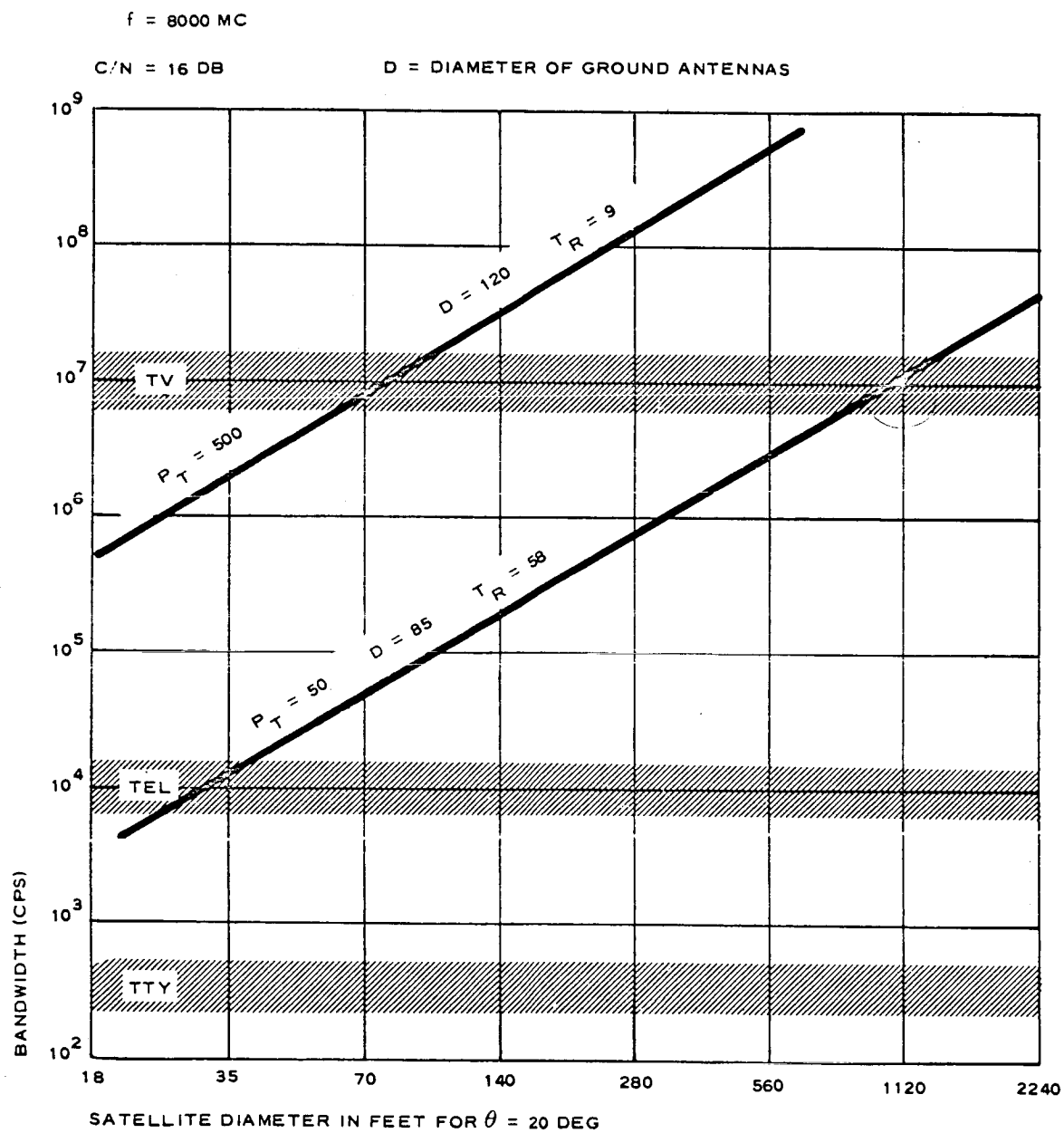


Figure 17 - Lenticular Synchronous Orbit System - Bandwidth versus Satellite Diameter

TABLE II - SATELLITE CHARACTERISTICS

Launch vehicle	Satellite diameter (ft)	Satellite weight (lb)	Satellite radius of curvature (ft)	Gain over 70 ft diameter (db)	Reflection cross section*
Thor-Delta	70	100	200	0	16
Atlas-Agena B	140	390	400	6	61
Titan III	400	3,200	1150	15	1024
Saturn C-5	1120	25,000	3200	24	4096

* With reference to Echo I.

(2) two 120-ft antennas similar to the Haystack antenna⁴ and a 500-kw transmitter.

If a Saturn C-5-launched 1120-ft lenticular satellite is used, a television circuit could be established via the 85-ft Syncom II antennas and receivers with a 50-kw transmitter.⁵ Moreover, since the lenticular satellite has a frequency reflection characteristic that is thousands of megacycles wide, many other ground links could use the satellite simultaneously.

3. VOICE AND TELEVISION BROADCAST

Figures 18 and 19 show the audio and television broadcast capability afforded by the parameters indicated on the figures.

The 1000-ft antenna and the 150-kw, 400-mc transmitter installation at ARECIBO, Puerto Rico,⁶ together with a 1120-ft lenticular satellite described below could provide the broadcast facility for audio programs.

Broadcast reception could be achieved via an oriented antenna with a 15-db gain and audio receiver equipped with the appropriate frequency converter.

Since the bandwidth capabilities of a passive communication satellite increase as the square of the link frequency, when both antenna apertures areas and other link parameters are held constant, a TV broadcast capability could be achieved with the above 1000-ft antenna and a 4-db increase in transmitter power if the transmitter frequency raised to 8000 mc. However, since 1000-ft antennas capable of operating at 8000 mc

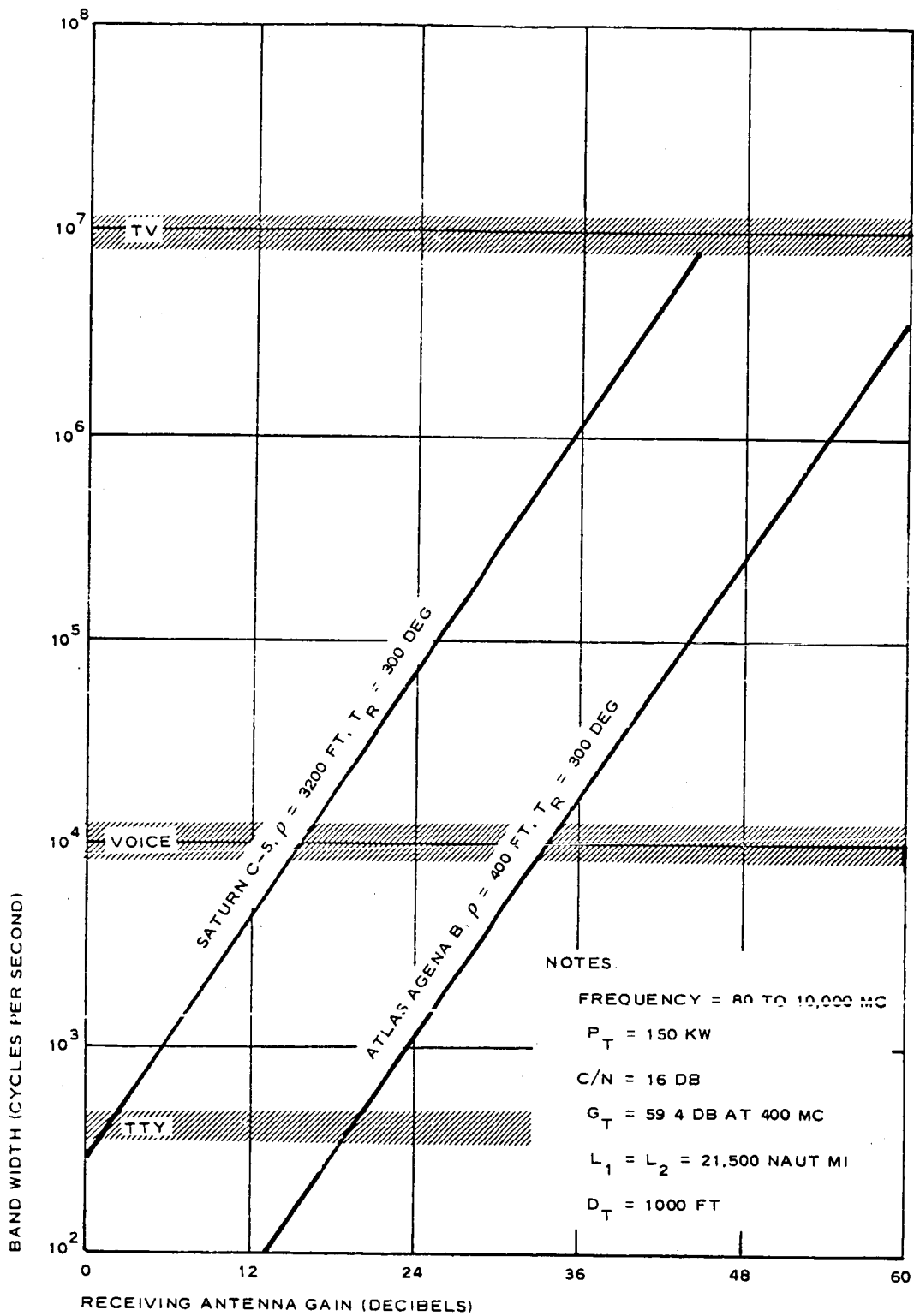


Figure 18 - Voice Broadcast Synchronous Orbit - System Bandwidth versus Receiving Antenna Gain

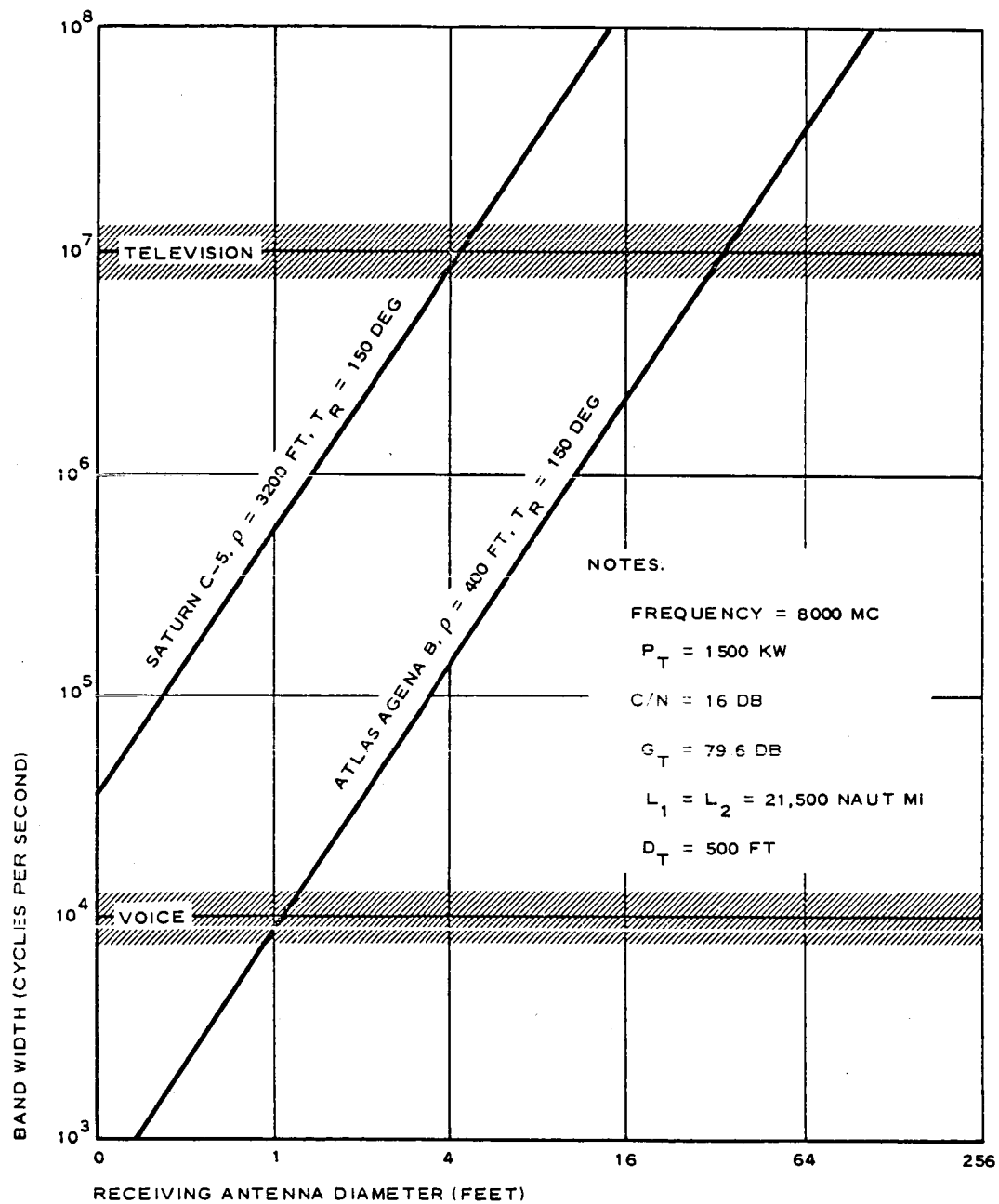


Figure 19 - Television Broadcast Synchronous Orbit System

are almost impracticable because of structural tolerances, the television broadcast transmitting terminal could be more appropriately implemented with 1500-kw transmitter and a 500-ft antenna (twice the diameter of the Jordell Bank antenna).

Broadcast television reception could be accomplished via a 4-ft oriented parabolic antenna, a low-noise 8000 mc to uhf converter, and a conventional television receiver.

Audio signals could be transmitted from the broadcast receiver locations back to the large antenna terminal by a transmitter in the tens of watts range at 8000 mc and in the tens of kilowatts range at 400 mc.

4. SATELLITES

The lenticular satellite configuration and construction details discussed in Section II for lower-orbit satellites generally apply for synchronous orbit, except for the change in lenticular angle and modifications to the gravity-gradient stabilization and solar-sailing subsystems (Figure 20). These changes are discussed in the following paragraphs.

5. LENTICULAR ANGLE

A lenticular angle of 20 deg was selected for synchronous orbit applications rather than 17 deg to allow for possible perturbations in the gravity-gradient stabilization system. If the satellite were perfectly stabilized and relaying of the signal through a ground terminal were permitted, line of sight coverage could be provided with a lenticular angle of less than 10 deg and a satellite weight reduction of about 4 to 1.⁷

With materials and structural improvements, it is possible that the satellite weights listed in Table II could be reduced many times, thereby permitting several satellites to be orbited with the respective spacecraft.

6. SYNCHRONOUS ORBIT STABILIZATION

Recent analyses indicate that gravity-gradient stabilization at synchronous orbit altitudes appears feasible. Moreover, studies by the Applied Physics Laboratory of The John Hopkins University in connection with the Transit satellite also indicate the promise of gravity-gradient stabilization at synchronous orbit.⁸

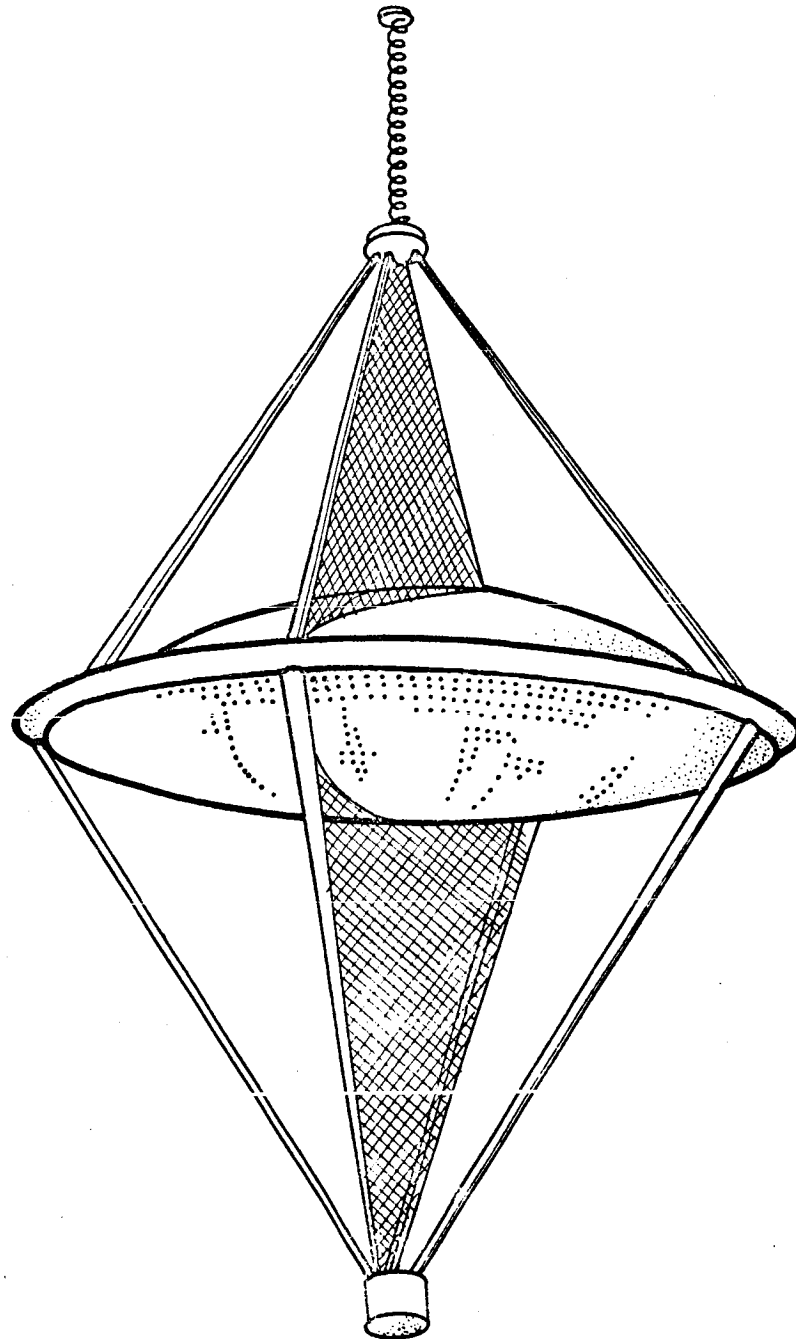


Figure 20 - Early Concept of Lenticular Gravity-Gradient Satellite with Solar Sail and Damper

Gravity orientation torques need only be large enough to overcome disturbing forces in a reasonable time. The primary cause of satellite perturbing forces are nonsymmetrical solar radiation pressure forces on the satellite structure and the reaction forces resulting from the solar sail subsystems. As shown in References 3 and 8, the gravity-gradient restoration torque is $T \cong 3/2\omega_o^2 (I_x - I_z) \sin 2\theta$, where ω_o is the orbital frequency, I_z and I_x are the moments of inertia of the boom and transverse axis, and θ is the angle of the boom axis with respect to the local vertical. Because restoration torque varies as the cube of the ratio of orbit radius, the restoration torque at synchronous orbit for a given satellite is

$$\left(\frac{5440}{22700}\right)^3$$

or 1.36 percent of that for a 2000-naut-mi orbit. This loss in torque can be compensated for by the following techniques.

1. Selecting satellite surface material to minimize solar pressure perturbation torques, such as the highly solar radiation transparent wire grid material of the subject lenticular satellites.
2. Increasing the length of the lightweight booms.
3. Increasing the mass at the end of the booms or minimizing the weight of the wire grid reflection lens.

7. SOLAR SAILING FUNDAMENTALS

The following discussion is presented to promulgate the solar sailing concept and to show the general boundary constraints associated with solar sailing.

A lenticular gravity-gradient satellite with a solar sail and gravity-gradient stabilization system is shown orbiting the earth in Figure 21. For circular orbits the period and angular velocity (ω) are related to the specific energy (E)* of the orbit in accordance with equations (1) and (1A). The satellite's position and period can be changed by adding or subtracting energy.

*Specific energy = satellite's energy divided by weight.

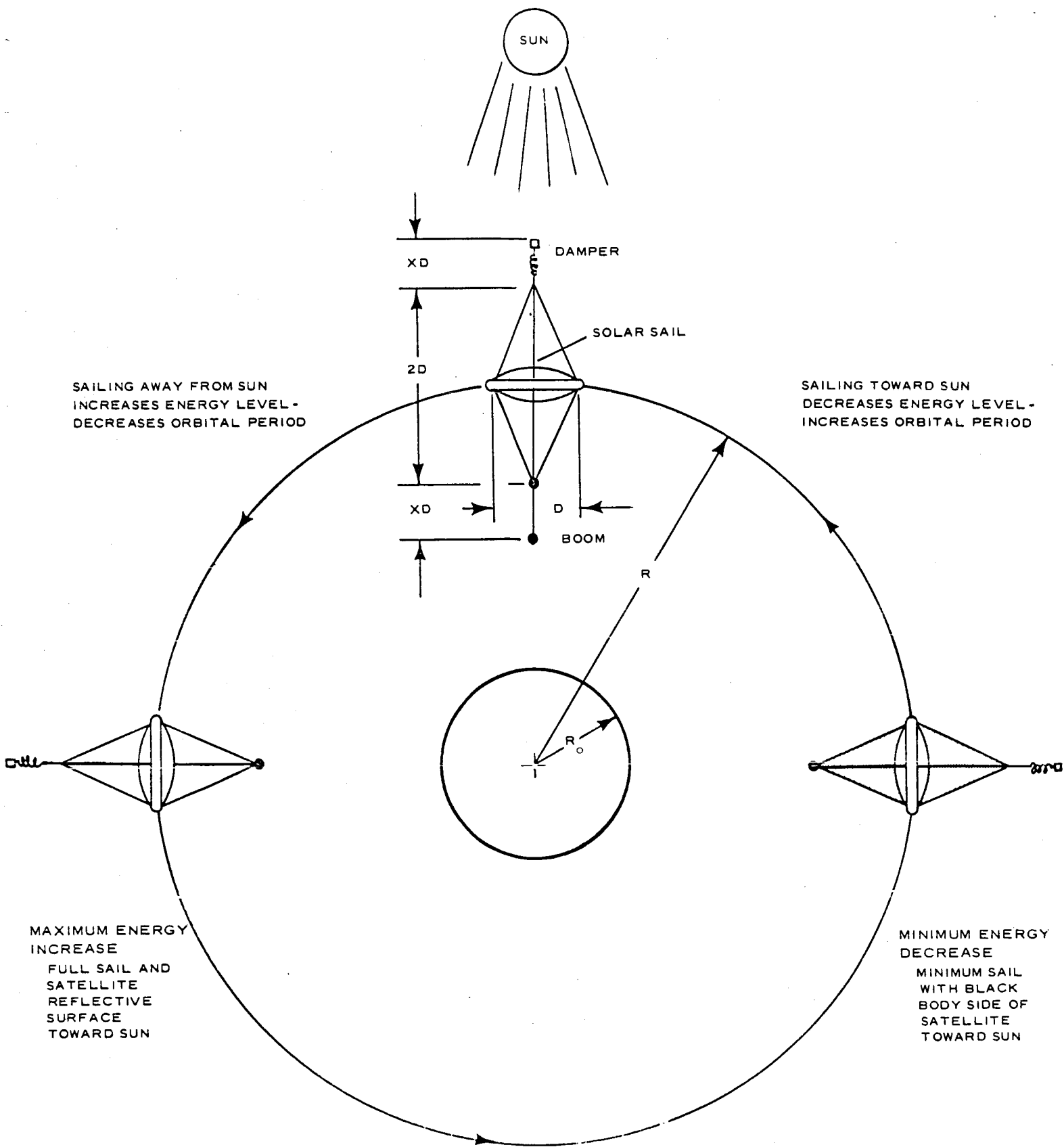


Figure 21 - Solar Sailing Fundamentals

$$\begin{aligned}\omega &= 107 \left[2 \left(1 - \frac{E}{R_o} \right) \right]^{3/2} \\ &= \frac{107}{\left(\frac{R}{R_o} \right)^{3/2}} \text{ radians/day}\end{aligned}\quad (1)$$

$$\frac{E}{R_o} = \frac{\frac{R}{R_o} - \frac{1}{2}}{\frac{R}{R_o}} \frac{\text{ft}\cdot\text{lb}}{\text{ft}\cdot\text{lb}} \quad (1A)$$

As discussed in Reference 2, the solar radiation pressure acting on the satellite structure can add or subtract energy from the satellite. The pressure exerted on a structure is proportional on the electromagnetic energy density in the region of the satellite and is equal to 1.94×10^{-7} lb/ft² and 1/2 of 1.94×10^{-7} lb/ft² for a fully reflecting and absorbing satellite surface respectively. Using the above values, the force on an ideal perfectly reflecting 10^5 sq-ft sail would be 2×10^{-2} lb.

The orbital energy level of a solar sailing satellite can be controlled by changing the sail area or the satellite surface electromagnetic energy reflectivity and absorbtivity characteristics while it is traveling toward and away from the sun.

Equations (2) and (3) indicate the distance traveled by the satellite and the maximum change of specific energy rate (E) available when the sun is pushing in the direction of satellite velocity 100 percent of the time.

$$d = \frac{2.24 \times 10^9}{\sqrt{\frac{R}{R_o}}} \text{ ft/day} \quad (2)$$

$$\begin{aligned}E &= d \times 1.94 \times 10^{-7} \\ &= \frac{435 \text{ ft}\cdot\text{lb}}{\sqrt{\frac{R}{R_o}} \text{ ft}^2 \text{ day}}\end{aligned}\quad (3)$$

A satellite with a sail area of S sq ft and a weight of W lb could have the specific energy increase indicated by equation (4):

$$\dot{E} = \frac{435}{\sqrt{\frac{R}{R_o}}} \times \frac{S}{W} \times B \text{ ft/day} \quad (4)$$

B is a general efficiency factor less than unity that depends on such things as satellite surface material, sail angle with respect to the sun, and ratio of time sailing toward and away from the sun.

The total energy of the orbiting satellite (E) is equal to the initial energy (E_o) - the energy disregarding solar pressure effects - plus the change of energy ($\dot{E}t$) due to solar pressure effects. This relationship is expressed in equation (5) where t indicates time:

$$E = E_o + \dot{E} t \quad (5)$$

From equations (5) and (1) the angular velocity achieved in solar radiation pressure environment can be obtained.

$$\begin{aligned} \omega &= 107 \left[2 \left(1 - \frac{E_o + \dot{E}t}{R_o} \right) \right]^{3/2} \\ &= 107 \left[2 \left(1 - \frac{E_o}{R_o} - \frac{\dot{E}t}{R_o} \right) \right]^{3/2} \\ &= \omega_o \left[1 - \frac{\dot{E}t}{R_o \left(1 - \frac{E_o}{R_o} \right)} \right]^{3/2} \end{aligned} \quad (6)$$

Since

$$\dot{E}t \ll R_o \left(1 - \frac{E_o}{R_o} \right) \quad (7)$$

$$\omega \cong \omega_o \left[1 - \frac{3/2 \dot{E}t}{R_o \left(1 - \frac{E_o}{R_o} \right)} \right] \text{ radians/day} \quad (8)$$

Integrating (7) yields the total angular displacement capability θ .

$$\theta = \omega_o t - \frac{3/4 \dot{E} t^2}{R_o \left(1 - \frac{E_o}{R_o}\right)} \text{ radians} \quad (9)$$

and rearranging

$$\theta - \omega_o t = - \frac{3/4 \dot{E} t^2}{R_o \left(1 - \frac{E_o}{R_o}\right)} \text{ radians} \quad (10)$$

where $\theta - \omega_o t$ is the angular displacement capability caused by solar pressure forces acting on the sail under the above constraints.

Substituting the value of E from equation (4) into equation (10) yields equation (11):

$$\begin{aligned} \theta - \omega_o t &= \frac{-(3/4)(435)(S/W) B t^2}{R_o \left(1 - \frac{E_o}{R_o}\right)^{1/2}} \\ &= \frac{2.2 \times 10^{-5} B (S/W) t^2}{\left(1 - \frac{E_o}{R_o}\right)^{1/2}} \text{ radians} . \end{aligned} \quad (11)$$

To indicate how $\theta - \omega_o t$ varies with orbital altitude, equation (1A) is combined with equation (11) to give equation (12).

$$\theta - \omega_o t = 3.11 \times 10^{-5} B \frac{S}{W} \sqrt{\frac{R}{R_o}} t^2 \text{ radians} . \quad (12)$$

For synchronous orbit,

$$\frac{R}{R_o} = 6.61 ,$$

$$\frac{S}{W} = 50 ,$$

B is assumed to be 0.1 .

If $t = 30$ days, the angular displacement caused by solar radiation pressure $\theta - \omega_o t$ is = 0.358 radians or an average of about 0.68 deg per day. This example indicates a capability of sailing the satellite about 1000 miles a

month. If the S/W is increased by using a larger sail, more distance could easily be covered.

8. MAGNETIC TORQUING

Magnetic torquing appears to be a promising method for orienting the solar sail with respect to the sun because the earth's magnetic field vector is relatively constant with respect to the earth for equatorial orbits. Although sunstorms effect the earth's magnetic field, it appears that magnetic torquing of a synchronous orbit quasi-stationary satellite is much simpler than for other orbits.

The satellite can be torqued by using a current-carrying wire coil inside the hollow unfurlable sail support tubes. A flow of direct current through the coil will align the satellite, like a compass needle, with the earth's magnetic field. A reversal of the current will align the satellite in the opposite direction. A coil is also provided in the adjacent pair of booms to provide an alignment position of 90 deg from the above positions. Rotation or sail locking to the earth's magnetic field can be accomplished by the remote control of the coil currents via a command link from the ground. Power for the coils is supplied from a battery-solar cell supply located in the canister, which is normally secured to the ends of the boom quadropad. At the present time studies are being made to determine the extent of sail torquing required for a practicable orbital placement and station keeping system. Power requirements and coil weights appear quite modest, since a satisfactory torquing period is on the order of hours. In fact, one turn of 18-gage copper wire carrying a current of one amp will provide a torquing time constant of 24 hours for a 267-ft lenticular satellite. With this arrangement the power consumption during torquing will be less than 10 w.

9. BENEFITS OF SYNCHRONOUS ORBIT

Synchronous orbit satellite systems have the following advantages.

1. Only one ground antenna per terminal is required.
2. Antenna steering system is simpler and less expensive, particularly for very large antennas.
3. Lower receiver system noise temperatures can be

achieved at many stations since the antennas do not have to be operated at low angles above the horizon.

4. The satellite's radio reflection cross-section-to-mass ratio is improved about 100 to 1 over very low orbits.
5. Solar sail orbital placement and station keeping techniques are greatly simplified.
6. In the broadcast mode inexpensive high-gain receiving antennas can be used.
7. Multiple access bookkeeping and common satellite availability problems are solved automatically by the system geometry and wide inherent bandwidth capability of passive satellites.
8. Less interference to other services is expected because of the essentially fixed position in space of the satellite.
9. Doppler frequency shift would be minor, thus permitting simpler receivers and more efficient use of the frequency spectrum.
10. Because of ease of acquisition and bandwidth availability, the satellite could be used for the transmission of time signals, navigation, etc.

SECTION V - CONCLUSIONS

Passive communications satellites show great promise, but more research is recommended to enhance the technology in the areas of proving and implementing satellite system capabilities. Further work is recommended in the following areas.

Stabilization	Models
Materials	Solar sailing
Reliability	Systems
Microwave	

With additional research and development, passive communication satellites show promise of being more economical than active satellites for many applications.

Lenticular gravity-gradient satellites, because of their inherent long life, capability to provide broad communication bandwidths and ability to operate with thousands of inexpensive terminals, truly have the promise of providing a passive satellite communications system for all nations.

In closing, it appears appropriate to point out that the technology and philosophy derived from airship implementation experience has been of great assistance in realizing practical satellite designs.

The philosophy of Count von Zeppelin is as appropriate for gravity-gradient stabilized, solar sailing passive communication satellites as it is for airships.

"The forces of nature cannot be eliminated but they may be balanced one against the other."

Count von Zeppelin
Friedrichshofen, May 1914

LIST OF REFERENCES

1. Joseph R. Burke, NASA-Headquarters, Washington, D.C., Passive Satellite Development and Technology. Pgs 72-75 Aeronautics and Astronautics, September 1963. Published by the American Institute of Aeronautics and Astronautics.
2. W. J. O'Sullivan, Jr., NASA-Langley Research Center Passive Communications Satellites - Paper presented at Conference on Artificial Satellites August 12-16, 1963 at Virginia Polytechnic Institute, Blacksburg, Virginia.
3. C. M. Kelly - Gravity Oriented Passive Communications Satellites, paper presented at the Internal Symposium of the IEEE Professional Group on Antennas and Propagation. 9 July 1963 at the National Bureau of Standards, Boulder, Colorado.
4. Sidney Metzger, Communications Satellite Corporation, "Communications", Pgs 110-113, Astronautics and Aeronautics, November 1963. Published by the American Institute of Aeronautics and Astronautics.
5. F. P. Alder, Space Systems Division, Hughes Aircraft Company, "Syncom" paper n^o 82, presented at the XIV International Astronautics Congress, September 1963, Paris, France.
6. Thomas Maguire, "Arecibo New Era in Radio Astronomy" Electronics Pgs 29-31, McGraw-Hill Publishing Co., New York.
7. Pierce, J. R., and Cutter, C. C., "Interplanetary Communications", Advances in Space Science, Academic Press, New York, N. Y., Vol. 1, Pg 96, 1959.
8. Fischell, R. E., The TRAAC Satellite - Applied Physics Laboratory, Technical Digest 1, 2-9 March 1962.

GOODYEAR AEROSPACE

